Cumhuriyet Science Journal
Faculty of Science, Cumhuriyet University
58140 - Sivas - Türkiye
Phone: +90(346) 487 13 72
Fax: +90(346) 219 11 86
e-mail: csj@cumhuriyet.edu.tr
http://csj.cumhuriyet.edu.tr/en
http://dergipark.org.tr/en/pub/csj

Cumhuriyet Science Journal Vol: 44 No: 1 Year 2023

Sivas Cumhuriyet University

ISSN : 2680-2587
e-ISSN : 246-2587X
dergipark.org.tr/tr/pub/csj
e-mail: csj@cumhuriyet.edu.tr

Cumhuriyet Science Journal

Cumhuriyet Science Journal (CSJ) is an official publication of Sivas Cumhuriyet University, Science Faculty. The high quality research papers related to the natural sciences are published as online four times a year. CSJ is an open access, free of charge journal and all articles in CSJ have undergone peer review and upon acceptance are immediately and permanently free for everyone to read and download.

Volume: 44 Number: 1 Year: 2023

ISSN: 2587-2680
e-ISSN: 2587-246X
Period: Quarterly
Founded: 2002
Publisher: Sivas Cumhuriyet University

Cumhuriyet Science Journal (CSJ)

Journal Previous Name: Cumhuriyet Üniversitesi Fen-Edebiyat Fakültesi Fen Bilimleri Dergisi

Old ISSN: 1300-1949

Abstracted&Indexeding

ULAKBİM TR-Dizin

Index Copernicus (ICI Journals Master List)

Clarivate Analytics Zoological Record

Crossref

WorldCat

Akademik Dizin

Arastirmax Bilimsel Yayın İndeksi

Bielefeld Academic Search Engine (BASE)

Directory of Research Journal Indexing (DRJI)

Google Scholar

Research Gate

Idealonline

Publication Type: Peer Reviewed Journal

Cite Type: Cumhuriyet Sci. J.

Contact Information

Faculty of Science Cumhuriyet University
58140 Sivas- TURKEY
Phone: +90 (346) 487 13 72
Fax: +90 (346) 219 11 86
e-mail: csj@cumhuriyet.edu.tr
http://dergipark.gov.tr/csj

	CONTENTS		PAGES

Cumhuriyet Sci. J., 44(1) (2023) 1-6
DOI: https://doi.org/10.17776/csj.1128138

Cumhuriyet Science Journal

| csj.cumhuriyet.edu.tr | Founded: 2002 ISSN: 2587-2680 e-ISSN: 2587-246X Publisher: Sivas Cumhuriyet University

Screening of Probiotic Properties of *Bacillus Licheniformis* Isolated from Yoghurt

Samet Kocabay [1,a,*]

[1]*Department of Molecular Biology and Genetics, Faculty of Science and Art, Inonu University, Malatya, Türkiye.*
**Corresponding author*

Research Article

History
Received: 09/06/2022
Accepted: 27/12/2022

ABSTRACT

Probiotic microorganisms are an indispensable part of a healthy life. The usage areas of the probiotic *Bacillus licheniformis* bacteria are quite wide, from contributing to the development of the immune system to reducing cholesterol, which is an important cause of cardiovascular diseases. In this study, *Bacillus licheniformis* (*isolate 29)* was isolated from traditional yoghurt sample obtained from town of Hatipli/ Tokat/ Türkiye. And it's genotypic and probiotic characterizations were performed. Our results showed that the isolated *Bacillus licheniformis* grew better at pH 5. The survival rate of the bacteria in artificial gastric and intestinal fluid was determined as 47.51% and 65.29%, respectively. The isolate degraded all tested sodium salts, including Sodium glycocholate hydrate, Sodium taurodeoxy Cholate, Sodium taurocholic acid, Sodium tauroglyco Cholate, Sodium thioglycolate. Its surface hydrophobicity was found to be moderately 30.31 ± 0.009% in *n*-Hexadecane. Although RA5 antibiotic had the largest zone diameter (10 mm), antibiotic susceptibility of *Bacillus licheniformis* was not among the antibiotic discs tested. These findings indicated that the isolate can be a good probiotics candidate to lower the cholesterol levels.

Keywords: Cholesterol, *Bacillus licheniformis*, Probiotic, Sodium salts, Yoghurt

[a] *samet.kocabay@inonu.edu.tr* *https://orcid.org/0000-0002-0120-2910*

Introduction

Probiotic organisms are defined by the World Health Organization/Food and Agriculture Organization of the United Nations as living organisms that, when consumed in sufficient quantities, make some adjustments in the large intestine of the consuming person and contribute positively to host health [1, 2]. Although there are many different classes of probiotic microorganisms, lactic acid bacteria (LAB) are one of the largest groups including *Lactobacillus*, *Lactococcus*, *Carnobacterium*, *Enterococcus*, *Streptococcus*, *Pediococcus*, *Propionibacterium*, and *Leuconostoc* [3, 4]. The use of LAB bacteria in the production of dairy products such as cheese and yogurt has a long history [5, 6].

Although the first study on *Bacillus licheniformis* was made in 1945, it has found the expected interest in the last 20 years. The number of studies over the last 20 years resembles a bacterial logarithmic growth curve [7]. *Bacillus* and its metabolites have been used in biotechnological applications such as enzymes, amino acids, antibiotic production, preparation of fermented foods, and insect control production for many years [7]. *Bacillus* species gram positive rod shape [8] may have advantages over different probiotic bacteria species due to their ability to form endospores. For example, in the preparation of high temperature fermented products, the survival potential of the bacteria is high. *B. subtilis, B. licheniformis, B. clausii, B. coagulans, B. cereus, B. pumilus*, and *B. laterosporus* are some species which used human consumption as probiotics [9, 10]. Biosporine® is a probiotic product consisting of a mixture of *Bacillus subtilis* and *Bacillus licheniformis*, commercially available in Russia and Ukraine today [8, 9, 11]. Primal Defense™ (USA), MegaSporeBiotic™ (USA), Prescript-Assist® SBO Probiotic (USA), Body biotics (UK), Zhengchangsheng®(Korea) are other commercial products including *Bacillus licheniformis* for human consumption [7].

Probiotic bacteria are important for human health because of killing pathological microorganisms, increase the immune system, and regulate the cholesterol level in the blood vessel. Cholesterol in the blood increases the risk of cardiovascular disease by causing vascular occlusion. This disease is known as hypercholesterolemia. It is estimated that a 1% decrease in serum cholesterol level will cause a 2% to 3% reduction in cardiovascular occlusion [12]. Cardiovascular disease is one of the leading health issues with high mortality rates. By 2030, the disease course is predicted to nearly triple [13]. Some probiotic bacteria could reduce cholesterol levels by digesting bile salts, which are the precursors of cholesterol. Mechanisms of cholesterol reduction by probiotic bacteria are hypothesized in the literature [14]. In the mouse experiment, it was observed that the body fat accumulation decreased and the lipid metabolism rate decreased in mice fed with yoghurt containing *Bacillus licheniformis.* These bacteria have bile salt hydrolysis enzyme activity [7, 15, 16]. Other potential way can be decreasing of the cholesterol solubility to prevent the uptake from gut [12]. In today's study on a mouse model, it is seen that *Bacillus licheniformis* bacteria inhibit obesity by regulating intestinal flora [17].

In this study, *Bacillus licheniformis* were purified as a new isolate from the yoghurt sample of the town of Hatipli/Türkiye and some probiotic properties such as pH stability, surface hydrophobicity, antibiotic sensitivity, and degradation of sodium salts were determined.

Material Methods

Bacillus licheniformis was isolated from single yoghurt sample from Hatipli/Tokat/Türkiye (40.547117, 37.228158). LB (Luria−Bertani) broth (CONDA), Agar Fluka (05039) (sigma). Pepsin (sigma), trypsin from beef pancreas (thermo), Sodium glycocholate hydrate, Sodium taurodeoxy Cholate, Sodium taurocholic acid, Sodium tauroglyco Cholate (*Chemcruz* D1317), Sodium thioglycolate (Sigma 101851207), antibiotic discs (Bioanalyse), n-Hexadecane (Merck 596470), Xylene (sigma16446), used in our experiments. The others used chemicals are analytical grade. The all experiments were made as triplicate.

Isolation and Identification of Bacillus Licheniformis

Bacillus licheniformis was isolated from traditional yoghurt sample and kept at +4 °C. An overnight cell culture was obtained by inoculation an aliquot of the sample into 10 ml LB broth (pH 7.2), and incubated at 37 °C. Single bacterial colonies were grown from the overnight culture by using the pour-plate method. Some of the colonies were then transferred onto LB-agar plates. The pure cultures were stored at −80 °C. For the molecular characterization, we bought service from BM Company at Ankara/Türkiye [18]. DNA was prepared and used for the amplification of 16S rRNA gene as general steps. The sequences obtained from an automatic DNA sequencer were subjected to BLAST analysis and similarities were determined using the National Center of Biotechnology Information databases (http://www.ncbi.nlm.nih.gov) [19]. An accession number for the sequence was also obtained (as ON496990).

Survivals of Bacterial Strain in Low pH

Bacillus licheniformis species were growth in 10 ml sterile LB broth pH 7.2 with shaking at 110 rpm at 37 °C during overnight [20]. Ten milliliters of the bacteria were centrifuged for 10 min at 4,000 rpm at +4°C. The pellet was suspended in fresh LB broth (pH 7.2, pH 5, pH 4, pH 3, and pH 2). Bacterial survival in pH 7.2, pH 5, pH 4, pH 3, and pH 2 was determined. Their growing absorbance values were recorded versus time. Cell growth rates were presented as growth curves with standard deviation. The experiment was made triplicate.

Survival in Simulated Gastric Juice

The survival rate of the bacteria in the simulated gastric juice was determined. For this, 10 ml sterile and fresh 1^x PBS pH 2 solution with 3 g/L concentration of pepsin was prepared [19]. The solution was passed through a 0.45 µm filter. Concentrated bacterial culture supernatant was poured out. 10 ml of prepared artificial gastric juice was added to it. Serial dilution was made in 4.5 ml sterile saline (0.85%) by taking 0.5 ml sample. 100 µl were cultivated from various dilute tubes. After spreading the sample on the LB agar plate by smear method, it was kept at 37 °C every other day. The exposed colonies were counted. After the bacteria were waited for 5 hours at 37 °C in the artificial stomach environment, the sample count was done again. The survival rate of the bacteria was calculated with the following formula [21].

$$\text{Survival rate \%} = (N1 / N0) \times 100 \quad (1)$$

Here (N0= Total bacterial number at first time in simulated gastric juice and N1 = Total bacterial number after 5 hours in simulated gastric juice).

Survival in Simulated Intestinal Juice

The survival rate of the bacteria was determined in the simulated intestinal juice. For this, 10 ml sterile and fresh 1^x PBS pH 8 solution with a concentration of 1 g/L of trypsin was prepared [19]. The solution was passed through a 0.45 µm filter. Concentrated bacterial culture supernatant was poured out. 10 ml of prepared artificial intestine juice was added to it. Serial dilution was made in 4.5 ml sterile saline (0.85%) by taking 0.5 ml sample. 100 µl were cultivated from various dilute tubes. After spreading the sample on the LB agar plate by smear method, it was kept at 37 °C every other day. The exposed colonies were counted. After the bacteria were waited at 37 °C for 24 hours in the artificial intestinal environment, the sample count was repeated. The survival rate of the bacteria was calculated with the formula above (simulated gastric juice).

Antibiotic Sensitivity

Disc diffusion method was used according to our previously published article [22]. Fresh LB agar (1.5%) medium was prepared and 100 µl bacterial cultures was spread on the agar plates. Antibiotic discs included kanamycin (K30), ampicillin (AM10), streptomycin (S10), tetracycline (TE30), gentamicin (CN30), chloramphenicol (C30), penicillin (P2 units), erythromycin (E15), rifampin (RA5), neomycin (N30), vancomycin (VA30), and empty disc (00). The antibiotic discs were placed on the agar surface. After overnight incubation under the optimum growth conditions, dimeters of inhibition zones were measured with a ruler and the measurements were recorded.

Surface Hydrophobicity

Surface hydrophobicity of bacteria was investigated using reference articles in the literature [23, 24]. The bacterial sample was freshly propagated and the culture aliquoted in 3 ml aliquots in sterile falcon tubes. Cells were centrifuged (10 minutes at 4000 rpm at +4°C). The supernatant was decanted and 10 ml of phosphate urea magnesium sulfate buffer (pH 6.5) was added. After the pellet was dissolved, centrifugation was performed under the same conditions. This process was repeated 3 times.

Initial cell densities were determined at 450 nm, and then 0.6 ml of n-Hexadecane, n-Hexane and xylene were slowly added to the cell suspensions (3 ml). The mixed solution was placed in a 37°C water bath and incubated for 15 minutes. The samples were then vortexed for 15 seconds at 2 minute intervals and left on the bench for 25 minutes. Absorbance values were recorded at 450 nm. The percent hydrophobicity was calculated using the following formula:

$$\text{Hydrophobicity}\,\% = ((OD_{450nm}\,N0 - OD_{450nm}\,N1)/OD_{450nm}\,N0) \times 100 \quad (1)$$

(OD_{450nm} N1: the absorbance value for final bacteria concentration, after the experiment, OD_{450nm} N0: the absorbance value for initial bacteria concentration before the experiment).

Degradation of Sodium Salts

The isolate was grown overnight on LB agar at 37 °C. Sodium salts, 0.005 g/ml, (Sodium glycocholate hydrate, Sodium taurodeoxy Cholate, Sodium taurocholic acid, Sodium tauroglyco Cholate, Sodium thioglycolate), MRS (MAN, ROGOSA and SHARPE) agar were prepared at pH 6.3. The colonies formed were immersed in sodium salt solid medium. Incubated under optimum conditions. The activity of the *Bacillus licheniformis* against sodium salts was checked. The white transparent structure formed around the colony was determined as positive [14, 22, 23].

Results

Genomic Characterization

Genotypic characterization studies of pure culture isolated from yoghurt culture were carried out. *Bacillus licheniformis* was determined as a result of NCBI BLAST analysis (Figure 1).

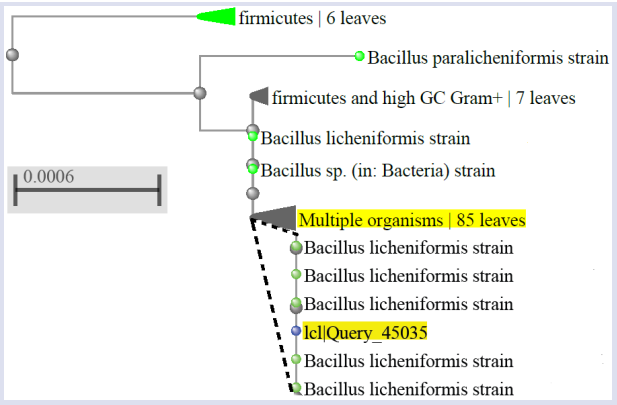

Figure 1. The dendrogram result of *Bacillus licheniformis*.

Tolerance to low pH

The growth graph of bacteria in low pH environments is indicated in figure 2. No growth OD increase was observed in the bacterial pH 2 medium. It is seen that bacterial growth is better in the pH 5, 4, 3 than pH 7.2 medium.

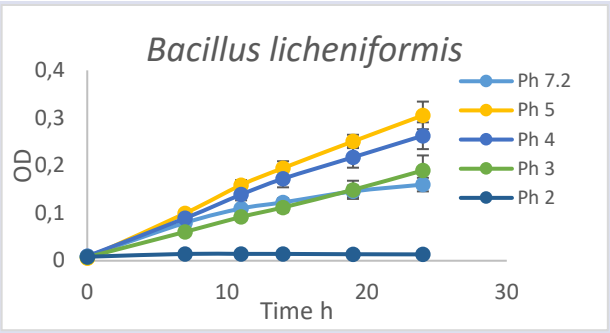

Figure 2. Bacterial growth in different pH including 7.2, 5, 4, 3, and 2. The absorbance values were recorded by the spectrophotometer at different intervals for 24 hours.

Survival Rate in Simulated Gastric and Intestinal Juice

The survival rate of bacteria in artificial gastric and intestinal fluid was determined as 47.51% and 65.29%, respectively (Table 1 and Figure 3).

Bacillus licheniformis	Initial bacterial number (log(CFU/ml))	Final bacterial number (log(CFU/ml))	Survival rate
Simulated gastric juice	21.91 ± 1.14	10.41 ± 0.31	47.51%
Simulated intestinal juice	14.55 ± 1.22	9.5 ± 0.78	65.29%

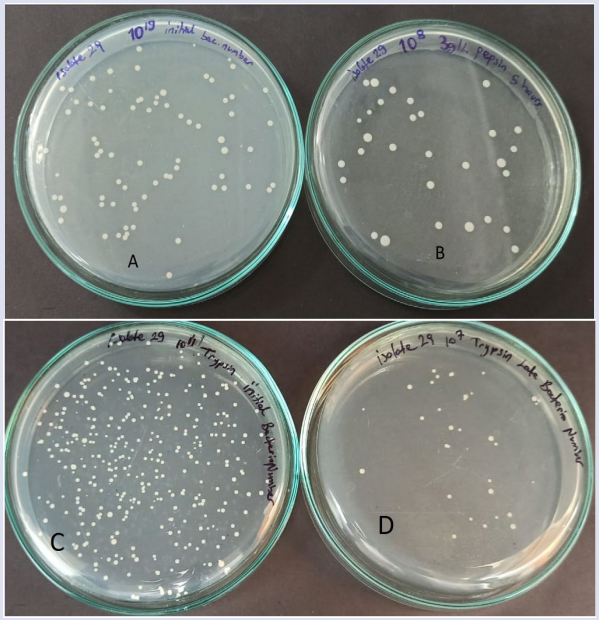

Figure 3. The test results of the survival of bacteria in the artificial stomach and intestinal environment. A) The number of initial colonies in the artificial stomach medium, B) The number of bacteria cultivated after 5 hours in the artificial stomach medium, C) The initial number of bacteria in the artificial intestinal medium, D) The number of bacteria cultivated after 24 hours in the artificial intestinal medium.

Antibiotic Sensitivity

The bacteria were found to be resistant to the tested antibiotics (figure 4). The best inhibition zone was seen with RA5 antibiotic (10 mm).

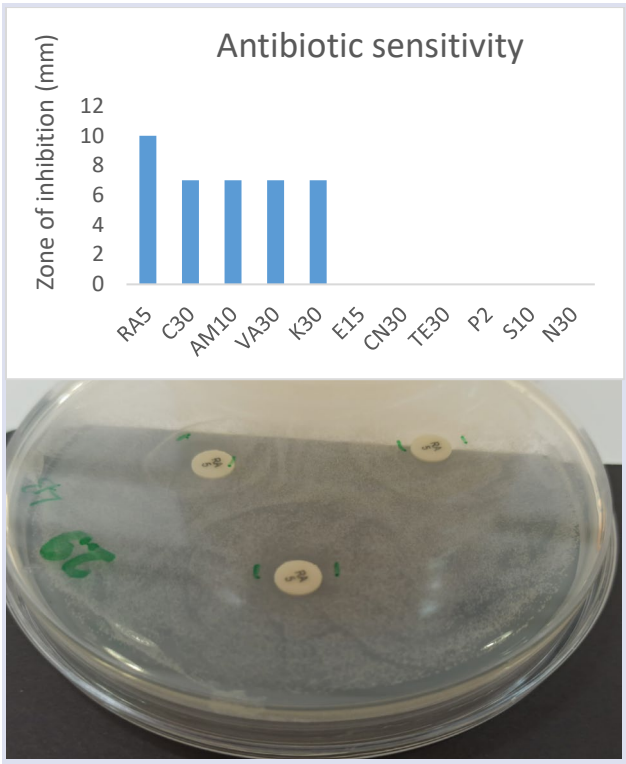

Figure 4. The antibiotic susceptibility test results of *Bacillus licheniformis* (above). Indicates the zone diameter measured on the LB agar plate (below).

3.4 Surface Hydrophobicity

Among the tested hydrophobic solvents, the surface hydrophobicity values of the bacteria were 31.75 ± 0.014%, 30.31 ± 0.009%, 34.87 ± 0.008% n-Hexane, n-Hexadecane, Xylene, respectively (Table 2).

Table 2: Bacterial surface hydrophobicity

Hydrophobic solvent	n-Hexane	n-Hexadecane	Xylene
Surface hydrophobicity %	31.75±0.014	30.31 ± 0.009	34.87±0.008

Degradation of Sodium Salts

Table 3: Degradation ability of sodium salts by *Bacillus licheniformis*

Sodium Salts	Sodium glycocholate hydrate	Sodium taurodeoxy Cholate	Sodium taurocholic acid	Sodium tauroglyco	Sodium thioglycolate
Bacillus licheniformis	+	+	+	+	+

Considering the result of the bacteria in terms of its ability to break down sodium salts (Table 3 and Figure 5), it was seen that it could destroy all the tested salts.

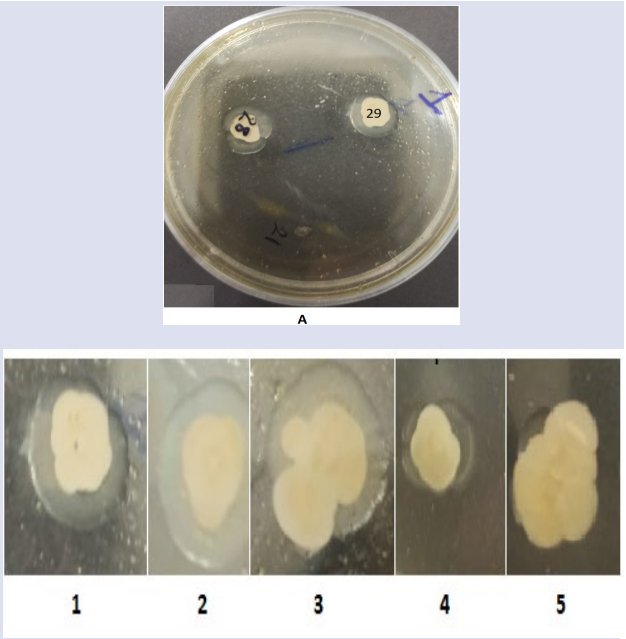

Figure 5. The degradation of sodium salts by the bacteria. A) Shows the colony structure and transparent zone formed by the bacteria grown on MRS agar with specific sodium glycocholate hydrate medium. 1) Sodium glycocholate hydrate, 2) Sodium taurodeoxy Cholate, 3) Sodium taurocholic acid, 4) Sodium tauroglyco Cholate, 5) Sodium thioglycolate.

Discussion

As a result of the genotypic characterization of the bacterial strain obtained from the yoghurt culture, it was determined that it belonged to the *Bacillus licheniformis* bacterium. The bacteria, which are probiotic strains, have been used in previous studies. In addition, there are *Bacillus licheniformis* probiotic bacteria obtained from different traditional foods [9, 25].

A good probiotic bacteria must be able to survive or tolerate acidic stress conditions and the presence of bile salts [26]. When the growth curve of the bacteria is examined in extreme environments, it is seen that it performs the best growth at pH 5 among the tests. In pH 4 and pH 3 environments, the growth curve of the bacteria is better than pH 7.2. These data show that the bacteria can multiply in an acidic environment. For the pH 2, there was no increase in bacterial absorbance during the tested time.

When the logarithmic survival results of the bacteria in the artificial stomach and intestinal environment were evaluated, it was observed that their survival rates were 47.51% and 65.29% respectively. In the literature, it was observed that no *Bacillus licheniformis* after incubation for 90 minutes [27] and above 90% at 3 h incubation in simulated gastric juice at pH 2 [28]. According to Niu, K. M et al., it has been shown to fully survive after 3 hours in a

pH 2.5 acid environment [29], it can be said that the isolate is better than various isolates in terms of survival in the artificial stomach environment. This is the desired property of probiotic bacteria.

The bacteria was found to be resistant to all antibiotics tested. Although the rifampin antibiotic has the most effective zone diameter among the antibiotics tested, the bacteria are still resistant. In a similar study performed by R. Sharma et al., it was concluded that *Bacillus licheniformis* was resistant to 16 tested antibiotics [27]. Patients receiving antibiotic therapy against *Bacillus licheniformis* show antibiotic resistance, which is an important probiotic feature for the survival of *Bacillus licheniformis [30]*.

Hydrophobicity studies are important for understanding the adhesion of bacterial cells to surface epithelial cells. Adhesion to surface epithelial cells results from the interaction between bacterial cell and epithelial cell. This is also associated with hydrophobicity and autoaggregation properties. The interaction between bacteria and epithelial cells may be caused by proteins and exopolysaccharide molecules reflecting the auto-aggregation feature. Stronger binding may be due to hydrophobic interaction [31]. As a result of surface hydrophobicity, the bacteria appears to be moderately hydrophobic. Similar results were obtained by P. Shobharani et al. [32] and Khan, Md Idrish Raja, et al. [33]. However K. Ragul et al., obtained better results in terms of surface hydrophobicity [26].

The bacteria are very effective against sodium salts. It can break down the precursors of cholesterol [34]. This means that it can contribute to the reduction of cholesterol level. It was observed that lipid metabolism accelerated and body fat accumulation decreased in the rat model fed with yoghurt sample containing *Bacillus licheniformis* bacteria [35]. It was concluded that the G.T. Cao et al., study's decreased the final body weight in mice, increased glucose intolerance and decreased hepatic fat accumulation [17]. It has been observed by Mahdi et al., that *Bacillus licheniformis* bacteria have a significant effect on lowering the cholesterol level [36].

Conclusion

The *Bacillus licheniformis* grew in acidic environments. The survival rate of bacteria in artificial gastric and intestinal fluid was good. It degraded all tested sodium salts, including sodium glycocholate hydrate, sodium taurodeoxycholate, sodium taurocholic acid, sodium thioglycolate. These results can meaning as cholesterol lowering bacteria. Its surface hydrophobicity was found to be moderately. As a result, it can be stated that the isolated bacteria is a good probiotic organism according to the tested parameters.

Acknowledgement

Thanks to my mommy because of preparation of traditional dairy yoghurt.

Conflict interests

The author(s) declared no potential conflicts of interest.

References

[1] Papizadeh M., Nahrevanian H., Rohani M., Hosseini S.N., Shojaosadati S.A., Lactobacillus rhamnosus Gorbach-Goldin (GG): a top well-researched probiotic strain, *Journal of Medical Bacteriology,* 5(5-6) (2016) 46-59.

[2] Pinto A., Barbosa J., Albano H., Isidro J., Teixeira P., Screening of bacteriocinogenic lactic acid bacteria and their characterization as potential probiotics, *Microorganisms,* 8(3) (2020) 393.

[3] Amara A., Shibl A., Role of Probiotics in health improvement, infection control and disease treatment and management, *Saudi pharmaceutical journal,* 23(2) (2015) 107-114.

[4] Sathyabama S., Vijayabharathi R., Priyadarisini V.B., Screening for probiotic properties of strains isolated from feces of various human groups, *Journal of Microbiology,* 50(4) (2012) 603-612.

[5] Granato D., Branco G.F., Nazzaro F., Cruz A.G., Faria J.A., Functional foods and nondairy probiotic food development: trends, concepts, and products, *Comprehensive Reviews in Food Science and Food Safety,* 9(3) (2010) 292-302.

[6] Espitia P.J., Batista R.A., Azeredo H.M., Otoni C.G., Probiotics and their potential applications in active edible films and coatings, *Food Research International,* 90 (2016) 42-52.

[7] Muras A., Romero M., Mayer C., Otero A., Biotechnological applications of Bacillus licheniformis, *Critical Reviews in Biotechnology,* 41(4) (2021) 609-627.

[8] AL-Yahya A.A., Alhomoud M., Asad M., Alhussaini M.S., Ibrahim K.E., Probiotic bacteria bacillus licheniformis attenuates gastric ulcer healing and antagonizes the ulcer healing effect of ranitidine in rats, *Advances in Bioresearch,* 6(1) (2015) 25-30.

[9] Nithya V., Halami P.M., Evaluation of the probiotic characteristics of Bacillus species isolated from different food sources, *Annals of Microbiology,* 63(1) (2013) 129-137.

[10] Li P, Tian W, Jiang Z, Liang Z, Wu X., Du B., Genomic characterization and probiotic potency of Bacillus sp. DU-106, a highly effective producer of L-lactic acid isolated from fermented yogurt, *Frontiers in Microbiology,* 9 (2018) 2216.

[11] Gracheva N.M., Gavrilov A.F., Solov'eva A.I., Smirnov V.V., Sorokulova I.B., Reznik S.R., Chudnovskaia N.V., The efficacy of the new bacterial preparation biosporin in treating acute intestinal infections, *Zhurnal Mikrobiologii, Epidemiologii, i Immunobiologii,* 1 (1996) 75-77.

[12] Nguyen T., Kang J., Lee M., Characterization of Lactobacillus plantarum PH04, a potential probiotic bacterium with cholesterol-lowering effects, *International Journal of Food Microbiology,* 113(3) (2007) 358-361.

[13] Sivamaruthi B.S., Kesika P., Chaiyasut C., A mini-review of human studies on cholesterol-lowering properties of probiotics, *Scientia Pharmaceutica,* 87(4) (2019) 26.

[14] Shobharani P., Halami P.M., In vitro evaluation of the cholesterol-reducing ability of a potential probiotic Bacillus spp, *Annals of Microbiology,* 66(2) 82016) 643-651.

[15] Jeong S.M., Lee H.J., Park Y.M., Kim J.S., Lee S.D., Bang I.S., Inducible spy transcription acts as a sensor for envelope stress of Salmonella typhimurium, *Korean Journal for Food Science of Animal Resources,* 37(1) (2017) 134-138.

[16] Park S., Chang H.C., Lee J.J., Rice Bran Fermented with Kimchi-Derived Lactic Acid Bacteria Prevents Metabolic Complications in Mice on a High-Fat and-Cholesterol Diet, *Foods,* 10(7) (2021) 1501.

[17] Cao G., Dai B., Wang K., Yan Y., Xu Y., Yang, C. M., Bacillus licheniformis, a potential probiotic, inhibits obesity by modulating colonic microflora in C57BL/6J mice model, *Journal of Applied Microbiology,* 127(3) (2019) 880-888.

[18] Arabacı N., Arıkan B., Isolation and characterization of a cold-active, alkaline, detergent stable α-amylase from a novel bacterium Bacillus subtilis N8, *Preparative Biochemistry and Biotechnology,* 48(5) (2018) 419-426.

[19] Ghosh K., Ray M., Adak A., Halder S.K., Das A., Jana A., Parua (Mondal) S., Vágvölgyi C., Das Mohapatra P.K., Pati B.R., Mondal K.C., Role of probiotic Lactobacillus fermentum KKL1 in the preparation of a rice based fermented beverage, *Bioresource Technology,* 188 (2015)161-168.

[20] Samet K., Taskın I.I., Screening of Potential Probiotic Properties of Lactobacillus and Lactococcus strains, *Research Journal of Biotechnology, Vol* 17 (2022) 1.

[21] Guo, Z., Wang, J., Yan, L., Chen, W., Liu, X. M., & Zhang, H. P., In vitro comparison of probiotic properties of Lactobacillus casei Zhang, a potential new probiotic, with selected probiotic strains, *LWT-Food Science and Technology,* 42(10) (2009) 1640-1646.

[22] Kocabay S., Çetinkaya S., Probiotic properties of a Lactobacillus fermentum isolated from new-born faeces, *Journal of Oleo Science,* 69(12) (2020) 1579-1584.

[23] Çetinkaya S., Kocabay S., Yenidünya A.F., An investigation of the probiotic properties of Lactobacillus fermentum, *International Journal of Life Sciences and Biotechnology,* 3(2) (2020) 180-191.

[24] Iyer R., Tomar S., Kapila S., Mani J., Singh R., Probiotic properties of folate producing Streptococcus thermophilus strains, *Food Research International,* 43(1) (2010) 103-110.

[25] Mehta D., Metzger L., Hassan A., Nelson B., Patel H., The ability of spore formers to degrade milk proteins, fat, phospholipids, common stabilizers, and exopolysaccharides, *Journal of Dairy Science,* 102(12) (2019) 10799-10813.

[26] Ragul K., Syiem I., Sundar K., Shetty P.H., Characterization of probiotic potential of Bacillus species isolated from a traditional brine pickle, *Journal of Food Science and Technology,* 54(13) (2017) 4473-4483.

[27] Sharma R., Sharma N., Probiotic potential of Bacillus licheniformis isolated from indigenous traditional fermented beverage, *Indian Journal of Traditional Knowledge,* 16(1) (2017) 153-157

[28] Wang, Y., Zhang, H., Zhang, L., Liu, W., Zhang, Y., Zhang, X., Sun, T., In vitro assessment of probiotic properties of Bacillus isolated from naturally fermented congee from Inner Mongolia of China, *World Journal of Microbiology and Biotechnology,* 26(8) (2010) 1369-1377.

[29] Niu KM, Kothari D, Lee WD, Lim JM, Khosravi S., Lee S.M., Lee B.J., Kim K.W., Han H.S., Kim S.K., Autochthonous Bacillus licheniformis: Probiotic potential and survival ability in low-fishmeal extruded pellet aquafeed, *MicrobiologyOpen,* 8(6) (2019) e00767.

[30] Kim K.T., Yang S.J., Paik H.D., Probiotic properties of novel probiotic Levilactobacillus brevis KU15147 isolated from radish kimchi and its antioxidant and immune-enhancing activities, *Food Science and Biotechnology,* 30(2) (2021) 257-265.

[31] Yang S.J., Kim K.T., Kim T.Y., Paik H.D., Probiotic properties and antioxidant activities of Pediococcus pentosaceus SC28 and Levilactobacillus brevis KU15151 in fermented black gamju, *Foods,* 9(9) (2020) 1154.

[32] Shobharani P., Halami P.M., Cellular fatty acid profile and H+-ATPase activity to assess acid tolerance of Bacillus sp. for potential probiotic functional attributes, *Applied microbiology and biotechnology,* 98(21) (2014) 9045-9058.

[33] Khan M.I.R., Choudhury T.G., Kamilya D., Monsang S.J., Parhi J., Characterization of Bacillus spp. isolated from intestine of Labeo rohita—Towards identifying novel probiotics for aquaculture, *Aquaculture Research,* 52(2) (2021) 822-830.

[34] Habib B., Vaid S., Bangotra R., Sharma S., Bajaj B.K., Bioprospecting of probiotic lactic acid bacteria for cholesterol lowering and exopolysaccharide producing potential, *Biologia,* 77 (2022) 1931–1951.

[35] Yeon, S. J., Hong, G. E., Kim, C. K., Park, W. J., Kim, S. K., Lee, C. H., Effects of yogurt containing fermented pepper juice on the body fat and cholesterol level in high fat and high cholesterol diet fed rat, *Korean Journal for Food Science of Animal Resources,* 35(4) (2015) 479.

[36] Mahdi M.H., Khalil Y.I., The Effect of Bacillus licheniformis on weight gain, Blood picture and Lipid Profiles in rats feed high Cholesterol diet, *Tikrit Journal for Agricultural Sciences,* 22(2) (2022) 36-43.

Cumhuriyet Sci. J., 44(1) (2023) 7-12
DOI: https://doi.org/10.17776/csj.1150823

Cumhuriyet Science Journal

| csj.cumhuriyet.edu.tr | Founded: 2002 ISSN: 2587-2680 e-ISSN: 2587-246X Publisher: Sivas Cumhuriyet University

Toxicity of Paraquat and Dicamba on Caenorhabditis Elegans LC50 Value

Alper Zöngür [1,a,*], Musa Sari [2,b]

[1] *Gemerek Vocational School, Sivas Cumhuriyet University, Sivas, Türkiye.*
[2] *Department of Biology, Faculty of Science, Sivas Cumhuriyet University, Sivas, Türkiye.*
**Corresponding author*

Research Article

History
Received: 29/07/2022
Accepted: 24/02/2023

ABSTRACT

Paraquat and dicamba are chemicals commonly used in agriculture for plant control. The US Environmental Protection Agency (EPA) has classified paraquat into a restricted use class for use only by practitioners, as it is highly toxic. In this study, the effects of different concentrations of paraquat and dicamba toxic substances on *C. elegans* were studied. In tests, *C. elegans* were directly exposed to different concentrations of paraquat and dicamba for 6h, 12h, 18h, 24h. In particular, it was determined at which paraquat and dicamba doses that half of the *C. elegans* individuals (LC50) died. In the analysis results, paraquat LC50 values were found as LC50 6h= $LC_{50\ 6h}$= 7412 µM, $LC_{50\ 12h}$= 459 µM, $LC_{50\ 18h}$= 123 µM, $LC_{50\ 24h}$= 61 µM. Similarly, dicamba LC50 values were found as $LC_{50\ 6h}$= 14610 µM, $LC_{50\ 12h}$= 1404 µM, $LC_{50\ 18h}$= 906 µM, $LC_{50\ 24h}$= 463 µM.

Keywords: C. elegans, Paraquat, Dicamba, Lethal concentration (LC), Paraquat and dicamba toxicity.

[a] *bzongur@cumhuriyet.edu.tr* *https://orcid.org/0000-0003-4946-3199* [b] *musasari@cumhuriyet.edu.tr* *https://orcid.org/0000-0002-6431-643X*

Introduction

Paraquat (1,1'-dimethyl-4-4'-bipyridinium dichloride, PQ) is a fast, effective and non-selective highly toxic dipyridyl herbicide widely used especially in developing countries [1,2]. Paraquat toxicity is mediated by oxidative stress-induced mechanisms [3]. Paraquat exerts its effectiveness by interfering with intracellular electron transfer photosystems by inhibiting the reduction of oxidized nicotinamide adenine dinucleotide phosphate ($NADP^+$) to nicotinamide adenine dinucleotide phosphate (NADPH) during photosynthesis. Instead of NADPH, the paraquat ion is reduced and a monocation-free radical is formed. The electron transferred to the paraquat is then rapidly converted to oxygen with the production of superoxide, leading to the formation of reactive oxygen species (ROS) such as superoxide anion (O_2^-), singlet oxygen ($^1O_2$), peroxyl radicals (ROO-) [4]. As a result, oxidative damage occurs due to reactive oxygen species [5-7]. Mitochondrial dysfunction results in decreased cellular energy supply, inability to maintain cellular homeostasis, and activation of cell death [8,9]. At the same time, paraquat causes respiratory depression through inhibition of mitochondrial complexes [10]. Paraquat also has acute systemic effects. In particular, the lungs and kidneys are the organs most susceptible to paraquat-induced injuries [11]. An acceptable daily intake (ADI) of 0.004 mg/kg has been established for Paraquat. Also, the minimum lethal dose of paraquat in humans is about 35 mg/kg body weight [12]. In case of exposure to lethal doses of paraquat, death can occur within a few days after inhalation [13]. Paraquat (PQ) has been associated with Parkinson's (PD) in epidemiological studies in rodents and it has been reported that paraquat is an environmental risk factor for PD disease [14]. In particular, paraquat was thought to cause parkinsonism by increasing oxidative stress and affecting a pathophysiological genetic mechanism (alpha-synuclein, PINK-1, DJ-1 and PARKIN mutations) [15,16]. However, the evidence that human exposure to chemicals poses an increased risk for PD is quite limited and is based on insufficient epidemiological data [17].

Dicamba (3,6-dichloro-2-methoxybenzoic acid) is a white solid crystalline compound with a molecular formula ($C_8H_6Cl_2O_3$) and a molecular weight of 221.03 g/mol. Dicamba is a chlorinated derivative of o-anisic acid, first registered in the United States in 1967. O-Anisic acid, (ortho-methoxybenzoic acid or 2-methoxybenzoic acid) is a crystalline solid and is an isomer of anisic acid [18]. The biodegradation metabolites of Dicamba are 2,5-dichlorophenol and 3,6-dichlorosalicylic acid. After biodegradation, 3,6-dichlorosalicylic acid converts to more carbon dioxide, water and chloride [19]. These compounds can be dangerous if not handled properly, and many (even though not all of them) pose a potential hazard to the environment due to contamination of food, water and air [20]. In addition, hazardous anthropogenic activities continuously release large amounts of these compounds into the environment, regardless of their bioaccumulation and toxicity. However, it is well known that this chemical not only affects target organisms, but also exerts adverse effects on non-target organisms [21]. Dicamba has been detected as a contaminant in agricultural, urban and mixed agriculture/urban areas, surface drinking water reservoirs and even estuarine waters [22]. Much is known about the effects of dicamba

on aquatic plants and its risks to terrestrial organisms. So far, the potential genotoxic hazard of dicamba has been demonstrated by various in vivo and in vitro tests [23]. Some recent research has shown that dicamba should be viewed as a DNA-damaging agent. Similarly, studies have reported that dicamba causes induction of sister chromatid exchanges (SCEs) and mitotic changes in human lymphocytes and Chinese hamster ovary (CHO-K1) cells [24]. Although the information on the potential toxic effects of dicamba is limited, it is known how unsaturated membrane fatty acids affect cis-trans isomerization, toxicity and membrane activity, and the toxicity of dicamba increases with the increase in the length of the alkyl chain lengths of dicamba [25].

The nematode *Caenorhabditis elegans* is frequently preferred in biological research due to its convenient use in intergenerational studies, short breeding period and low cost. Studies have revealed that *C. elegans* contains many genes homologous to mammals [26]. Moreover, the similarity of *C. elegans* biological processes with human processes has made *C. elegans* a useful model for genetic and developmental biological research [27]. In addition, the clear traceability of genetic and biochemical processes of *C. elegans* provides the opportunity to use this organism as a biosensor for toxicological studies [28]. For these reasons, many pharmaceutical companies use the positive predictive power of *C. elegans* in their drug development processes and chemical toxicity tests [29,30].

In this study, the effects of different concentrations of paraquat and dicamba toxic substances on *C. elegans* were studied. In particular, it was determined at which paraquat and dicamba doses that half of the *C. elegans* individuals (LC_{50}) died.

Materials and Methods

Collection of Materials

In this study, it was aimed to investigate the toxicological effects of analytically pure dicamba and paraquat chemicals on Caenorhabditis elegans. Dicamba was stored at room temperature in the dark until use, while Paraquat was stored at +4 °C. In the study conducted to examine the toxicological effects of dicamba and paraquat chemicals, living organisms (wild type C. elegans N2) and bacterial colonies (*E. coli* OP50 strain) were provided by the University of Minnesota *Caenorhabditis* Genetics Center (CGC).

Preparation of TBX Agar Medium and Purification of E. coli OP50

Tryptone Bile X-glucuronide (TBX) Agar medium was preferred to determine the presence of *E. coli* OP50 strain in cultures and to purify the strains. 3.65 g of TBX Agar required to prepare 100 mL of medium was weighed and prepared in dH_2O. The prepared medium solution is kept at 125°C for 15 minutes. After autoclaving, it was cooled (55 °C) and poured into 60 mm petri dishes as 10 mL. Solidified TBX Agar media were seeded from the stock *E. coli* OP50 strain. The inoculated petri dishes were incubated for 24 hours at 37 °C and the blue colonies formed were determined.

Preparation of LST Broth and Propagation of E. coli OP50

Lauryl Sulfate Broth (LST) broth was used to propagate *E. coli* OP50 strain. The medium was prepared to contain 9.125 g of LST in 250 ml of dH_2O. 15 min at 125°C. Pure *E. coli* Op50 colonies determined in TBX medium were transferred to the broth that came to 37 °C after autoclaving. The medium was kept in an incubator at 37 °C for 24 hours. The stock broth containing the *E. coli* OP50 strain determined using the McFarland method was kept in the refrigerator at +4 °C to be used.

Preparation of Nematode Medium (NGM) and C. elegans Cultures

C. elegans can be cultured in laboratories on Nematode Growth Medium (NGM) agar. To prepare NGM; 2.5 g Peptone, 3 g NaCl and 20 g Agar were mixed in 1 L dH2O until boiling point. 15 minutes at 120 ºC. After autoclaving, it was kept in a water bath at 55 ºC. For homogenization of NGMs; 1 mL of $MgSO_4$ (1M), 1 mL of cholesterol (5 mg/mL), 1 mL of $CaCl_2$ (1M), 25 mL of KPO_4 buffer (pH:7) were filtered through cellulose filters and added to the medium solution. Approximately 10 mL of homogenized NGMs were poured into 60 mm petri plates. Next, 500 µL of LST medium containing *E. coli* Op50 was placed in the midpoint of NGM. Afterwards, small incisions were taken from the *C. elegans* stock culture medium and placed in the middle of the prepared NGM, and fresh *C. elegans* cultures were created.

C. elegans Synchronization

An alkaline hypochlorite solution was used to synchronize cultures of *C. elegans*, which dissolves the eggs of hermaphrodites without damaging them [31]. The petri dish was washed by pipetting with 2 ml of dH_2O to loosen the eggs. The liquid was collected in a capped sterile 5 mL conical centrifuge tube and the total volume was made up to 3.5 mL with dH_2O. 0.5 mL NaOH (1g/5ml) and 1 mL NaOCl were added into the tube. The tube was shaken every 2 minutes for a total of 10 minutes. To pellet the released eggs, the tube was run at 3400 rpm for 5 minutes centrifuged. The liquid in the tube was aspirated up to 0.25 mL and transferred to a bottle containing 25 mL of M9 buffer (0.3 g KH_2PO_4, 0.6 g Na_2HPO_4, 0.5 g NaCl, 0.1 mL 1 M $MgSO_4$) and incubated for 1 day at 20°C to obtain highly starved L1 larvae. The flask was then placed on ice for 15 minutes and centrifuged to allow *C. elegans* to settle. After re-aspiration after centrifugation, 0.25 mL of liquid remaining was transferred with a Pasteur pipette to a clean NGM petri dish containing *E. coli* OP50. Thus, *C. elegans* life forms were synchronized by growing at the same time and were used in studies.

Preparation of Dicamba and Paraquat Solutions

The dicamba and paraquat stock solutions used in the study were taken with a micropipette and diluted to a final concentration of 15.625- 31.25- 62.5- 125- 250- 500- 1000 and 2000 µM in the tubes. In the tubes used as control, dicamba and paraquat were not added. *C. elegans* were transferred directly into the prepared solutions.

Statistical Analysis

In the study, SPSS 26.00 probit test was used and LC_{50} values between dose groups were determined. In addition, differences between doses with Anova were determined. In addition, various statistical data including survival time and survival rate using Kaplan-Meier test and Chi-square test are presented together in the findings section. All of the analyzes made in the study were evaluated by taking the averages and graphs and charts were created using the data found.

Results

C. elegans Survival Analyzes

In the study, 60 *C. elegans* individuals were exposed to 8 different doses of paraquat (15.6- 31.2- 62.5- 125- 250- 500- 1000 and 2000 µM) in tubes for 6,12,18 and 24 hours. After the lowest dose exposure of 6, 12, 18 and 24 hours, 3, 6, 11 and 18 of the *C. elegans* individuals died, respectively. After 6, 12, 18 and 24 hours of exposure at the highest dose, 19, 39, 52 and 56 *C. elegans* individuals died, respectively (Table 1).

Table 1 The effect of paraquat doses on the number of deaths

Number of individuals Concentration (µM)		Mortality (number of dead individuals)			
		6 h	12 h	18 h	24 h
60	15.6	3	6	11	18
60	31.2	3	8	16	22
60	62.5	6	15	23	28
60	125	8	20	28	34
60	250	14	28	40	47
60	500	16	33	44	53
60	1000	18	36	50	55
60	2000	19	39	52	56

Table 2 The effect of dicamba doses on the number of deaths

Number of individuals Concentration (µM)		Mortality (number of dead individuals)			
		6 h	12 h	18 h	24 h
60	15.6	1	3	3	4
60	31.2	3	3	5	7
60	62.5	4	8	9	12
60	125	7	11	13	17
60	250	10	17	20	26
60	500	11	19	24	32
60	1000	13	30	33	39
60	2000	17	31	35	41

Similarly, C. elegans individuals were exposed to 8 different doses of dicamba (15.6- 31.2- 62.5- 125- 250- 500- 1000 and 2000 µM). After the lowest dose exposure of 6, 12, 18 and 24 hours, 1, 3, 3 and 4 of the C. elegans individuals died, respectively. After 6, 12, 18 and 24 hours of exposure at the highest dose, 17, 31, 35 and 41 C. elegans individuals died, respectively (Table 2). There were differences between doses in the anova and chi-square tests performed with survival numbers ($p<0.05$). In addition, paraquat and dicamba survival function graphs were created using the Kaplan-Meier method to show the differences between dose groups (Figure 1 and 2).

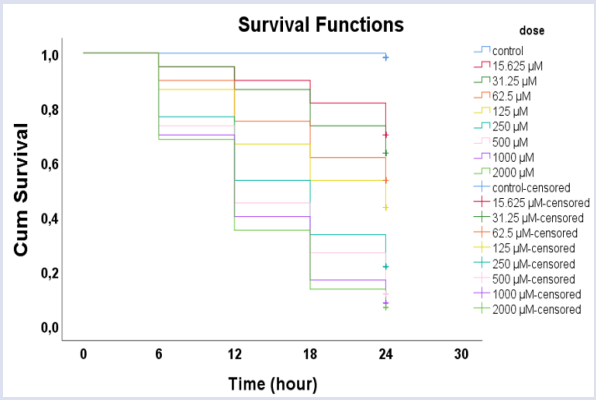

Figure 1 Paraquat survival function graph prepared with Kaplan-Meier analysis

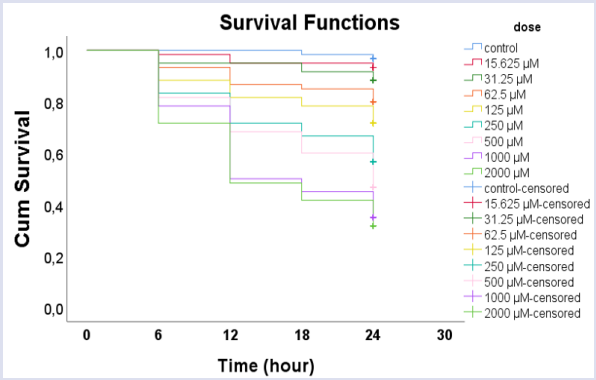

Figure 2 Dicamba survival function graph prepared with Kaplan-Meier analysis

C. elegans LC_{50} Determination with Different Paraquat Doses

C. elegans individuals were exposed to 8 different doses of paraquat (15.6- 31.2- 62.5- 125- 250- 500- 1000 and 2000 µM) for 6-12-18 and 24 hours. After exposure, *C. elegans* LC_{50} values were determined by the probit test. Analysis results showed paraquat LC_{50} 6h= 7412 µM, $LC_{50\ 12h}$= 459 µM, $LC_{50\ 18h}$= 123 µM, $LC_{50\ 24h}$= 61 µM (Figure 3).

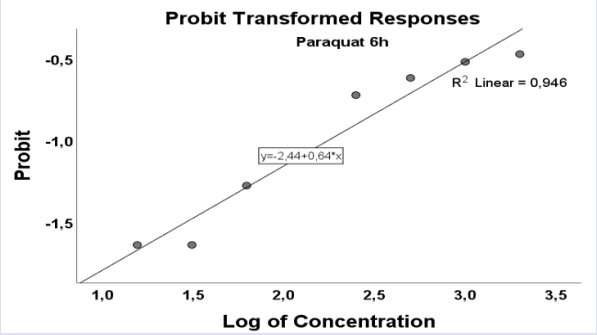

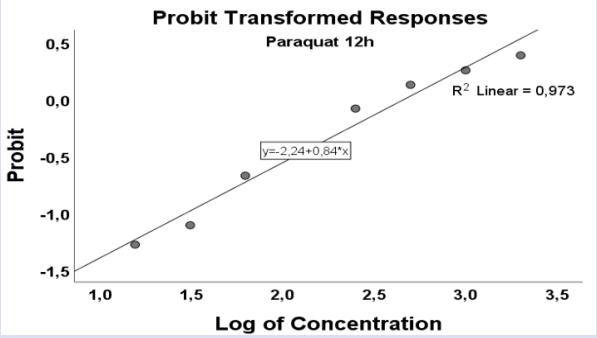

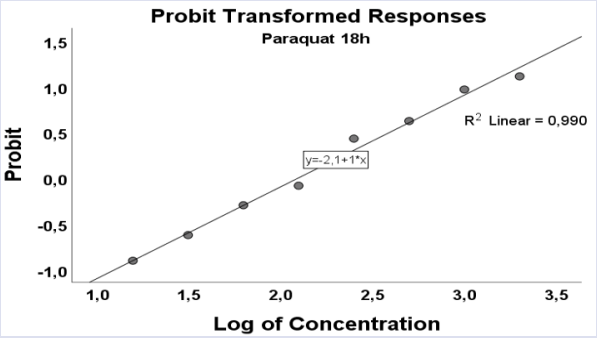

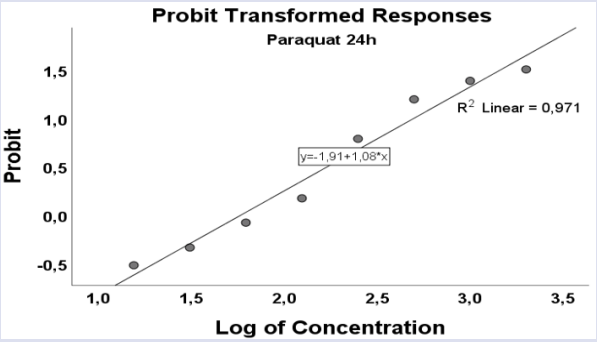

Figure 3 Paraquat dose applications probit values (6h,12h,18h and 24h)

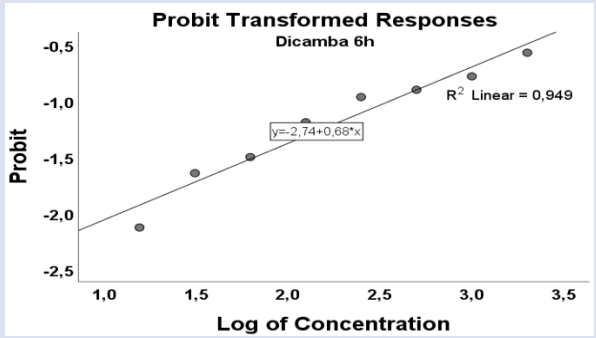

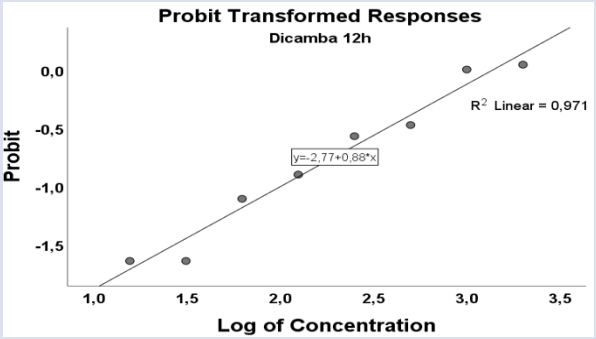

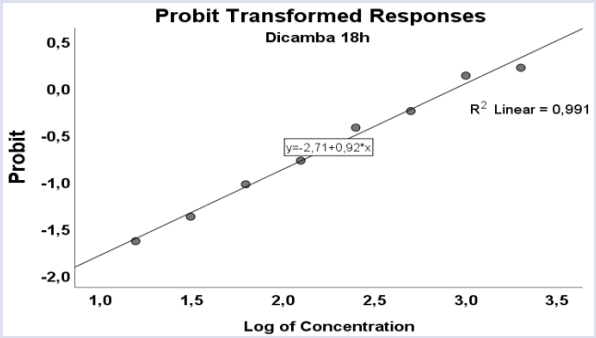

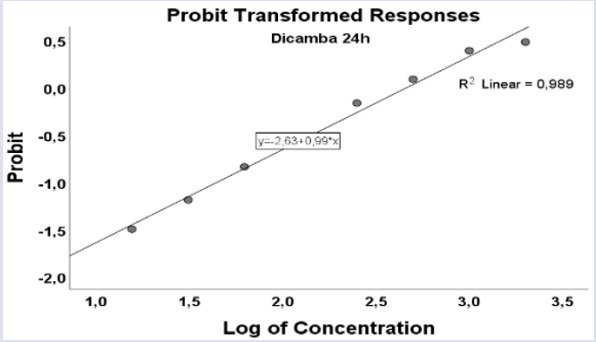

Figure 4 Dicamba dose applications probit values (6h,12h,18h and 24h)

C. elegans LC_{50} Determination with Different Dicamba Doses

C. elegans individuals were exposed to 8 different doses (15.6- 31.2- 62.5- 125- 250- 500- 1000 and 2000 µM) of dicamba for 6-12-18 and 24 hours. After exposure, C. elegans LC50 values were determined by the probit test. Analysis results showed dicamba LC50 6h= 14610 µM, LC50 12h= 1404 µM, LC50 18h= 906 µM, LC50 24h= 463 µM (Figure 4).

Discussion

In our study, the number of live and dead worms was counted by visual inspection with the aid of a camera microscope [32]. At the highest dose of paraquat (2000 µM) at the end of 6,12,18,24 hours, 31.6%, 65%, 86.6% and 93.3% mortality rates were observed, respectively. In the highest (2000 µM) dose application of dicamba, 68.3%, 58.3%, 51.6% and 28.3% mortality rates were observed after 6,12,18,24 hours, respectively. When

these mortality rates are evaluated, it is seen that paraquat and dicamba have an intense toxic effect on C. elegans individuals. The fact that these toxic chemicals affect C. elegans individuals so much after 24 hours has shown that young animals are more sensitive to toxic substances than adult forms [33].

C. elegans is a popular living model for examining the toxicological relevance of chemical-induced toxicity at the molecular level [34,35]. In this study, LC_{50} (50% lethal concentration) values of paraquat and dicamba were determined for *C. elegans*. Paraquat $LC_{50\ 6h}$= 7412 µM, $LC_{50\ 12h}$= 459 µM, $LC_{50\ 18h}$= 123 µM, $LC_{50\ 24h}$= 61 µM (Figure 3). Similarly, dicamba $LC_{50\ 6h}$= 14610 µM, $LC_{50\ 12h}$= 1404 µM, $LC_{50\ 18h}$= 906 µM, $LC_{50\ 24h}$= 463 µM (Figure 4). These determined LC_{50} values showed that even a short time (6h,12h,18h,24h) exposure of *C. elegans* directly to paraquat and dicamba can cause 50% of these organisms to die.

Paraquat is a known mitochondrial toxicant. It is important to know the effects caused by mitochondrial toxicants in order to interpret lifespan analyses. In a study, using the *C. elegans* model, it was stated that paraquat affects reproduction, longevity, gene expression and mitochondrial physiology. Moreover, paraquat has been shown to induce mitochondrial unfolded protein response (mtUPR), increase mitochondrial superoxide dismutase expression, and decrease mitochondrial membrane potential (Δψm). In particular, chronic exposure to paraquata (0.035 mM) has been reported to cause gradual decline in fertility, resulting in complete loss of fertile embryo production by the third generation. Similarly, it is known that paraquat increases oxidative stress by generating reactive oxygen species (ROS), and this increased oxidative stress is one of the main causes of aging and plays a role in the pathogenesis of many diseases. In a study, it was shown that 200 mM paraquat in the NGM medium killed approximately half (LC50) of *C. elegans* individuals in the L2 and L4 form in 6 hours, and all of them in 15 hours [36]. In our study, however, paraquat was not applied in the NGM medium, and *C. elegans* individuals were directly exposed to paraquat. Therefore, the toxic effect of the applied paraquat increased and $LC_{50\ 6h}$= 7412 µM, $LC_{50\ 12h}$= 459 µM, $LC_{50\ 18h}$= 123 µM, $LC_{50\ 24h}$= 61 µM.

Although there is no study on dicamba on *C. elegans* individuals, there are some studies on the toxic effect of dicamba on some living species. In one study, the acute lethal effects of dicamba on Rhinella arenarum larvae were determined and demonstrated to induce primary DNA breaks in amphibians. In addition, dicamba was found as $LC_{50\ 24h}$ = 742 mg /L [37]. Similarly, zebrafish embryos were exposed to dicamba for 120 hours and the dicamba was found as $LC_{50\ 120h}$ = 56 mg /L [38]. When the studies on Paraquat and dicamba and our study results are evaluated together, it has been seen that LC50 values are generally directly affected by the exposure method and exposure time.

Conclusion

As with any model system, the *C. elegans* LC50 results determined in the paraquat and dicamba toxicity screening were considered useful in predicting toxic responses in other organisms. In particular, considering the similarity of biological processes of *C. elegans* with human processes, the LC50 values of paraquat and dicamba found in the study will provide information for human toxicology studies. Similarly, the results of the study provided additional information for assessing correlations between toxicity responses in *C. elegans* and mammals, with up to 69% concordance between mammals and *C. elegans*.

Conflicts of Interest

The authors stated that did not have conflict of interests.

References

[1] Wesseling C., De Joode B.V.W., Ruepert C., León C., Monge P., Hermosillo H., Partanen L.J., Paraquat in developing countries. *International Journal of Occupational and Environmental Health*, 7 (4) (2001) 275-286.

[2] Cicchetti F., Drouin-Ouellet J., Gross R.E., Environmental toxins and Parkinson's disease: what have we learned from pesticide-induced animal models, *Trends in Pharmacological Sciences*, 30 (9) (2009) 475-483.

[3] Suntres Z.E., Role of antioxidants in paraquat toxicity, *Toxicology*, 180 (1) (2002) 65-77.

[4] Vicente J.A., Peixoto F., Lopes M.L., Madeira V.M., Differential sensitivities of plant and animal mitochondria to the herbicide paraquat, *Journal of Biochemical and Molecular Toxicology*, 15 (6) (2001) 322-330.

[5] Han J.F., Wang S.L., He X.Y., Liu C.Y., Hong J.Y., Effect of genetic variation on human cytochrome p450 reductase-mediated paraquat cytotoxicity, *Toxicological Sciences*, 91 (1) (2006) 42-48.

[6] Mohammadi-B.A., Ghazi-Khansari M., Alternative electron acceptors: proposed mechanism of paraquat mitochondrial toxicity, *Environmental Toxicology and Pharmacology*, 26 (1) (2008) 1-5.

[7] Figueiredo-Fernandes A.M., Fontaínhas-Fernandes A.A., Monteiro R.A., Reis-Henriques M.A., Rocha E., (2006) Temperature and gender influences on the hepatic stroma (and associated pancreatic acini) of *Nile tilapia*, *Oreochromis niloticus* (Teleostei, Cichlidae): A stereological analysis by light microscopy, *Journal of Morphology*, 267 (2) (2006) 221-230.

[8] Beal M.F., Mitochondria take center stage in aging and neurodegeneration, *Annals of Neurology: Official Journal of the American Neurological Association and the Child Neurology Society*, 58 (4) (2005) 495-505.

[9] Banerjee R., Starkov A.A., Beal M.F., Thomas B., Mitochondrial dysfunction in the limelight of Parkinson's disease pathogenesis, *Biochimica et Biophysica Acta (BBA)-Molecular Basis of Disease*, 1792 (7) (2009) 651-663.

[10] Palmeira C.M., Moreno A.J., Madeira V.M., Mitochondrial bioenergetics is affected by the herbicide paraquat, Biochimica et Biophysica Acta (BBA)-*Bioenergetics*, 1229 (2) (1995) 187-192.

[11] Costa L.G., Toxic effects of pesticides. Casarett and Doull's toxicology, *Tthe Basic Science of Poisons*, 8 (2008) 883-930.

[12] Maroni M., Colosio C., Ferioli A., Fait A., Quaternary Ammonium Compounds, *Toxicology*, 143 (2000) 85-89.

[13] Lin H.M., Liu H.L., Yang M.C., Tsai T.H., Chou C.C., Chang C.F., Lin Y.R., Clinical features and outcome analysis of patients suffer from paraquat intoxication in central Taiwan, *Journal of Emergency Medicine,* 12 (4) (2010) 99-106.

[14] Oliveira R.J., Remiao F., Carmo H., Duarte J.A., Navarro A.S., Bastos M.L., Carvalho F., Paraquat exposure as an etiological factor of Parkinson's disease, *Neurotoxicology*, 27 (6) (2006) 1110-1122.

[15] Henchcliffe C., Beal M.F., Mitochondrial biology and oxidative stress in Parkinson disease pathogenesis, *Nature Clinical Practice Neurology*, 4 (11) (2008) 600-609.

[16] Klein C., Schneider S.A., Lang A.E., Hereditary parkinsonism: Parkinson disease look-alikes—An algorithm for clinicians to "PARK" genes and beyond. *Movement disorders, Official Journal of the Movement Disorder Society*, 24 (14) (2009) 2042-2058.

[17] Berry C., La Vecchia C., Nicotera P., Paraquat and Parkinson's disease, *Cell Death & Differentiation*, 17 (7) (2010) 1115-1125.

[18] Tomlin C.D.S., The pesticide manual: a world compendium. 12th Ed. British Crop Protection Council, Bracknel, 14 (2000) 502-504.

[19] Yang J., Wang X.Z., Hage D.S., Herman P.L., Weeks D.P., Analysis of dicamba degradation by *Pseudomonas maltophilia* using high-performance capillary electrophoresis, *Analytical Biochemistry*, 219 (1) (1994) 37-42.

[20] Kaushik G., Satya S., Naik S.N., Food processing a tool to pesticide residue dissipation–A review, *Food Research International*, 42 (1) (2009) 26-40.

[21] Fischer B.B., Pomati F., Eggen R.I., The toxicity of chemical pollutants in dynamic natural systems: the challenge of integrating environmental factors and biological complexity, *Science of the Total Environment*, 449 (2013) 253-259.

[22] Woudneh M.B., Sekela M., Tuominen T., Gledhill M., Acidic herbicides in surface waters of lower Fraser valley, British Columbia, Canada, *Journal of Chromatography A*, 1139 (1) (2007) 121-129.

[23] Perocco P., Ancora G., Rani P., Valenti A.M., Mazzullo M., Colacci A., Grilli S., Evaluation of genotoxic effects of the herbicide dicamba using in vivo and in vitro test systems, *Environmental and Molecular Mutagenesis*, 15 (3) (1990) 131-135.

[24] González N.V., Soloneski S., Larramendy M.L., The chlorophenoxy herbicide dicamba and its commercial formulation banvel® induce genotoxicity and cytotoxicity in Chinese hamster ovary (CHO) cells. *Mutation Research/Genetic Toxicology and Environmental Mutagenesis*, 634 (1-2) (2007) 60-68.

[25] Piotrowska A., Syguda A., Wyrwas B., Chrzanowski Ł., Heipieper H.J., Toxicity evaluation of selected ammonium-based ionic liquid forms with MCPP and dicamba moieties on *Pseudomonas putida, Chemosphere*, 167 (2017) 114-119.

[26] Lehner B., Crombie C., Tischler J., Fortunato A., Fraser A.G., Systematic mapping of genetic interactions in *Caenorhabditis elegans* identifies common modifiers of diverse signaling pathways, *Nature Genetics*, 38 (8) (2006) 896-903.

[27] Boyd W.A., Smith M.V., Freedman J.H., *Caenorhabditis elegans* as a model in developmental toxicology, *In Developmental Toxicology*, Humana Press, Totowa, NJ (2012) 15-24

[28] David H.E., Dawe A.S., de Pomerai D.I., Jones D., Candido E.P.M., Daniells C., Construction and evaluation of a transgenic hsp16-GFP-lacZ *Caenorhabditis elegans* strain for environmental monitoring, *Environmental Toxicology and Chemistry: An International Journal*, 22 (1) (2003) 111-118.

[29] Artal-Sanz M., de Jong L., Tavernarakis N., *Caenorhabditis elegans*: a versatile platform for drug discovery, *Biotechnology Journal: Healthcare Nutrition Technology*, 1 (12) (2006) 1405-1418.

[30] Leung M.C., Williams P.L., Benedetto A., Au C., Helmcke K.J., Aschner M., Meyer J.N., *Caenorhabditis elegans*: an emerging model in biomedical and environmental toxicology, *Toxicological Sciences*, 106 (1) (2008) 5-28.

[31] Baugh L.R., To grow or not to grow: nutritional control of development during *Caenorhabditis elegans* L1 arrest, *Genetics*, 194 (3) (2013) 539-555.

[32] Helmcke K.J., Aschner M., Hormetic effect of methylmercury on *Caenorhabditis elegans*, *Toxicology and Applied Pharmacology*, 248 (2) (2010) 156-164.

[33] Chu K.W., Chow K.L., Synergistic toxicity of multiple heavy metals is revealed by a biological assay using a nematode and its transgenic derivative, *Aquatic Toxicology*, 61 (1-2) (2002) 53-64.

[34] Menzel R., Rödel M., Kulas J., Steinberg C.E., CYP35: xenobiotically induced gene expression in the nematode *Caenorhabditis elegans*, *Archives of Biochemistry and Biophysics*, 438 (1) (2005) 93-102.

[35] Reichert K., Menzel R., Expression profiling of five different xenobiotics using a *Caenorhabditis elegans* whole genome microarray, *Chemosphere*, 61 (2) (2005) 229-237.

[36] Senchuk M.M., Dues D. J., Van Raamsdonk, J.M., Measuring oxidative stress in *Caenorhabditis elegans*: paraquat and juglone sensitivity assays, *Bio-protocol*, 7 (1) (2017) 2086-2086.

[37] Soloneski S., De Arcaute C.R., Larramendy M.L., Genotoxic effect of a binary mixture of dicamba-and glyphosate-based commercial herbicide formulations on *Rhinella arenarum* (Hensel, 1867)(Anura, Bufonidae) late-stage larvae. *Environmental Science and Pollution Research*, 23 (17) (2016) 17811-17821.

[38] Turner L.W., Defining the Developmental Toxicity of the Herbicide Dicamba Using the Zebrafish Model System. *The Journal of Purdue Undergraduate Research*, 9 (1) (2019) 30.

Cumhuriyet Sci. J., 44(1) (2023) 13-18
DOI: https://doi.org/10.17776/csj.1161889

Cumhuriyet Science Journal

| csj.cumhuriyet.edu.tr | Founded: 2002 ISSN: 2587-2680 e-ISSN: 2587-246X Publisher: Sivas Cumhuriyet University

Variation in Measurements of Some Body Parts of *Laodelphax striatella* (Fallén, 1826) (Hemiptera: Fulgoromorpha: Delphacidae) due to Altitude

Murat Karavin [1,a,*], Ünal Zeybekoğlu [2,b]

[1] *Vocational School, Amasya University, Suluova, Amasya, Türkiye.*
[2] *Biology Department, Arts and Science Faculty, Ondokuz Mayıs University, Samsun, Türkiye.*
**Corresponding author*

Research Article

History
Received: 14/08/2022
Accepted: 13/03/2023

ABSTRACT

The small brown planthopper *Laodelphax striatella* (Fallén, 1826), which belongs to Delphacidae family, is widespread in Palearctic. It is one of the important pests of agricultural crops such as rice, maize, oat, wheat etc. Because of its economic importance, identification of the factors that effective on *L. striatella* populations is required. Size of body parts closely related with vital processes such as metabolic performance, fecundity, and longevity. Several ecological factors such as light, temperature, water supply and moisture were effective on body size. The aim of the study was to determine the effect of altitude on some body measurements of *L. striatella*. Because light, temperature, precipitation and some of the other factors vary based on altitude, it is an important ecological factor for organisms. Understanding the effects of altitude on insect species may give useful information about them. The specimens were collected from three localities at different altitudes in Central Black Sea Region, Turkey. Except wing length, all the measurements of the body parts varied proportionally with increasing altitude. Statistically significant variations were determined in the measurements of head width, pronotum length, pronotum width, mesonotum width and forewing width. The maximum head, pronotum, mesonotum and forewing width (0.623, 0.686,0.707 and 0.730 mm, respectively) and pronotum length (0.172 mm) was measured at 50 m. The minimum measurements of these body parts were at 900 m. Additionally, relationships were determined between measured body parts and altitude.

Keywords: *Laodelphax striatella*, Altitude, Body parts, Insect, Variation.

[a] *murat.karavin@amasya.edu.tr* *https://orcid.org/0000-0003-0957-859X* [b] *unalz@omu.edu.tr* *https://orcid.org/0000-0001-7595-9572*

Introduction

Ecological factors play important roles in fitness of organisms. Topographic characteristics of an area are effective directly or indirectly on ecological factors. For example, altitude is the major determinant of light, temperature, precipitation. The variation in climatic factors and other characteristics due to altitude is related to species composition and fitness.

There are some key features which provide monitoring the ecological, biological, and physiological status of organisms and give information about their fitness. One of these key factors is the body size that give information about metabolic performance, fecundity, and longevity of organisms [1]. Body size is one of the most important characteristics of organisms. While it is associated with a variety of ecological and physiological characteristics, it also influences life histories [2-8].

Insects are important organisms of the world due to their ecological niches such as pollen transport, effects on plants as pests, and vector status. Because of their vital roles in ecosystems, understanding the ecological factors which are effective on insect body size and fitness is important.

There are several studies in the literature showing that the effect of elevation on insect body size [1,9-15]. While some of the studies reported increase in body size based on elevation, the others determined decrease. It was thought that these differences may be resulted from diversity of insect species and the multiple ecological factors in the area. However, there was no significant relationship between body size and elevation in some studies [16-17].

As the results vary widely according to the insect species, geographical region and ecological factors, no clear conclusion has yet been reached regarding the relationship between body size and height of insects. Therefore, new studies on various families and species are needed.

In the current study, it was aimed to determine the variation in the measurement of some body parts of *L. striatella* according to altitude. Delphacidae Leach, 1815 is a large family of the suborder Fulgoromorpha (Hemiptera), and it has approximately 2000 species placed in 300 genera and six subfamilies [18-19]. It is known that 250 species belonging to the Delphacidae family are distributed in the Europe, and about half of these species are from Central Europe [20]. Delphacids are easily distinguished from other members of Hemiptera by the presence of a posttibial spur on the tibia of their hind legs. With their piercing-sucking mouthparts, they generally feed by sucking the sap from plant species belonging to the Cyperaceae and Poaceae families. Most of the species are found on the plant parts which are close

to soil surface, such as roots and stems. For this reason, they do not attract much attention and can easily be overlooked. Delphacids damage plants directly by feeding and laying eggs, and indirectly by transmitting viruses, rickettsia, bacteria and mycoplasmas [21-22].

The small brown planthopper, *L. striatella*, is one of the harmful species for rice. It is widely distributed in Asia, Europe, and Northern Africa of Palearctic region. Both adults and nymphs feed directly on rice, and spread important viral diseases, such as rice black streaked dwarf disease [23-27]. The body size of specimens has less than 4 mm. Vertex is square in shape. The pronotum is straight anteriorly, concave posteriorly, and the lateral carinas do not extend to the posterior margin. The pronotum is about the length of the vertex. The mesonotum is approximately three times the length of the pronotum and its median carina extends to the mesoscutellum (Figure 1). There are more than 10 teeth of the same size on the ventral edge of the posttibial spur. The front wings are membranous.

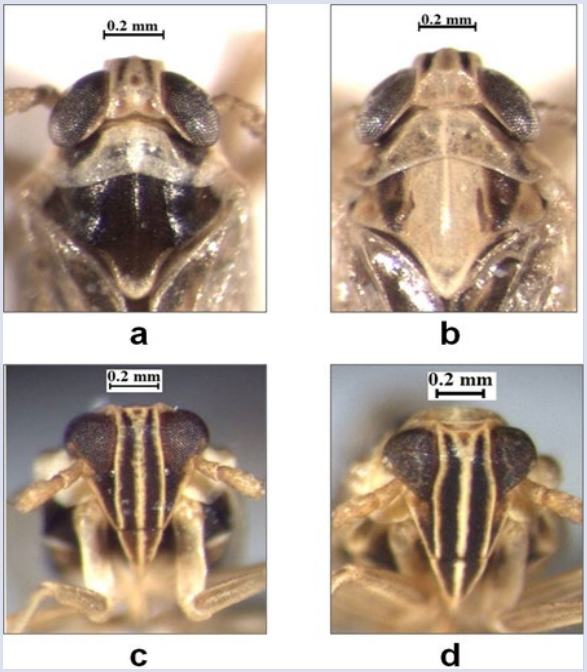

Figure 1. *L. striatella*, a, b) head, pronotum and mesonotum from dorsal (a: male, b: female), c, d) head from anterior (c: male, d: female).

According to the literature survey, no study was found on the variation in body size of Delphacidae family members based on elevation. For this reason, the study is original and may give useful information about both entomology and agriculture.

Materials and Methods

The *L. striatella* specimens were collected from three different localities with 50, 550 and 900 m. above sea level in the Central Black Sea Region, Turkey. Specimens were collected by sweep net in the daytime. Specimens were prepared according to standard methods and identified by comparing with the descriptions and figures given in Holzinger et al. [20]. Measurements of body length, body width, forewing length, forewing width (Figure 2a), head width, pronotum length, pronotum width, mesonotum length, mesonotum width, vertex length and vertex width (Figure 2b) were measured by Leica IM-50 module in Leica MZ 12.5 stereomicroscope. Statistical analyses were performed with SPSS 20.0 statistical software. Differences between measurements were determined by one-way ANOVA and Tukey post-hoc test. Relationships between measurements and altitude were examined by Pearson correlation. Materials were deposited in the collection of Suluova Vocational School, Amasya University, Turkey.

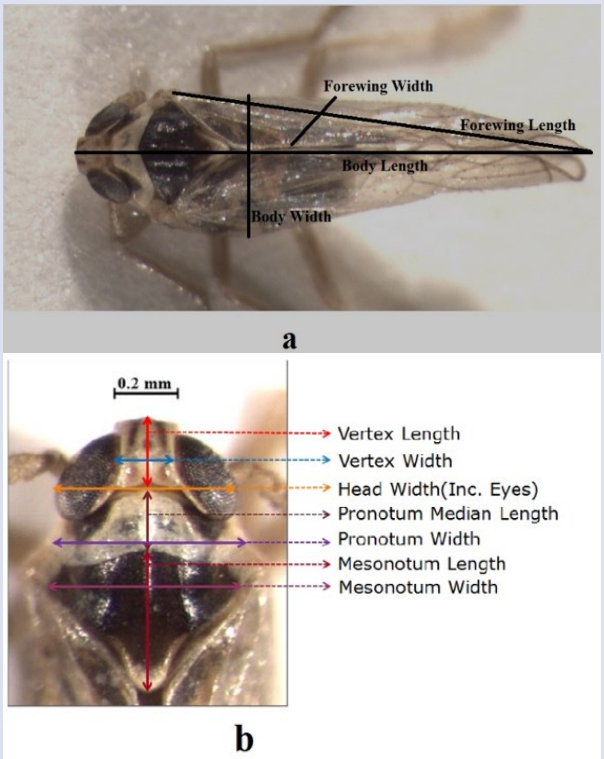

Figure 2. The measured body parts.

Results and Discussion

Results showed that, head width, pronotum length, pronotum width, mesonotum width and forewing width were significantly varied according to elevation (Table 1). There were not statistically significant differences in body, mesonotum, forewing, vertex length, and body and vertex width due to elevation. Measurements of these characters tended to decrease with increasing altitude (Figure 3). While the maximum values of body measurements were determined at 50 m, the minimum values are obtained at 900 m. Results showed that measurements of head width, pronotum length, pronotum width, mesonotum width and forewing width were obviously affected by elevation.

Declines in body measurements of L. striatella based on elevation may be caused by the influence of different

multiple ecological factors due to altitude. It is known that ecological factors such as temperature, wind speed, precipitation, vegetation composition and food quality differ by altitude. Environmental conditions in exposed habitat factors are important determinants for characteristics of organisms and may cause differences in features. It is known that temperature gradually decreases with increasing elevation. According to the temperature-size rule hypothesis, high temperature may promote growth rate and this result in smaller body size for adults. But findings of both our study and the some of the previous studies did not verify this rule. For example, in the studies on *Dichroplus pratensis* (Acrididae) [28], *Onthophagus* spp. (Scarabaeidae) [29] and *Paropsis atomaria* (Chrysomelidae) [30], decrease in body size were reported [1]. It was thought that this may be caused by combined effect of the exposed ecological factors and insect species. When we thought diversity of insects, the physiological differences among the insect species may be an important factor in this context. In addition, it should be explained that the results obtained from laboratory and natural areas also differed.

Table 1. ANOVA table of differences in measurements of body parts according to altitude (df: Degrees of freedom; F: F value; P: Significance)

Body Part	Sum of Squares	df	Mean Square	F	P
Body Length	0.196	2	0.098	1.887	0.202
Body Width	0.001	2	0.000	2.914	0.101
Head Width	0.020	2	0.010	10.505	**0.003**
Pronotum Length	0.003	2	0.002	6.005	**0.019**
Pronotum Width	0.056	2	0.028	30.341	**0.000**
Mesonotum Length	0.002	2	0.001	0.596	0.570
Mesonotum Width	0.049	2	0.025	17.874	**0.000**
Forewing Length	0.049	2	0.025	0.757	0.494
Forewing Width	0.058	2	0.029	10.602	**0.003**
Vertex Length	0.003	2	0.001	2.993	0.096
Vertex Width	0.001	2	0.000	2.914	0.101

Taking head width, pronotum width, mesonotum width and forewing width into account, it seems that, the major effective factor was wind speed (or airflows) in the light of previous studies [10]. As a contrast, Sullivan and Miller [31] reported that forewing length increased significantly with increasing altitude in the studied six species of Macrolepidoptera. Similar with the results of Sullivan and Miller [31] for Lepidoptera, Mikitová et al. [32] determined increased forewing lenght based on altitude for *Argynnis paphia* (Lepidoptera). Differences in the tendency of forewing length size based on altitude may be related with insect species, body size and structure for easy fly.

Except forewing length, the decreas in the measurements may be caused by temperature reduction and nutrient quality. Hodkinson [10] explained that variation in nutrient content of plants through altitude determines food quality and this may be effective on insect body measurements. The results of the current study showed that, size of some body parts of *L. striatella* decreased according to increasing altitude.

In the previous studies, altitude-related decrease in insect body size was reported by Sveum and Solem [9], Rodríguez-Jimenez and Sarmiento [12], Bernadou et al. [13], and reverse by Geraghty et al. [11], Osorio- Canadas et al. [15], Lozier et al. [33]. The studies which reported increase in body size with increasing altitude explained the results by Bergan's rule. In contrast, decrease in body size based on altitude also found in the other studies. For example, Brehm and Fiedler [34] expressed no or only weak support for Bergmann's rule. Furthermore, an opposite tendency was reported in Geometridae and Ourapterygini. Similar with our results, body size decreased with increasing altitude in Geometridae.

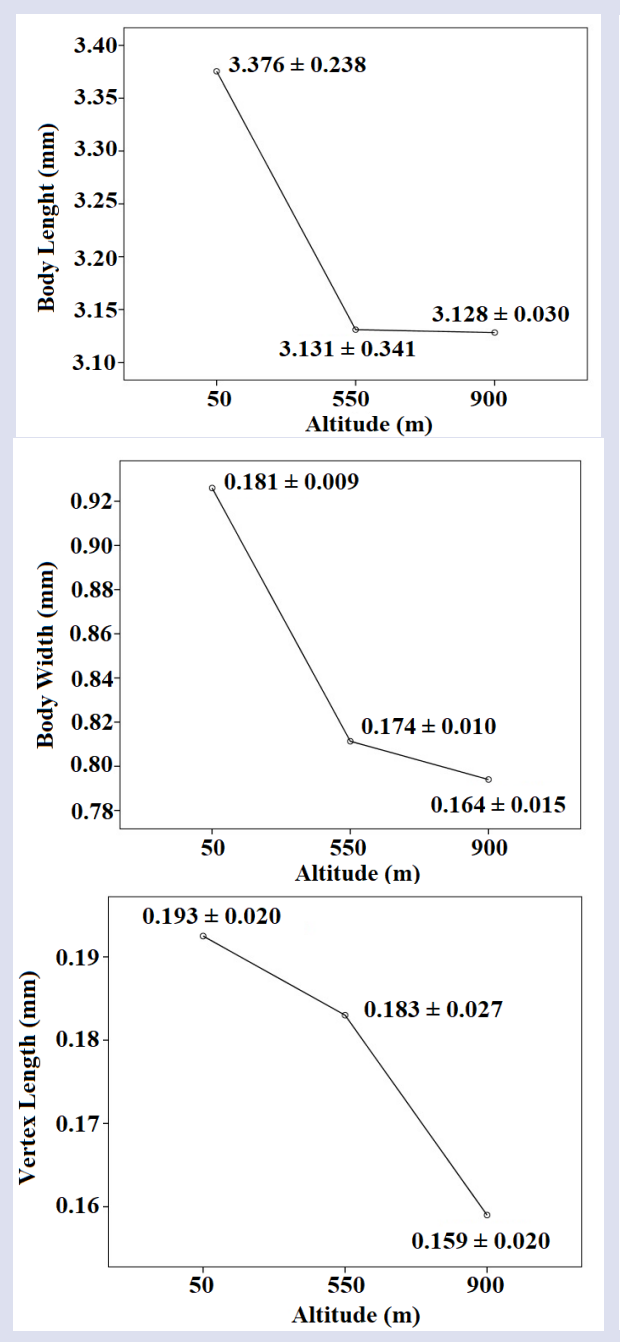

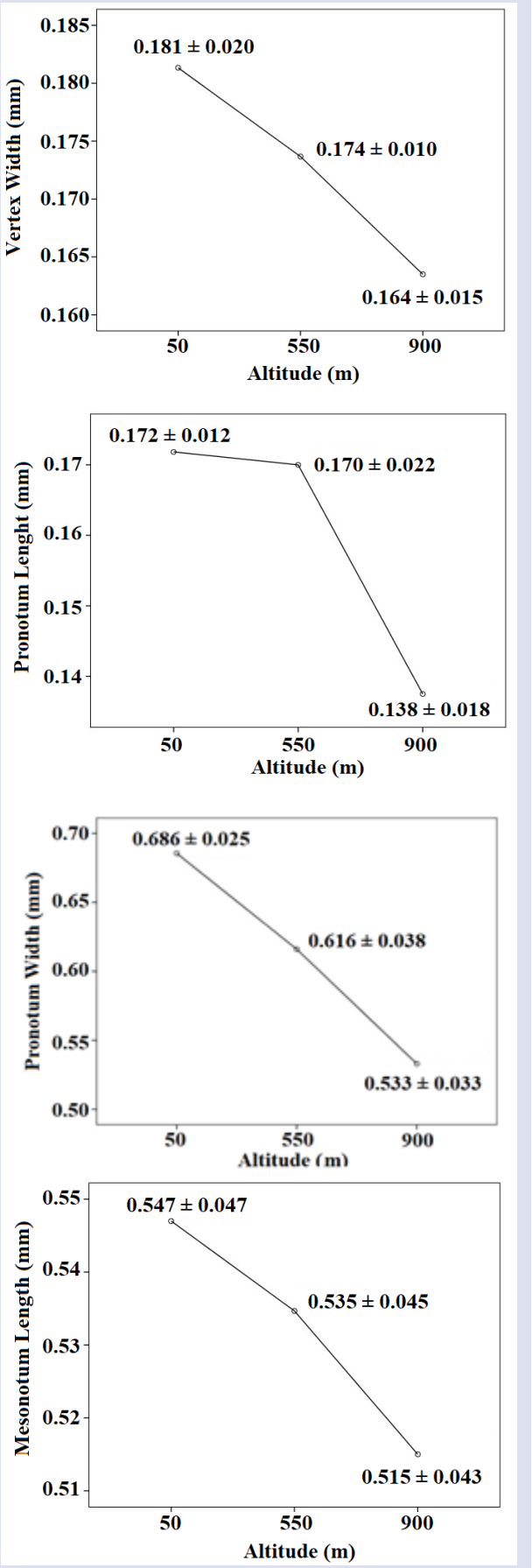

Figure 3. Mean values of measurement according to the altitude.

Significant relationships were determined between altitude and measurements of body width, head width, vertex length, vertex width, pronotum length, pronotum width, mesonotum width and forewing width (Table 2). These results verified the effect of altitude on insect body measurements.

Table 2. Relationships between measurements and altitude

Altitude	**Body length**	**Body width**	**Head width**	**Vertex length**	**Vertex width**	
	-0.477	-0.605**	-0.822**	-0.598*	-0.605*	
Altitude	**Pronotum length**	**Pronotum width**	**Mesonotum length**	**Mesonotum width**	**Forewing length**	**Forewing width**
	-0.673*	-0.926**	-0.324	-0.882**	-0.257	-0.816**

**. Correlation is significant at the 0.01 level (2-tailed).

*. Correlation is significant at the 0.05 level (2-tailed).

Conclusion

As a conclusion, results showed that except wing length, all the measurements of the body parts varied proportionally with increasing altitude. Head width, pronotum length, pronotum width, mesonotum width and forewing width significantly decreased with increasing altitude. Relationships were determined between measured body parts and altitude, and these results verify the effect of altitude on *L. striatella*. The altitude-related variations in insect body size derived from combined ecological factors such as temperature, precipitation, wind, vegetation composition, food quality. According to the previous studies it was thought that temperature is the most effective factor for this variation. Because the physiology and structure of the insects differ from species to species, effect of altitıude on body measurements considerably vary among insects.

There are different results about impacts of altitude on insect body size. Since there are very different results on the effects of altitude on insect body size, a clear judgment has not yet been reached. So, it is thought that detailed studies on various species from different ecosystems may be required to clarifying the effect of altitude on body measurements of insects.

Acknowledgment

This study was funded by Ondokuz Mayıs University Scientific Research Foundation (Project No: PYO.FEN.1904.09.013).

Conflicts of interest

The authors stated that did not have conflict of interests.

References

[1] Kang, N., Hu H., Huang Z., Luo, S., Guo S. Environmental Factors Drive Chalcid Body Size Increases with Altitudinal Gradients for Two Hyper-Diverse Taxa, *Insects*, 14 (1) (2023) 67.

[2] Peters R.H., The ecological implications of body size. Cambridge: Cambridge University Press, (1983).

[3] Schmidt-Nielsen K., Scaling. Why is animal size so important? Cambridge: Cambridge University Press, (1984).

[4] Roff D.A., The evolution of life histories: Theory and analysis. New York: Chapman and Hall, (1992).

[5] Stearns S.C., The evolution of life histories. Oxford: Oxford University Press, (1992).

[6] Gaston K.J., Blackburn T.M., Pattern and process in macroecology. Oxford: Blackwell Science, (2000).

[7] Blackburn T.M., Gaston K.J., Linking patterns in macroecology, J. *Anim. Ecol*., 70 (2) (2001) 338-352.

[8] Chown S.L., Klok C.J., Altitudinal body size clines: latitudinal effects associated with changing seasonality, *Ecography*, 26 (4) (2003) 445-455.

[9] Sveum, P., Solem, J.O. *Anaphes cultripennis* Debauché, 1948 (Hymenoptera, Mymaridae) in Norway. *Fauna Nor*., 27 (1980) 17–18.

[10] Hodkinson I.D., Terrestrial insects along elevation gradients: species and community responses to altitude, Biol. Rev., 80 (3) (2005) 489-513.

[11] Geraghty M.J., Dunn R.R., Sanders N.J. Body Size, Colony Size, and Range Size in Ants (Hymenoptera: Formicidae): Are Patterns along Elevational and Latitudinal Gradients Consistent with Bergmann's Rule?, *Myrmecol. News*, 10 (2007) 51–58.

[12] Rodríguez-Jimenez A., Sarmiento C.E. Altitudinal Distribution and Body Resource Allocation in a High Mountain Social Wasp (Hymenoptera: Vespidae), Neotrop, Entomol., 37 (2008) 1–7.

[13] Bernadou A., Römermann C., Gratiashvili N., Heinze J. Body Size but Not Colony Size Increases with Altitude in the Holarctic Ant, Leptothorax acervorum: Bergmann's Rule in a Holarctic Ant, *Ecol. Entomol*., 41 (2016) 733–736.

[14] Nowrouzi S., Andersen A.N., Bishop T.R., Robson S.K.A. Is Thermal Limitation the Primary Driver of Elevational Distributions? Not for Montane Rainforest Ants in the Australian Wet Tropics, *Oecologia*, 188 (2018) 333–342.

[15] Osorio-Canadas S., Flores-Hernández N., Sánchez-Ortiz T., Valiente-Banuet A. Changes in Bee Functional Traits at Community and Intraspecific Levels along an Elevational Gradient in a Mexical-Type Scrubland, *Oecologia*, 200 (2022) 145–158.

[16] Horne C.R., Hirst A.G., Atkinson D. Insect Temperature–Body Size Trends Common to Laboratory, Latitudinal and Seasonal Gradients Are Not Found across Altitudes, *Funct. Ecol.,* 32 (2018) 948–957.

[17] Beerli N., Bärtschi F., Ballesteros-Mejia L., Kitching I.J., Beck J. How Has the Environment Shaped Geographical Patterns of Insect Body Sizes? A Test of Hypotheses Using Sphingid Moths, *J. Biogeogr,* 46 (2019) 1687–1698.

[18] Asche M., Zur Phylogenie der Delphacidae Leach, 1815 (Homoptera, Cicadina, Fulgoromorpha), *Marburger Entomologische Publikationen*, 2 (1) (1985) 399-910.

[19] Asche M., Vizcayinae, a new subfamily of Delphacidae with revision of *Vizcaya* Muir (Homoptera: Fulgoroidea)-a significant phylogenetic link, *Bishop Museum Occasional Papers*, 30 (1990) 154-187.

[20] Holzinger W.E., Kammerlander I., Nickel H., The Auchenorrhyncha of Central Europe. Fulgoromorpha, Cicadomorpha excl. Cicadellidae. Leiden: Koninklijke Brill NV, (2003).

[21] Ossiannilsson F., The Auchenorrhyncha (Homoptera) of Fennoscandia and Denmark. Part 1: Introduction, infraorder Fulgoromorpha, *Fauna Entomologica Scandinavica*, 7 (1) (1978) 1-222.

[22] O'Brien L.B., Wilson S.W., Planthopper systematics and external morphology. In Nault L.R., Rodriguez J.G., (Eds). The Leafhoppers and Planthoppers, New York: John Wiley and Sons, (1985) 61-101.

[23] Kisimoto R., Genetic variation in the ability of a planthopper vector; *Laodelphax striatellus* (Fallén), to acquire the rice stripe virus, *Virology*, 32 (1) (1967) 144-152.

[24] Wilson M.R., Claridge M.F., Handbook for the identification of leafhoppers and planthoppers of rice, Wallingford: CAB International (1991).

[25] Yin X., Zheng F.Q., Tang W., Zhu Q.Q., Li X.D., Zhang, G.M., Liu H.T., Liu B.S., Genetic structure of rice black streaked dwarf virus populations in China, *Arch. Virol*., 158 (12) (2013) 2505-2515.

[26] Park J., Jung J.K., Koh Y.H., Park J., Seo B.Y., The complete mitochondrial genome of Laodelphax striatellus (Fallén, 1826) (Hemiptera: Delphacidae) collected in a mid-Western part of Korean peninsula, *Mitochondrial DNA Part B,* 4 (2) (2019) 2229-2230.

[27] Zhang S., Wang X., Gu F., Gong C., Chen L., Zhang Y., Hasnain A., Shen L., Jiang C., Sublethal Effects of Triflumezopyrim on Biological Traits and Detoxification Enzyme Activities in the Small Brown Planthopper *Laodelphax striatellus* (Hemiptera: Delphacidae), *Frontiers in Physiology*, 11 (261) (2020) 1-11.

[28] Bidau C.J., Martí D.A. Clinal Variation of Body Size in *Dichroplus pratensis* (Orthoptera: Acrididae): Inversion of Bergmann's and Rensch's Rules, *Ann. Entomol. Soc. Am.,* 100 (2007) 850–860.

[29] Salomão R.P., Arriaga-Jiménez A., Kohlmann B. The Relationship between Altitudinal Gradients, Diversity, and Body Size in a Dung Beetle (Coleoptera: Scarabaeinae: Onthophagus) Model System, *Can. J. Zool*., 99 (2021) 33–43.

[30] Schutze M.K., Clarke A.R. Converse Bergmann Cline in a *Eucalyptus* Herbivore, *Paropsis atomaria* Olivier (Coleoptera: Chrysomelidae): Phenotypic Plasticity or Local Adaptation?, *Glob. Ecol. Biogeogr*. 17 (2008) 424–431.

[31] Sullivan J.B., Miller W.E. Intraspecific body size variation in macrolepidoptera as related to altitude of capture site and seasonal generation, *Journal of the Lepidopterists Society,* 61 (2) (2007) 72-77.

[32] Mikitová B., Šemeláková M., Panigaj Ľ. Morphological variability of *Argynnis paphia* (Lepidoptera: Nymphalidae) across different environmental conditions in eastern Slovakia, *Biologia*, 76 (10) (2021) 2941-2956.

[33] Lozier J.D., Parsons Z.M., Rachoki L., Jackson J.M., Pimsler M.L., Oyen K.J., Strange J., Dillon M.E. Divergence in Body Mass, Wing Loading, and Population Structure Reveals Species-Specific and Potentially Adaptive Trait Variation Across Elevations in Montane Bumble Bees, *Insect Syst. Divers*., 5 (5) (2021) 3.

[34] Brehm G., Fiedler K. Bergmann's rule does not apply to geometrid moths along an elevational gradient in an Andean montane rain forest, *Global Ecology and Biogeography*, 13 (1) (2004) 7-14.

Cumhuriyet Sci. J., 44(1) (2023) 19-27
DOI: https://doi.org/10.17776/csj.1180547

Cumhuriyet Science Journal

| csj.cumhuriyet.edu.tr | Founded: 2002 ISSN: 2587-2680 e-ISSN: 2587-246X Publisher: Sivas Cumhuriyet University

The Effect of Two Different Botulinum Neurotoxin A On The Cortical Neuron Cells In Terms of Apoptosis and MMP 2, MMP 7, and MMP9 Localizations

Zeynep Deniz Şahin İnan [1,a,*], Zübeyda Akın Polat [2,b], Rasim Hamutoğlu [1,c]

[1] *Department of Histology-Embryology, Faculty of Medicine, Sivas Cumhuriyet University, Sivas, Türkiye.*
[2] *Department of Parasitology, Faculty of Medicine, Sivas Cumhuriyet University, Sivas, Türkiye.*
**Corresponding author*

Research Article

History
Received: 26/09/2022
Accepted: 14/03/2023

ABSTRACT

This study aimed to associate the possible cytotoxic and apoptotic effects of Botox (Allergan) and Dysport (Ipsen) and immunolocalization of matrix metalloproteinase (MMP) proteins with HCN2 cortical neuron cell line. Accordingly, cytotoxic potentials of Botox and Dysport were determined on different concentrations. Then, the apoptosis rates of these cells were evaluated by TUNEL method. MMP2, MMP7, and MMP9 proteins were also visualized using immunofluorescence method. There was a significant difference in cytotoxicity between those treated with 3.2, 6.4, and 12.8IU compared with the control. The Dysport 12.8 IU group was statistically more toxic than Botox group at the same concentration. Therefore, the number of apoptotic cells increased from 0.1 IU in Botox and 0.01 IU in Dysport groups compared to the control. The number of apoptotic cells was significantly higher in Dysport group at 1.6, 3.2, 6.4, and 12.8 IU concentrations than in Botox group. It was determined that MMPs increased gradually at the concentrations where the number of apoptotic cells was highest compared to the control group. As a result, we consider that it may be necessary to deal with the dose adjustment in Botox and Dysport applications, together with detailed studies to be carried out in the future.

Keywords: Apoptosis, Botulinum neurotoxin A, HCN2, MMP, TUNEL.

[a] *zinan@cumhuriyet.edu.tr* *https://orcid.org/0000-0002-0292-4448*
[b] *zakinpolat@cumhuriyet.edu.tr* *https://orcid.org/0000-0002-1130-4953*
[c] *rasim.hamutoglu@gmail.com* *https://orcid.org/0000-0002-2474-5336*

Introduction

Botulinal neurotoxins (BoNTs) are derived from an anaerobic bacteria of the genus *Clostridium*. They are neurotoxins that paralyze the nerves and prevent contraction of the related muscle. These toxins reduce the release of acetylcholine on the nerve terminals and inhibit neuromuscular connection. Seven similar subtypes (A, B, C, D, E, F, G) of BoNTs that act with the hyperactivity of cholinergic nerve terminals for a long time are described [1,2]. It has been shown that botulinum neurotoxin A (BoNTA) is widely preferred in clinical application. BoNTs have been used effectively in the treatment of many diseases [2]. However, some undesirable side effects might be seen, in addition to its therapeutic effects. These effects can be seen as excessive local muscle weakness or can be caused by the undesirable distribution of the toxin due to the diffusion of neurotoxin. The leakage of BoNT into the systemic circulation is known as Botulism, which can clinically stop the respiratory system and cause death [3]. However, these neurotoxins, which are used in many areas, including cosmetics, are administered to patients at clinically safe amounts at certain intervals or continuously. It is not known whether these neurotoxins, which are likely to enter the systemic bloodstream, will affect both the surrounding cells and brain cells in the long term [4].

Nowadays, three formulations of BoNTA are administered. These are Botox (Allergan, Irvine, California), Dysport (Ipsen, Slough, UK) and Xeomin (Merz Pharmaceuticals, Greensborough, North Carolina) [3]. BoNT treatment has a large safety precaution, and this is partly dependent on the ability of the toxin to remain localized at the injection site. The diffusion to nearby muscles is one of the most common side effects of this therapy. For example, in ptosis, known as eyelid drooping, sternocleidomastoid muscle transition may occur after the injection has made into the extraocular muscle. These undesirable effects are related to the local diffusion of BoNT [5]. However, it may show different migration/diffusion properties, depending on the different compositions of BoNTA. Botox and Dysport are structurally composed of a neurotoxin (150 kDa) and a non-toxic component (Dysport 300-900 kDa, Botox 900 kDa). It has been claimed that the diffusion of the neurotoxin into adjacent tissues is slower in those with high molecular weight due to its size [5]. A study was conducted to compare the diffusion of Botox and Dysport formulation in the mouse muscle tissue, and it was emphasized that two different formulations show limited diffusion to adjacent muscles in the diffusion region, but this spread is not significant [3]. Some studies have been conducted to compare the safe use of BoNTA formulations, but its effect on cortical neuron cells in different concentrations, including safe concentration ranges, is highly limited in the literature.

Evidence that the intramuscular BoNTA injection passes directly into the central nervous system is not yet available. However, several studies reported that BoNTA had an indirect effect on the central nervous system organization through the peripheral mechanism [4-7]. This toxin reported to spread through the bloodstream in *in vivo* studies. Studies on passing the blood-brain barrier at low therapeutic doses are quite limited [4]. However, it was emphasized that BoNTA affects the brain with motor afferent feedback and changes brain activity but could not pass the blood-brain barrier [8]. There is no study investigating the effect of BoNTAs on brain tissue cells comparatively, but in some culture studies, it has been stated that neurons show sensitivity to this toxin [9,10].

Apoptosis is a vital component of many events, such as normal cell cycle and embryonic development. Disorders occurring in this mechanism can cause uncontrolled processes and serious damage [11]. Matrix metalloproteinases (MMPs) are structures containing the zinc-dependent family of endopeptidases [12], which can break down the components of the extracellular matrix (ECM). MMPs normally play a role in the development of the nervous system, wound healing, and regulation of neuron or glial cell functions, or increasing their expression in cells during abnormal processes such as cancer. There are currently 24 different MMPs, and it has been reported that MMP2 and MMP9 are especially expressed from the neuron and glial cells of the brain, cerebellum, and hippocampus and their expression increases significantly in cases such as ischemia [12]. The balance of ECM components in cultured human adult neuron cells allows synapses of the neurons' extensions to occur regularly. In particular, the role of MMP2, MMP7 and MMP9 in synapse formation has been determined [12]. It is assumed that MMP1, MMP2, MMP9, and MMP13 in the nuclei of the brain, endothelial cells and cardiac myocytes regulate the activity of proteins involved in DNA repair and apoptosis [13].

Increased MMP expression in brain cells disrupts the blood-brain barrier. The disruption of the blood-brain barrier increases neuronal apoptosis [14,15]. Considering all these data, the relationship between the increased MMP2, MMP7, MMP9 localization in cells with cell apoptosis has not been fully evaluated, especially in the central nervous system pathologies in the literature.

There are many methods to detect apoptosis. TUNEL (Terminal dUTP Nick End Labeling) method is used to determine endonuclease cleavage products by enzymatically ending DNA strand breaks [16]. Terminal transferase is used to add labeled UTP to the 3 'end of DNA fragments. dUTP can then be examined under a light microscope or fluorescent microscope. Tests are available from various companies as kits. These tests also allow precise examination of fluorescence microscopy until the detection of a single cell [16]. In the present study, we aimed to evaluate the effect of Botox and Dysport application at different concentrations on HCN2 cortical neuron cells in terms of differences in apoptotic cell numbers. It was investigated whether these BoNTAs applied in different concentrations affected on the localization of MMP2, MMP7, and MMP9 in increasing apoptotic cell numbers. In this way, the safe range of these two commonly used BoNTA can be determined through the hyperpolarization-activated cyclic nucleotide-gated (HCN2) cortical neuron cells and lead to more reliable preferences in clinical practice.

Materials and Methods

Obtaining Botulinum Toxin type A

Botox (Allergan, Irvine, California) and Dysport (Ipsen, Slough, UK) were commercially obtained in 100 IU packs lyophilized. Toxins were prepared with Dulbecco's Modified Eagle's Medium (DMEM) at concentrations of 0.01, 0.1, 0.2, 0.4, 0.8, 1.6, 3.2, 6.4, 12.8 IU [17].

Cell Culture

In our study, HCN2 (ATCC ® CRL-10742 ™) cortical neuron cell line was used. These cells were reproduced in DMEM by adding Penicillin-streptomycin, L-glutamine, and Fetal Bovine Serum (FBS). Passages were created in order to maintain the continuity and viability of the HCN2 cell line to be used throughout the study, and passages 6th and 11th of the HCN2 cortical neuron cell series were used in our study [18].

Cytotoxicity Test

The XTT (2,3-bis (2-methoxy-4-nitro-5-sulfophenyl)-5-[(phenylamino) carbonyl]-2H-tetrazolium hydroxide) test (Roche) method was used to determine the cytotoxic potential of toxins. In the reaction of XTT solution with mitochondria of living or early-stage apoptosis cells, the tetrazolium ring in this solution breaks down by dehydrogenase enzymes in cell mitochondria to form colored formazan crystals. The intensity of the color formed with the reaction is directly related to the mitochondrial activity. Formazan crystal does not form in the presence of dead cells. In our study, cortical neuron cells were transferred into microplate wells to 100 µl of the suspension, which is 1x105/mL. Different concentrations of Botox and Dysport (0.01, 0.1, 0.2, 0.4, 0.8, 1.6, 3.2, 6.4 and 12.8 IU) were added to these cells after waiting for 4 hours for the cells to adhere and kept for 24 hours. 10 µl of XTT solution was added to the wells at the end of this period. After 2 hours of incubation, the wavelength was determined to be 570 nm and observed in microplate readers (Thermo Scientific, USA) [19].

Microscobe analysis

TUNEL assay

The TUNEL (Roche, Germany) procedure applied in our study was carried out as specified by the manufacturer. Briefly, the HCN2 cortical neuron cell line was seeded on sterile 18×18 coverslips placed in 6-well plates at 10×10^4 cells each well. Groups were then formed as outlined in the XTT cytotoxicity section, and the cells

were treated in the same way. The media on the coverslips was removed, washed twice with PBS, and air dry. Freshly prepared 4% paraformaldehyde/PBS (Sigma, Germany) was fixed at pH 7.4 at room temperature for 60 min and washed again with PBS. The cells were infused in freshly prepared Triton X-100 in 1% sodium citrate at 2–8°C for 2 min. Negative controls were treated with 50 µL label solution. The enzyme solution in the kit was mixed with the label solution and incubated. 10 min in micrococcal nuclease or DNase 1 recombinant solution (50 mM Tris–HCL, pH 7.5, 3000 U/mL-3 U/mL in 1 mg mL^{-1} BSA) to detect DNA breaks was suspended before applying the prepared mixture to the positive controls. Cells that had been passed through PBS twice were then applied to each sample with 50 µL of TUNEL blend solution (label and enzyme solution mixture) and incubated at 37°C in humid dark for 60 min. Groups were washed 3 times with PBS-Triton-X. The TUNEL was stained with 4'6'-diamidine-2-phenyl-indole dihydrochloride (DAPI) (200 nm mL^{-1}) for 5 min to observe nuclear morphology after staining. The cells were rewashed with PBS-Triton-X 100 and examined under a fluorescence microscope. The coverslip we placed under the culture plate on the slide was carefully inverted (Olympus BX51 Japan) [20].

Immunofluorescence labeling

Immunofluorescent staining was performed with monoclonal mouse anti-human MMP2, MMP7 and MMP9 primary antibodies to HCN2 cortical neuron cells treated with Botox and Dysport in 3 different concentration ranges (3.2 IU, 6.4 IU, 12.8 IU), which were statistically significant with TUNEL. Cells were grown on sterile 18×18 coverslips in 6-well culture dishes. Cells were purified from the medium and washed with phosphate-buffered saline (PBS) (Sigma Aldrich, Germany). Washed cells were fixed in pH 7.4% paraformaldehyde (Merk, Germany) for 10 minutes at the room temperature. It was washed 3 times with cold PBS after fixation. Subsequently, pH 6.5 Sodium Citrate buffer heated at 95°C was treated for 10 minutes to expose tissue antigen (Sigma Aldrich, Germany). Cells were washed 2 times with PBS for 5 minutes. Cells were incubated for permeabilization in 0.1% Triton ™ X-100 (Sigma Aldrich, Germany) solution for 10 minutes. Cells were then washed with PBS for 5 minutes. The Ultra V Block (Thermo Scientific, PBQ180830, USA) was dropped and incubated for 30 minutes at room temperature to prevent non-specific binding after washing. Then, the primary antibodies MMP2, MMP7, AND MMP9 (Santa Cruz Biotechnology) were instilled onto the cells. Cells were incubated overnight at +4°C in a dark and humid environment. At the end of the period, cells were washed twice with PBS for 5 minutes. Goat Anti-Mouse IgG H&L (Alexa Fluor® 488) (ab150113) (Abcam, USA) secondary antibody was used for primary antibody. Secondary antibody was diluted to 1:300 with antibody diluent reagent (Invitrogen, USA) and applied to the cells for 1 hour in a humidity chamber. Then, nuclear staining was carried out in 4'6'-diamidine-2-phenyl-indole dihydrochloride (DAPI) (200 nm/mL) for 5 min after washing with PBS. The coverslips in the culture dishes were removed and inverted on the slide. The results were analyzed by fluorescence microscopy (Olympus BX51, Japan) using appropriate filters followed by recording [19].

Statistical analysis

Apoptotic cells stained with the TUNEL method were counted under the microscope at 20× magnification from 5 independent regions. Apoptotic cell numbers were analyzed using the non-parametric Kruskal-Wallis test. Each group was compared with the other using the Dunn multiple comparison test.

All statistical analyses were performed using GraphPad Prism 6 (GraphPad Software, CA, USA). Each group was evaluated separately with each other using Mann-Whitney U, parametric one-way ANOVA was performed for comparing XTT results. $p < 0.05$ was considered significant.

Results

Different concentrations of Botox and Dysport 0.01, 0.1, 0.2.0.4, 0.8, 1.6, 3.2, 6.4 and 12.8 IU were applied to HCN2 cortical neurons, and the findings obtained after XTT analysis were evaluated with GraphPad Prism. Botox and Dysport 3.2, 6.4, 12.8 IU values were found to differ significantly compared to the control group. However, the Dsyport group 12.8 IU concentration value was significantly different from the Botox group in terms of cytotoxicity ($p < 0.05$) (Graph 1).

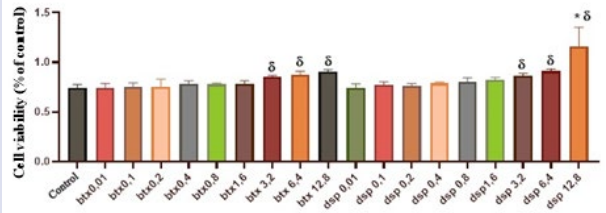

Graph 1. Graphical drawing of findings obtained from XTT analysis as a result of Botox and Dysport treatment at different concentrations to HCN2 cortical neurons with GraphPad Prism program. There is a difference in 3.2.6.4 and 12.8 IU values when the Botox and Dysport groups are compared with the control. The Dysport group differs significantly from the Botox group in terms of cytotoxicity at a concentration of 12.8 IU ($p < 0.05$).

Apoptosis cells were determined by applying in different concentrations of Botox and Dysport to HCN2 cortical neurons and marking them with TUNEL method. Apoptotic cells began to appear from a concentration of 0.1 IU in the Botox group and 0.01 IU in the Dysport group. Considering these cells labeling at similar concentrations, the number of apoptotic cells in the Dysport group is higher than in the Botox group. Apoptotic cell numbers increased in both groups as the concentration increased (Figure 1).

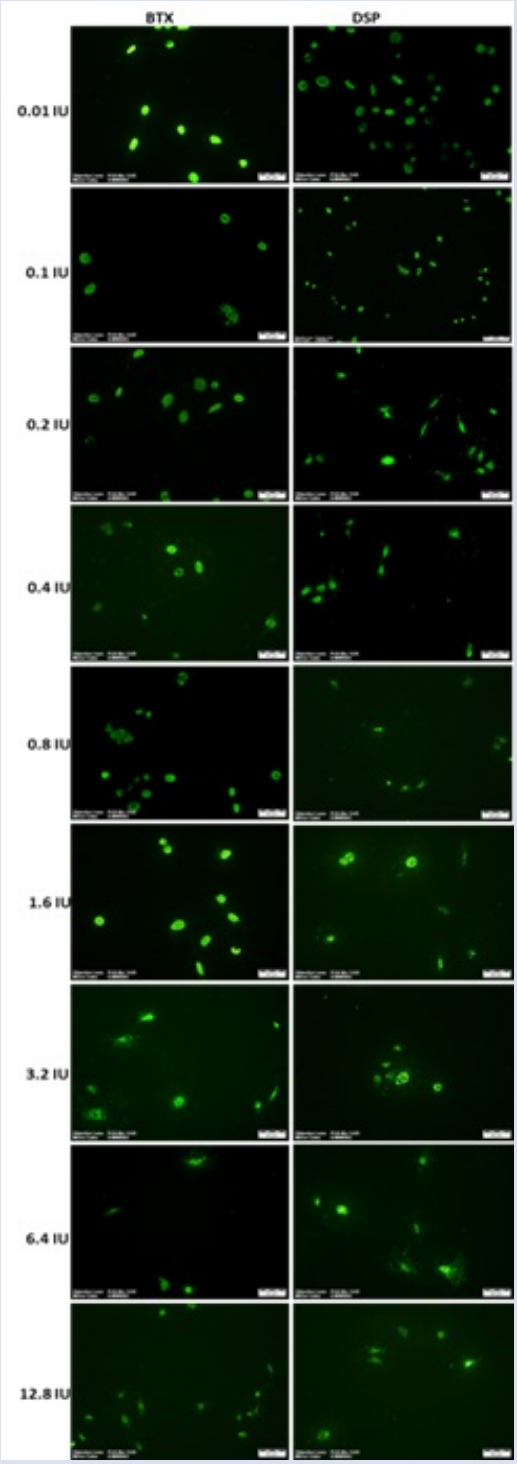

Figure 1. Fluorescence microscope image showing apoptosis cells by marking with TUNEL method as a result of Botox and Dysport treatment to the HCN2 cortical neurons at different concentrations. Apoptotic cells began to appear in the BTX group from 0.1 IU and in the DSP group from 0.01 IU concentration. As the amount of concentration increased, the number of apoptotic cells also increased (20x magnification).

The numbers obtained by applying different concentrations of Botox and Dysport to HCN2 cortical neurons and semi-quantitative scoring of apoptotic cells were evaluated in the GraphPad Prism program. The number of apoptotic cells began to increase from the concentration of Botox 0.1 IU and Dysport 0.01IU compared to the control group. In addition, Botox 6.4, 12.8 IU concentrations and Dysport 1.6, 3.2, 6.4, and 12.8 IU concentrations differ significantly in terms of cells leading to apoptosis ($p < 0.05$) (Graph 2).

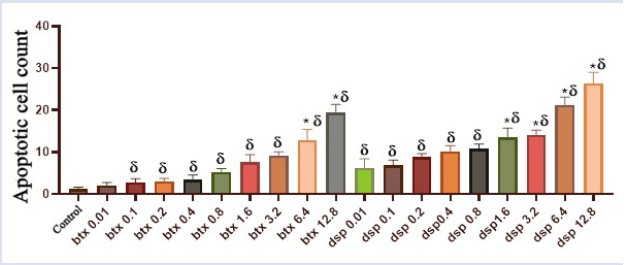

Graph 2. Graphical drawing of findings obtained by semi-quantitative scoring of apoptosis cells at different concentrations of Botox (btx) and Dysport (dsp) treatments to HCN2 cortical neurons with GraphPad Prism program.

In our study, the importance of MMP2, MMP7, and MMP9 was remarkable on the number of apoptotic cells in cortical neurons that increased with increasing concentration. Therefore, MMP antibodies were labeled with the immunofluorescence method in the concentration ranges where apoptotic cells increased significantly. As the concentrations of MMP2, MMP7, and MMP9 increased in Botox and Dysport groups, the nucleus and cytoplasmic MMP localization also increased, and this ratio was found to be higher in the Dysport group than the Botox group when semi-quantitative findings were evaluated (Figures 2-7).

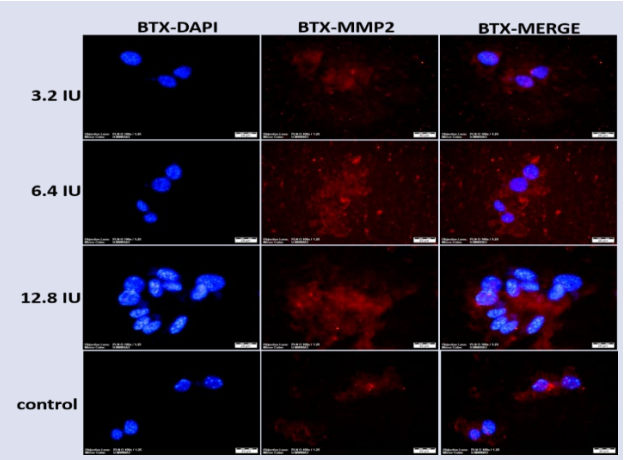

Figure 2. Immunofluorescence profile of HCN2 cortical neurons treated with Botox 3.2, 6.4, and 12.8 IU concentrations and stained with MMP2 primer antibody. The nuclei were stained by DAPI (blue). Cells were fixed in paraformaldehyde and examined under fluorescent microscope. Scale bar represents 20 µm.

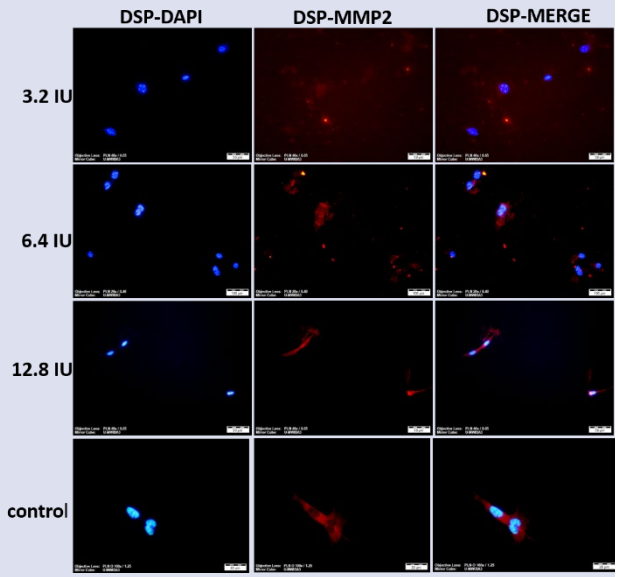

Figure 3. Immunofluorescence profile of HCN2 cortical neurons treated with Dysport 3.2, 6.4, and 12.8 IU concentrations and stained with MMP2 primer antibody. The nuclei were stained by DAPI (blue). Cells were fixed in paraformaldehyde and examined under fluorescent microscope. Scale bar represents 50 µm.

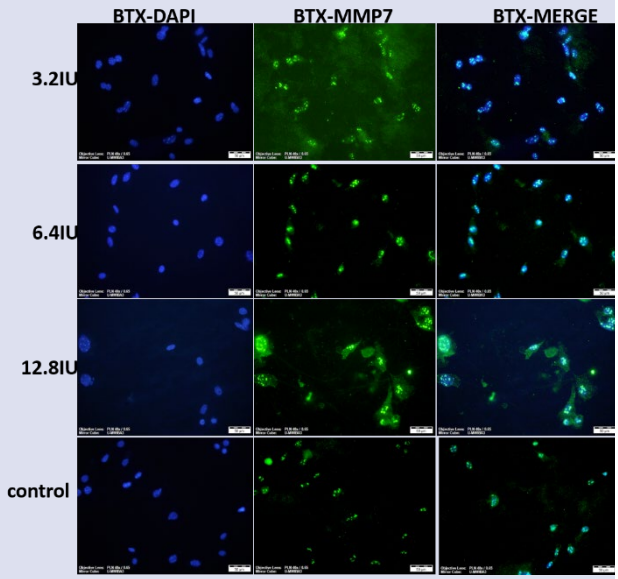

Figure 4. Immunofluorescence profile of HCN2 cortical neurons treated with Botox 3.2, 6.4, and 12.8 IU concentrations and stained with MMP7 primer antibody. The nuclei were stained by DAPI (blue). Cells were fixed in paraformaldehyde and examined under fluorescent microscope. Scale bar represents 50 µm.

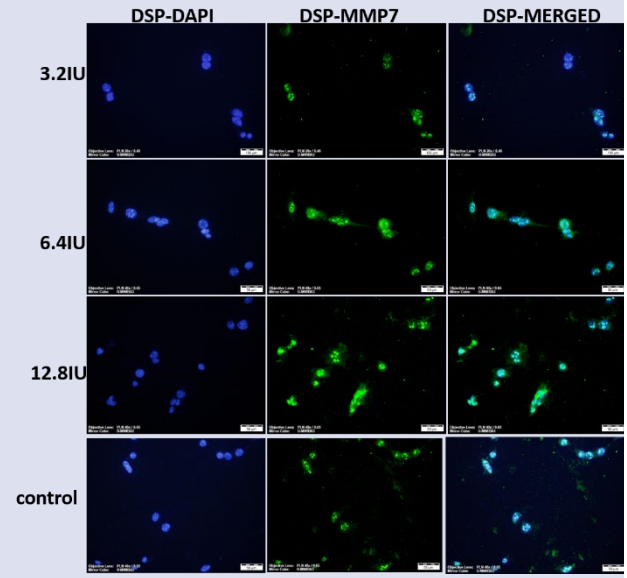

Figure 5. Immunofluorescence profile of HCN2 cortical neurons treated with Dysport 3.2, 6.4, and 12.8 IU concentrations and stained with MMP7 primer antibody. The nuclei were stained by DAPI (blue). Cells were fixed in paraformaldehyde and examined under fluorescent microscope. Scale bar represents 50 µm.

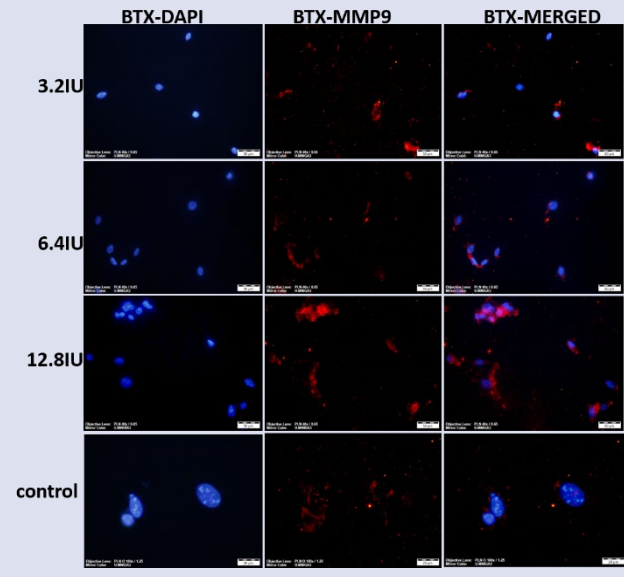

Figure 6. Immunofluorescence profile of HCN2 cortical neurons treated with Botox 3.2, 6.4, and 12.8 IU concentrations and stained with MMP9 primer antibody. The nuclei were stained by DAPI (blue). Cells were fixed in paraformaldehyde and examined under fluorescent microscope. Scale bar represents 50 µm.

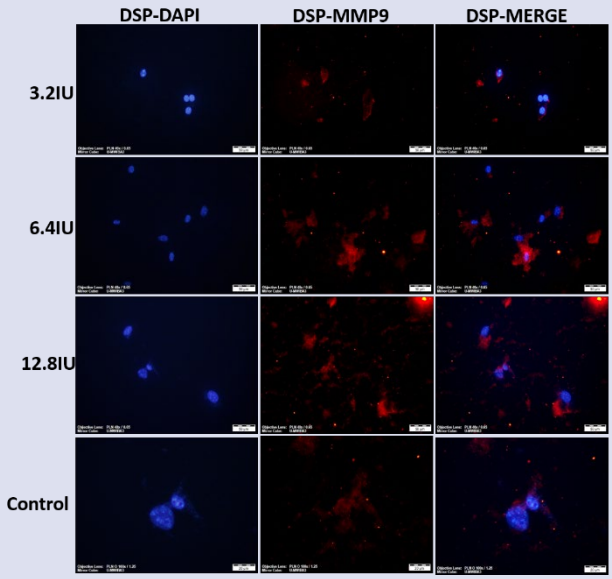

Figure 7. Immunofluorescence profile of HCN2 cortical neurons treated with Dysport 3.2, 6.4, and 12.8 IU concentrations and stained with MMP9 primer antibody. The nuclei were stained by DAPI (blue). Cells were fixed in paraformaldehyde and examined under fluorescent microscope. Scale bar represents 50 µm.

Discussion

Clostridium botulinum toxin type-A inhibits the release of acetylcholine (ACh) from stimulating pre-synaptic nerve terminals in peripheral neuromuscular junctions and the mechanism is still not fully understood [15]. BoNT consists of 7 types of neurotoxins, however, Type-A and Type-B toxins are mainly used in the clinic. BoNTA is used in medicine, especially in dermatology for various cosmetic disorders and also in the treatment of many diseases. The first type of BoNT presented is onabotulinum toxin A. It was proposed to be used as therapeutic by the Food and Drug Administration (FDA) in 2002 [21]. The second form of onabotulinum toxin A produced in France was licensed from the European Union for use for aesthetic purposes in 2006 and was approved by the FDA in 2009. BoNTA has been used for treatment in many fields, especially cosmetics [22].

Botox has a molecular mass of 900kDa and Dysport has a molecular mass of 300-900kDA. Both toxins contain the nuclear neurotoxin weighing 150 kDa and varying amounts and types of non-toxin accessory proteins. This situation changes the molecular weights and mechanisms of action of Botox and Dysport. This is expressed as bioavailability during clinical practice and therefore the neurotoxin load per hundred units varies. On the other hand, injection of a given dose of BoNT-A in a larger volume increases the area to which it initially diffuses, thus increasing the risk of excessive diffusion [23]. Possible negative effects that may occur due to the varying amount of toxin per injection and toxin load require looking at these frequently used toxins from a different place.

Local BoNT administration results in muscle paralysis or immobility of cholinergic glands. There is evidence that botulinum toxin is carried retrograde transport in the spinal cord through the motor and sensory nerves. However, there are no pathological signs or symptoms caused by the retrograde transport of botulinum toxin to the central nervous system. It is still known that the dose of Botox varies according to the type of BoNTA used and the area injected. There is no clear guideline for proper dosing. Botox must be diluted with sterile 0.9% saline before injection. In general, if the muscle is small in size, the injected solution should be more diluted. For example, several 0.1ml applications were proposed to different areas of the face and forehead for migraine treatment. In cervical dystonia patients, it varies up to 30-100 units and treatment is recommended several times, while in the clinic, this rate is 5-100 units [24]. The appropriate dose of Botox in the cosmetic field is between 20-40 units. In our literature research, we determined the dose range of Botox and Dysport applied to HCN2 cortical neurons as wide as 0.01, 0.1, 0.2, 0.4, 0.8, 1.6, 3.2, 6.4 and 12.8 IU concentrations. The effect of Botox and Dysport, which are frequently used in many areas in the clinic, on cytotoxic cortical neuron cells is not previously studied. In the study, a significant difference was found between the groups treated with 3.2, 6.4 and 12.8 IU in Botox and Dysport groups compared to the control in terms of cytotoxicity. However, Dysport 12.8 IU concentration is more significant than all other groups ($p < 0.05$).

Every cell in our body lives for a certain time and dies on time. There is a controlled balance between cell death and cell proliferation. Apoptosis is an event that is regulated by many complex internal and external mechanisms in which cells are self-destroying, regulated by genes, programmed, requiring RNA, protein synthesis and energy, and maintaining homeostasis in the organism. Different methods are used to determine and display apoptosis, and one of them is TUNEL method. Terminal deoxynucleotidyl transferase (TdT) mediated dNTP nick-end labeling (TUNEL) is often used to detect *in situ* cell death. DNA strand breaks in apoptotic cells can be identified by labeling the free 3p-OH terminus with altered nucleotides (fluorescein-labeled dNTP) in a TdT enzymatic reaction. It is one of the methods frequently used in the determination of cellular apoptosis especially in neurotoxicity studies [25]. In our study, after the application of Botox and Dsyport to HCN2 cortical neurons in different concentrations, apoptotic cells were stained by TUNEL method, and the number of cells obtained was compared with the control and each other. As a result of this comparison, an increase in apoptotic cells was observed from the concentration of 0.1 IU in the Botox group and the concentration of 0.01 IU in the Dysport group. In addition, apoptotic cells are significantly higher in the Dysport group at concentrations of 1.6, 3.2, 6.4 and 12.8 IU than the Botox group.

It has been reported in the literature that the use of BoNTAs is safe (lethal dose in humans can reach 50% (LD50) up to 40 U/kg BW). Therefore, it is stated that its use in cosmetics is particularly safer [26]. It has been reported that BoNTA does not cause permanent changes in nerve terminals and targeted muscles, therefore it cannot cause long-term adverse or side effects in the field of dermatology [26]. However, complications are rarely reported after the application of cosmetic Botox. The most common complications are ecchymosis and purpura at the injection sites [27]. These side effects can be prevented by simple clinical precautions [28]. On the other hand, in a case report, it was emphasized that sudden death developed in a patient who was given Botox, and this situation occurred after Botox treatment for cosmetic purposes and revealed that it was positive in terms of hypersensitivity tests in forensic medicine findings. In September 2005, the FDA reported that the use of Botox caused 28 deaths between 1989 and 2003, but none of them were directly linked to cosmetic use [29]. The most common local side effect is swelling or bruising at the injection site. Serious local reactions such as blurred vision, swelling, itching, and dry mouth have also been reported. It also causes headaches or flu-like symptoms as a systemic reaction. Moreover, severe findings such as urinary retention, difficulty breathing, difficulty swallowing, and dysphonia can be seen after Botox injection [30]. In addition to all these clinical findings, in a study by Wiegand et al. [6], it is stated that BoNTA is delivered to the spinal cord system by retrograde transport in an intramuscular injection. They stated that BoNTA, which was given by marking the cat gastrocnemius muscle, was moved first in the sciatic nerve, then in the ipsilateral spinal ventral roots, then in the spinal cord segments and some dorsal roots. This information suggests that BoNTA is moved over motor and intrafusal afferent axons. Neurophysiological techniques used in cats and other animals have been reported to occur with the movement of toxins into the alpha motor neuron soma membrane [6]. In addition, BoNTA was administered directly into the spinal cord in cats under anesthesia. In the study, it was stated that BoNTA reduced cholinergic transition to Renshaw cells and the function of inhibitory interneurons [7]. In studies conducted in the rat brain, it was found that BoNTAs are primarily bound to synaptosomes and the regions of the rat brain rich in synapses such as the hippocampus and cerebellum [31]. It has been reported that toxin is spread through the bloodstream in *in vivo* studies. Studies, in which it passes the blood-brain barrier at low therapeutic doses, are quite limited [4]. However, it was reported that BoNTA affects brain tissue with motor afferent feedback and changes brain activity but does not cross the blood-brain barrier [8]. In a study investigating the effect of botulinum neurotoxins on cells obtained from the embryonic rat dorsal root ganglia by primary culture, it has been reported that neurons show high sensitivity to toxins, and especially BoNTA significantly paralyzes synaptic transmission [9]. Similarly, there are findings in fetal mouse spinal cord neurons that especially BoNTA blocks neural transmission [32]. In another study, it was thought that BoNTC causes widespread synaptic damage in the central nervous system neurons, with the structural disruption of the neuron extensions, the disruption of the communication of the cells with each other, the loss of interneuron connections and eventually disappearing these cells by undergoing apoptosis process [10]. Similarly, in a study conducted by Zhao et al. [33] in *in vitro* and *in vivo*, mouse neurons exposed to BoNTC have degenerated. They stated that BoNTs can block synaptic vesicle exocytosis and cause damage to synapses and neurons. However, they did not report that BoNTAs caused a significant neuronal disorder [33]. In our study, it was determined that two different BoNTAs applied to HCN2 cortical neurons at different concentrations increased cytotoxicity and apoptotic cell number. We consider that Dysport undergoes more cells to apoptosis than Botox due to the molecular weight difference [23] especially at high concentrations.

Based on the potential peripheral leakage and the ability of BoNTs to reach neurons, we consider that the role of MMPs, known to regulate the brain matrix of neurons and glial cells, has gained more importance with the increase in apoptotic cell number of Botox and Dysport applied in different concentrations. It is known that MMP2, MMP7, MMP9 are especially related to the regulation of the brain extracellular matrix, DNA repair and apoptosis in the brain [21,22]. The MMP protein family primarily impairs the blood-brain barrier integrity [34]. In addition to neurons in the central nervous system, they are also expressed in endothelial cells in mammals and contribute to the blood-brain barrier integrity. Kanda et al. [14] stated that with the application of BoNTAs on Drosophila, it disrupts the blood-brain barrier with the increase of MMP2 expression.

Studies have shown that MMPs can degrade the nuclear matrix and poly (ADP-ribose) polymerase (PARP), which is one of the components of the nuclear matrix [35]. PARP is activated by single-stranded DNA breaks induced by peroxynitrite and is responsible for repairing single-stranded DNA breaks. Thus, PARP can be inactivated by MMPs via proteolytic cleavage. Inhibition of DNA repair can cause apoptosis, and excessive amounts of PARP also cause energy depletion of cells, resulting in apoptosis. It has been stated that apoptosis is induced in various tissues and cells by increasing the expression of MMP2, MMP7 and MMP9 [36]. Studies on the damage caused by Botox and Dysport on neurons are very few and controversial. In some histological and electron microscopic study findings, it is stated that Botox causes muscle atrophy by disrupting the thin structure of the muscle [37]. It has been stated that Botox treatment induces apoptosis in glioblastoma and neuroblastoma cells due to mitochondrial damage together with excessive ROS production [38]. Recently, it has been reported that the positive effects of Botox treatment especially on peripheral nerve damage and damage after

spinal cord injuries [39]. However, due to the long-term and continuous nature of these treatments, their possible effects on the neurons of the central nervous system cannot be ignored. In a study, it was emphasized that botulinum toxins cause intense degeneration in human primary neuron culture cell lines, not only in the perisynaptic areas of neurons, but also in their perikaryons [40]. The receptors are exposed to the toxin in cultured neurons because the neurons lack both the myelin sheath and the perineurium that normally surrounds peripheral nerves from the outside at their ends (the presynaptic terminals of the endplate). Thus, the toxin can cause more significant damage. It is still insufficient to explain the cause of death of healthy neurons by apoptosis at clinical concentrations recommended for therapy. However, the cells undergo apoptosis as a result of Botox and Dysport applied to healthy cortical neuron cells at various concentrations. Cells undergoing apoptosis were remarkably significant at 3.2, 6.4 and 12.8 IU Botox and Dysport concentrations. The toxin applied on healthy cells may have caused mitochondrial damage with the increase in the amount of intracellular ROS, as well as an increase in MMP2, MMP7, and MMP9 immunolocalizations. Studies can be developed and expanded, which may lead to dose limitations in the use of these toxins, which have a wide area of use.

Conflicts of interest

There are no conflicts of interest in this work.

Acknowledgments

The work was supported by grants from Sivas-Cumhuriyet University, Scientific Research Project under grant number T-756.

References

[1] Li Z., Lu J., Tan X., Wang R., Xu Q., Yu Y., Yang Z., Functional EL-HN Fragment as a Potent Candidate Vaccine for the Prevention of Botulinum Neurotoxin Serotype E, *Toxins*, 14 (2022) 135.

[2] Alberts T., Antipova V., Holzmann C., Hawlitschka A., Schmitt O., Kurth J., Stenzel J., Lindner T., Krause B.J., Wree A., Witt, M., Olfactory Bulb D2/D3 Receptor Availability after Intrastriatal Botulinum Neurotoxin-A Injection in a Unilateral 6-OHDA Rat Model of Parkinson's Disease, *Toxins*, 14 (2022) 94.

[3] Carlı L., Montecucco C., Rossetto O., Assay of diffusion of different Botulinum neurotoxin type A formulations injected in the mouse leg, *Muscle Nerve*, 40 (2009) 374-380.

[4] Curra A., Trompetto C., Abbruzzese G., Berardelli A., Central Effects of Botulinum Toxin Type A: Evidence and Supposition, *Movement Disorders*, 19 (8) (2004) 60-64.

[5] Aoki K.R., Ranoux D., Wissel J., Using translational medicine to understand clinical differences between botulinum toxin formulations, *Eur. J. Neurol*., 13 (4) (2006) 10–19.

[6] Wiegand H., Erdmann G., Wellhoner H.H., 125I-labelled botulinum A neurotoxin: pharmacokinetics in cats after intramuscular injection, *Naunyn Schmiedebergs Arch. Pharmacol*., 292 (1976) 161-165.

[7] Hagenah R., Benecke R., Wiegand H., Effects of type A botulinum toxin on the cholinergic transmission at spinal Renshaw cells and on the inhibitory action at Ia inhibitory interneurones, *Naunyn Schmiedebergs Arch. Pharmacol*., 299 (1977) 267-272.

[8] Boroff D.A., Chen G.S., On the question of permeability of the blood-brain barrier to BoNT, *Int. Arch. Allergy Appl. Immunol*., 48 (1975) 495-504.

[9] Welch M.J., Purkiss J.R., Foster K.A., Sensitivity of embryonic rat dorsal root ganglia neurons to *Clostridium botulinum* neurotoxins, *Toxicon*, 38 (2000) 245-258.

[10] Berliocchi L., Fava E., Leist M., Horvat V., Dinsdale D., Read D., Nico P., Botulinum neurotoxin C initiates two different programs for neurite degeneration and neuronal apoptosis, *J. Cell Biol*., 168 (2005) 607-618.

[11] Bertheloot D., Latz E., Franklin B.S., Necroptosis, pyroptosis and apoptosis: an intricate game of cell death, *Cel Mol. Immunol*., 18 (2021) 1106–1121.

[12] Gualdoni G., Castro G.G., Hernandez R., Barbeito C., Cebral E., Comparative matrix metalloproteinase-2 and -9 expression and activity during endotheliochorial and hemochorial trophoblastic invasiveness, *Tissue and Cell*, 74 (2022) 101698.

[13] Kwan J.A., Schulze C.J., Wang W., Leon H., Sariahmetoglu M., Sung M., Sawicka J., Sims D.E., Sawicki G., Schulz R., Matrix metalloproteinase-2 (MMP-2) is present in the nucleus of cardiac myocytes and is capable of cleaving poly (adp-ribose) polymerase (parp) *in vitro*, *FASEB J*., 18 (2004) 690-692.

[14] Kanda H., Shimamura R., Koizumi-Kitajima M., Okano H., Degradation of Extracellular Matrix by Matrix Metalloproteinase 2 Is Essential for the Establishment of the Blood-Brain Barrier in Drosophila, *iScience*, 16 (2019) 218-229.

[15] Wu M.Y., Gao F., Yang X.M., Qin X., Chen G.Z., Li D., Dang B.Q., Chen G., Matrix metalloproteinase-9 regulates the blood brain barrier via the hedgehog pathway in a rat model of traumatic brain injury, *Brain Res*., 727 (2020) 146553.

[16] Sharma R., Cakar Z., Agarwal A., TUNEL assay by benchtop flow cytometer in clinical laboratories. In: Zini A., Agarwal A., (Eds). A Clinician's guide to sperm DNA and chromatin damage. Berlin: Springer, (2018) 103–118.

[17] Pellett S., Progress in cell based assays for botulinum neurotoxin detection, *Curr. Top. Microbiol. Immunol.,* 364 (2013) 257–285.

[18] Bibi F., Ullah I., Ki, M.O., Naseer M.I., Metformin attenuate PTZ-induced apoptotic neurodegeneration in human cortical neuronal cells, *Pakistan Jjournal of Medical Sciences*, 33 (3) (2017) 581.

[19] Sozmen F., Kucukoflaz M., Ergul M., Inan Z.D.S., Bozkurt Y., Taydas D., Synthesis of Multifunctional Organic Nanoparticles Combining Photodynamic Therapy and Chemotherapeutic Drug Release, *Macromolecular Research*, 30 (1) (2022) 61-69.

[20] Sozmen F., Kucukoflaz M., Ergul M., Inan Z.D.S., Nanoparticles with PDT and PTT synergistic properties working with dual NIR-light source simultaneously, *RSC Advances*, 11 (4) (2021) 2383-2389.

[21] Awan K.H., The therapeutic usage of botulinum toxin (Botox) in non-cosmetic head and neck conditions–an evidence based review, *Saudi Pharm. J*., 25 (1) (2017) 18-24.

[22] Flynn T.C., Advances in the use of botulinum neurotoxins in facial esthetics, *J. Cosmet. Dermatol*., 11 (1) (2012) 42-50.

[23] Bhattacharjee K., Mehta A., Journey of a therapeutic poison: Botulinum toxin A and its biosimilars, *Indian J Ophthalmol*, 69 (10) (2021) 2568-2569.

[24] Ferguson K., Wolfgram N., Botulinum Toxin. In: Deer T., Pope J., Lamer T., Provenzano D., (Eds). Deer's Treatment of Pain. Cham: Springer, (2019) 163-169.

[25] Deng X., Wang Y., Chou J., Cadet J.L., Methamphetamine causes widespread apoptosis in the mouse brain: evidence from using an improved TUNEL histochemical method, *Mol. Brain Res*., 93 (1) (2001) 64-69.

[26] Hexsel C., Hexsel D., Porto M.D., Schilling J., Siega C., Botulinum toxin type A for aging face and aesthetic uses, *Dermatol. Ther*., 24 (1) (2011) 54-61.

[27] Ascher B., Talarico S., Cassuto D., Escobar S., Hexsel D., Jaen P., Monheit G.D., Rzany B., Viel M., International consensus recommendations on the aesthetic usage of botulinum toxin type A (Speywood Unit)–part II: wrinkles on the middle and lower face, neck and chest, *J. Eur. Acad. Dermatol. Venereol*., 24 (11) (2010) 1285–1295.

[28] Rzany B., Zielke H., Safety of botulinum toxin in aesthetic medicine. In: de Maio M., Rzany B., (Eds). Botulinum Toxin in Aesthetic Medicine. New York: Springer-Verlag Berlin Heidelberg, (2007) 19-25.

[29] Food and Drug Administration, How Drugs Are Developed and Approved. Available at: https://www.fda.gov/drugs/developmentapprovalprocess/howdrugsaredevelopedandapproved. 2019.

[30] Irvine C.A., BOTOX Cosmetic Product Information. BOTOX Cosmetic. Available at: http://www.allergan.com/products/medical_aesthetics/botox_cosmetic.htm. 2012.

[31] Kitamura M., Binding of botulinum neurotoxin to the synaptosome fraction of rat brain, *Naunyn Schmiedebergs Arch. Pharmacol*., 295 (1976) 171-175.

[32] Kellera J.E., Nealeb E.A., Oylerc G., Adler M., Persistence of botulinum neurotoxin action in cultured spinal cord cells, *FEBS Letters*, 456 (1999) 137-142.

[33] Zhao L.C., Yang B., Wang R., Lipton S.A., Zhang D., Type C botulinum toxin causes degeneration of motoneurons *in vivo*, *Neuroreport*, 21 (2010) 14-18.

[34] Ralf G.R., Anika M.S.H., Emma L.B.S., Brent S.S., Satya R.A., Erin L.A., Richard J.K., Anton P., Juli S., Björn B., Matrix Metalloproteinase-Mediated Blood-Brain Barrier Dysfunction in Epilepsy, *J. Neurosci*., 38 (18) (2018) 4301-4315.

[35] Kwan J.A., Schulze C.J., Wang W., Leon H., Sariahmetoglu M., Sung M., Savicka J., Sims D.E., Savicki G., Schulz R., Matrix metalloproteinase-2 (MMP-2) is present in the nucleus of cardiac myocytes and is capable of cleaving poly (ADP-ribose) polymerase (PARP) *in vitro*, *FASEB J*, 18 (2004) 690–692.

[36] Xie Y., Mustafa A., Yerzhan A. Merzhakupova D., Yerlan P., Orakov A.N., Wang X., Huang Y., Miao L., Nuclear matrix metalloproteinases: functions resemble the evolution from the intracellular to the extracellular compartment, *Cell Death Discov*., 3 (2017) 17036.

[37] Kocaelli H., Yaltirik M., Ayhan M., Aktar F., Atalay B., Yalcin S., Ultrastructural evaluation of intramuscular applied botulinum toxin type A in striated muscles of rats, *Hippokratia*, 20 (2016) 292–298.

[38] Akpınar O., Özşimşek A., Güzel M., Nazıroğlu M., *Clostridium botulinum* neurotoxin A induces apoptosis and mitochondrial oxidative stress via activation of TRPM2 channel signaling pathway in neuroblastoma and glioblastoma tumor cells, *Journal of Receptors and Signal Transduction*, 40 (6) (2020) 620-632.

[39] Luvisetto S., Botulinum Toxin and Neuronal Regeneration after Traumatic Injury of Central and Peripheral Nervous System, *Toxins*, 12 (7) (2020) 434.

[40] Kurokawa Y., Oguma K., Yokosawa N., Syuto B., Fukatsu R., Yamashita I., Binding and cytotoxic effects of Clostridium botulinum type A, C1 and E toxins in primary neuron cultures from foetal mouse brains, *Journal of General Microbiology*, 133 (9) (1987) 2647-2657.

Cumhuriyet Sci. J., 44(1) (2023) 28-35
DOI: https://doi.org/10.17776/csj.1196804

Cumhuriyet Science Journal

| csj.cumhuriyet.edu.tr | Founded: 2002 ISSN: 2587-2680 e-ISSN: 2587-246X Publisher: Sivas Cumhuriyet University

DNA Barcoding of Commercial Cockroaches in Turkey

Şeyda Berk [1,2,a,*], Ayşe Nur Pektaş [2,b]

[1] *Department of Molecular Biology and Genetics, Faculty of Science, Sivas Cumhuriyet University, Sivas, Türkiye.*
[2] *Advanced Technology Research Center (CUTAM), Sivas Cumhuriyet University, Sivas, Türkiye.*
**Corresponding author*

Research Article

History
Received: 31/10/2022
Accepted: 14/03/2023

ABSTRACT

Accurate species identification has become a precondition for accomplished biodiversity administration and further genetic research. Species acquaintance technics require molecular tools such as DNA barcoding as well as morphological identification for accurate identification. Particularly, the application of subunit I of the mitochondrial *cytochrome c oxidase (COI)* gene for DNA barcoding for insects has approved to be very useful in species acquaintance. The main aim of this study is to generate the first reference library of DNA barcode for cockroaches in Turkey using previously published data. As a result of the literature research, it has been observed that no study has been carried out on the DNA barcode of Turkish cockroaches. Therefore, in this study, we evaluated the advantage of DNA barcoding applied to two cockroach samples from Turkey for the first time. Our working samples implicated 10 DNA barcodes grounded on sequences created from our present study and 109 other DNA barcodes from BOLD. Various molecular analyzes including genetic distance-origin assessment (NeighborJoining and Maximum Likelihood trees) has been applied to accurately identify and describe species. In addition, *Blaptica dubia (B. dubia)* (Serville, 1838) and *Nauphoeta cinerea (N. cinerea)* (Olivier, 1789) have been reported as the first country records. It has been observed that reference libraries like BOLD are not yet sufficiently populated with *COI* sequences of Turkish cockroach species. In order for Turkish cockroach bio-assessment and biodiversity studies to benefit from the advantages of DNA barcoding, it is of great importance that cockroach inventories and taxonomic studies include DNA barcodes.

Keywords: *Blaptica dubia, Nauphoeta cinerea*, Cockroaches, DNA barcoding.

[a] *sberk@cumhuriyet.edu.tr* *https://orcid.org/0000-0003-4687-0223* [b] *aysenurpektas@cumhuriyet.edu.tr* *https://orcid.org/ 0000-0001-5621-2844*

Introduction

The concept of using DNA in taxonomic identification of species was first proposed by Hebert and Gregory [1]. The concept of DNA barcoding means "small standard DNA sequence" that can be used to distinguish species from one another. It is a technique based on PCR amplification of selected specific regions in the genome and used for species identification. Since the first barcoding study, over 6000 barcoding articles have been published [2]. The idea of a barcoding zone where species could distinguish life forms from one another was quickly adopted. Later, barcoding studies expanded with the idea that other organelle regions, markers and associated primer sets could also be used for barcoding [3].

For instance *MatK* for plants [4] and *rbcL* [5]; *ITS* for fungi [6] gene regions were used as barcode gene regions. Zoological DNA barcoding continues to grow as a popular way to identify animal specimens by similarity comparison of *cytochrome c oxidase subunit I (COI)* sequences of the mitochondrial genome [7-10]. The reasons why the *COI* region is a good barcode indicator; it does not contain insertions and deletions, is easy to isolate, has great differences between species although conserved, has a high copy number, relatively few differences within the species, does not contain introns, and the range of mutation rates in different regions of the molecule [11].

Essentially, barcoding includes two key elements, each as indirectly vital as the other in allowing precise identification through molecular characterization. These are the query and the target. The query is normally represented by a partial sequence of COIs of unknown origin (approximately 650 base pairs), while the target is a sequence of COIs located in a predetermined (typically by morphology and preferably species level) database or other repository. The purpose of DNA barcoding is to help recognize the diversity of species in our ecosystem, and species-level identification is crucial to achieving this goal [12].

Recently, those who do DNA barcoding have tried to create large-scale, carefully selected storage databases such as the Barcode Of Life Data System (BOLD), [10] and it serves securely because barcodes in databases are created in coordination with GenBank (NCBI). In addition, DNA barcoding offers the most convenient method for detecting cryptic species [13, 14].Moreover, differences at the molecular level also help to identify (marking) new species. Besides to the use of barcoding for sample identification, the fact that it can also be used in fields such as biosecurity, conservation biology, epidemiology and the food industry is proof that these studies should increase [12].

While the use of morphological data in the diagnosis and identification of insect species is a requirement in classical taxonomy, it is a time-consuming and species-specific method. However, DNA barcoding is a uniform

and practical techniques for insect species identification. It offers the opportunity to detect insect species at all developmental stages (egg, pupa, nymph, adult). It also works well in cases where morphological differentiation cannot be achieved. In addition, DNA barcoding is important for the rapid detection of invasive insect species. Diagnostic studies using the DNA barcoding approach have provided better solutions than other molecular techniques in terms of identifying new species and monitoring existing pest species. It is believed that the DNA barcoding technique can reliably resolve ecological and evolutionary connections in insect-host-plant relationships. In addition, DNA barcoding studies with flies are important in terms of human health and agriculture, especially in determining the vector-disease relationship [15].

Barcode data (*COI* gene region) has been entered for approximately 217,000 species from insect groups to date (September 2022) in the BOLD database and GenBank (NCBI) databases. Of these, about 76000 species are in the order Lepidoptera, 39000 species are in the order Hymenoptera and about 40000 species are in the order Coleoptera. The BOLD system (http://www.barcodinglife.org) has data for 1436 species from the order Blattodea (October 2022).

Cockroaches are a highly diverse group of insects, with over 4000 species commonly found worldwide [16]. Because cockroaches are capable of living in habitats containing various amounts of toxic substances, including environmental pollutants, microbial toxins, insecticides, it has been proposed as a good experimental model to study stress responses and detoxification abilities [17]. In addition, because cockroaches often live close to humans, they constitute an important reservoir for human pathogens. Therefore, they are of medical importance due to their potential to spread bacteria and other pathogens [18, 19]. Especially *N. cinerea* (Olivier, 1789) is important in that it is used as a model for correlations between sexual selection, bacterial infections, toxicology studies and metabolic rate and adaptation studies [20, 21]. The aim of this study is to investigate the suitability of DNA barcodes of commercially purchased *B. dubia* (Serville, 1838) and *N. cinerea* (Olivier, 1789) to identify cockroaches in Turkey and to create the first reference library of DNA barcode for cockroach species in Turkey using previously published data.

Material and Methods

Sample statement

Adults of *B. dubia* and *N. cinerea* (Blattodea: Blaberidae) were commercially obtained from a producer in Antalya/Turkey in February 2020 (https://www.antalyacekirge.net/). *B. dubia* and *N. cinerea* adults were brought to the laboratory by controlled storage in the RNAlater® (Qiagen) that is RNA stabilization reagent and stored at freezer (-20°C) until used in further experiments.

Total Genomic DNA Isolation, PCR Amplification and Sequencing

Total genomic DNA isolation from insect tissues was carried out with the sing a commercial DNA extraction kit (PureLink Genomic DNA Mini Kit, Invitrogen, USA) in accordance with the manufacturer's recommended protocol. Additional blank negative controls without tissue samples were used to exclude possible contamination during DNA isolation. All DNA samples were stored at -20 °C until further analysis. Universal *COI* barcode region primers, sequenced below, were used for amplification of the *COI* gene region [22].

LCO1490: 5'-GGTCAACAAATCATAAAGATATTGG-3'
HC02198: 5'-TAAACTTCAGGGTGACCAAAAAATCA-3'

With a final volume of 25 µL, the PCR mix contents are as follows: 2.5 µl 10X reaction buffer (KCL buffer), 1.25 µl (1.5 mM/µl) $MgCl_2$, 10pmol of each of the primers, 0.5 µl (0.2 mM) dNTPs, 5 U Taq DNA polymerase, and 1 µl (50 ng/µl) template DNA. PCR conditions for cockroaches' species included initial denaturation at 94 °C for 2 min; followed by 35 cycles of denaturation at 94 °C for 30 s, annealing at 51.3 °C for 1 min, extension at 72 °C for 2 min; and a final elongation at 72 °C for 10 min. PCR reactions were performed in a thermal cycler (T100, BioRad). Negative controls without a DNA template were included in all PCR runs. To ensure reproducibility and accuracy, PCR products were visualized by 1% agarose gel electrophoresis to assess success in amplification. By observing under UV transilluminator (Syngene), the presence of the expected amplicons was assessed by comparing with a standard DNA marker (Fermantas, EU).

After PCR anaysis, DNA sequencing was conducted by Macrogen through BMLabosis company. Sequence operations were performed bidirectionally with the primers in the PCR process. The files with the .ab1 extension obtained after this process were checked by reciprocating the forward and reverse sequences in the Geneious Prime program. After the Contig files were created, false peaks were corrected and BLAST scan was performed. These unique gene sequences have been uploaded to NCBI and Barcode of Life Data System (BOLD) databases (Supplementary data). Genbank accession numbers and BOLD accession numbers are shown in Table 1.

Bioinformatics and Phylogenetic Data Analysis

COI barcode region sequences were downloaded from 102 Blattodea orders from the NCBI gene bank to be used in phylogenetic analyzes and from 7 Mantodea orders to be used as outgroups. The accession numbers of the sequences are shown on the trees. A data set consisting of 119 sequences was obtained by combining all sequences. Sequence alignments were made in the MAFFT program. FASTA format was converted to NEXUS and PYHLIP formats by using ALTER alignment (http://www.sing-group.org/ALTER/) program so that the data can be used in different formats in phylogenetic analysis.

In order to obtain a tree with the maximum likelihood approach, BIC (Bayesian Information Criterion) and AICc (Akaike Information Criterion, corrected) values were determined by modeltesting in the MEGA 11 program, and the model was determined accordingly. Based on this model, PhyML and RaxML trees were constructed using the heuristic search method in the Geneious program. While creating the tree, Bootstrap (1000 bootstrap) method was used based on the Maximum likelihood method. The reproducibility of the measurement and its ability to give reliable and accurate results were effective in the selection of the Boostrap method. It also has applicability to all methods used for phylogenetic structuring and is able to assign probability-like repetition percentages to each possible part of the datasets in the branches of the resulting tree. The Boostrap method was preferred because it creates many new matrices with original dimensions and makes it possible to find the best tree for the analysis of each one, and the reliability of the branches in the tree is considered to be directly proportional to the frequency of branch exposure. In addition to these, giving information about how well the node to which the boostrap values belong is supported in terms of the model used in creating the phylogenetic tree has been another reason for the use of the method. Since it is aimed to establish a phylogenetic relationship in which phenetic characters are not used in the study; Maximum likelihood, which is a method that uses a clear criterion for the comparison of all possible trees and takes into account all possible trees in order to establish a relationship with the highest similarity in the trees created, to define and reveal the best one. The bootstrap discrimination power values are written on the branches. In addition, the evolutionary distance test based on the use of the Neighbor-joining evolution principle was carried out using the Kimura 2-Parameter (K2-P) model [23], which tests multiple displacements based on the characteristic that transitional nucleotide changes are higher than transversional changes in nature. All transitions and transversions are included in the nucleotide changes, and the value of "nst=6" is entered by choosing the gamma distribution for the variation between nucleotide positions.

Results and Discussion

Total DNA Quality

Figure 1. Image of PCR products produced with universal barcode primers in 1% agarose gel electrophoresis for the *COI* region. D1-D5: *B. dubia*, L1-L5*: N. cinerea*. M: marker

Mitochondrial *COI* gene barcode region was amplified by conventional PCR in five individuals of two cockroach species and PCR products were validated by running on 1% agarose gel. Band images were obtained in the correct gene region (~ 700bp) of all samples (Figure 1).

The Properties of DNA Sequence

The products obtained after PCR were sequenced and approximately 700 bp sequence was obtained, including the 658 bp barcode region. Barcode sequences of 696 bases for *B. dubia* (n=5) and 682 bases for *N. cinerea* (n=5) were created by editing the raw sequences in the Geneious Prime program. These sequences were uploaded to the NCBI GenBank system and BOLD systems and their accession numbers are given in Table 1. No deletion, insertion or stop codons were noted in the newly amplified sequences, indicating that the amplified sequences specify functional mitochondrial *COI* sequences. Overall, 99,5% sequence similarity was accomplished during the BLAST searching in the NCBI database. NJ tree-based identification via BOLD demonstrated cockroach species clustering in our study with other similar species in the database of *COI* sequences. This allowed these species to be defined precisely at the species level. The BIN analysis includes 10 BIN sets that are compatible with other barcode data in BOLD (Table 1). At the species level, BINs were determined in agreement with the morphology-based identification. Among these BINs, 5 (55%) are specified as the other 5 (18%), meaning that BIN refers to only one species (Table 1). BIN analyzes showed that the mean intraspecific distance of BIN varied between 0.18% and 0.55%, the maximum specific distance 0.62% and 0.61%, and the mean genetic distance to nearest neighbour 7.41 and 13.86 for *B. dubia* and *N. cinerea*, respectively (Table 1). For an exact resulting of *COI* genetic similarities, we merged our newly obtained *COI* sequence with *COI* sequences from other cockroach species in the BOLD system. Taken together, our dataset for phylogenetic analyzes included 102 individuals belonging to the order Blattodea. The approximately 700 bp *COI* sequence was aligned after the indeterminate bases were trimmed. Overall, GC percentages were recorded as 35% and 38% for *B. dubia* and *N. cinerea*, respectively (Table 1). All *COI* sequences were obtained heavily AT biased, with an average A+T content of 62.7%. Estimates of Evolutionary Divergence Between Sequences are shown in Table 2 and 3. The percentage of bases that are the same among *B. dubia* sequences is min. 98%, while for *N. cinerea* this ratio is 97%.

Table 1. Information of GenBank and BOLD database

Species	GenBank Accession No	BOLD ID	BIN URI	Average Distance in BIN (%)	Max Divergence in BIN (%)	Distance to NN (nearist neigbour) (%)	Marker Code	Sequence Length	GC %
Nauphoeta cinerea	MT861034	DLB006-20	BOLD:AAG9934	0.55 (p-dist)	1.61 (p-dist)	13.86 (p-dist)	COI-5P	682	37.2
Nauphoeta cinerea	MT861035	DLB007-20	BOLD:AAG9934					682	37.4
Nauphoeta cinerea	MT861036	DLB008-20	BOLD:AAG9934					682	37.2
Nauphoeta cinerea	MT861037	DLB009-20	BOLD:AAG9934					682	37.4
Nauphoeta cinerea	MT861038	DLB010-20	BOLD:AAG9934					682	37.4
Blaptica dubia	MT861039	DLB001-20	BOLD:ADC6507	0.18 (p-dist)	0.62 (p-dist)	7.41 (p-dist)		696	35.9
Blaptica dubia	MT861040	DLB002-20	BOLD:ADC6507					696	35.8
Blaptica dubia	MT861041	DLB003-20	BOLD:ADC6507					696	35.9
Blaptica dubia	MT861042	DLB004-20	BOLD:ADC6507					696	35.8
Blaptica dubia	MT861043	DLB005-20	BOLD:ADC6507					696	35.8

Table 2. Estimates of evolutionary divergence between sequences of *B. dubia*

	D1	D2	D3	D4	D5
D1		98.849	98.750	98.851	98.189
D2	98.849		98.886	98.499	98.464
D3	98.750	98.886		98.470	98.574
D4	98.851	98.499	98.470		98.082
D5	98.189	98.464	98.574	98.082	

Table 3. Estimates of evolutionary divergence between sequences of *N. cinerea*

	N1	N2	N3	N4	N5
N1		98.107	98.519	98.090	97.535
N2	98.107		98.796	98.629	98.277
N3	98.519	98.796		99.386	99.169
N4	98.090	98.629	99.386		98.886
N5	97.535	98.277	99.169	98.886	

Phylogenetic Analyses

In order to obtain trees with the maximum likelihood approach in phylogenetic analyses, first the model was determined. Accordingly, the results obtained are as in Table 4. On the basis of hierarchical likelihood-ratio tests as implemented in Modeltest 3.0, the model General Time Reversible (GTR) model + Gamma distribution + invariable sites were used (GTR + G + I, -lnL = 16,941.61, P < 0.001, AIC = 34,374.77, BIC = 36,642.61). The gamma distribution and proportion of invariant sites were set as 0.77 and 0.42 (estimated by Modeltest), respectively (Table 4).

The K2P/NJ tree, *COI* gene datasets, clustered individuals of the same species with high bootstrapping values (Figure 2). In our present study, most of the morphologically identified species formed distinct *COI* clusters that were well differentiated and supported by high bootstrapping values (Figure 2). When we look at the information given to us by the phylogenetic tree created by the NJ method, we see three main clades except the outgroups. *B. dubia* and *N. cinerea* individuals are located in different clades (Figure 2). Considering the branch values in the tree, considering the entire Blattodea order, this tree shows the accuracy of the barcoding work, although the distinction between species is not perfect within the clades. ML trees (1000bootsrap) created with the Maximum likelihood approach have patterned to support the NJ tree (Figure 3, 4). It supports the distinction between the 3 main clades subsets. The selection of outgroups in the Mantodea order increased the success of all trees (Figure 2-4).

Our study demonstrates the first cockroach DNA barcode analysis in Turkey containing mitochondrial COI gene sequences. In present study, the general achievement rate of DNA sequencing and barcode creation varies between 81.3 and 94.8%. These values represent the percentage of sequencing quality of unclipped bases in a sequence (a total of 20 forward and reverse reads for 10 samples).

The main purpose of this study is to show the compatibility of DNA barcodes for identification of cockroaches in Turkey and to create the first DNA barcode reference library for cockroaches in Turkey using previously published data. Tree-based identifying usage of ML and NJ techniques, particularly applicable to newly barcoded samples, demonstrated that both species were clearly determinable from all other species by the formation of distinct, non-overlapping *COI* clusters. When we compared species identification methods, our study showed that it is compatible with tree-based identification using ML and NJ technics. When we examine the DNA barcoding studies on cockroaches in the literature, Evangelista et al., used molecular identification using the *COI* DNA barcode gene to confirm that the new invasive insect species, *Periplaneta japonica* Karny, 1908, which does not conform to the typical morphology of the American cockroach *Periplaneta americana L* [24]. In another study by Farah Haziqah et al., they conducted research on *Blastocystis spp* infections. They collected a total of 151 cockroaches, mostly nymph and adult stages, from various residential species in the Malaysian state of Perak and Selangor, and reported that approximately half of the scanned cockroach gut contents were positive and determined that this infection was closely related to the host stage and housing types using DNA barcoding [25]. In a review by Miskelly and Paiero, it was reported that DNA barcodes are available for more than 60% of the species belonging to the order *Blattodea*, *Orthoptera, Dermaptera*, and *Phasmida* known to be found in Canada [26]. Liao et al., used *COI* DNA barcodes in Hainan Province, China to confirm sexual dimorphism occurring in the cockroach species, *Laevifaciesquadrialata gen. et sp.*

nov [27]. Von Beeren et al., analyzed mitochondrial DNA barcodes in American cockroach (*Periplaneta americana*) by collecting 284 cockroach samples from various states of America. *P. americana* barcode sequences formed a distinct monophyletic lineage from other *Periplaneta* species, and they found three distinct *P. americana* haplogroups between groups. They suggested that this genetic pattern likely reflects multiple introductions from genetically different source populations and subsequent interbreeding in the invasive range [28]. A new species of 2021 *Bundoksia lucañas* from China has been identified and Li et al. performed molecular identification by DNA barcoding with mitochondrial *COI* data to reveal relationships between *Bundoksialongissima sp. nov.* populations. They reported details of the female genitalia in addition to the known external morphology and male genitalia of this new species found [29]. Considering all these studies, DNA barcoding is important in determining the biodiversity of a country, determining the disease vector relationship in anthropophilic species, molecular identification of agriculturally important insects, determining the place of cryptic species in classical taxonomy and identifying new species. The first DNA barcoding records from cockroaches to NCBI and BOLD databases were made with this study. Molecular identification of these commercially available species was carried out in this study. These records in the database form the basis for future *COI* barcoding studies. It has been observed that reference libraries like BOLD do not yet contain information on the *COI* sequences of Turkish cockroach species. In order for the bio-assessment and biodiversity studies of Turkish cockroaches to benefit from the advantages of DNA barcoding, it is of great importance that the inventories and taxonomic studies of cockroaches include DNA barcodes.

Table 4. Maximum Likelihood fits of 24 different nucleotide substitution models

Model	#Param	BIC	AICc	lnL	Invariant	Gamma	R	Freq A	Freq T	Freq C	Freq G	A=>T	A=>C	A=>G	T=>A	T=>C	T=>G	C=>A	C=>T	C=>G	G=>A	G=>T	G=>C
GTR+G+I	245	36642.61192	34374.77342	-16941.6103	0.4156809	0.771571429	2.52581738	0.306124546	0.322370195	0.203821901	0.167683358	0.08	0.01	0.05	0.08	0.23	0	0.01	0.37	0.03	0.09	0.01	0.04
GTR+G	244	36801.84756	34543.25924	-17026.85953	n/a	0.298374522	2.7181121	0.306124546	0.322370195	0.203821901	0.167683358	0.07	0.01	0.04	0.07	0.24	0	0.01	0.38	0.04	0.08	0.01	0.05
TN93+G	242	36987.60595	34747.51814	-17131.00154	0.419021182	0.794629732	2.02144266	0.306124546	0.322370195	0.203821901	0.167683358	0.05	0.03	0.06	0.05	0.2	0.03	0.05	0.31	0.03	0.11	0.05	0.03
TN93+G	241	37206.64976	34975.81228	-17246.15486	n/a	0.334693965	1.8457286	0.306124546	0.322370195	0.203821901	0.167683358	0.06	0.04	0.06	0.05	0.19	0.03	0.05	0.29	0.03	0.12	0.06	0.04
HKY+G+	241	37389.86874	35159.03127	-17337.76435	0.428963016	0.816970799	2.24549667	0.306124546	0.322370195	0.203821901	0.167683358	0.05	0.03	0.12	0.05	0.14	0.02	0.05	0.23	0.02	0.22	0.05	0.03
T92+G+I	239	37564.49977	35352.16312	-17436.34269	0.429664807	0.822659706	2.21482764	0.314247371	0.314247371	0.185752629	0.185752629	0.05	0.03	0.13	0.05	0.13	0.03	0.05	0.22	0.03	0.22	0.05	0.03
HKY+G	240	37632.26109	35410.674	-17464.59194	n/a	0.354104454	2.02569462	0.306124546	0.322370195	0.203821901	0.167683358	0.05	0.03	0.11	0.05	0.14	0.03	0.05	0.22	0.03	0.21	0.05	0.03
T92+G	238	37818.01563	35614.92946	-17568.73203	n/a	0.359260404	1.96345054	0.314247371	0.314247371	0.185752629	0.185752629	0.05	0.03	0.13	0.05	0.13	0.03	0.05	0.21	0.03	0.21	0.05	0.03
GTR+I	244	38420.48621	36161.8979	-17836.17886	0.452345793	n/a	1.90651637	0.306124546	0.322370195	0.203821901	0.167683358	0.11	0.03	0.07	0.1	0.19	0	0.04	0.31	0.01	0.13	0.01	0.01
K2+G+I	238	38599.1877	36396.10153	-17959.31806	0.436419573	0.989560432	2.0874251	0.25	0.25	0.25	0.25	0.04	0.04	0.17	0.04	0.17	0.04	0.04	0.17	0.04	0.17	0.04	0.04
K2+G	237	38672.94286	36479.10723	-18001.82705	n/a	0.271724165	1.83970723	0.25	0.25	0.25	0.25	0.04	0.04	0.16	0.04	0.16	0.04	0.04	0.16	0.04	0.16	0.04	0.04
TN93+I	241	39091.9442	36861.10673	-18188.80208	0.451613299	n/a	1.7198867	0.306124546	0.322370195	0.203821901	0.167683358	0.06	0.04	0.06	0.06	0.18	0.03	0.06	0.28	0.03	0.12	0.06	0.04
HKY+I	240	39409.94038	37188.35329	-18353.43158	0.445714872	n/a	1.67024548	0.306124546	0.322370195	0.203821901	0.167683358	0.06	0.04	0.11	0.06	0.13	0.03	0.06	0.21	0.03	0.2	0.06	0.04
T92+I	238	39557.78066	37354.69449	-18438.61454	0.451371089	n/a	1.6630279	0.314247371	0.314247371	0.185752629	0.185752629	0.06	0.03	0.12	0.06	0.12	0.03	0.06	0.2	0.03	0.2	0.06	0.03
JC+G+I	237	39674.12233	37480.2867	-18502.41679	0.433418551	1.12460805	0.5	0.25	0.25	0.25	0.25	0.08	0.08	0.08	0.08	0.08	0.08	0.08	0.08	0.08	0.08	0.08	0.08
JC+G	236	39735.92002	37551.33499	-18538.94705	n/a	0.270083466	0.5	0.25	0.25	0.25	0.25	0.08	0.08	0.08	0.08	0.08	0.08	0.08	0.08	0.08	0.08	0.08	0.08
K2+I	237	40234.18256	38040.34694	-18782.44691	0.45106856	n/a	1.49767968	0.25	0.25	0.25	0.25	0.05	0.05	0.15	0.05	0.15	0.05	0.05	0.15	0.05	0.15	0.05	0.05
JC+I	236	41254.31454	39069.72951	-19298.14431	0.45264965	n/a	0.5	0.25	0.25	0.25	0.25	0.08	0.08	0.08	0.08	0.08	0.08	0.08	0.08	0.08	0.08	0.08	0.08
GTR	243	43187.63347	40938.29538	-20225.38389	n/a	n/a	1.47827418	0.306124546	0.322370195	0.203821901	0.167683358	0.13	0.03	0.07	0.12	0.18	0	0.05	0.28	0	0.12	0.01	0.01
TN93	240	44194.81603	41973.22894	-20745.86941	n/a	n/a	1.46373195	0.306124546	0.322370195	0.203821901	0.167683358	0.06	0.04	0.06	0.06	0.17	0.03	0.06	0.26	0.03	0.11	0.06	0.04
HKY	239	44512.24136	42299.90471	-20910.21348	n/a	n/a	1.43248236	0.306124546	0.322370195	0.203821901	0.167683358	0.06	0.04	0.1	0.06	0.12	0.03	0.06	0.19	0.03	0.18	0.06	0.04
T92	237	44647.91347	42454.07785	-20989.31236	n/a	n/a	1.43214119	0.314247371	0.314247371	0.185752629	0.185752629	0.06	0.04	0.11	0.06	0.11	0.04	0.06	0.19	0.04	0.19	0.06	0.04
K2	236	44983.71947	42799.13444	-21162.84677	n/a	n/a	1.60385748	0.25	0.25	0.25	0.25	0.05	0.05	0.15	0.05	0.15	0.05	0.05	0.15	0.05	0.15	0.05	0.05
JC	235	45938.14175	43762.80736	-21645.68932	n/a	n/a	0.5	0.25	0.25	0.25	0.25	0.08	0.08	0.08	0.08	0.08	0.08	0.08	0.08	0.08	0.08	0.08	0.08

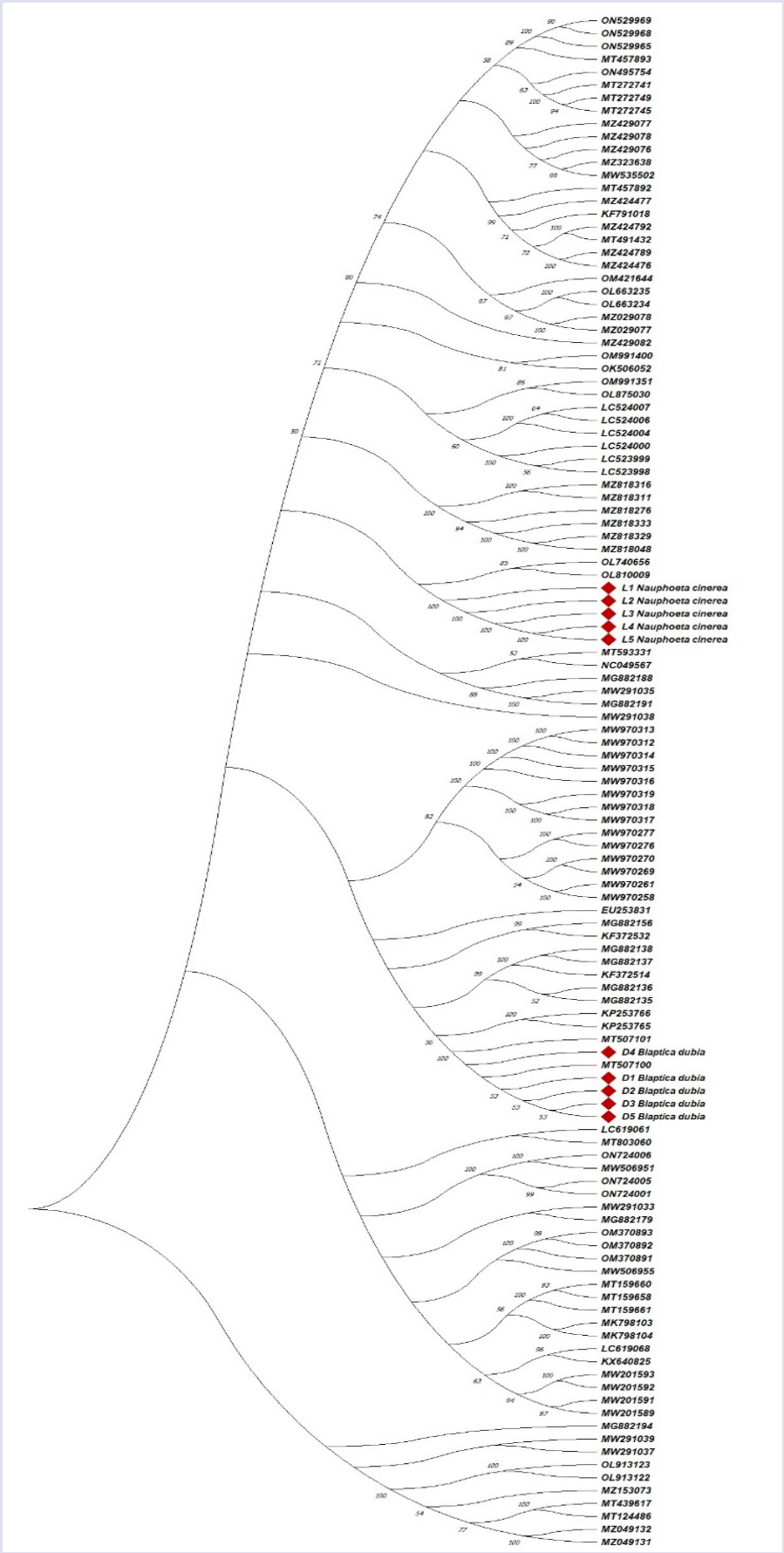

Figure 2. K2P/Neighbour-Joining (NJ) tree with bootstrap support (1000 replicates) showing clustering of species for *COI* sequences. Red nodes are the sequences obtained in this study.

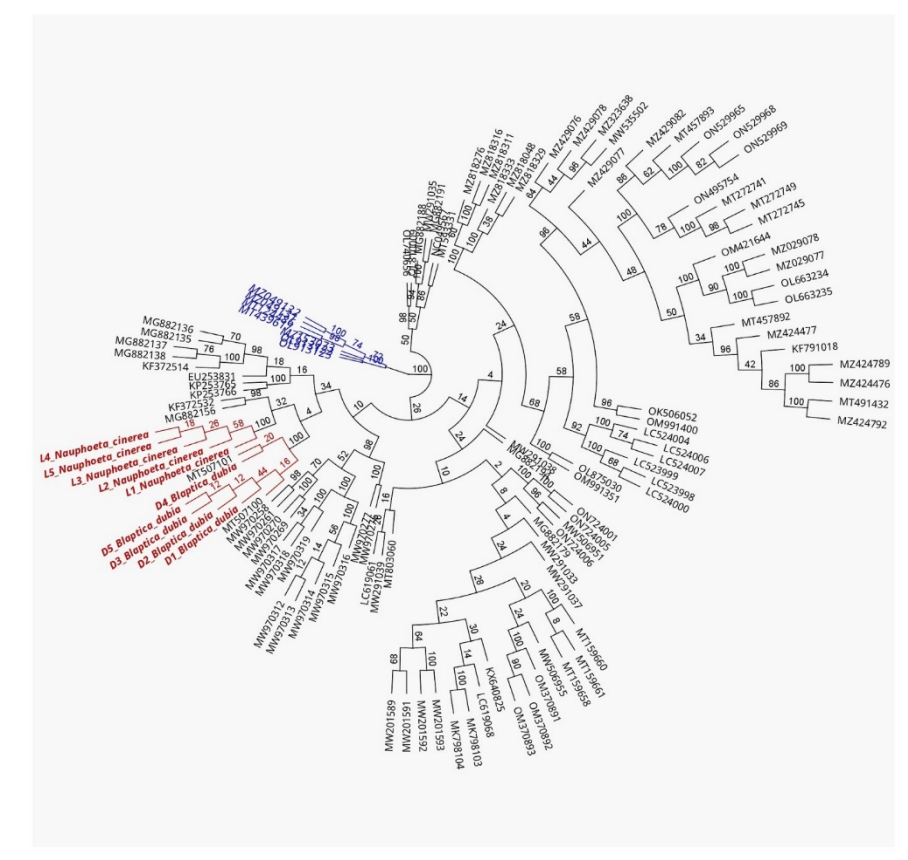

Figure 3. Mitochondrial *COI* barcode Maximum likelihood (PhyML) tree. In the tree obtained by bootstrap method, branch values are shown above. Sequences obtained in this study are shown in red and outgroup in blue.

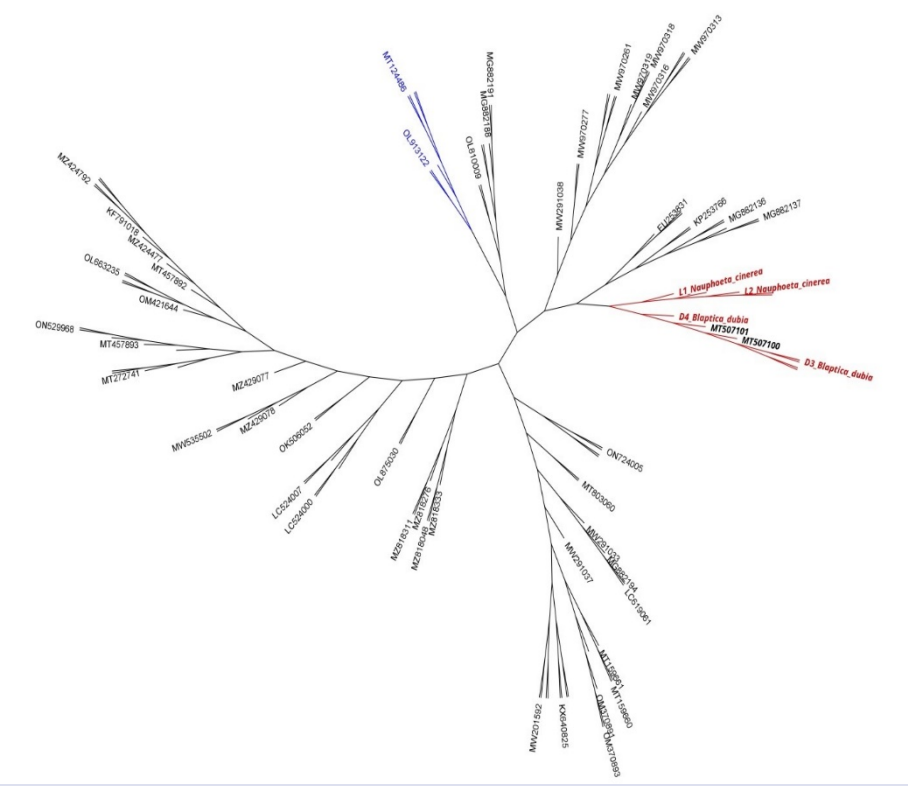

Figure 4. Mitochondrial *COI* barcode Maximum likelihood (RaxML). Sequences obtained in this study are shown in red and outgroup in blue.

Acknowledgment

All analyses in this study were performed in the Molecular Biology laboratory of the Sivas Cumhuriyet University Advanced Technology and Research Center (CUTAM).

Conflict of Interest

The authors state that did not have conflict of interests

References

[1] Hebert P.D., Gregory T.R. The promise of DNA barcoding for taxonomy, *Syst. Biol.,* 54 (2005) 852-859.

[2] Dormontt E.E., Van Dijk K.-J., Bell K.L., Biffin E., Breed M.F., Byrne M., Caddy-Retalic S., Encinas-Viso F., Nevill P.G., Shapcott A. Advancing DNA barcoding and metabarcoding applications for plants requires systematic analysis of herbarium collections—an Australian perspective, *Front. Ecol. Evol. FRONT ECOL EVOL.,* 6 (2018) 134.

[3] Bohmann K., Mirarab S., Bafna V., Gilbert M.T.P. Beyond DNA barcoding: The unrealized potential of genome skim data in sample identification, *Wiley Online Library*, 2020.

[4] Lahaye R., Van der Bank M., Bogarin D., Warner J., Pupulin F., Gigot G., Maurin O., Duthoit S., Barraclough T.G., Savolainen V. DNA barcoding the floras of biodiversity hotspots, *PNAS.*, 105 (2008) 2923-2928.

[5] Fazekas A.J., Burgess K.S., Kesanakurti P.R., Graham S.W., Newmaster S.G., Husband B.C., Percy D.M., Hajibabaei M., Barrett S.C. Multiple multilocus DNA barcodes from the plastid genome discriminate plant species equally well, *PloS one.*, 3 (2008) e2802.

[6] Schoch C.L., Seifert K.A., Huhndorf S., Robert V., Spouge J.L., Levesque C.A., Chen W., Consortium F.B., List F.B.C.A., Bolchacova E. Nuclear ribosomal internal transcribed spacer (ITS) region as a universal DNA barcode marker for Fungi, *PNAS.*, 109 (2012) 6241-6246.

[7] Hebert P.D., Cywinska A., Ball S.L., DeWaard J.R. Biological identifications through DNA barcodes, *Proc. R. Soc. B: Biol.*, 270 (2003) 313-321.

[8] Hebert P.D., Penton E.H., Burns J.M., Janzen D.H., Hallwachs W. Ten species in one: DNA barcoding reveals cryptic species in the neotropical skipper butterfly Astraptes fulgerator, *PNAS.*, 101 (2004) 14812-14817.

[9] Hajibabaei M., Janzen D.H., Burns J.M., Hallwachs W., Hebert P.D. DNA barcodes distinguish species of tropical Lepidoptera, *PNAS.*, 103 (2006) 968-971.

[10] Ratnasingham S., Hebert P.D. BOLD: The Barcode of Life Data System (http://www.barcodinglife.org), *Mol. Ecol. Notes.*, 7 (2007) 355-364.

[11] Elyasigorji Z., Izadpanah M., Hadi F., Zare M. Mitochondrial genes as strong molecular markers for species identification, *The Nucleus*, (2022).

[12] Kvist S. Barcoding in the dark? A critical view of the sufficiency of zoological DNA barcoding databases and a plea for broader integration of taxonomic knowledge, *Mol. Phylogenet Evol.*, 69 (2013) 39-45.

[13] Witt J.D., Threloff D.L., Hebert P.D. DNA barcoding reveals extraordinary cryptic diversity in an amphipod genus: implications for desert spring conservation, *Mol. Ecol.*, 15 (2006) 3073-3082.

[14] Pfenninger M., Schwenk K. Cryptic animal species are homogeneously distributed among taxa and biogeographical regions, *BMC Evol. Biol.*, 7 (2007) 1-6.

[15] Jalali S., Ojha R., Venkatesan T. DNA barcoding for identification of agriculturally important insects, New horizons in insect science: Towards sustainable pest management, *Springer,* (2015) 13-23.

[16] Pomés A., Arruda L.K. Investigating cockroach allergens: aiming to improve diagnosis and treatment of cockroach allergic patients, *Methods*, 66 (2014) 75-85.

[17] Zhang J., Zhang Y., Li J., Liu M., Liu Z.,Midgut Transcriptome of the Cockroach *Periplaneta americana* and Its Microbiota: Digestion, Detoxification and Oxidative Stress Response, *PLoS One.*, 11 (2016) e0155254.

[18] Fakoorziba M.R., Eghbal F., Hassanzadeh J., Moemenbellah-Fard M.D. Cockroaches (*Periplaneta americana* and *Blattella germanica*) as potential vectors of the pathogenic bacteria found in nosocomial infections, *Ann Trop Med Parasitol.*, 104 (2010) 521-528.

[19] Atiokeng Tatang R.J., Tsila H.G., Wabo Poné J. Medically Important Parasites Carried by Cockroaches in Melong Subdivision, Littoral, Cameroon, *J Parasitol Res.*, 2017 (2017) 7967325.

[20] Bouchebti S., Durier V., Pasquaretta C., Rivault C., Lihoreau M. Subsocial Cockroaches Nauphoeta cinerea Mate Indiscriminately with Kin Despite High Costs of Inbreeding, *PLoS One.*, 11 (2016) e0162548.

[21] Schimpf N.G., Matthews P.G., White C.R.,Standard metabolic rate is associated with gestation duration, but not clutch size, in speckled cockroaches Nauphoeta cinerea, *Biol Open.*, 1 (2012) 1185-1191.

[22] Folmer O., Black M., Hoeh W., Lutz R., Vrijenhoek R. DNA primers for amplification of mitochondrial cytochrome c oxidase subunit I from diverse metazoan invertebrates, *Mol Mar Biol Biotechnol.*, 3 (1994) 294-299.

[23] Kimura M. A simple method for estimating evolutionary rates of base substitutions through comparative studies of nucleotide sequences, *J Mol Evol.*, 16 (1980) 111-120.

[24] Evangelista D., Buss L., Ware J.L. Using DNA barcodes to confirm the presence of a new invasive cockroach pest in New York City, *J Econ Entomol.*, 106 (2013) 2275-2279.

[25] Farah Haziqah M.T., Nur Asyiqin M.N., Mohd Khalid M.K.N., Suresh K., Rajamanikam A., Chandrawathani P., Mohd Zain S.N. Current status of Blastocystis in cockroaches, *Trop Biomed.*, 34 (2017) 741-745.

[26] Miskelly J., Paiero S.M. Mantodea, Blattodea, Orthoptera, Dermaptera, and Phasmida of Canada, *Zookeys*, (2019) 255-269.

[27] Liao S., Wang Z., Che Y. A new genus and a new species in the subfamily *Polyzosteriinae* (Blattodea, Blattidae) from China, *Zookeys*, 852 (2019) 85-100.

[28] von Beeren C., Stoeckle M.Y., Xia J., Burke G., Kronauer D.J. Interbreeding among deeply divergent mitochondrial lineages in the American cockroach (*Periplaneta americana*), *Sci Rep.*, 5 (2015) 8297.

[29] Li Y., Luo X., Zhang J., Wang Z., Che Y. A new species of Bundoksia Lucañas, 2021 with comments on its subfamilial placement, based on morphological and molecular data, *Zookeys*, 1085 (2022) 145-163.4

Cumhuriyet Sci. J., 44(1) (2023) 36-40
DOI: https://doi.org/10.17776/csj.1221192

Cumhuriyet Science Journal

| csj.cumhuriyet.edu.tr | Founded: 2002 ISSN: 2587-2680 e-ISSN: 2587-246X Publisher: Sivas Cumhuriyet University

Determination of the Optimum Number of Short Reads to Obtain the Mitogenome in some Insect Orders

Mahir Budak [1,a,*]

[1] *Department of Molecular Biology and Genetics, Faculty of Science, Sivas Cumhuriyet University, Sivas, Türkiye.*
**Corresponding author*

Research Article

History
Received: 19/12/2022
Accepted: 16/03/2023

ABSTRACT

Sanger sequencing is frequently used as the final step in time-consuming extraction and enrichment processes for examining the mitochondrial genome (mitogenome). The development of next-generation or massively parallel sequencing has made it possible to consistently gather data at the nucleotide level with comparatively little difficulty. Additionally, reference-based genome assembly is now achievable thanks to the growing amount of mt genome data in databases. Consequently, acquiring the genome with fewer short-read counts reduces the financial load on research projects. The use of mitogenomes, particularly in the studies of systematic and population genetics of insects, have increased, and sequencing mitogenomes in non-model animals have become critical. Twelve species from four insect orders, each having a different-sized genome, were employed in the study. Short reads of these species, used in the study, were acquired from the SRA (The Sequence Read Archive) database. Alignments to the reference genome were carried out in triplicate for five different short read counts. It was observed that 0.092 (*Chrysotoxum bicinctum*) to 14.04 (*Anopheles coluzzii*) sequencing depth was needed to obtain the mitogenome with 100X coverage. This work aims to give researchers a better understanding of how much sequencing depth is necessary for mitogenome investigations.

Keywords: Next-generation sequencing, Mitogenome, Short-reads, Coverage, Insects.

[a] *mbudak@cumhuriyet.edu.tr* *https://orcid.org/0000-0001-5610-486X*

Introduction

Mitochondria are essential organelles for eukaryotic cells due to their crucial functions in the production of bioenergetics intermediates. This organelle also participates in important cellular processes, such as signalling, apoptosis, ageing, metabolic homeostasis, and biosynthesis of lipids [1]. The maternally inherited mitochondrial genome is present in nearly all eukaryotic organisms, possessing double-stranded circular DNA molecules of approximately 16 kb in size in general [2]. They typically appear to be consisted of thousands of copies in each cell with widely varying copy number among different tissue cells. The genome of mitochondria (mitogenome) are also commonly preferred in the studies on the genome architecture, evolutionary relationships and adaptive evolution, providing valuable information from intraspesific level to interspesific or higher level of taxa [3-5]. Performing analyses such as hybridization, population genetics, geographical cline has also become essential to reveal the effects of changing environmental conditions. Mitochondrial genes are frequently used in this type of analyses [6].

Insects have become an important model group for figuring out how organisms respond to global warming from an ecological and evolutionary point of view. They are important to the environment and the economy (e.g., as pollination, pests, and as vectors), but they are also vulnerable to environmental conditions [7]. An insect mitogenome generally consists of 13 protein coding genes (PCGs), 24 RNA genes (22 transfer RNAs (tRNAs) and two ribosomal RNAs (rRNAs)) and A + T-rich region (one large control region) with 14–25 kb in length [3,8]. In the result of a rapid search in the organelle section of the public database of NCBI (November 2022) using the “Insecta, mitochondrion” as keywords and filtering the sequence length >10,000 bp, there were complete insect mitogenomes of more than 5,300 species, corresponding approximately 0.5% of described insect species. Despite the most widely studied marker of insect genomes, some technical difficulties have limited benefit for the full potential of mitogenomes. The purification of mitochondria and isolation its DNA in sufficient quantities to perform direct mitogenome sequencing from the large organism such as vertebrates are relatively possible from fresh material [9,10]. However, this approach is not achievable for insect tissues [11,12].

Recent advances in high-throughput sequencing approaches have overcome many of these difficulties and it is possible to rapidly and economically produce very large numbers of relatively short reads from both the nuclear and mitochondrial DNA contained in an insect sample [12,13]. This facility makes this huge data a valuable resource for extracting and assembling insect mitogenomes. However, we need to determine the minimum short-read data required to identify the mitogenomes from insects with varying genome sizes. We can take advantage of mtDNA being present

approximately 10-100 times more than the nuclear DNA in an animal cell [14]. For this aim, we here selected and analyzed twelve species representing the orders of Hymenoptera, Diptera, Lepidoptera and, Coleoptera with variable genome sizes and sequencing depths. Remarkably, it was found that the genome size of the organism did not correlate with the proportion reads belong to mitogenome in the short-read data. It has been found that approximately 1-2X read depth from mixed DNA sample is required to reliably sequence and assemble a typical insect mitogenome.

Materials and Methods

Data Preparation

Within the scope of the study, 12 species belonging to four distinct insect orders were examined. The short reads and reference mitochondrial genomes representing these species used for the analyses were retrieved from the GenBank database. Table 1 lists the accession numbers for each insect species. Fastq-dump v2.8.0 (https://github.com/ncbi/sra-tools) software was used to convert short reads downloaded in SRA format into forward and reverse *fastq* files. Using a custom python script (https://github.com/budakmah/fastq_sub_reads), sub-datasets with various read counts were produced for each fastq file. Each analysis was conducted in triplicate for each sub-dataset.

Mapping of short-reads to Reference Genomes

For alignment to the reference, the bowtie2 software package [15] was used with default settings. To calculate consensus sequences from aligned reads, sam2consensus program (https://github.com/edgardomortiz/sam2consensus) was used. The sam2consensus program takes as input a SAM file resulting from mapping short reads to a reference, then it calculates the consensus sequence from the aligned reads alone. The findings of the mapping to the reference genome and the consensus computations were recorded in log files that contained statistics of analyses.

Statistical Analysis and Data Visualization

For the results of the reference genome mapping and consensus calculations, log files containing the statistics of the analyzes were generated and exported to R v.4.0.2 [16] for statistical analysis. The R custom script was used to extract information about the read counts of each fastq file (RCF), read counts aligned to the target genome (RCTG), coverage (COV), and overall alignment rate (AR) from the log files. The ggplot2 R package [17] was used to visualize data and generate graphs. Threshold value for COV value was accepted as 100. The following formula was used to determine each fastq file's read depth (RD) based on the genome size (GS):

$$RD = \frac{read\ length\ (RL)\ x\ RCF}{GS}$$

The following equation was used to calculate the ratio of RCF to the mitogenome length (ML):

$$\text{ratio of RCF (RDml)} = \frac{RL\ x\ RCF}{ML}$$

The minimum sequencing depth for 100X (RD_{100}) mitogenome coverage was determined using linear least squares regression analysis. The Kendall correlation method was used to figure out if there was a link between the size of the genome and the number of short reads that were needed to cover 100X of the mitogenome.

Results and Discussion

Twelve species with different genome size from the four largest insect orders—Coleoptera, Hymenoptera, Lepidoptera, and Diptera—were selected for the study (Table 1).

Table 1: GenBank accession numbers for SRA and mitogenome, genome sizes and Orders of the species used in the study

Species	Genome Size (bp)	SRA ID	Order	Mitochondrion ACC	Mitochondiron_l
Anopheles coluzzii	262,617,596	SRR17828126	Diptera	KT382819.1	15.441
Apis mellifera	225,234,541	SRR15173878	Hymenoptera	CM040891.1	16.654
Chironomus riparius	191,837,449	ERR7059573	Diptera	OU815687.1	15.666
Chrysotoxum bicinctum	912,938,338	ERR6054968	Diptera	OU426992.1	19.366
Danaus plexippus	245,173,502	ERR4613992	Lepidoptera	KC836923.1	15.314
Harmonia axyridis	425,524,972	ERR6054991	Coleoptera	OU611935.1	19.884
Heliconius numata	351,227,686	ERR4614539	Lepidoptera	Assembled	14.784
Leptidea sinapis	685,583,065	ERR6054634	Lepidoptera	FR990201.1	15.959
Leptinotarsa decemlineata	641,992,784	SRR1055549	Coleoptera	MZ189364.1	16.741
Pachycephus smyrnensis	225,000,000	SRR18358779	Hymenoptera	KX907846.1	15.203
Syrista parreyssii	160,000,000	SRR15850959	Hymenoptera	OK104785.1	18.666
Tenebrio molitor	287,839,991	ERR5859003	Coleoptera	CM025077.1	15.794

The short read data that was retrieved from the database is used to build sub-data with randomly chosen reads. *de-novo* assembly was carried out for the sake of the study because there was no mitogenome sequence belong to *H. numata* in the database. *C. bicinctum* had the biggest genome (about 912 Mb), while *S. parreyssii* had the shortest genome (about 160 Mb).

Each sub-data set has been aligned to the reference mitogenomes, and summary statistics is provided in Table 2. The ratio of sequences matched to the reference mitogenome to the number of reads in the used data (AR) was highest in *A. mellifera* (3.21), while it was lowest in *A. coluzzii* (0.02). There are several explanations for why mitogenome reads in total may vary so greatly between species. This is probably due to three main factors: the first is the mitochondrial copy number, the second is potential experimental variances, and third is body part used for sequencing. Insects' energy requirements vary due to their diverse life strategies. This condition also results in variations in mitochondrial copy number present in cells [18–20].

Table 2: Summary results of each sub-dataset

Species	Order	RCF	RCTG	AR	COV	Ns	Gsize	mtGS	MGR	RD	RL
Anopheles coluzzii		6448193.3	2817.7	0.02	26.64	201	262617596	15441	0.0000588	3.68	151
	Diptera	12897770.7	5638.0	0.02	53.29	51	262617596	15441	0.0000588	7.37	151
		19349235.7	8330.3	0.02	78.73	8	262617596	15441	0.0000588	11.05	151
		25797822.7	11122.7	0.02	105.12	2	262617596	15441	0.0000588	14.74	151
		32246096.0	13839.0	0.02	130.81	2	262617596	15441	0.0000588	18.42	151
Apis mellifera		3346972.3	214829.7	3.21	1951.72	182	225234541	16654	0.0000739	2.23	150
	Hymenoptera	13388126.3	858011.7	3.20	7794.95	160	225234541	16654	0.0000739	8.92	150
		23424563.0	1501845.0	3.21	13644.94	43	225234541	16654	0.0000739	15.60	150
		33463792.0	2145393.0	3.21	19492.24	32	225234541	16654	0.0000739	22.29	150
		33463792.0	2145393.0	3.21	19492.24	32	225234541	16654	0.0000739	22.29	150
Chironomus riparius		12275648.7	111738.0	0.46	1069.46	62	191837449	15666	0.0000817	9.60	150
		16369765.7	149404.7	0.46	1429.42	27	191837449	15666	0.0000817	12.80	150
		20463386.7	186594.3	0.46	1786.30	5	191837449	15666	0.0000817	16.00	150
		22097706.7	201586.0	0.46	1929.09	25	191837449	15666	0.0000817	17.28	150
	Diptera	24554698.0	223832.3	0.46	2142.25	0	191837449	15666	0.0000817	19.20	150
Chrysotoxum bicinctum		97351.0	2219.0	1.14	16.70	808	912938338	19366	0.0000212	0.02	151
		194128.3	4493.3	1.16	33.82	40	912938338	19366	0.0000212	0.03	151
		290865.3	6827.0	1.17	51.34	22	912938338	19366	0.0000212	0.05	151
		387865.0	8937.7	1.15	67.27	1	912938338	19366	0.0000212	0.06	151
		485057.0	11227.3	1.16	84.49	0	912938338	19366	0.0000212	0.08	151
Danaus plexippus		1439176.7	7935.0	0.27	78.01	37	245173502	15314	0.0000625	0.88	151
		2158216.0	11747.0	0.27	115.49	7	245173502	15314	0.0000625	1.32	151
	Lepidoptera	2875802.0	15675.3	0.27	154.12	9	245173502	15314	0.0000625	1.76	151
		3596881.7	19699.3	0.27	193.69	1	245173502	15314	0.0000625	2.20	151
		4314262.7	23533.3	0.27	231.41	0	245173502	15314	0.0000625	2.64	151
Harmonia axyridis		412631.3	2289.3	0.28	16.84	262	425524972	19884	0.0000467	0.15	151
		1237167.0	6831.7	0.28	50.24	4	425524972	19884	0.0000467	0.44	151
		2061552.0	11186.7	0.27	82.25	0	425524972	19884	0.0000467	0.73	151
	Coleoptera	2889836.0	15842.3	0.27	116.51	0	425524972	19884	0.0000467	1.02	151
		3715467.3	20627.0	0.28	151.68	0	425524972	19884	0.0000467	1.31	151
Heliconius numata		1580636.0	28642.3	0.91	242.22	53	351227686	14784	0.0000421	0.68	125
		3160763.7	57245.3	0.91	484.19	14	351227686	14784	0.0000421	1.35	125
		4738753.3	85911.7	0.91	726.66	11	351227686	14784	0.0000421	2.02	125
	Lepidoptera	6321199.0	114477.0	0.91	968.27	1	351227686	14784	0.0000421	2.70	125
		7902389.3	142869.0	0.90	1208.40	1	351227686	14784	0.0000421	3.37	125
Leptidea sinapis		2442035.7	2887.7	0.06	26.29	65	685583065	15959	0.0000233	0.53	151
		4883440.0	6003.0	0.06	54.64	16	685583065	15959	0.0000233	1.07	151
		7326785.3	8897.0	0.06	81.01	2	685583065	15959	0.0000233	1.60	151
		9767001.7	11849.0	0.06	107.86	1	685583065	15959	0.0000233	2.14	151
		12210228.7	14816.7	0.06	134.89	1	685583065	15959	0.0000233	2.67	151
Leptinotarsa decemlineata		17632471.3	9299.0	0.03	56.07	1964	641992784	16741	0.0000261	4.12	101
		35264625.0	18528.0	0.03	111.70	866	641992784	16741	0.0000261	8.24	101
	Coleoptera	35264625.0	18528.0	0.03	111.70	866	641992784	16741	0.0000261	8.24	101
		35264625.0	18528.0	0.03	111.70	866	641992784	16741	0.0000261	8.24	101
		35264625.0	18528.0	0.03	111.70	866	641992784	16741	0.0000261	8.24	101
Pachycephus smyrnensis		1448487.7	9918.7	0.34	97.60	140	225000000	15203	0.0000676	0.97	150
		2896938.7	19712.3	0.34	193.98	116	225000000	15203	0.0000676	1.93	150
		4345744.7	29611.3	0.34	291.36	114	225000000	15203	0.0000676	2.90	150
	Hymenoptera	5793263.0	39278.0	0.34	386.52	109	225000000	15203	0.0000676	3.86	150
		7241341.0	49159.0	0.34	483.73	108	225000000	15203	0.0000676	4.83	150
Syrista parreyssii		3387611.7	79966.7	1.18	640.78	56	160000000	18666	0.0001167	3.18	150
		6772713.3	159137.3	1.17	1275.19	40	160000000	18666	0.0001167	6.35	150
		10159627.7	239514.7	1.18	1919.27	30	160000000	18666	0.0001167	9.52	150
		13548000.0	320148.0	1.18	2565.39	1	160000000	18666	0.0001167	12.70	150
		16935220.7	399503.0	1.18	3201.20	10	160000000	18666	0.0001167	15.88	150
Tenebrio molitor		230950.3	1414.7	0.30	13.33	243	287839991	15794	0.0000549	0.12	151
		461837.7	2920.7	0.32	27.52	21	287839991	15794	0.0000549	0.24	151
		693059.0	4364.7	0.32	41.25	6	287839991	15794	0.0000549	0.36	151
	Coleoptera	1156782.0	7297.7	0.32	68.69	3	287839991	15794	0.0000549	0.60	151
		1617781.0	10097.7	0.31	95.09	0	287839991	15794	0.0000549	0.84	151

RCF: read counts of each fastq file; RCTG: read counts aligned to the target genome; AR: overall alignment rate; COV: coverage; Gsize: genome size; mtGS: mitochondrial genome size; MGR: ratio of mitochondrial genome size to genome size; RD: fastq file's read depth; RL: read length.

The method used to prepare sequencing libraries for next-generation sequencing is another key component. The outcomes of sequencing are significantly impacted by errors and variations in the library preparation procedure.In this situation, the target genome may be represented by fewer reads [21]. Insects have more mitochondrial DNA in their thoracic muscles than their chitinous legs. If the researcher extracts DNA from the insect's legs rather than its thoracic muscles, then the short-read data will contain very few mitogenome sequences. In addition, utilizing the whole insect for genomic DNA isolation implies isolating the microflora that lives in the abdomen [22]. In this case, a portion of the data will be associated with the microorganisms.

The minimum sequencing depth for 100X (RD_{100}) mitogenome coverage was determined using linear least squares regression analysis. Table 3 displays RD_{100} and p-values for each species. The RD_{100} value is highest for *A. coluzzii* (14.04), and it is lowest for *C.bicinctum* (0.09). According to these findings, the RD_{100} values for the majority of species are quite close to 1, and there is no discernible trend according to the different orders of insects.

Table 3: The minimum sequencing depth for 100X mitogenome coverage

Species	RD_{100}	p value
Anopheles coluzzii	14.04	<0.01
Apis mellifera	0.12	<0.01
Chironomus riparius	0.92	<0.01
Chrysotoxum bicinctum	0.09	<0.01
Danaus plexippus	1.14	<0.01
Harmonia axyridis	0.87	<0.01
Heliconius numata	0.28	<0.01
Leptidea sinapis	1.98	<0.01
Leptinotarsa decemlineata	7.37	<0.01
Pachycephus smyrnensis	0.99	<0.01
Syrista parreyssii	0.51	<0.01
Tenebrio molitor	0.88	<0.01

RD_{100}: The minimum sequencing depth for 100X mitogenome coverage

Insect species with different-sized genomes were chosen to see how genome size affects mitogenome assembly. The Kendall rank correlation coefficient or *Kendall's tau* statistic is used to estimate a rank-based measure of association between RD_{100} and genome size. It is likely that as the size of the genome increases, the proportion of short reads that come from the genome will also grow. Concurrently, it is expected that the ratio of reads from mitogenomes will decrease. However, the values for R(tau) and p- value were determined to be 0.03 and 0.95, respectively (Figure 1).

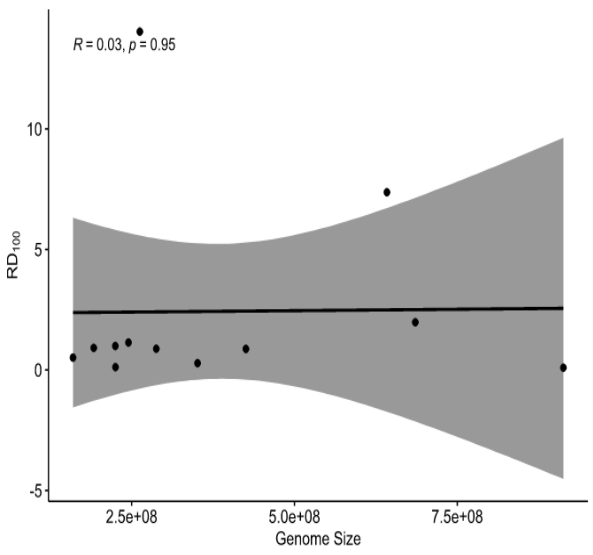

Figure 3. The Kendall rank correlation coefficient statistic graph estimate a rank-based measure of association between RD_{100} and genome size.

It is safe to say that there was no link between the size of the genome and the number of mitogenome reads in the short reads. Perhaps even more surprising is the finding that the insect with the largest genome size (*C. bicinctum*) also had the lowest RD_{100} score (0.09) of all the examined insects (Table 3). As a result, 1-2X reading depth seems sufficient to obtain a full mitogenome with high throughput sequencing approach.

For instance, for a next-generation sequencing analysis employing short-reads of 150 bp in length, roughly 4 million short-reads would be adequate to retrieve the mitogenome of an insect with a genomic size of approximately 500 Mb.

Conclusion

This study determined the minimum short-read data required to identify the mitochondrial genomes of twelve species belonging to the orders Hymenoptera, Diptera, Lepidoptera and, Coleoptera with varied genome sizes. Remarkably, it was found that the genome size of the organism did not correlate with the proportion reads belong to mitogenome in the short-read data. It has been found that approximately 1-2X read depth is required to reliably sequence a typical insect mitogenome.

Conflicts of Interest

The author declares no conflicts of interest. No competing financial interests exist.

References

[1] Ladoukakis, E. D., Zouros, E., Evolution and inheritance of animal mitochondrial DNA: Rules and exceptions, *Journal of Biological Research-Thessaloniki*, 24 (2) (2017) 1–7.

[2] Carlucci, A., Lignitto, L., Feliciello, A., Control of mitochondria dynamics and oxidative metabolism by cAMP, AKAPs and the proteasome, *Trends in Cell Biology*, 18 (12) (2008) 604–613.

[3] Cameron, S. L., Insect mitochondrial genomics: Implications for evolution and phylogeny, *Annual Review of Entomology*, 59 (2014) 95–117.

[4] Aydemir, M. N., Korkmaz, E. M., Comparative mitogenomics of hymenoptera reveals evolutionary differences in structure and composition*, International Journal of Biological Macromolecules*, 144 (2020) 460–472.

[5] Ballard, J. W. O., Pichaud, N., Mitochondrial DNA: More than an evolutionary bystander, *Functional Ecology*, 28 (1) (2014) 218–231.

[6] Okamura, Y., Sato, A., Kawaguchi, L., Nagano, A. J., Murakami, M., Vogel, H., Kroymann, J., Microevolution of pieris butterfly genes involved in host plant adaptation along a host plant community cline, *Molecular Ecology*, 31 (11) (2022) 3083–3097.

[7] González-Tokman, D., Córdoba-Aguilar, A., Dáttilo, W., Lira-Noriega, A., Sánchez-Guillén, R. A., Villalobos, F., Insect responses to heat: Physiological mechanisms, evolution and ecological implications in a warming world, *Biological Reviews*, 95 (3) (2020) 802–821.

[8] Boore, J. L., Animal mitochondrial genomes, *Nucleic Acids Research*, 27 (8) (1999) 1767–1780.

[9] Güler, M., Güler, F. T., Korkmaz, E. M., Budak, M., Böcek dokularından DNA İzolasyonu yöntemlerinin kalite, verim ve maliyet açısından karşılaştırılması, *Selçuk Üniversitesi Fen Fakültesi Fen Dergisi*, 44 (2018) 135–148.

[10] Budak, M., Korkmaz, E. M., Basibuyuk, H. H., A molecular phylogeny of the cephinae (hymenoptera, cephidae) based on mtDNA COI gene: A test of traditional classification, *ZooKeys*, 130 (2011) 363–378.

[11] Hu, M., Jex, A. R., Campbell, B. E., Gasser, R. B., Long PCR amplification of the entire mitochondrial genome from individual helminths for direct sequencing, *Nature Protocols,* 2 (10) (2007) 2339–2344.

[12] Jex, A. R., Hall, R. S., Littlewood, D. T. J., Gasser, R. B., An integrated pipeline for next-generation sequencing and annotation of mitochondrial genomes, *Nucleic Acids Research,* 38 (2) (2010) 522–533.

[13] Ye, F., Samuels, D. C., Clark, T., Guo, Y., High-throughput sequencing in mitochondrial DNA research, *Mitochondrion*, 17 (2014) 157–163.

[14] Al-Nakeeb, K., Petersen, T. N., Sicheritz-Pontén, T., Norgal: Extraction and de novo assembly of mitochondrial DNA from whole-genome sequencing data, *BMC Bioinformatics*, 18 (1) (2017) 1–7.

[15] Langmead, B., Salzberg, S. L., Fast gapped-read alignment with bowtie 2, *Nature Methods*, 9 (2012) 357–359.

[16] R Core Team, R: A language and environment for statistical computing, R Foundation for Statistical Computing, Vienna, Austria (2022).

[17] Wickham, H., ggplot2: Elegant graphics for data analysis. 2nd ed., New York: Springer-Verlag (2016) 18 – 30.

[18] Reinhold, K., Energetically costly behaviour and the evolution of resting metabolic rate in insects, *Functional Ecology,* 13 (1999) 217–224.

[19] Li, F., Zhao, X., Li, M., He, K., Huang, C., Zhou, Y., Li, Z., Walters, J. R., Insect genomes: Progress and challenges, *Insect Molecular Biology*, 28 (6) (2019) 739–758.

[20] Cameron, S. L., How to sequence and annotate insect mitochondrial genomes for systematic and comparative genomics research, *Systematic Entomology*, 39 (3) (2014) 400–411.

[21] Gómez-Rodríguez, C., Intraspecific genetic variation in complex assemblages from mitochondrial metagenomics: Comparison with DNA barcodes, *Methods in Ecology and Evolution*, 8 (2) (2017) 248–256.

[22] Patzold, F., Zilli, A., Hundsdoerfer, A. K., Advantages of an easy-to-use DNA extraction method for minimal-destructive analysis of collection specimens*, PloS one*, 15 (7) (2020) e0235222.

Cumhuriyet Sci. J., 44(1) (2023) 41-45
DOI: https://doi.org/10.17776/csj.1060972

Cumhuriyet Science Journal

| csj.cumhuriyet.edu.tr | Founded: 2002 ISSN: 2587-2680 e-ISSN: 2587-246X Publisher: Sivas Cumhuriyet University

Investigation of the Analgesic Properties L-759,633 and SER 601 in Experimental Neuropathic Pain Model in Rats and their Comparison with Pregabalin

Ziad Joha [1,a,*], Şahin Yıldırım [1,b], Levent Hacısüleyman [1,c], Ahmet Sevki Taşkıran [2,d]

[1] *Department of Pharmacology, Faculty of Pharmacy, Sivas Cumhuriyet University, Sivas, Türkiye.*
[2] *Department of Pharmacology, Faculty of Medicine, Sivas Cumhuriyet University, Sivas, Türkiye.*
**Corresponding author*

Research Article

History
Received: 21/01/2022
Accepted: 06/02/2023

ABSTRACT

Despite the fact that narcotics and NSAIDs are the mainstays of nociceptive pain care, only a small proportion of neuropathic pain patients benefit from them. Cannabinoid agents could be a viable alternative to opioids in the management of chronic pain. The goal of our investigation was to assess the analgesic efficacy of SER 601 and L-759,633, cannabinoid receptor 2 (CB2) agonists, at various doses in a model of neuropathic pain generated in rat. The analgesic effect of CB2 agonists L-759,633 and SER 601 at various doses in a rat model of neuropathic pain created by partial sciatic nerve ligation was examined by the hot plate method. Furthermore, a comparison of analgesic effects of both drugs with pregabalin is also conducted. The two substances demonstrated a dose-dependent analgesic effect in this model. The analgesic response of SER601 and L-759,633 in the neuropathic pain model was higher compared to that of pregabalin. All in all, our data suggest that SER601 and L-759,633 may offer a beneficial treatment option for neuropathic pain in future.

Keywords: Neuropathic pain, L-759,633, SER 601, Hot plate, Pregabalin.

[a] *zead-geha@hotmail.com* *https://orcid.org/0000-0001-8520-3760*
[b] *syildirim1965@gmail.com* *https://orcid.org/0000-0003-1312-7273*
[c] *ps4.levent@gmail.com* *https://orcid.org/0000-0001-2345-6789*
[d] *a.sevkitaskiran@gmail.com* *https://orcid.org/0000-0002-5810-8415*

Introduction

According to research, 13-50% of UK individuals suffer from chronic pain [1]. Neuropathic pain has been described as pain caused by a sensorimotor system damage or dysfunction, and it affects about one-fifth of people with chronic pain. [2, 3]. The sensory system is immediately affected by tissue destruction in neuropathic pain, resulting in ectopic discharges that circumvent transmission [4].

Two characteristics distinguish neuropathic pain from non-neuropathic pain. There is no transduction in neuropathic pain and the prognosis is bad. Nerve injury has a higher risk of causing persistent pain than injury to non-nervous tissues. Additionally, neuropathic pain is more resistant to standard painkillers than non-neuropathic pain (morphine derivatives and steroidal anti-inflammatory medicines) [5].

The absence of effective treatments is one explanation for the high incidence of neuropathic pain [5]. Despite the fact that morphine derivatives and non-steroidal anti-inflammatory medicines are the cornerstones of nociceptive pain medications, they have only a minor effect in the medication of neuropathic pain in a small percentage of patients. The primary cause for this is that the fundamental mechanisms are not fully targetable [6].

Tricyclic antidepressants (amitriptyline), serotonin-norepinephrine reuptake inhibitors (duloxetine), calcium channel α2- δ ligands (pregabalin) and lidocaine have exhibited effectiveness in neuropathic pain and they are used as first-line treatment. Opioid analgesics or tramadol, which are second-line drugs, can be used in patients that do not respond to the first-line treatment. In cases such as acute neuropathic pain, morphine derivatives such as tramadol are used as first-line drugs. Cannabinoids are used as a second-line drug in neuropathic pain caused by multiple sclerosis [7].

CB_2R expression has been demonstrated in the rodent in pain-related brain regions, including cerebral cortex, hippocampus, striatum, amygdala, thalamic nuclei, periaqueductal gray, cerebellum, and several brainstem nuclei. The upregulation of CB2R in the dorsal horn of the spinal cord during neuropathic or inflammatory pain was observed . Cannabinoids have a long history of medical application and are ~~growingly~~ increasingly approved for pain management. This advancement has been established by pre-clinical and experimental human research. Over the past ten years, six controlled trials have been reported evaluating the pain-relieving activities of cannabinoid-based medicines in experimental human settings. Cannabinoids have demonstrated efficacy in multiple chronic inflammatory and neuropathic pain models. There are tremendous evidences that specific cannabinoid receptor (CB_2R) agonists have anti-nociceptive effects and reduce the neuroinflammatory component of neuropathic pain [8].

It has been suggested that CB_2R selective agonists could be used to treat human neuropathic pain, a condition for which there are currently no consistently effective treatments. CB_2R selective agonists are not

estimated to have central nervous system side effects that limit the effectiveness of currently available drugs [9]. Up to now, the analgesic effect of L-759,633 and SER 601, cannabinoid receptor 2 (CB_2) agonists, in the rat model of neuropathic pain was not studied. In view of these findings, the analgesic effect of L-759,633 and SER 601, at various doses in the rat model of neuropathic pain was investigated in our experimentation using the hot plate method and the analgesic activity of these CB_2R agonists was compared to that of pregabalin.

Materials and Methods

Animals

In the experiments, 66 male adult Wistar albino rats ranging 210-235 g were employed. Four animals were located in each cage at 23 ± 0.5 ° C, with a 12-hour dark /12-hour light cycle and limitless connection with water and nutrient. There were six rats in each group. Cumhuriyet University's Animal Ethics Committee authorized the study protocols (Ethical Number: 65202830-050.04.04-280). Prior to testing, the animals were acclimatized to laboratory settings. Between 10 and 15 hours, all of the experiments were conducted blindly.

Drugs

SER601 and L-759,633 (Cayman Chemical Company, USA) were dissolved in the solution containing 10% dimethyl sulfoxide (DMSO) and 90% normal saline. Pregabalin (Cumhuriyet University Hospital, Sivas, Turkey) was dissolved in 0.9% NaCl solution. On the days of the experiments, fresh solutions were prepared. L-759,633, SER601 (3, 6, 12 mg/kg) and pregabalin (30 mg/kg) were injected intraperitoneally. A pilot study was carried out to determine the doses of L-759,633, SER601. However, the dose of pregabalin was determined according to the study conducted by Meymandi [10].

Analgesia Tests

The thermal pain was measured using a hot plate method (May AHP 0603 Analgesic HP, Commat) [11]. The animals were located on a hot plate. The temperature was determined as 53 ± 0.6 ° C. The time taken for the first action (licking or jumping) to avoid heat was calculated and taken as a measure of pain threshold.. The cut of time is 30 seconds to avoid damaging the claw. This test's hyperalgesic responses demonstrate pain processes in the central nervous systems [11].

Surgical Intervention

A neuropathic pain model was created by partially ligating the sciatic nerve. Surgical procedures were carried out in the Experimental Animals Laboratory of Sivas Cumhuriyet University. Intramuscular ketamine at dose of 90 mg/kg and xylazine at dose of 3 mg/kg were used for anesthesia. An about 1 cm incision was made in the biceps femoris under aseptic circumstances. After that the sciatic nerve was reached in the right leg's middle thigh level. The sciatic nerve was then carefully separated from the supporting tissues and firmly bound with 4.0 chromic catgut. 4.0 silk was used to close the incision. In sham group, the rat's nerve was separated but not tied [12,13].

Protocol

Rats were randomly divided into 11 groups. In order to create a neuropathic pain model, the sciatic nerve binding method was applied to rats and it was predicted that neuropathic pain would occur during two weeks. At the end of this period, basal latencies were obtained before applying the drugs and compared with basal latencies obtained before surgery. Then the agonists were applied in 3 various doses. The antihyperalgesic effects of L-759,633, SER601 and pregabalin in the rats were examined at 0, 15, 30, 60, 90, and 120 minutes by hot-plate method. In the sham group, rats received DMSO. Table 1 below explains the animal groups (11 groups) in detail.

Table 1. Some topological parameters of BCPs for gas phase calculations.

	Experimental and Control Groups (Each dose was administered once intraperitoneally)	Number of Rats
1	Sham (DMSO)	6
2	Sham (saline)	6
3	Neuropathic Pain (saline)	6
4	Neuropathic Pain (DMSO)	6
5	L-759,633 3 mg/kg	6
6	L-759,633 6 mg/kg	6
7	L-759,633 12 mg/kg	6
8	SER 601 3 mg/kg	6
9	SER 601 6 mg/kg	6
10	SER 601 12 mg/kg	6
11	Pregabalin 30 mg/kg	6

Data Analysis and Statistical Analysis

To determine percentage of the maximal anti-nociceptive effects (% MPE), lick/escape latencies were translated to percentage of anti-nociceptive effects using this formula:

% MPE = [(test latency – baseline) / (cutoff (30) – baseline)] * 100 [14]

The results were evaluated using paired student t-test and one-way analysis of variance (ANOVA) and repeated measures ANOVA followed by a Tukey post hoc test (SPSS 20.0 for Windows) for multiple comparisons between groups. All results are displayed as a mean ± SEM. The level of significance was set at $p < 0.05$.

Results and Discussion

Detection of Neuropathic Pain Generation by Sciatic Nerve Ligation

The hot plate basal latencies obtained after surgery were significantly lower than those obtained before it ($p<0.05$) (Fig. 1). In this context, the formation of neuropathic pain in rats was established.,

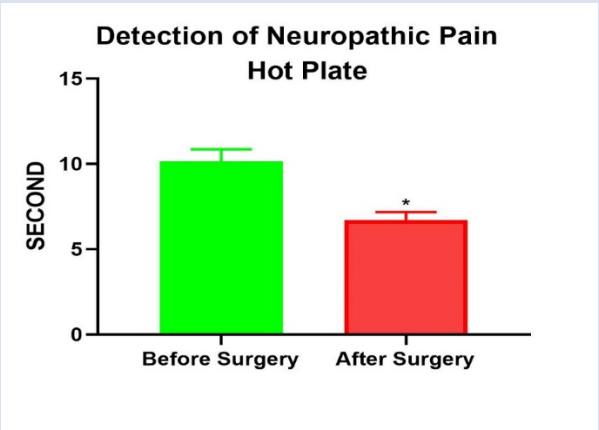

Figure 1. The basal latencies of rats before and after operation (paired student t-test, *p<0.05)

The Effect of Various Doses of SER601 on Neuropathic Pain

The effect of SER601 at doses of 3, 6 and 12 mg/kg on neuropathic pain was assessed using a hot plate test to determine the anti-hyperalgesic responses for the different doses of this agent from 15 to120 minutes using hot plate test. All doses of SER601 were demonstrated to be efficient on neuropathic pain in comparison with the sham group at all minutes (Fig. 2). In addition, statistically significant differences were found between %MPE values produced by these three doses. As a result, it was revealed that the drug's effect on neuropathic pain is dose-dependent (Fig. 2).The maximum %MPE was recorded after 60 minutes of administration of these three doses.

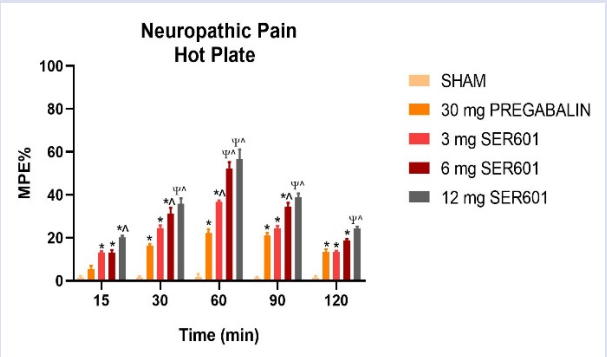

Figure 2. The effect of SER601 on the neuropathic pain model represented as a percentage of the maximum potential effect (MPE). Pregabalin was used as positive control. The agents were administered intraperitoneally. The results are presented as mean ± SEM for 6 rats. One-way ANOVA was applied.*p < 0.05, MPE% is significantly higher when compared to the correspondence time of sham group. Ψp< 0.05, MPE% is significantly higher when compared to the correspondence time of sham and 3 mg/kg SER601 groups. ^p < 0.05, MPE% is significantly higher when compared to the correspondence time of pregabalin group.

The Effect of Various Doses of L-759,633 on Neuropathic Pain

The effect of L-759,633 at doses of 3, 6 and 12 mg/kg on neuropathic pain was assessed using a hot plate test to determine anti-hyperalgesic responses for the different doses of this agent from 15 to120 minutes using hot plate test. 6 and 12 mg/kg L-759,633 were demonstrated to be efficient on neuropathic pain in comparison with the sham group at all minute points. 3 mg/kg L-759,633 from 30 to 120 minutes was demonstrated to be efficient on neuropathic pain in comparison with the sham group (Fig. 3). In addition, statistically significant differences were found between %MPE values produced by these three doses. As a result, it was revealed that the drug's effect on neuropathic pain is dose-dependent (Fig. 3). The maximum %MPE was recorded after 60 minutes of administration of these three doses.

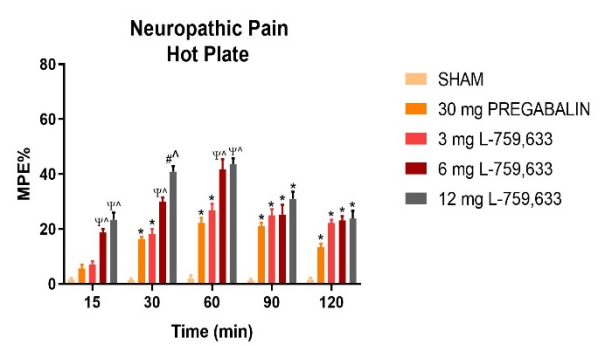

Figure 3. The effect of L-759,633 on the neuropathic pain model represented as a percentage of the maximum potential effect (MPE). Pregabalin was used as positive control. The agents were administered intraperitoneally. The results are presented as mean ± SEM for 6 rats. One-way ANOVA was applied. *p < 0.05, MPE% is significantly higher when compared to the correspondence time of sham group. Ψp< 0.05, MPE% is significantly higher when compared to the correspondence time of sham and 3 mg/kg L-759,633 groups .#p< 0.05 MPE% is significantly higher when compared to the correspondence time of sham, 3 mg/kg L-759,633 and 6 mg/kg L-759,633 groups. ^p< 0.05, MPE% is significantly higher when compared to the correspondence time of pregabalin group.

For comparison, the effect of 30 mg/kg dose of pregabalin on neuropathic pain was assessed at 0, 15, 30, 60, 90, and 120 minutes. Compared to the sham group, it was determined that pregabalin was effective against neuropathic pain at all minutes (except the 15-minute). The effect of the drug reached its peak at the 60-min then started to decrease. The antihyperalgesic effect of 12 mg/kg SER601 from 15 to 120 minutes, 6 mg/kg SER601 from 30 to 90 minutes and 3 mg/kg SER601 at 60-min on neuropathic pain were higher than the effect of

pregabalin group (Fig. 2). The antihyperalgesic effect of 12 and 6 mg/kg L-759,633 from 15 to 60 minutes on neuropathic pain were greater than the effect of pregabalin group (Fig. 3).

There is an inadequately treated pain epidemic, and it has been considered as a main public health issue. Sever and chronic pain management is the burden of clinicians [15]. Nonsteroidal anti-inflammatory medications opiates, antidepressants, anti-convulsants, ketamine, and other drugs have been used to manage a variety of pathological pain conditions. However, the side effects lead to a limitation of the amount of doses that can be used in the treatment and thus a decrease in the therapeutic efficacy. Though there are advances in the comprehension of pathophysiological processes that generate chronic pain status and in the determination of different analgesic pathways, there is still an excessive need for treatment approaches for chronic pain that are effective and don't cause undesirable central side effects [16]. CB2 receptor expression has also been discovered to be altered in different regions of the pain pathways during inflammatory and neuropathic pain conditions. An elevation of CB2 receptor mRNA level in the medulla spinalis was discovered in neuropathic pain situations caused by ligation of sciatic or spinal nerve. In animal models of neuropathic pain generated by nerve injury or chemotherapeutic drugs, systemic or local treatment of a variety of selective CB2 receptor agonists was found to be useful in alleviating neuropathic pain.[17]. Cannabinoid-based therapies may be a feasible alternative to opioids for the chronic pain management. Cannabinoids have been demonstrated in clinical studies to considerably relieve chronic pain in multiple sclerosis, fibromyalgia, diabetic or other neuropathy, and rheumatoid arthritis patients. [18,19]. Due to undesirable properties of opioids, drug discovery and development efforts have become more focused on finding effective new drugs that do not have these unwanted properties [20,21]. Undesirable effects of cannabinoids are reported to be relatively mild and well tolerated, and some studies have also shown that these drugs may cause improvements in sleep [18,19]. Sheng et al. showed that CB2 receptor agonists JWH015, Gp1a, and JWH133 were efficacious in lowering mechanical allodynia caused by prolonged retroviral infection in mice when evaluated 2 hours after injections [22]. In a similar study, It has been demonstrated that CB2 agonist GW405833 eliminated the mechanical allodynia generated in inflammatory and neuropathic pain models in wild type WT mice and the effect was dose-dependent [23]. Pasquiniet al., showed that SER-601, a selective and potent CB2 agonist, has antinociceptive effect in a formalin-induced pain model at 3 mg/kg and because of its poor affinity for the CB1 receptor, it has no cannabis-like behavioral activities [24,25].

No research has been conducted to determine the effect of the selective CB2 agonists L-759,633 and SER-601 on neuropathic pain. In our research, the effects of these agents on neuropathic pain were evaluated. SER601 and L-759,633 were administered at doses of 3, 6, and 12 mg/kg. These two drugs showed dose-dependent analgesic activity in neuropathic pain model induced by sciatic nerve ligation. Our results are consistent with earlier data as CB2R agonists have analgesic activities on neuropathic pain. The analgesic effects of SER601 and L-759,633 achieved their peak at 60- minute and then began to diminish. The antinociceptive effects of these agents were evaluated as %MPE (maximal possible effect). The analgesic response of SER601 and L-759,633 in the neuropathic pain model was higher compared to that of pregabalin. When comparing the analgesic response to SER601 and L-759,633, no statistically significant differences were found. The effect of 10% diluted DMSO on pain response was detected and compared with saline. 10% Diluted DMSO did not produce any alteration in the pain response. In addition, the control solution was 10% diluted DMSO, which prevents errors in outcome assessment.

We did not examine the mechanisms contributing to the analgesic effects of SER601 and L-759,633. However, other studies have reported that activation of cannabinoid type 2 receptors produce antinociceptive effects by inhibiting glutamatergic transmission [26], calcium influx [27] and stimulating β-endorphin release [28].

In summary, L-759,633 and SER601 showed an analgesic effect in neuropathic pain and could be candidate drugs for neuropathic pain treatment. The study of analgesic effects of CB2 agonists deserves further effort, as these agents do not cause central side effects and exert strong analgesic activity. In addition, the mechanisms of analgesic effect of SER601 and L-759,633 were not investigated in our study so further studies should be done to reveal the mechanisms involved in this effect.

Acknowledgment

This study was supported by a grant from (T-848i, Doctoral Thesis Projecti, iCUBAP, Turkey). The authors appreciate the help they received in the lab from Ahmet Atun and Ihsan Bagcivan.

Conflicts of interest

There are no conflicts of interest in this work.

References

[1] Mills S. E., Nicolson K. P., Smith B. H., Chronic pain: a review of its epidemiology and associated factors in population-based studies, *British Journal of Anaesthesia*, 123(2) (2019) 273-283.

[2] Ricci L., Luigetti M., Florio L., Capone F., Di Lazzaro V., Causes of chronic neuropathies: a single-center experience, *Neurological Sciences*, 40(8) (2019) 611-1617.

[3] Koetsier E., Franken G., Debets J., Heijmans L., van Kuijk S. M., Linderoth B., Maino P., Mechanism of dorsal root ganglion stimulation for pain relief in painful diabetic polyneuropathy is not dependent on GABA release in the dorsal horn of the spinal cord, *CNS Neuroscience & Therapeutics,* 26(1) (2020) 136-143.

[4] Devor M., Neuropathic pain and injured nerve: Peripheral mechanisms, *Br. Med. Bull.,* 47 (1991) 619–30.

[5] Cohen S.P., Mao J., Neuropathic pain: Mechanisms and their clinical implications, *BMJ,* 348 2014.

[6] Henningsen P., Zipfel S., Herzog W., Management of functional somatic syndromes, *Lancet,* 369 (2007) 946–55.

[7] Dworkin R.H., O'Connor A.B., Backonja M., Farrar J.T., Finnerup N.B., Jensen T.S., Pharmacologic management of neuropathic pain: Evidence-based recommendations, *Pain,* 132 (2007) 237–51.

[8] Lötsch J., Weyer-Menkhoff I., Tegeder I., Current evidence of cannabinoid-based analgesia obtained in preclinical and human experimental settings, *Eur. J. Pain,* 22 (2018) 471–84.

[9] Ibrahim M.M., Deng H., Zvonok A., Cockayne D.A., Kwan J., Mata H.P., Activation of CB2 cannabinoid receptors by AM1241 inhibits experimental neuropathic pain: Pain inhibition by receptors not present in the CNS, *Proc. Natl. Acad. Sci.,* 100 (2003) 10529–33.

[10] Meymandi M. S., Sepehri G., Abdolsamadi M., Shaabani M., Heravi G., Yazdanpanah O., Aghtaei M. M., The effects of co-administration of pregabalin and vitamin E on neuropathic pain induced by partial sciatic nerve ligation in male rats, *Inflammopharmacology*, 25(2) (2017) 237-246.

[11] Kanaan S.A., Saadé N.E., Haddad J.J., Abdelnoor A.M., Atweh S.F., Jabbur S.J., Endotoxin-induced local inflammation and hyperalgesia in rats and mice: A new model for inflammatory pain, *Pain,* 66 *(*1996) 373–379.

[12] Malmberg A.B., Basbaum A.I., Partial sciatic nerve injury in the mouse as a model of neuropathic pain: Behavioral and neuroanatomical correlates, *Pain,* 76 (1998) 215–222.

[13] Seltzer Z., Dubner R., Shir Y., A novel behavioral model of neuropathic pain disorders produced in rats by partial sciatic nerve injury, *Pain,* 43 (1990) 205–18.

[14] Altun A., Yildirim K., Ozdemir E., Bagcivan I., Gursoy S., Durmus N., Attenuation of morphine antinociceptive tolerance by cannabinoid CB1 and CB2 receptor antagonists, *J. Physiol. Sci.,* 65 (2015) 407–15.

[15] Kirsh K.L., Passik S.D., Rich B.A., Failure to Treat Pain. Treat. Chronic Pain by Integr. Approaches, Springer New York; (2015) 307–312.

[16] Guindon J., Hohmann A.G., Cannabinoid CB 2 receptors: A therapeutic target for the treatment of inflammatory and neuropathic pain, *Br. J. Pharmacol.,* 153 (2008) 319–34.

[17] Hossain M.Z., Ando H., Unno S., Kitagawa J., Targeting peripherally restricted cannabinoid receptor 1, cannabinoid receptor 2, and endocannabinoid-degrading enzymes for the treatment of neuropathic pain including neuropathic orofacial pain, *Int. J. Mol. Sci.,* (2020) 21-28.

[18] Craft R.M., Greene N.Z., Wakley A.A., Antinociceptive effects of JWH015 in female and male rats, *Behav Pharmacol.,* 29 (2018) 280–289.

[19] Lynch M.E., Ware M.A., Cannabinoids for the Treatment of Chronic Non-Cancer Pain: An Updated Systematic Review of Randomized Controlled Trials, J. Neuroimmune Pharmacol., 10 (2015) 293–301.

[20] Yekkirala A.S., Roberson D.P., Bean B.P., Woolf C.J., Breaking barriers to novel analgesic drug development, *Nat. Rev. Drug Discov.,* 16 (2017) 545–64.

[21] Li A.L., Lin X., Dhopeshwarkar A.S., Thomaz A.C., Carey L.M., Liu Y., Cannabinoid CB2 agonist AM1710 differentially suppresses distinct pathological pain states and attenuates morphine tolerance and withdrawal, *Mol. Pharmacol.,* 95 (2019) 155–68.

[22] Sheng W.S., Chauhan P., Hu S., Prasad S., Lokensgard J.R., Antiallodynic effects of cannabinoid receptor 2 (CB2R) agonists on retrovirus infection-induced neuropathic pain, *Pain Res. Manag.,* (2019) 245-254

[23] Li A.L., Carey L.M., Mackie K., Hohmann A.G., Cannabinoid CB2 agonist GW405833 suppresses inflammatory and neuropathic pain through a CB1 mechanism that is independent of CB2 receptors in mice, *J. Pharmacol. Exp. Ther.,* 362 (2017) 296–305.

[24] Pasquini S., Botta L., Semeraro T., Mugnaini C., Ligresti A., Palazzo E., Investigations on the 4-quinolone-3-carboxylic acid motif. 2. Synthesis and structure-activity relationship of potent and selective cannabinoid-2 receptor agonists endowed with analgesic activity in vivo, *J. Med. Chem.,* 2008 (51) 5075–84.

[25] Contartese A., Valoti M., Corelli F., Pasquini S., Mugnaini C., Pessina F., A novel CB2 agonist, COR167, potently protects rat brain cortical slices against OGD and reperfusion injury, *Pharmacol. Res.,* 2012 (66) 555–563.

[26] Starowicz K., Finn D.P., Cannabinoids and Pain: Sites and Mechanisms of Action, *Adv., Pharmacol.,* 80 (2017) 437–75.

[27] Strangman N.M., Walker J.M., Cannabinoid WIN 55,212-2 inhibits the activity-dependent facilitation of spinal nociceptive responses, *J. Neurophysiol.,* 1999 (82) 472–477.

[28] Ibrahim M.M., Porreca F., Lai J., Albrecht P.J., Rice F.L., Khodorova A., CB2 cannabinoid receptor activation produces antinociception by stimulating peripheral release of endogenous opioids, *Proc. Natl. Acad. Sci.* 2005 102 3093–3098.

Cumhuriyet Sci. J., 44(1) (2023) 46-52
DOI: https://doi.org/10.17776/csj.1167703

Cumhuriyet Science Journal

| csj.cumhuriyet.edu.tr | Founded: 2002 ISSN: 2587-2680 e-ISSN: 2587-246X Publisher: Sivas Cumhuriyet University

Toll-like Receptor 3 c.1377C/T and -7C/A Polymorphisms Associated with COVID-19 and COVID-19 Severity

Nil Özbilüm Şahin [1,a,*], Burcu Bayyurt [2,b], Serdal Arslan [3,c], Sevgi Baltacı [4,d], Mehmet Bakır [4,e]

[1] *Department of Molecular Biology and Genetic, Faculty of Science, Sivas Cumhuriyet University, Sivas, Türkiye.*
[2] *Department of Medical Biology, Faculty of Medicine, Sivas Cumhuriyet University, Sivas, Türkiye.*
[3] *Department of Medical Biology, Faculty of Medicine, MersinUniversity, Mersin, Türkiye.*
[4] *Departments of Infectious Diseases and Clinical Microbiology, Faculty of Medicine, Sivas Cumhuriyet University, Sivas, Türkiye.*
**Corresponding author*

Research Article

History
Received: 27/08/2022
Accepted: 01/03/2023

ABSTRACT

Chinese officials have reported the novel coronavirus to the world health organization, which is called the SARS-CoV-2. Toll-like receptor 3 (TLR3) induces antiviral immune responses via the production of type I interferons and inflammatory cytokines. In this study, we aimed to examine TLR3 c.1377C/T and -7C/A polymorphisms in COVID-19 and the association between some clinical parameters. We investigated the frequencies of TLR3 (c.1377C/T and -7C/A) polymorphisms in 150 patients with COVID-19 and 171 healthy individuals as controls. We performed polymerase chain reaction (PCR) based on restriction fragment length polymorphism (RFLP). We also investigated whether TLR3 c.1377C/T and-7C/A were associated with the severity of COVID-19. In addition, CHAID tree-based classification algorithm was created to investigate the severity of the patients in our study. TLR3 c.1377C/T TT genotype frequencies were statistically significant between cases and controls (p= 0.02). For TLR3 -7C/A polymorphism, the findings showed a statistically significant difference in A allele frequencies (p= 0.03). There was a statistically significant difference in the distribution of TLR3 -7C/A CA genotype frequency (p= 0.04). Our findings suggest that TLR3 c.1377C/T and -7C/A polymorphisms may be important on susceptibility or clinical course of COVID-19.

Keywords: COVID-19, Genetic polymorphism, Severity, Toll like receptor 3, CHAID tree-based classification algorithm.

[a] nozbilum@cumhuriyet.edu.tr https://orcid.org/0000-0002-2889-3600
[b] ebayyurt@cumhuriyet.edu.tr https://orcid.org/0000-0002-5618-457X
[c] serdalarslan@mersin.edu.tr https://orcid.org/0000-0002-3921-8061
[d] sevgibaltaci@cumhuriyet.edu.tr https://orcid.org/0000-0002-2466-777X
[e] mbakir@cumhuriyet.edu.tr https://orcid.org/0000-0003-3702-1932

Introduction

Coronaviruses (CoVs) have been known for many years as enveloped viruses with single-stranded RNA genomes ranging from 26 to 32 kb that may cause diseases in domestic and wild animals and humans [1]. CoVs belong to the order-Nidovirus, family-Coronaviridae, subfamily-Coronavineae [2]. In December 2019, the novel coronavirus, which was identified as SARS-CoV-2, caused pneumonia was reported to the world health organization (WHO) [3] and is named COVID-19. In February 2022, it was reported that the number of cases worldwide exceeded 424 million, and the total number of deaths approached six million [4]. Several publications have reported a high incidence of coagulation abnormalities in these patients [5]. Lymphopenia, leukocytosis, neutrophilia, thrombocytopenia, d-dimer height, c-reactive protein height, prothrombin time height, troponin increase and lactate dehydrogenase (LDH) height are the most commonly defined haematological parameters in COVID-19 [6]. The complete genome of the Wuhan-Hu-1 coronavirus, a strain of SARS-CoV-2 isolated from a COVID-19 pneumonia patient, is 29.9 kb and has a poly(A) tail at the 3' end; it has a capped structure at the 5' end [7]. Two-thirds of viral RNA encodes pp1a, pp1ab proteins, and 16 non-structural proteins, while the remaining open reading frames encode and structural and accessory proteins. The remainder of the virus genome encodes four major structural proteins, including spike glycoprotein (S), an envelope protein (E), matrix protein (M) and nucleocapsid protein (N) [8]. During transmission, virus penetrates into the cell using angiotensin-converting enzyme 2 (ACE2) [9]. ACE2 is the cell receptor for coronavirus and regulates both interspecies and human-to-human transmission [10]. The S proteins of the SARS-CoV-2 can bind to host cells with ACE2 by fusing to the membrane and releasing viral RNA. Viral RNAs are recognized by pattern recognition receptors (PRRs) as pathogen-linked molecular patterns (PAMP). TLR3, 7, 8 and 9 detect viral RNA and DNA in the endosome [11]. Until now, TLR1-TLR13 has been detected and characterized; TLR 1-9 are expressed in mice and humans, while TLR10–13 are only expressed in mice [12]. Some TLRs, such as TLR1, 2, 4, 5, 6 and 10, are expressed on the cell surface, while TLR3, TLR7, TLR8, TLR9, TLR11, TLR12, and TLR13 are expressed in the cell, especially in endosomes, lysosomes, and endolysosomes. TLR3 is determined in both intracellular places and the plasma membrane of human astrocytes [13]. TLR3 is nucleotide-sensing and located on chromosome 4q35 [14]. TLR3 is expressed in many cell types, such as macrophages, mast cells, natural killer cells, fibroblasts, endothelial and epithelial cells, myeloid dendritic cells, neuronal cells and astrocytes [15]. TLR3 is considered a very important receptor that recognizes

negative sense double-stranded RNA (dsRNA) from pathogenic virus [16]. In recent years, TLR3 polymorphisms have been studied in a wide range of infectious diseases, such as Hepatitis C infection [17], HPV infection [18] and Crimean Congo hemorrhagic fever disease (CCHF) [19]. However, to our knowledge, until now, TLR3 c.1377C/T and -7C/A polymorphism have not been studied in COVID-19. Thus, we aimed to investigate the frequencies of these polymorphisms and whether they were associated with the severity of COVID-19 in the present study.

Materials and Methods

We investigated association TLR3 c.1377C/T (rs3775290) and -7C/A (rs3775296) polymorphisms with SARS-CoV-2 infection in this study. Blood samples were collected from 150 COVID-19 patients. This study was approved by Sivas Cumhuriyet University Clinical Research Ethic Committee (Desicion No: 2021-02/07). Control group was composed of 171 healthy individuals whose blood had been taken during the absence of the COVID-19 outbreak (Ethic Committe Desicion No: 2009-02/5). The informed consent forms were taken from all volunteers. Firstly, DNA was extracted from blood samples of COVID-19 patients. We performed PCR-based RFLP for genotyping rs3775290 and rs3775296. The patients had no other infections and chronic disease according to hematological, biochemical and serological laboratory findings. Cases were classified as severe and non-severe in terms of severity of the disease. COVID-19 patients hospitalized in intensive unit care and asymptomatic were severe and non-severe, respectively. Healthy volunteers had no disease complaints in anamnesis, as well as their examination was normal.

TLR3 c.1377C/T and -7C/A Genotyping

Genomic DNA was extracted from blood samples in EDTA containing tubes using phenol-chloroform method. PCR-RFLP method was used for determining genotype of TLRs. In a thermal cycler (BIORAD T100); PCR was performed in a total volume of 25 ml including 1 mM of each deoxynucleotide triphosphates (dCTP, dATP, dTTP and dGTP), approximately 100 ng DNA, 10X PCR buffer (A.B.T.TM cat.: E01-01-50), 0.2 mM each of primers (Table 1), 2.5 U/µL Taq DNA polymerase (A.B.T.TM lot: W911-A911) and 1.5 mM MgCl2. PCR reaction conditions for the 35-cycle amplification were as follows: initial denaturation at 94°C for 5 minute, denaturation at 94°C for 30 second, annealing at appropriate temperature of primers in Table 1 for 30 second and extension at 72°C for 1 minute, and final extension at 72°C for 5 minute. PCR products (5mL) were visualized in a 2% agarose gel. Amplification products were cut with restriction enzymes (NEB) in the Table 1 overnight.

Table 1. Experimental conditions for genotyping of the SNPs by RFLP

Gene polymophism	SNP	Primers	Annealing temp (°C)	Restriction endonuclease
TLR3 c.1377C/T	rs3775290	5'-CCAGGCATAAAAAGCAATATG-3' 5'-GGACCAAGGCAAAGGAGTTC-3'	52	TaqI
-7C/A	rs3775296	5'-GCATTTGAAAGCCATCTGCT-3' 5'-AAGTTGGCGGCTGGTAATCT-3'	52	MboII

SNP: Single nucleotide polymorphism; temp: Temperature

The fragments and undigested products were separated with 4% agarose gel electrophoresis and observed after stained with ethidium bromide (Figure 1).

In addition, ABI PRISM 377 automatic sequencer (Applied Biosystems, Foster City, CA) was used to verify sequence of three types (homozygous wild, heterozygous and homozygous mutant) of TLRs.

Statistical Analysis

All statistical analyses were carried out using the SPSS version 25. Statistical significance of the differences in TLR3 alleles and genotypes of all groups were calculated by Pearson's chi-squared test (Table 2). Genotype and allele frequency differences were considered significant when p-values were ≤0.05. One-way ANOVA was used to compare different genotypes in terms of clinical parameters for TLR3 c.1377C/T and -7C/A polymorphisms. Tukey test was used for lettering the groups. In addition, CHAID tree-based classification algorithm was created to determine the severity of the patients in our study (Fig. 2).

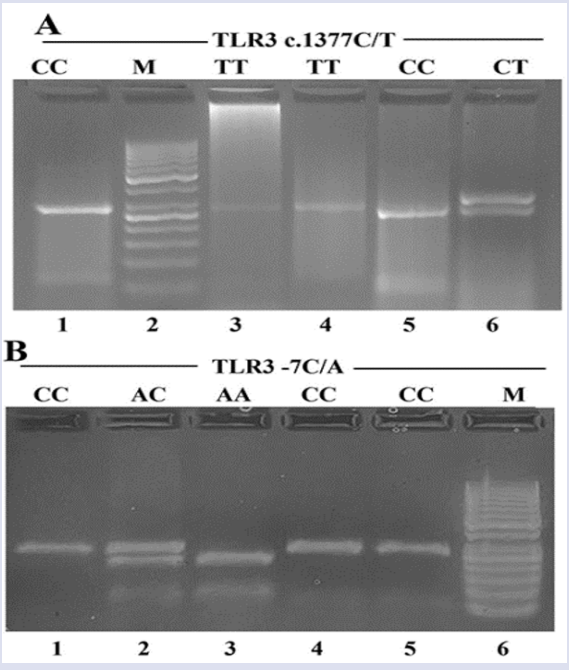

Figure 1: PCR-RFLP analysis of TLR3 c.1377C/T and -7A/C polymorphisms

A Homozygous wild genotype (CC): 275+62 bp (lane 1 and 5), heterozygous genotype (CT): 337+275+62 bp (lane 6), homozygous mutant genotype (TT): 337 bp (lane 3 and 4) for TLR3 c.1377C/T. B Homozygous wild genotype (CC): 279 bp (lane 1, 4 and 5), heterozygous genotype (CA): 279+207+72 bp (lane 2), homozygous mutant genotype (AA): 207+72 bp (lane 3) for TLR3 -7A/C. Bp: base pair, CI: Confidence interval, M: molecular weight marker (50 bp DNA ladder, Fermentas), OR: Odds ratio, PCR-RFLP: Polymerase chain reaction based restriction fragment length polymorphism. Two replicates were made all experiments

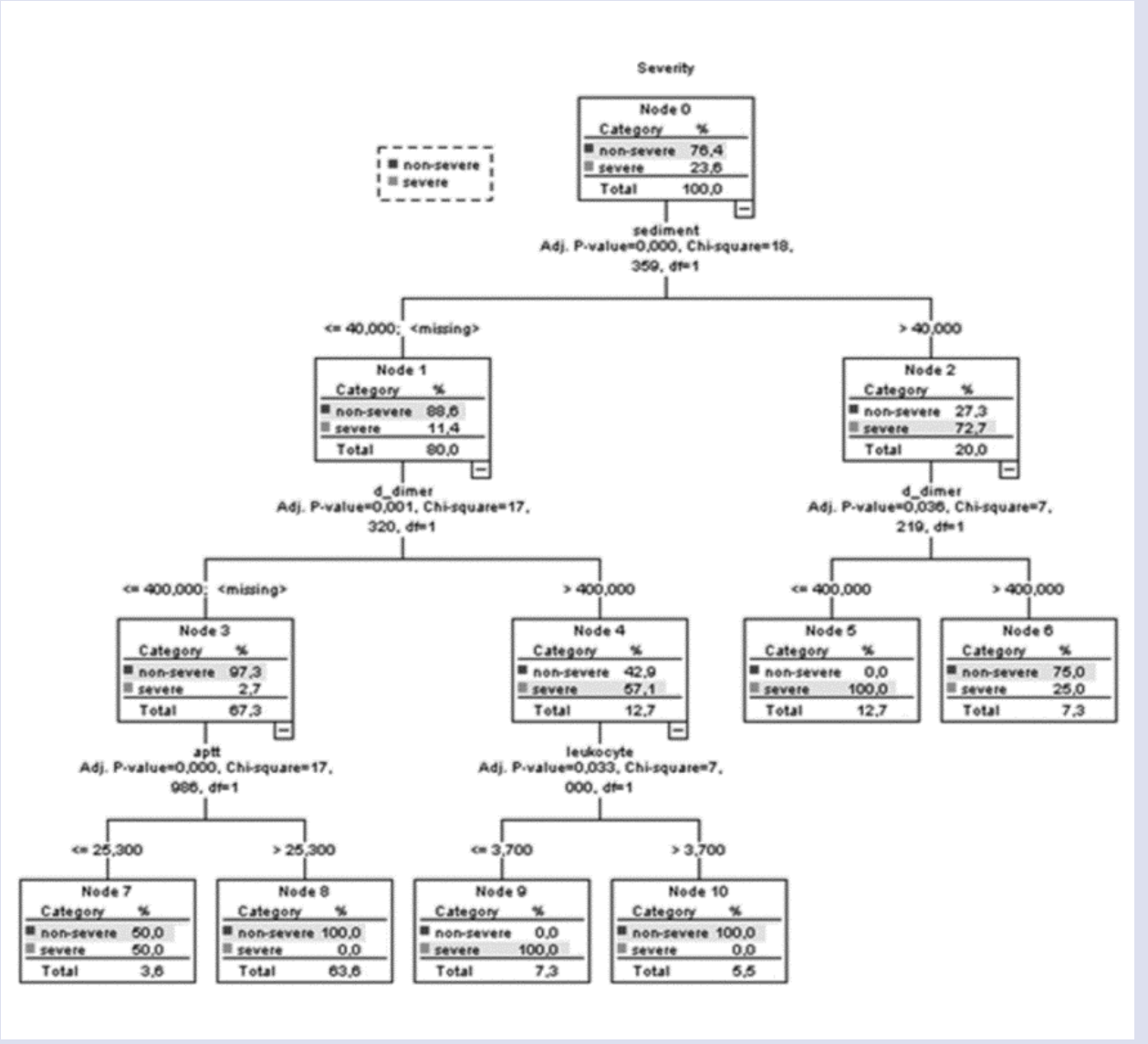

Figure 2 Determination severity of COVID-19 patients using CHAID tree-based classification algorithm Adj. p-value: Adjusted p value; activated partial thromboplastin time: Aptt; df: Degree of freedom.

Results

In this study, 150 patients with COVID-19 and 171 healthy individuals were included in our study population for TLR3 c.1377C/T (rs3775290) and -7C/A (rs3775296) polymorphisms. We compared allele and genotype frequencies of study population regarding disease severity (not demonstrated in Table). We found a statistically significant difference in TT genotype distribution between patients with COVID-19 and healthy controls (p= 0.02, OR= 2.80) in TLR3 c.1377C/T polymorphism (Table 2). There was a statistically significant difference in distribution of CA genotype (p= 0.04) and allele frequencies (p= 0.03) (Table 2) between two groups in TLR 3 -7C/A polymorphism. We also compared allele and genotype frequencies of patients with COVID-19 regarding disease severity for TLR3 c.1377C/T and -7C/A. There was no statistically significant difference between severe and non-severe groups in these polymorphisms (p> 0.05). In addition, we compared genotype and allele frequencies of case and controls in terms of gender. For TLR3 c.1377C/T, we found a statistically significant difference in male patients with TT genotype compared to control individuals (p= 0.04). We found 3.92 times higher risk in males with

TT genotype (Table 2). For TLR3 -7A/C, there was statistically significant difference in distribution A allele of females with COVID-19 (p= 0.05, OR= 0.55). The data of the present study are summarized in Table 2.

Table 2. Risk estimates and frequencies of allele and genotypes for TLR3 (c.1377C/T and -7C/A) polymorphisms in COVID-19 patients and healthy controls.

TLR3 polymorphism	Case, n (%)	Control, n (%)	P value	OR (95%CI)
c.1377C/T				
Allele				
C	203 (67.67)	248 (72.51)		
T	97 (32.33)	94 (27.49)	0.18	1.26 (0.90-1.77)
Genotype				
CC	72 (48.33)	85 (49.71)		
CT	59 (39.17)	78 (45.61)	0.63	0.89 (0.56-1.42)
TT	19 (12.5)	8 (4.68)	0.02*	2.80 (1.16-6.79)
Female				
C	118 (71.95)	154 (72.64)		
T	46 (28.05)	58 (27.36)	0.85	1.05 (0.66-1.65)
CC	44 (54.32)	53 (50)		
CT	30 (37.04)	48 (45.28)	0.40	0.77 (0.42-1.41)
TT	7 (8.64)	5 (4.72)	0.27	1.93 (0.59-6.31)
Male				
C	87 (63.04)	93 (71.54)		
T	51 (36.96)	37 (28.46)	0.14	1.47 (0.88-2.47)
CC	29 (42.03)	31 (47.69)		
CT	29 (42.03)	31 (47.69)	1.00	1.0 (0.49-2.05)
TT	11 (15.94)	3 (4.62)	0.04*	3.92 (0.99-15.48)
-7C/A				
Allele				
C	265 (88.33)	282 (82.46)		
A	35 (11.67)	60 (17.54)	0.03*	0.62 (0.40-0.97)
Genotype				
CC	117 (77.61)	115 (67.25)		
CA	31 (20.90)	52 (30.41)	0.04*	0.59 (0.35-0.98)
AA	2 (1.49)	4 (2.34)	0.68	0.49 (0.09-2.74)
Female				
C	152 (89.41)	153 (82.26)		
A	18 (10.59)	33 (17.74)	0.05*	0.55 (0.30-1.02)
CC	68 (80)	62 (66.67)		
CA	16 (18.82)	29 (31.18)	0.05*	0.50 (0.25-1.01)
AA	1 (1.18)	2 (2.15)	0.61	0.46 (0.40-5.15)
Male				
C	112 (86.15)	129 (82.69)		
A	18 (13.85)	27 (17.31)	0.42	0.77 (0.40-1.47)
CC	48 (73.85)	53 (67.95)		
CA	16 (24.61)	23 (29.49)	0.49	0.77 (0.36-1.62)
AA	1 (1.54)	2 (2.56)	1.00	0.55 (0.50-6.28)

*: p≤0.05; n: individual number; OR: Odds ratio; p: Significant value.

As a result of the ANOVA test for TLR3 c.1377C/T, we observed that platelet, sediment, d-dimer, LDH and alanine aminotransferase (ALT) parameters were statistically significant in CT and TT genotypes (p< 0.05) (Table 3). Tukey test was used to investigate the differences of clinical parameters between the genotypes. Platelet, sediment, d-dimer, LDH and ALT levels were statistically significant in individuals with CT and TT genotypes according to the Tukey test results. The findings obtained in this study showed that platelet level was statistically significant different in individuals with CT genotype. In addition, we observed that sediment (p= 0.02) and d-dimer (p= 0.04) were statistically significant in CC, CA and AA genotypes for TLR3 -7A/C. Individuals with CC, CA and AA genotypes showed statistically significant difference regarding sediment and d-dimer (Table 3).

In this study, a decision tree based on the CHAID tree-based classification algorithm was created to determine the severity of the patients with COVID-19 (Figure 2). We found that sediment, d-dimer, leukocyte and activated partial thromboplastin time (aptt) variables were important predictors in determining the severity of patients (Adj p= 0.00). The findings showed that 76.4% of the patients were non-severe and 23.6% were severe patients according to the root node (Node 0), which is at the top of the classification tree diagram. Sediment showed a more significant effect on the severity of patients than the other variables found in the classification tree (Adj p=0.000; Chi-square=18.359; df1=1) (Figure 2).

Table 3. Association between genotype and clinical parameters of COVID-19 patients

TLR3 c.1377C/T Genotype	Platelet (mean ±std. error)	Sediment (mean ±std. error)	D-dimer (mean ±std. error)	LDH (mean ±std. error)	ALT (mean ±std. error)
CC	206.59 ± 9.38b	31.92 ± 3.11a	638.86 ± 149.07a	269 ± 14.18a	19.82 ± 1.73b
CT	244.92 ± 12.51a	24.40 ± 3.38b	269.27 ± 60.74b	221.65 ± 12.56b	24.41 ± 2.54a
TT	223.94 ± 11.87b	20.07 ± 2.56b	223.33 ± 57.86b	239.06 ± 16.25b	29 ± 4.26a
Sig.	0.03*	0.04*	0.04*	0.04*	0.04*
TLR3 -7C/A Genotype					
CC	217.22 ± 7.4	31.25 ± 2.41a	553.47 ± 105.12a	253.70 ± 10.67	23.03 ± 1.76
CA	234.09 ± 14.9	19.55 ± 2.99c	152.68 ± 21.26c	235.60 ± 14.25	23.90 ± 3.04
AA	222 ± 0.00	27.05 ± 0.05b	431 ± 0.00b	246 ± 0.00	23 ± 0.00
Sig.	0.53	0.02*	0.04*	0.64	0.96

*: $p \leq 0.05$; [a, b, c] Mean values with different symbols in the same column differ from each other ($p<0.05$). ALT: Alanine aminotransferase; LDH: Lactate dehidrogenase; Sig.: Significant value; std. error: Standard error

Also, descriptive statistics for d-dimer, aptt and leukocyte were shown in the classification tree (Figure 2). Statistically insignificant clinical parameters were removed from the classification tree.

Discussion

In the last 20 years, there have been pandemics worldwide that have been exposed to important coronavirus strains outbreaks. These outbreaks have been most often caused by severe acute respiratory syndrome (SARS) coronavirus (SARS-CoV). The SARS-CoV-2 has caused the COVID-19 outbreak and continues to be effective worldwide. Today, genetic polymorphisms are efficient in pathways that demonstrate a crucial role in the binding of microbiological agents to the host cell, host disease resistance, disease susceptibility and severity. There are few studies in the literature on COVID-19 and gene polymorphisms. Genetic variations in the TLR pathway contribute to resistance or susceptibility to various infections. Thus, in this study, we examined the effects of TLR3 c.1377C/T (rs3775290) and TLR3 -7C/A (rs3775296) polymorphisms on COVID-19 infection.

TLR3, TLR7, TLR8 and TLR9 recognize viral pathogen-associated particles, and these molecules are called antiviral TLRs. Such TLRs have a major role in reducing viral infection, causing a decrease in disease severity. Any mutation or SNPs in the TLR pathway may cause impairment in signal transduction, and this impairment may cause recurrence of viral infections [20]. In this study, there was no statistically significant difference in TLR3 c.1377C/T T allele frequencies between the case and control group (p= 0.18). We found that T allele frequency was 27.49% (Table 1). The T allele frequency of healthy control ranges from 19% to 38% in different populations. T allele frequency was 33.7% in Chinese Han population [21]; 35.66% in Eastern Indian population [22]; 25.5% in Egyptian population [23]. We found a significant difference in TT genotype between COVID-19 cases and controls (p= 0.02; Table 1). We also found that individuals with TT genotype had approximately three times greater risk than individuals with CC genotype for COVID-19 (OR= 2.80; Table 2). In a recent study, this polymorphism was investigated in COVID-19 disease. Consistent with our results, the TT genotype was found to be statistically significant between patient and control group [24].TLR3 c.1377C/T polymorphism has been associated with another viral disease as our present study result. One of them, an association analysis by Huang (2015), showed that the TT genotype of TLR3 c.1377C/T polymorphism was related to decreased risk for chronic hepatitis B, HBV-related liver cirrhosis, and HBV-related hepatocellular carcinoma diseases [25]. In another study, frequency of polymorphic genotype TLR3 c.1377C/T TT was not significantly different between hepatitis C virus (HCV) infection-positive patient and control group, whereas TLR-3 c.1377 T allele was found to be associated with advanced hepatic fibrosis stage [23]. Engin et al. found that the homozygous mutant genotype (TT) frequency of TLR3 c.1377C/T in patients with CCHF was significantly higher than that of the controls [19]. A study among patients with DENV-CHIKV co-infection and CHIKV mono-infection revealed that patients with the TLR3 rs3775290 TT genotype exhibited a significant susceptibility to co-infection [22]. Mosaad et al. (2019) found that a significant higher frequency was found for the CT genotype of TLR3 rs3775290 in chronic HCV infection [26].

In humans, the TLR3 promoter region maintains promoter integrity and promoter-specific virus responsive elements. It has been suggested that promoter polymorphisms, such as TLR3 -7C/A, may cause transcriptional regulation of TLR3 and alter gene expression in response to inflammatory cytokines [27]. TLR3s have the ability to initiate a signaling cascade that activates type 1 interferons and inflammatory cytokines [28]. Thus, they trigger the initiation of the immune response against both DNA and RNA viruses. When the human body is exposed to a viral infection, interferons are induced by the TLR3/TRIF pathway within a few hours. TLR3 identifies dsRNA and viral infection causes dsRNA generation either as a replication intermediate for ssRNA viruses or as a by-product of symmetrical transcription in DNA viruses. Since dsRNA is a universal viral pathogen-associated molecule, TLR3 may have an effective role in

antiviral immunity against both DNA and RNA viruses [29]. In our study, we have also investigated TLR3 -7C/A promoter polymorphism in COVID-19 infection. There was a significant difference TLR3 -7C/A A allele frequency between case and control group (p= 0.03; Table 2) We have found that mutant A allele frequency was 17.54% in the control group (Table 2). A allele frequency ranged from 0.00% to 27% in different population. A allele frequency was 26.7% in Iran population [30]; 10% in Egyptian population [22]; 21.5% in Chinese population [31]; 0.00% in Cyprus population [32]. We found that CA genotype frequency was significantly different between the case and control (p= 0.04; Table 2). We also found that individuals with CA genotype have approximately 0.6 times greater protective effects than individuals with the CC genotype for COVID-19. However, there was any significant difference in allele and genotype frequencies between severe and non-severe. In a study of CCHF disease, there was no significant difference in distribution of TLR3 -7C/A genotype and allele frequencies [19]. In another study, frequency of polymorphic genotypes in TLR3 -7C/A were not significantly different between studied HCV-positive patients and controls. Consistent with the findings obtained in the present study, Deeba et al. (2019) reported that the distribution of polymorphic TLR3 -7C/A A allele showed a statistical significance in natural killer cells [31]. There was also a significant difference in the frequency distribution of TLR3 -7C/A CA heterozygous genotypes and mutant A alleles in the human T-lymphotropic virus type 1 (HTLV-1) disease like our result. Habibabdi et al. (2020) reported that these observations might indicate a protective factor to prevent HTLV-1 infection for the Iranian population [30]. Similar to the findings obtained in Habibabdi et al.'s (2020) study, we observed CA genotype and mutant A allele might have a protective role for COVID-19 infection (OR= 0.59 and OR= 0.62, respectively; Table 2).

Patients with COVID-19 presented with higher coagulatory potential [5]. Liver biochemical parameters like aspartate aminotransferase (AST), ALT and LDH were strongly correlated with COVID-19 mortality. Non-survivors had higher levels of AST, ALT and LDH [33]. In this study, we have also analyzed the relationship between allele-genotype distribution and clinical parameters that affects disease severity. We found that patients with COVID-19 with CC genotype had the highest sediment, d-dimer, LDH level regarding two polymorphisms. Patients with CT genotype had the highest platelet level, whereas patients with TT genotype had the highest ALT level for TLR3 c.1377C/T (Table 3). In addition, individuals with CA genotype had the highest platelet and ALT level for TLR3-7C/A (Table 3).

Gender differences may exist in patients with COVID-19 of severe type. Male patients may have more complicated clinical conditions and worse in-hospital outcomes than women [34]. We found that male patients with TT genotype showed a statistically significant difference for TLR3 c.1377C/T. Also, females with A allele and CA genotype differed statistically significant for TLR3-7C/A.

In conclusion, TLR3 c.1377 TT genotype frequency in patients with COVID-19 was higher than the healthy controls. TLR3 c.1377 TT genotype, especially in males, might increase susceptibility to COVID-19 disease. TLR3 -7C/A A allele and TLR3 -7C/A CA genotype may be protective factors for COVID-19. In addition, clinical parameters like sediment and d-dimer are among the most important factors that may affect COVID-19 severity for TLR3 c.1377C/T and -7C/A polymorphisms.

Acknowledgements

This study was supported by the Scientific Research Council of Sivas Cumhuriyet University (Grant number: F-2021-635), Sivas, Turkey.

Conflict of interest

The authors state that did not have a conflict of interests

References

[1] Shang J., Wan Y., Liu C., Yount B., Gully K., Yang Y., Structure of mouse coronavirus spike protein complexed with receptor reveals mechanism for viral entry, *PLoS Pathog,* 3 (2020) 9-16.

[2] Chen Y., Liu Q., & Guo D., Emerging coronaviruses: genome structure, replication, and pathogenesis, *Journal of Medical Virology, 92 (*2020) 418-423.

[3] Gorbalenya A.E., Baker S.C., Baric R.S., Groot R.J., Drosten C., Gulyaeva A.A., The species severe acute respiratory syndrome related coronavirus: classifying 2019-nCoV and naming it SARS-CoV-2, *Nat Microbiol.,* 5 *(*2020) 536–544.

[4] WHO 2022 (2022, February 23). Retrieved from https://www.who.int/emergencies/diseases/novel-coronavirus-2019

[5] Hoechter D.J., Becker-Pennrich A., Langrehr J., Bruegel M., Zwissler B., Schaefer S., Higher procoagulatory potential but lower DIC score in COVID-19 ARDS patients compared to non-COVID-19 ARDS patients, Thromb Res., 196 (2020) 186-192.

[6] Park S.E., Epidemiology, virology, and clinical features of severe acute respiratory syndrome-coronavirus-2 (SARS-CoV-2; Coronavirus Disease-19), *Clinical and Experimental Pediatric, 63*(4) (2020) 119.

[7] Wu F., Zhao S., Yu B., Chen Y.M., Complete genome characterisation of a novel coronavirus associated with severe human respiratory disease in Wuhan, China, *BioRxiv*, (2020).

[8] Cui J., Li F., Shi Z.L., Origin and evolution of pathogenic coronaviruses, *Nature Reviews Microbiology, 17*(3) (2019) 181-192.

[9] Zhou P., Yang X.L., Wang X.G., Hu B., Zhang L., Zhang W., A pneumonia outbreak associated with a new coronavirus of probable bat origin, *Nature, 579*(7798) (2020) 270-273.

[10] Wan Y., Shang J., Graham R., Receptor recognition by the novel coronavirus from Wuhan: an analysis based on decade-long structural studies of SARS coronavirus, *Journal of Virology. 94*(7) (2020) e00127-20.

[11] Wu J., & Chen Z.J,. Innate immune sensing and signaling of cytosolic nucleic acids, *Annual review of immunology*, 32 (2014) 461-488.

[12] Kawai T., & Akira S., The role of pattern-recognition receptors in innate immunity: update on Toll-like receptors, *Nature Immunology, 11*(5) (2010) 373.

[13] Triantafilou M., Gamper FG., Haston RM., Mouratis MA., Morath S., Hartung T., et al. Membrane sorting of toll-like receptor (TLR)-2/6 and TLR2/1 heterodimers at the cell surface determines heterotypic associations with CD36 and intracellular targeting, *Journal of Biological Chemistry,* 281(41) (2006) 31002-31011.

[14] Takeda K., Kaisho T., & Akira S., Toll-like receptors*, Annual Review of Immunology*, 21(1) (2003) 335-376.

[15] Matsumoto M., & Seya T., TLR3:interferon induction by double-stranded RNA including poly (I: C), *Advanced Drug Delivery Reviews,* 60(7) (2008) 805-812.

[16] Mukherjee S., Karmakar S., Babu S.P.S., TLR2 and TLR4 mediated host immune responses in major infectious diseases: a review, *The Brazilian Journal of Infectious Diseases, 20*(2) (2016) 193-204.

[17] Abdelwahab S.F., Hamdy S., Osman A.M., Zakaria Z.A., Association of the polymorphism of the Toll-like receptor (TLR)-3 and TLR-9 genes with hepatitis C virus-specific cell-mediated immunity outcomes among Egyptian health-care workers, *Clinical & Experimental Immunology, 203*(1) (2021) 3-12.

[18] Jin Y., Qiu S., Shao N., Zheng J., Association of toll-like receptor gene polymorphisms and its interaction with HPV infection in determining the susceptibility of cervical cancer in Chinese Han population, *Mammalian Genome, 28*(5) 2017 213-219.

[19] Engin A., Arslan S., Özbilüm N., Bakir M., Is there any relationship between Toll-like receptor 3 c. 1377C/T and−7C/A polymorphisms and susceptibility to Crimean Congo hemorrhagic fever?, *Journal of medical virology, 88*(10) (2016) 1690-1696.

[20] Frazao J.B., Errante P.R., Condino-Neto A., Toll-like receptors' pathway disturbances are associated with increased susceptibility to infections in humans, *Archivum Immunologiae et Therapiae Experimentalis*, 61(6) 2013 427-443.

[21] Wang J., Liu Y., Liu Y., The association between TLR3 rs3775290 polymorphism and sporadic Parkinson's disease in Chinese Han population, *Neuroscience Letters,* 728 (2020) 135005.

[22] Sengupta S., Mukherjee S., Bhattacharya N., & Tripathi A., Differential genotypic signatures of Toll-like receptor polymorphisms among dengue-chikungunya mono-and co-infected Eastern Indian patients, *European Journal of Clinical Microbiology & Infectious Diseases*, 40(7) (2021) 1369-1381.

[23] Zayed R.A., Omran D., Mokhtar D.A., Association of toll-like receptor 3 and toll-like receptor 9 single nucleotide polymorphisms with hepatitis C virus infection and hepatic fibrosis in Egyptian Patients, *Am. J. Trop. Med. Hyg.,* 96(3) (2017) 720–726.

[24] Alseoudy, M. M., Elgamal, M., Abdelghany, D. A., Borg, A. M., El-Mesery, A., Elzeiny, D., & Hammad, M. O., Prognostic impact of toll-like receptors gene polymorphism on outcome of COVID-19 pneumonia: A case-control study, *Clinical Immunology (Orlando, Fla.),* 235 (2022) 108929

[25] Huang X., Li H., Wang J., Huang C., Lu Y., Qin X., Genetic polymorphisms in Toll-like receptor 3 gene are associated with the risk of hepatitis B virus-related liver diseases in a Chinese population, *Gene*, *569*(2) 2015 218-224.

[26] Mosaad Y.M., Metwally S.S., Farag R.E., Lotfy Z.F., AbdelTwab H.E., Association between toll-like receptor 3 (TLR3) rs3775290, TLR7 rs179008, TLR9 rs352140 and chronic HCV, *Immunological Investigations*, *48*(3) (2019) 321-332.

[27] Zhou P., Fan L., Yu K.D., Zhao M.W., Toll-like receptor 3 C1234T may protect against geographic atrophy through decreased dsRNA binding capacity, *The FASEB Journal*, 25(10) (2011) 3489-3495.

[28] Huik K., Avi R., Pauskar M., Kallas E., Jõgeda E.L., Karki T., Association between TLR3 rs3775291 and resistance to HIV among highly exposed Caucasian intravenous drug users, *Infection, Genetics and Evolution, 20* (2013) 78-82.

[29] Akira S., Uematsu S., & Takeuchi O., Pathogen recognition and innate immunity, *Cell, 124*(4) (2006) 783-801.

[30] Habibabadi H.M., Parsania M., Pourfathollah A.A., Haghighat S., Sharifi Z., Association of TLR3 single nucleotide polymorphisms with susceptibility to HTLV-1 infection in Iranian asymptomatic blood donors, *Rev. Soc. Bras. Med. Trop*., 22 (53) (2020) e20200026.

[31] Fan L., Zhou P., Hong Q., Chen A.X., Liu G.Y., Yu K.D., Toll-like receptor 3 acts as a suppressor gene in breast cancer initiation and progression: a two-stage association study and functional investigation, *Oncoimmunology,* 30 (2019) 8(6).

[32] Deeba E., Koptides D., Lambrianides A, Pantzaris M., Krashias G., Christodoulou C., Complete sequence analysis of human toll-like receptor 3 gene in natural killer cells of multiple sclerosis patients, Mult. Scler. Relat. Disord., 33 (2019) 100-106.

[33] Ye L., Chen B., Wang Y., Yang Y., Zeng J., Deng G., Prognostic value of liver biochemical parameters for COVID-19 mortality, *Ann Hepatol*, 21 (2021) 100279.

[34] Li J., Zhang Y., Wang F., Liu B., Li H., Tang G., Chang Z., Sex differences in clinical findings among patients with coronavirus disease 2019 (COVID-19) and severe condition, *MedRxiv*., (2020).

Cumhuriyet Sci. J., 44(1) (2023) 53-61
DOI: https://doi.org/10.17776/csj.1230387

Cumhuriyet Science Journal

| csj.cumhuriyet.edu.tr | Founded: 2002 ISSN: 2587-2680 e-ISSN: 2587-246X Publisher: Sivas Cumhuriyet University

An *In Silico* Approach to Define Potential Biomarkers of miRNA-Associated ceRNAs for Breast Cancer

Serap Ozer Yaman [1,a,*], Sema Mısır [2,b]

[1] *Department of Medical Biochemistry, Faculty of Medicine, Karadeniz Technical University, Trabzon, Türkiye.*
[2] *Department of Biochemistry, Faculty of Pharmacy, Sivas Cumhuriyet University, Sivas, Türkiye.*
**Corresponding author*

Research Article

History
Received: 06/01/2023
Accepted: 17/03/2023

ABSTRACT

Breast cancer (BC) is the most common type of cancer with the highest incidence in women. Particularly in breast cancer, competing endogenous RNAs (ceRNAs) play crucial roles in a variety of metabolic pathways including proliferation, migration, and apoptosis. The aim of the present study is to identify combinatorial target genes (ceRNAs) by employing *in silico* research to identify miRNAs specific to BC. The other aim was to determine possible biomarkers for the diagnosis of BC by selecting those containing the Transcribed Ultra Conserved Region (T-UCR). Using the miRWalk database, 40 miRNAs that have been experimentally shown to be clinically linked with BC were found. T-UCR-containing genes with potential ceRNA activity were identified. Genes with statistically significant changes in expression between BC and normal breast tissue were identified using the *GEPIA*. The relationship of the *CLK3* and *NFAT5* genes was found using the Spearman correlation test. The Spearman correlation test was used to determine the association between the *CLK3* and *NFAT5* genes, and the genes were found to be significantly less expressed in BC. The *NFAT5* and *CLK3* gene pair have been found to be associated with BC ($p<0.001$; $r=0.35$), and may function as useful biomarkers for BC.

Keywords: Biomarker, Breast cancer, ceRNA, miRNA.

[a] *serapozer@ktu.edu.tr* *https://orcid.org/0000-0002-5089-0836* [b] *smisir@cumhuriyet.edu.tr* *https://orcid.org/0000-0002-5919-3295*

Introduction

Breast cancer (BC) accounts for 25.2% of all female cancers in the world. The prevalence of female cancer is highest in BC, and rates are rising quickly [1]. BC is a complex disease that greatly strains human health and reduces the quality of life. In 2018, it is predicted that there were 626.679 BC related deaths (6.6% of 9.6 million deaths) and 2,088,849 newly recognized BC cases (11.6% of 18.1 million new cases) [2]. Among the imaging medical diagnostic methods used for the early detection of BC, the only clinically proven test method is mammography [3]. The prevalence and fatality of BC highlight the importance of studying the processes behind the breast cancer development as well as developing new methods of diagnosis and therapy [3, 4].

A group of non-coding RNAs with a length of 18–22 nucleotides are called microRNAs (miRNAs) which acts as post-transcriptional modulators of gene expression. miRNAs bind directly to the mRNA of the target molecule, regulating gene expression by inhibiting translation and causing mRNA degradation. Finding important miRNA targets for cancer research is crucial because each miRNA has the ability to regulate hundreds of target genes. [5]. By targeting the expression of oncogenes or tumor suppressor genes, miRNAs have been shown to play vital roles in the genesis, development and progression of BC. To determine the roles of miRNAs in BC, it is necessary to examine miRNA expression profiles between normal and tumor tissues, then to understand differentially expressed miRNAs [6].

By competing with one another for miRNAs, transcripts known as competing endogenous RNA (ceRNAs) can regulate one another at the post-transcriptional level. CeRNA connections link the roles of non-coding RNAs such as microRNA, long non-coding RNA, pseudogenic RNA, and circular RNA to those of protein-coding mRNAs. CeRNAs, which are transcripts that have the miRNA response element, can be used to regulate post-transcriptional gene expression in both health and disease. Numerous elements, including the quantity and subcellular location of ceRNA components, the affinity of miRNAs to their sponges, RNA sequences, and regulation, all have an impact on ceRNA function. Differences in these factors can release ceRNA networks and thus cause many pathological conditions, including cancer [7].

In recent years, non-coding RNAs (ncRNAs) have attracted major interest in cell transformation. By comparing the genomes of the mouse, rat, and human using bioinformatics tools, ultra-conserved regions (UCRs) were identified in 2004. UCRs consist of at least 481 genomic sequences between 200-779 bp lengths that are strictly conserved across the three vertebrate species. Although the function of T-UCRs is not fully known, it is stated that their conservation across the species is important for mammalian ontogenesis/phylogenesis. T-UCRs have diverse profiles in different types of human malignancies, according to the current genome profiling research, which further supports their significance in human carcinogenesis [8].

MiRNAs, which are well-known to play a crucial functional role in cancer, have promised hope in elucidating the molecular pathophysiology of the disease and creating molecularly targeted treatments.

The aim of this study is to determine BC-specific miRNAs, find combinatorial target genes (ceRNAs), select among them those containing the Transcriptionally Ultra Conserved Region (T-UCR) among them, and identify potential predictive biomarkers for BC diagnosis by *in silico* analysis.

Methods

Identification of miRNAs in BC

Forty miRNAs that have been experimentally proven to be clinically associated with BC were identified using the miRWalk database. The anticipated and verified information on miRNA-target interaction is available from the miRWalk database. The "Validated Target module" utilized in this study is updated every month [9].

Identification of BC-specific miRNA-mediated ceRNAs

1009 genes predicted to be characterized by these 40 miRNAs simultaneously were found using ComiR (combinatorial microRNA database), and 869 genes with a ComiR score above 0.911 were taken into consideration. The combinatorial arrangement of miRNA pairs of the observed transcriptome was determined. In line with the results obtained, comprehensive ones for combinatorial editing by miRNAs are presented. The probability of combinatorial miRNA activity was estimated in annotating data with the ComiR score. Therfore, combinatorial arrangement and statistical constraints were applied to recover the correct miRNA in BC and identify hundreds of genes from miRNA sets. ComiR is a web tool for predicting the targets of miRNAs. ComiR calculates the potential for targeting by a set of miRNAs, each of which may have one or more targets in its 3'untranslated region. ComiR utilizes user-provided miRNA expression levels [10].

Determination of BC-associated ceRNA with genes including T-UCR

T-UCRs play role in the development of many diseases, including cancer. For this reason, it was ensured that these genes were matched. Therefore, the data of the study by Bejerano et al. were taken as a basis, and genes containing T-UCR in their exonic regions were determined [11].

Differential Expression of Genes in Breast Cancer and Healthy Tissues

Based on data from the Genotype-Tissue Expression (GTEx) and Cancer Genome Atlas (TCGA), GEPIA is an interactive web application. Many visualization and analysis tools for gene expression have been made available by GEPIA. Using the gene expression profiling database GEPIA, we discovered *NFAT5* and *CLK3* genes among breast cancer-associated ceRNAs, including T-UCR, with significant expression changes between BC and normal breast tissue.

Distribution of *NFTA5* and *CLK3* gene expressions according to TCGA normal and GTEx data in GEPIA was performed using ANOVA. And also, |Log2FC| Cutoff:1 and q-value Cutoff: 0.01 were taken [12].

Correlation analysis of NFAT5 and CLK3 genes

Using the Spearman correlation test in the GEPIA, a comparison of the *NFAT5* and *CLK3* genes in BC and normal breast tissue was performed [12].

Figure 1 shows the schematic flow chart illustrates the general methodology including miRNA selection, miRNA-mediated ceRNAs analysis, matching of ceRNAs with the genes containing T-UCR and correlation analysis.

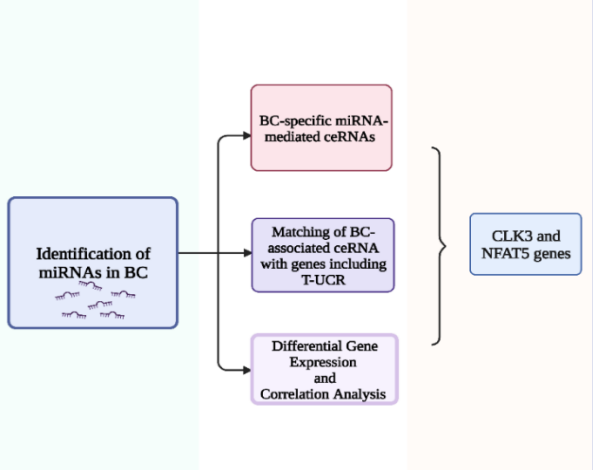

Figure 1. A schematic flow chart of the in silico process in the study.

Results

40 miRNAs that have been experimentally proven to be associated with breast cancer (MCF-7) were detected. 1009 genes targeted simultaneously by these 40 miRNAs were identified and 869 genes with a ComiR score above 0.911 were considered (Table 1, 2, 3).

Table 1. List of miRNAs involved in MCF-7 cells

hsa-let-7f-5p	hsa-miR-10b-5p	hsa-miR-1226-3p	hsa-miR-7-5p	hsa-miR-145-5p	hsa-miR-21-5p
hsa-miR-146b-5p	hsa-miR-155-5p	hsa-miR-196a-5p	hsa-miR-520e	hsa-miR-185-5p	hsa-miR-17-5p
hsa-miR-196b-5p	hsa-miR-199b-5p	hsa-miR-200a-3p	hsa-miR-22-3p	hsa-miR-205-5p	hsa-miR-206
hsa-miR-20a-5p	hsa-miR-146a-5p	hsa-miR-200b-3p	hsa-miR-221-3p	hsa-miR-222-3p	hsa-miR-27a-3p
hsa-miR-27b-3p	hsa-miR-299-5p	hsa-miR-29a-3p	hsa-miR-29b-3p	hsa-miR-328-3p	hsa-miR-328-5p
hsa-miR-339-5p	hsa-miR-342-3p	hsa-miR-345-5p	hsa-miR-375	hsa-miR-451a	hsa-miR-520b
hsa-miR-181b-5p	hsa-miR-125b-5p	hsa-miR-9-3p	hsa-miR-92a-3p		

Table 2. Genes likely to show the highest ceRNAs function for 40 miRNAs by the ComiR.

Gene ID	Comir equal abundance score	Gene ID	Comir equal abundance score	Gene ID	Comir equal abundance score	Gene ID	Comir equal abundance score
CFLAR	0.9233	GAS7	0.9182	AGPS	0.9111	SLC39A9	0.9115
SLC7A2	0.9148	CDKL5	0.9228	PRDM11	0.9144	IKZF2	0.9191
SARM1	0.9197	REV3L	0.9224	MRE11A	0.913	PIAS1	0.9143
LIG3	0.9123	IYD	0.9206	NDUFS1	0.9192	DAPK2	0.9144
KMT2E	0.9149	ZNF207	0.9226	KPNA6	0.9185	CYP46A1	0.9113
MAP3K9	0.9168	BRCA1	0.9168	AGPAT4	0.9197	INPP4A	0.9206
FARP2	0.9119	NUDCD3	0.9191	POU2F2	0.9135	ADAM28	0.911
DCUN1D1	0.9135	HDAC9	0.9176	RSF1	0.9187	CELF2	0.9173
ADAMTS6	0.9189	H6PD	0.9191	KIAA2022	0.9135	SLC4A8	0.9206
HEBP2	0.9203	ALX4	0.9156	AP5M1	0.9207	FAM168A	0.918
EIF2AK2	0.9168	KMT2C	0.9239	PRDM6	0.9152	NCKAP1	0.9233
MON2	0.9198	EPN1	0.9236	CDON	0.9123	HIPK2	0.9227
GNAI3	0.9241	WDR3	0.9126	TRAM2	0.9195	SNAP91	0.9138
CYB5R4	0.9183	GSTO2	0.9159	SLC9A7	0.9172	CD84	0.9178
ATXN3	0.9241	MYO9A	0.9119	RRP15	0.9166	POLR1A	0.9137
RORA	0.9216	GNB5	0.9222	SLC44A1	0.9116	EXOC5	0.9161
MGAT4A	0.917	MBD3	0.9154	ZFYVE26	0.9134	SMC1A	0.9151
CHFR	0.9224	TRHDE	0.9201	AP1M1	0.9216	MAP3K13	0.916
RASAL2	0.9233	ZNF37A	0.9114	FNDC3B	0.9137	BCAP29	0.911
RBM7	0.9112	RBMS2	0.9145	PAG1	0.9179	MBNL3	0.9222
PPP1R12B	0.9233	DNAJC10	0.9238	DCX	0.9188	ACER3	0.9171
PIK3C3	0.9143	N4BP2	0.9202	SAR1A	0.9163	STX7	0.9222
RFX3	0.9113	RAB21	0.9234	CDH7	0.9153	PGR	0.9205
FAM135A	0.911	TRPM3	0.9205	TNPO1	0.9167	DIS3	0.9187
ZNF264	0.9214	REST	0.9115	SSH1	0.9205	ATRX	0.9154
HSD17B2	0.9213	SH3BP2	0.9197	C14orf166	0.9204	MAVS	0.9226
ZBTB25	0.9229	GPATCH2L	0.9231	ZNF268	0.923	PDPR	0.9151
TNRC6A	0.9228	WDR7	0.9192	RGS17	0.9189	AGO1	0.9214
RFFL	0.9122	SEC22C	0.9195	CBX5	0.9211	FKBP5	0.9176
CECR2	0.9169	MAPK1	0.9207	ADRBK2	0.9152	MTMR3	0.9179
TNRC6B	0.9236	KIAA0930	0.9187	KCNK10	0.917	DDHD1	0.9227
SPTLC2	0.917	ZC3H14	0.9238	RPS6KA5	0.9241	RNF24	0.9167
RASSF2	0.9145	CDS2	0.9217	ST8SIA5	0.9234	CEP192	0.9197
LIPG	0.9188	XIAP	0.9143	PCYT1B	0.913	FGF14	0.9225
STK24	0.9219	DGKH	0.9237	INTS6	0.9235	NUP93	0.9134
NFAT5	0.9236	LONP2	0.9189	PLLP	0.9152	SLC7A6	0.9175
CMC2	0.9184	MLYCD	0.9211	USP31	0.9135	XYLT1	0.9126
HOMER2	0.9212	DTWD1	0.9223	BMF	0.9116	FZD3	0.923
UBE2W	0.9152	NOVA2	0.9136	AVL9	0.9148	GTPBP10	0.917
CDK6	0.9218	ITGB8	0.9195	FKBP14	0.9123	PLEKHA8	0.9199
ZKSCAN1	0.9187	RBM28	0.9237	TMEM106B	0.922	PSMA2	0.9144
FKTN	0.9178	FSD1L	0.9165	MEGF9	0.9143	TRDMT1	0.9229
PLEKHA1	0.9231	CCSER2	0.912	BMPR1A	0.9192	CPEB3	0.9184
SH3PXD2A	0.9188	TSPAN14	0.9239	NUFIP2	0.9202	FBXL20	0.9184
TMEM33	0.9134	GABRA4	0.9162	USP46	0.92	GAB1	0.914
TRIM2	0.916	WHSC1	0.9144	CBL	0.9218	KIAA1549L	0.9134
SLC1A2	0.9205	SOX6	0.9177	CAPRIN2	0.9213	PPM1H	0.9147
KCNA1	0.9199	C12orf49	0.9195	CAND1	0.9126	KRR1	0.9207
FRK	0.9232	SOD2	0.9236	MDGA1	0.9137	ZNF451	0.9161
BAG2	0.9112	KIAA1244	0.9209	SLC16A10	0.9227	PHACTR2	0.9145
QKI	0.9188	SEMA5A	0.9198	RNF130	0.9162	CNOT6	0.9145
LNPEP	0.9179	PRLR	0.9184	SKP1	0.9192	HEMK1	0.9237
ACVR2B	0.9228	NKTR	0.9137	FOXP1	0.912	INO80D	0.9216
TTL	0.923	TFCP2L1	0.9137	GGCX	0.915	KDM3A	0.916
ZNF142	0.9147	STRN	0.9124	KYNU	0.9235	AAK1	0.924
PLEKHA3	0.9234	TNR	0.9137	QSOX1	0.9125	KCNC4	0.9238
C1orf21	0.921	SLC35D1	0.912	TTF2	0.9159	LGALS8	0.9121
MTR	0.9166	RIMS3	0.9186	DR1	0.9202	PTBP2	0.9214
DIEXF	0.9114	ATF6	0.9184	CREB1	0.915	KLF7	0.9198
PHF3	0.9114	FBXO30	0.9113	MED28	0.9228	SLC16A7	0.9228
KLF12	0.9203	CCND2	0.9158	CYP20A1	0.9209	FBXW2	0.9145
ONECUT2	0.9238	DNAL1	0.9201	NRDE2	0.9221	DNMT3A	0.9145

YIPF4	0.9227	OGFRL1	0.9151	PANK3	0.9202	PLXDC2	0.9218
DNAJC15	0.9167	KDM3B	0.9123	PAPD5	0.9166	ZMYM2	0.9123
PIK3CA	0.9122	GTDC1	0.9221	SV2C	0.9196	RPAP2	0.9236
FAM126A	0.9196	KIAA1549	0.9135	SLC25A16	0.9119	RASSF8	0.9141
NCKAP1L	0.9124	ACVR1C	0.916	LPGAT1	0.9182	VAPB	0.9115
RAB22A	0.9217	NQO2	0.9184	SSR1	0.9192	ATXN1	0.9217
ATP5S	0.9188	GTF3C4	0.9143	PSD4	0.9179	OPA3	0.919
AP5S1	0.9146	CEP250	0.9222	AGO3	0.9236	KLC1	0.9233
PCNXL4	0.9218	PLEKHG3	0.9178	HELB	0.9219	RAP1B	0.9234
RAB3IP	0.9195	PTPRB	0.9112	DYRK2	0.9171	SLC35E1	0.9126
HIP1	0.9132	ZNF780B	0.9159	PODXL	0.9163	FOXP2	0.9209
MKLN1	0.9212	PDE11A	0.9165	TMOD2	0.9219	TTBK2	0.9172
C15orf57	0.9142	ICE2	0.9114	FAM63B	0.9152	MAS1	0.9217
PGPEP1	0.9172	RAB11FIP4	0.9181	RLIM	0.9159	CHRM3	0.9166
SCO1	0.9179	MPRIP	0.9202	FAM83F	0.9235	TMTC1	0.9149
MBD2	0.9142	SORT1	0.9172	WNT2B	0.9216	KIDINS220	0.9165
NAV1	0.9136	EMP1	0.9133	KLRD1	0.9231	DSC2	0.921
C5AR2	0.9122	CLOCK	0.9202	APC	0.9185	MTO1	0.9192
PRRG4	0.9118	GDF11	0.9145	ESPL1	0.9182	USP15	0.9234
GNS	0.9114	MDM2	0.9223	NTPCR	0.9142	KIAA1614	0.9135
RC3H1	0.9152	TMEM127	0.9113	GCC2	0.9177	ALDH1L2	0.9166
ITM2B	0.9147	TNS3	0.9156	DBNL	0.9188	ALPK3	0.9142
DCAF7	0.9157	KAT7	0.9168	UGGT1	0.9152	GOLGA1	0.9114
TAF8	0.9165	RAB30	0.9199	SLCO5A1	0.917	UNC13C	0.9151
PAQR5	0.9116	DBT	0.9205	EPT1	0.9177	ENTPD1	0.9213
SSFA2	0.9142	ABI2	0.9241	USP8	0.9239	TMOD3	0.9194
KIAA1644	0.9196	FGD4	0.9112	NDUFA9	0.9211	LLPH	0.9166
TMEM132B	0.9168	SLC7A1	0.9121	ANKRD52	0.919	ZNF740	0.9137
WDFY2	0.9213	NOVA1	0.9205	SYT16	0.9227	NAA30	0.9151
KCNH5	0.9201	SLC24A4	0.9192	TSPAN3	0.9158	IGF1R	0.9152
ABHD2	0.9205	NTRK3	0.9235	FTO	0.9211	VPS53	0.9233
RNF165	0.9161	NFIC	0.9206	FEM1A	0.9181	WTIP	0.9229
CACNG8	0.9115	GPR161	0.9123	POU2F1	0.9231	ILDR2	0.9206
SDHC	0.9234	ABL2	0.9232	TOR1AIP1	0.9144	SNX27	0.9145
GABPB2	0.9196	SYT14	0.9199	KCNN3	0.9223	GATAD2B	0.9134
LYST	0.9192	MBOAT2	0.915	SYT2	0.9145	ASXL2	0.9173
KIAA1715	0.9159	LIMD1	0.9196	LPP	0.9237	STXBP5L	0.9112
ANK2	0.9159	SPATA5	0.9162	SETD7	0.9142	MARCH6	0.9172
RPL37	0.922	SSBP2	0.9178	PPIP5K2	0.9203	ARHGAP26	0.916
G3BP1	0.9138	GFOD1	0.9136	FAXC	0.9199	CLVS2	0.918
RNF217	0.9212	SHPRH	0.9207	CREB5	0.9145	EGFR	0.9208
PURB	0.9161	TMEM168	0.9119	LANCL3	0.9216	CASK	0.9123
FBXO25	0.9154	WHSC1L1	0.9159	MTDH	0.9127	VLDLR	0.9176
NFIB	0.9151	CEP78	0.9192	NTRK2	0.9144	SNX30	0.9203
NR6A1	0.9188	USP6NL	0.9179	ZEB1	0.9205	EIF4EBP2	0.916
NPFFR1	0.9215	LRRC27	0.9164	CNNM2	0.923	CELF1	0.9177
SESN3	0.9137	SOGA1	0.9162	HMGA2	0.9173	CDH8	0.9172
LPHN3	0.9182	CD226	0.9197	FREM2	0.9135	SLC7A11	0.9187
THRB	0.9134	DLG5	0.911	GXYLT1	0.9188	EIF4E	0.9199
AKAP6	0.9198	MIPOL1	0.9166	FER	0.9214	WWC2	0.9181
GABRA2	0.9133	GFRA1	0.9153	CACUL1	0.9199	PTPN14	0.9199
MGAT5	0.9151	PDK1	0.9227	UHMK1	0.9182	GUCY1A2	0.9227
JMY	0.9124	CCDC50	0.9135	CAMK4	0.9199	GPR180	0.9182
FARP1	0.9152	RAB3C	0.921	SREK1IP1	0.9134	MR1	0.9136
BCL2L11	0.9119	ASAP1	0.9112	PLEKHG4B	0.9216	CNKSR3	0.924
DGKE	0.9134	HS2ST1	0.9157	CHST9	0.9213	ANKH	0.9113
OTULIN	0.9195	LRRK1	0.9226	ENAH	0.9213	PDE1C	0.9177
ADAMTS5	0.9113	TTC39B	0.9183	GOLGA7B	0.9112	MIER3	0.911
FAM126B	0.9167	PPARGC1B	0.9187	SLC24A2	0.922	AFF2	0.9222
PSD3	0.9127	MMP16	0.9215	KCNMA1	0.9127	PPP2R2B	0.9212
SAMD8	0.918	RAB11FIP1	0.9165	UNC5D	0.9113	MPV17L	0.911
ST3GAL2	0.9112	KCNJ6	0.9238	ZNF618	0.9201	DGKI	0.9162
UBN2	0.9213	BRAF	0.9161	AGAP1	0.9224	CLSTN2	0.9221
KCNB1	0.9214	ELK4	0.9197	ADAMTS4	0.9197	IGF2BP1	0.9181
ZBTB8A	0.914	KALRN	0.9186	PDXK	0.9124	ICOSLG	0.9182
TAOK1	0.9214	ORAI2	0.9207	IKZF3	0.9207	EMC10	0.9138

FMNL3	0.9219	PRKAA2	0.9195	GMEB1	0.9137	DRAXIN	0.9142
RBBP4	0.9124	NFIA	0.9206	ZNF326	0.9178	SLC30A7	0.9159
DDR2	0.9136	ACP6	0.9124	KIF26B	0.9171	REL	0.9207
DISC1	0.9124	PAQR3	0.9205	EIF4E3	0.9222	LRRC58	0.9124
PPM1L	0.9219	ICA1L	0.9113	RYBP	0.9166	GMPS	0.9207
SMIM14	0.9133	RPP14	0.9136	APBB2	0.9143	ZNF148	0.9124
GRIK3	0.9113	LRPAP1	0.9169	UBXN7	0.9184	INTU	0.9224
HSPA4L	0.9201	RAD54L2	0.9112	RICTOR	0.9125	CCDC127	0.9184
CREBRF	0.9156	SAP30L	0.911	KIF6	0.9197	USP49	0.916
ZNF704	0.9239	ADCY1	0.9216	FOXK1	0.9138	KIAA1958	0.9192
PTCHD1	0.9229	BRWD3	0.9149	SLITRK5	0.9238	CFL2	0.918
SUGT1	0.9238	PGM2L1	0.9165	AMER2	0.9195	PDZD8	0.9176
FAM204A	0.922	NSD1	0.9147	TSC1	0.9191	FUNDC2	0.9159
TTC7B	0.9236	CPSF2	0.9207	CLMN	0.9189	HIF1AN	0.9237
FRS2	0.9148	ARIH1	0.924	STXBP4	0.9217	TRIM44	0.9227
TUB	0.9147	PLD4	0.9142	TRIM66	0.9213	RNF169	0.9134
PRTG	0.9224	PRKCB	0.9185	TMED3	0.9232	GALR1	0.9216
SLFN5	0.9187	DCTN5	0.9199	ELFN2	0.9113	GREM1	0.9232
FBXO22	0.9188	TBC1D16	0.9205	IRGQ	0.9137	ZNF226	0.9159
ANKRD11	0.9187	ZNF641	0.9144	TTYH1	0.9155	SLC43A2	0.9181
HOOK3	0.9226	MPLKIP	0.9114	LDLRAD4	0.9194	SNTB2	0.9207
SPRY3	0.9137	IRS1	0.9122	MECP2	0.9225	AR	0.9211
CSNK1G1	0.9172	RAB3B	0.9232	SH3TC2	0.9171	SHE	0.9171
C15orf40	0.9219	HIC2	0.9154	OTUD7A	0.9192	KLF13	0.9121
MAP3K2	0.9218	TMEM154	0.9179	TMEM192	0.9214	ZNF778	0.9162
NIPA1	0.9148	SIK2	0.9124	RNF150	0.9183	CRTAP	0.917
LONRF2	0.9229	ELOVL6	0.9179	NUDCD2	0.9172	SGCD	0.9137
ATF7	0.9134	TANC2	0.9135	PYGO1	0.9166	KCNMB3	0.9169
CLCN5	0.9198	KSR2	0.9234	ZNF562	0.9226	WIPF2	0.9134
BCL2	0.9141	NEGR1	0.9218	ALG14	0.9198	FUT9	0.9226
ZNF24	0.9145	ZMAT3	0.9145	DCP2	0.9198	BNC2	0.9221
VANGL1	0.9188	GOLGB1	0.9232	STOX2	0.9114	PEAK1	0.9239
GMPPB	0.911	SNX33	0.9123	NABP1	0.9212	NUDT4	0.9153
SCAI	0.9162	HEG1	0.9168	AGFG1	0.9166	RNF213	0.9134
ZNF791	0.9204	PHC3	0.923	UBXN2A	0.9137	ZHX3	0.9152
CNTNAP2	0.918	C4orf32	0.9188	FZD4	0.9124	PDE12	0.9187
CA5A	0.9216	CADM2	0.9183	SMAD2	0.9241	ARL10	0.9214
PPP2R2D	0.9229	MLXIP	0.9149	SLC35E3	0.9237	ZDHHC21	0.9192
KCMF1	0.9113	SPRYD4	0.9203	SYNE3	0.9234	KIAA2018	0.9126
SOX11	0.9161	POLE	0.9135	ZBTB34	0.9162	RIMKLA	0.9202
NR2C2	0.9212	ST8SIA3	0.921	SAMD12	0.9195	PGBD5	0.923
ZBTB41	0.9139	FAM26E	0.9162	PDE4DIP	0.9141	GEN1	0.9126
NT5DC1	0.9168	CD28	0.9113	ERBB4	0.9211	ERN1	0.9149
CSRNP3	0.9162	CLK3	0.9221	CIITA	0.9198	SERTAD2	0.9129
SOCS4	0.9111	ZADH2	0.9186	ZNF609	0.9111	SSTR2	0.9122
YOD1	0.9207	LRRC57	0.9202	EHMT1	0.9181	PLAG1	0.9122
RFX7	0.915	IBA57	0.9209	MGAT4C	0.9237	CREB3L2	0.9201
UNC5C	0.9125	RGMA	0.9218	EXT1	0.9168	BACE2	0.9114
GABRG3	0.9174	FIGN	0.9219	CLN8	0.9179	PAPPA	0.9133
NGRN	0.9142	C16orf72	0.9228	GJC1	0.9192	CADM1	0.9211
SLC8A1	0.9239	CALN1	0.9173	POTEC	0.919	CTNNA3	0.9115
GRIN2A	0.9225	MACC1	0.9124	KCTD16	0.9229	B3GALT5	0.9229
BTBD9	0.9177	KCNH8	0.9137	KCNQ3	0.9173	PCDH9	0.924
ZBTB40	0.9132	SDR42E1	0.9226	ZFP90	0.9136	FAM227A	0.922
BRI3BP	0.9133	FLRT2	0.9241	PURA	0.9229	ZBTB37	0.924
HS6ST3	0.9144	RAD51D	0.9192	GPRIN3	0.9207	SV2B	0.9146
LSAMP	0.9168	OLFML2A	0.912	PBX1	0.9112	C16orf52	0.9149
PIGP	0.9187	PTCH1	0.9216	LRCH3	0.9156	MKL2	0.9175
ZNF555	0.9192	KPNA4	0.9172	PPARA	0.922	TEAD1	0.9168
NAP1L1	0.923	SESTD1	0.9153	TET3	0.9135	ZNF286A	0.912
LIN28B	0.914	NWD1	0.9172	ZNF383	0.9145	CENPP	0.9204
ASAH2	0.9121	PTAR1	0.9205	VWC2	0.9169	TMEM120B	0.9203
MTF1	0.917	BEND4	0.9145	LRRK2	0.9134	PTPLAD2	0.9145
ZNF527	0.9155	FAM179A	0.9221	PTPRT	0.9198	LCOR	0.9214
XPNPEP3	0.9193	ZNF765	0.9172	TSC22D2	0.9115	ZNF605	0.9226
MYO18A	0.9181	AJAP1	0.9196	HDAC2	0.9126	WNK3	0.9176

ZNF431	0.922	VKORC1L1	0.9168	COL27A1	0.9134	NHLRC2	0.921
FLNA	0.9159	SRGAP1	0.924	ZNF470	0.9117	ZNF441	0.9119
GMFB	0.921	PGAP1	0.9161	ZNF720	0.9158	DDI2	0.9214
LRP10	0.9153	ZNF655	0.9157	SPN	0.9149	MYO5A	0.9151
FAM212B	0.9122	ZNF121	0.9142	MPZL1	0.9143	MBP	0.9226
DLGAP2	0.9221	MRPL42	0.9237	ZNF544	0.9116	CACNA1E	0.9212
ZKSCAN8	0.9151	ASPH	0.9149	ZNF26	0.9233	NUDT16	0.9124
MDM4	0.9173	C6orf89	0.9165	IPO9	0.9221	SLC5A3	0.9222
FAM169A	0.9121	LRIG2	0.9162	RORB	0.9137	C1orf95	0.919
PHACTR4	0.9124	BMPR2	0.9192	MBD5	0.9179	FAM155A	0.9152
PCDHA4	0.9192	SLC35B4	0.9148	ZBTB10	0.9177	TMEM170B	0.9153
CCDC85C	0.9239	ITSN1	0.9226	ITPRIPL2	0.9133	DOK6	0.9182
TMEM200C	0.9173	CFAP44	0.9142	VGLL3	0.9153	TRIM71	0.9203
XKR4	0.9239	C17orf51	0.9223	SFT2D2	0.9221	FGFR1OP	0.9236
LEPROT	0.9119	DNASE1	0.9116	ZNF891	0.9225	LYRM4	0.9167
ZNF788	0.9134	PEX26	0.9235	SIAH3	0.9124	PLXNA4	0.9137
APOL6	0.9207	HSBP1	0.9183	TMEM189	0.9151	ARPIN	0.9178
FMN1	0.9207	ZNF286B	0.9119	PCDHA10	0.9224	KIAA1456	0.9177
SOGA3	0.9116	NOX5	0.9177	TIFAB	0.9123	CUX1	0.9221
<a>KIAA0408							
FRRS1L	0.9176	XKR7	0.9125	TMEM178B	0.9218	GAN	0.9235
DYNLL2	0.9177	OTUD7B	0.9124	RNF115	0.9198	TRABD2B	0.9192
GTF2H5	0.9167	NUDT3	0.9174	GRIN2B	0.9241	ZBTB8B	0.923
SOCS7	0.9124	NPHP3-ACAD11	0.9124	ZNF8	0.9204	CLN8	0.9179
ZNF229	0.9141						

Table 3: List of genes containing T-UCR in their exonic regions according to the study of Bejerano et al.

UCR number	Length (bp)	Gene (ID)
uc.143	218	AB014560
uc.203	203	AB067798
uc.135	201	AK096400
uc.339	252	ATP5G2
uc.413	272	BC060758
uc.49	207	BC060860
uc.61	326	BCL11A
uc.324	225	C11orf8
uc.285	232	CARP-1
uc.233	266	CENTG3
uc.393	**275**	**CLK3**
uc.185	411	CLK4
uc.184	230	CPEB4
uc.471	239	DDX3X
uc.331	218	DLG2
uc.13	237	EIF2C1
uc.194	201	EPHA7
uc.183	236	FBXW1B
uc.333	270	FLJ25530
uc.478	252	GRIA3
uc.479	302	GRIA3
uc.282	207	GRIN1
uc.97	442	HAT1
uc.144	205	HNRPDL
uc.186	305	HNRPH1
uc.263	207	HNRPK
uc.264	267	HNRPK
uc.443	239	HNRPM
uc.45	203	HNRPU
uc.46	217	HNRPU
uc.409	244	L32833
uc.174	260	MATR3
uc.129	212	MBNL1
uc.356	251	MBNL2
uc.375	300	MIPOL1
uc.292	217	MLR2
uc.406	**211**	**NFAT5**
uc.473	222	NLGN3
uc.378	251	NRXN3
uc.475	397	OGT
uc.280	220	PBX3
uc.338	223	PCBP2
uc.376	290	PRPF39
uc.377	217	PRPF39
uc.33	312	PTBP2
uc.102	338	PTD004
uc.48	298	PUM2
uc.477	209	RAB9B
uc.395	249	RBBP6
uc.330	207	RBM14
uc.455	245	RNPC2
uc.419	289	SFRS1
uc.138	419	SFRS10
uc.28	355	SFRS11
uc.189	573	SFRS3
uc.456	320	SFRS6
uc.50	222	SFRS7
uc.454	208	SLC23A1
uc.193	319	SYNCRIP
uc.436	210	TCF4
uc.414	246	THRA
uc.313	231	TIAL1
uc.208	218	TRA2A
uc.209	250	TRA2A
uc.77	296	ZFHX1B
uc.151	214	ZFR
uc.474	210	ZNF261

NFAT5 (nuclear factor 5 of activated t cells), *CLK3* (dual specificity protein kinase 3) genes, which contain T-UCR and show ceRNA activity, were detected (Table 4).

Table 4. Breast cancer-associated ceRNAs, including T-UCR in their exonic region

Gene ID	BC	Normal breast tissue
NFAT5	4.29*	9.63
CLK3	36.03*	52.28

*Significantly different between BC and normal breast tissues

This investigation revealed that the expression of the *NFAT5* and *CLK3* genes was considerably lower in breast cancer than in healthy breast tissue (Figure 2). GEPIA database was used for statistical analysis of the relationship between the *NFAT5* and *CLK3* genes and breast cancer (Figure 3).

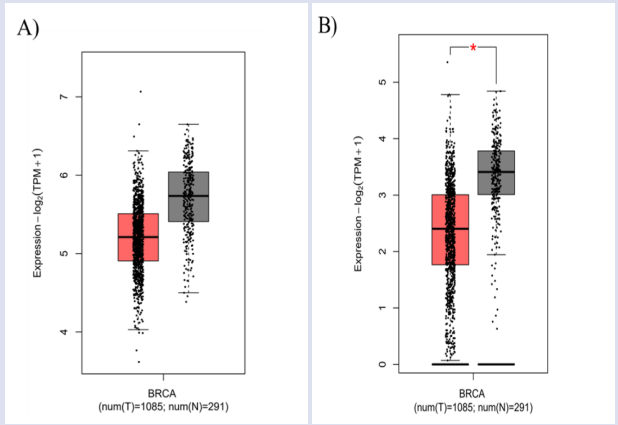

Figure 2. Distribution of *CLK3* and *NFAT5* gene expressions in BC and normal breast tissues according to TCGA normal and GTEx data in GEPIA. A) *CLK3*, B) *NFAT5* (BRCA: Breast cancer, T: tumour tissue, N: Normal breast tissue)

The *NFAT5* and *CLK3* gene pair has been found to be associated with breast cancer.

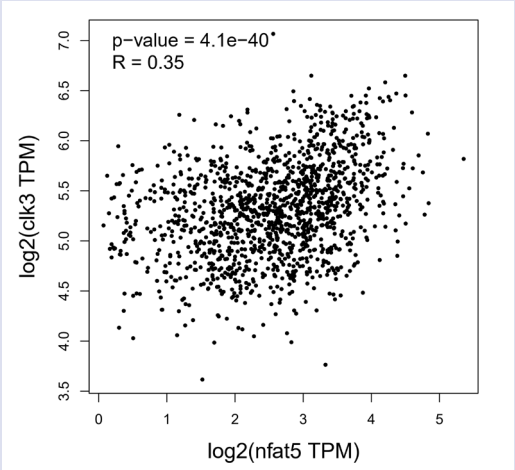

Figure 3. Spearman correlation analysis of CLK3 and NFAT5 genes in BC in the GEPIA

Discussion

Breast cancer has a high incidence and mortality rate worldwide and is among the most common types of cancer [13]. To comprehend the mechanisms involved in the treatment, control, onset, and advancement of this disease, new prospective biomarkers must be discovered [14]. The determination of these molecules can contribute to the prevention and cure of the disease. Thus, an improvement in the quality of life of BC patients, and a decrease in mortality and morbidity can be observed [15, 16]. miRNAs have major functions in a variety of diseases, including cancers, where they act as oncogenes and/or tumor suppressors. Several studies have demonstrated that miRNAs regulate gene expression by interacting with multiple networks [17].

In recent years, a mechanism has been discovered that indicates that RNAs interact with each other [18]. The first time the ceRNA theory was put forth was by Salmena et al [19]. All RNA transcripts with miRNA binding sites are supposed to compete for post-transcriptional regulation, according to the competing endogenous RNA (ceRNA) hypothesis [19-22]. Endogenous competitive RNAs that regulate the binding of miRNAs to their targets have been identified [20], and this network established between miRNAs and ceRNAs has been expressed as ceRNA networks (ceRNET). As ceRNAs can act as regulators of miRNAs, ceRNAs may have an important role in miRNA-related diseases. Therefore, understanding the function of ceRNAs will provide understanding of the development process of diseases, including cancer, and the development of new treatment methods [18]. It has been stated that ceRNAs are important regulators in many cancer types [23]. Studies in the literature have revealed a strong correlation between the prevalence and development of breast cancer and abnormal expression of ceRNAs. [24].

The purpose of the present study was to use *in silico* analysis to find miRNA-associated ceRNAs that may be used as BC biomarkers. The other objective was to find those which also included ceRNAs and T-UCRs. Thus, it will be possible to identify new potential biomarkers supporting the diagnosis and diagnosis of BC. In this study, 40 miRNAs associated with BC (MCF-7 cells), which we determined in our previous study using the miRWalk database, are shown in Table 1. 1009 genes simultaneously targeted by these 40 miRNAs have been identified. Genes with a ComiR score above 0.911 are shown Table 2. [25].

For the matching of breast cancer-associated ceRNA to genes including T-UCR, genes with T-UCR in exon regions were selectively identified according to Bejerano et al. (Table 3) [11]. Using the gene expression profiling database GEPIA, genes with notable expression variations between breast cancer and normal breast tissue were found among breast cancer-associated ceRNAs, including T-UCR. In addition, correlation analysis was performed using the same database [12].

The present findings revealed that the expression of the *NFAT5* and *CLK3* genes in BC was statistically considerably lower than in healthy breast tissue (Figure 2). Others did not exhibit a statistically relevant pattern of differential expression. In addition, Spearman correlation analysis test determined that *NFAT5* and *CLK3* genes were associated with BC (Figure 3). According to the literature review, it was seen that *NFAT5* and *CLK3* genes were not experimentally detected in BC and their relationship with this cancer type was not determined. This study shows that these two genes may be associated with BC. Then, the genes with remarkable expression differences between BC and normal breast tissues were included from MCF7-associated ceRNAs that included. The *NFAT5* and *CLK3* genes were significantly less expressed in BC than in normal breast tissues according to the analysis in this study. On the other hand, other genes did not show any significant differences in expression pattern. According to the findings of the Spearman correlation analysis, *NFAT5* and *CLK3* genes were shown to have remarkable relationship with BC.

The *NFAT* family consists of five transcription factors, and NFAT5 is an osmotic stress transcription factor [26]. The role of *NFAT5* is to stimulate the synthesis of transmembrane transporters of ions and osmolytes at the gene level. Thus, osmotic stress responses see a coordination function [27]. It has also been reported that *NFAT5* modulates angiogenesis, invasion, glycolysis and osmotic stress, and is responsible for the regulation of many types of cancer [28, 29]. *NFAT5* specifically transcriptionally regulates calcium-binding protein S100A4 and vascular endothelial growth factor C (VEGF-C). Since *NFAT5* regulates many genes transcriptionally, it is stated that *NFAT5* probably has a key role in breast cancer [30, 31]. The signals and metastatic processes that induce *NFAT5* expression in metastatic BC have not been fully determined [32]. These findings imply a causal role for "constitutive activation" or elevated *NFAT5* transcriptional activity in the pathogenesis of BC. For this reason, *in silico* analysis results will contribute to the determination of the function of *NFAT5* in the metastatic process in BC.

CDC-like kinase 3 (CLK3) is a nuclear kinase that acts on serine/threonine and tyrosine-containing substrates [33]. *CLK3* modulates RNA splicing by phosphorylating serine/arginine-rich proteins [34]. Although the various tumor activities have not been precisely described, dysregulation of *CLK3* levels has been identified to be a highly penetrating factor in various types of human malignancies [35]. Therefore, the results of the analysis in this study suggest that *CLK3* associated with BC may provide a new therapeutic strategy. In the current investigation, the genes *NFAT5* and *CLK3* were linked to BC, and it was emphasized that these genes may have a role in the development of cancer. According to the analyses in this study, it has been hypothesized that these genes may function as tumor suppressor genes and that their expression is reduced in BC.

Conclusion

To better understand the molecular pathways behind cancer, many scientists are currently concentrating on ceRNA-based gene regulation. This *in silico* approach will enable the discovery of new undiscovered candidate genes for the pathogenesis of BC. This study confirmed that the *NFAT5* and *CLK3* genes downregulate expression in BC. The *NFAT5* and *CLK3* genes can be used as reliable biomarkers to differentiate between BC patients and healthy people. The assignment of phenotype-specific treatment agents could be aided by the identification of BC and the activation of the *NFAT5* and *CLK3* signaling pathway. According to these *in silico* results, we identified two miRNA-related genes as a novel biomarker in BC that could potentially be developed in clinical trials. Future *in vitro* and *in vivo* investigations may benefit from a novel viewpoint from our preliminary findings. These genes might help us understand the specific mechanisms behind BC. However, further and more comprehensive research on this topic is required.

Acknowledgement

S.Ö.Y. and S.M. planned, designed and performed the research. S.Ö.Y. and S.M. analyzed the data and wrote the manuscript. All authors contributed to editorial changes in the manuscript. All authors read and approved the final manuscript.

Conflicts of interest

There are no conflicts of interest in this work.

References

[1] Ferlay J., Soerjomataram I., Dikshit R., Eser S., Mathers C., Rebelo M., Parkin D.M., Forman D., Bray F., Cancer incidence and mortality worldwide: Sources, methods and major patterns in GLOBOCAN 2012, *Int. J. Cancer*., 136 (5) (2015) E359–E386.

[2] Bray F., Ferlay J., Soerjomataram I., Siegel R.L., Torre L.A., Jemal A., Global cancer statistics 2018:GLOBOCAN estimates of incidence and mortality worldwide for 36 cancers in 185 countries, *CA Cancer J Clin.,*68(6) (2018) 394-424.

[3] Wang L., Early diagnosis of breast cancer, *Sensors*., 17(7) (2017) 1-20.

[4] Loh H. Y., Norman B. P., Lai K. S., Rahman N. M. A. N. A., Alitheen N. B. M., Osman M. A., The regulatory role of microRNAs in breast cancer, *Int. J. Mol. Sci.,* 20(19) (2019) 1-27.

[5] Szczepanek J., Skorupa M., Tretyn A., MicroRNA as a potential therapeutic molecule in cancer, *Cells*, 11(6) (2022) 1-24.

[6] Jang J. Y., Kim Y. S., Kang K. N., Kim K. H., Park Y. J., Kim, C. W., Multiple microRNAs as biomarkers for early breast cancer diagnosis, *Mol Clin Oncol.,* 14(2) (2021) 1-9.

[7] Qi X., Zhang D.H., Wu N., Xiao J.H., Wang X., Ma W., CeRNA in cancer: possible functions and clinical implications, *J Med Genet.,* 52(10) (2015) 710-8.

[8] Fassan M., Dall'Olmo L., Galasso M., Braconi C., Pizzi M., Realdon S., Volinia S., Valeri N., Gasparini P., Baffa R., Souza R.F., Vicentini C., D'Angelo E., Bornschein J., Nuovo G.J., Zaninotto G., Croce C. M., Rugge M., Transcribed ultraconserved noncoding RNAs (TUCR) are involved in Barrett's esophagus carcinogenesis, *Oncotarget*, 5(16) (2014) 7162-71.

[9] Dweep H., Gretz N., miRWalk2. 0: a comprehensive atlas of microRNA-target interactions, *Nat Methods*., 12 (8) (2015) 697-697.

[10] Coronnello C., Benos P.V., ComiR: combinatorial microRNA target prediction tool, *Nucleic Acids Res.,* 41(W1) (2013) W159-W164.

[11] Bejerano G., Pheasant M., Makunin I., Stephen S., Kent W.J., Mattick J.S., Haussler D., Ultraconserved elements in the human genome. Science., 304(5675) (2004) 1321-5.

[12] Tang Z., Li C., Kang B., GEPIA: a web server for cancer and normal gene expression profiling and interactive analyses, *Nucleic Acids Res.,* 45(W1) (2017) W98-W102

[13] Ghoncheh M., Pournamdar Z., Salehiniya H., Incidence and mortality and epidemiology of breast cancer in the world. *Asian Pac. J. Cancer Prev*, 17(sup3) (2016) 43-46.

[14] Bettaieb A., Paul C., Plenchette S., Shan J., Chouchane L., Ghiringhelli F., Precision Medicine in Breast Cancer: Reality or Utopia? *J Transl Med*, 15 (1) (2017) 1-13.

[15] Ahmed K. T., Sun J., Chen W., Martinez I., Cheng S., Zhang W., Zhang W., In silico model for miRNA-mediated regulatory network in cancer. Brief. *Bioinform.,* 22(6), 2021, 1–13.

[16] Sadeghi M., Cava C., Mousavi P., Sabetian S., Insilico-based identification of survival-associated lncRNAs, mRNAs and, miRNAs in breast cancer, *Research Square*, (2022) 1-21.

[17] Kartha R.V., Subramanian S., Competing endogenous RNAs (ceRNAs): new entrants to the intricacies of gene regulation, *Front Genet*., 5 (8) (2014) 1-9.

[18] Akkaya Z.Y., Dinçer P., The new era in therapeutic approaches: Non-coding RNAs and diseases, *Marmara Medical Journal*, 26 (1) (2013) 5-10.

[19] Salmena L., Poliseno L., Tay Y., Kats L., Pandolfi P.P., A ceRNA Hypothesis: The Rosetta Stone of a Hidden RNA Language? *Cell*, 146 (3) (2011) 353–358.

[20] Ebert M.S., Neilson J.R., Sharp P.A., MicroRNA sponges: Competitive inhibitors of small RNAs in mammalian cells, *Nat. Methods*, 4 (9) (2007) 721–726.

[21] Arvey A., Larsson E., Sander C., Leslie C.S., Marks D.S., Target mRNA abundance dilutes microRNA and siRNA activity. *Mol. Syst. Biol.*, 6 (1) (2010) 1-7.

[22] Ebert M.S., Sharp P.A., Emerging Roles for Natural MicroRNA Sponges, *Curr. Biol.*, 20 (19) (2010) R858–R861.

[23] Sen R., Ghosal S., Das S., Balti S., Chakrabarti J., Competing endogenous RNA: the key to posttranscriptional regulation. *Sci. World J*., 2014 (896206) (2014) 1-7.

[24] Wu D., Zhu J., Fu Y., Li C., Wu B., LncRNA HOTAIR promotes breast cancer progression through regulating the miR-129-5p/FZD7 axis. *Cancer Biomarkers,* 30(2) (2021) 203–212.

[25] Misir S., Hepokur C., Aliyazicioglu Y., Enguita F. J., Biomarker potentials of miRNA-associated circRNAs in breast cancer (MCF-7) cells: an in vitro and in silico study, *Mol Biol Rep.,* 48(3) (2021) 2463-2471.

[26] Brown T.C., Murtha T.D., Rubinstein J.C., Korah R., Carling T., SLC12A7 alters adrenocortical carcinoma cell adhesion properties to promote an aggressive invasive behavior. *Cell Commun Signal.,*16(1) (2018) 1-13.

[27] Burg M.B., Ferraris J.D., Dmitrieva N.I., Cellular response to hyperosmotic stresses. *Physiol Rev.,* 87(4) (2007) 1441-1474.

[28] Chen M., Sastry S.K., O'Connor K.L., Src kinase pathway is involved in NFAT5-mediated S100A4 induction by hyperosmotic stress in colon cancer cells, *Am J Physiol Cell Physiol.*, 300(5) (2011) C1155-C1163.

[29] Küper C., Beck F.X., Neuhofer W., NFAT5-mediated expression of S100A4 contributes to proliferation and migration of renal carcinoma cells, *Front Physiol.*,5 (293) (2014) 1-10.

[30] Mishra S.K., Siddique H.R., Saleem M., S100A4 calcium-binding protein is key player in tumor progression and metastasis: preclinical and clinical evidence, *Cancer Metastasis Rev*., 31 (2012) 163–172.

[31] Su J.L., Yen C.J., Chen P.S., Chuang S.E., Hong C.C., Kuo I.H., Chen H.Y., Hung M.C., Kuo M.L., The role of the VEGF-C/VEGFR-3 axis in cancer progression, *Br J Cancer*. 96 (2007) 541–545.

[32] Remo A., Simeone I., Pancione M., Parcesepe P., Finetti P., Cerulo L., Bensmail H., Birnbaum D., Van Laere S.J., Colantuoni V., Bonetti F., Bertucci F., Manfrin E., Ceccarelli M., Systems biology analysis reveals NFAT5 as a novel biomarker and master regulator of inflammatory breast cancer, *J. Transl. Med.,* 13(1) (2015) 1-13.

[33] Nayler O., Stamm S., and Ullrich A., Characterization and comparison of four serine- and arginine-rich (SR) protein kinases, *Biochem. J.,* 326 (1997) 693–700.

[34] Cesana M., Guo M.H., Cacchiarelli D., Wahlster L., Barragan J., Doulatov S., Vo L.T., Salvatori B., Trapnell C., Clement K., Cahan P., Tsanov K. M., Sousa P.M., Tazon-Vega B., Bolondi A., Giorgi F.M., Califano A., Rinn J.L., Meissner A., Hirschhorn J.N., Daley G. Q., A CLK3-HMGA2 alternative splicing axis impacts human hematopoietic stem cell molecular identity throughout development, *Cell Stem Cell*., 22 (e7) (2018) 575–588.

[35] Bowler E., Porazinski S., Uzor S., Thibault P., Durand M., Lapointe E., Rouschop K.M.A., Hancock J., Wilson I., and Ladomery M., Hypoxia leads to significant changes in alternative splicing and elevated expression of CLK splice factor kinases in PC3 prostate cancer cells, *BMC Cancer*., 18 (2018) 1-11.

Cumhuriyet Sci. J., 44(1) (2023) 62-66
DOI: https://doi.org/10.17776/csj.1158670

Cumhuriyet Science Journal

| csj.cumhuriyet.edu.tr | Founded: 2002 ISSN: 2587-2680 e-ISSN: 2587-246X Publisher: Sivas Cumhuriyet University

Antimicrobial Properties of Biocompatible Poly (Ɛ-Caprolactone) Treated with Plant Extract

Sibel Selçuk Pekdemir [1,a,*], Şule İnci [2,b], Mustafa Ersin Pekdemir [3,c], Sevda Kırbağ [2,d]

[1] *Department of Chemistry, Faculty of Science, Fırat University, Elazığ, Türkiye.*
[2] *Department of Biology, Faculty of Science, Fırat University, Elazığ, Türkiye.*
[3] *Department of Chemistry, Faculty of Science, Fırat University, Elazığ, Türkiye.*
**Corresponding author*

Research Article

History
Received: 21/01/2022
Accepted: 06/02/2023

ABSTRACT

Poly (ε-caprolactone) (PCL) was synthesized using ethylene glycol initiator and catalyst accompanied by ring-opening polymerization method. The number average molecular weight (Mn) of the obtained polymer was found to be 4000 gmol-1. In addition, the characteristic signals of PCL were determined with Fourier-transform infrared spectroscopy (FT-IR). Decomposition temperatures were investigated by Thermogravimetric Analysis (TGA) and melting temperatures (Tm) were investigated by Differential Scanning Calorimetry (DSC). Tm of PCL at 57.3 °C was observed. PCL was treated with Rumex patientia L. ethanolic plant extract and its effects on Klebsiella pneumoniae ATCC 700603, Bacillus megaterium DSM32, Staphylococcus aureus ATCC25923, Escherichia coli ATCC25322, and Candida albicans FMC17 microorganisms were examined. It was determined that PCL, which did not show antimicrobial activity, showed antimicrobial activity on some microorganisms after being treated with the plant.

Keywords: Antmicrobial, Crystallinity, FT-IR, Poly ε-caprolactone, *Rumex patientia.*

[a] *sibelselcuk85@gmail.com* *https://orcid.org/0000-0002-8643-7590*
[b] *sule.inci@hotmail.com* *https://orcid.org/0000-0002-4022-5269*
[c] *ersinpkdmr58@gmail.com* *https://orcid.org/ 0000-0002-4979-1777*
[d] *skirbag@firat.edu.tr* *https://orcid.org/0000-0002-4337-8236*

Introduction

With the increase in diseases, it is seen that herbal medicines among the drugs used in the treatment have been preferred more in recent years [1]. It is known that these herbal medicines are frequently used to prevent cancer, fight against microorganisms, and eliminate the harmful effects of free radicals [1-3].

Rumex pateintia L. is a medicinal plant belonging to the Polygonaceae family and has more than 200 species [4]. Species of this genus have different pharmacological activities such as anti-inflammatory, antioxidant, cytotoxic, antifertility, antibacterial, laxative, antidiarrheal, antifungal, antipyretic, antiviral activities [5-10]. There are about 25 species of this genus in Turkey and the most common species are *R. patientia L.*, *R. crispus L.*, *R. acetosa L. R. caucasicus RECH.* and *R. alpinus L.* [11]. *Rumex patientia L.* is a perennial herb commonly found and grown in Eastern Europe, especially used in the treatment of different diseases in traditional medicine (Jovin et al., 2011). The root parts of the plant are known to have some preventive effects. The most important of these are antipyretic, anti-inflammatory, wound healing and diuretic effects [12].

As well as, antimicrobial polymers attract attention in the fight against pathogenic microorganisms [13]. Polymers with antimicrobial action or polymers with the ability to be conjugated with other materials with antimicrobial action can be effective in controlling pathogenic microorganisms [14]. For this reason, traditional methods and new generation antimicrobial agents with antimicrobial effect are in high demand.

Poly(ε-caprolactone) PCL, an aliphatic polyester, is of great interest in surgical fields such as drug delivery and tissue engineering [15,16]. PCL has a biocompatible, biopermeable, biodegradable and hydrophobic semi-crystalline structure [17-19]. Bioabsorbable and non-toxic to living organisms, PCL has been developed as a copolymer or blend polymer, providing an even wider field of application [20,21].

PCL with shape memory properties was synthesized using the ring-opening technique. During the synthesis, ethylene glycol was used as initiator and tin(II) octanoate was used as catalyst. The synthesized PCL was characterized by FT-IR, TGA, DSC and XRD. PCL was treated with *Rumex patientia L.* extract in an ultrasonic homogenizer in dimethyl sulfoxide (DMSO) solution. Antimicrobial activities of the blend obtained against *Staphylococcus aureus*, *Escherichia coli*, *Klebsiella pneumoniae*, *Bacillus megaterium* and *Candida albicans* microorganisms were investigated.

Materials and Methods

Synthesis of Poly (ε-caprolactone)

The synthesis of Poly (ε-caprolactone) in the presence of ethylene glycol and tin(II) octanoate is schematized in Figure 1 [22]. 5 grams ε-caprolactone was weighed into the reaction flask and then stirred until completely

dissolved in 10 mL of toluene. Then, 0.07 gram ethylene glycol and 2 drops tin (II) octanoate were added and mixed in a magnetic stirrer at room temperature. Ar gas was passed through the reaction flask and the flask was tightly closed. It was taken into an oil bath and the temperature was gradually increased up to 120 °C and stirring was continued for 24 hours. The viscous polymer obtained after 24 hours was precipitated by adding dropwise in cold n-hexane. The resulting poly (ε-caprolactone) was dried in a vacuum oven at 40 °C for 24 hours and then stored in the refrigerator.

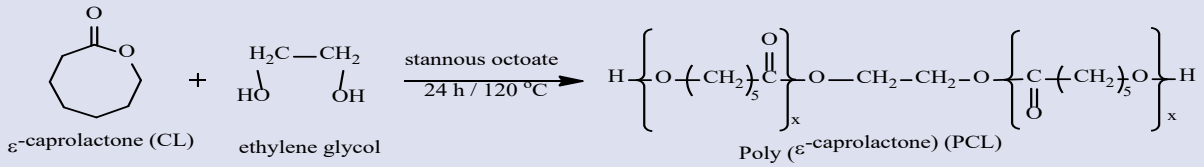

Figure 1. Polymerization of ε-caprolactone

Preparation of the Rumex patientia extract

The *Rumex Patientia* plant collected from Elazığ, Turkey, was dried in a cool, sun-free environment. Then, 20 grams the plant, which was pulverized with a blender, was taken and dissolved in 200 mL ethanol. The plant solution, which was dispersed in an ultrasonic homogenizer for 30 minutes, was shaken in a shaker incubator at 100 rpm for 24 hours at room temperature. The filtrate obtained by filtration of the solution was removed with ethanol at 35 °C with the evaporator [23]. *R. patientia* extract, the solvent of which was removed, was stored at -20 °C to interact with the polymer.

Treatment of PCL with Rumex patientia

R.patientia plant, the extract of which was prepared, was dispersed with PCL in Dimethyl sulfoxide solvent at a ratio of 1:1 for 1 hour in an ultrasonic homogenizer. After mixing for about 30 minutes on a magnetic stirrer, it was prepared for antimicrobial measurements [24].

Test Microorganisms

Bacillus megaterium DSM32, *Staphylococcus aureus* ATCC25923, *Klebsiella pneumoniae* ATCC 700603, *Escherichia coli* ATCC25322 and *Candida albicans* FMC17 microorganisms obtained from the culture collection of Fırat University Faculty of Science Department of Biology Microbiology Laboratory were used.

Antimicrobial Assay of Poly (ε-caprolactone) Treated with Rumex Patientia

The antimicrobial activity of PCL treated with *R.patientia* were determined according to the disk diffusion method [25]. Bacterial strains were inoculated into Nutrient Broth (Difco) for 24 hours at 35 ± 1°C, and the yeast strain was incubated for a longer time (48 hours) in Malt Extract Broth (Difco) at 25 ± 1°C. While the prepared bacterial culture was inoculated on Müeller Hinton Agar as 10^6 bacteria ml^{-1}, the yeast broth was inoculated on Sabouraud Dextrose Agar as 10^4 yeast ml^{-1} (Both inoculations were made at 1% rate). Then, after the shaking process was finished, 25 mL was taken and placed in sterile petri dishes with a diameter of 9 cm. In this way, homogeneous distribution of the medium was achieved. Antimicrobial discs with a diameter of 6 mm were impregnated with 100 µl of the prepared extracts at a concentration of 10 ppm and carefully placed on solid agar medium. Prepared petri dishes were incubated at 4 °C for 1.5-2 hours. Yeast inoculated plates were incubated at 25 ± 0.1°C for 72 hours, while bacteria inoculated plates were incubated at 37 ± 0.1°C for 24 hours. Standard discs of streptomycin sulfate 10 µg $disk^{-1}$ and Ceftrioxan 30 µg $disk^{-1}$ were used as controls. Dimethyl sulfoxide (DMSO) was used as negative control and inhibition zones were measured in mm.

Results and Discussion

FTIR Results

In Figure 1, the FTIR spectrum of poly (ε-caprolactone) is given. The characteristic signal of PCL at 1713 cm^{-1} in the FTIR spectrum belongs to the –C=O stretching vibration. The binary signal at 2943-2860 cm^{-1} belongs to aliphatic -CH, -CH_2 asymmetric and symmetric stretching vibrations, respectively [26]. Signals in the range of 1468 cm^{-1} – 1165 cm^{-1} are attributed to the -CH_2 deformation signals of PCL [27]. In addition, the signals of asymmetric and symmetric stretching vibrations of the C-O-C bond in the polymer structure were observed at 1240 cm^{-1} and 1165 cm^{-1}, respectively [28].The signal at 725 cm^{-1} is the shaking vibration of the methylene group in PCL [29, 30].

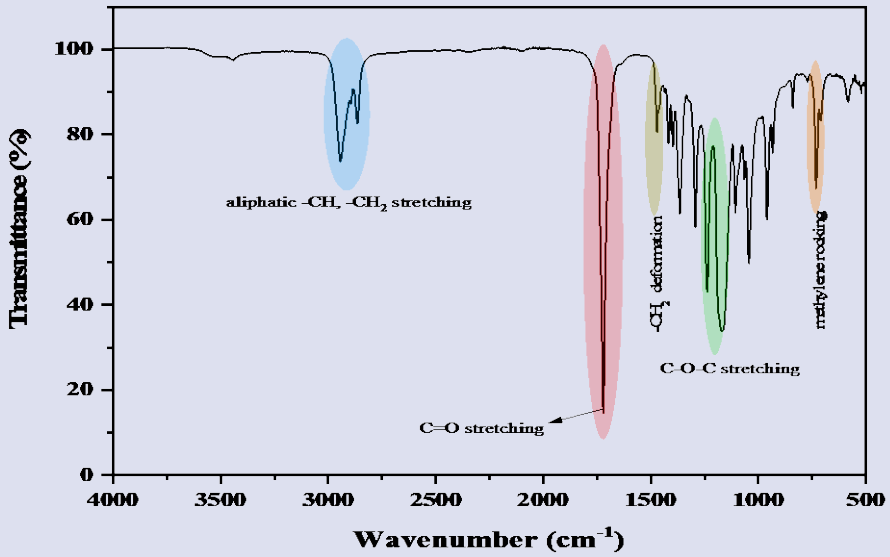

Figure 2. FTIR spectra of PCL

Thermal Results

The thermal properties of PCL synthesized by ring-opening polymerization were investigated. While the TGA curve of PCL is given in Figure 3, the DSC curve that gives the melting temperature of PCL is seen in Figure 4. In the TGA curve, it was observed that PCL decomposed in a single step. It was determined that the initial decomposition temperature (T_i) was 249.5 °C and the amount of residue at 500 °C was 5.9%. The peak of melting temperature (T_m) of PCL is around 57.5 °C, glass transition (T_g) was not observed in our experimental group.

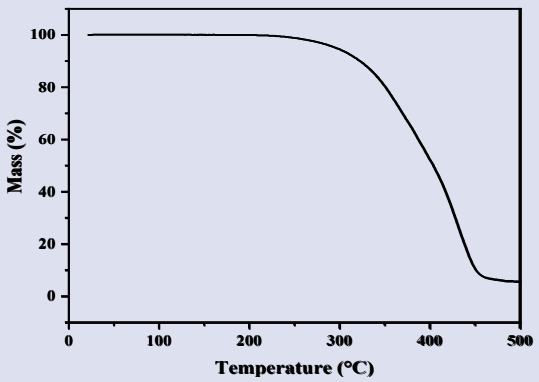

Figure 3. TGA curve of PCL

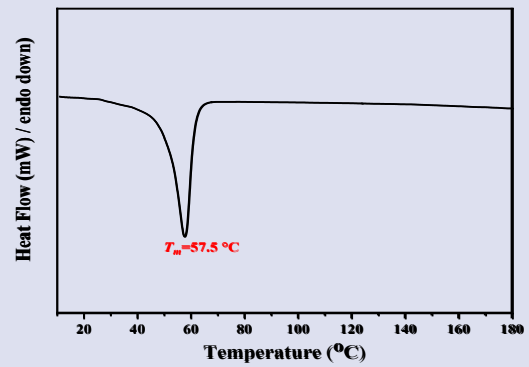

Figure 4. DSC curve of PCL

XRD Results

Figure 4 shows the XRD pattern of PCL at room temperature. PCL, which has a semi-crystalline orthorhombic structure, has 21.3 degrees (110) plane and 23.6 degrees (200) plane signals in the XRD spectrum. In addition, using the Debye-Scherer equation, the crystallinity of PCL was calculated as 53.6% from the XRD spectrum.

$$D = K\lambda/(\beta cos\theta) \quad (1)$$

β: The full width of the maximum half-peak (FWHM)
λ: The wavelength of the x-ray
θ: The angle of the maximum peak

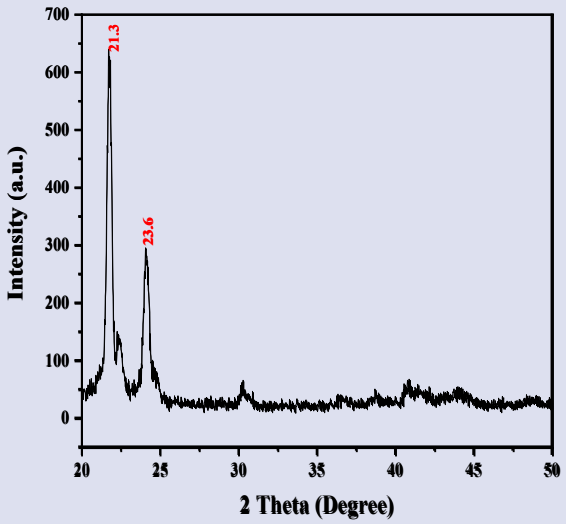

Figure 5. XRD spectra of PCL

Antimicrobial Activity Results

The antimicrobial activities of the ethanolic extract of *R. Patientia*, PCL, and PCL samples treated with *R. Patientia* against *Staphylococcus aureus, Klebsiella pneumoniae, Escherichia coli, Bacillus megaterium* and *Candida albicans* microorganisms are given in Figure 5, and the zone diameters are given in Table 1.

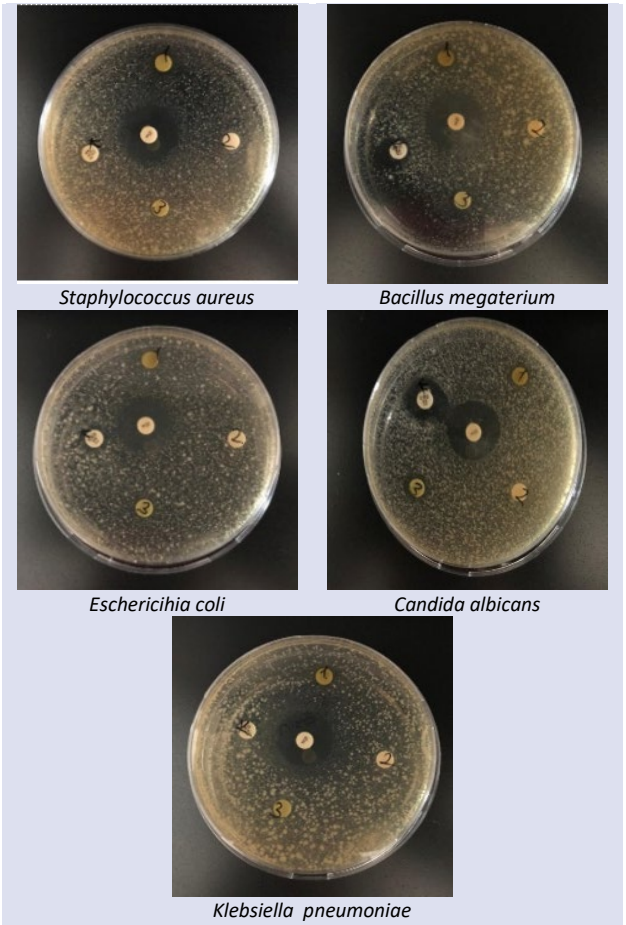

Figure 6. The antimicrobial assay of *Rumex patientia* treated with Poly ε-caprolactone against the bacterial pathogens

While R. patientia extract did not have an antimicrobial effect against E. coli, B. megaterium, K. pneumoniae and C. albicans, it showed an antimicrobial effect (10 mm) against S. aureus. PCL did not form an inhibition zone against the microorganisms used. It was determined that PCL treated with R. Patientia had antimicrobial activity against gram-positive bacteria (B.megaterium, S.aures) and yeast strain (C.albicans), but did not show antimicrobial activity against gram-negative bacteria (E.coli, K.pneumoniae). Antimicrobial polymers have often designed by mimic antimicrobial peptides [31]. Although the polymer used in the study does not have the potential to be an antimicrobial polymer, it is very important in terms of being an antimicrobial peptide in combination with the plant. PCL treated with R. patientia appears to have little antimicrobial effect compared to controls. The reason for this varies according to the solvent used, the amount of concentration, polymer and plant species.

Table 1. Inhibitory zone diameters (mm) of *Rumex patientia L.* treated with PCL

Microorganism	*R. patientia*	PCL	*R. patientia* Interacted with PCL	Streptomycin	Ceftriaxone
E. coli	-	-	-	20	8
B. megaterium	-	-	8	20	11
K. peumoniae	-	-	-	19	9
S. aureus	8	-	7	20	8
C. albicans	-	-	9	21	16

Conclusion

The number average molecular weight (M_n) of PCL synthesized by ring opening was determined to be 4000 $gmol^{-1}$. The characteristic signals of the synthesized PCL (-C=O stretching vibration at 1713 cm^{-1}) were determined by the FT-IR spectrum. In addition, it was calculated from the XRD spectrum that the crystallinity of PCL was 53%. It was determined that *R. Patientia* plant extract had antimicrobial effect only against *S. aureus,* while *R. Patientia* plant, which interacted with PCL, showed antimicrobial effect against *B. Megaterium*, *S. Aureus* and *C. Albicans* microorganisms. As a result, it was observed that the polymer, which did not show any antimicrobial effect, increased its antimicrobial properties in the plant after being treated with the plant extract.

Acknowledgment

It was supported within the scope of the individual project numbered FF.22.11 of the Fırat University Research Project Unit (FUBAP).

Conflicts of interest

The authors state that did not have conflict of interest.

References

[1] Şule İ., Dalkiliç L. K., Kirbag S. And Dalkiliç S. Determination of The Antimicrobial, Antioxidant and Cytotoxic Activity of Paulownia tomentosa Steud, *Kahramanmaraş Sütçü İmam Üniversitesi Tarım ve Doğa Dergisi*, 24 (2021) 701-706.

[2] Ocak E., Inci S., Ozturk D., Safak S. A., Ozdeniz E., Kirbag S., Evren A. H. and Kurt L. Antimicrobial activities of some narrow endemic gypsopyhte, *Journal of the Faculty of Pharmacy of Istanbul University*, 51 (2021) 118-123.

[3] Kirbağ S., Keser S., Tekin S., İnci Ş. and Sandal S. Cytotoxic effect of endemic Tchihatchewia isatidea Boiss. from Turkey, *Israel Journal of Plant Sciences*, 68 (2021) 161-165.

[4] Tonny T. S., Sultana S. and Siddika F. Study on medicinal uses of Persicaria and Rumex species of polygonaceae family, *Journal of Pharmacognosy and Phytochemistry*, 6 (2017) 587-600.

[5] Süleyman H., Demirezer L. Ö., Kuruüzüm A., Banoğlu Z., Göçer F., Özbakir G. and Gepdiremen A. Antiinflammatory effect of the aqueous extract from Rumex patientia L. roots,*Journal of ethnopharmacology*, 65 (1999) 141-148.

[6] Ghosh L., Gayen J., Murugesan T., Sinha S., Pal M. and Saha B. Evaluation of purgative activity of roots of Rumex nepalensis, *Fitoterapia*, 74 (2003) 372-374.

[7] Demirezer L. Ö., Kuruüzüm-Uz A., Bergere I., Schiewe H.-J. and Zeeck A. The structures of antioxidant and cytotoxic agents from natural source: anthraquinones and tannins from roots of Rumex patientia, *Phytochemistry*, 58 (2001) 1213-1217.

[8] Rouf A., Islam M. and Rahman M. Evaluation of antidiarrhoeal activity Rumex maritimus root, *Journal of ethnopharmacology*, 84 (2003) 307-310.

[9] Gebrie E., Makonnen E., Debella A. and Zerihun L. Phytochemical screening and pharmacological evaluations for the antifertility effect of the methanolic root extract of Rumex steudelii, *Journal of Ethnopharmacology*, 96 (2005) 139-143.

[10] Cos P., Hermans N., De Bruyne T., Apers S., Sindambiwe J., Witvrouw M., De Clercq E., Berghe D. V., Pieters L. and Vlietinck A. Antiviral activity of Rwandan medicinal plants against human immunodeficiency virus type-1 (HIV-1),*Phytomedicine*, 9 (2002) 62-68.

[11] Elife K., Akbaş P., Ceyhan G., Erdem T. K. And Alkan H. Determination the Fatty Acid Composition of the Rumex patientia L. Leaves and in vitro Antimicrobial Activity of their Different Extracts, *Süleyman Demirel Üniversitesi Fen Bilimleri Enstitüsü Dergisi*, 24 (2020) 362-367.

[12] Jovin E., Simin N., Orcic D., Balog K., Beara I., Lesjak M. and Dukic N. M. Antioxidant and anti-inflammatory properties of Rumex patientia L, *Planta Medica*, 77 (2011) PM157.

[13] Jain A., Duvvuri L. S., Farah S., Beyth N., Domb A. J. and Khan W. Antimicrobial polymers, *Advanced healthcare materials*, 3 (2014) 1969-1985.

[14] Kamaruzzaman N. F., Tan L. P., Hamdan R. H., Choong S. S., Wong W. K., Gibson A. J., Chivu A. and Pina M. d. F. Antimicrobial polymers: the potential replacement of existing antibiotics?, *International Journal of Molecular Sciences*, 20 (2019) 2747.

[15] Jia W. J., Gu Y. C., Gou M. L., Dai M., Li X. Y., Kan B., Yang J. L., Song Q. F., Wei Y. Q. and Qian Z. Y. Preparation of biodegradable polycaprolactone/poly (ethylene glycol)/polycaprolactone (PCEC) nanoparticles. *Drug delivery*, 15 (2008) 409-416.

[16] Zhang Y. and Zhuo R.-x. Synthesis and in vitro drug release behavior of amphiphilic triblock copolymer nanoparticles based on poly (ethylene glycol) and polycaprolactone, *Biomaterials*, 26 (2005) 6736-6742.

[17] Xu Q., Ren X., Chang Y., Wang J., Yu L. and Dean K. Generation of microcellular biodegradable polycaprolactone foams in supercritical carbon dioxide, *Journal of Applied Polymer Science*, 94 (2004) 593-597.

[18] Pekdemir M. E., Qader I. N., Öner E., Aydoğmuş E., Kök M. and Dağdelen F. Investigation of structure, mechanical, and shape memory behavior of thermally activated poly (ε-caprolactone): azide-functionalized poly (vinyl chloride) binary polymer blend films, *The European Physical Journal Plus*, 136 (2021) 1-14.

[19] Li Q., Li G., Yu S., Zhang Z., Ma F. and Feng Y. Ring-opening polymerization of ε-caprolactone catalyzed by a novel thermophilic lipase from Fervidobacterium nodosum, *Process Biochemistry*, 46 (2011) 253-257.

[20] Peeters J. W., van Leeuwen O., Palmans A. R. and Meijer E. Lipase-catalyzed ring-opening polymerizations of 4-substituted ε-caprolactones: mechanistic considerations, *Macromolecules*, 38 (2005) 5587-5592.

[21] Woodruff M. A. and Hutmacher D. W. The return of a forgotten polymer—Polycaprolactone in the 21st century, *Progress in polymer science*, 35 (2010) 1217-1256.

[22] Pekdemir M. E., Öner E., Kök M. and Qader I. N. Thermal behavior and shape memory properties of PCL blends film with PVC and PMMA polymers, *Iranian Polymer Journal*, 30 (2021) 633-641.

[23] Pekdemir S., Çiftci M. and Karatepe M. Elazığ'da Yetişen Polygonum cognatum Meissn (Madımak) Bitki Ekstraktlarının In vitro Biyolojik Aktiviteleri ve Bazı Fitokimyasal Bileşenlerinin Belirlenmesi, *Avrupa Bilim ve Teknoloji Dergisi*, (2020) 368-378.

[24] Pekdemir M. E., Pekdemir S., İnci Ş., Kırbağ S. and Çiftci M. Thermal, magnetic properties and antimicrobial effects of magnetic iron oxide nanoparticles treated with Polygonum cognatum, *Iranian Journal of Science and Technology, Transactions A: Science*, 45 (2021) 1579-1586.

[25] Sönmez P. E., Kirbağ S. and Şule İ. Antifungal and antibacterial effect of dodder (Cuscuta campestris) used for hepatitis treatment of mothers and newborn infants in province Mardin in Turkey, *Yüzüncü Yıl Üniversitesi Tarım Bilimleri Dergisi*, 29 (2019) 722-730.

[26] Pekdemir S., Özen Öner E., Pekdemir M. E., Dalkılıç S. and Kadıoğlu Dalkılıç L. An Investigation into the Influence of C. moschata Leaves Extract on Physicochemical and Biological Properties of Biodegradable PCL/PLA Blend Film, *Journal of Polymers and the Environment*, (2022) 1-11.

[27] Shoja M., Shameli K., Ahmad M. and Zakaria Z. Preparation and characterization of Poly (ε-Caprolactone)/TiO 2 micro-composites, *Digest Journal of Nanomaterials and Biostructures*, 10 (2015) 471-477.

[28] Qader I. N., Pekdemir M. E., Coşkun M., Kanca M. S., Kök M. And Dağdelen F. Biocompatible PLA/PCL blends nanocomposites doped with nanographite: Physico-chemical, and thermal behaviour, *Journal of Polymer Research*, 29 (2022) 1-8.

[29] İlboğa S., Pekdemir E. and Coşkun M. Cloud Point Temperature, Thermal and Dielectrical Behaviors of Thermosensitive Block Copolymers Based N-Isopropylacrylamide, *Polymer Science, Series B*, 61 (2019) 32-41.

[30] Silverstein R. M. and Bassler G. C. Spectrometric identification of organic compounds, *Journal of Chemical Education*, 39 (1962) 546.

[31] Xing H., Lu M., Yang T., Liu H., Sun Y., Zhao X., Xu H., Yang L. and Ding P. Structure-function relationships of nonviral gene vectors: Lessons from antimicrobial polymers, *Acta biomaterialia*, 86 (2019) 15-40.

Cumhuriyet Sci. J., 44(1) (2023) 67-71
DOI: https://doi.org/10.17776/csj. 1134711

Cumhuriyet Science Journal

| csj.cumhuriyet.edu.tr | Founded: 2002 ISSN: 2587-2680 e-ISSN: 2587-246X Publisher: Sivas Cumhuriyet University

Investıgatıon of the Effects of Favipiravir and Oseltamivir Active Substances Used in the Treatment of Covid-19 on Carbonic Anhydrase I-II Isoenzymes and Acetylcholine Enzyme Activities in Vitro

Sueda Arık [1,a,*], Ümit Muhammet Koçyiğit [1,b]

[1] *Department of Basic Pharmaceutical Sciences, Sivas Cumhuriyet University, Sivas, Türkiye.*
**Corresponding author*

Research Article

History
Received: 23/06/2022
Accepted: 16/01/2023

ABSTRACT

Covid-19, originating from Wuhan, China, is a worldwide health problem. Immune system abnormalities caused by covid-19 lead to infections, septic shock, and severe multi-organ dysfunction. The drugs used for treatment are palliative pharmacological alternatives and help manage symptoms or complications that occur during the course of the disease. Both carbonic anhydrases and cholinesterases can be target enzymes for drugs. The goal of this study is to determine how the drugs used in covid-19 affect patients being treated for Alzheimer's disease, myasthenia gravis, glaucoma, or epilepsy, and to determine if there are drug-drug interactions. In case of possible interactions, it is crucial for these patients to consider alternative treatments and to recheck the dosage of the drugs used. To this end, the effects of the drugs favipiravir and oseltamivir, which are used in the covid-19 clinic and whose relationship with these enzymes has not been previously studied, on the isoenzymes of carbonic anhydrase I- II and the enzyme acetylcholinesterase were studied in vitro. No inhibition or activation was observed on the enzyme acetylcholinesterase, while inhibition was observed for the isoenzyme carbonic anhydrase I - II.

Keywords: Alzheimer's disease, Carbonic anhydrase, Favipiravir, Oseltamivir, Covid-19

[a] *ariksueda@gmail.com* *https://orcid.org/0000-0003-3275-7035* [b] *ukocyigit@cumhuriyet.edu.tr* *https://orcid.org/ 0000-0001-8710-2912*

Introduction

Investigations into a group of patients who experienced respiratory symptoms (fever, cough, and shortness of breath) in Wuhan Province, China led to the discovery of covid-19 on January 13, 2020. After that, the pathogen spread very quickly and became a global threat, affecting millions of people around the world and causing the death of thousands.

In the treatment of covid-19 during the pandemic: Lopinavir/ritonavir, danoprevir/ritonavir, oseltamivir, favipiravir, remdesivir, umifenovir, molnupiravir, antivirals, camostat mesylate/nafamostat mesylate, ivermectin, chloroquine/hydroxychlorozone, anticoagulant drugs, drugs such as dexamethasone, treatment trials, such as dexamethasone, treatment. However, none of the proposed treatments have proven effective in completely eradicating covid-19. The drugs used are palliative pharmacological alternatives and have helped to treat the symptoms or complications that occur during the course of the disease [1].

Acid-base balance is one of the most important requirements for the survival of an organism and is achieved by the combined efforts of the kidneys and lungs [2]. CA Enzymes, on the other hand, maintain acid-base balance by catalyzing the reversible hydration of carbon dioxide to bicarbonate and H^+ ions. It has been characterized as a pH-regulating enzyme [3].

One of the most prevalent neurological conditions in clinical medicine is seizures. Although the exact causes of seizures are still unknown, it is believed that variations in brain pH and intracellular potassium concentration as well as ion variability are involved. The pH buffering of the extracellular and intracellular spaces is mainly carried out by the CO_2/HCO_3 buffer, and the balance of the two species is maintained by the zinc enzyme carbonic anhydrase (CA). Some carbonic anhydrase inhibitors (CAIs) are prescribed to treat epilepsy as anticonvulsants[4].

In glaucoma, one of the eye diseases that lead to blindness in 15-20%, the enzyme carbonic anhydrase has a triggering effect. For this reason, carbonic anhydrase inhibitors such as acetazolamide and dorzolamide have been used to treat glaucoma for years [5].

Recently, it has been suggested that activators of carbonic anhydrase may be one of the key factors in pathologies related to pharmacological development of synaptic activity, learning, and memory.

It has been demonstrated that administering amino acid-type CAAs enhances spatial learning, which is counteracted by concurrently administering a sulfonamide inhibitor such acetazolamide. These trials also revealed impairment in the consolidation of fear memories, which may open the door to pharmacological uses in new therapies for phobias and post-traumatic shock. Extracellular signal-regulated kinase (ERK) pathways, which are engaged in a crucial stage of memory formation in both the cortex and hippocampus, were

found to be quickly activated by CAA administration. The use of CAAs for memory treatment in aging or neurodegenerative illnesses like Alzheimer's disease may result from these intriguing findings [6]. As a result, it has been proposed that CA activators may be helpful in the management of phobias and cognitive impairment.

The fact that acid-base balance dysregulation observed in covid patients has not been adequately defined has attracted the attention of researchers; in the study by Gaetano Alfano et al. ABG analyzes of 211 covid patients were examined, and acid-base balance irregularity was observed in 79.7% of patients [7]. It is suggested that CA enzymes, which are characterized as pH-regulating enzymes and provide acid-base balance in many tissues, may be a crucial factor in the pathogenesis of the disease; CA, ACE2 and MMA biomolecules contribute to the RAS system in the pathogenesis of covid, and dysregulation of these biomolecules triggers respiratory acidosis, pulmonary edema, cardiac and renal failure [8]. In the study of Seçil Deniz et al, it was hypothesized that patients with covid-19 problems have an acid-base state affected by the activity of CA, and the blood levels of CA were measured in acute covid patients, noncovid patients, and post-covid patients. It was found that the activity of CA in blood was significantly increased in covid-19 patients and was higher in post-covid patients than in acute covid patients. In the same study, it was suggested that CA inhibitors could be used as pharmacological treatment in the treatment of covid [9].

Our study involves investigating the effects of favipiravir- and oseltamivir-based drugs used in the treatment of covid-19 on acid-base balance through the enzymes carbonic anhydrase isoenzyme I and II (hCA I and hCA II). This study, which examined the use of drugs in specific patient groups based on acid-base balance and the drug-enzyme relationship, is a contribution to the literature.

For the brain to function properly, acetylcholine (ACh), norepinephrine, dopamine, gamma-aminobutyric acid, serotonin, and glutamate all need to be in balance [10]. Alzheimer's disease (AD) is characterized by behavioral signs as well as a steady decline in cognitive ability. Acetylcholinesterase/cholinesterase inhibitors are the principal type of medications now used to treat AD. A crucial aspect of AD is cholinergic neurotransmission [11].

Targeted antibodies to the muscle's acetylcholine receptors (AChRs) are the main cause of the rare autoimmune disease myasthenia gravis, which affects the neuromuscular junction. Muscle weakness and exhaustion are brought on by the loss of AChRs, which affects neuromuscular transmission. Myasthenia gravis can today be effectively controlled with reasonably safe and effective medications, despite the fact that the condition used to typically be deadly. Acetylcholinesterase inhibitors (AChEI), which enhance neuromuscular transmission, are the first step in treatment and are crucial for early diagnosis [12].

The relationship between vascular deficits and retinal ganglion cell (RGC) loss in glaucoma was investigated. They wanted to know if the acetylcholinesterase inhibitor galantamine, which supports RGC survival, might shield the retinal microvasculature and enhance blood flow in an experimental glaucoma model. The outcomes demonstrated that systemic administration of galantamine improved retinal blood flow, preserved the density of microvessels in glaucomatous retinas, and mediated the vasoactive effect of galantamine on retinal microvessels through activation of muscarinic acetylcholine receptors both in vitro and in vivo [13].

As shown in the above studies, acetylcholinesterase inhibitors are used in the treatment of serious diseases such as Alzheimer's disease, myasthenia gravis, and glaucoma. It is very important to know how acetylcholinesterase is affected when these patients need to take these two antiviral drugs used at covid-19 clinic and to determine if there is a drug interaction. In the event of an interaction, it is imperative that these patients consider alternative treatments and recheck the dosage of the medications used.

Materials and Methods

Chemicals

p-nitrophenylacetate, Tris-SO_4 (0.5 M pH 7.4), Tris-HCl buffer (1M, pH 8), acetylcholine iodate solution (10 mM), DTNB solution (10 mM), enzyme solution (carbonic anhydrase I-II isoenzymes and acetylcholinesterase), purified water, favipiravir (favicovir film-coated tablet 200 mg 40 tablets) and oseltamivir phosphate (oseflu 30 mg 10 capsules) active ingredient drug samples

Tools and Devices Used

Spectrophotometer (SOIFoptical instruments/China), Magnetic stirrer (Elektro-MAG/Turkey), Precision balance (Weightlab Instrument/Turkey), pH meter (HANNA/ United States), Vortex instrument (Velp Scientifica/Italy),Micropipette types (Weightlab Instrument/Turkey, Nichipet EXII/Japan, ISOLAB/Turkey, A.B.T. Laboratory Industry/Turkey)

Activity Assignments

Esterase activity method investigation of the effects of drugs on carbonic anhydrase (Ca) isoenzymes

Carbonic anhydrase is an enzyme with esterase activity, so this method was studied. The principle of the esterase activity method is that the enzyme carbonic anhydrase hydrolyzes the compound *p*-nitrophenyl acetate as a substrate to p-nitrophenolate, which absorbs at a wavelength of 348 nm. In this method, *p*-nitrophenol and *p*-nitrophenolate in both compounds have the same absorbance values at a wavelength of 348 nm. Therefore, the formation of phenol or phenolate during the reaction affects the measured values [83-86].

In this experiment, p-nitrophenyl acetate, which has very low absorbance at a wavelength of 348 nm, was used

as a blank sample. 1-ml quartz cuvettes were also used in the measurements. In the method, the procedure for activity determination was applied in the following order.

Table 1. Contents of 1ml cuvette used in esterase activity studies for carbonic anhydrase isoenzymes

Substances	Control (Blind) (µl)	Sample (µl)
Tris-SO_4 (0,5 M) pH 7,4	400	400
p-Nitrophenol acetate	360	360
H_2O	240	230
Enzyme solution	-	10
Total final volume	1000	1000

The absorbance values of the reaction mixture prepared according to Table 1 were measured every 15 seconds, and the absorbance value at a wavelength of 348 nm at 25°C was read at the end of 3 minutes, and the difference between the absorbance value at zero second and the absorbance value was taken. [14-17]. In the kinetic studies applied in the study, the procedures for activity determination were applied according to the procedure for esterase activity of the enzyme. In this study, the effects of favipiravir and oseltamivir phosphate-based drugs on the isoenzymes of carbonic anhydrase I- II were investigated. IC_{50} and K_i values were calculated using data obtained by this method.

Determination of the effects of drugs on Acetylcholinesterase enzyme

The effects of the drugs under study on the enzyme acetylcholinesterase were investigated. The acetylcholinesterase method was used for this purpose. The principle of the method: AChE catalyzes the hydrolysis of acetylcholine and the formation of its degradation products thiocholine and acetate.

5-Thio-2-nitrobenzoic acid, a yellow compound, is formed by the interaction of the DTNB chemical used in the research with thiocholine, one of the degradation products. The absorbance value of this colored compound is measured at 412 nm [18]. In this method, the measurements of samples and blanks are performed at a wavelength of 412 nm. It should be noted that the absorbance values are measured and recorded at the beginning and after the fifth minute.

Table 2. The contents of the cuvette used during the kinetic studies of the acetylcholinesterase enzyme

Substances	Control (Blind) (µl)	Sample (µl)
Tris-HCl	100	100
H_2O	790	780
Inhıbıtor	-	10
DTNB	50	50
Enzyme solution	10	10
Acetylcholinthioiodide	50	50

Results

The inhibition potentials of drugs against two physiologically relevant CA isoforms, the slower cytosolic isoform (hCA I), the more rapid cytosolic isoenzyme (hCA II) were investigated by using an esterase assay method. The inhibition data of compounds against CA I, and II isoforms were summarized in Table 3 (IC_{50} and K_i values expressed as micromolar (**µ**M)).

Table 3. The enzyme inhibition results of the drugs against carbonic anhydrase I and II iszoenzymes

Compounds	IC_{50} (µM)				Ki (µM)	
	hCA I	r^2	hCA II	r^2	hCA I	hCA II
Favipiravir	6.9810	0.9531	5.3950	0,9526	6.2507 ±1.0564	5.9018±0.2938
Oseltamivir phosphate	1.2459	0.9461	1.0279	0.9783	2.2773±0.4405	1.5910±0.6036
AZA*	12.6200	0.9712	19.810	0.9706	12.08±2.00	18.2200±4.900

*AZA: acetazolamide, standard.

The drug concentrations (IC_{50}) at which 50% of CA enzymes activities were inhibited were calculated.The drugs were remarkably inhibited both the cytosolic isoforms hCA I (IC_{50} 6.9810 and 1.2459 µM) and hCA II (IC_{50} ranging between 5.3950 and 1.0279 µM). Figure 1 show IC_{50} plots.

Finally, inhibition constants (K_i) were determined for t CA enzymes from Lineweaver-Burk plots. K_i values were calculated as 6.2507 ±1.0564 µM and 2.2773±0.4405 µM for hCA I and 5.9018±0.2938 µM and 1.5910±0.6036 µM for h CA II, respectively. The K_i value for the standard item AZA was found to be 18.2200±4.900 µM. Figure 2 show K_i plots.

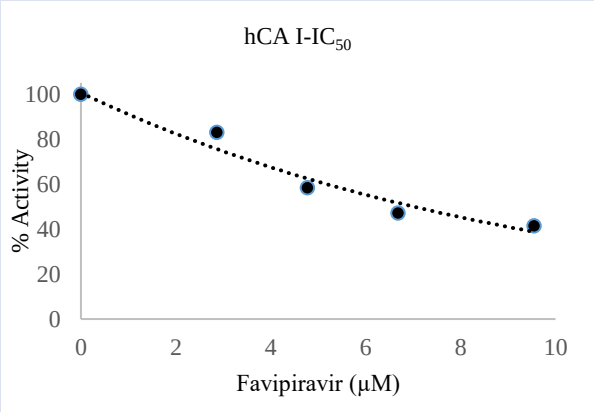

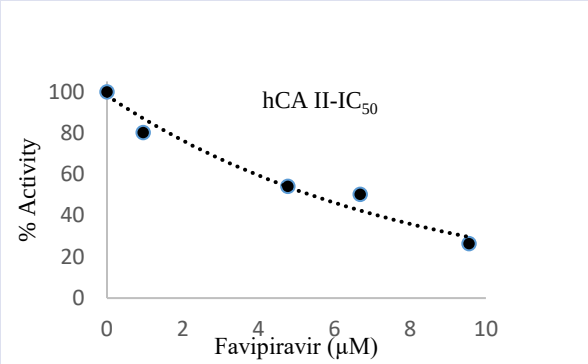

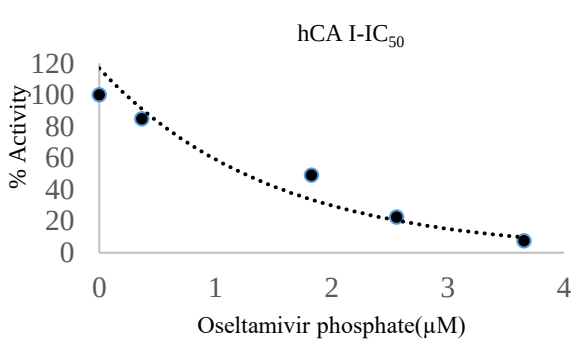

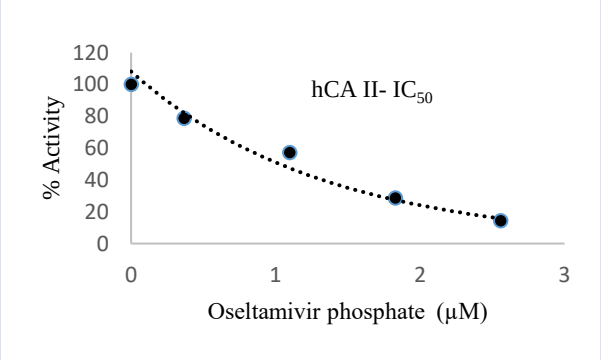

Figure 1. IC_{50} graphics of the drugs against carbonic anhydrase I and II isoenzymes

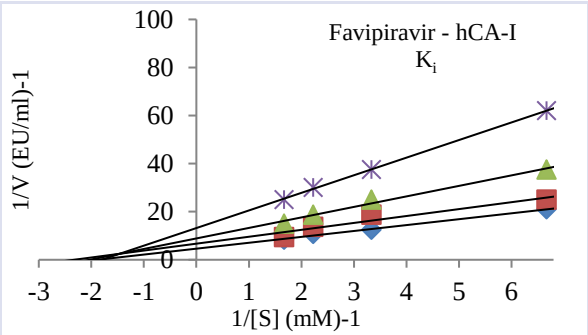

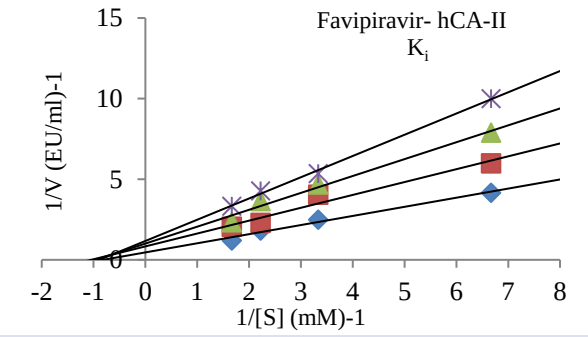

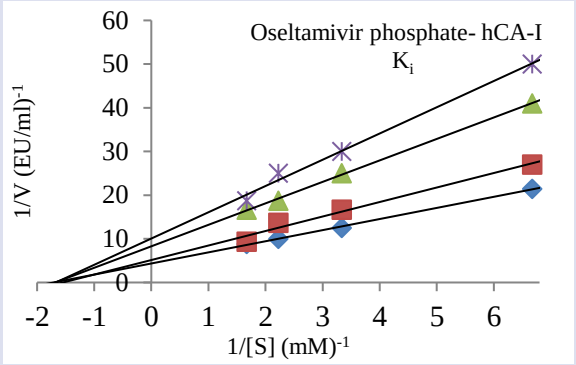

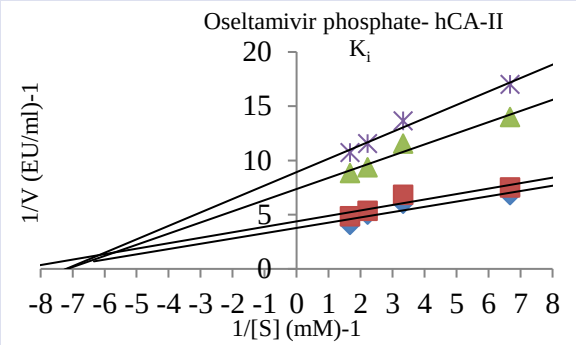

Figure 2. K_i graphics of the drugs against carbonic anhydrase I and II isoenzymes

Finally, the effects of these drugs on acetylcholinesterase enzyme activity were investigated in vitro using the acetylcholiniodate method. No effect of drugs on enzyme activity was found.

Discussion and Conclusion

In the study of Gaetano Alfano et al., it was mentioned that 79.7% of 211 covid-19 patients had acid-base disorders. Based on this study, it was thought that favipiravir and oseltamivir phosphate active agents used in the treatment of covid-19 may have inhibition or activation effects on carbonic anhydrase I-II isoenzymes. IC_{50} and K_i results were calculated for both drugs, and it was observed that the absorbance difference value decreased as the amount of inhibitor substance studied increased. The results showed that favipiravir and oseltamivir phosphate-based drugs have inhibitory effects on carbonic anhydrase I-II isoenzymes. No inhibition or activation was observed on the acetylcholinesterase enzyme.

Carbonic anhydrase enzymes, which are characterized as pH-regulating enzymes and provide acid-base balance in tissues, are a critical factor in the pathogenesis of covid-19 disease. In this context, carbonic anhydrase inhibition by favipiravir and oseltamivir phosphate active substances used in treatment is very important.

Carbonic anhydrase inhibitors are used clinically as diuretics, anti-glaucoma agents, and anti-epileptics, but new applications have recently been reported in the treatment of cancer, neuropathic pain, sleep apnea, migraine, lowering intracranial pressure, and cerebral ischemia. The carbonic anhydrase inhibition observed for

favipiravir and oseltamivir phosphate active substances used in covid-19 may contribute to the development of new treatment strategies.

When special patient groups with conditions such as epilepsy and glaucoma have to receive treatment with these antivirals, the drug doses used by the experts in the field should be reviewed and the appropriate dose determined, taking into account drug-drug interactions.

As a result, enzyme inhibitors are very important in the discovery of new therapeutic agents and in a detailed understanding of protein-drug interactions at the molecular level. This study contributed to the literature by investigating the effects of favipiravir and oseltamivir phosphate-based drugs on acetylcholinesterase and carbonic anhydrase I-II isoenzymes. Drug research is generally a long and laborious process. Our results will provide insight to researchers and may be a preliminary step for many new projects.

Acknowledgments

This study has been partly supported by Cumhuriyet University Faculty of Pharmacy as the research project.

Conflicts of interest

There are no conflicts of interest in this work.

References

[1] Marcolino V. A., Pimentel T. C., Barao C. E., What to expect from different drugs used in the treatment of COVID-19: A study on applications and in vivo and in vitro results, *European Journal of Pharmacology*, 887 (2020) 173467.

[2] Nechipurenko Y. D., Semyonov D. A., Lavrinenko I. A., Lagutkin, D. A., Generalov, E. A., Zaitceva, A. Y., Yegorov, Y. E., The Role of Acidosis in the Pathogenesis of Severe Forms of COVID-19. *Biology*, 10(9) (2021) 852.

[3] Akkemik E., Çalışır Ü., Çiçek B., İnsan karbonik anhidraz I, II izoenzim aktiviteleri üzerine bazı tiyocrown eterlerin etkisi, *Balıkesir Üniversitesi Fen Bilimleri Enstitüsü Dergisi*, 19(2) (2017) 192-199.

[4] Thiry A., Dogne J. M., Supuran C. T., Masereel B., Carbonic anhydrase inhibitors as anticonvulsant agents, *Current Topics in Medicinal Chemistry*, 7(9) (2007): 855-864.

[5] Supuran, CT Karbonik anhidraz inhibitörleri: hipoksik tümörlerin tedavisi ve görüntülenmesi için deneysel ajanlar hakkında bir güncelleme, *Araştırma İlaçları Hakkında Uzman Görüşü* , 30(12) (2021) 1197-1208.

[6] Supuran, C. T. Carbonic anhydrase inhibitors and their potential in a range of therapeutic areas. *Expert opinion on therapeutic patents*, 28(10) (2018) 709-712.

[7] Alfano G., Fontana F., Mori G., Giaroni F., Ferrari A., Giovanella S., Guaraldi G., COVID-19 hastalarında asit baz bozuklukları, *Uluslararası Üroloji ve Nefroloji* , 54(2) (2022) 405-410.

[8] Emameh R. Z., Falak R., Bahreini E., Application of system biology to explore the association of neprilysin, angiotensin-converting enzyme 2 (ACE2), and carbonic anhydrase (CA) in pathogenesis of SARS-CoV-2, *Biological Procedures Online*, 22(1) (2020) 1-9.

[9] Deniz S., Uysal T. K., Capasso C., Supuran C. T., Ozensoy Guler O., Is carbonic anhydrase inhibition useful as a complementary therapy of Covid-19 infection?, *Journal of Enzyme Inhibition and Medicinal Chemistry*, 36(1) (2021) 1230-1235.

[10] Watkins P. B., Zimmerman H. J., Knapp M. J., Gracon S. I., Lewis K. W., Hepatotoxic effects of tacrine administration in patients with Alzheimer's disease, *Jama*, 271(13) (1994) 992-998.

[11] Marucci G., Buccioni M., Dal Ben D., Lambertucci C., Volpini R., Amenta F., Efficacy of acetylcholinesterase inhibitors in Alzheimer's disease, *Neuropharmacology*, 190 (2021) 108352.

[12] Komloova M., Musilek K., Dolezal M., Gunn-Moore F., Kuca K., Structure-activity relationship of quaternary acetylcholinesterase inhibitors-outlook for early myasthenia gravis treatment, *Current Medicinal Chemistry*, 17(17) (2010) 1810-1824.

[13] Almasieh M., MacIntyre J. N., Pouliot M., Casanova C., Vaucher E., Kelly M. E., Di Polo A., Acetylcholinesterase inhibition promotes retinal vasoprotection and increases ocular blood flow in experimental glaucoma, *Investigative Ophthalmology & Visual Science*, 54(5) (2013) 3171-3183.

[14] Armstrong J.M., Myers D.V., Verpoorte J.A., Edsall J.T., Purification and Properties of Human Erythrocyte Carbonic Anhydrase, *The Journal of Biological Chemistry,* 241(21) (1966) 5137-5149.

[15] Verpoorte JA, Mehta S, Edsall JT. Esterase activities of human carbonic anhydrases B and C. Journal of Biological Chemistry, 242.18 (1967): 4221-4229.

[16] Göçer H., Akıncıoğlu A., Öztaşkın N., Göksu S., Gülçin İ., Synthesis, Antioxidant, and Antiacetylcholinesterase Activities of Sulfonamide Derivatives of Dopamine-Related Compounds, *Archiv der Pharmazie*, 346(11) (2013) 783-792.

[17] Gürdere M. B., Budak Y., Kocyigit U. M., Taslimi P., Tüzün B., Ceylan M., ADME properties, bioactivity and molecular docking studies of 4-amino-chalcone derivatives: new analogues for the treatment of Alzheimer, glaucoma and epileptic diseases, *In Silico Pharmacology,* 9(1) (2021) 1-11.

[18] Ellman G.L., Courtney K.D., Andres J.V., Featherstone R.M., A new and rapid colorimetric determination of acetylcholinesterase activity, *Biochemical Pharmacology*, 7(2) (1961) 88-95.

Cumhuriyet Sci. J., 44(1) (2023) 72-80
DOI: https://doi.org/10.17776/csj.1117056

Cumhuriyet Science Journal

| csj.cumhuriyet.edu.tr | Founded: 2002 ISSN: 2587-2680 e-ISSN: 2587-246X Publisher: Sivas Cumhuriyet University

Structural, Electronic, ADME and p450 Analyses of Boron Containing Compounds against Omicron Variant (B.1.1.529) in SARS-CoV-2

Koray Sayın [1,a,*], Hilmi Ataseven [2,b]

[1] *Department of Chemistry, Faculty of Science, Sivas Cumhuriyet University, Sivas, Türkiye.*
[2] *Department of Gastroenterology, Faculty of Medicine, Sivas Cumhuriyet University, Sivas, Türkiye.*
**Corresponding author*

Research Article

History
Received: 15/05/2022
Accepted: 12/02/2023

ABSTRACT

Eight boron compounds are investigated in this study. Structural and spectral characterization is done at M062X/6-311G(d) level in the water. Active sites of these compounds are determined using contour plots of frontier molecular orbital, molecular electrostatic potential (MEP) maps and MEP contour.. Electrophilic and nucleophilic attack regions are determined. We aimed to determine whether boron compounds inhibitor used in the treatment of omicron variant of SARS-CoV-2. Since SARS-CoV-2 is a worldwide health problem, anti-viral properties of studied boron compounds were investigated using in silico techniques. Bioavaliability analyses were performed using ADME and p450. It was found that compound B7 can be good drug candidate against omicron variant of SARS-CoV-2.

Keywords: Boron-Imine compounds, SARS-CoV-2_Omicron, p450, ADME, Molecular docking.

[a] *krysayin@gmail.com* *https://orcid.org/0000-0001-6648-5010* [b] *hilmiataseven@yahoo.com* *https://orcid.org/0000-0001-5458-509X*

Introduction

In December 2019, the novel coronavirus is broked out in Wuhan, Hubei province of China and it is called as novel coronavirus 2019 (2019-nCoV) or severe acute respiratory syndrome coronavirus 2 (SARS-CoV-2) and appeared as a pandemic threatening the world [1]. To date, many variants of SARS-CoV-2 have been encountered and the threat still continues [1]. To date, seven variants of this virus which are alpha, beta, gamma, delta, omicron, lambda, and mu, are reported and summarized by the world health organization. The most common symptoms of this disease are fever, cough, tiredness, loss of taste and smell. However, the serious symptoms are difficulty breathing, loss of speech or mobility, and chest pain. Currently, many people suffer from this disease, and some end up with death. Additionally, many drugs are used for the treatment of COVID-19 while many vaccines are used for the preventation from SARS-CoV-2. Furthermore, many drug candidates are investigated by researchers [2-6].

Nowadays, the omicron variant of SARS-CoV-2 is the most important threat and many people suffer from this variant. The Omicron variant of SARS-CoV-2 is known as B.1.1.529 variant and has been reported firstly on 24 November 2021 in South Africa [7]. Normally, three genes/proteins of SARS-CoV-2 are reported as the most important ones which are main protease, spike-glycoprotein, and RNA polymerase. However, the spike glycoprotein of the omicron variant of SARS-CoV-2 is not detected at first. In subsequent analyzes, it was reported that the spike protein belonging to the omicron variant was not similar to that of the other variants. Protein structure of omicron variant is shown in Fig. 1.

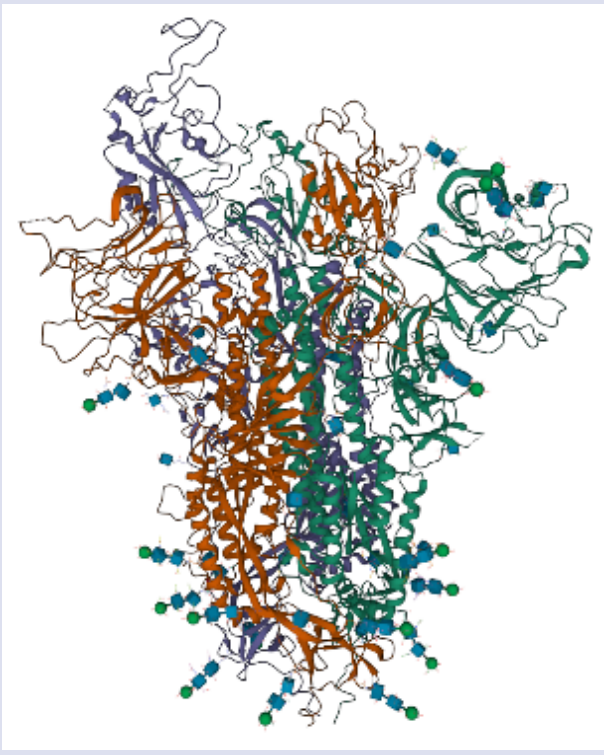

Fig. 1. The protein structure of omicron variant of SARS-CoV-2.

In this study, boron-imine structured compounds are taken into consideration and these compounds have been synthesized by Pasa and co-workers [8]. These compounds are initially optimized at M06-2X/6-311G(d) level in water. In this study, it is accepted that M062X/6-311G(d) level is popular ones for the boron compounds. The Polarizable Continuum Model (PCM) using the integral equation formalism variant (IEF-PCM) model is used to taking of solute – solvent interaction in optimizations. Electronic properties of these boron compounds are investigated using contour diagram of frontier moleculer orbitals, molecular electrostatic potential (MEP) maps and MEP contours. Finally, molecular docking analysis which is the popular analysis in the recent time to determine the biological activity of chemicals are performed between target proteins and selected compounds [9-11]. Target proteins are main protease, RNA polymerase, and spike glycoproteins of SARS-CoV-2. Additionally, alpha and omicron variant of this virus is considered. Finally, selected compounds are found as more inactive against alpha variant of SARS-CoV-2 while they are found as highly active against that of the omicron variant. Compounds B4, B5 and B7 can be good inhibitor candidates in the treatment of the omicron variant of SARS-CoV-2.

Materials and Methods

Optimization

Fully optimization calculations were performed using Gaussian software [12, 13]. Initally, the whole compounds in this study was pre-optimized in universal force field (UFF) molecular mechanic method in order not to waste time and not to encounter errors in future optimization calculations. In subsequent optimization calculations, M06-2X method was used with the 6-311G(d) basis set. Furthermore, IEF-PCM method was used to consider solute-solvent interaction. All calculations were done in the water phase. Furthermore, ChemDraw software was used as utilities throughout the study [14].

Molecular Docking

Studied compounds were prepared for docking calculation using LigPrep module in Maestro software. Acidity of calculations is selected as 7±2. Then target proteins which are 6NUS [15], 6VSB [16], 6WNP [17] and 7QO7 [18] were prepared using Protein Preperation module. 6NUS, 6VSB and 6WNP are related with alpha variant of SARS-CoV-2 while 7QO7 was related with omicron variant. 6NUS, 6WNP, 6WNP and 7QO7 were related with RNA polymerase, main protease, spike glycoprotein of alpha variant and spike glycoprotein of omicron variant, respectively. The receptor binding domain of them are defined using Grid Generation. Then molecular docking calculations were performed [19-22]. In these calculation four parameters which are docking score (DS), van der Walls energy (E_{vdW}), Coloumb interaction energy (E_{Coul}) and total interaction energy (E_{Total}), were examined and evaluated. ADME and p450 analyses were performed for the studied boron containg compounds.

Results and Discussion

Optimized Structures

The examined compounds are optimized at M06-2X/6-311G(d) level in the water. Optimized structures of them are represented in Fig. 2.

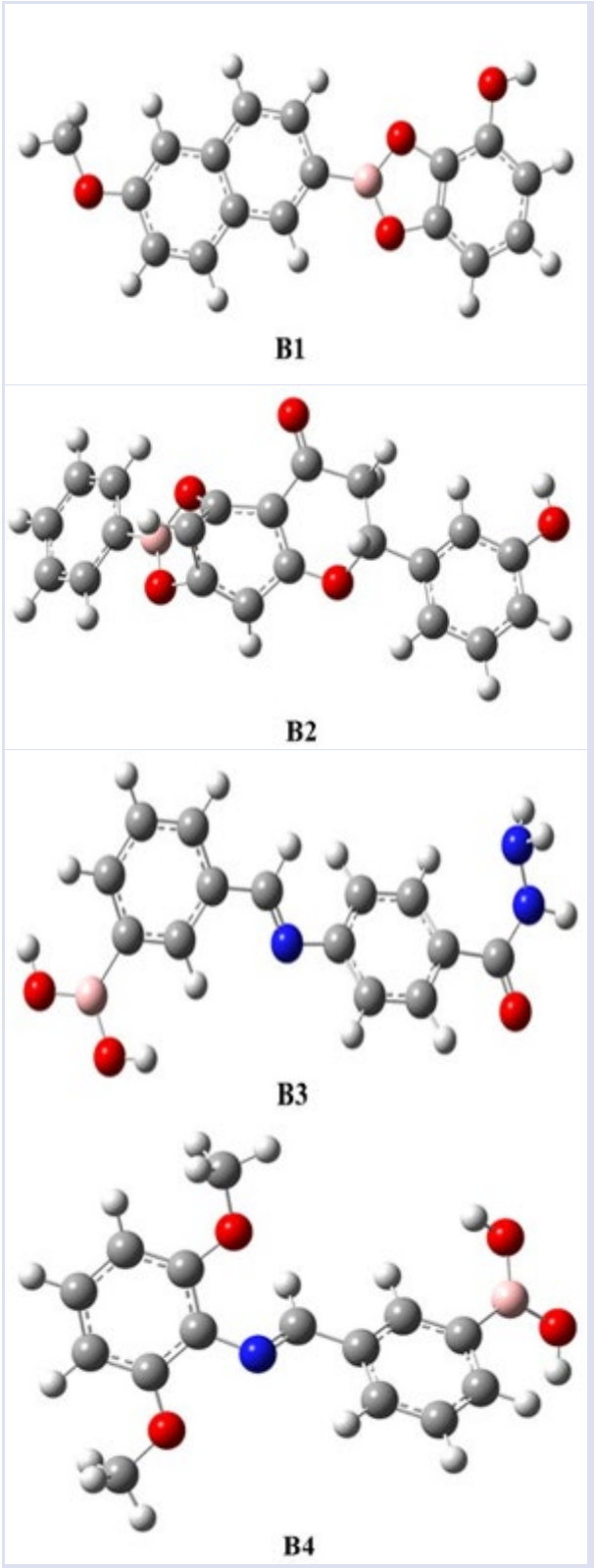

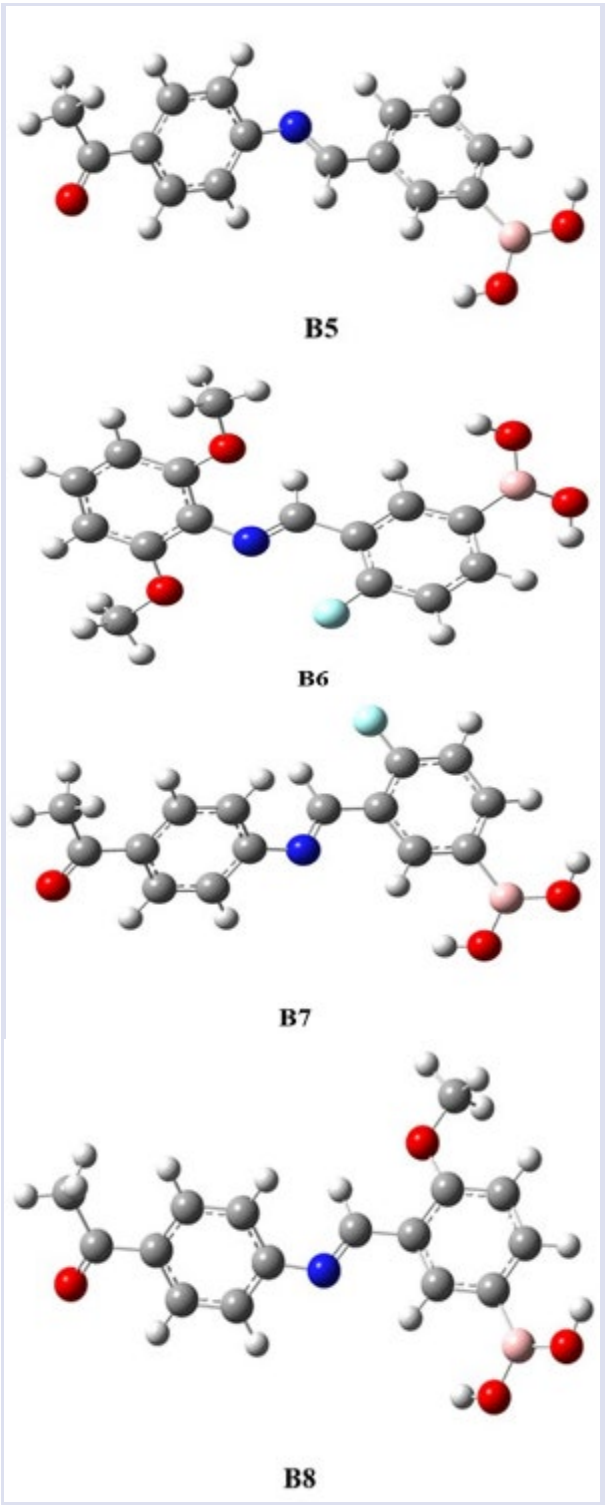

Fig. 2. The optimized structure of studied boron compounds.

According to optimized structures, studied boron compounds are mainly look alike to each other. Only the attached substituents cause the structural branching of the compounds. IR spectrum of studied compounds are calculated and potential energy distribution (PED) analyses of these spectrum are performed. IR spectrum and PED analyses are represented in Fig. 3 and Table 1, respectively.

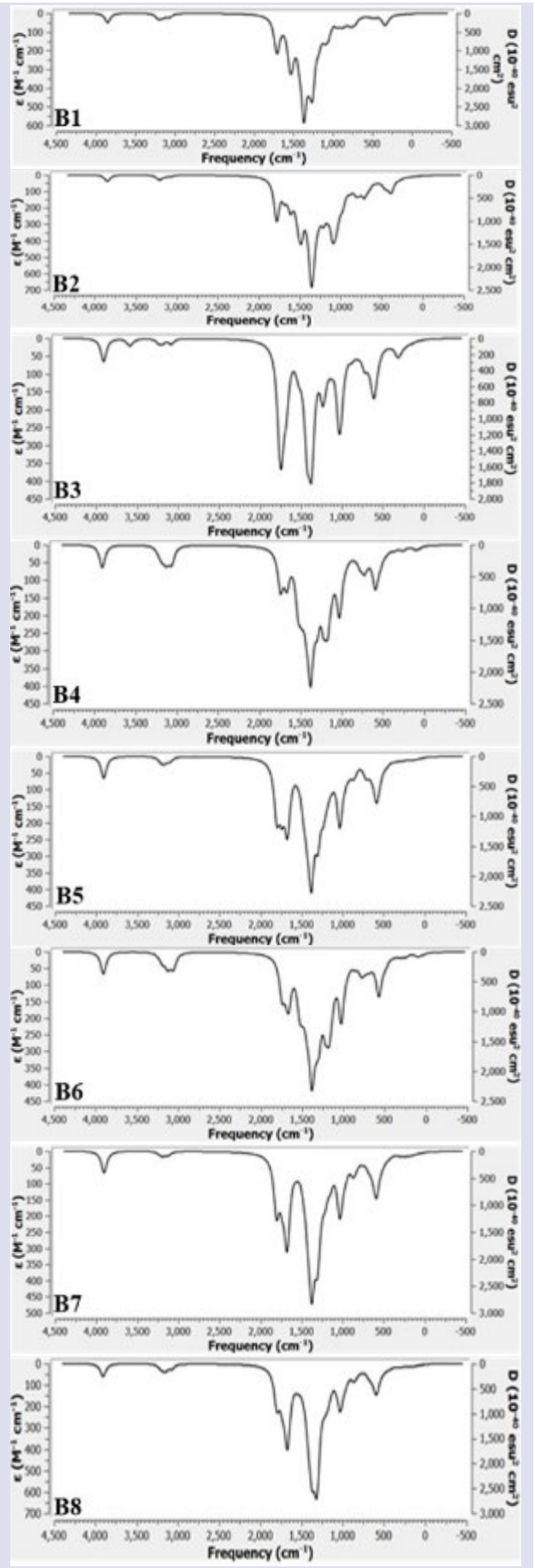

Fig. 3. The IR spectrum of boron compounds.

Table 1. The calculated frequencies (cm^{-1}) in PED Analyses

B1	
3850	STRE(OH)
3180	STRE(CH)
1703	STRE(CC), STRE(CC)
1544	BEND(HCC), BEND(HCH)
1367	STRE(CB)
1293	STRE(CC), BEND(HCC), BEND(HCC)
335	BEND(CCC), BEND(OCC), BEND(CBO), BEND(COC)
B2	
3848	STRE(OH)
3214	STRE(CH)
1781	STRE(OC)
1612	STRE(CC)
1504	BEND(HCC), BEND(CCC)
1361	STRE(CB), BEND(HCC), BEND(HCO)
1218	BEND(HOC), BEND(HCC)
1102	STRE(OC)
815	STRE(CH), TORS(HCCC), OUT(CCOC)
711	BEND(COB), TORS(HCCC), TORS(CCCC)
380	STRE(OC), TORS(HOCC), STRE(CC)
B3	
3906	STRE(OH), STRE(CC)
3585	STRE(NH)
3233	STRE(CH)
3083	STRE(CH)
1762	STRE(OC), BEND(HNH)
1375	STRE(OB), STRE(CB), BEND(HCC)
1234	STRE(CC), STRE(NN), BEND(HNN)
1011	BEND(HNH), TORS(HNNC)
607	STRE(OH), STRE(NC)
309	TORS(HNNC)
B4	
3903	STRE(OH)
3067	STRE(CH)
1742	STRE(NC)
1666	STRE(CC), BEND(CCC)
1377	STRE(OB), STRE(CB)
1214	BEND(HCC)
1033	STRE(OB), BEND(HOB)
781	TORS(HCCC), TORS(CCCC), OUT(OCCC)
592	TORS(HOBC)
B5	
3907	STRE(OH)
3167	(STRE(CH)
1801	STREOC)
1674	STRE(CC)
1378	STRE(OB), STRE(CB)
1301	STRE(CC)
1037	BEND(HOB)
589	TORS(HOBC)
B6	
3905	STRE(OH)
3064	STRE(CH)
1744	STRE(NC)
1688	STRE(CC), BEND(HCC)
1382	STRE(OB), STRE(CB)
1171	STRE(OC), BEND(HCC)
1027	BEND(HOB)
783	TORS(HCCC), OUT(OCCC)
567	TORS(HOBC)
B7	
3904	STRE(OH)
3123	STRE(CH)
1804	STRE(OC)
1678	STRE(CC)
1375	STRE(OB), STRE(CB), BEND(HCC)
1311	STRE(CC), STRE(FC), BEND(HCC)
1036	STRE(OB), BEND(HOB)
875	TORS(HCCC)
592	BEND(OCC), TORS(HOBC)
B8	
3902	STRE(OH)
3074	STRE(CH)
1799	STRE(OC)
1672	STRE(NC), STRE(CC)
1372	STRE(OB), STRE(CB), BEND(HCC)
1321	STRE(CC), STRE(OC)
1034	STRE(OB), BEND(HOB)
852	TORS(HCCC), OUT(OCCC)
592	TORS(HOBC)

Electronic Properties

Electronic properties of chemicals play important role on the determination of interaction mechanism, active site of compounds and molecular effectiveness of compound surface etc. For these aims, different plots of maps can be used and contour diagram of frontier molecular orbitals, molecular electrostatic potential (MEP) maps and MEP contours are calculated for each boron compounds. While contour diagram of frontier molecular orbitals of B1-B8 are represented in Fig. 4.

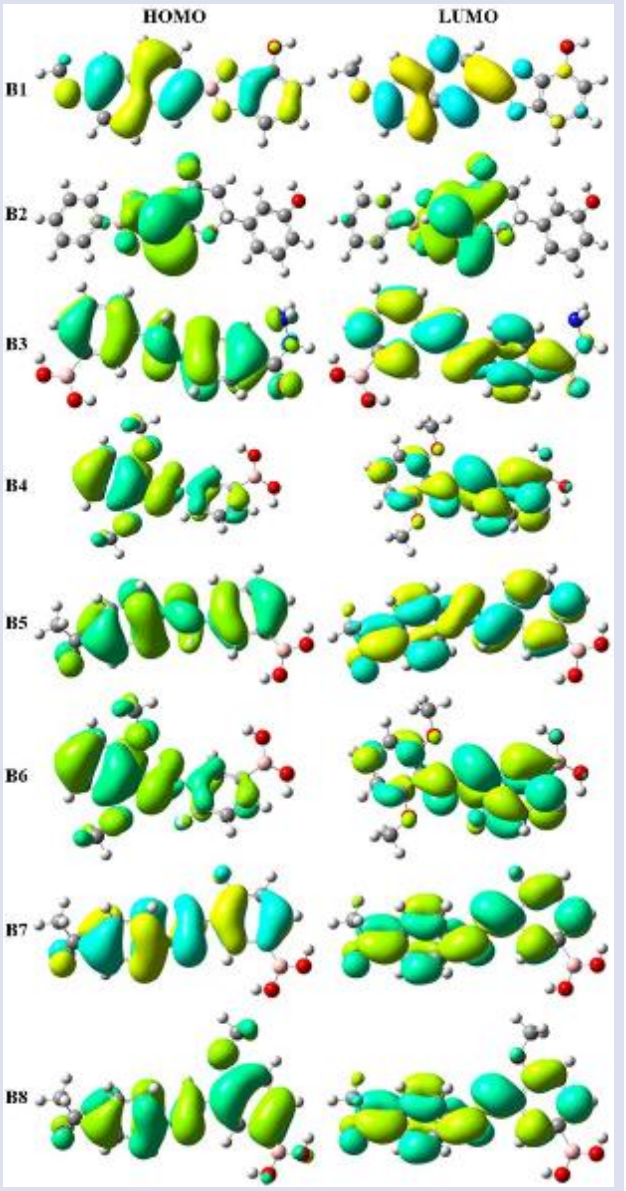

Fig. 4. Contour diagram of frontier molecular orbitals of B1-B8

According to Fig. 4, HOMO electrons are mainly delocalized on the whole structure of the studied compound. In the contour plot of LUMO, electrons could be delocalized on the whole structure. To exmine more detail, MEP maps and contours are calculated and respresented in Fig. 5.

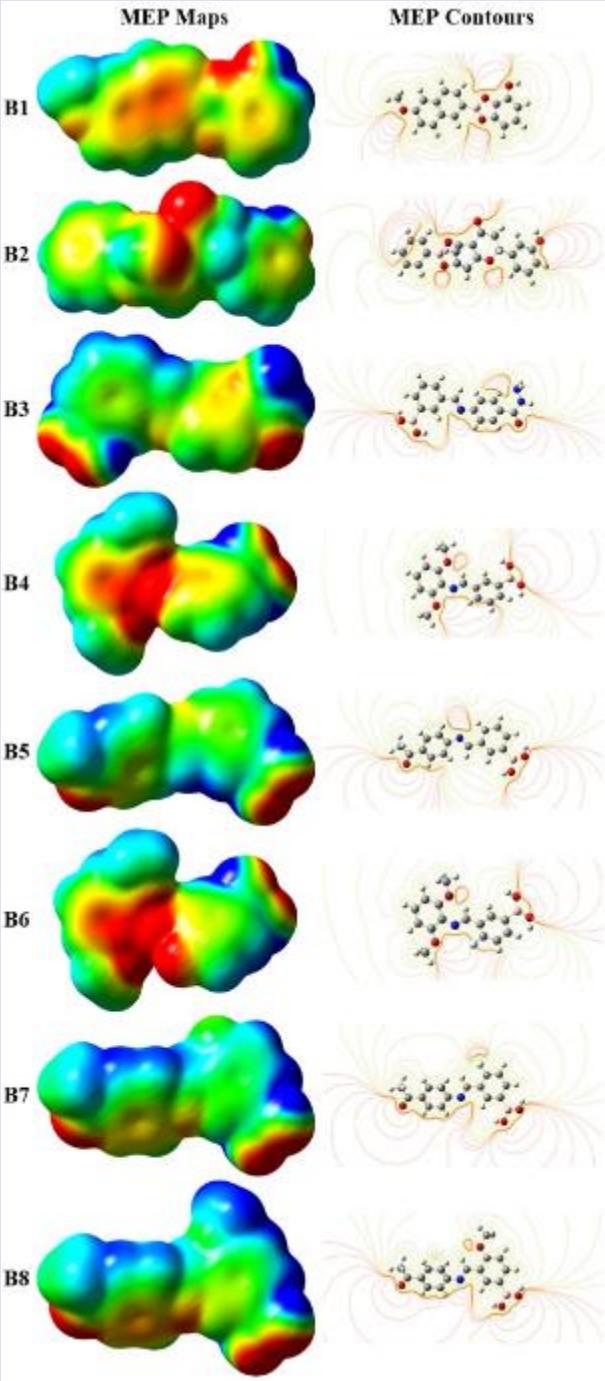

Fig. 5. MEP maps and MEP contours of B1-B8.

Especially, it can be seen easily that π electrons play an essential role in having this feature. MEP maps and contours show the reactive zones on the molecular surface. The reactivity of π electrons is seen easily from MEP maps of related compounds, too. Additionally, reactivity of heteroatoms which are oxygen, nitrogen etc. can be easily seen from MEP contours.

Molecular Docking Analysis

The best method to foresee the biological activity of chemicals is molecular docking calculations. In this study, biological reactivity of studied compounds are investigated against SARS-CoV-2. Especially, alpha and omicron variants are taken into consideration. For this aim, four proteins are selected which are 6NUS, 6VSB, 6WNP and 7QO7. The docking results are summurized and given in Table 2.

Table 2. Summarized docking results

Compounds	6NUS[a]	6VSB[a]	6WNP[a]	7QO7[a]
B1	D	ND	D	D
B2	D	ND	D	D
B3	D	ND	D	D
B4	D	ND	D	D
B5	D	ND	D	D
B6	D	ND	D	D
B7	D	ND	D	D
B8	D	ND	D	D

[a] D: Docked; ND: No Docked

Docking score (DS), van der Walls energy (E_{vdW}), Coulomb interaction energy (E_{Coul}) and total interaction energy (E_{Total}) are given in Table 3.

Table 3. The molecular docking results

Comp.	DS[a]	E_{vdW}[a]	E_{Coul}[a]	E_{Total}[a]
6WNP				
B1	-4.025	-18.607	-2.412	-21.019
B2	-4.459	-23.707	-4.969	-28.675
B3	-3.999	-18.383	-10.056	-28.440
B4	-3.459	-20.045	-4.633	-24.678
B5	-4.175	-19.363	-6.274	-25.637
B6	-3.208	-17.640	-6.718	-24.358
B7	-4.387	-19.878	-7.344	-27.222
B8	-3.961	-16.111	-10.001	-26.112
6NUS				
B1	-4.970	-25.791	-2.226	-28.017
B2	-4.061	-30.073	-3.423	-33.496
B3	-5.026	-32.006	-4.806	-36.812
B4	-4.589	-30.838	-5.315	-36.153
B5	-5.814	-24.050	-9.323	-33.373
B6	-4.566	-28.114	-7.157	-35.271
B7	-4.338	-31.376	-2.472	-33.847
B8	-5.581	-31.039	-6.366	-37.405
7QO7				
B1	-6.490	-35.881	-1.848	-37.729
B2	-6.389	-43.435	-2.425	-45.860
B3	-6.092	-39.063	-1.179	-40.242
B4	-7.258	-31.499	-10.517	-42.016
B5	-7.018	-37.780	-2.730	-40.509
B6	-5.399	-31.124	-3.888	-35.012
B7	-7.352	-39.375	-1.904	-41.278
B8	-6.657	-36.210	-4.512	-40.722

[a] in kcal/mol

According to obtained results, studied boron compounds are more effective against omicron variant than alpha variant of SARS-CoV-2.

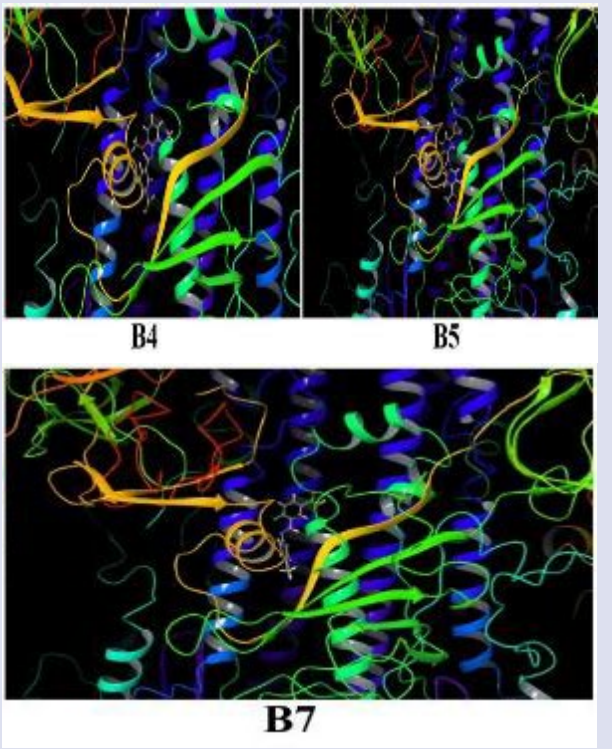

Fig. 6. Docking structure of B4, B5 and B7 compounds

Especially, docking score in alpha variant are so small. However, this case is not same in omicron variant. The docking score is the first parameter due to the fact that it shows the key-lock harmony between inhibitor candidate and target protein. In obtained results, the docking score of B4, B5 and B7 is better than the other in omicron variant of SARS-CoV-2. Their interaction energies are better, too. The complex structure of B4, B5 and B7 with 7QO7 are represented in Fig. 6. Additionally, interaction maps of them are represented in Fig. 7.

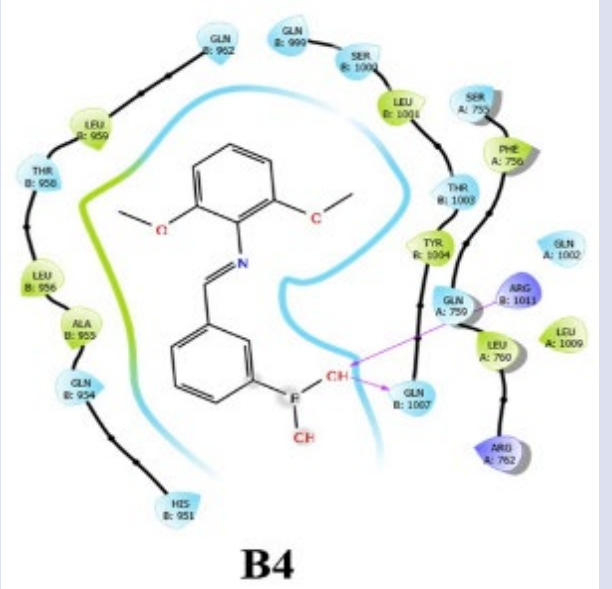

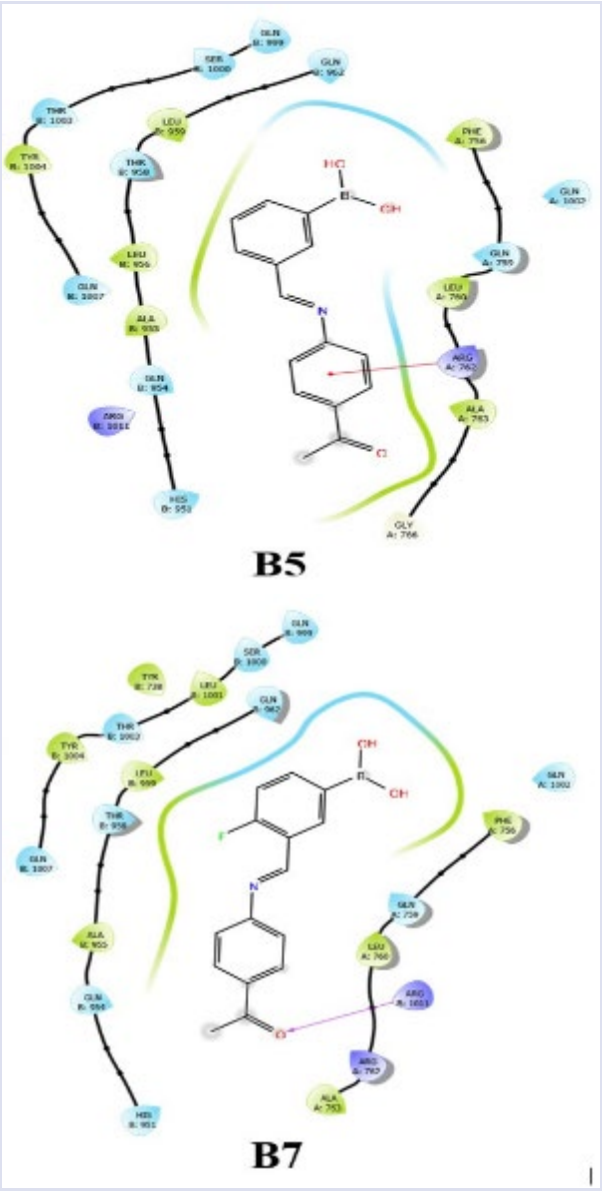

Fig. 7. Interaction maps of B4, B5 and B7 with spike glycoprotein of omicron variant of SARS-CoV-2.

As a result, B4, B5 and B7 compounds can be effective against omicron variant of SARS-CoV-2. The further analyses should be done in detail to today's problem to fight COVID19

ADME Analysis

ADME is an abbreviation for "absorption, distribution, metabolism and excretion" in pharmacokinetics and pharmacology and describes the localization of a pharmaceutical compound within an organism. The whole criterias affect drug levels and drug exposure kinetics to tissues and so affect the performance and pharmacological activity of the drug candidates. QikProp descriptors of studied boron containing compounds are calculated using Maestro 12.8 software to determine the ADME properties. However atomic properties of boron is changed as any special atom to calculate the parameters. QikProp parameters are given in Table 4.

Table 4. Calculated QikProp parameters of studied boron compounds for ADME analyses

Parameters[a]	B1	B2	B3	B4	B5	B6	B7	B8	RV[b]
Stars	0	1	1	0	1	0	1	0	0-5
Amine	0	0	0	0	0	0	0	0	0-1
rtvFG	1	1	2	1	1	1	1	1	0-2
SASA	521.9	627.1	543.1	558.4	547.0	567.5	552.8	586.4	300.0-1000.0
FOSA	98.0	76.7	15.4	196.6	97.3	195.1	94.0	186.3	0.0-750.0
FISA	56.1	104.5	243.3	103.2	163.2	109.0	163.0	162.5	7.0-330.0
PISA	367.7	445.9	284.4	258.6	286.5	231.9	258.6	237.6	0.0-450.0
WPSA	0	0	0	0	0	31.5	37.2	0	0.0-175.0
donorHB	1	1	5	2	2	2	2	2	0.0-6.0
AccptHB	3	5	7.4	5.9	6.4	5.9	6.4	7.2	2.0-20.0
QPpolrz	32.0	40.7	28.0	29.2	28.9	29.9	29.1	30.9	13.0-70.0
QPPCaco	2907.5	1011.8	48.9	1041.0	280.7	916.4	282.0	284.9	<25 poor >500 great
QPlogBB	-0.1	-0.5	-2.2	-0.9	-1.4	-0.9	-1.3	-1.5	-3.0- 1.2
QPPMDCK	1568.1	501.0	19.0	516.7	125.3	669.6	201.4	127.3	<25 poor >500 great
QPlogKp	-1.1	-1.8	-4.2	-1.7	-2.9	-1.9	-2.9	-2.9	-8.0- -1.0
metab	2	4	0	2	0	2	0	1	1-8
QPlogKhsa	0.4	0.5	-0.7	-0.3	-0.4	-0.2	-0.3	-0.4	-1.5- 1.5
Percent Human-Oral Absorption	100	100	58.1	94.2	79.7	94.4	80.8	80.5	>80% is high <25% is poor
PSA	47.6	75.1	121.2	65.9	85.4	68.5	85.3	91.5	7.0- 200.0
RuleOfFive	0	0	0	0	0	0	0	0	Max is 4
RuleOfThree	0	1	0	0	0	0	0	0	Max is 3

[a] Stars: Number of property or descriptor values that fall outside the 95% range of similar values for known drugs; Amine: Number of non-conjugated amine groups; rtvFG: Number of reactive functional groups; SASA: Total solvent accessible surface area; FOSA: Hydrophobic component of the SASA; FISA: Hydrophilic component of the SASA; PISA: π (carbon and attached hydrogen) component of the SASA; WPSA: Weakly polar component of the SASA; donorHB: Estimated number of hydrogen bonds that would be donated; AccptHB: Estimated number of hydrogen bonds that would be accepted; QPpolrz: Predicted polarizability in cubic angstroms; QPPCaco: Predicted apparent Caco-2 cell permeability in nm/sec; QPlogBB: Predicted brain/blood partition coefficient; QPPMDCK: Predicted apparent MDCK cell permeability in nm/sec; QPlogKp: Predicted skin permeability; metab: Number of likely metabolic reactions; QPlogKhsa: Prediction of binding to human serum albumin; PercentHuman-OralAbsorption: Predicted human oral absorption on 0 to 100% scale; PSA: Van der Waals surface area of polar nitrogen and oxygen atoms; RuleOfFive: Number of violations of Lipinski's rule of five; RuleOfThree: Number of violations of Jorgensen's rule of three.
[b] RV: Recommended Value

According to Table 4, calculated parameters are in the good agreement with the recommended value for each parameters. These parameters reveal the druglikeness properties of the investigated compounds. Especially, these compounds have skin permeability, MDCK cell permeability, Caco-2 cell permeability, brain/blood permeability. Additionally, some compounds can be taken part in metabolic reactions which it is undesirable. In such cases, the dose of the drugs taken into the body should be adjusted. According to all results in Section 3.5 and 3.6, **B5 and B7** is the most significant drug candidates for the SARS-CoV-2. However, p450 metabolism analyzes are required for a clearer prediction and the affinities of the compounds (B4, B5 and B7) against CYP enzymes should be investigated.

p450 Analyses

p450 metabolism analysis is so critical for the drug desing processes. It is vital to investigate the interaction of the designed drugs with CYP enzymes, which are cytochrome p450 enzymes.

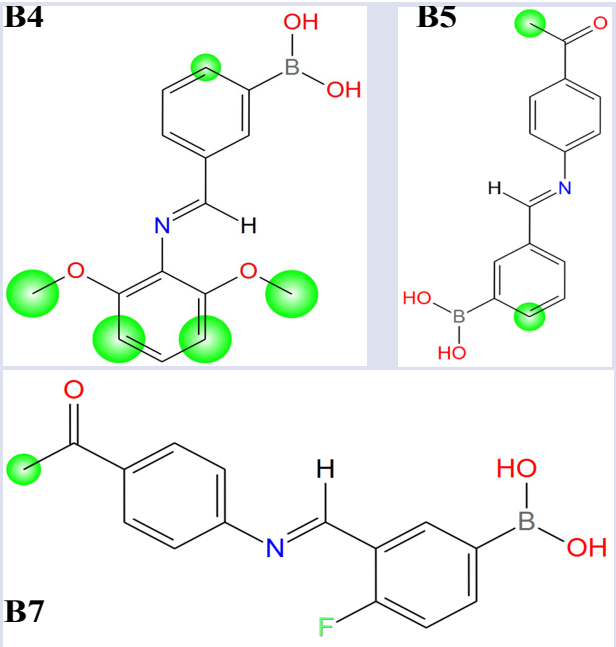

Fig. 8. The overall SOM score of B4, B5 and B7

CYP enzymes have been identified in animals, plants, fungi, protists, bacteria, and archaea, as well as in viruses. However, it is known that it is not found in some living things, although it is rare. It is known that there are more than 300000 CYP proteins. CYP enzymes are essential for the metabolism of many medications. Three CYP enzymes are so important and the most known ones which are CYP2C9, CYP2D6 and CYP3A4 and they metabolize ninty percent of drugs. p450 metabolism prediction can be done by in silico techniques. In this study, p450 metabolism analyses of synthesized boron compound are performed against CYP2C9. It is seen that each compound inhibits the CYP2C9. Overall SOM score of B4, B5 and B7 compounds against the CYP2C9 is represented in Fig. 8. The docking results of B4, B5 and B7 compounds are given in Table 5.

Table 5. The docking results against CYP2C9

Compound	DS[a]	E_{vdW}[a]	E_{Coul}[a]	E_{Total}[a]
B4	-6.242	-29.436	-7.957	-37.393
B4	-6.831	-24.896	-8.228	-33.124
B4	-6.772	-30.584	-8.036	-38.619
B5	-6.748	-40.903	-0.600	-41.502
B5	-5.955	-25.085	-5.737	-30.822
B7	-6.154	-35.734	-6.130	-41.864

[a] in kcal/mol

According to Fig. 8, the results are displayed as green circles, in which the radius is proportional to the score. Larger scores mean higher reactivity. The most reactive compound is found as B4 while B7 is the least reactive one. These results are agreement with docking results given in Table 5. While more than one binding pattern of the B4-labeled compound to CYP2C9 is determined, this value is two in B5 and one in B7. While the strongest key-lock compatibility is observed in B4, this value of B7 is in the middle level among the results. The docking structure of B7 with CYP2C9 is represented in Fig. 9.

Fig. 9. The complex structure between B7 and CYP2C9.

Conclusion

Eight boron compounds were investigated. Firstly, these compounds were fully optimized M06-2X/6-311G(d) level in water. IR spectrum of them were calculated to characterization of these structure. Electronic properties of studied compounds were investigated contour plots of frontier molecular orbitals, MEP maps and MEP contours. Especially active atoms and zones on the structure were determined in detail. Biological activity of these compounds were examined against SARS-CoV-2. Alpha variant and omicron variant were taken into consideration. Four proteins were selected which are 6NUS, 6VSB, 6WNP and 7QO7. The 7QO7 protein belongs to the omicron variant, while the others belong to the alpha variant. The results obtained show that the investigated compounds did not exhibit the desired effect against the alpha variant, but were highly effective against the omicron variant. In particular, B4, B5 and B7 compounds were found to be highly effective against the omicron variant. ADME properties and p450 analyses of related compounds are performed. As a result, B7 is found as the best drug candidate against Omicron variant of SARS-CoV-2.

Acknowledgment

This work is supported by the Scientific Research Project Fund of Sivas Cumhuriyet University under the project numbers RGD-020. This research was made possible by TUBITAK ULAKBIM, High Performance, and Grid Computing Center (TR-Grid e-Infrastructure).

Conflicts of interest

There are no conflicts of interest in this work.

References

[1] Singhal T., A review of coronavirus disease-2019 (COVID-19), *Indian J. Pediatr*, 87(4) (2020) 281–286.

[2] Ataseven H., Sayin K., Tüzün B., Gedikli M.A., Could boron compounds be effective against SARS-CoV-2?, *Bratislava Medical Journal*, 122(10) (2021) 753-758.

[3] Tüzün B., Nasibova T., Garaev E., Sayin K., Ataseven H., Could Peganum harmala be effective in the treatment of COVID-19?, *Bratislava Medical Journal*, 122(9) (2021) 670-679.

[4] Gokalp F., Sayin K., The highly protective natural medical agents against COVID-19, *Bratislava Medical Journal* 122(9) (2021) 631-635.

[5] Cetiner E., Sayin K., Tüzün B., Ataseven H., Could boron-containing compounds (BCCs) be effective against SARS-CoV-2 as anti-viral agent?, *Bratislava Medical Journal*, 122(4) (2021) 263-269.

[6] Aktaş A., Tüzün B., Aslan R., Sayin K., Ataseven H., New anti-viral drugs for the treatment of COVID-19 instead of favipiravir, *Journal of Biomolecular Structure and Dynamics*, 39(18) (2021) 7263-7273.

[7] Enhancing response to Omicron SARS-CoV-2 variant: Technical brief and priority actions for Member States. World Health Organization: Headquarters, Geneve, Switzerland, Update #6: 21 January 2022,

https://www.who.int/publications/m/item/enhancing-readiness-for-omicron-(b.1.1.529)-technical-brief-and-priority-actions-for-member-states.

[8] Pasa S., Aydın S., Kalaycı S., Boğa M., Atlan M., Bingul M., Şahin F., Temel H., The synthesis of boronic-imine structured compounds and identification of their anticancer, antimicrobial and antioxidant activities, *Journal of Pharmaceutical Analysis*, 6 (2016) 39-48.

[9] Gömeç M., Yulak F., Gezegen H., Özkaraca M., Sayin K., Ataseven H., Synthesis of diaryl urea derivatives and evaluation of their antiproliferative activities in colon adenocarcinoma, *Journal of Molecular Structure*, 1254 (2022) 132318.

[10] Vanitha U., Elancheran R., Manikandan V., Kabilan S., Krishnasamy K., Design, synthesis, characterization, molecular docking and computational studies of 3-phenyl-2-thioxoimidazolidin-4-one derivatives, *Journal of Molecular Structure*, 1246 (2021) 131212.

[11] Govindarasu M., Ganeshan S, Ansari M.A., Alomary M.N., Alyahya S., Alghamdi S., Almehmadi M., Rajakumar G., Thiruvengadam M., Vaiyapuri M., In silico modeling and molecular docking insights of kaempferitrin for colon cancer-related molecular targets, *Journal of Saudi Chemical Society*, 25(9) (2021) 101319.

[12] GaussView, Version 6.1, Roy Dennington, Todd A. Keith, and John M. Millam, Semichem Inc., Shawnee Mission, KS, 2016.

[13] Gaussian 16, Revision B.01, Frisch M.J., Trucks G.W., Schlegel H.B., Scuseria G.E., Robb M.A., Cheeseman J.R., Scalmani G., Barone V., Petersson G.A., Nakatsuji H., Li X., Caricato M., Marenich A.V., Bloino J., Janesko B.G., Gomperts R., Mennucci B., Hratchian H.P., Ortiz J.V., Izmaylov A.F., Sonnenberg J.L., Williams-Young D., Ding F., Lipparini F., Egidi F., Goings J., Peng B., Petrone A., Henderson T., Ranasinghe D., Zakrzewski V.G., Gao J., Rega N., Zheng G., Liang W., Hada M., Ehara M., Toyota K., Fukuda R., Hasegawa J., Ishida M., Nakajima T., Honda Y., Kitao O., Nakai H., Vreven T., Throssell K., Montgomery J.A. Jr., Peralta J.E., Ogliaro F., Bearpark M.J., Heyd J.J., Brothers E.N., Kudin K.N., Staroverov V.N., Keith T.A., Kobayashi R., Normand J., Raghavachari K., Rendell A.P., Burant J.C., Iyengar S.S., Tomasi J., Cossi M., Millam J.M., Klene M., Adamo C., Cammi R., Ochterski J.W., Martin R.L., Morokuma K., Farkas O., Foresman J.B., Fox, Gaussian, Inc., Wallingford CT, 2016.

[14] Perkin Elmer, ChemBioDraw Ultra Version (13.0.0.3015), 2012.

[15] Kirchdoerfer R.N., Ward A.B, Structure of the SARS-CoV nsp12 polymerase bound to nsp7 and nsp8 co-factors, *Nat. Commun.*, 10 (2019) 2342.

[16] Wrapp D., Wang N., Corbett K.S., Goldsmith J.A., Hsieh C.L., Abiona O., Graham B.S., McLellan J.S., Cryo-EM structure of the 2019-nCoV spike in the prefusion conformation, *Science*, 367 (2020) 1260-1263.

[17] Anson B., Mesecar A., X-ray Structure of SARS-CoV-2 main protease bound to Boceprevir at 1.45 A. https://www.rcsb.org/structure/6WNP.

[18] Ni D., Lau K., Turelli P., Raclot C., Beckert B., Nazarov S., Pojer F., Myasnikov A., Stahlberg H., Trono D., Structural analysis of the Spike of the Omicron SARS-COV-2 variant by cryo-EM and implications for immune evasion, *Biorxiv.*, (2021).

[19] Release S. 3: Maestro, Schrödinger, LLC: New York, NY, USA, 2019.

[20] Schrödinger L. Schrödinger Release 2019-4: LigPrep. New York, NY: Schrödinger, LLC. 2019.

[21] Friesner R.A., Murphy R.B., Repasky M.P., Frye L.L., Greenwood J.R., Halgren T.A., Sanschagrin P.C., Mainz D.T., Extra precision glide: Docking and scoring incorporating a model of hydrophobic enclosure for protein− ligand complexes, *J. Med. Chem.*, 49(21) (2006) 6177–6196.

[22] Friesner R.A., Banks J.L., Murphy R.B., Halgren T.A., Klicic J.J., Mainz D.T., Repasky M.P., Knoll E.H., Shelley M., Perry J.K., Shaw D.E., Francis P., Shenkin P.S., Glide: a new approach for rapid, accurate docking and scoring. Method and assessment of docking accuracy, *J. Med. Chem.*, 47(7) (2004) 1739–1749.

Cumhuriyet Sci. J., 44(1) (2023) 81-89
DOI: https://doi.org/10.17776/csj.1221864

Cumhuriyet Science Journal

| csj.cumhuriyet.edu.tr | Founded: 2002 ISSN: 2587-2680 e-ISSN: 2587-246X Publisher: Sivas Cumhuriyet University

Novel Bis-1,3,4-Thiadiazoles Derivatives: Synthesis, Spectroscopic Characterization, DFT Calculations and Evaluation of their Antimicrobial and Antioxidant Activities

Şukriye Çakmak [1,a,*], Muhammet Serdar Çavuş [2,b]

[1]*Department of Medical Services and Techniques, Vocational School of Health Services, Sinop University, Sinop, Türkiye.*
[2]*Biomedical Engineering Department, Faculty of Engineering and Architecture, Kastamonu University, Kastamonu, Türkiye.*
**Corresponding author*

Research Article

History
Received: 20/12/2022
Accepted: 01/03/2023

ABSTRACT

Two new, bis-1,3,4-thiadiazoles derivatives (**I** and **II**), were prepared by cyclization reaction of oxalic acid with *N*-alkyl/allyl thiosemicarbazides and phosphorous oxychloride ($POCl_3$). Then the newly prepared products screened for their antimicrobial and antioxidant activities. The biological activity results shown that tested compounds exhibited effective antibacterial activity against six different bacteria. However, the compound **II** demonstrated greater $ABTS^{\cdot+}$ scavenging ability. The characterization of the synthesized molecules was done by FT-IR, ^1H NMR, ^{13}C NMR spectroscopic methods and elemental analysis. Moreover, the experimental FT-IR and NMR spectra of the molecules were compared with the results calculated at the cc-pvtz, 6-311g(2d,2p), and 6-311++g(2d,2p) levels of theory. The effect of substituted groups on the spectral and electronic properties of the compounds was investigated. NCI and QTAIM analyses were performed to examine the effects of allyl group and intramolecular interactions on σ and π bonds. How the N-H bonds of the substituted groups affect the bond degrees was investigated using Fuzzy, Laplacian and Mayer approaches, and the relationship of the data with the antioxidant properties of the compounds was examined. In addition, the relationship between bond stretching force constant and intrinsic bond strength index, electron density, and delocalization index for some bonds was revealed.

Keywords: Bis-thiadiazoles, Biological activity, DFT, IBSI, Force constant (FC).

[a] *scakmak@sinop.edu.tr* *https://orcid.org/0000-0002-2221-0098*
[b] *mserdarcavus@kastamonu.edu.tr* *https://orcid.org/0000-0002-3721-0883*

Introduction

Thiadiazoles are five-membered heterocyclic compounds consisting of two nitrogen and one sulfur atom in the ring. Compounds having thiadiazole moiety possess medicinal characteristics and unique biological activity due to their strong aromaticity. When different functional groups that interact with biological receptors are added to this ring, moiety compounds with extraordinary properties are obtained. Thiadiazoles and their derivatives have various biological and medicinal characteristics such as antimicrobial [1], anticancer [2], antibacterial, antiviral [3], antifungal [4] antitubercular [5], antihypertensive [6], anticonvulsant [7], diuretic [8], antioxidant [9] properties. They are also used for various applications such as pesticides, herbicides, and insecticides in the agriculture field [10].

Accordingly, we have synthesized two new bis-1,3,4-thiadiazoles derivatives and investigated their antimicrobial and antioxidant characteristics. *In vitro* antimicrobial activity tests on the synthesized two new compounds were performed against six different bacteria and two fungi using the microdilution method (MIC). The results of the biological activity analyses reveal that these synthesized two new compounds show effective antibacterial activity against *B. subtilis*, *S. aureus*, *E. faecalis*, *E. coli*, *K. pneumoniae*, and *P. aeruginosa*. Besides, the antioxidant activities of these molecules were explored by employing ABTS radical scavenging method.

In the theoretical approaches, DFT calculations of the compounds were made first and the data were compared with the experimental results. Subsequently, the effects of intramolecular interactions on IR and NMR spectra were revealed. Quantum theory of the atom in the molecule (QTAIM) [11, 12] and non-covalent interaction (NCI) [13] analyses were performed to examine the relationship between intramolecular interactions, bond orders, and spectral data, depending on the electron charge distribution on the bonds. Furthermore, the relationship between properties such as bond length, Laplacian bond order (LBO), Fuzzy bond order (FBO), Mayer bond order (MBO) and bond stretching force constant (FC), Intrinsic bond strength index (IBSI), electron density (Rho) at the bond critical point (BCP), and DI were analyzed.

Materials and Methods

Instrumentation

All the reagents and solvents were acquired from Sigma Aldrich or Merck Chemical Company and were used without further purification. The melting points were

determined using a Stuart SMP30 apparatus. Eurovector EA3000 elemental analyser was used to define elemental analysis. Infrared spectra were recorded with a Bruker Alpha Fourier transform FT-IR spectrometer. ^{1}H and ^{13}C-NMR spectra were registered using a Bruker Avance DPX-400 spectrophotometer (400 and 101 MHz) in DMSO-d_6.

General Synthesis Procedure for Novel bis- 1,3,4-thiadiazoles (I and II)

The mixture of oxalic acid (n mol) and N-alkyl/allyl thiosemicarbazide (2n mol) was chilled in a refrigerator and phosphorous oxychloride (3n mol) was added drop-wise by stirring. Then, refluxing was continued 90 °C for 4 h. After completion of the reaction, the mixture was cooled to room temperature, poured into ice-cold water with stirring, and then neutralized with ammonia. The final product was filtered, washed with water, and crystallized in a suitable solvent. These novel thiadiazoles were prepared according to indicated the prodecure [14] in Scheme 1.

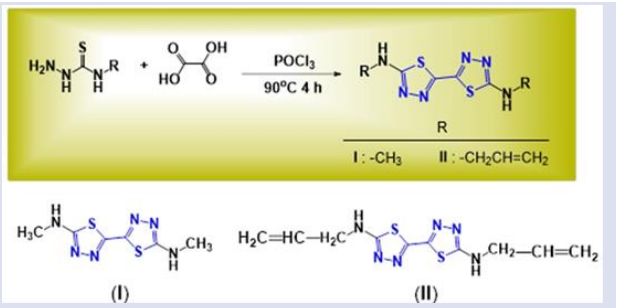

Scheme 1. Synthetic route for new bis- 1,3,4-thiadiazoles compounds.

Detection of Antimicrobial Activity

The antimicrobial activities were tested against the following eight microorganisms including Gram-staining-positive (*B. subtilis* ATCC 6633; *S. aureus* ATCC 25923; *E. faecalis* ATCC 29212), Gram-staining-negative (*E. coli* ATCC 25922; *K. pneumoniae* ATCC 70060; *P. aeruginosa* ATCC 27853) bacteria and fungi (*A. niger* ATCC 16404; *C. albicans* ATCC 1023). The antimicrobial screening activity was determined in 96-well microplates by microdilution method (MIC) [15]. Synthesized compounds were dissolved in dimethyl sulfoxide (DMSO) at the appropriate concentration. The cultures were obtained from nutrient broth for all the bacterial strains after 24 h of incubation at 37 °C. Fungi were maintained in nutrient broth after incubation for 24 h at 28 °C. Bacterial and fungi cells were homogenized in nutrient broth. The turbidity of bacterial and fungi suspensions was set at a concentration of approximately 10^6 cells/ml. Only inoculated broth was used as controls. 100 mL suspension of each microorganism and 100 mL suspension of compound tested were added into the wells. The microplate with no growth of microorganism was recorded to represent the MIC enounced in µg/mL.

Measurements of Antioxidant Activity

$ABTS^{\cdot+}$ radical scavenging activity of the samples were measured spectrophotometrically at 734 nm on the results of the oxidation of 2,2-azinobis-(3-ethylbenzothiozine-6-sulfonic acid) ammonium salt ($ABTS^{2-}$) with of peroxydisulphate based on form $ABTS^{\cdot+}$ radical and butylated hydroxyanisole (BHA), *tert*-butylhydroquinone (TBHQ) and α-tocopherol standards were used [16, 17]. IC_{50} (µg/mL) values of the results were calculated.

Theoretical Processes

The ground state optimized geometries of the compounds and the calculations of the electronic parameters of these geometries were performed using the Gaussian 09 software package [18]. Becke three-parameter hybrid functional combined with Lee-Yang-Parr correlation functional (B3LYP) was used in the Kohn-Sham DFT [19, 20] calculations. Calculations were performed at the cc-pvtz, 6-311g(2d,2p), and 6-311++g(2d,2p) levels of the theory without any geometry restrictions. The optimized geometries with minimum energy correspond to the actual minimum points on the potential energy surface, and no imaginary frequencies were observed in the calculations.

Frontier molecular orbital (FMO) energy eigenvalues and chemical reactivity parameters such as HOMO-LUMO energy gap, chemical hardness, electronegativity, electrophilic index depending on these eigenvalues were also calculated in the gas phase using the aforementioned basis sets.

IR calculations were performed in the gas phase for all three basis sets mentioned. NMR calculations were performed with the Gauge-Including Atomic Orbital (GIAO) approach, using conductor-like polarizable continuum model (CPCM) in the DMSO phase in accordance with the experiment. The calculated TMS values of ^{1}H and ^{13}C NMR for cc-pvtz, 6-311g(2d,2p), and 6-311++g(2d,2p) basis sets are 31.7450 and 184.4735; 31.8181 and 183.8257; 31.8149 and 183.7737, respectively.

QTAIM analyses, NCIs, electron density distributions, FBO and LBO, and IBSI [21, 22] calculations of the certain bonds were performed using Multiwfn [23] software. Bond stretching force constant (FC) were calculated separately with the mentioned three basis sets using Forcegen [24] software.

Results and Discussion

Analytical Data

Table 1. Analytical data for the synthesized compounds.

Entry	Compound's Names	M. P. (°C)	Yields (%)	Colour	Calculated/Found C%	H%	N%
I	*N5,N5'*-dimethyl-[2,2'-bi(1,3,4-thiadiazole)]-5,5'-diamine	>320	72	Light Yellow	31.57/31.69	3.53/3.55	36.81/36.76
II	*N5,N5'*-diallyl-[2,2'-bi(1,3,4-thiadiazole)]-5,5'-diamine	230-232	83	Yellow	42.84/42.93	4.31/4.34	29.98/29.92

FT-IR Spectral Analysis

In the IR spectra data of the compounds, the corresponds to carboxylic acid (-COOH) absorption bands of the starting material were not observed at approximately 3500-2800 cm^{-1}. Furthermore, asymmetric and symmetric stretching absorption bands of the NH_2 group were not appeared around 3400–3150 cm^{-1}. For compounds I and II, the peaks of the -NH were showed at 3188 and 3189 cm^{-1}, the -C=N stretching frequencies of thiadiazole ring were observed at 1556 and 1576 cm^{-1}; the -C–N stretching frequencies were showed at 1158 and 1143 cm^{-1}; the -C–S signals of aryl ring were observed at 697 and 691 cm^{-1}, respectively as shown in Figure 1. These frequency values of the target compounds were nearly in accordance with the literature [25-27]. The IR stretching vibration frequencies of the compounds are summarized in Table 2.

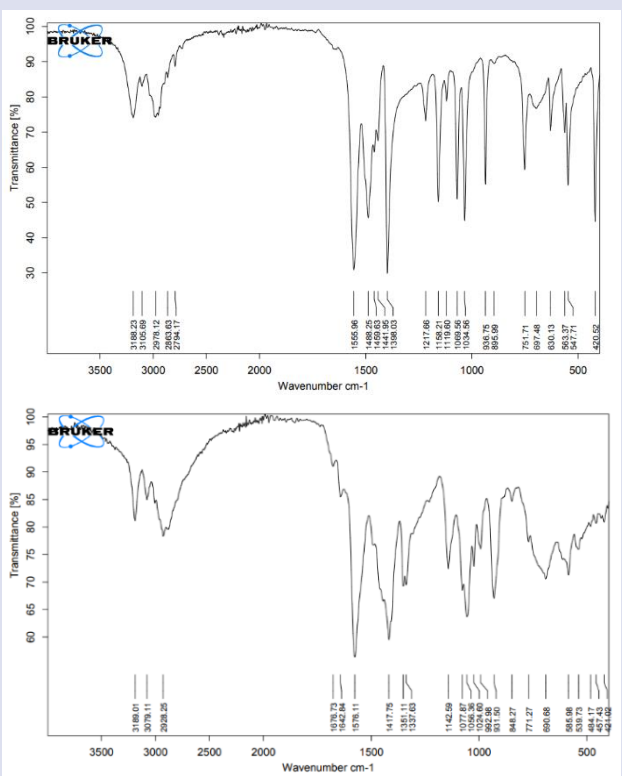

Figure 1. IR spectra of the compounds.

Table 2. Experimental and calculated IR values of the target compounds (cm^{-1}).

		Comp.	-NH	Aliph. CH	C=N	C-N	C-S
Exp.		I	3188	2978- 2863	1556	1158	697
		II	3189	2928-2827	1576	1143	691
Calculated	BS1	I	3647.7	3131.4-3021.9	1476.7	1560.4	731.8
		II	3621.9	3216.2-3007.8	1476.9	1537.2	730.5
	BS2	I	3641.3	3139.8-3026.1	1478.0	1558.1	727.5
		II	3621.1	3218.7-3014.3	1478.2	1534.0	725.9
	BS3	I	3649.1	3140.0-3032.5	1472.7	1553.5	728.1
		II	3621.8	3221.3-3020.2	1472.7	1526.9	726.8

BS1: B3lyp/cc-pvtz, BS2: B3lyp/6-311g(2d,2p), BS3: B3lyp/6 311++g(2d,2p).

H NMR Spectral Analysis

The ^1H NMR spectra of the compounds are given in Figure 2. For compound I, the proton signal of –NH was detected as a quartet at 8.13-8.09 ppm. The methoxy group (OCH_3) peak on the aryl ring was resonated as a doublet at 2.95-2.94 ppm. For compound II, the proton

signal of –NH was detected as a triplet at 8.37-8.35 ppm. The methylene (–N-CH_2) group peak on the aryl ring was observed as a triplet at 4.00-3.97 ppm. The methine (–C-CH=) group peak on the aryl ring was observed as a multiplet at 5.96-5.89 ppm. The methylene (–C=CH_2) group peak on the aryl ring was appeared as a multiplet at 5.30-5.14 ppm. DMSO-d_6 and water in DMSO (HOD, H_2O) signals are shown around at 2.00, 2.50 (quintet) and 3.30 ppm, respectively [28]. These observed are compatible with the literature [25-27]. The chemical shift values are presented in Table 3.

Table 3. ^{1}H NMR values of the compounds (δ, ppm, in nDMSO-d_6).

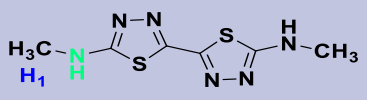

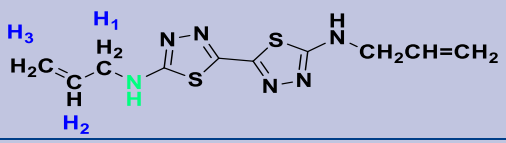

Exp.		Comp.	NH	H1	H2	H3
		I	8.13-8.09 (q)	2.95-2.94 (d)	-	-
		II	8.37-8.35 (t)	4.00-3.97 (t)	5.96-5.89 (m)	5.30-5.14 (m)
Calculated	BS1	I	5.17	3.17, 3.01	-	-
		II	4.75	4.76, 3.78	6.41	5.75, 5.58
	BS2	I	4.97	3.23-2.92	-	-
		II	4.60	4.73, 3.71	6.37	5.73, 5.58
	BS3	I	5.19	3.27-3.03	-	-
		II	4.76	4.69, 3.82	6.52	5.81, 5,64

d: doublet, t: triplet, q: quartet, m: multiplied.
BS1: B3lyp/cc-pvtz, BS2: B3lyp/6-311g(2d,2p), BS3: B3lyp/6-311++g(2d,2p).

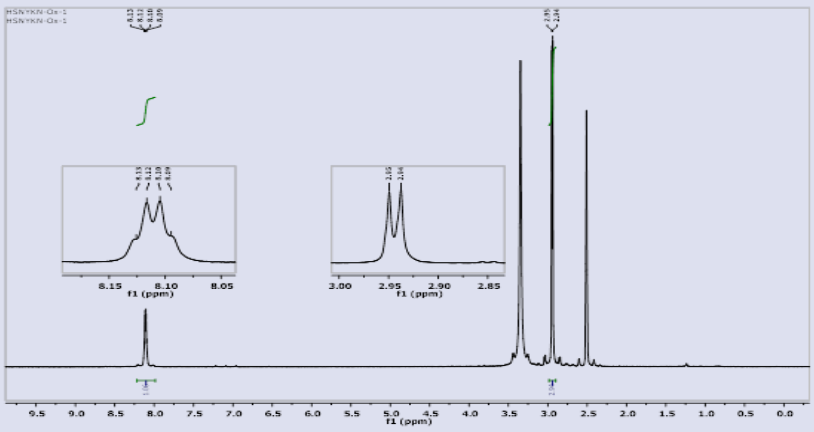

(I)

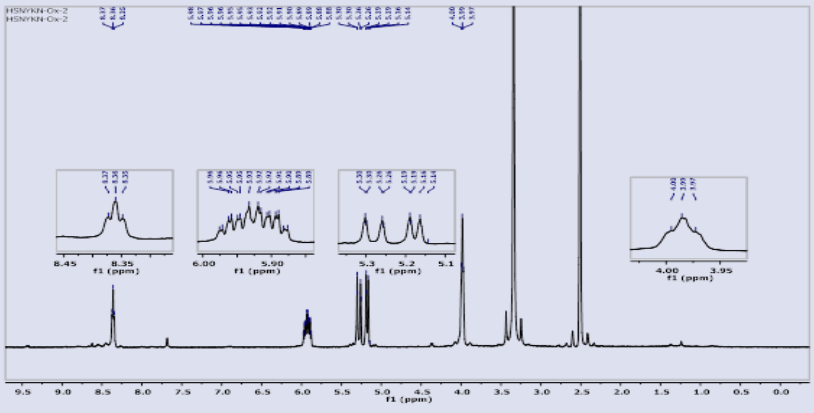

(II)

Figure 2. ^{1}H NMR spectra of compounds I and II.

^{13}C NMR Spectral Analysis

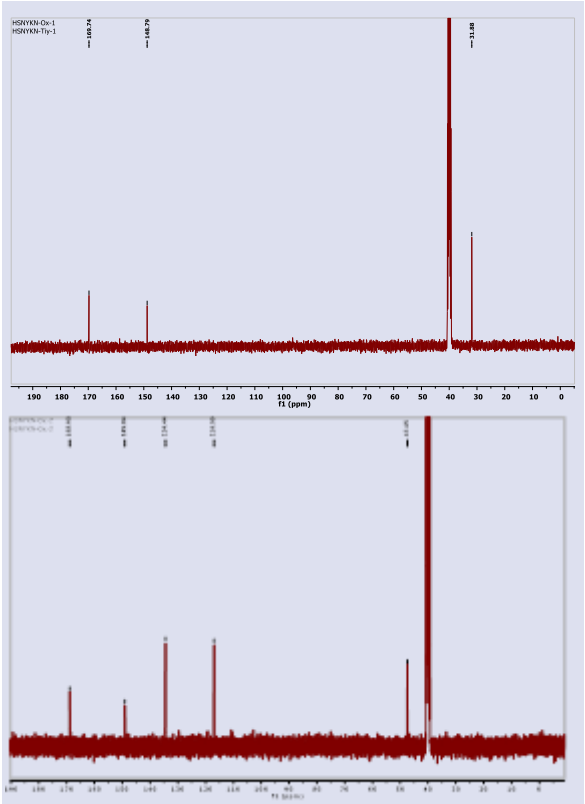

Figure 3. ^{13}C NMR spectra of compounds I and II.

The ^{13}C NMR spectra of the compounds I and II recorded in DMSO-d_6 showed 3 and 5 different carbon atoms resonances respectively, in good agreement with the proposed structure as shown in Figure 3. The chemical shift results are given in Table 4.

In compound I, the carbon signals (C1 and C2) of thiadiazole ring were detected at 148.79 and 169.74 ppm, respectively. The C2 carbon (C2-NH) is shifted down-field (high values, δ) at 169.74 ppm due to the presence of amino group (NH). The carbon atom of methyl (N-CH_3) group on the aryl ring was observed at 31.88 ppm.

For compound II, the carbon signals (C1 and C2) of thiadiazole ring were detected at 149.04 and 168.90 ppm, respectively. The C2 carbon (C1-NH) is shifted down-field (high values, δ) at 168.90 ppm due to the presence of amino group (NH). The carbon atom of methylene (N-CH_2) group on the aryl ring was observed at 47.45 ppm. The carbon atom of methine group (-CH=) was detected at 134.44 ppm. The methylene (–C=CH_2) carbon atom was resonated at 116.99 ppm. These spectroscopic data are in agreement with values previously reported in the literature [25].

Table 4. ^{13}C NMR values of the title compounds (δ, ppm, in DMSO-d_6)

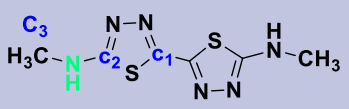

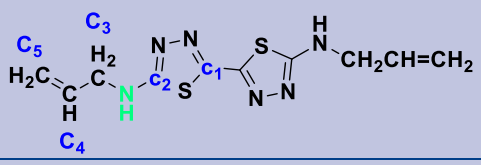

Exp.		Comp.	C_1	C_2	C_3	C_4	C_5
		I	148.79	169.74	31.88	-	-
		II	149.04	168.90	47.45	134.44	116.99
Calculated	BS1	I	158.99	175.84	32.62	-	-
		II	159.52	175.83	52.41	142.67	124.91
	BS2	I	157.97	175.55	32.58	-	-
		II	158.27	175.04	52.22	142.19	125.02
	BS3	I	160.08	177.47	32.67	-	-
		II	160.64	177.30	52.59	143.81	125.88

Antimicrobial Evaluation

Antimicrobial activity tests of the compounds were performed against six different bacteria and two fungi using the microdilution method (MIC). In this study based on serial dilution, MIC value for DMSO used as a control was found to be > 4000 µg/mL. When the effect of the one compound on bacteria is examined, it is seen that MIC values are 1000 µg/ml for *B.subtilis*, 1000 µg/ml for *S.aureus*, 500 µg/ml for *E. faecalis*, 500 µg/ml for *E. coli*, 1000 µg/ml for *K. pneumonia* and 1000 µg/ml for *P.aeruginosa*. Likewise, when the effect of the second compound on bacteria is examined, it is seen that MIC values are 250 µg/ml for *B.subtilis*, 500 µg/ml for *S.aureus*, 500 µg/ml for *E. faecalis*, 125 µg/ml for *E. coli*, 250 µg/ml for *K. pneumonia* and 1000 µg/ml for *P.aeruginosa*. Two new compounds synthesized did not show antifungal activity against *A. niger* and *C. albicans*. The MIC values were showed in Table 5.

Table 5. The minimum inhibition concentrations (MIC's) of the tested compounds.

Sample	Minimum inhibition concentration (µg/mL)							
	Gram-staining-positive			*Gram-staining-negative*			*Fungi*	
	B. subtilis	*S. aureus*	*E. faecalis*	*E. coli*	*K. pneumoniae*	*P. aeruginosa*	*A. niger*	*C. albicans*
Compound I	1000	500	500	500	1000	1000	-	-
Compound II	250	500	500	125	250	1000	-	-

Compound I: *N5,N5'*-dimethyl-[2,2'-bi(1,3,4-thiadiazole)]-5,5'-diamine;
Compound II: *N5,N5'*-diallyl-[2,2'-bi(1,3,4-thiadiazole)]-5,5'-diamine.

In 2009 Demirbaş et al. [29] conducted a similar study. They synthesized some new 1,3,4-thiadiazol-2-ylmethyl-1,2,4-triazole derivatives and found them to moderate activity against all the tested microorganisms (*E. coli*, *Y. pseudotuberculosis, P. aeruginosa, E. faecalis, S. aureus, B. cereus*) except *C. tropicalis* and *C. albicans*. Muglu et al. (2018) [14] synthesized new 1,3,4-thiadiazole compound and all the tested compounds showed good antimicrobial activities against *S. aureus*.

Antioxidant Evaluation

The antioxidant activities of the samples (I and II) were determined through the $ABTS^{\cdot+}$ scavenging activity test. In the present study, the $ABTS^{\cdot+}$ scavenging activity results of the tested compounds have shown in Table 6. The compound II (IC_{50} value of 68.93±0.79 µg/mL) was found to be the most active with comparison to compound I. It was even found to have activity close to the α-tocopherol standard. This effect may be owing to its role of the allyl group ($-CH_2CH=CH_2$) and activating the bithiadiazole rings [30]. In compound I, the methyl group ($-CH_3$) at position 2,2' of the bis- 1,3,4-thiadiazole nucleus is substituted whereas in II this has an allyl group. This indicates that the allyl group on the bithiadiazole rings enhances the activity. As result, the $ABTS^{\cdot+}$ scavenging activity was significantly ameliorated when the methyl groups were replaced by allyl groups. According to the IC_{50} values, the antioxidant capacities of the tested compounds were observed lower than that of the standards products. The $ABTS^{\cdot+}$ scavenging effect of the title compounds and standards decreased in the following order: TBHQ> BHA> α-tocopherol> II> I.

Table 6. IC_{50} values for the compounds.

Compounds	ABTS radical scavenging activity, IC_{50}^{*} (µg/mL)
Compound I	103.26±1.39
Compound II	68.93±0.79
BHA	33.91±2.09
TBHQ	32.09±2.02
α -tokoferol	64.86±3.28

Values are expressed as means (n = 3).
*IC_{50} = the concentration (µg /mL) exhibiting 50% inhibition of ABTS radical.

These results further demonstrated that the structure of the products and electronic effects of groups/substituents in the structures plays an important role of antioxidant activity [31]

Theoretical Calculations

Calculations reveal that the allyl group decreases the E_{HOMO} and E_{LUMO} energies of the compound while increasing the energy gap $\Delta E=E_{LUMO}-E_{HOMO}$ (Figure 4).

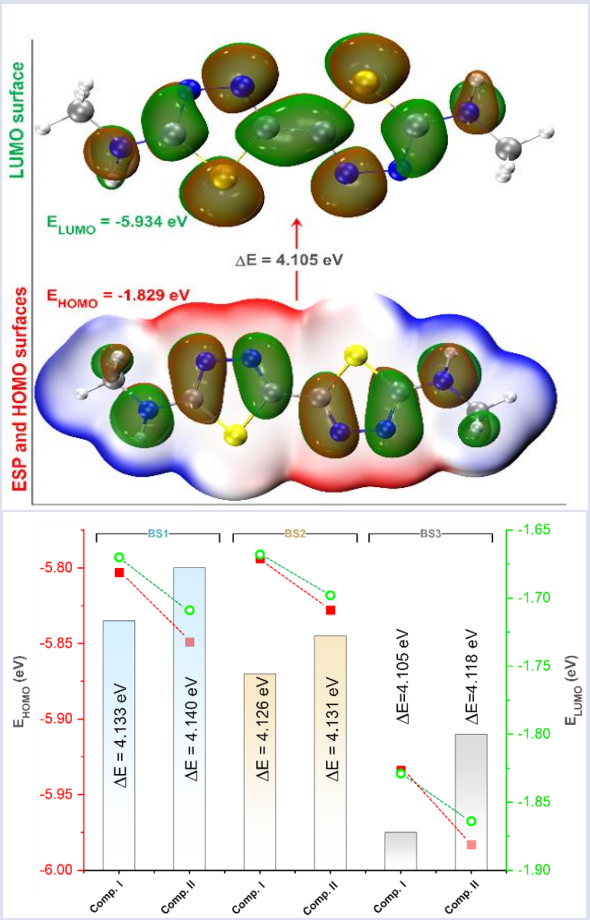

Figure 4. HOMO-ESP and LUMO surface of comp. I (BS3). The graph shows the HOMO-LUMO energy eigenvalues and Energy gap, ΔE, values of the compounds calculated by the basis sets BS1, BS2, and BS3.

In this context, we can say that compound I is more reactive. In parallel, the chemical hardness of compound I is lower.Contrary to these data, compound II was both more electronegative and had higher electrophilic index (Figure 5). However, there are many variables that dominate chemical reactions, and such static variables of the whole molecular structure can be partially helpful in predicting reaction mechanisms, but it can be misleading

to determine the reactivity of a compound in a particular reaction by considering these values. Certain reaction mechanisms are directly related to specific local regions of the compounds. For example, the antioxidant behavior of synthesized thiadiazole derivative compounds is closely dependent on both the conformative and electronic properties of the N–H bond. Although these are not the only parameters that determine the antioxidant reactions, an analysis of the static and dynamic parameters of the N–H bond is a useful method to predict the antioxidant property of the compound. Intramolecular interactions are among the factors that affect bond dissociation energy, and in polyatomic molecules, treating two atoms in a particular bond in isolation from other bonds and atoms can yield false results. In addition, bond strengths (or bond force constants) are strongly dependent on bond order of the bonded atoms and molecular conformation, which affects intramolecular interactions and thus charge distribution. NCI analysis shows that the non-covalent interaction of the allyl moiety with the thiadiazole region is stronger than that of the methyl group (Figure 6). This may result in compound II retaining its current conformation more than compound I. In addition, both the allyl group and intramolecular interactions affected the electronic data of the bonds in the reactive region in parallel in terms of IBSI, FC, Rho, and DI variables.

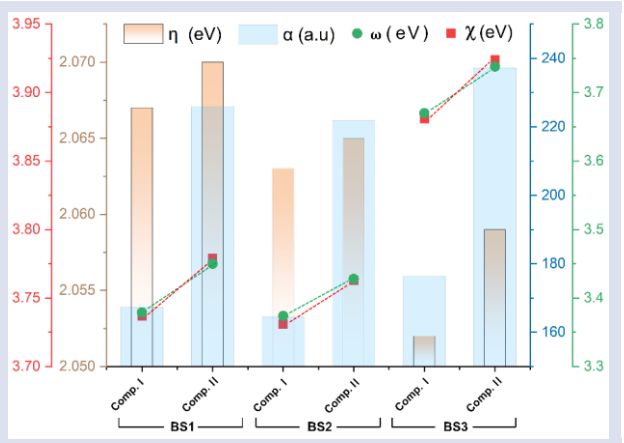

Figure 5. Chemical hardness (η), Electronegativity (χ), Polarizability (α), and Electrophilic index (**ω**) values of compounds, calculated by BS1, BS2, and BS3.

The decrease in the charge density at BCP of the N–H bond resulted in a weakening of the delocalization on the bond and thus an increase in the polarization coefficient of the N hybridization from 0.8351 to 0.8358 ($\sigma_{NH} = 0.8351(sp^{2.95})_N + 0.5501(s)_H$ for compound I, and $\sigma_{NH} = 0.8358(sp^{2.99})_N + 0.5490(s)_H$ for compound II, calculated by BS3 in the NBO analysis).

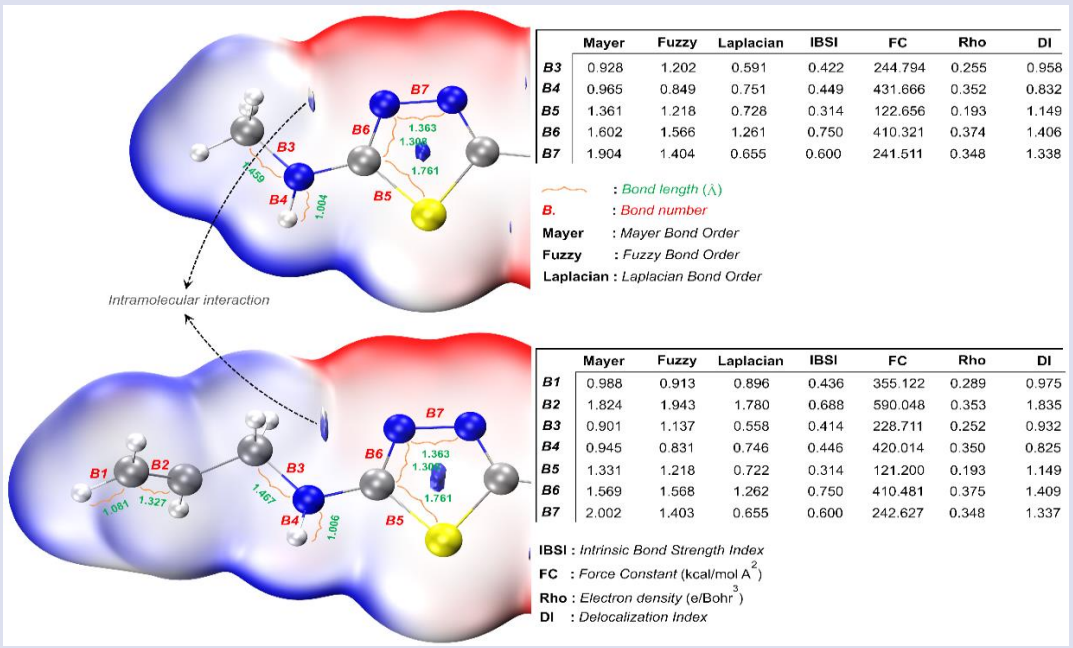

Figure 6. NCI, QTAIM, and some electronic data of the compounds I and II., calculated by 6-311++g(2d,2p).

Although the electronic variables considered for compound II were generally compatible with each other for the bonds of interest, the FBO and DI values did not change in parallel with the other variables, especially in the N–H and C–S bonds (Figure 7). FC values of sigma bonds B1, B3, and B5 were calculated lower than FC of electronegative atom groups and π bond (H_2C=CH–), but there is no linear relationship between FCs of σ and π bonds.

Although the prediction of antioxidant properties of the target compounds has difficulties due to the dynamic nature of the reactions, the bond stretching FC data reveal that compound II will exhibit higher antioxidant properties. It has been determined that the Allyl group weakens the N–H bond (the bond length also increased from 1.004 to 1.006 Å), that is, it causes bond strength reducing effects and therefore reduces the bond dissociation energy.

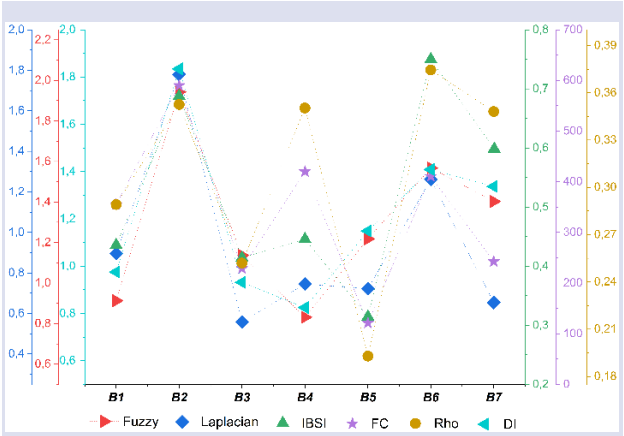

Figure 7. FBO, LBO, IBSI, FC, Rho, and DI values of the compound II, calculated by BS3.

Furthermore, it was observed that the electron density of the N–H bond, which plays an active role in antioxidant reactions, in BCP decreased (0.352 *e*/Bohr^3 for compound I, 0.350 *e*/Bohr^3 for compound II), and accordingly, both IBSI and bond stretching FC values also decreased (IBSI and FC values for compound I were calculated as 0.449 and 431,666 kcal/mol A^2, respectively; 0.446 and 420.014 kcal/mol A^2 for compound II). It can be said that this decrease in the bond strength and force constant of N–H bond results in easier breakage of the bond and therefore an increase in antioxidant properties. It is also a useful tool as the degree of a bond is usually related to the number of electrons forming the bond, and hence the bond strength; and overall, greater proportionality between bond strength and LBO emerged compared to the Fuzzy and Mayer approaches. MBO calculations increased the degree of =N–N= bond above 2 by adding the diffuse functions to the calculations. Especially adding the diffuse functions to the calculations may give wrong results in terms of MBO calculations. Moreover, there is a close relationship between IBSI and bond stretching FC, and it can be predicted that these parameters can be used to describe the chemical reactivity of compounds with predictable reactive sites.

Conclusions

In this study, new bis- 1,3,4-thiadiazole compounds were prepared in excellent yields of 72–83%. The compounds were characterized by IR, ^{1}H NMR, ^{13}C NMR and elemental analysis. In the next step, the compounds screened for their *in vitro* for their antimicrobial and antioxidant activities. The results of microbial activity studies show that the two synthesized compound exhibited effective antibacterial activity against *B. subtilis*, *S. aureus*, *E. faecalis*, *E. coli*, *K. pneumoniae*, and *P. aeruginosa*. Among the tested molecules, compound **II** exhibited greater ABTS$^{\cdot+}$ radical scavenging ability. This effect can be explained with in presence of the allyl group in the structures. Therefore, the new two synthesized compounds can be considered as bioactive substances for pharmacological and medical applications.

Although HOMO-LUMO energy eigenvalues of molecules and parameters such as energy gap, chemical hardness, and electronegativity obtained from these eigenvalues are useful, they are insufficient to explain the reaction mechanisms in which local regions are reactive because they are obtained from the molecular orbital approach. Calculations on selected bonds of compounds reveal that parameter such as LBO, IBSI, and bond stretching FC can be helpful tools in understanding antioxidant reaction mechanisms. An inverse relationship was observed between the IBSI and bond stretching FC values of the N–H bond and its reactivity in antioxidant reactions, that is, the IBSI and FC values of the N–H bond of the compound decreased while the antioxidant property increased. QTAIM analysis plays an especially important role in correlating the charge densities (Rho) of the bonds in the BCP and the DI data with the strength of the bond. By which atomic groups the bonds are formed affects the way these analyses are used. LBO calculations yielded more consistent results for bonds with electronegative atoms, and a close relationship was also observed between LBO, IBSI and FC.

Acknowledgements

The authors wish to thank Prof. Dr. Tevfik Özen (Chemistry Department, Ondokuz Mayis University) for helping during biological studies.

Conflicts of interest

The authors declare that they have no conflict of interest.

References

[1] Kaur P., Kaur R., Thiadiazole as an antimicrobial scaffold, *Ann Trop Med & Public Health*, 23 (2020) SP231542.

[2] Szeliga M., Thiadiazole derivatives as anticancer agents, *Pharmacological Reports*, 72 (2020) 1079-1100.

[3] Zhong X., Wang X., Chen L., Ruan X., Li Q., Zhang J., Chen Z., Xue W., Synthesis and biological activity of myricetin derivatives containing 1,3,4-thiadiazole scaffold, *Chem. Cent. J.,* 11 (2017) 106.

[4] Chudzik B., Bonio K., Dabrowski W., Pietrzak D., Niewiadomy A., Olender A., Pawlikowska-Pawlęga B., Gagoś M., Antifungal effects of a 1,3,4-thiadiazole derivative determined by cytochemical and vibrational spectroscopic studies, *PLoS One*, 14 (2019) 0222775.

[5] Gautam A., Tyagi M., An insight into antitubercular activity associated with 1,3,4-thiadiazoles, *Chemistry & Biology Interface*, 10 (2020) 140-148.

[6] Mayura K., Kirtee B., Biological potential of thiadiazole linked heterocycles: An overview, *Journal of Current Pharma Research*, 5 (2015)1578-1585.

[7] Sharma B., Verma A., Prajapati S., Sharma U K., Synthetic methods, chemistry, and the anticonvulsant activity of thiadiazoles, *Int. J Med. Chem*, 2013 (2013) 348948.

[8] Drapak I.V., Zimenkovsky B.S., Slabyy M.V., Holota S.M., Perekhoda L.O., Yaremkevych R.V., Nektegayev I.O., Synthesis and diuretic activity of novel 5-amino-1,3,4-

thiadiazole-2-thiol derivatives, *Biopolymers and Cell*, 37 (2021) 33-45.

[9] Parlak A.E., Koparır P., In vitro antioxidant properties of novel compound (1r, 2r) -1,2-bis- (5- (4-hydroxynaphthalen-1-ylazo) - [1,3,4] thiadiazol-2-yl) - ethane- 1,2-diole, *Cumhuriyet Sci. J*, 39-3 (2018) 658-667.

[10] Madkour H.F., Azab M.E., Aly A.F., Khamees M.S.M., Novel heterocycles based on 1,3,4-Thiadiazole scaffold as insecticides, *J. Environ. Sci.*, 40 (2017) 19-44.

[11] Bader R.F.W., A quantum theory of molecular structure and its applications, *Chem. Rev*., 91 (1991) 893-928.

[12] Bader R. F. W., Atoms in molecules, *Acc. Chem. Res*., 18 (1985) 9-15.

[13] Johnson E.R., Keinan S., Mori-Sánchez P., Contreras-García J., Cohen A. J., Yang W., Revealing noncovalent interactions, J. *Am. Chem. Soc*., 132 (2010) 6498-6506.

[14] Muğlu H., Şener N., Emsaed H. A. M., Özkınalı S., Özkan O.E., Gür M., Synthesis and characterization of 1, 3, 4-thiadiazole compounds derived from 4-phenoxybutyric acid for antimicrobial activities, *J. Mol. Struct*, 1174 (2018) 151-159.

[15] Schwalbe R., Steele-moore L., Goodwin A., Antimicrobial susceptibility testing protocols. 1nd ed. Boca Raton, (2007) 432.

[16] Dechayont B., Ruamdee P., Poonnaimuang S., Mokmued K., Chunthorng-Orn J., Antioxidant and antimicrobial activities of Pogostemon cablin (Blanco) Benth., *Journal of Botany*, 2017 (2017) 1-6.

[17] Re R., Pellegrini N., Proteggente A., Pannala A., Yang M.C., Rice-Evans C., Antioxidant activity applying an improved ABTS radical cation decolorization assay, *Free Radic Biol Med*, 26 (1999) 1231-1237.

[18] Frisch, M.J., Trucks, G.W., Schlegel, H.B., Scuseria, G.E., Robb, M.A., Cheeseman, J.R., Scalmani, G., Barone, V., Mennucci, B., Petersson, G.A., Nakatsuji, H., Caricato, M., Li, X., Hratchian, H.P., Izmaylov, A.F., Bloino, J., Zheng, G., Sonnenberg, J.L., Hada, M., Ehara, M., Toyota, K., Fukuda, R., Hasegawa, J., Ishida, M., Nakajima, T., Honda, Y., Kitao, O., Nakai, H., Vreven, T., Montgomery Jr., J.A., Peralta, J.E., Ogliaro, F., Bearpark, M., Heyd, J.J., Brothers, E., Kudin, K.N., Staroverov, V.N., Kobayashi, R., Normand, J., Raghavachari, K., Rendell, A., Burant, J.C., Iyengar, S.S., Tomasi, J., Cossi, M., Rega, N., Millam, J.M., Klene, M., Knox, J.E., Cross, J.B., Bakken, V., Adamo, C., Jaramillo, J., Gomperts, R., Stratmann, R.E., Yazyev, O., Austin, A.J., Cammi, R., Pomelli, C., Ochterski, J.W., Martin, R.L., Morokuma, K., Zakrzewski, V.G., Voth, G.A., Salvador, P., Dannenberg, J.J., Dapprich, S., Daniels, A.D., Farkas, O., Foresman, J.B., Ortiz, J.V., Cioslowski, J. and Fox, D.J. Gaussian 09, (2010).

[19] Kohn W., Sham L.J., Self-consistent equations including exchange and correlation effects, *Phys. Rev*., 140 (1965) A1133-A1138.

[20] Hohenberg P., Kohn W., Inhomogeneous electron gas, *Phys. Rev.,* 136 (1964) B864-B871.

[21] Klein J., Khartabil H., Boisson J. C., Contreras-Garciá J., Piquemal J. P., Hénon E., New way for probing bond strength, *J. Phys. Chem*. A., 124 (2020) 1850-1860.

[22] Lefebvre C., Rubez G., Khartabil H., Boisson J.C., Contreras-García J., Hénon E., Accurately extracting the signature of intermolecular interactions present in the NCI plot of the reduced density gradient versus electron density, *Phys. Chem. Chem. Phys*, 19 (2017) 17928-17936.

[23] Lu T., Chen F., Multiwfn: A multifunctional wavefunction analyzer, *J. Comput. Chem*., 33 (2012) 580-592.

[24] Nash A., Collier T., Birch H. L., de Leeuw N. H., ForceGen: atomic covalent bond value derivation for Gromacs, *J. Mol. Model*, 24 (2017).

[25] Muğlu H., Yakan H., Shouaib H. A., New 1, 3, 4-thiadiazoles based on thiophene-2-carboxylic acid: Synthesis, characterization, and antimicrobial activities, *J. Mol. Struct*., 1203 (2020) 127470.

[26] Popiołek Ł., Kosikowska U., Mazur L., Dobosz M., Malm A., Synthesis and antimicrobial evaluation of some novel 1, 2, 4-triazole and 1, 3, 4-thiadiazole derivatives, *Med. Chem. Res*., 22 (2013) 3134-3147.

[27] Zamani K., Faghihi K., Tofighi T., Shariatzadeh M. R., Synthesis and antimicrobial activity of some pyridyl and naphthyl substituted 1, 2, 4-triazole and 1, 3, 4-thiadiazole derivatives, *Turk. J. Chem*., 28 (2004)95-100.

[28] Williams D., Fleming I., RNA structure and NMR spectroscopy, Spectroscopic Methods in Organic Chemistry, McGraw-Hill, New York, (1996).

[29] Demirbas A., Sahin D., Demirbas N., Karaoglu S. A., Synthesis of some new 1,3,4-thiadiazol-2-ylmethyl-1,2,4-triazole derivatives and investigation of their antimicrobial activities, *Eur. J. Med. Chem*, 44 (2009) 2896-2903.

[30] Okada Y., Tanaka K., Fujita I., Sato E., Okajima H., Antiodidant activity of thiosulfinates derived from garlic, *Redox Report*, 10 (2005) 96-102.

[31] Bendary E., Francis R. R., Ali H. M. G., Sarwat M. I., El Hady S., Antioxidant and structure–activity relationships (SARs) of some phenolic and anilines compounds, *Ann. Agric. Sci.*, 58 (2013) 173-181.

Cumhuriyet Sci. J., 44(1) (2023) 90-98
DOI: https://doi.org/10.17776/csj.1223357

Cumhuriyet Science Journal

| csj.cumhuriyet.edu.tr | Founded: 2002 ISSN: 2587-2680 e-ISSN: 2587-246X Publisher: Sivas Cumhuriyet University

Biosynthesis, Characterization and Antioxidant Properties of ZnO Nanoparticles Using Punica Granatum Peel Extract as Reducing Agent

Zehra Seba Keskin [1,a,*], Ünsal Açıkel [2,b]

[1] *Health Services Vocational School, Department of Pharmacy, Sivas Cumhuriyet University, Sivas, Türkiye.*
[2] *Department of Chemical Engineering, Sivas Cumhuriyet University, Sivas, Türkiye.*
**Corresponding author*

Research Article

History
Received: 23/12/2022
Accepted: 02/03/2023

ABSTRACT

The green synthesis method of nanoparticles using plant extracts attracts great attention as a reliable, low-cost, sustainable, environmentally friendly protocol that prevents or minimizes waste generation. In this study, *Punica granatum* peel extract was used as the reducing plant material and zinc acetate dihydrate ($Zn(CH_3COO)_2.2H_2O$) solution was used as the starting metal. In the synthesis, optimum conditions were determined by UV visible spectroscopy using different metal ion concentrations, plant extract amount, temperature, and pH parameters. For characterization of ZnONPs synthesized at optimum conditions, Scanning Electron Microscopy (SEM), Energy Dispersive X-ray spectroscopy (EDX), X-ray diffraction (XRD), Fourier Transform Infrared spectroscopy (FTIR), Dynamic Light Scattering (DLS), Zeta potential and Atomic Force Microscope (AFM) analyzes were made. It has been determined that the synthesized ZnONPs are spherical, have good stability, high purity, and nanoscale. The free radical scavenging capacity of biosynthesized ZnONPs was evaluated by DPPH analysis with different concentrations. The IC50 value was determined as 250µg ml^{-1}.

Keywords: Neuropathic pain, L-759,633, SER 601, Hot plate, Pregabalin.

[a] *zkeskin@cumhuriyet.edu.tr* *https://orcid.org/0000-0003-1334-5158* [b] *uacikel@cumhuriyet.edu.tr* *https://orcid.org/0000-0003-4969-8502*

Introduction

Nanotechnology is a new and rapidly developing technology field that enables applications such as processing, measurement, design, modeling, and arrangement performed on materials between 1-100 nm, aiming to provide advanced features at the atomic and molecular level or completely new physical, chemical and biological properties to the substance [1]. Considered as the building block of nanotechnology, nanoparticles (NP) describe a broad class of materials that contain particulate matter with a size less than 100 nm [2].

In recent years, biological methods are preferred as an alternative to chemical and physical methods in synthesizing metal oxide nanoparticles. Biological methods increase the efficiency of the process by catalyzing reactions in aqueous media at standard temperature and pressure. Also, they have the advantage of increasing the flexibility of the process by being applied in almost any environment and at any scale [3]. The green synthesis method involves the reduction of metal ions using biomass/extract, such as bacteria, fungi, yeast, virus, microalgae, and plant as an extracellular or intracellular source of reducing agents (see [4] and the references therein) The use of plant biomass/extracts instead of other biomaterials has advantages such as eliminating the detailed maintenance of cell cultures, rapid synthesis, finding various metabolites that can aid reduction, being easily accessible [5], [6]. In various studies in the literature, it has been stated that compounds found in plants such as polyphenols, proteins, terpenoids, alkaloids, amino acids, alcoholic compounds, glutathions, polysaccharides, antioxidants, organic acids, contribute to the reduction of metal ions to nanoparticles and to ensure their stability [7, 8].

Within the large metal oxide nanoparticle family, ZnONPs have an important potential in various applications such as electronics, communication, sensor, cosmetics, environmental protection, biology, and medical industry [9] due to the properties antifungal, antibacterial, antiviral, wound healing, high catalytic and photochemical activity, UV filtering, optical. Besides, the US FDA recognizes ZnO as a GRAS (generally considered safe) metal oxide (see [10]. and the references therein).

Punica granatum L. is a perennial plant belonging to the genus Punica of the Lythraceae family [11]. The peel, which constitutes 50% of the fruit weight, is a good source of high molecular weight phenolics, elagitanen, proanthocyanidins, complex polysaccharides, flavonoids, and microelements and has strong antimutagenic, antioxidant, and antimicrobial properties [12]. Various studies have reported that polyphenolic and flavonoid compounds act as reducing, stabilizing, limiting growth, and preventing agglomeration during the production of nanoparticles by biosynthesis (see [13] and the references therein).

The aim of this study is to synthesize ZnONPs using *Punica granatum* peel extract as a reducing and stabilizing agent and to determine the antioxidant activities of biosynthesized nanoparticles. Optimum conditions of the reaction in different parameters such as plant extract amount, metal ion concentration, temperature, and pH

were determined by UV-visible spectrophotometer. All properties of ZnONPs synthesized at optimum conditions were investigated in detail with Scanning Electron Microscopy (SEM), Energy Dispersive X-ray analysis (EDX), Zeta Potential, Dynamic Light Scattering (DLS), Fourier Transform Infrared Spectroscopy (FTIR), X-Ray Diffraction (XRD) and Atomic Force Microscopy (AFM) analyzes to be used in bionanocomposites in later studies.

Materials and Methods

Preparation of Pomegranate (Punica granatum) Peel Extract

The fruits obtained from local markets in Sivas/Turkey were washed several times to remove dust, then peel and inner parts were separated and dried in the laboratory for 2 weeks. *Punica granatum* fruit peels extract was obtained by boiling 5 g of powdered peel in 100 ml of sterile distilled water in 250 ml of flask until it turns yellow-brown for 15 minutes. Then it was cooled to room temperature and filtered with filter paper Whatman No. 1 and stored at +4 ^{o}C in a refrigerator to be used for further experiments.

Synthesis of ZnONPs by green method

50 ml of 0.15 M $Zn(CH_3COO)_2.2H_2O$ solution was prepared. 10 ml of fruit peel extract was added drop by drop to this prepared solution and adjusted to pH 12 with 1 M NaOH and mixed in a magnetic stirrer for 2 hours. The extract, which was initially yellow-brown in color, turned into a light yellow mixture [14]. This mixture was centrifuged at 10.000 rpm for 10 minutes and then dried at 50 ^{o}C for 2 days [15].

Determination of Optimum Synthesis Conditions of ZnONPs

In some studies, it has been reported that the optimum synthesis conditions in the green synthesis method are determined by changing the parameters such as plant extract amount, metal ion solution concentration, incubation time, medium pH and temperature [16, 17]. During the synthesis, different metal ion solution concentrations of 0,03 M, 0,05 M, 0,1 M, 0,15 M, and 0,2 M were applied by keeping the plant extract amount, incubation time, medium pH and temperature constant. To determine the optimum amount of plant extract, 2 ml, 4 ml, 6 ml, 8 ml, and 10 ml of extract were added to 50 ml of zinc acetate dihydrate solution. Keeping the other parameters the same, the pH value of the environment was brought to 9, 10, 11, and 12 and the optimum pH value was determined. Finally, synthesis was carried out at 20 ^{o}C, 40 ^{o}C, 50 ^{o}C and 60 ^{o}C to determine the optimum reaction temperature for NP synthesis.

UV–Visible Absorption Spectroscopy

UV-visible spectroscopy is a widely used technique for determining the optical properties of metallic nanoparticles [18]. Since the extract and nanoparticle solution was dark and concentrated, dilution was made before UV analysis was performed. After diluting these solutions with distilled water at a ratio of 1/40, they were placed in a quartz cuvette and their optical properties were determined in the UV-Vis spectrophotometer (UV-2600, Shımadzu) in the wavelength range of 200 to 900 nm.

X-ray Diffraction (XRD)

XRD is a characterization method used for phase identification and characterization of the crystal structure of nanoparticles [19]. XRD measurements of synthesized ZnONPs were made in X-Ray Diffractometer (Rigaku Miniflex 600). XRD shapes were obtained with a step size of 0.05 between Cu-Kα radiation (k = 1.54 A) and 2θ = 10 °-90 ° values. Crystal sizes of the nanoparticles were calculated using the Debye-Scherrer formula.

Scanning Electron Microscopy (SEM) and Energy-Dispersive X-ray Analysis (EDS)

SEM analysis to determine the structure, shape, and size of ZnONPs obtained by the green synthesis method and EDX analysis to determine the basic composition of the NPs were obtained by using Scanning Electron Microscope (TESCAN MIRA 3 XMU). Before analysis, the samples were plated with gold in an automatic coater. This process increases the surface conductivity and provides better quality images.

Fourier-Transform Infrared Spectroscopy (FTIR)

FT-IR spectrum was used to define functional groups in ZnONPs obtained by green synthesis method and *Punica granatum* peel extract used as a reducing agent. The FT-IR spectrum of the extract and ZnONPs was realized with Bruker Tensor II and adjusted to work at 2 cm^{-1} resolution in the range of 400-4000 cm^{-1} to obtain a good signal/noise ratio.

Dynamic Light Scattering (DLS) Analysis

Average size, size distribution, and polydispersity index (PDI) measurements of the synthesized nanoparticles were made with Malvern Brand, Zetasizer model particle size analysis device. After diluting the nanoparticles with pure water, the sonication process was applied for 15 minutes to disintegrate the agglomerated structures, and analysis was performed by placing them in 1.5 ml cuvettes.

Zeta Potential Analysis

Zeta potential analysis was performed with the Malvern, Nano ZS Model zeta sizer device to determine the colloidal distribution stability of ZnONPs. Measurements were made at 25 °C with a back reflection angle of 173°. The nanoparticles prepared for analysis were diluted with distilled water, taken with a syringe in 1 ml, and placed in disposable zeta potential cells, and measurements were made.

Atomic Force Microscopy

The particle size, distribution, and morphology of nanoparticles were analyzed using atomic force microscope (Veeco Multimode 8). The prepared nanoparticle solutions were diluted at a ratio of 1/100, then spread a drop on a clean glass surface with a size of 1 cm x 1 cm and dried. The surface topographies of the nanoparticle sample prepared in this way were scanned in 2D and 3D in an area of 3x3 μm^2 and 20x20 μm^2.

Antioxidant Assay (DPPH Free Radical Scavenging)

The radical scavenging activities of *Punica granatum* extract and biosynthesized ZnONPs were determined by the method reported by Sathiskumar et al. [20]. Samples were prepared at different concentrations (50,75, 100, 250 and 500 µg/mL) for ZnONPs, extract and Ascorbic acid (as positive control). Then, 1 ml of each sample at different concentrations was added to 2 ml of 0.1 mM DPPH (in ethanol) solution. After 30 minutes of incubation in the dark, absorbance values were measured at 517 nm in a UV spectrophotometer. The radical scavenging activity was determined using equation 1 given below.

$$Sc\ (\%) = (1-(As/Ac))*100 \quad [1]$$

Here, Sc represents the DPPH scavenging activity (%), Ac represents the absorbance of the positive control, and As represents the absorbance of the sample.

Results and Discussion

Visual Observation and UV–visible spectroscopy

The visual color change is accepted as a preliminary test to confirm the formation of NPs obtained by green synthesis. The first indication of the reduction of Zn ions to ZnONPs by the *Punica granatum* peel extract was determined as the yellow-brown color of the extract turning into a light yellow color.

Determination of Optimum Zinc Acetate Dihydrate [$Zn(CH3COO)_2$].$2H_2O$ Concentration

In this study, the effect of different zinc acetate dihydrate concentrations (0,03 M, 0,05 M, 0,1 M, 0,15 M, and 0,2 M) on the formation of ZnONPs obtained by green synthesis was determined by UV-visible absorption spectroscopy. While no absorption peak was observed at 0,03 M, 0,05 M, and 0,1 M (Figure 1a), the maximum absorbance peak was determined at a concentration of 0,15 M. This peak read at 358 nm confirms the synthesis since it is the characteristic peak of ZnONPs. However, despite the increase in 0,2 M zinc acetate dihydrate concentration, it was observed that there was a decrease in absorbance and an expansion at the peak point. Therefore, it is concluded that increasing the metal ion concentration to the optimum level will increase the NP formation while increasing the metal ion concentration will decrease the NP formation.

Determining the Optimum Extract Amount

In the synthesis of ZnONPs, *P. granatum* extract was used as a stabilizing, reducing, and capping agent. In the optimization study for biosynthesis, the effect of the amount of extract on absorption and peak priority was observed by UV-Vis absorption spectroscopy. 2 ml, 4 ml, 6 ml, 8 ml, and 10 ml of extract were added to 0,15 M Zn $(CH_3COO)_2.2H_2O$ used as the starting solution and UV spectra of the solutions were obtained as a result of the reaction. As seen in Figure 1b, it was determined that the maximum absorbance peak occurred at 356 nm and 10 ml extract usage. In some studies, it has been stated that by increasing the plant extract rate, the NP synthesis rate increases in direct proportion [21, 22].

Determining the Optimum Temperature

It is known that the temperature of the reaction medium is an important factor regulating the structure of the synthesized nanoparticles [21]. To determine the optimum reaction temperature of the synthesis using 0,15 M Zn $(CH_3COO)_2.2H_2O$ solution and 10 ml extract, the synthesis was carried out at 20 ^{O}C, 40 ^{O}C, 50 ^{O}C, and 60 ^{O}C. In the UV spectrum seen in Figure 1c, it is seen that the absorbance peak intensities increase as the temperature increases.

The highest absorbance peak determined at 60 ^{O}C and 344 nm shows that zinc acetate is converted into ZnONPs. Synthesis of ZnONPs performed at higher rates at higher temperatures has been reported in various studies in the literature [23, 24].

Determining the Optimum pH Value

The pH of the medium is an important parameter affecting the NP size. During the synthesis, it has been noted that there is an increase in the absorbance value as a result of the pH increase from 9 to 12. This event is due to the formation of nucleation centers that increase with the increase of pH. As the nucleation center increases, the reduction of metallic ions to metal nanoparticles also increases [25]. While no absorption peak was observed at pH 9 and pH 10, the characteristic maximum absorption peak was observed at 358 nm at pH 12 (Figure 1d) . These results are consistent with studies in the literature [17, 23].

While the characteristic absorption peak of ZnONPs solution synthesized at specified optimum conditions was determined at 359 nm, no peak of peel extract was observed (Figure 2).

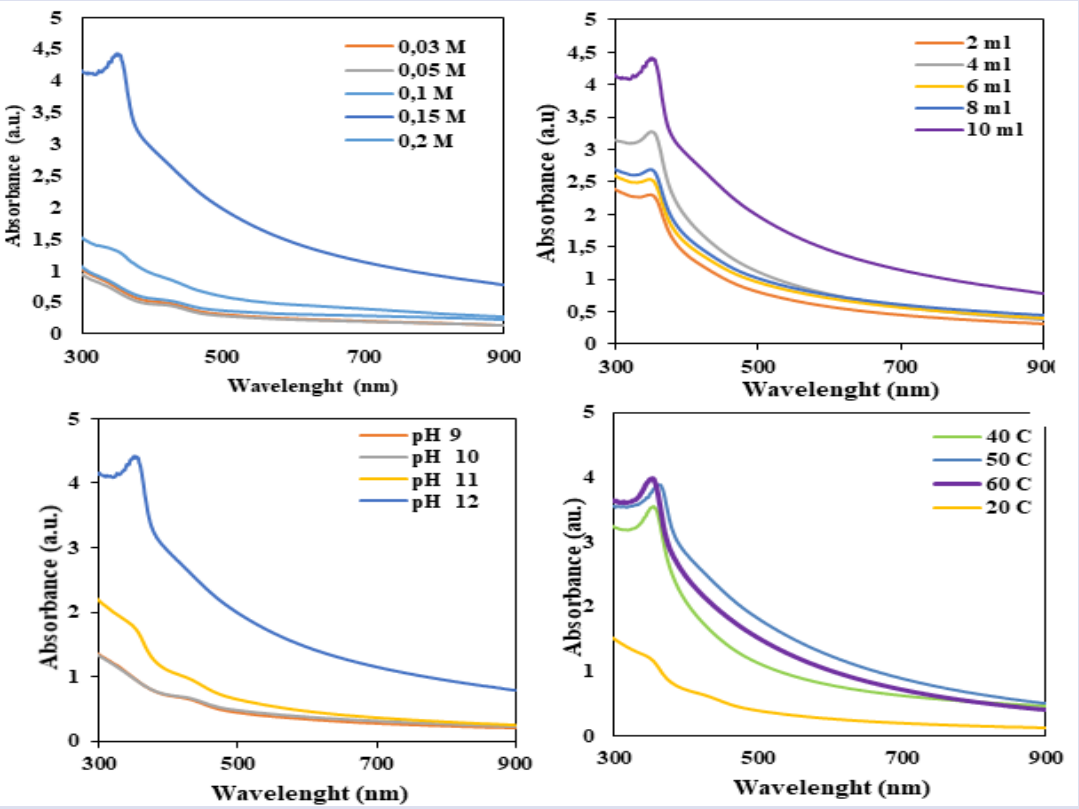

Figure1. Optimization of synthesis parameters, a. zinc acetate concentrations, b. amount of extract, c. pH. d. Temperature

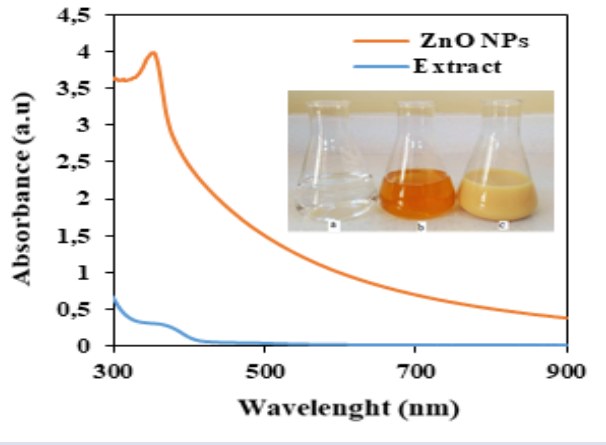

Figure 2. Synthesis of ZnONPs in optimum conditions

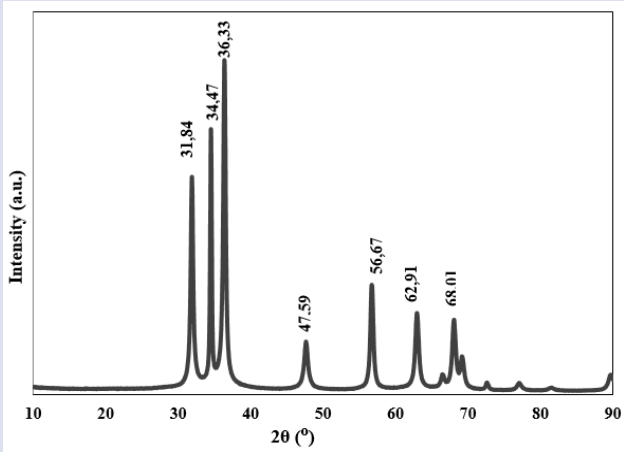

Figure 3. XRD graph of synthesized ZnONPs

XRD

The XRD diffraction peaks of the ZnONPs samples obtained by the green synthesis method are shown in Figure 3. It was determined that the characteristic peaks observed at 2θ=31,84°, 34,47°, 36,33°, 47,59°, 56,67°, 62,91, 68,01 of the ZnONPs correspond to the planes (100), (002), (101), (102), (110), (103) and (112), respectively. These obtained data match the card numbered JCPDS Data Card No: 36–1451 in the Joint Committee on Powder Diffraction Standards (JCPDS) database [26]. Besides, since all the peaks seen in the graphic are characteristic peaks of ZnO, it confirms that they do not contain impurities.

Crystal size measurement for synthesized ZnONPs was calculated using the Debye-Scherrer equation [2] [27].

$$D = \frac{K\lambda}{\beta \cos\theta} \qquad [2]$$

D: crystal size,
K: Debye Scherrer constant (0.94)
λ: Cu-Kα radiation (1.54 A),
β: half-length width of maximum peak (FWHM),
θ: It is the Bragg angle value obtained from the 2θ value of the maximum peak in the XRD diffraction pattern.

The average crystal size of ZnONPs was calculated as approximately 19.51 nm according to the Debye-Scherrer formula [2]. FWHM values for each peak point determined to calculate particle size are shown in Table 1.

Table 1. Crystal sizes and peak values of ZnONPs

2 θ	h k l	FWHM	D(nm)
31,84	100	0,49192	17,55
34,47	002	0,29878	29,10
36,33	101	0,5026	17,39
47,59	102	0,67818	13,38
56,67	110	0,53313	17,70
62,91	103	0,63896	15,23
68,01	112	0,63676	15,73

SEM and EDX

The structure, shape, and size of ZnONPs obtained by the green synthesis method were determined by SEM images (Figure 4). SEM images obtained with 50 kx and 200 kx magnifications show that synthesized ZnONPs have a spherical structure and particle sizes in the range of 33.6 nm and 51.47 nm. The obtained results are similar to some studies in the literatüre [28, 29].

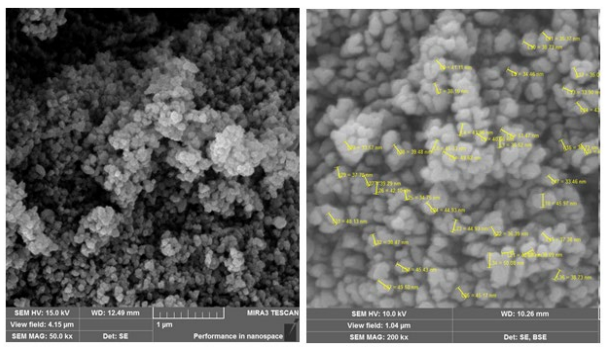

Figure 4. SEM image of ZnONPs

Chemical purity, elemental composition, and stoichiometry of ZnONPs were determined by EDX analysis. In EDX spectra shown in Figure 5, it is seen that the peaks belong only to Zn and O. Therefore, it is confirmed that the synthesized ZnONPs are of high purity. The stoichiometric mass percentage for Zn and O were determined 76.77% and 23.23%, respectively. These results are seen to be consistent with the results of other studies in the literature [15, 30, 31].

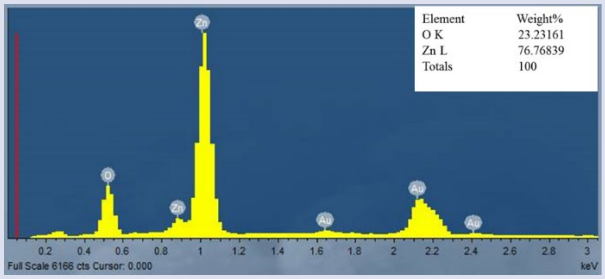

Figure 5. EDX spectrum of ZnONPs

FTIR

FTIR spectrum analysis shows the relationship of absorption bands with chemical compounds in pomegranate peel and ZnONPs. The availability of functional groups in ZnONPs is given in Figure 6. In the spectrum, absorption peaks are seen at 3219 cm^{-1}, 1578 cm^{-1}, 1399 cm^{-1},1088 cm^{-1}, 1032 cm^{-1}, 841 cm^{-1}, 717 cm^{-1} and 480 cm^{-1}. The wide peak observed at 3219 cm^{-1} is due to O-H stress vibrations. While the peak at 1578 cm^{-1} corresponds to C = C stress in aromatic rings and C = O stress in polyphenols, it is thought that the absorption peak at 1399 cm^{-1} is caused by the C = N amide-1 stress in the protein. The peak at 1088 cm^{-1} showed the C-O stretch in amino acid and the peak at 1032 cm^{-1} showed the presence of the C-N stretch [15]. Also, in the spectrum, it was determined that peaks were formed at 841 cm^{-1} and 717 cm^{-1} correspondings to the C-H stretching of alkanes [17]. Metal oxides form an absorption peak in the region between 600 - 400 cm^{-1} due to interatomic vibrations.

The characteristic peak corresponding to the ZnO stretch band showing ZnO formation, which is stated in the literature, was observed at a wavenumber of 481 cm^{-1} [32]. Therefore, it is confirmed that the water-soluble compounds in *Punica granatum* peel extract are effective in determining the shape of nanoparticles and in reducing metal ions.

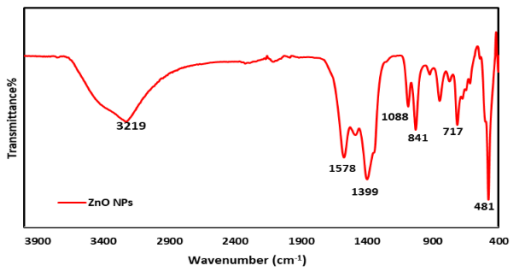

Figure 6. FTIR spectrum for ZnONPs

DLS Analysis Results

The size distribution, average particle size, and *polydispersity index* (PDI) of ZnONPs synthesized by the green method were determined by the dynamic light scattering method. The size distribution of ZnONPs is shown in Figure7. The average particle size for ZnONPs in solution was found to be 348 nm with DLS. It was determined that the ZnONPs size obtained by DLS was higher than the average NP size determined in SEM images. This is thought to be because the NP size measured by DLS is the hydrodynamic diameter of the particle swollen with water or solvent, while the value measured by SEM corresponds to the dried NP size. Another reason can be shown as the measurement of clustered particle sizes rather than individual particle sizes since NPs tend to coalesce in an aqueous medium [33].The PDI value, which is a dimensionless value, ranges from 0.01 to 0.5-0.7 for monodisperse particles, while the PDI value for particles with very wide size distribution is

greater than 0.7 [34]. The fact that the PDI value of ZnONPs synthesized in the study was 0.457 shows that ZnONPs are monodisperse. In addition, it was determined that the ZnO NP size obtained with DLS was higher than the average NP size determined in SEM images. This is because the NP size measured by DLS is not water or solvent dependent. It is the hydrodynamic diameter of the particle swollen by SEM, while the value measured by SEM is considered to correspond to the dried NP size. Another reason can be cited as a measurement of aggregated particle sizes rather than individual particle sizes, as NPs tend to coalesce in aqueous media [33].

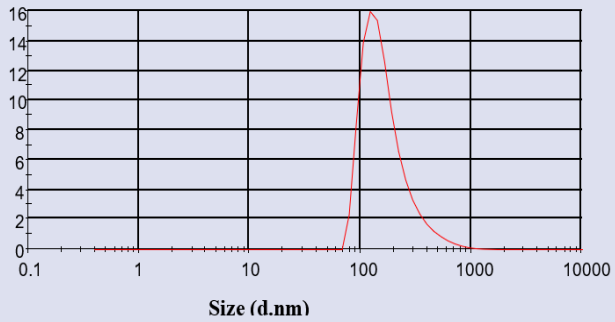

Figure 7. Size distribution of ZnONPs

Stability of ZnONPs

Zeta potential analysis was performed to determine the potential stability depending on the NP surface charges and the electrostatic repulsive forces between the NPs. The zeta potential of colloidal ZnONPs synthesized by the green method was found to be -46.0 mV as seen in Figure 8.

The negatively charged surface of the nanoparticles confirms the repulsion between particles and proves that it results in stable suspensions [35]. Because agglomeration/aggregation seen between NPs occurs due to van der Waals forces and chemical bonding [36].

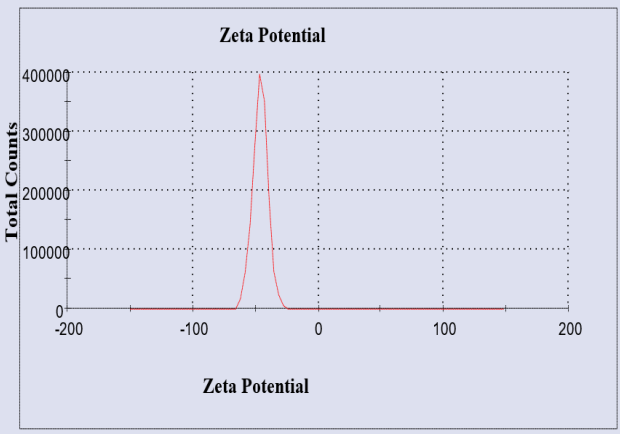

Figure 8. Zeta potential of synthesized ZnONPs

AFM

One of the characterizations that enable us to determine the morphology and size of the synthesized ZnONPs is the atomic force microscope with high resolution.

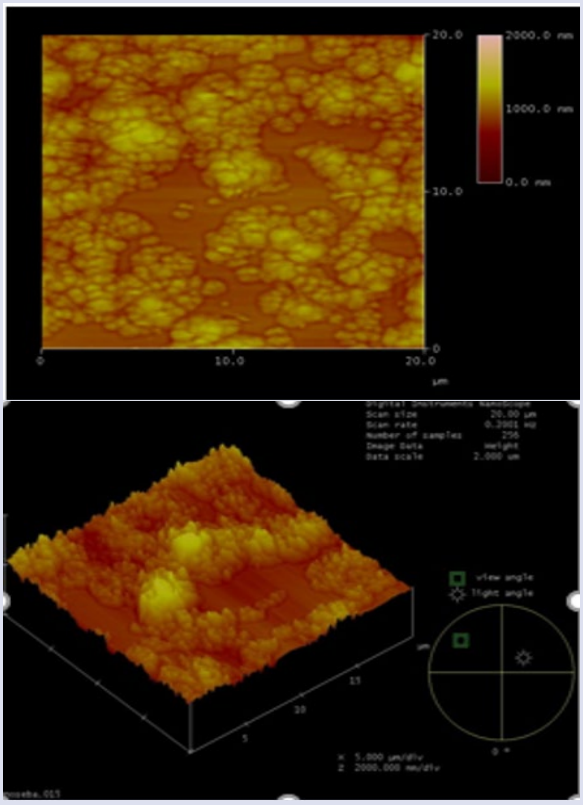

Figure 9. AFM images of ZnONPs at 20x20 µm^2 a) 2D b) 3D

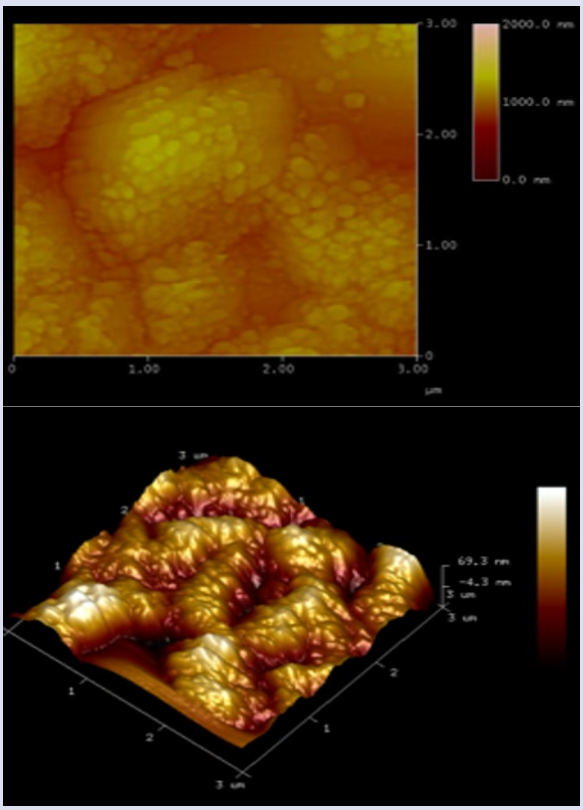

Figure 10. AFM images of ZnONPs at 3x3 µm^2 a) 2D b) 3D

2D and 3D surface images and surface roughness values were obtained by scanning NPs with magnification ranges of 20x20 μm^2 and 3x3 μm^2 (Figure 9- 10). When 2D and 3D images with a magnification range of 3x3 μm^2, which give the NP size, were examined, the size of the largest nanoparticle in the 3D image was determined to be 69,3 nm. The average roughness value (Ra) of the nanoparticles was measured as 19,88 nm, and the maximum roughness value (Rmax) was 201,55 nm.

Antioxidant Activity

In this study, antioxidant capacity of *Punica granatum* peel extract and biosynthesized ZnONPs was investigated by DPPH method. As seen in Figure 11, ZnONPs and Ascorbic acid used as a control produced strong inhibitory activity against DPPH radical. It was determined that the free radical scavenging activities increased as the ZnONPs concentration increased. The % inhibition values of 250 µg/ml and 500 µg/ml concentrations of ZnONPs (92.3% and 93.3%, respectively) showed strong antioxidant capacity when compared with ascorbic acid. It is known that the significant antioxidant potential of ZnONPs is due to the hydrogen donating abilities of active phytochemicals such as alkaloids, anthocyanins, anthocyanidins, tannins, flavonoids, phenolics, proanthocyanidins, sterols, terpenes, and xanthonoids in *Punica granatum* peel [19]. As seen in Table 2, the IC_{50} value of biosynthesized ZnONPs falls within the range of IC_{50} values of previously studied ZnONPs.

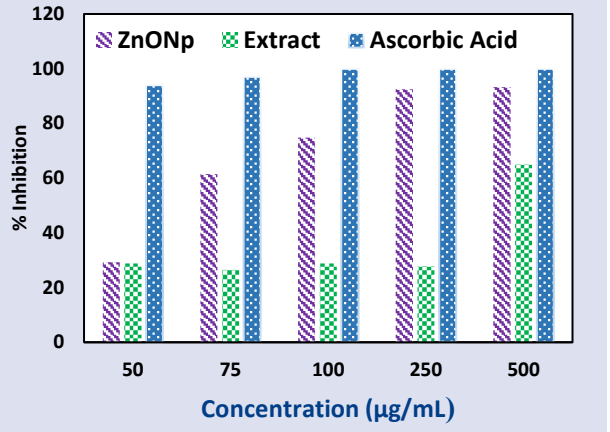

Figure 11. DPPH radical scavenging activity of ZnONPs, extract of *Punica granatum* and ascorbic acid

Table 2. The comparison of DPPH radical scavenging activity of synthesized ZnONPs of the present study with other biosynthesized ZnONPs

ZnONPs	IC_{50} (µg/ml)	Reference
ZnONPs –*Beta vulgaris*	4400	[37]
ZnONPs-*Mussaenda frondosa*	857	[38]
ZnONPs- *Citrullus colocynthis*	290	[39]
ZnONPs- *Punica granatum*	250	This present
ZnONPs-*Lutfa acutangula*	134,12	[40]
ZnONPs-*Coccinia abyssinica*	127,74	[41]

Conclusions

In this study, ZnONPs was synthesized by green synthesis method using *Punica granatum* peel extract, which is food waste. The characterizations of ZnONPs synthesized at optimum conditions were made by SEM, EDX, XRD, FTIR, DLS, zeta potential, and AFM analysis. The sizes of the NPs, which are seen to be in spherical structure in SEM images, were determined to be between 33.6 nm and 51.47 nm, and it was confirmed that they do not contain impurities with the results of XRD and EDX analysis. Besides, the high negative zeta potential value (-46 mV) determined for the ZnONPs proves that the NPs have good stability, as it shows the repulsive force between the particles. The IC_{50} value of biosynthesized ZnONPs was found to be 250 µg ml^{-1} by DPPH analysis. It was determined that it has strong antioxidant activity from % inhibition values.

As a result, a clean, antioxidant, environmentally friendly, inexpensive, the non-toxic approach is reported for the synthesis of zinc oxide nanoparticles.

Acknowledgment

The **PhD** thesis research process was supported by the Scientific Research Project Fund Sivas Cumhuriyet University (Grant No. M-721).

Conflicts of interest

The authors declare that they have no conflict of interest.

References

[1] Beykaya M., Çağlar A. Bitkisel özütler kullanılarak gümüş-nanopartikül (AgNP) sentezlenmesi ve antimikrobiyal etkinlikleri üzerine bir araştırma, *Afyon Kocatepe Üniversitesi Fen ve Mühendislik Bilimleri Dergisi*, *16* (3) (2016) 631-641.

[2] Laurent S., Forge D., Port M., Roch A., Robic C., Vander Elst L., Muller R. N., Magnetic iron oxide nanoparticles: synthesis, stabilization, vectorization, physicochemical characterizations, and biological applications, *Chemical Reviews*, *108* (6) (2008) 2064-2110.

[3] Schröfel A., Kratošová G., Šafařík I., Šafaříková M., Raška I., Shor L. M., Applications of biosynthesized metallic nanoparticles–a review, *Acta Biomaterialia*, *10*(10) (2014) 4023-4042.

[4] Shah M., Fawcett D., Sharma S., Tripathy S. K., Poinern G. E. J., Green synthesis of metallic nanoparticles via biological entities, *Materials*, *8* (11) (2015) 7278-7308.

[5] Iravani S., Green synthesis of metal nanoparticles using plants, *Green Chemistry*, *13* (10) (2011) 2638-2650.

[6] Shankar S. S., Rai A., Ahmad A., Sastry M., Rapid synthesis of Au, Ag, and bimetallic Au core–Ag shell nanoparticles using Neem (Azadirachta indica) leaf broth, *Journal of Colloid and Interface Science*, *275* (2) (2004) 496-502.

[7] Asmathunisha N., Kathiresan K., A review on biosynthesis of nanoparticles by marine organisms, *Colloids and Surfaces B: Biointerfaces*, *103* (2013) 283-287.

[8] Canbaz G. T., Açıkel U., Açıkel Y. S., ZnO-Kitosan Kompoziti ile Ağır Metal Giderimi, *Avrupa Bilim ve Teknoloji Dergisi*, (35) (2022) 603-609.

[9] Sharma D., Sabela M. I., Kanchi S., Mdluli P. S., Singh G., Stenström T. A., Bisetty K., Biosynthesis of ZnO nanoparticles using Jacaranda mimosifolia flowers extract: synergistic antibacterial activity and molecular simulated facet specific adsorption studies., *Journal of Photochemistry and Photobiology B: Biology*, *162* (2016) 199-207.

[10] Ghaseminezhad S. M., Hamedi S., Shojaosadati S. A. Green synthesis of silver nanoparticles by a novel method: Comparative study of their properties, *Carbohydrate Polymers*, *89* (2) (2012) 467-472.

[11] Çetinkaya H. K., Güvercin D., Karakurt Y., Molecular characterization of pomegranate (*Punica granatum* L.) Genotypes with SSR Markers, *Süleyman Demirel Üniversitesi Fen Edebiyat Fakültesi Fen Dergisi*, *14* (2) (2019) 345-351.

[12] Okumuş G., Yıldız E., Bayizid A. A., Doğal antioksidan bileşikler: Nar yan ürünlerinin antioksidan olarak değerlendirilmesi, *Uludağ Üniversitesi Ziraat Fakültesi Dergisi*, *29* (2) (2015).

[13] Vijayaraghavan K., Ashokkumar T., Plant-mediated biosynthesis of metallic nanoparticles: a review of literature, factors affecting synthesis, characterization techniques and applications, *Journal of Environmental Chemical Engineering*, *5* (5) (2017) 4866-4883.

[14] Dobrucka R., Długaszewska J., Biosynthesis and antibacterial activity of ZnO nanoparticles using Trifolium pratense flower extract, *Saudi J Biol Sci* 23 (2016) 517–523.

[15] Yedurkar S. M., Maurya C. B., Mahanwar P. A., A biological approach for the synthesis of copper oxide nanoparticles by Ixora coccinea leaf extract, *J. Mater. Environ. Sci*, *8* (4) (2017) 1173-1178.

[16] Bhuyan T., Mishra K., Khanuja M., Prasad R., Varma A., Biosynthesis of zinc oxide nanoparticles from Azadirachta indica for antibacterial and photocatalytic applications, *Materials Science in Semiconductor Processing*, *32* (2015) 55-61.

[17] Gupta M., Tomar R. S., Kaushik S., Mishra R. K., Sharma D., Effective antimicrobial activity of green ZnO nano particles of Catharanthus roseus, *Frontiers in Microbiology*, *9*, (2018) 2030.

[18] Pal S., Tak Y. K. Y Song J. M., Does the antibacterial activity of silver nanoparticles depend on the shape of the nanoparticle? A study of the gram-negative bacterium Escherichia coli., *Appl Environ Microbiol*, *73* (6) (2007) 1712-1720.

[19] Sun S., Murray C. B., Weller D., Folks L., Moser A., Monodisperse Fe Pt nanoparticles and ferromagnetic Fe Pt nanocrystal superlattices, *Science*, *287*(5460) (2000) 1989-1992.

[20] Sathishkumar G., Pradeep K. Jha, Vignesh V., Rajkuberan C., Jeyaraj M., Selvakumar M., Rakhi Jha, Sivaramakrishnan S., Cannonball fruit (Couroupita guianensis, Aubl.) extract mediated synthesis of gold nanoparticles and evaluation of its antioxidant activity, *Journal of Molecular Liquids* 21 (2016) 229–236.

[21] Mittal J., Batra A., Singh A., Sharma M. M., Phytofabrication of nanoparticles through plant as nanofactories, *Advances in Natural Sciences: Nanoscience and Nanotechnology*, *5* (4) (2014) 043002.

[22] Song J. Y., Kwon E. Y., Kim B. S., Biological synthesis of platinum nanoparticles using Diopyros kaki leaf extract. *Bioprocess and Biosystems Engineering*, *33* (1) (2010) 159-164.

[23] Jamdagni P., Khatri P., Rana J. S., Green synthesis of zinc oxide nanoparticles using flower extract of Nyctanthes arbor-tristis and their antifungal activity, *Journal of King Saud University-Science*, *30* (2) (2018) 168-175.

[24] Chunfa D., Fei C., Xianglin Z., Xiangjie W., Xiuzhi Y., Bin Y., Rapid and green synthesis of monodisperse silver nanoparticles using mulberry leaf extract, *Rare Metal Materials and Engineering*, *47* (4) (2018) 1089-1095.

[25] Bali R., Harris A. T., Biogenic synthesis of Au nanoparticles using vascular plants, *Industrial & Engineering Ehemistry Research*, *49* (24) (2010) 12762-12772.

[26] Firooz A. A., Mirzaie R. A., Kamrani F., Effect of morphological ZnO nanostructures on the optical and decolorization properties, *Journal of Structural Chemistry*, *59* (3) (2018) 739-743.

[27] Taghavi Fardood, S., Ramazani A., Asiabi P. A., Joo S. W., A novel green synthesis of copper oxide nanoparticles using a henna extract powder, *Journal of Structural Chemistry*, *59* (7) (2018) 1737-1743.

[28] Anbuvannan M., Ramesh M., Viruthagiri G., Shanmugam N., Kannadasan N., Anisochilus carnosus leaf extract mediated synthesis of zinc oxide nanoparticles for antibacterial and photocatalytic activities, *Materials Science in Semiconductor Processing*, *39* (2015) 621-628.

[29] Yuvakkumar R., Suresh J., Nathanael A. J., Sundrarajan M., Hong S. I., Novel green synthetic strategy to prepare ZnO nanocrystals using rambutan (*Nephelium lappaceum* L.) peel extract and its antibacterial applications, *Materials Science and Engineering: C*, *41* (2014) 17-27.

[30] Velmurugan P., Anbalagan K., Manosathyadevan M., Lee K. J., Cho M., Lee S. M., Oh B. T., Green synthesis of silver and gold nanoparticles using Zingiber officinale root extract and antibacterial activity of silver nanoparticles against food pathogens, *Bioprocess and Biosystems Engineering*, *37* (10) (2014) 1935-1943.

[31] Salam H. A., Sivaraj R., Venckatesh R., Green synthesis and characterization of zinc oxide nanoparticles from Ocimum basilicum L. var. purpurascens Benth.-Lamiaceae leaf extract, *Materials Letters*, *131* (2014) 16-18.

[32] Anžlovar A., Crnjak Orel Z., Kogej K., Polyol-mediated synthesis of zinc oxide nanorods and nanocomposites with poly (methyl methacrylate), *Journal of Nanomaterials*, *2012 (31)* (2012).

[33] Sharma V., Shukla R. K., Saxena N., Parmar D., Das M., Dhawan A., DNA damaging potential of zinc oxide nanoparticles in human epidermal cells, *Toxicology Letters*, *185* (3) (2009) 211-218.

[34] Nidhin M., Indumathy R., Sreeram K. J., Nair B. U., Synthesis of iron oxide nanoparticles of narrow size distribution on polysaccharide templates, *Bulletin of Materials Science*, *31* (1) (2008) 93-96.

[35] Anandalakshmi K., Venugobal J., Ramasamy V., Characterization of silver nanoparticles by green synthesis method using *Pedalium murex* leaf extract and their antibacterial activity, *Applied Nanoscience*, *6* (3) (2016) 399-408.

[36] Jayapriya M., Dhanasekaran D., Arulmozhi M., Nandhakumar E., Senthilkumar N., Sureshkumar K., Green synthesis of silver nanoparticles using *Piper longum* catkin extract irradiated by sunlight: antibacterial and catalytic activity, *Research on Chemical Intermediates*, *45*(6) (2019) 3617-3631.

[37] Kumar P., Suresh D., Nagabhushana H., Sharma S. C., *Beta vulgaris* aided green synthesis of ZnO nanoparticles and their luminescence, photocatalytic and antioxidant properties, *The European Physical Journal Plus*, *130* (6) (2015) 1-7.

[38] Jayappa M. D., Ramaiah C. K., Kumar M. A. P., Suresh D., Prabhu A., Devasya R. P., Sheikh S., Green synthesis of zinc oxide nanoparticles from the leaf, stem and in vitro grown callus of *Mussaenda frondosa* L.: characterization and their applications, *Applied Nanoscience*, *10* (8) (2020) 3057-3074.

[39] Azizi S., Mohamad R., Mahdavi Shahri M., Green microwave-assisted combustion synthesis of zinc oxide nanoparticles with *Citrullus colocynthis* (L.) Schrad: characterization and biomedical applications, *Molecules*, *22* (2) (2017) 301.

[40] Ananthalakshmi R., Rajarathinam S. R., Sadiq A. M., Antioxidant activity of ZnO Nanoparticles synthesized using peel extract, *Research Journal of Pharmacy and Technology*, *12* (4) (2019) 1569-1572.

[41] Safawo T., Sandeep B. V., Pola S., Tadesse A., Synthesis and characterization of zinc oxide nanoparticles using tuber extract of anchote (*Coccinia abyssinica* (Lam.) Cong.) for antimicrobial and antioxidant activity assessment. *Open Nano*, *3*, (2018) 56-63.

Cumhuriyet Sci. J., 44(1) (2023) 99-105
DOI: https://doi.org/10.17776/csj.1191282

Cumhuriyet Science Journal

| csj.cumhuriyet.edu.tr | Founded: 2002 ISSN: 2587-2680 e-ISSN: 2587-246X Publisher: Sivas Cumhuriyet University

Water-Soluble Quaternized Serotonin Substituted Zinc-Phthalocyanine for Photodynamic Therapy Applications

Ebru Yabaş [1,a], Fuat Erden [2,b,*]

[1] *Advanced Technology Application and Research Center, Sivas Cumhuriyet University 58140, Sivas, Türkiye.*
[2] *Department of Aeronautical Engineering, Sivas University of Science and Technology, 58140 Sivas, Türkiye.*
**Corresponding author*

Research Article

History
Received: 18/10/2022
Accepted: 09/03/2023

ABSTRACT

Poor water solubility is the main drawback of phthalocyanine (Pc)-based second generation photosensitizing agents in photodynamic therapy (PDT). To resolve this, we proposed preparation of quaternized serotonin substituted zinc phthalocyanine (q-Ser-ZnPc) since the positive charge on quaternary amines could improve water-solubility and might limit self-interactions of hydrophobic aromatic surface of Pc in aqueous solutions. Briefly, serotonin substituted phthalonitrile was prepared by reaction of 4-nitrophthalonitrile with 5-hydroxytryptamine (Serotonin). Serotonin substituted zinc(II) phthalocyanine (Ser-ZnPc) was prepared by cyclotetramerization of serotonin substituted phthalonitrile. Then, q-Ser-ZnPc was prepared by the quaternization reaction of Ser-ZnPc. The synthesized compounds were characterized by ^{1}H-NMR, UV-Vis, FT-IR, fluorescence, and elemental analysis. Importantly, unlike ZnPc, which is among most widely used second generation photosensitizing agents, we report that q-Ser-ZnPc is actually water-soluble. Besides, q-Ser-ZnPc also absorbs light in the wavelengths corresponding to the therapeutic window. What's more, q-Ser-ZnPc exhibits a higher fluorescence quantum yield than that of ZnPc. Thus, the material might be useful particularly for image-guided PDT applications.

Keywords: Photodynamic therapy, Photosensitizer, Water-soluble, Phthalocyanine, Serotonin.

[a] *eyabas@cumhuriyet.edu.tr* *https://orcid.org/0000-0001-7163-3057* [b] *fuaterden@sivas.edu.tr* *https://orcid.org/0000-0002-8261-4844*

Introduction

A human body consists of more than 30 trillion cells with various functions. Normally, these cells grow, perform their functions, die when they grow old or get damaged and replaced with new cells. Sometimes, damaged or abnormal cells continue to grow and divide in an uncontrollable fashion instead of dying, resulting in cancer. The cancer cells grow out of control, avoid the immune system, spread to the other parts of the body, invade normal tissues and organs, can destroy healthy cells and disrupt vital organ functions. According to the World Health Organization (WHO), cancer is the disease with the highest cause of death worldwide [1]. Even only in 2020, cancer is responsible for the loss of nearly 10 million lives, accounting for one in every six deaths [1]. These facts are leading scientists from all around the globe to work hard towards finding an efficient cancer treatment.

Currently, depending on the kind, stage, and location of cancer cells in the body, surgery, chemotherapy, and radiotherapy are the most frequently used cancer treatment methods. The problem is none of these options are actually flawless. In surgery, a reaction to medication, bleeding, internal organ damage, pain, scar tissue, and infection might occur as possible side effects [2, 3]. Regarding chemotherapy, its main drawback is that highly cytotoxic anti-neoplastic drugs are used in chemotherapy, and thus, a fraction of healthy cells are destroyed along with cancerous ones [3]. Besides, being susceptible to infections, fatigue, dizziness, hair loss, dryness of skin, change of taste, loss of memories, and diarrhea are also other common side effects of chemotherapy [3, 4]. Similar to chemotherapy, healthy cells are also damaged to some extent in radiotherapy by ionizing radiation that is targeted towards cancerous cells [2, 3].

Alternatively, photodynamic therapy (PDT) has been proposed as a promising method for cancer treatment. In PDT, a light source, photosensitizing agent and oxygen in the tissue, all of which are non-toxic alone, work together to destroy cancerous cells [2, 5]. Briefly, the photosensitizers could selectively be accumulated in only cancer cells via use of enhanced permeability and retention (EPR) effect, cancer biomarkers, functionalized nanomaterials or RNA-targeting [6-10]. Then, upon application of a long wavelength red light, photosensitizers are activated and transfer energy to molecular oxygen in the tissue, which results in the formation of reactive oxygen species like singlet oxygen [7]. Singlet oxygen is a cytotoxic agent, and can directly kill cancer cells [7, 8]. Luckily, it exhibits a very low diffusion range of 10 to 55 nm and has a short lifetime of 10 to 320 ns, thus, limiting any damage on healthy cells in the process and reducing side effects [2].

Ideally, an effective photosensitizer should be non-toxic in the dark, chemically pure, photostable, absorb

light in the wavelength of about 600-800 nm since this region is known to be the most suitable therapeutic window for PDT, exhibit high efficiency to yield reactive oxygen species, and soluble in aqueous solutions [11-13]. Photofrin is the first clinically approved photosensitizing agent for PDT, and is actually used now to cure various cancer types [14-16]. However, its main limitations are lack of purity, low absorption of light in the wavelengths of therapeutic window, which results in poor tissue penetration, and absorption of light in the wavelengths of about 400-600 nm, which cause skin phototoxicity as a side effect [2, 7, 17]. These drawbacks have led scientists to search alternative photosensitizing agents for PDT.

Eventually, in the mid-1980s, various phthalocyanine (Pc) derivatives were proposed as second generation photosensitizing agents since they meet most of the requirements of PDT [18]. First, Pcs exhibit strong light absorption in the red and deep red wavelengths of spectrum with a maximum peak at about 700 nm, and thus, they offer enhanced skin penetration. Also, since Pcs don't exhibit a significant light absorption between 400-600 nm, their use could reduce the skin phototoxicity [2]. What's more, Pcs have a large conjugated π-system, which enhances energy and charge transfer, and hence, boosting generation of singlet oxygen [19]. On the other hand, the main drawback of Pcs is low solubility in aqueous mediums, making their transport in the body difficult [20, 21]. This is due to the extended flat hydrophobic aromatic surface of Pcs that cause their aggregation in aqueous solutions through self-interactions [20, 21]. Yet, particularly Zn, Al, and Si containing Pc derivatives are among most promising second generation photosensitizers, and even some of them are commercially available [21-25]. However, an intense research effort is still ongoing to develop third generation photosensitizing agents that could not only exhibit properties of afore-mentioned second generation photosensitizers, but also have high water solubility.

In this context, we propose that serotonin substituted Pc might be a promising candidate in terms of improving solubility without deteriorating PDT properties. This is because serotonin is a non-toxic, water-soluble (25.5 mg/mL) primary amino compound with direct roles in human metabolite [26]. Further, serotonin does not exhibit light absorption peaks in the region of 400-600 nm, and one would not expect skin phototoxicity upon its attachment to Pc [27]. Although serotonin could be expected to attach Pc towards an oxygen bridge, its free NH_2 groups can be cationized for conversion to quaternary amines. The positive charge on quaternary amines could improve water-solubility and might limit self-interactions of hydrophobic aromatic surface of Pc in aqueous solutions, hence solving aggregation problem. In this sense, we prepared serotonin substituted ZnPc (Ser-ZnPc) and quaternized serotonin substituted ZnPc (q-Ser-ZnPc) compounds, since zinc (II) phthalocyanines (ZnPcs) are the most widely studied second generation photosensitizers in PDT. Then, we investigated the solubility of as-synthesized serotonin substituted ZnPc derivatives in aqueous solutions as well as their PDT performance. Strikingly, we report that not only the water solubility, but also fluorescence quantum yield is improved in case of q-Ser-ZnPc, as compared to Ser-ZnPc. These results suggest that q-Ser-ZnPc might be useful for image-guided PDT applications.

Materials and Methods

Materials

All reactions were carried out under nitrogen atmosphere and all solvents were dried by molecular sieves or proper methods [28]. Preparation of 4-nitrophthalonitrile was carried out according to previous reports in three steps [29]. In the first step, 4-nitrophthalimide was obtained as a result of the nitration reaction of phthalimide. In the second step, 4-nitrophthalamide was obtained by treating 4-nitrophthalimide and ammonia. In the last step, 4-nitrophthalonitrile was obtained by treating 4-nitrophthalamide with thionyl chloride. Solvents and all other chemical reagents were purchased from Merck.

Characterization

FT-IR spectra were recorded on a Perkin Elmer Spectrum 100 spectrometer by preparing KBr pellets. Absorption spectra were recorded by a Shimadzu 1601 UV-Vis spectrometer. Fluorescence spectra of compounds were collected by a Shimadzu RF 5301 fluorescence spectrophotometer. ^{1}H-NMR spectra were obtained by using a JEOL 400 MHz spectrometer. Melting points are recorded on Electrothermal 9100 digital melting point apparatus.

Synthesis

Synthesis procedures are described below and schematized in Figure 1.

Synthesis of serotonin substituted phthalonitrile (1)

The 4-nitrophthalonitrile (1.0 g, 5.78 mmol) and 5-hydroxytryptamine hydrochloride (1.47 g, 6.93 mmol) were dissolved in dimethyl sulfoxide (DMSO) (20 mL). Anhydrous potassium carbonate (K_2CO_3) (2.40 g, 17.34 mmol) was added to the reaction solution over period of 2 h with efficient stirring. The reaction mixture was stirred at 40°C for 2 days. The reaction was controlled by thin layer chromatography (TLC). Then the mixture was poured into a solution of salt-water (1%), and the precipitate was filtered off, washed with water and dried in vacuum oven at 40°C. Crude products were purified by column chromatography on silica gel using tetrahydrofuran (THF) and chloroform ($CHCl_3$) (50:10). Finally, a light yellow solid was obtained and found to be soluble in $CHCl_3$, THF, acetone, methanol (MeOH), N,N-dimethylformamide (DMF) and DMSO. Yield 750 mg (43%). Mp: 205°C. ^{1}H-NMR (400 MHz, $CDCl^3$, 25°C): δ= 10.7 (s, 3H, N-H); 7.3-7.0 (m, 7H, Ar-H); 2.6 (s, 4H, Aliphatic-H). FT-IR (KBr pellet) υ (cm^{-1}) 3444; 3122; 3028; 2244; 1572; 1251;760. Anal. Calc. for $C_{18}H_{14}N_4O$: C, 71.51; H, 4.67; N, 18.53%, found: C, 71.43; H, 4.60; N, 18.49%.

Synthesis of serotonin substituted zinc(II) phthalocyanine (Ser-ZnPc) (2)

Compound **1** (100.0 mg, 0.33 mmol) and dry zinc(II) acetate ($Zn(CH_3COO)_2$) (15.17 mg, 0.08 mmol) in DMF (2 mL) was heated at 180°C for 12h in the presence of 1,8-Diazabicyclo[5.4.0]undec-7-ene (DBU). After cooling, the mixture was precipitated with MeOH, filtered off and dried in vacuum. The dark green compound was dissolved in THF and filtered off. The THF solution was passed over a silica gel column. The organic phase was precipitated with diethyl ether and filtered off and dried in vacuum. Finally, a dark green solid was obtained and found to be soluble in $CHCl_3$, THF, DMF and DMSO. Yield 32.0 mg (37%). Mp: >300°C. ^{1}H-NMR ($CDCl_3$, 400 MHz): δ= 8.2-7.00 (br m, 28H, Ar-H); 2.92 (s, 16H, $-CH_2$); 9.8 (br s, 3H, N-H, disappeared on D_2O addition). UV-Vis (DMSO) λ_{max}/nm 679, 608, 350. FT-IR (KBr pellet) υ (cm^{-1}) 3429; 3052; 2856; 1599; 1308; 764. Anal. Calc. for $C_{54}H_{56}N_{16}O_4Zn$: C, 61.27; H, 5.33; N, 21.17%, found: C, 60.95; H, 5.26; N, 21.08%.

Synthesis of quaternized serotonin substituted zinc(II) phthalocyanine (q-Ser-ZnPc) (3)

The solution of compound **2** (100.0 mg, 0.09 mmol) in $CHCl_3$ (2 mL) was added methyl iodide (CH_3I) (1.0 mL) and stirred at 40°C for 48 hours. After cooling, the organic phase was precipitated with diethyl ether and filtered. The solid was then washed with diethyl ether (2x 5mL) and dried in vacuum. Finally, a green solid was obtained and found to be soluble in water. Yield 88.0 mg (57%). Mp: >300°C. ^{1}H-NMR ($CDCl_3$, 400 MHz): δ= 8.10-7.00 (br m, 28H, Ar-H); 2.86 (s, 16H, $-CH_2$); 9.5 (br s, 3H, N-H, disappeared on D_2O addition); 1.36 (s, 12H, $N-CH_3$). UV-Vis (DMSO) λ_{max}/nm 688, 613, 351. FT-IR (KBr pellet) υ (cm^{-1}) 3420; 3180; 2816; 1603; 1311; 767.

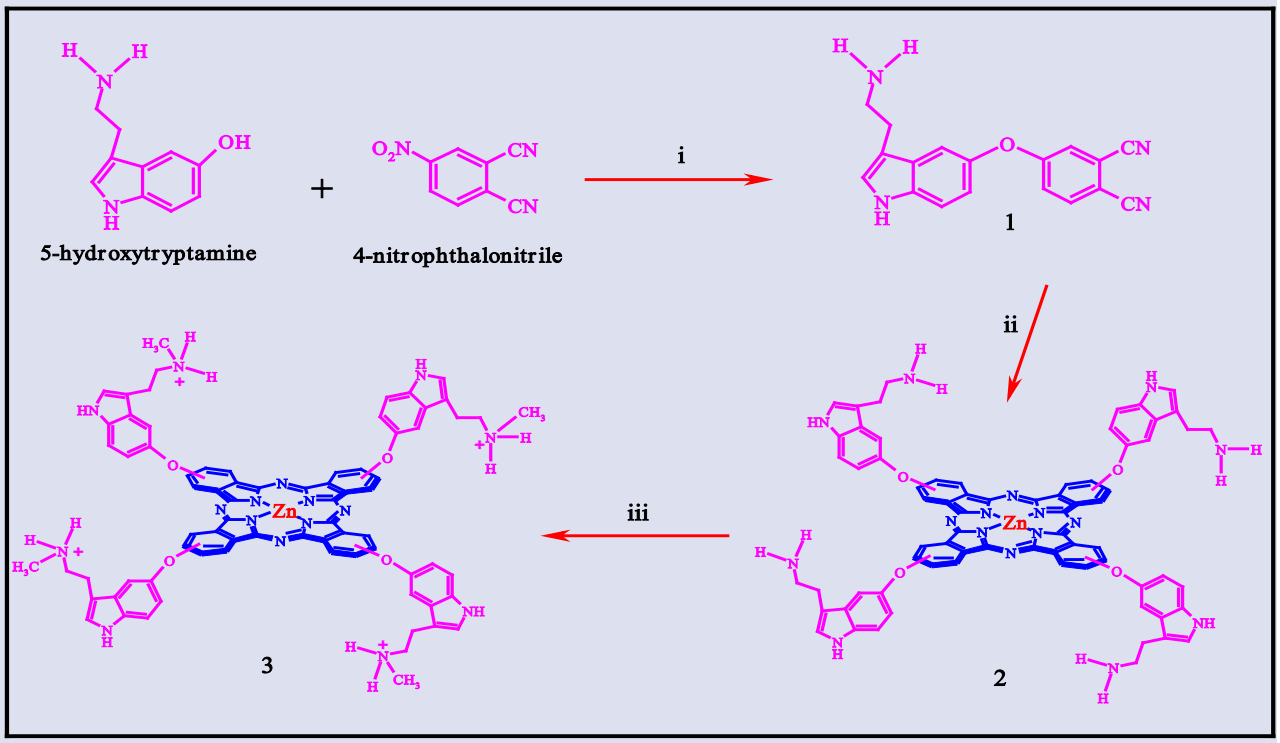

Figure 1. Synthesis of Compounds (i: dry DMSO, 2 days, K_2CO_3, 40°C, ii: dry DMF, zinc acetate, DBU, 12h, 180°C, iii: $CHCl_3$, CH_3I, 48h, 40°C).

Results and Discussion

Serotonin substituted phthalonitrile derivative (Compound 1) was synthesized by the nucleophilic substitution reaction of 4-nitrophthalonitrile and 5-hydroxytryptamine hydrochloride in DMSO in the presence of K_2CO_3. The Compound 1 was then purified by column chromatography with silica gel. The Ser-ZnPc (Compound 2) was obtained by tetramerization reaction of compound 1 with $Zn(CH_3COO)_2$. The q-Ser-ZnPc (Compound 3) was synthesized by the quaternization reaction of Ser-ZnPc. The FT-IR, UV-Vis, ^{1}H-NMR, and elemental analysis results confirmed the proposed structure of new compounds.

The characteristic vibration band of the -C≡N group appeared at 2244 cm^{-1} in the IR spectrum of compound 1 and it disappeared after conversion to Ser-ZnPc (Figure 2) [30]. The peaks corresponding to aliphatic C-H groups were realized at 3122-3028 cm^{-1}, 3052-2856 cm^{-1} and 3180-2816 cm^{-1} in the FT-IR spectra of synthesized compounds 1-3, respectively [31]. Also, the peak at 3444-3420 cm^{-1} was ascribed to the stretching vibration of N-H, the peak at 1603-1572 cm^{-1} was ascribed to the stretching

vibration of C=C, and the peak at 1311-1251 cm^{-1} was ascribed to the stretching vibration of Ar-O-C [31]. Finally, a peak for the substituted benzene ring was observed at 767-764 cm^{-1} in all compounds [31].

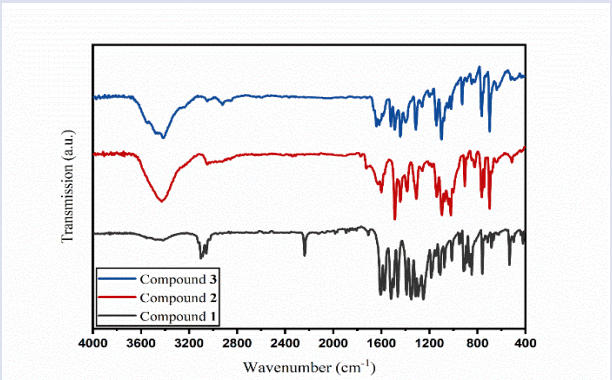

Figure 2. The FT-IR spectra of compounds 1, 2 and 3.

The characteristic absorptions were observed in the Q-band (650-700 nm) and B-band (300-400 nm) region in the UV-Vis spectra (Figure 3) of Ser-ZnPc and q-Ser-ZnPc in DMSO, as expected [31]. The characteristic Q-band is due to the π–π* transition of the Pc ring from Highest Occupied Molecular Orbital (HOMO) to Lowest Unoccupied Molecular Orbital (LUMO), while the characteristic B-band is due to deep π–π* transitions [33]. Specifically, the Ser-ZnPc and q-Ser-ZnPc show characteristic Q-bands of metallophthalocyanines at around 679 nm and 688 nm, respectively. In addition, B-bands of the compounds Ser-ZnPc and q-Ser-ZnPc appeared at around 350 nm and 351 nm, respectively. The formation of these peaks confirms the formation of Pc structure as a result of the tetramerization reaction. The UV-Vis spectra of Ser-ZnPc and q-Ser-ZnPc in DMSO show that the absorption wavelength was redshifted after the quaternization of Ser-ZnPc. Importantly, the increase in the absorption wavelength might be an indicator of a more effective PDT performance for q-Ser-ZnPc. More importantly, we report that the q-Ser-ZnPc is soluble in water. This feature is especially important in PDT applications, as it could allow easier transportation of the photosensitizer to the target in the body. Also, the redshift of the Q-band peak was found to be more pronounced in H_2O as compared to DMSO (Figure 3). This suggests that there might be a possibility of H-bond formation between q-Ser-ZnPc and water molecules.

In the ^{1}H-NMR spectrum of compound 1 which was taken in $CDCl_3$ at room temperature, the aromatic protons and aliphatic protons appeared at 7.30-7.00 ppm and at 2.60 ppm, respectively. The ^{1}H-NMR spectra of compounds Ser-ZnPc and q-Ser-ZnPc showed aromatic protons at 8.20-7.00 ppm and 8.10-7.00 ppm, aliphatic protons at 2.90 ppm and 2.86 ppm, respectively [34]. In addition, the ^{1}H-NMR spectrum of q-Ser-ZnPc showed N-CH_3 protons at 1.36 ppm [31].

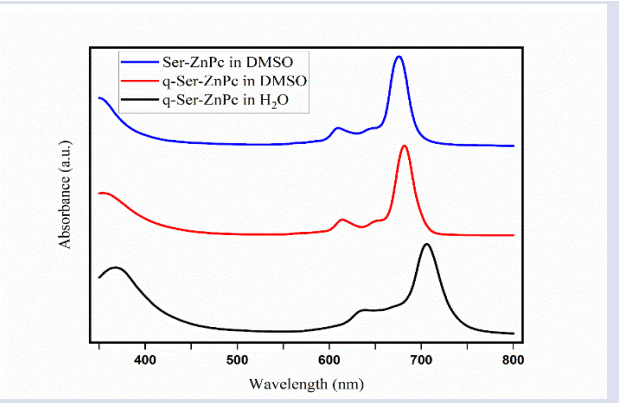

Figure 3. UV-Vis spectra of Ser-ZnPc and q-Ser-ZnPc in various solvents.

Finally, the -NH protons of compounds 1-3 appeared as singlets at 10.70 ppm, 9.80 ppm and 9.50 ppm, respectively, all of which disappeared after the D_2O exchange, as expected [34]. The integration of ^{1}H-NMR peaks are correlated with structure of compounds.

Elemental analysis was conducted experimentally and theoretically, both of which are in harmony with the proposed structures of compounds 1-3 in Figure 1.

The fluorescence quantum yield (Φ_F) is an important parameter in PDT applications. Thus, we measured the fluorescence emission spectra and calculated the fluorescence quantum yields of Ser-ZnPc and q-Ser-ZnPc by using Equation 1 [34]:

$$\Phi_F = \Phi_{F_{(std)}} \frac{F.A_{std}.n^2}{F_{std}.A.n_{std}^2} \quad (1)$$

where Φ_F symbolizes the fluorescence quantum yield of the unknown sample, and $\Phi_{F(std)}$ symbolizes the fluorescence quantum yield of the standard compound used in the measurement. The A and A_{std} in the Equation 1 symbolize the absorbance of the sample and the standard at the excitation wavelength, respectively. The n and n_{std} in the Equation 1 are the refractive indices of the solvents used for the sample and the standard, respectively. Unsubstituted ZnPc (Φ_F=0.18 in DMSO) was used as the standard in the measurements.

Table 1. Spectral data comparison for Ser-ZnPc and q-Ser-ZnPc.

Compound	Solvent	Q-band λ (nm)	Emission λ (nm)	Φ_F
Ser-ZnPc	DMSO	679	686	0.30
q-Ser-ZnPc	DMSO	688	690	0.42
q-Ser-ZnPc	H_2O	707	709	0.37

As can be seen in Figure 4 and Table 1, the absorption and emission spectra of q-Ser-ZnPc are shifted to higher wavelengths in H_2O comparing to DMSO. This shift can be explained by the tendency to H-bonding formation

between the functional groups of q-Ser-ZnPc and H_2O molecules [35]. The Φ_F of unsubstituted ZnPc, Ser-ZnPc and q-Ser-ZnPc in DMSO were found to be 0.18, 0.30, and 0.42, respectively. Also, it was observed that the Φ_F of both Ser-ZnPc and q-Ser-ZnPc are higher than that of unsubstituted ZnPc. At the same time, it was also observed that the Φ_F tended to increase after the quaternization. As it is known, a simultaneous combination of high Φ_F and singlet oxygen quantum yield (Φ_Δ) is sought for image-guided PDT applications [36-38]. However, it is difficult in most cases to reach a high Φ_Δ while concurrently maintaining the Φ_F at acceptable levels for real-time image guidance. Although we couldn't measure the Φ_Δ of q-Ser-ZnPc, a considerable increase of the Φ_F after quaternization might be beneficial for image-guided PDT, particularly if the Φ_Δ of q-Ser-ZnPc is also high. Adding this to the our observations that absorption peaks of q-Ser-ZnPc are within the therapeutic window (600-800 nm), and more importantly the q-Ser-ZnPc is water soluble, it could be beneficial to identify the Φ_Δ of q-Ser-ZnPc in the future for the progress of PDT field.

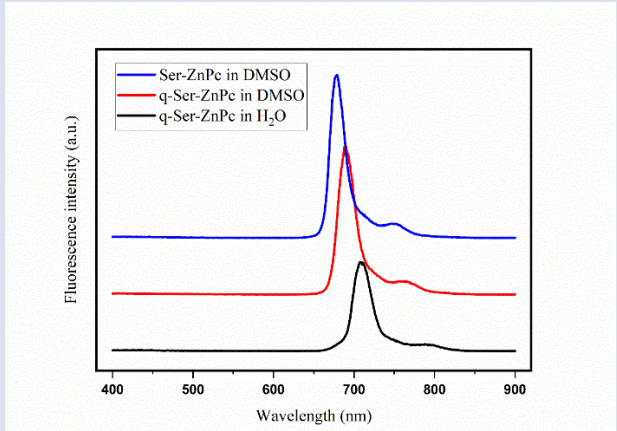

Figure 4. Emission spectra of compounds 2 and 3 in various solvents.

Regarding other factors that could affect emission spectra and fluorescence quantum yields, we also studied the effects of solvent selection and concentration. In particular, the emission spectra provide information about the fluorophore-solvent interaction, as the solvent and fluorophore molecule interactions affect the energy difference between the ground and excited states [35, 39]. Therefore, we used THF, $CHCl_3$, DMF and DMSO as solvents, in which Ser-ZnPc is readily soluble as can be seen in Figure 5. Importantly, we report that the Φ_F is increasing with a decrease of solvent polarity, since the polarities of these solvents increase in the order of THF<$CHCl_3$<DMF<DMSO, as listed Table 2 [40]. Likewise, the emission maximum shifted to shorter wavelengths with a decrease in solvent polarity [35, 39]. The variation of Φ_F with concentration was also investigated for compound 2 as illustrated in Figure 6 [39]. The results suggest no change in emission wavelength, but the Φ_F was found to be decreasing with a decrease in concentration in all of the solvents studied in this work (Figure 6).

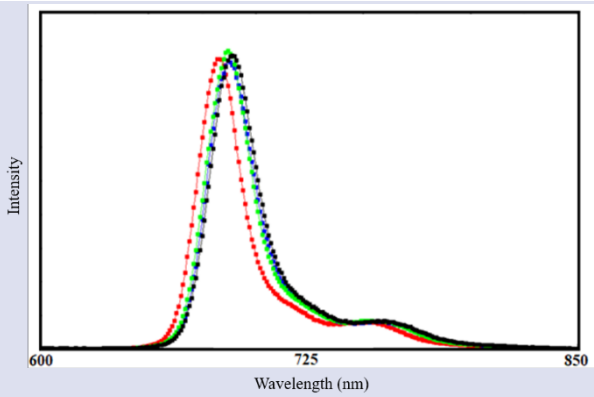

Figure 5. Emission spectra of Ser-ZnPc in various solvents (THF: red, $CHCl_3$: green , DMF: black, DMSO: blue).

Table 2. Spectral data for Ser-ZnPc in different solvents

Solvent	Dipole moment of solvents (μ)	Q-band λ (nm)	Emission λ (nm)	Φ_F
THF	1.69	673	680	0.39
$CHCl_3$	1.90	675	683	0.36
DMF	3.79	676	690	0.32
DMSO	3.96	679	686	0.30

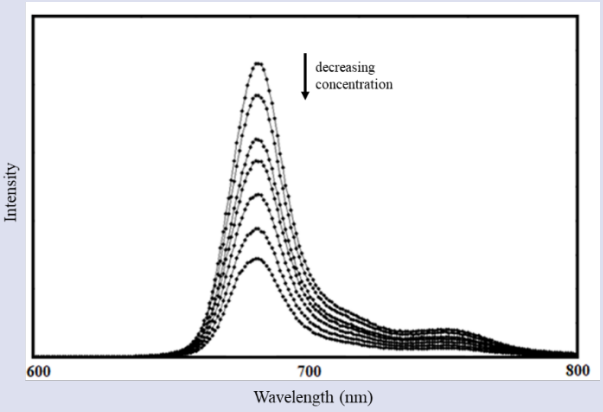

Figure 6. Emission spectra of Ser-ZnPc at various DMSO concentrations.

Conclusions

ZnPc is one of the most widely studied Pc-based photosensitizer materials in PDT applications. However, the main drawback of ZnPc that limits its application areas in PDT is the materials' poor water solubility that hinders its effective transfer to the target in the body. Accordingly, we synthesized serotonin substituted and quaternized serotonin substituted ZnPc to improve water solubility. The idea is that the positive charge on quaternary amines might limit self-interactions of the hydrophobic aromatic surface of Pc in aqueous solutions, and enhance the water-solubility. To do this, serotonin substituted phthalonitrile derivative was first synthesized by the nucleophilic substitution reaction of 4-nitrophthalonitrile and 5-hydroxytryptamine hydrochloride. Following this, serotonin substituted zinc(II) phthalocyanine (Ser-ZnPc)

was prepared by cyclotetramerization of serotonin substituted phthalonitrile. Finally, the Ser-ZnPc was quaternized to obtain q-Ser-ZnPc. The synthesized compounds were characterized by ^{1}H-NMR, UV-Vis, FT-IR, fluorescence, and elemental analysis. The results show that while unsubstituted ZnPc and Ser-ZnPc are not water-soluble, q-Ser-ZnPc is actually soluble in water. In addition, the absorption bands of q-Ser-ZnPc are within the so-called therapeutic window. Moreover, we report that the Φ_F of q-Ser-ZnPc is higher than that of both Ser-ZnPc and ZnPc. As it is known, a combination of both high Φ_F and Φ_Δ is necessary for image-guided PDT, and thus, q-Ser-ZnPc might become a promising candidate in PDT applications if it also exhibits a high Φ_Δ.

Conflict of interest

There are no conflicts to declare.

References

[1] WHO (2022). "Cancer". (Accessed: 10.03.2022) Available from:https://www.who.int/news-room/factsheets/detail/cancer#:~:text=Cancer%20is%20a%20leading%20cause,and%20rectum%20and%20prostate%20cancers.

[2] Borzecka W., Dominski A., Kowalczuk M., Recent Progress in Phthalocyanine-Polymeric Nanoparticle Delivery Systems for Cancer Photodynamic Therapy, *Nanomaterials (Basel),* 11(9) (2021) 2426-2458.

[3] Baykara O., Current Therapies and Latest Developments in Cancer Treatment, in Horizons in Cancer Research, Watanabe H. S., Editor., *Nova Science Publishers*, 57 (2015) 105-157.

[4] Monje M., Dietrich J., Cognitive side effects of cancer therapy demonstrate a functional role for adult neurogenesis, *Behav. Brain. Res.*, 227(2) (2012) 376-379.

[5] De Annunzio S.R., Costa N.C.S., Mezzina R.D., Graminha M. A. S., Fontana C.R., Chlorin, Phthalocyanine, and Porphyrin Types Derivatives in Phototreatment of Cutaneous Manifestations: A Review, *Int. J. Mol. Sci*, 20(16) (2019) 3861-3882.

[6] Hong E.J., Choi D.G., Shim M.S., Targeted and effective photodynamic therapy for cancer using functionalized nanomaterials, *Acta Pharm. Sin. B*, 6(4) (2016) 297-307.

[7] Wang X., Luo D., Basilion J.P., Photodynamic Therapy: Targeting Cancer Biomarkers for the Treatment of Cancers, *Cancers (Basel)*, 13(12) (2021) 2992-3010.

[8] Xu Y., Tan Y., Ma X., Jin X., Tian Y., Li M., Photodynamic Therapy with Tumor Cell Discrimination through RNA-Targeting Ability of Photosensitizer, *Molecules*, 26(19) (2021) 5990-6012.

[9] Lin L., Xiong L ., Wen Y ., Lei S., Deng X., Liu Z., Chen W., Miao X., Active Targeting of Nano-Photosensitizer Delivery Systems for Photodynamic Therapy of Cancer Stem Cells, *J. Biomed. Nanotechnol.*, 11(4) (2015) 531-554.

[10] Liu D., Cancer biomarkers for targeted therapy, *Biomark. Res.*, 7 (2019) 25-31.

[11] Yoon I., Li J.Z., Shim Y.K., Advance in photosensitizers and light delivery for photodynamic therapy, *Clin. Endosc.*, 46(1) (2013) 7-23.

[12] Allison R.R., Sibata C.H., Oncologic photodynamic therapy photosensitizers: a clinical review, *Photodiagnosis Photodyn. Ther.*, 7(2) (2010) 61-75.

[13] Chen Q., Dan H., Tang F., Wang J., Li X., Cheng J., Zhao H., Zeng X., Photodynamic therapy guidelines for the management of oral leucoplakia, *Int. J. Oral. Sci.*, 11(2) (2019) 14-18.

[14] Lightdale C.J., Role of Photodynamic Therapy in the Management of Advanced Esophageal Cancer, *Gastrointestinal Endoscopy Clinics of North America*, 10(3) (2000) 397-408.

[15] Schweitzer V.G., Photofrin-mediated photodynamic therapy for treatment of early stage oral cavity and laryngeal malignancies, *Lasers Surg. Med.*, 29(4) (2001) 305-313.

[16] Ormond A.B., Freeman H.S., Dye Sensitizers for Photodynamic Therapy, *Materials (Basel)*, 6(3) (2013) 817-840.

[17] Lo P.C., Rodríguez-Morgade M. S., Pandey R. K., Ng D.K. P., Torres T ., Dumoulin F., The unique features and promises of phthalocyanines as advanced photosensitisers for photodynamic therapy of cancer, *Chem. Soc. Rev.*, 49(4) (2020) 1041-1056.

[18] Ben-Hur E., Rosenthal I., The phthalocyanines: a new class of mammalian cells photosensitizers with a potential for cancer phototherapy, *Int. J. Radi. Biol. Rel. Stu. Phys., Chem.Med.*, 47(2) (1985) 145-147.

[19] Mehraban N., Freeman H.S., Developments in PDT Sensitizers for Increased Selectivity and Singlet Oxygen Production, *Materials (Basel)*, 8(7) (2015) 4421-4456.

[20] Bian Y., Chen J., Xu S., Zhou Y., Zhu L., Xiang Y., Xia D., The effect of a hydrogen bond on the supramolecular self-aggregation mode and the extent of metal-free benzoxazole-substituted phthalocyanines, *New J. Chem.*, 39(7) (2015) 5750-5758.

[21] de la Escosura A., Martı´nez-Dı´az M. V., Thordarson P., Rowan A. E., Nolte R.J.M., Torres T., Donor-Acceptor Phthalocyanine Nanoaggregates, *J. Am. Chem. Soc.*, 125(40) (2003) 12300-12308.

[22] Ma D., Ma D., Chen X., Wang Y., Guo Q., Ye Q., Guo R., Xiao S., Ye Q., Huang Y., Peng Y., Benzyl ester dendrimer silicon phthalocyanine based polymeric nanoparticle for in vitro photodynamic therapy of glioma, *J. Lumin.*, 207 (2019) 597-601.

[23] Makhseed S., Machacek M., Alfadly W., Tuhl A., Vinodh M., Simunek T., Novakova V., Kubat P., Rudolf E., Zimcik P., Water-soluble non-aggregating zinc phthalocyanine and in vitro studies for photodynamic therapy, *Chem. Commun.*, 49(95) (2013) 11149-11151.

[24] Idowu M., Nyokong T., Photophysical and photochemical properties of zinc and aluminum phthalocyanines in the presence of magnetic fluid, *J. Photochem. Photobiol. A*, 188(2) (2007) 200-206.

[25] Carobeli L.R., Meirelles L.E.F., Damke G., Damke E., Souza M.V.F., Mari N.L., Mashiba K.H., Shinobu-Mesquita C.S., Souza R.P., da Silva V.R.S., Gonçalves R.S., Caetano W., Consolaro M.E.L., Phthalocyanine and Its Formulations: A Promising Photosensitizer for Cervical Cancer Phototherapy, *Pharmaceutics*, 13(12) (2021) 2057-2084.

[26] Ubuka T., 131D Serotonin. In: Ando H, Ukena K, Nagata S, editors. Handbook of Hormones: Comparative Endocrinology for Basic and Clinical Research, 2nd Ed. *Academic Press*; (2021) 1049.

[27] Hernandez-Mendoza G.A., Aguirre-Olivas D., Gonzalez-Gutierrez M., Leal H.J., Qureshi N., Trevino-Palacios C.G., Peón J., De-Miguel F.F., Fluorescence of serotonin in the visible spectrum upon multiphotonic photoconversion, *Biomed. Opt. Express*.,11(3) (2020) 1432-1448.

[28] Armarego W.L.F., Chai C.L.L., Purification of Laboratory Chemicals, 5 third ed., Tokyo: Butterworth/Heinemann, (2003).

[29] Young J.G., Onyebuagu W., Synthesis and Characterization of Di-disubstituted Phthalocyanines, *J. Org. Chem.*, 55 (1990) 2156-2158.

[30] Granados-Tavera K., Zambrano-Angulo M., Montenegro-Pohlhammer N., Yaşa-Atmaca G., Sobotta L., Güzel E., C´ardenas-Jir´on G., Erdoğmuş A., Gürek A. G., Synergistic effect of ultrasound and light to efficient singlet oxygen formation for photodynamic purposes, *Dye Pigments*, 210 (2023) 110986-110995.

[31] Yabaş E., Bağda E, Bağda E., The water soluble ball-type phthalocyanine as new potential anticancer drugs, *Dyes Pigment.*, 120 (2015) 220-227.

[32] Yabaş E., Sülü M., Saydam S., Dumludağ F., Salih B., Bekaroğlu Ö., Synthesis, characterization and investigation of electrical and electrochemical properties of imidazole substituted phthalocyanines, *Inorg. Chem. Acta*, 365 (2011) 340-348.

[33] Günsel A., Kırbaç E., Tüzün B., Erdoğmuş A., Bilgiçli, A. T., Yaraşır M. N., Selective chemosensor phthalocyanines for Pd^{2+} ions; synthesis, characterization, quantum chemical calculation, photochemical and photophysical properties, *J. Mol. Struct.*, 1180 (2019) 127-138.

[34] Mısır M. N., Mısır G., Bekircan O., Kantekin H., Öztürk D., Durmuş M., Sulfur bridged new metal-free and metallo phthalocyanines carrying 1,2,4-triazole rings and their photophysicochemical properties, *Polyhedron*, 207 (2021) 115361-115369.

[35] Nagaraja D., Melavanki R.M., Patil N.R., Kusanur R.A., Solvent effect on the relative quantum yield and fluorescence quenching of 2DAM, *Spectrochim. Acta Part A*, 130 (2014) 122-128.

[36] Zou J., Yin Z., Wang P., Chen D., Shao J., Zhang Q., Sun L., Huang W., Dong X., Photosensitizer synergistic effects: D–A–D structured organic molecule with enhanced fluorescence and singlet oxygen quantum yield for photodynamic therapy, *Chem. Sci.*, 9 (2018) 2188-2194.

[37] Huang Y-Q., Liu K-L., Ni H-L., Zhang R., Liu X-F., Fan Q-L., Wang L-H., Huang W., Organic Theranostic Nanoplatform with Enhanced Fluorescence and Singlet Oxygen Quantum Yield for Tumor-Targeting Image-Guided Photodynamic/Photothermal Synergistic Therapy, *ACS Appl. Polym. Mater.*, 4 (2022) 7739-7750.

[38] Mai D.K., Kim C., Lee J., Vales T.P., Badon I.W., De K., Cho S., Yang J., Kim H-J., BODIPY nanoparticles functionalized with lactose for cancer-targeted and fluorescence imaging-guided photodynamic therapy, *Sci. Rep.*, 12 (2022) 2541.

[39] Bindhu C. V., Harilal S. S., Nampoori V. P. N., Vallabhan C. P. G., Solvent Effect On Absolute Fluorescence Quantum Yield Of Rhodamine 6g Determined Using Transient Thermal Lens Technique, *Modern Physics. Letters B*, 13 (1999) 563-576.

[40] Ogunsipe A., Maree D., Nyokong T., Solvent effects on the photochemical and fluorescence properties of zinc phthalocyanine derivatives, *J Mol. Struct.*, 650 (2003) 131-140.

Cumhuriyet Sci. J., 44(1) (2023) 106-111
DOI: https://doi.org/10.17776/csj.1228170

Cumhuriyet Science Journal

| csj.cumhuriyet.edu.tr | Founded: 2002 ISSN: 2587-2680 e-ISSN: 2587-246X Publisher: Sivas Cumhuriyet University

Development of Halloysite Loaded Polypropylene Sutures with Enhanced Mechanical and Thermal Properties

Fadime Nülüfer Kıvılcım [1,a,*]

[1] *Chemistry Department, Faculty of Arts and Science, İnönü University, Malatya, 44280, Türkiye.*
**Corresponding author*

Research Article

History
Received: 02/01/2023
Accepted: 16/03/2023

ABSTRACT

Polypropylene is a crucial polymeric material in modern life, especially in the packaging and food industry, as well as the biomedical field. This study aimed to enhance the mechanical properties of polypropylene structures used as surgical suture material by preparing polypropylene-halloysite (PP-halloysite) composites. Halloysite was added in varying amounts (1%, 3%, 5%, and 10%) to polypropylene, and the resulting composites were passed through a double heated extruder. Structural characterization of the PP-halloysite composites was carried out using Fourier Transform Infrared Spectroscopy (FTIR), elemental analysis, Scanning Electron Microscopy-Energy Dispersive X-Ray Analysis (SEM-EDX), Differential Thermal Analysis (DTA), Thermogravimetric Analysis (TGA)), and Differential Scanning Calorimetry (DSC) techniques to determine their thermal properties and softening temperatures. Mechanical tests were conducted to examine the composite suture structures obtained and determine the effect of halloysite doping on their mechanical properties. The results of the mechanical tests showed that the mechanical strength of the fiber structure increased with the amount of halloysite added. Therefore, the PP-halloysite suture structures could be used as non-melting suture material, especially in surgeries that require high strength compared to pure polypropylene structures.

Keywords: Polypropylene, Halloysite, Polypropylene composites, Suture mechanic properties.

[a] *Nilufer.kivilcim@inonu.edu.tr* *https://orcid.org/0000-0002-6017-5326*

Introduction

Medical suture materials are of critical importance, especially in terms of surgical applications, for the healthy termination of surgical applications [1,2]. The suture materials to be used in a healthy surgical operation must be biocompatible materials with high mechanical strength, structural and thermal stability [3]. In addition, some variable properties are requested in suture materials to be used in in-body and extra-body applications [4,5]. For example, while mechanical properties come to the fore in extracorporeal applications, features such as biocompatibility and being unaffected by body fluids come to the fore in intrabody applications. However, the suture materials to be used in surgeries such as tendons and hernias must show high mechanical strength as well as structural stability [6]. Therefore, many suture materials have been used up to now. Such as nylon [7,8], polyester[9], polypropylene [10], polyvinylenedifluoride [11], polydioxanone [12] are frequently preferred suture structures. Among these suture structures, Catgut and Silk are natural compounds. Polypropylene, polyamide, polydioxane, polyglycolic acid/polylactic acid and polyglycolic acid/polytrimethylene carbomate structures are synthetically produced structures. Silk, polypropylene, polyamide and stainless steel structures are permanent structures that are not self-absorbed. Other structures are dissolved in the body after ingestion. However, polypropylene is a highly preferred suture structure due to its high biocompatibility, low toxicity, high breaking resistance and high mechanical strength as monofilament compared to multi-filament structures.

In recent years, biodegradable polymers have started to be used as suture material, as well as such polymers. Polylactic acid [13,14], polyglycolic acid [15], poly(lactic-co-glycolic acid) copolymers [16], poly(ε-caprolactone) and poly(ε-caprolactam) [17] structures are frequently used in in-body applications. Since these structures have the property of dissolving in the body, there is no need for a second intervention after the surgery. Suture structures of different diameters and lengths are used according to the place of use, the purpose of use and the size of the wound. The diameter of the suture materials varies between 0.01 and 0.799 mm. Suture structures with high mechanical strength, such as polypropylene and nylon, are still used in many surgical operations today [18,19]. It is one of the most popular surgical suture materials, especially because of its polypropylene suture structures, non-adherent properties and not being affected by body fluids. Polypropylene sutures are widely used especially in vascular surgery because they are resistant to repeated torsion and do not contain monomer residues [20]. Since polypropylene can be produced as very thin, it has a structure that does not leave traces and does not stretch the tissue, therefore it is especially preferred in sports surgeries, meniscus and tendon surgeries. For this reason, it is necessary to restrict the movement of the polypropylene structure due to stretching and increase its mechanical strength in muscle tears and menisci that

require excessive movement. For this purpose, different additives were tested. Among these additives are structures such as carbon nanotubes, silica and chitosan. Within the scope of this study, the halloysite structure was used to increase the mechanical properties of polypropylene suture structures. Fiber structure in halloysite increased the secondary interactions between polypropylene chains and provided significant increases in mechanical properties. Depending on the increase in the amount of halloysite, the changes in the mechanical properties were interpreted.

Halloysite has a 2:1 structure and a tubular-wrapped clay structure showing phyllosilicate properties. The smooth tubular morphology leads to a reduction in size and an increase in efficiency in the resulting composites [21, 22]. Pure halloysite and halloysite composites are used in the production of biomedical gels and biomedical absorbents, enzyme immobilization, wound dressing materials, drug release systems and preparation of bone cement due to their biocompatibility. All of these applications are proof that halloysite structures provide the biocompatibility required for biomedical applications [23]. Halloysite has a large surface area due to its tubular structure. Depending on the increased surface area, the interaction between the matrix and the additive will increase in the composite structure, so the improvements in the mechanical properties will be quite high. Therefore, halloysite structure was preferred in this study to increase the mechanical properties of suture structures instead of organic inorganic nanomaterials with similar structures. PP-based suture structures are widely used in medical surgical operations. They have frequently preferred suture structures, especially due to their biocompatibility and low cytotoxicity. Halloysite added to the structure in this study is clay with high biocompatibility. In the study, an additional toxicity and biocompatibility test was not needed for two-component composites with high biocompatibility and low cytotoxicity. Within the scope of this study, the effect of this fairly new type of clay on polypropylene suture structures was studied in detail in terms of mechanical, thermal and morphological aspects. Its usability as a suture material has been commented on.

Materials and Methods

Materials

Halloysite structure used in this study was obtained from Sigma Aldrich Company and its metric dimensions are 30-70 nm × 1-3 µm and cation exchange capacity is 8.0 meq/g. The polypropylene was obtained from Exxon Mobil Company. The commercially available ExxonMobil™ PP3155E5 product for medical applications has a density of 0.900 g/cm³ and a melting point of 230 °C.

Characterization

Structural characterization of polypropylene-halloysite composites was determined by FTIR spectroscopy method. Perkin Elmer Spectrum 2 model FTIR spectrophotometer was used in the FTIR analysis. Analyses were performed in ATR mode, and spectra were recorded in the range of 400-4000 cm^{-1}.

DTA, DSC devices were used to analyse the thermal properties of composites. DTA measurements were carried out to determine the thermal strength of the composite structures obtained within the scope of this study. DSC analyses were performed to interpret the effects of halloysite added to the structure on the flexibility and glass transition temperature of the composite. The thermal stability of the composite structures was measured using the Shimadzu DTA-50 instrument. This analysis was performed against aluminium oxide reference material at a heating rate of 10 mg sample at 10 °C/min. The softening temperatures and glass transition temperature (Tg) of polymeric composite structures were measured with a Shimadzu DSC-60 model calorimeter. In these analyses, a heating rate of 5 °C/min and 5 mg sample were used. The samples to be analysed were studied in aluminium pans with alpha alumina reference material in a static air atmosphere at the range of 30-500 °C.

Mechanical Test

The mechanical properties of pure PP and halloysite added PP composite structures produced within the scope of the study were determined by MTS-Exceed model E42 mechanical test analyser. These analyses were performed at room temperature and at approximately 30% relative humidity. Measurement samples were used in a cylindrical geometry of 120 x 0.11 mm.

The Preparation of Polypropylene-Halloysite Composites

Polypropylene halloysite composites were obtained by adding 1%, 3, 5 and 10% halloysite into 10 g of polypropylene and passing it through a double heated extruder set at 220^{0}C.

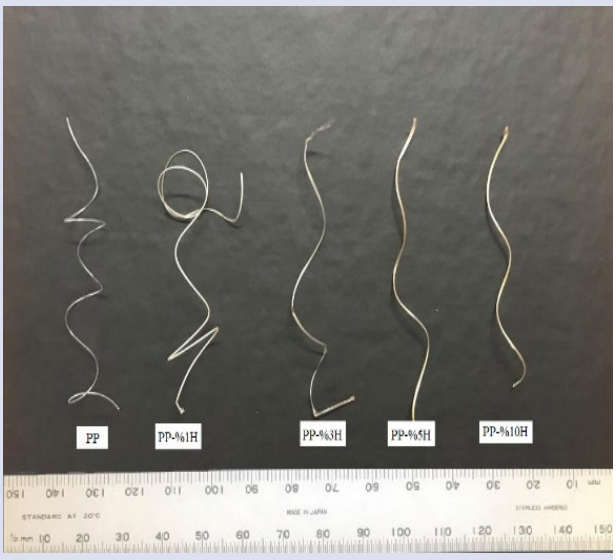

Figure 1. PP- Halloysite suture materials

Result and Discussion

Structural Characterization of Halloysite-Based PP Sutures

Structural characterization of PP-Halloysite composites obtained in this study was carried out by FTIR.

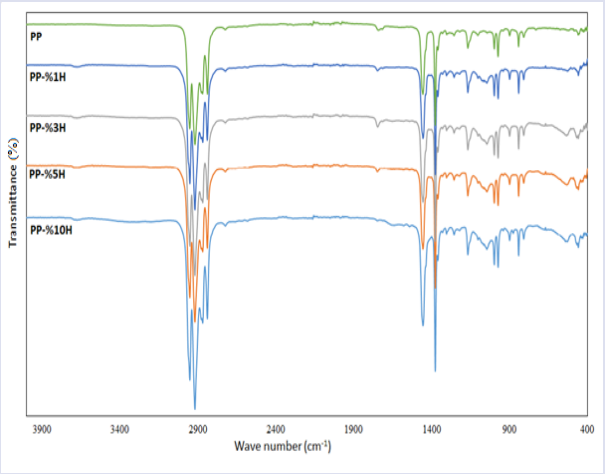

Figure 2. FTIR spectra of PP- Halloysite composites

In the FTIR spectrum given in Figure 2, the peak between 2850-2950 cm^{-1} is aliphatic C-H stretching vibrations and originates from the CH_2-CH groups on the polyprophylene main chain. The peaks at 2800-2830 cm^{-1} are the C-H aliphatic stretching vibrations of the CH_3 group in the side groups. The peak seen at 1450 cm^{-1} shows the C-C stretching vibration on the main chain, and the C-C bending vibration at 1380 cm^{-1}, C-H asymmetric stretching at 875 cm^{-1}, C-H out-of-plane bending at 825 cm^{-1} and C-H swinging peaks at 475 cm^{-1} belong to polypropylene. With the inclusion of halloysite in the structure, the Si-O-Si peak around 1000-1100 cm^{-1} appears as a band. Absorption bands at 3600 cm^{-1} in the FTIR spectrum belong to the tensile vibration originating from the inner surfaces of the O-H groups of halloysite. Furthermore, with the rise in the amount of halloysite in the composite, the peak due to Si-O at 550 cm^{-1} increases. Also, the inner Si-O stretching vibrations at 1039cm^{-1} demonstrate the increase of halloysite amount.

3.2. Thermal Properties of Halloysite- Based PP Sutures

From the DTA thermograms given in Figure 3, the classical melting peak of polypropylene at 160-180°C is seen. Starting from 220°C, two-stage decay is observed. It is seen that the peak area of the degradation peak decreases with the addition of halloysite to the polypropylene structure. Because while the amount of polypropylene in the structure decreases, the amount of halloysite increases.

From the DSC thermograms given in Figure 4, melting peaks of polypropylene at 180°C are seen.

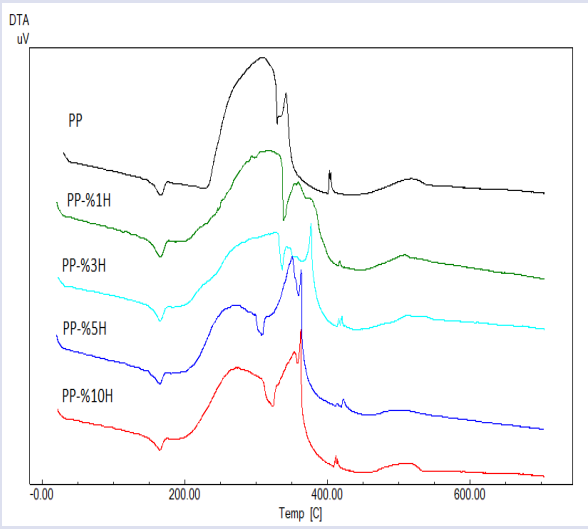

Figure 3. DTA thermograms of pure PP suture structure and sutures with PP-Halloysite composite structure.

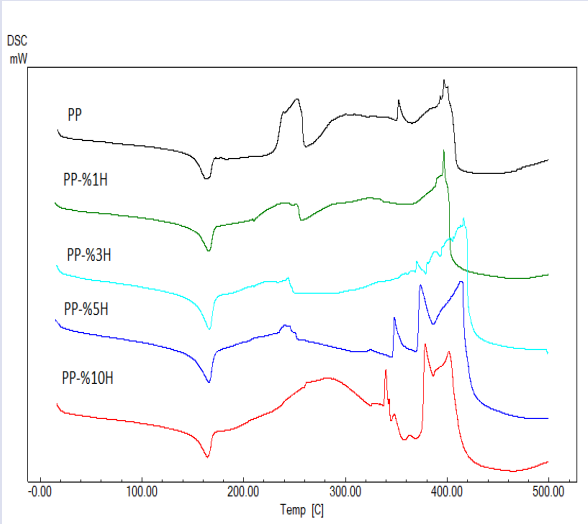

Figure 4. DSC thermograms of pure PP suture structure and sutures with PP-Halloysite composite structure.

The thermal stability of the PP-HA structures obtained within the scope of the study was confirmed by TGA analysis and the degradation steps were determined (Figure 5). In TGA analyses, a single mass loss was clearly seen in pure PP structure and all composite structures. This mass loss occurs at approximately 400 – 500°C and is seen as 100% for pure PP structure. In composite structures, the initial decomposition temperatures shift forward by about 50°C. However, the % residue amounts increase at 500°C. According to these analyses, the inclusion of halloysite groups in the PP structure partially reduces the thermal stability of the polymeric structure. This decrease is due to the inclusion of halloysite groups in the structure and the decrease in inter-chain stacking density. This leads to the formation of inter-chain spaces

in composite structures and the stretching of the structure. All these findings prove to us that the desired composite structures were obtained.

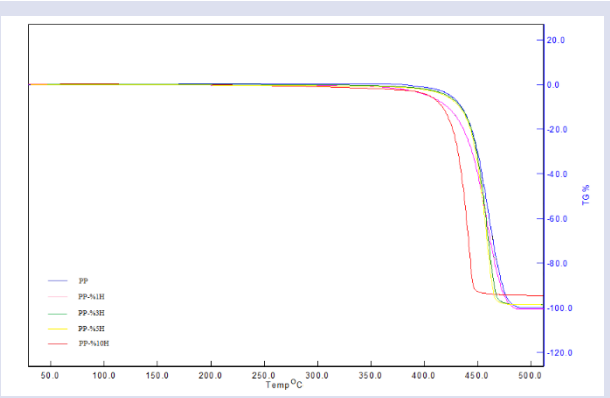

Figure 5. TGA thermograms of pure PP suture structure and sutures with PP-Halloysite composite structure.

Surface and Morphological Properties of Halloysite-Based PP Sutures

SEM images of PP-halloysite composite sutures produced within the scope of the study with different amounts of halloysite doped are given in Figure 6. When the SEM images are examined, it is seen that the pure pp structure in figure 5a has a smooth and monolithic structure. Fractal formations occur in the surface morphology of the structure with the inclusion of halloysite groups in the structure. Especially in structures with 1% and 3% halloysite additives, fractal formations are more prominent and distort the surface morphology. However, depending on the increased amount of halloysite, it is seen that the surface texture is improved again and smoother suture structures are obtained in structures containing 5% and 10% halloysite. For this reason, it can be said that the optimum 5% halloysite-containing structure has a smoother surface than other structures. In structures containing 10% halloysite, it has been determined that halloysite structures are clustered in places and there is agglomeration in the polymer.

The EDX spectra of the composite structures obtained within the scope of the study are given in Figure 6. While taking these spectra, the surfaces were coated with Au/Pd. When Figure 6 is examined, only the peak of the C atom is clearly seen in the spectrum of the pure PP structure. In addition, the peaks caused by the surface coating are evident. As halloysite is added to this structure, the peaks of O, Si and Al atoms in the halloysite structure are observed. The intensity of these peaks increases in direct proportion to the amount of halloysite. In these structures, in addition to these peaks, there are peaks originating from the 20 nm Au/Pd coating. The increase in the intensity of O, Al and Si peaks as the halloysite group's decrease in the composite structures proves that the desired composites are obtained.

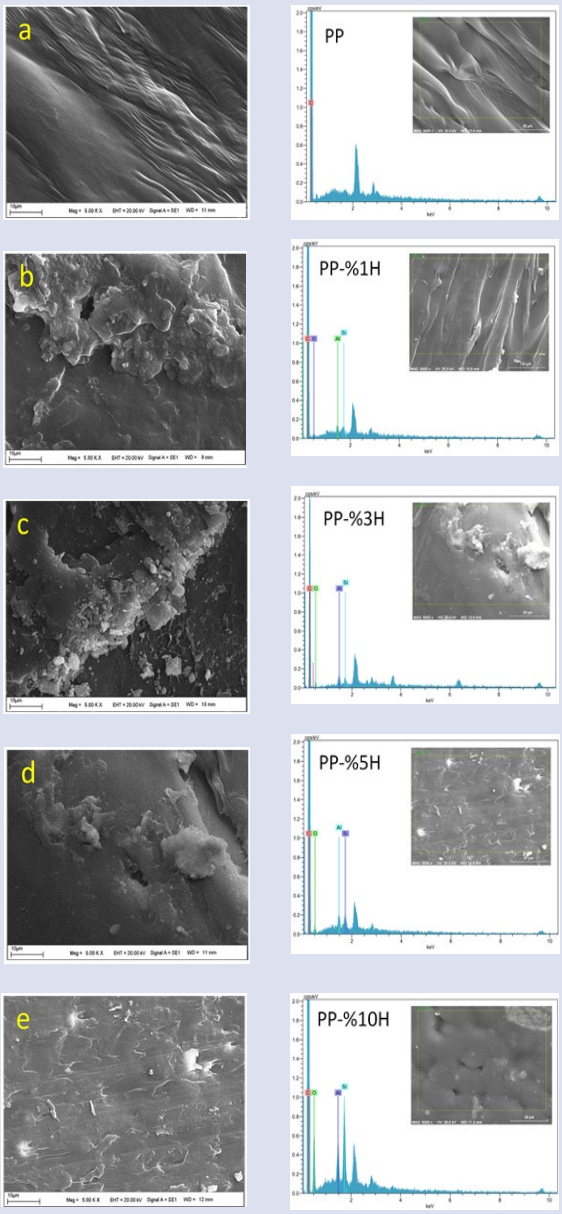

Figure6. SEM- EDX spectrum of PP-Halloysite suture structure (a); PP (b); 1%, (c); 3%, (d); 5% and (e); 10% by mass of halloysite.

Table 1. Chemical composition based on EDX analysis of the PP and the halloysite-based PP suture structures.

Sample	Chemical composition (wt%)			
	C	O	Si	Al
PP	95.26	4.74	-	-
PP-%1H	94.16	5.47	0.17	0.20
PP-%5H	93.58	5.54	0.42	0.45
PP-%10H	79.34	18.19	1.62	0.83

Chemical composition based on EDX analysis of the PP and the halloysite-based PP suture structures are given in Table 1. According to this table, only C and O elements are seen in the pure PP structure. Si and Al elements are also seen in halloysite-based PP suture structures. As the amount of halloysite in the structure increases, the percentages of Si and Al elements increase.

Mechanical Properties of Halloysite-Based PP Suture Structures

The most basic properties expected in suture materials used in the medical field; biocompatibility, non-toxicity, non-irritation, secure knotting and not breaking during use. In other words, its mechanical properties should be sufficient and strong. Therefore, PP-based suture materials used in this study are biocompatible and non-toxic materials. However, its mechanical properties may need to be strengthened according to the place of use. The mechanical properties of the suture structure are very important, especially in tissues and tendons with high mobility and exposed to force loads. Therefore, in this study, PP suture was doped with halloysite structure to increase the mechanical properties of the structures. The mechanical properties of the obtained halloysite-based PP suture structures were determined with a universal mechanical testing device. Each measurement was taken in triplicate and calculated as mean ± standard deviation. The mechanical test results obtained for Halloysite-based PP suture structures prepared with different halloysite ratios are given in Figure 7. According to this figure, as the amount of halloysite increased, the amount of elongation of the suture structure without breaking increased. Especially in the structure containing 10% halloysite, the highest mechanical flexibility was obtained. In this way, the tensions in the tissues and muscles after surgical operations may not cause the suture structure to break.

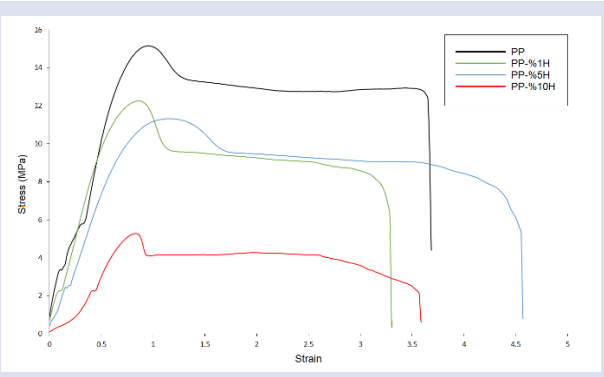

Figure 7. Mechanical test results of halloysite-based PP suture structures

Conclusion

In this study, PP-hallosite nanocomposite in the form of a series of sutures was prepared by adding halloysite into polypropylene matrix at different rates using the extrusion technique with physical interactions. These suture structures were characterized chemically, thermally and morphologically. According to morphological properties, especially homogeneous and crack-free structures were obtained. In the FTIR analysis, it was seen that the intensity of the Si-O-Si peak increased at 1000-1100 cm^{-1} as the amount of halloysite increased. As a result of thermal analysis, it was determined that the thermal stability of the composite obtained increased by 30-40 °C as the amount of halloysite increased. In terms of thermal properties, they were found to be thermally stable up to about 160°C. Therefore, they were found to be sterilizable before use. In the SEM images, it was seen that a homogeneous structure was obtained by the inclusion of halloysite in the structure. This shows that the halloysite groups are equally contributed to the whole structure. The mechanical properties of the obtained suture structures were analysed with a universal mechanical analysis system. Improvements in mechanical properties were observed as the amount of halloysite increased. It was observed that the structure containing 10% halloysite had advantages in terms of elongation and breaking strength compared to pure PP suture structures. For this reason, it is suggested that the PP-halloysite structures obtained within the study can be used as a suture.

Acknowledgments

Financial support from the İnönü University Research Fund Unit (Grant no. FBA-2022-2126) was gratefully acknowledged.

Conflicts of interest

There are no conflicts of interest in this work.

References

[1] Dennis C., Sethu S., Nayak S., Mohan L., Morsi Y., & Manivasagam G., Suture materials—Current and emerging trends, *Journal of Biomedical Materials Research*, *Part A*, 104 (6) (2016) 1544-1559.

[2] Abhari R. E., Martins J. A., Morris H., Mouthuy P. A., Carr A., Synthetic sutures: Clinical evaluation and future developments, *Journal of Biomaterials Applications*, 32 (3) (2017) 410-421.

[3] Chu C. C., Mechanical properties of suture materials: an important characterization, *Annals of Surgery*, 193 (3) (1981) 365.

[4] Zhukovskii V. A., Problems and prospects for development and production of surgical suture materials, *Fibre Chemistry*, 40 (3) (2008) 208-216.

[5] Srinivasulu K., Kumar N. D., A review on properties of surgical sutures and applications in medical field, *Int. J. Res. Eng. Technol.,* 2 (2) (2014) 85-96.

[6] Najibi S., Banglmeier R., Matta J. M., Tannast M., Material properties of common suture materials in orthopaedic surgery, *The Iowa Orthopaedic Journal*, 30 (2010) 84-88.

[7] Naleway S. E., Lear W., Kruzic J. J., Maughan C. B., Mechanical properties of suture materials in general and cutaneous surgery, *Journal of Biomedical Materials Research Part B: Applied Biomaterials*, 103 (4) (2015) 735-742.

[8] Byrne M., Aly A., The surgical suture, *Aesthetic Surgery Journal,* 39 (2) (2019) 67-72.

[9] Bloom B. S., Goldberg D J., Suture material in cosmetic cutaneous surgery, *Journal of Cosmetic and Laser Therapy,* 9 (1) (2007) 41-45.

[10] Saxena S., Ray A. R., Kapil A., Pavon-Djavid G., Letourneur D., Gupta B., Meddahi-Pellé A., Development of a new polypropylene-based suture: plasma grafting, surface treatment, characterization, and biocompatibility studies, *Macromolecular Bioscience*, 11(3) (2011) 373-382.

[11] Sun J., Yao L., Zhao Q. L., Huang J., Song R., Ma Z., Hao Y. M., Modification on crystallization of poly (vinylidene fluoride)(PVDF) by solvent extraction of poly (methyl methacrylate)(PMMA) in PVDF/PMMA blends*, Frontiers of Materials Science,* 5 (4) (2011) 388-400.

[12] Boland E. D., Coleman B. D., Barnes C. P., Simpson D. G., Wnek G. E., Bowlin G. L., Electrospinning polydioxanone for biomedical applications, *Acta Biomaterialia*, 1 (1) (2005) 115-123.

[13] Chen Y., Geever L. M., Killion J. A., Lyons J. G., Higginbotham C. L., Devine D. M., Review of multifarious applications of poly (lactic acid), *Polymer-Plastics Technology and Engineering,* 55 (10) (2016) 1057-1075.

[14] Singhvi M. S., Zinjarde S. S., Gokhale D. V., Polylactic acid: synthesis and biomedical applications*, Journal of Applied Microbiology*, 127 (6) (2019) 1612-1626.

[15] Budak K., Sogut O., Aydemir Sezer U., A review on synthesis and biomedical applications of polyglycolic acid, *Journal of Polymer Research,* 27 (8) (2020):1-19.

[16] Chu C. C., Materials for absorbable and nonabsorbable surgical sutures, In Biotextiles as Medical Implants, *Woodhead Publishing Series in Textiles*, (2013) 275-334.

[17] Linderman S. W., Kormpakis I., Gelberman R. H., Birman V., Wegst U. G., Genin G. M., Thomopoulos S., Shear lag sutures: Improved suture repair through the use of adhesives, *Acta Biomaterialia*, 23 (2015) 229-239.

[18] Wang B., Yang W., Sherman V. R., Meyers M. A., Pangolin armor: overlapping, structure, and mechanical properties of the keratinous scales, *Acta Biomaterialia*, 41 (2016) 60-74.

[19] Javed F., Al-Askar M., Almas K., Romanos G. E., Al-Hezaimi K., Tissue reactions to various suture materials used in oral surgical interventions, *International Scholarly Research Notices*, (2012) 762095

[20] Acosta S., Björck M., Wanhainen A., Negative-pressure wound therapy for prevention and treatment of surgical-site infections after vascular surgery, *Journal of British Surgery*, 104 (2) (2017) 75-84.

[21] Joussein E., Petit S., Churchman J., Theng B., Righi D., Delvaux B., Halloysite clay minerals—a review, *Clay Minerals*, 40 (4) (2005) 383-426.

[22] Yuan P., Tan D., Annabi-Bergaya F., Properties and applications of halloysite nanotubes: recent research advances and future prospects, *Applied Clay Science*, 112 (2015) 75-93.

[23] Danyliuk N., Tomaszewska J., Tatarchuk T., Halloysite nanotubes and halloysite-based composites for environmental and biomedical applications, *Journal of Molecular Liquids*, 309 (2020) 113077.

Cumhuriyet Sci. J., 44(1) (2023) 112-119
DOI: https://doi.org/10.17776/csj.1192585

Cumhuriyet Science Journal

| csj.cumhuriyet.edu.tr | Founded: 2002 ISSN: 2587-2680 e-ISSN: 2587-246X Publisher: Sivas Cumhuriyet University

Silver Nanoparticles Capped with Poly[(maleic anhydride)-*co*-(vinyl acetate)]

Gamze Ayas [1,a], Gulderen Karakus [2,b,*]

[1] *Faculty of Pharmacy, Sivas Cumhuriyet University, Sivas, Türkiye.*
[2] *Department of Pharmaceutical Basic Sciences, Faculty of Pharmacy, Sivas Cumhuriyet University, Sivas, Türkiye.*
**Corresponding author*

Research Article

History
Received: 21/10/2022
Accepted: 06/02/2023

ABSTRACT

Anhydride containing functional co-polymer, Poly[(maleic anhydride)-*co*-(vinyl acetate)] (pMAVAc) was synthesized by free radical polymerization reaction presence of methyl ethyl ketone (MEK) media with benzoyl peroxide radical initiation at 80 ◦C. Surface modification of pMAVAc was carried out with silver to obtain size specific silver nanocomposites by well-known chemical-reduction approach. Structural characterizations of the samples were performed spectroscopic measurement and surface morphology identification using Attenuated Total Reflectance-Fourier Transform Infrared (ATR-FTIR) spectroscopy and Scanning Electron Microscopy (SEM), respectively. Results obtained from the ATR-FTIR analysis, detection of the characteristic spectrum data of the co-polymer composition in pMAVAc-AgNPs nanocomposite is proof that the co-polymer structure remains unchanged after treatment. The size and morphological properties of the silver nanoparticles were compatible with the characteristic nanomaterial structure and their average size was found to be 35 nm. In addition, as expected, MAVA-AgNPs nanocomposite, the detection of 79.73% Ag by mass is evidence of the high silver content in the material, and it was concluded that the co-polymer was successfully coated with silver. In recent years, considering the increasing importance of biocompatible nanomaterials in drug delivery systems and in pharmaceutical industry, the synthesized nanocomposites are thought to be a useful drug carrier system with potential antibacterial activity.

Keywords: Maleic anhydride-vinyl acetate copolymer, Surface modification, Silver nanoparticle, FTIR, SEM.

[a] *eczgamzeayas@gmail.com* *https://orcid.org/0009-0009-7276-0897* [b] *gulderen@cumhuriyet.edu.tr* *https://orcid.org/0000-0003-2596-9208*

Introduction

The production and applications of polymers have attracted great interest in both academic and industrial research fields in the last twenty years due to their high potential to produce useful materials with desired properties [1]. Functional polymers have been designed specifically, as for example solubilizing agents, surface modification, nanoparticles, macromolecules as drug carriers, medical devices as diagnostic/imaging agents and implants etc. Functional polymers generally design for the purpose of biomedical applications, such as prostheses, dental filling materials, contact lenses, and pharmaceutical formulations as drugs, drug or enzyme conjugates, and gene delivery systems with having many biological activities [2].

Maleic anhydride (MA) containing materials, anhydride or acid form, indispensable tools that widely used for copolymer design for biomedical applications, especially in health research area to diagnosis and treatment of the diseases [3]. Polymer-drug conjugates were first introduced to research area by Helmut Ringsdorf in 1975. The model basically is based on synthetic covalent bond interaction between the pharmaceutically active substances and a polymer backbone [4]. On the other hand, the unique surface modification capability of maleic anhydride makes it possible to design different materials, drug carrier tools because of its unique functionalization capacity, for biomedical applications. These carriers can be easily produced by free radical chain polymerization as non-toxic, non-immunogenic, and biodegradable property under mild conditions with biological activities [5]. They are synthetically produced as targeted functional biomaterials using many types of reactions. Water solubility property makes them attractive for rational polymer-drug fabrication and controlled drug delivery systems.

MA, $C_4H_2O_3$, is a well-known functional monomer with electron acceptor property, which can undergo chemically versatile structural modification through its reactive anhydride moiety with nucleophiles. The functionality of the anhydride moiety allows the production of polymer-based pharmaceutical systems with the desired capacity thanks to special reactions, especially for the design of biocompatible drug carriers. Synthetic modification of polymer surfaces for various applications is an interesting research area, especially in developing new formulations and producing useful materials. Large amounts of anhydride moieties located along the alternating co-polymer backbone tend to react specifically with polar groups, -OH and $–NH_2$, easily [6]. One of the interesting studies on the surface properties of Poly(4-styrenesulfonic acid-*co*-maleic acid) (SMA) is SMA coated with silver nanoparticles (AgNPs) designed to have potential antibacterial activity [7]. Chemical reduction method used for co-polymer coated AgNPs preparation includes silver nanoparticles starting with the reduction of

a silver salt (silver nitrate, $AgNO_3$) with a reducing agent (sodium borohydride, $NaBH_4$) in the presence of colloidal stabilizer (1) [8,9].

$$AgNO_3+NaBH_4 \longrightarrow Ag+½H_2+½B_2H_6+NaNO_3 \quad (1)$$

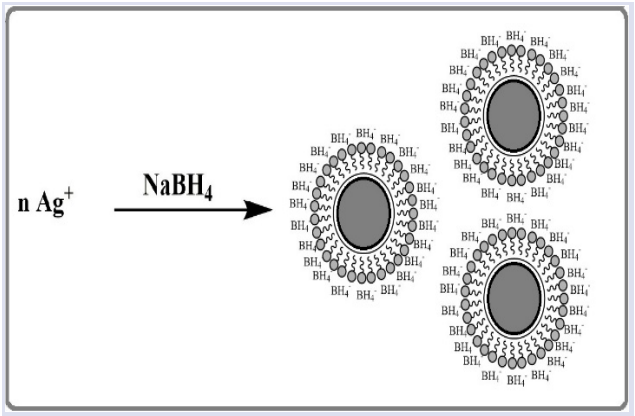

Scheme 1. Schematic representation of the repulsive forces separating Ag nanoparticles with the adsorbed borohydride layer [10].

Nanosilver-based materials plays a major role in nanotechnology and is widely used in nano-medicine. There are many factors linked to potential action and cytotoxicity of silver nanoparticles such as particle size, exposure dose, coating materials, and aggregation behaviour of the particles [11]. Coating is a remarkable method to enhance the advantages of nanoparticle-containing material, which can increase the stability of AgNPs and reduce their aggregation. One of the most striking roles of the coating is to minimize the potential cytotoxic effect of silver nanoparticle against living cells. Moreover, the function of the coating is highly dependent on the properties of the coating agents [12].

The coating process can be explained as the dispersion and bonding of nano-sized silver particles on the surface of the copolymer. Silver nanocomposite based on carboxymethyl cellulose exhibits antibacterial, antifungal, and anticancer activities [13], Poly(vinyl alcohol (PVA) and poly(*N*-vinyl 2-pyrrolidone (PVP) [14] cause angiogenesis via the production of an angiogenic factor [15], chitosan coating can act as a photothermal agents against human non-small lung cancer cells [16], a suture coating led to high anti-inflammatory activity in the intestinal anastomosis during early healing in mice [17]. Furthermore, polysulfone (PS) [18], polyethersulfone (PES) [19], polyvinylidene fluoride (PVDF) [20], cellulose acetate (CA) [21] is widely used other well-known polymers to obtain polymer-coated silver nanoparticles. For example, a recent study showed that the addition of PVA-AgNP ((poly(vinyl alcohol) doped by AgNPs) composites, prepared by spin coating and electrospinning and dip coating techniques, to the non-toxic and colourless polymer leads to a remarkable change in the optical and antibiofilm capacities of the polymer [22]. In another study, it was observed that by incorporating AgNPs into the PES polymer matrix, the antibacterial properties [23] and thermal stability [24] of the polymer composite were significantly improved. As for the animal models, healing has been observed in injured tissues, especially by triggering new collagen synthesis. Thus, modified-AgNPs with oligonucleotides accelerated wound healing without any adverse effects [25]. On the other hand, techniques using PVP-coated silver nanoparticles as colour indicators can be listed as biosensing, environmental protection, food control and medical diagnosis [26]. The coating of all these materials is intended to improve the properties of the surface, especially in terms of reducing initial toxicity and increasing stability.

In this study, pMAVAc, AgNPs, and pMAVAc-AgNPs were synthesized and characterized for size and morphology by SEM analysis. ATR-FTIR spectroscopy was also carried out for the enlightening of the copolymer composition. pMAVAc composed of equal proportions of maleic anhydride and vinyl acetate monomers that it was radically synthesized and using as a capping agent through its anhydride group. Surface modification of pMAVAc was performed with silver to obtain size specific silver nanocomposites by chemical-reduction approach. pMAVAc selected as a capping agent because our previous studies was also confirmed that pMAVAc have almost no cytotoxicity on cultured cell lines and it has been a suitable carrier for drugs or pharmaceutically active molecules such as noradrenaline and doxorubicin [27,28]. Since the synthesized Ag-nanocomposite is thought to potentially have antibacterial effects on Gram-positive and Gram-negative bacteria, it is planned to be investigated in our future studies.

Materials and Methods

Materials

Chemicals and reagents of analytical purity were used as follows: Maleic anhydride (MA, with anhydrous benzene recrystallization method), methyl ethyl ketone (MEK), and radical initiator benzoyl peroxide (BPO) were purchased from Merck. Absolute ethyl alcohol (95% purity) was supplied by Carlo-Erba. Vinyl acetate (VA), petroleum ether, and ethyl acetate, and silver nitrate ($AgNO_3$) were purchased from Sigma-Aldrich. The reducing agent (sodium borohydride, $NaBH_4$) was obtained from Merck.

Instrument

The ATR-FTIR spectra of all samples were recorded on a FTIR spectrophotometer (Bruker Mode: Tensor II) at 400–4000 cm^{-1}. Morphological characteristics (shape and size) of silver nanoparticles were determined by scanning electron microscope (SEM) equipped with Energy Dispersive X-Ray spectroscopy (EDX) at 30 keV (TESCAN MIRA3 XMU). The polymer and copolymer silver nanoparticle composite was coated with 5 nm gold at 10 keV and visualized with the SE detector.

Synthesis of pMAVAc Capping Agent

Alternating based maleic anhydride-vinyl acetate *co*-polymer (Scheme 2) was synthesized using the *in situ* charge transfer complex (CTC) radical polymerization method by free-radical polymerization in MEK for initiated with benzoyl peroxide (BPO) 24h at 80 °C (Table 1). An overnight ethyl acetate purification method and vacuum filtration system (at 50 °C, for 24 h) were used for co-polymer and liquid phase removing, respectively [27].

Preparation of Silver Nanoparticles

AgNPs Sample

AgNPs were prepared according to chemical-reduction method (Table 1) [7,8]. Briefly, 10 mM silver nitrate salt solution was prepared by adding 84.9 mg of $AgNO_3$ salt to 50 mL distilled water. The reducing solution was obtained by adding 18.915 mg of $NaBH_4$ (10 mM) to same volume of the distilled water (50 mL). Solvents mixed well and shaken for 10 min to obtain a greenish brown solution and then allowed to further incubation for 3h at 250 rpm at room temperature in dark conditions for the formation of new silver nanoparticles. As a result, it was observed that a black particle precipitated to the bottom and a very transparent liquid formed on it. The precipitate was carefully separated from the liquid and left to dry for 1 day in a cold environment and further solvent evaporation was also performed in a vacuum oven at 50 °C for 24h. Particles in the form of black powder (AgNPs) were formed stored in a vacuum desiccator until further use.

pMAVAc-AgNPs Sample

The chemical reduction method was used in the preparation of pMAVAc-AgNPs as described above for the preparation of AgNPs (Table 1) [7,8]. Briefly, same volume (50 mL) of the 10 mM $AgNO_3$ salt and 1 mM pMAVAc solution were mixed, then 50 mL solution of 10 mM $NaBH_4$ was rapidly poured into the co-polymer-$AgNO_3$ mixture in one step to reduce all of the silver ions. According to our previous study, the concentration of the copolymer solution was calculated using the average molecular weight (M_w), which was measured as 398.00 Da by size exclusion chromatography (SEC) [27]. The reaction was terminated after 3h incubation at 250 rpm, under room temperature in dark conditions until the mixture became a dark brown solution. The final solution was washed several times with ethyl alcohol, left in the cold for half an hour to allow the particles to become apparent and centrifuged at 14000 rpm for 15 min. Then, nanoparticles dried in a vacuum oven at 50 °C for 24h. Particles in the form of shiny silver powder (pMAVAc-AgNPs) were formed stored in a vacuum desiccator until further use.

Water Solubility of the Samples

Water-soluble polymers are widely used clinically for surface modification of biomaterials. Solubility is a mandatory property for biocompatibility in order to target biomedical applications. Considering the importance of this criterion, water solubility test was also performed for silver nanoparticles. Samples were incubated in ultrapure water (1 g/mL) for 1 h at 25 °C. Solubility in water was checked after one hour by centrifugation of the solution at 6000 rpm with mechanical stirring.

Table 1. Reaction conditions and mixing ratios for the synthesized AgNPs and the MAVA/AgNPs.

Sample code	Monomers/Components (mM)	Solvent (mL)	Initiator (g)	Temperature (°C)	Time (h)
MAVA	MA : VA (1:1)	MEK (5)	BPO (0.025)	80	24
AgNPs	$AgNO_3$ and $NaBH_4$	d.water (50)	-	25	3
MAVA-AgNPs	MAVA : AgNPs (1:1)	d.water (50)	-	25	3

**BPO: Benzoyl peroxide; MEK: Methyl ethyl ketone*

Results and Discussions

The chemical structure and morphological properties of the copolymer and the modification product were elucidated by ATR-FTIR spectroscopic method and SEM analysis, respectively.

FTIR Analysis

Characteristic spectral region of non-conjugated AgNPs recorded at 400–3900 cm^{-1} (Fig. 1a). Typically BH_4^- bending modes observed around at 1993 cm^{-1} and B–H stretching modes detected at 2116 cm^{-1} and 2329 cm^{-1} [29,30]. According to the selection rules, for a tetrahedral system (BH_4^- ion) only two different IR active modes exist; one bending and one stretching mode. The additional bands generally appeared approximately around at 2300 cm^{-1} as 2329 cm^{-1} [29].

Characteristic maleic anhydride functionality containing IR spectrum for poly(MA-*alt*-VA) was obtained (Fig. 1b). Briefly, capping polymeric agent had the characteristic anhydride group at 1857, and 1781 cm^{-1}, belongs to symmetric and asymmetric carbonyl (-C=O) characteristic vibrations of MA-anhydride as expected, respectively [31]. Characteristic vibration modes recorded at 1026 and 934 cm^{-1} attributed to the C–O–C fragment on MA moiety. Stretching modes of $-CH_3$ and $-CH_2$ groups on VA were detected at 1374 and 1432 cm^{-1}, respectively [32]. In addition, $-COCH_3$ stretching modes on VA

appeared around at 1095 cm^{-1} and 1216 cm^{-1} was assigned to the ester groups (CO–O–C) on VA [33]. FTIR results confirmed the pMAVAc copolymer structure [31,32].

The FTIR spectrum of the modification product pMAVAc-AgNPs is shown in Figure 1c as compared to both pure AgNPs and capping agent-pMAVAc. Characteristic vibrations of the anhydride ring belongs to capping agent poly(MA-*alt*-VAc) were appeared in pMAVAc-AgNPs spectrum. In addition the IR spectrum of the modification product consists of two parts, including the characteristic peaks of both capped AgNPs and capping agent pMAVAc. Briefly, on the left side of the spectrum characteristic peaks observed at 2116 cm^{-1} frequencies arising from BH_4^- following the electron capture by BH_4 radical [30] and 2663 cm^{-1} attributed to vibrational frequencies BH_4 [30], 2329 cm^{-1} bending mode of BH_4 [34], and 1993 cm^{-1} assigned to BH_4^- bending modes [40]. On the other hand, on the left side of the spectrum characteristic anhydride asymmetric carbonyl (C=O) vibrations observed at 1788 cm^{-1} [31]. Finally, the antisymmetric and symmetric stretching vibrations of the C-O-C bond in MA detected around at 1166 cm^{-1} and 886 cm^{-1}, respectively [35,36].The remaining frequency observed at 3665 cm^{-1} assigned to hydrophilic groups according to the O–H stretching vibrations, ensuring good water solubility [37].

This result revealed that silver nanoparticles successfully capped with pMAVAc copolymer. These findings obviously demonstrated that a new nanoparticle structure formed following the surface functionality.

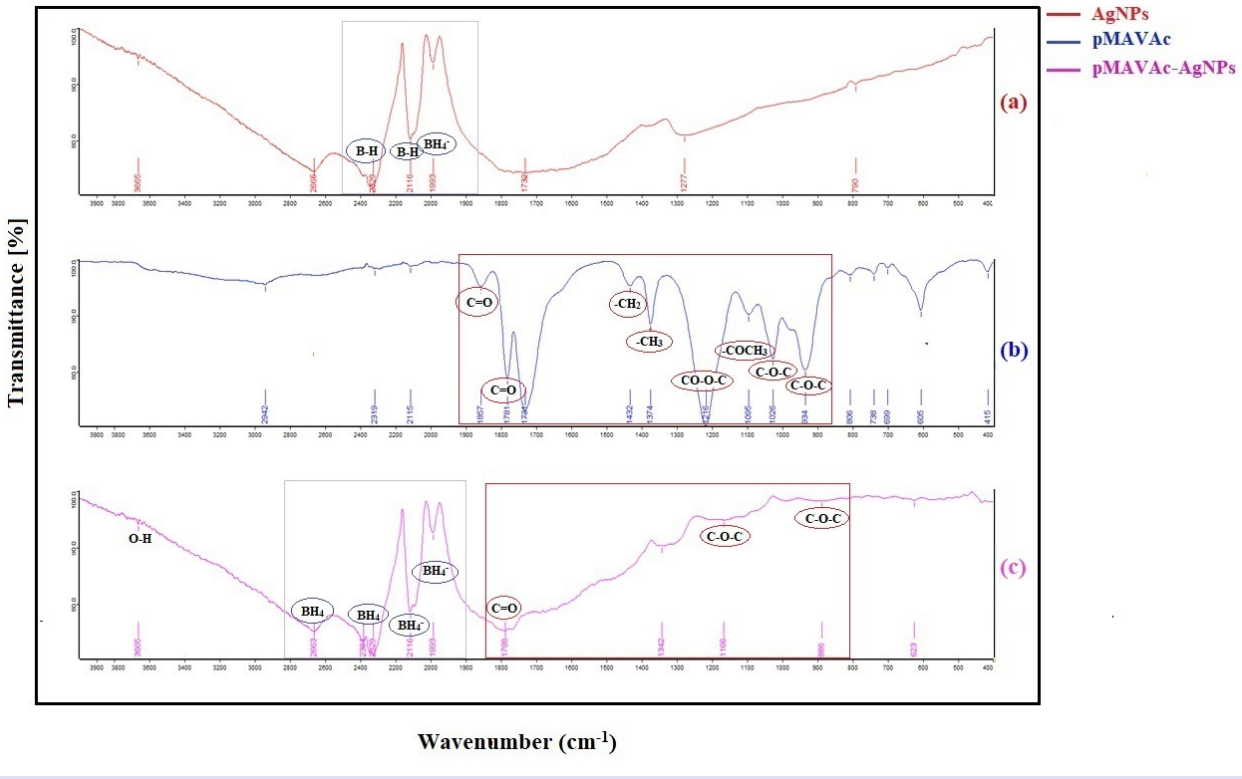

Figure 1. FTIR spectra of the copolymer and the modification product. (a) AgNPs, (b) pMAVAc, and (c) pMAVAc/AgNPs.

SEM Analysis

Scanning electron microscopy (SEM) was employed to enlighten of the main characteristics of the copolymer and synthesized silver nanoparticles such as size, shape and surface morphologies. Energy dispersive spectrometry (EDX) analysis was also performed to confirm the presence of elemental silver. SEM images of copolymer and copolymer-silver nanoparticle taken at 5µm 10.0 KX given in Fig. 2a and Fig. 3a. The size and morphological properties of the copolymer uncoated silver nanoparticle are also given in Fig. 4. As can be seen, the size and morphological properties of uncoated silver particles are compatible with the characteristic nanomaterial structure because of its spherical in shape with narrow size distribution. Their sizes range from 12 nm to 70 nm, with an average size of 35 nm [38].

Morphological characteristics of silver nanoparticles were determined by scanning electron microscope (SEM) equipped with EDX at 30 keV. Figure 2b and 3b show EDX analyses of MAVA copolymer and MAVA-AgNPs nanocomposite. Elemental analysis results were also recorded for reduced silver nanoparticles. Since the copolymer used as the coating agent has only carbon (C) and oxygen (O) atoms in the main chain, the presence of carbon and oxygen was observed, while in the silver-containing nanocomposite, only C, O and Ag elements were determined as % composition, as expected. In the spectrum, the presence of high levels of O and C elements in the structure of the MAVA copolymer and high amount of Ag elements in the silver surface modified copolymer (MAVA-AgNPs) the most important evidence of the inclusion of silver elements in the copolymer structure.

Quantitatively, the weight percent of atoms for the pMAVAc copolymer was determined as 70.02% C and 75.68% O atoms (atomic percentage; % 29.98 C and % 24.32 O), while 7% C, 13.26% O and 79.73% Ag atoms (atomic percentage; % 27.14 C, % 38.52 O, and % 34.35 Ag) were determined for the modification product pMAVAc-AgNPs, as expected [38].

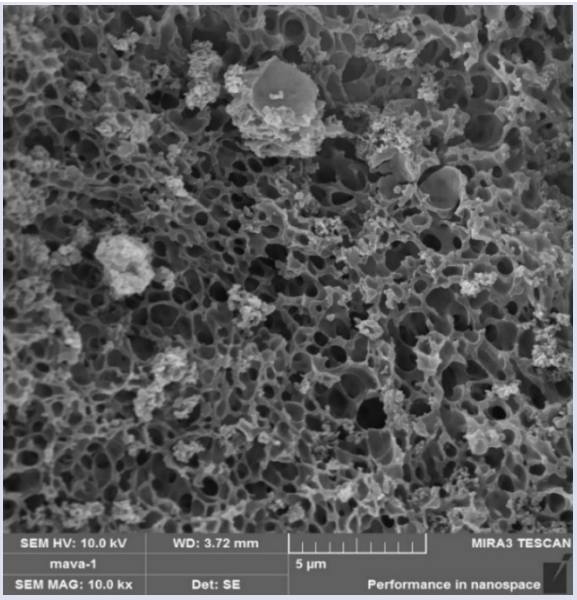

(a)

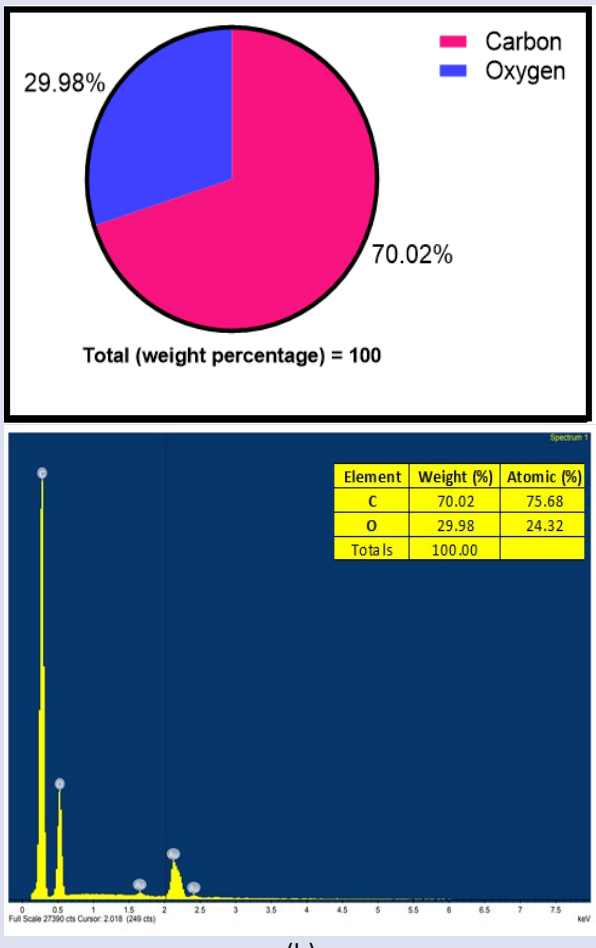

(b)

Figure 2. a) SEM image (5µm, 10.0 KX magnification) and b) EDX spectrum of pMAVAc copolymer.

It can be obviously concluded that silver nanoparticles reduced by pMAVAc copolymer have the weight percentage of silver atoms as 79.73%.

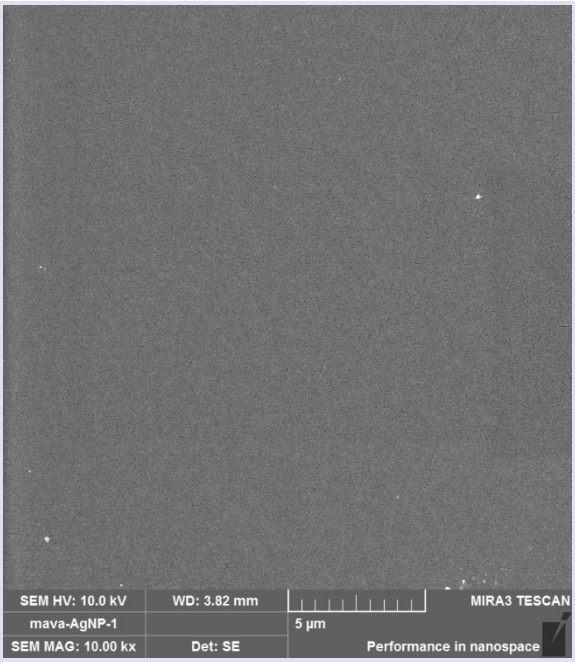

(a)

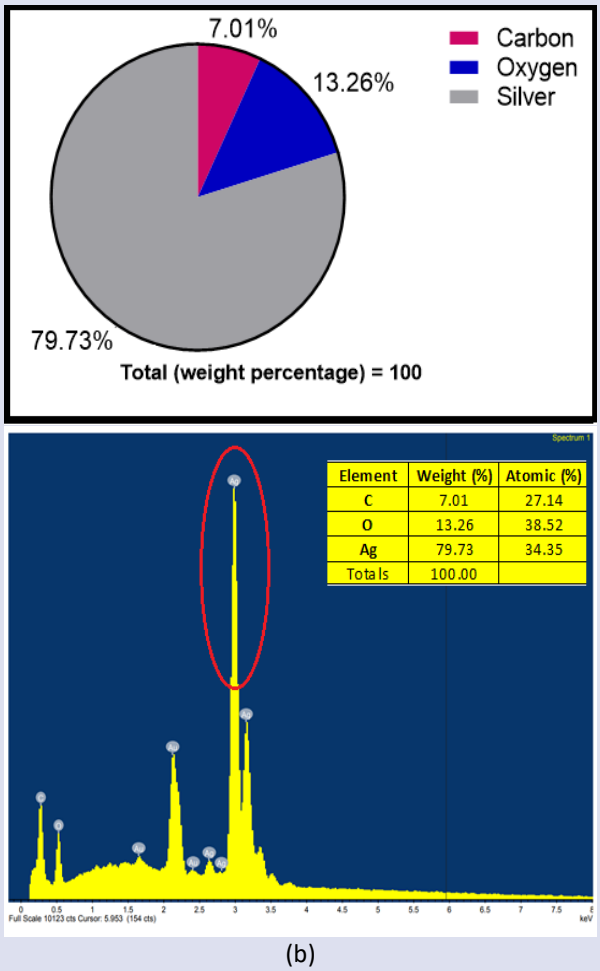

(b)

Figure 3. a) SEM image (5µm, 10.0 KX magnification) and b) EDX spectrum of pMAVAc-AgNPs.

In the light of the spectroscopic and morphological findings obtained, it was concluded that the surface of the copolymer was successfully coated with silver nanoparticles.

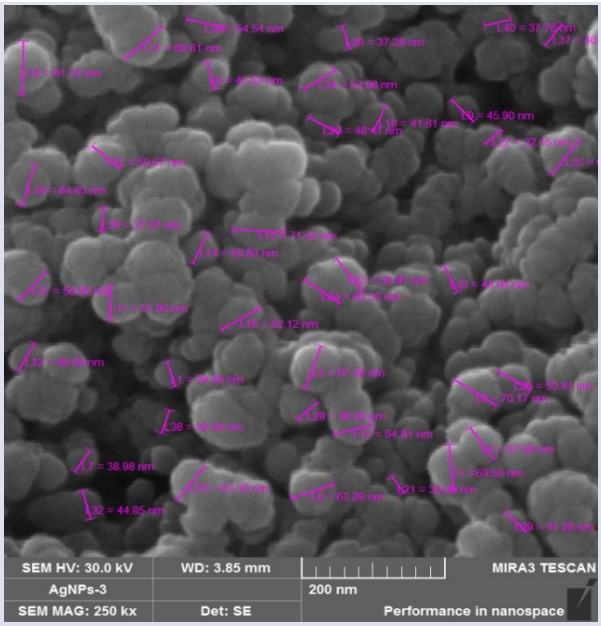

Figure 4. SEM image of AgNPs (200 nm, 250 KX magnification).

Water Solubility of the Samples

According to "like dissolves like" rules polar/ionic solvents dissolve polar/ionic compounds, nonpolar solvents dissolve nonpolar compounds. The water solubility test clearly showed that the newly designed pMAVAc-AgNPs nanocomposite is highly soluble in water. As supported by the FTIR results of the functional groups of the copolymer and nanocomposite, its *polyanionic character* provides high water solubility.

Proposed Reaction Mechanisms for Copolymer and Silver Nanoparticle

Spectroscopic analysis results, FTIR, clearly showed that the mechanism of synthesis reaction for MA containing copolymer is compatible with radical initiated free-radical polymerization and AgNPs nanoparticles capping with this copolymer according to chemical-reduction method (Scheme 2 and 3) [28].

The physical appearances of the synthesized copolymer, silver nanoparticle and the modified product copolymer-silver nanoparticle (after drying and purification) coated with the copolymer are given in Figure 5.

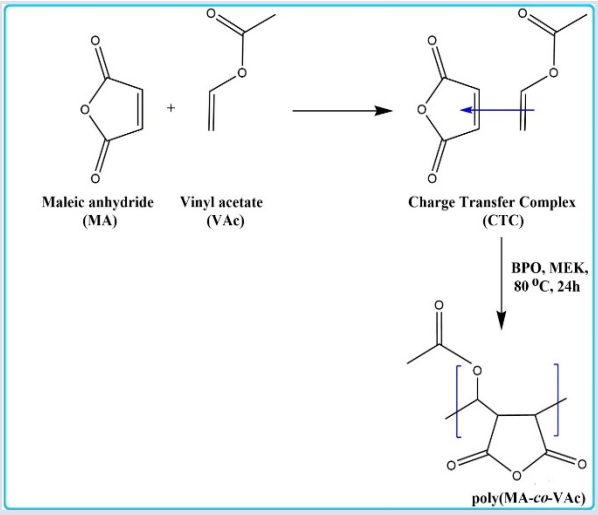

Scheme 2. Schematic illustration of the preparation of maleic anhydride-vinyl acetate (pMAVAc) copolymer.

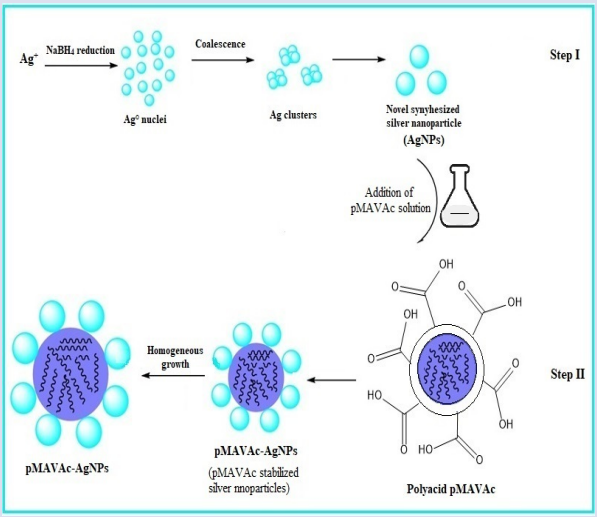

Scheme 3. Schematic illustration of the preparation of silver nanoparticles and its surface modification.

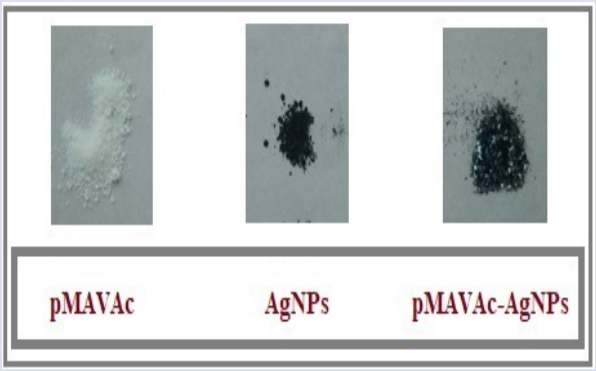

Figure 5. Physical appearance of the prepared copolymer, silver nanoparticle and surface modified silver nanoparticle.

Conclusions

Polymer-based nanocarriers are known as the most versatile biomaterials useful for controlled drug delivery systems. AgNPs are widely used in the many diverse research areas such as cosmetics, food, electronics, optics and also medical purposes as biosensors and drug delivery systems. Current therapeutic applications of AgNPs, especially in healthcare, are closely related to their size, shape and surface coating properties. The chemical-reduction methods used in this study for anhydride containing functional co-polymer, pMAVAc, *via* surface coating process to obtain size specific silver nanocomposites. The characteristic spherical shape and size-specific properties of the designed silver nanoparticles were confirmed by the current literature data, which they gained by surface coating process.

Spectroscopic and surface morphology analyses were used for the samples to structure characterization by ATR-FTIR and SEM, respectively. Detection of the ATR-FTIR spectrum revealed that the characteristic copolymer composition in the pMAVAc-AgNPs nanocomposite remained unchanged after surface modification. The size, shape and morphology of the silver nanoparticles were compatible with the characteristic nanocomposite structure and their average size was found to be 35 nm. The detection of 79.73% Ag atoms as a weight percent for the pMAVAc-AgNPs nanocomposite is proof of the high silver content in the material, as well as the successful silver coating of the copolymer surface. Water solubility and biocompatibility of polymers used as coating materials are very important parameters for the design of size-specific and also stable silver nanocomposites [39]. In this study, used functional co-polymer, pMAVAc with average molecular weight (Mw) 398.00 Da, convenient capping agent for the design of novel silver nanoparticle because of its promising properties, such as water solubility, biocompatibility and non-cytotoxicity etc [27]. According to our previous studies, it was also proposed as a very suitable and stable drug-carrier to be synthesized copolymer-drug conjugates [28].

In addition, polymers with functional groups such as ester, thiol and thioether used as capping agents are suitable surface ligands for design and synthesizing nanoparticles (NPs) with reproducibility and high yield stable properties [40]. Therefore, the selected pMAVAc with a vinyl ester monomer such as vinyl acetate, thanks to its ester functional group, allowed the successful production of nano-scale, water-soluble and stable pMAVAc-AgNPs nanomaterial with high silver content by capping process. As stated before, water solubility is a mandatory property for biocompatibility for biomedical applications. The polyanionic nature of the pMAVAc-AgNPs nanocomposite gives the material the advantage of high solubility in water. In recent years, as researchers have focused on biocompatible nanomaterials in drug delivery systems and the pharmaceutical industry, the synthesized nano-sized composite could be a useful drug delivery system with potential antibacterial activity, and also an easy, short-term and inexpensive way to produce new coated materials.

As a result, it has been shown that pMAVAc tends to yield smaller and narrowly dispersed silver nanoparticles with desirable properties in various applications. It is suggested that the synthesized nano-sized composite can be developed for next-generation drug delivery systems for antibacterial treatment and detailed bioactivity studies can be made.

Conflicts of interest

There are no conflicts of interest in this work.

References

[1] Sung Y.K., Kim, S.W. Recent advances in polymeric drug delivery systems, *Biomater. Res.,* 24 (12) (2020).

[2] Popescu I., Suflet D.M., Pelin I.M., Chitanu G.C., Biomedical applications of maleic anhydride copolymers, *Rev. Roum. Chim.,* 56 (2011) 173–188.

[3] Scognamiglio F., Travan A., Rustighi I., Tarchi P., Palmisano S., Adhesive and sealant interfaces for general surgery applications, *J. Biomed. Mater. Res. B. Appl. Biomater*., 104(3) (2016) 626-639.

[4] Ringsdorf H., Structure and properties of pharmacologically active polymers, *J. Polym. Sci*., 51 (1975) 135–153.

[5] Spridon D., Panaitescu L., Ursu D., Uglea C.V., Synthesis and biocompatibility of maleic anhydride copolymers: 1. Maleic anhydride–vinyl acetate, maleic anhydride methyl methacrylate and maleic anhydride-styrene, *Polym. Int*., 43 (1997) 175–181.

[6] Bortel E., Styslo M., On the chemical modifications of poly(maleic anhydride-co-isobutene) by means of hydrolysis ammonisation or aminations, *Makromol. Chem. Macromol. Chem. Phys.,* 191 (1990) 2653.

[7] Hathaichanok T., Somboon T., Stephan T.D., Warangkana W., Antibacterial Potential of Silver Nanoparticles Capped with Poly(4-styrenesulfonic acid-co-maleic acid) Polymer, *Adv. Mat. Res*., 1088 (2015) 64-68.

[8] Mavani K., Shah M., Synthesis of Silver Nanoparticles by using Sodium Borohydride as a Reducing Agent, *Int. J. Eng. Res. Technol. (IJERT)* , 2(3) (2013) 2278-018.

[9] Agnihotri S., Mukherjiabc S., Mukherji S., Size-controlled silver nanoparticles synthesized over the range 5–100 nm using the same protocol and their antibacterial efficacy, *RSC Adv*., 4 (2014) 3974–3983.

[10] Haque Md. N., Kwon S., Daechul C., Formation and stability study of silver nano-particles in aqueous and organic medium, *Korean J. Chem. Eng*., 34(7) (2017) 2072-2078.

[11] Cameron S., Hosseinian F., Willmore W., A Current Overview of the Biological and Cellular Effects of Nanosilver, Int. J. Mol. Sci., 19(7) (2018) 2030.

[12] Travan A., Pelillo C., Donati I., Marsich E., Benincasa M., Scarpa T., Semeraro S., Turco G., Gennaro R., Paoletti S., Non-cytotoxic Silver Nanoparticle-Polysaccharide Nanocomposites with Antimicrobial Activity, Biomacromolecules., 10(6) (2009) 1429–1435.

[13] S. Salem S., H. Hashem A., M. Sallam A., S. Doghish A., A. Al-Askar A.,.A. Arishi A, M. Shehabeldine A., Synthesis of Silver Nanocomposite Based on Carboxymethyl Cellulose: Antibacterial, Antifungal and Anticancer Activities, *Polymers*, 14, (2022) 3352.

[14] Nikolić, N., Spasojević, J., Radosavljević, A., Milošević, M., Barudžija, T., Rakočević, L., Kačarević-Popović, Z., Influence of poly(vinyl alcohol)/poly(N-vinyl-2-pyrrolidone) polymer matrix composition on the bonding environment and characteristics of Ag nanoparticles produced by gamma irradiation, *Radiat. Phys. Chem*., 202 (2023) 110564.

[15] Kang K., Lim D.H., Choi I.H., Kang T., Lee K., Moon E.Y., Yang Y., Lee M.S., Lim J.S., Vascular tube formation and angiogenesis induced by polyvinylpyrrolidone-coated silver nanoparticles, *Toxicol Lett.,* 10;205(3) (2011) 227-234.

[16] Boca S., Potara, M., Gabudean, A.M., Juhem, A., Baldeck, P., Astilean, S., Chitosan-coated triangular silver nanoparticles as a novel class of biocompatible, highly effective photothermal transducers for in vitro cancer cell therapy, *Cancer Lett*., 311 (2011) 131–140.

[17] Liu X., Gao P., Du J., Zhao X., Wong K.K.Y., Long-term anti-inflammatory efficacy in intestinal anastomosis in mice using silver nanoparticle-coated suture, *J Pediatr Surg*., 52(12) (2017) 2083-2087.

[18] Koseoglu-Imer, D.Y., Kose, B., Altinbas, M., Koyuncu, I., The production of polysulfone (PS) membrane with silver nanoparticles (AgNP): Physical properties, filtration performances, and biofouling resistances of membranes, *J. Membr. Sci.,* 428 (2013) 620–628.

[19] Huang, J., Zhang, K., Wang, K., Xie, Z., Ladewig, B., Wang, H., Fabrication of polyethersulfone-mesoporous silica nanocomposite ultrafiltration membranes with antifouling properties, *J. Membr. Sci*., 423–424 (2012) 362–370.

[20] Zhang, S., Qiu, G., Peng Ting, Y., Shung Chung, T., Silver-PEGylated dendrimer nano-composite coating for anti-foulingthin film composite membranes for water treatment, *Colloid Surf. A*., 436 (2013) 207–214.

[21] Arthanareeswaran, G., Thanikaivelan, P., Fabrication of cellulose acetate-zirconia hybrid membranes for ultrafiltration applications: Performance, structure and fouling analysis, *Sep. Purif. Technol*., 74 (2010) 230–235.

[22] Velgosova O., Mačák L., Múdra E., Vojtko M., Lisnichuk M., Preparation, Structure, and Properties of PVA-AgNPs Nanocomposites, *Polymers*, 15(2) (2023) 379.

[23] Basri, H., Ismail, A.F., Aziz, M., Polyethersulfone (PES)-silver composite UF membrane: Effect of silver loading and PVP molecular weight on membrane morphology and antibacterial activity, *Desalination,* 273 (2011) 72–80.

[24] Huang, J., Arthanareeswaran, G., Zhang, K., Effect of silver loaded sodium zirconium phosphate (nanoAgZ) nanoparticles incorporation on PES membrane performance. *Desalination*, 285 (2012) 100–107.

[25] Keleştemur S., Kilic E., Uslu Ü., Cumbul A., Ugur M., Akman S., Culha M., Wound healing properties of modified silver nanoparticles and their distribution in mouse organs after topical application, Nano Biomed. Eng., 4(4) (2012), 160-176

[26] Endo T., Shibata A., Yanagida Y., Higo Y., Hatsuzawa T., Localized surface plasmon resonance optical characteristics for hydrogen peroxide using polyvinylpyrrolidone coated silver nanoparticles, *Mater. Lett*., 64(19) (2010) 2105-2108.

[27] Karakus G., Zengin H.B., Akin Polat Z., Yenidunya A.F., Aydin S., Cytotoxicity of three maleic anhydride copolymers and common solvents used for polymer solvation, *Polym. Bull*., 70 (2013) 1591–1612.

[28] Karakus G., Akin Polat Z., Yenidunya A. F., Zengin H. B., Karakus C. B., Synthesis, characterization and cytotoxicity of novel modified poly[(maleic anhydride)-*co*-(vinyl acetate)]/noradrenaline conjugate, *Polym. Int*., 62 (2013) 492–500.

[29] Karakus G., Ece A., Sahin Yaglioglu A., Zengin H. B., Karahan M., Synthesis, structural characterization, and antiproliferative/cytotoxic effects of a novel modified poly(maleic anhydride-*co*-vinyl acetate)/doxorubicin conjugate, *Polym. Bull*., 74 (2017) 2159–2184.

[30] D'Anna V., Spyratou A., Sharma M., Hagemann H., FT-IR spectra of inorganic borohydride, *Spectrochim. Acta A Mol. Biomol*. Spectrosc., 128 (2014) 902–906.

[31] Lester A., Xuefeng W., Infrared Spectrum of the Novel Electron-Deficient BH_4 Radical in Solid Neon, *J. Am. Chem. Soc*., 124 (2002) 7280-7281.

[32] Xiao C.M., Tan J., Xue G.N., Synthesis and properties of starch-g-poly(maleic anhydride-*co*-vinyl acetate), Express. *Polym. Lett*., 4 (2010) 9–16.

[33] Sunel V., Popa M., Stoican A.D., Popa A.A., Uglea C., Poly (maleic anhydride-*alt*-vinyl acetate) conjugate with alkylating agents, *Mater. Plast*., 45 (2008) 149–153.

[34] Ghosh S., Banthia A.K., An approach to novel polyamidoamine (PAMAM) side chain dendritic polyesterurethane (SCDPEU) block copolymer architectures, *Eur. Polym. J*., 39 (2003) 2141–2146.

[35] Assi Z., Schneider A.G., Ulpe A.C., Bredow T., Rüscher C.H., The Rigidity of the (BH_4)-Anion Dispersed in Halides AX, A = Na, K; X = Cl, Br, I, and in MBH_4 with M = Na, K, Rb, Cs, *Crystals* 12 (2022) 510.

[36] Wu J.H., Hsieh T.Y., Lin H.Y., Shiau I.L., Chang S.T., Properties of wood plasticization with octanoyl chloride in a solvent-free system, *Wood. Sci. Technol.* 37 (2004) 363–372.

[37] Schramm C., High temperature ATR-FTIR characterization of the interaction of polycarboxylic acids and organotrialkoxysilanes with cellulosic material, *Spectrochim. Acta A Mol. Biomol*. Spectrosc. 243 (2020) 118815.

[38] Yulong A., Xu L., Yuxi Z., Yan L., Yunwu Z., Chunhua W., Kaimeng X., Xijuan C., Can L., Red, green, and blue light-emitting carbon dots prepared from *o*-phenylenediamine, *RSC Adv*., 11 (2021) 26915–26919.

[39] Alahmad A., Feldhoff A., Bigall N.C., Rusch P., Scheper T., Hypericum perforatum L.-Mediated Green Synthesis of Silver Nanoparticles Exhibiting Antioxidant and Anticancer Activities, *Nanomaterials*, 11 (2021) 487.

[40] Razzaque S., Hussain S. Z., Hussain I., Tan B., Design and Utility of Metal/Metal Oxide Nanoparticles Mediated by Thioether End-Functionalized Polymeric Ligands, *Polymers* (8) (2016) 156.

Cumhuriyet Sci. J., 44(1) (2023) 120-129
DOI: https://doi.org/10.17776/csj.1229221

Cumhuriyet Science Journal

| csj.cumhuriyet.edu.tr | Founded: 2002 ISSN: 2587-2680 e-ISSN: 2587-246X Publisher: Sivas Cumhuriyet University

Interpretation of Geochemical Data of Eocene Volcanism in Eastern Sivas Province (Central Anatolia, Türkiye)

Taner Ekici [1,a,*]

[1] *Department of Geology, Engineering Faculty, Sivas Cumhuriyet University, Sivas, Türkiye.*
**Corresponding author*

Research Article

History
Received: 04/01/2023
Accepted: 08/03/2023

ABSTRACT

The study area covers the eastern part of Zara district (Sivas) located in East-Central Anatolia. The units found in the region from bottom to top are characterized by the Upper Creataceous-Paleocene Refahiye Complex, the Middle-Upper Eocene Akıncılar Formation, the Karataş volcanics and Kösedağ Syenite, the Lower Miocene Onarı Formation, the Upper Miocene-Pliocene İsola volcanics, the Şerefiye volcanics, the Kadıköy Formation and the uppermost Quaternary sediments. In the frame of this study, the Karataş volcanics, which were formed as a result of the second magmatic activity of the Eocene period, are studied in detail. The Karataş volcanics are greenish black on their undisturbed clean surfaces, and some parts are brown-purple in color and have distinctive crack systems. It shows a reddish-pinkish color distribution in regions where degradation is observed intensely. The SiO2 content, which is the main criterion for determining the magma character of Karataş volcanics, is between 52.09 % and 58.45 %. MgO contents of similar importance are between 0.53 % and 2.21 %. Some of the light rare earth elements, La have 22.2-40.7 ppm, Ce 44.4-67.3 ppm, Pr 5.23-8.88 ppm, Sm 4.41-7.15 ppm, Eu 1.24-1.83 ppm; one of the heavy rare earth elements, Lu have 0.20-0.45 ppm and Yb 1.88-2.98 ppm values. The Karataş volcanics consist of basaltic-trachyandesite and trachyandesite. Evidence of liquid-crystal fractional crystallization (FC) in the phenocryst phase during the formation of the Karataş volcanics is clearly observed in the geochemical diagrams. Traces of partial melting and crustal contamination were found in geochemical studies. Following the closure of the Neo-Tethys ocean in the region, a widespread crustal thickening occurred in the region with the northward divergence of the northern branch of Neo-Tethys, and a suture zone was formed along this line. The Karataş volcanics were formed as a product of active volcanism after the collision in the region.

Keywords: Geochemistry, Geochemical data, Major-minor-rare earth element analysis, Volcanics, Petrology.

[a] *tanere@cumhuriyet.edu.tr* *https://orcid.org/0000-0002-7420-3877*

Introduction

İzmir-Ankara-Erzincan Suture Zone (IAESZ) which is one of the most important tectonic units of Turkey. As a result of the subduction of the Neo-Tethys Ocean in the northern part of Turkey, the İzmir-Ankara-Erzincan suture zone (IAESZ) has developed. After the end of the suturation process, tension and magmatism developed simultaneously on both sides of the IAESZ and above. Products of Eocene volcanism cover large areas along the northern and southern border of this suture zone. Volcanic products are widely observed in the post-collisional basins that developed after the continental collision between the Anatolide and Pontide belt. The Middle Eocene magmatism is represented by volcano-sedimentary units, and at the same time, gabbro and diorite type plutonic rocks constitute the other element of this magmatism. The Middle Eocene volcano-sedimentary units in north-central Anatolia can be regarded as post-collisional. IAESZ and Intra Pontide suture zones with a regional unconformity. Geological records indicate that the lower levels of the Middle Eocene formations are represented by subaerial to shallow marine clastic sediments, but the middle and upper levels are made up almost entirely of subaerial volcanic units. All these findings imply that the suture zone was subjected to a sudden uplift around Lutetian, before the initiation of a widespread volcanism. Karataş volcanics (KV) products also crop out in large areas in the Zara (Eastern Sivas) region. The KV seems to be post-collisional volcanics and are very wide spread along the IAESZ.

The Middle-Upper Eocene KV, which form the basis of this study, cover the north and surrounding areas of the Zara district located in the northeastern parts of the Sivas basin in east Central Anatolia (Figure 1). While the units in the study area generally consist of magmatic and sedimentary rocks, the main subject of the study is the Middle-Upper Eocene KV. Although sedimentary rocks are not very common, there are lacustrine fluvial deposits belonging to the Upper Miocene-Pliocene Kadıköy Formation in the study area. The Refahiye complex, which consists of Upper Cretaceous-Paleocene serpentinized peridotites forming the oldest of the units not only in the study area but also in the region. The Refahiye complex is unconformably overlain by the Akıncılar Formation, which contains Eocene green-black colored serpentinized peridotite, yellow-colored dolomite

interbedded gray-green-black colored sandstone siltstone alternation, black-gray thick bedded agglomerate levels. The Akıncılar Formation is overlain by the Middle-Upper Eocene KV consist of greenish-black colored porphyritic textured basaltic trachyandesite, trachyandesite, and trachyte-containing KV, which are the basic units of this study. In addition, Kösedağ syenite has a hot-hot contact relationship with Karataş volcanic [1]. The Kösedağ syenite mainly has alkaline feldspar syenite, quartz alkaline feldspar syenite, syenite and quartz syenite and locally monzonitic composition.

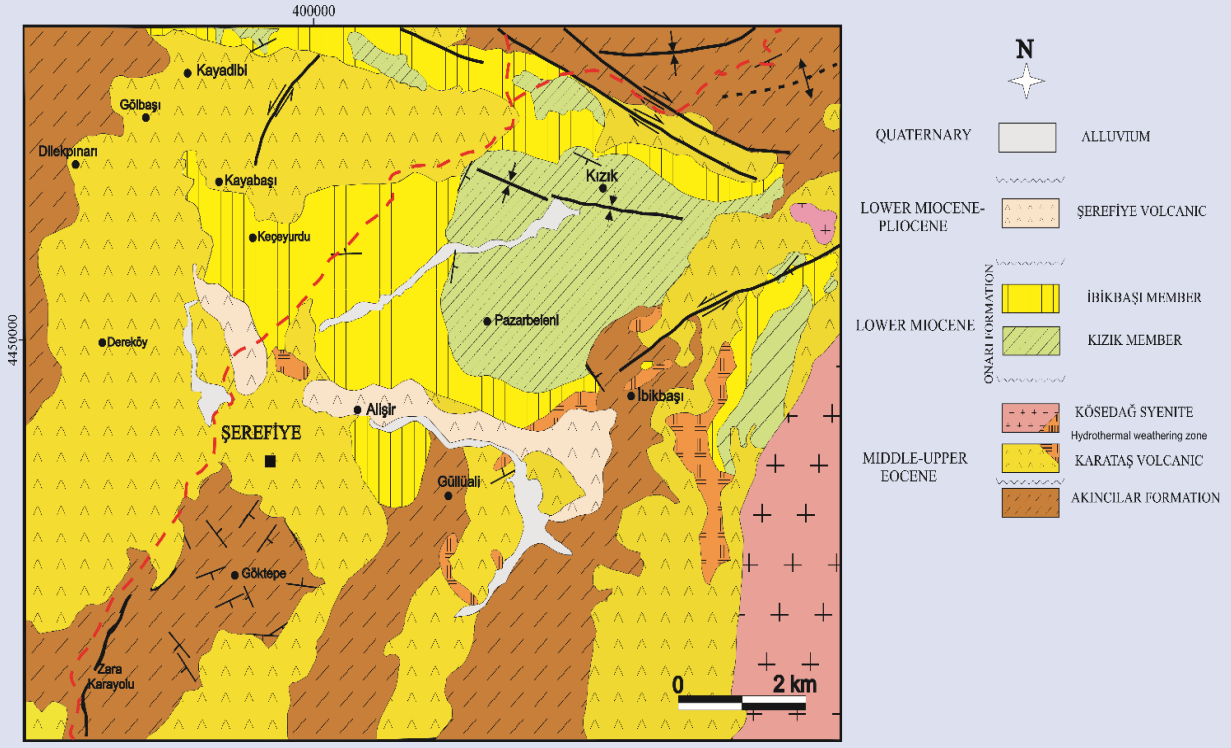

Figure 1. Geological map of the study area (modified from [1-4]).

These units are unconformably overlain by Lower Miocene red-orange colored conglomerate, yellowish medium-thin-bedded limestone and claystone-marl intercalations of white-gray colored thick-bedded gypsum, sandstone and the Onarı Formation, which contains yellowish-gray colored limestone with conglomerate intercalations, sandy and pebbly limestone layers in places. The Isola volcanics and the Upper Miocene-Pliocene Şerefiye volcanic, which are black color and contain abundant gas cavities, overlie the Onarı Formation. Kadıköy Formation, which consists of lacustrine-fluvial sediments unconformably, overlies these units. All these successions are covered by Quaternary alluvium (Figure 2).

Middle-Upper Eocene KV within the study area; It crops out around Dereköy, Keçeyurdu, Dilekpınarı, Kayabaşı, Güllüali and Pazarbelen. While the KV are generally greenish-black, in some parts brown-purple, the weathered areas are observed in the light brown-yellow-white color range. In addition, some parts contain distinctive fissure systems [1].

Materials and Methods

Petrographic thin sections of the rock samples collected from the study area were made in Sivas Cumhuriyet University Geological Engineering Department laboratories. Mineralogical-petrographic thin sections were made by McKenzie and Guilford [6], Yardley [7], Erkan [8], using a backlit Nikon Eclipse 50i POL type binocular research microscope, according to optical mineralogical criteria.

The rock samples, which were geochemically analyzed, were first brought to a particle size of less than 0.5 cm with a Fritisch brand crusher in the crushing-grinding-sieving laboratories of Sivas Cumhuriyet University, Department of Geological Engineering. Then, silicon-carbide was ground with a vibrating mill with a mortar until it reached a grain size that could pass under a 200 mesh sieve. Major, trace and rare earth element (REE) analyzes of 20 rock samples were analysed in ACME laboratories in Canada. The method of geochemical analysis is given on the website of the relevant company.

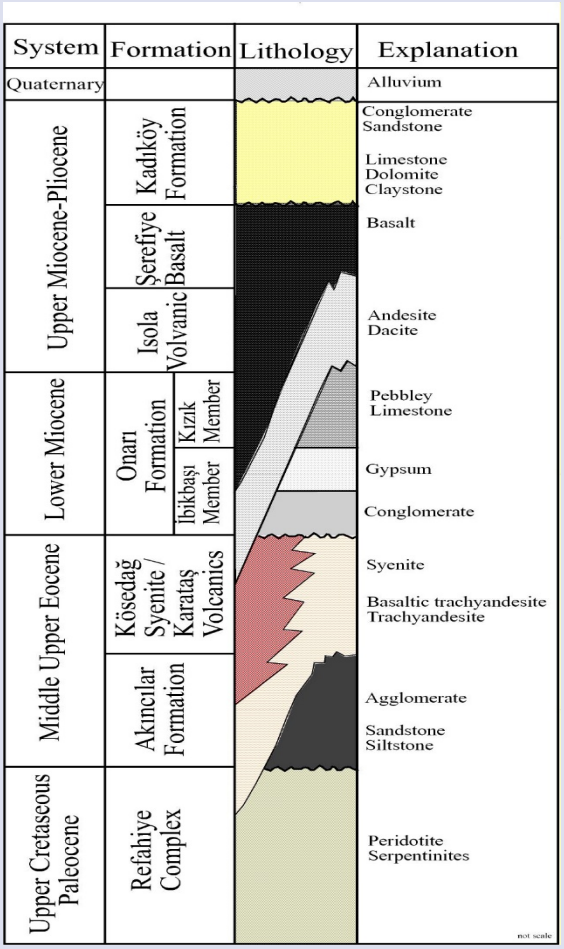

Figure 2. Generalized stratigraphic column section of the study area ([2-5].

Results and Discussion

Petrography

Thin sections of unaltered rock samples taken from the Middle-Upper Eocene KV were made and examined under a polarized light microscope[6-8]. Field and the textural observations on these rocks and the pulp of the rock have been very helpful in defining the volcanic rocks in the study area. These observations were examined under a polarized light microscope, and defining methods based on whole-rock geochemistry data [9] were used to name volcanic rocks (Figure 3). When we look at the positions of the Middle-Upper Eocene aged KV in the total alkali-silica [9] description diagram; It consists of basaltic trachyandesite and trachyandesite (Figure 3).

Plagioclase minerals in the form of microphenocryst and phenocryst have been observed intensively in the rock. Sanidine phenocrysts, augite and olivine minerals have been detected together with plagioclases. While hypocrystalline porphyric texture is commonly observed in the investigations made in KV, hypohyaline porphyric texture is also rarely observed. Plagioclase minerals are particularly common and are colorless and gray-white interference colored, low optically bumpy, subhedral/euhedral and prismatic shaped.

Polysynthetic twinning and zoned textured phenocrysts are observed.

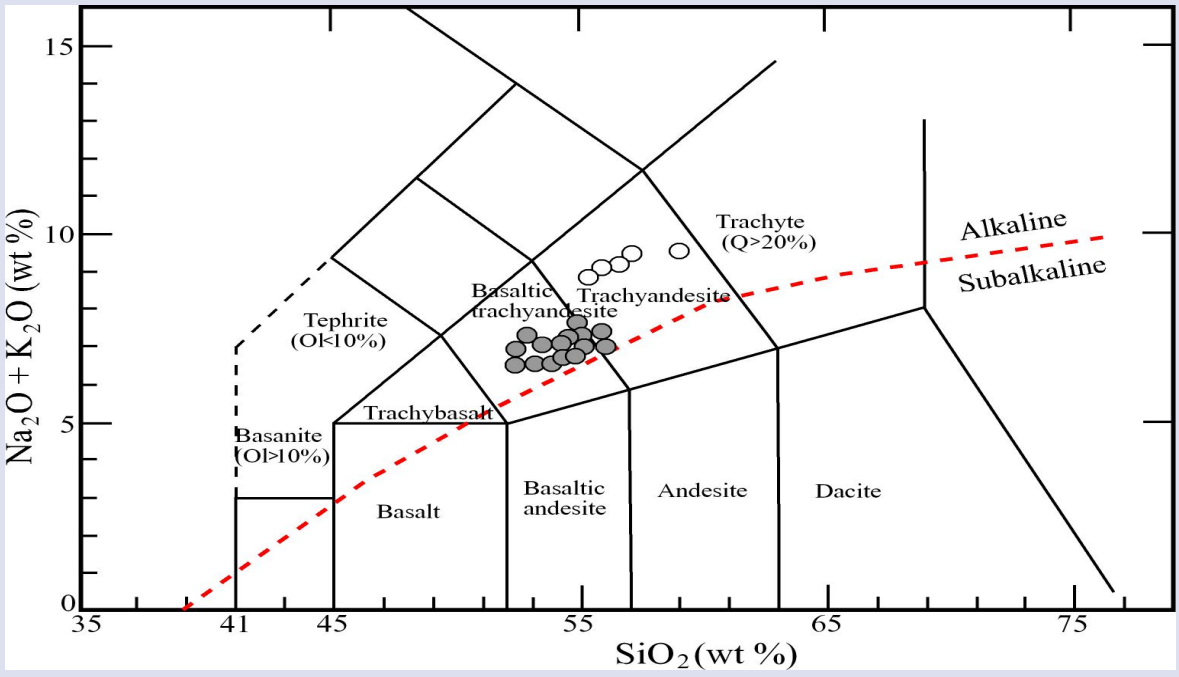

Figure 3. Total alkali-silica nomenclature diagram for Karataş volcanics (A: Alkali, SA: Subalkali, [9]).

There is interaction with magma at edges of plagioclase phenocrysts (Figure 4a,b). Plagioclase minerals are observed as phenocrysts and also microliths in thin sections. A sieve texture is rarely observed at the edges of the plagioclase phenocrysts. Sanidine mineral, which is rarely observed in the rock, is colorless in thin section and has low optical roughness. They display usually karsbald twinning, and rarely polysynthetic twinning, with euhedral crystal shapes. Rarely, sanidine phenocrysts containing plagioclase microphenocryst as inclusions were also observed (Figure 4c). Augite minerals, which are almost colorless in thin section, are generally observed as phenocrysts and microliths (Figure 4d). Augites observed as euhedral to subhedral in crystal shape and are also encountered as octagonal. The augite mineral shows vivid interference colors with its high optical roughness. Abundant carbonated augite phenocrysts are observed to be surrounded by the plagioclase. Olivine minerals in KV are generally seen as microphenocryst sizes. Olivine minerals are seen as highly optically rugged and completely iddingsitized.

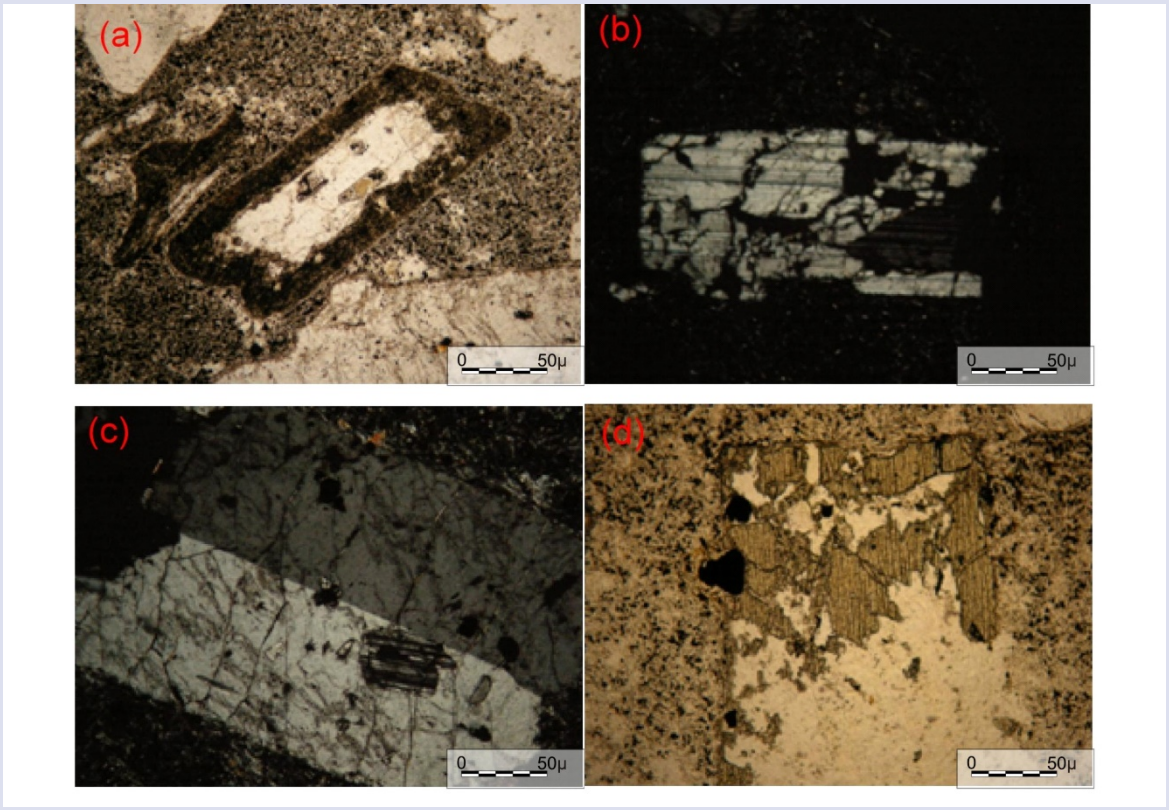

Figure 4. Thin section views of the Karataş volcanics. a-Cooling interactions with plagioclase minerals in the groundmass; b- Sieve texture in palgioclase mineral; c- Sanidine phenocryst and plagioclase microphenocryst seen as inclusions; d-Augite phenocrystal.

Geochemistry

The major, trace and rare earth element contents of the Middle-Upper Eocene KV are given in Table 1. Middle-Upper Eocene KV, which exhibit geochemically alkaline character, are composed of basaltic-trachyandesite and trachyandesite (Figure 3).

Fractional Crystallization

Evidence of liquid-crystal fractional crystallization (FC) in the phenocryst phase during the formation of the KV is clearly observed in the harker diagrams. Fractionation is quite evident in the variation diagrams of the major elements against SiO_2 (Figure 5). A distinct hyperbolic trend is exhibited in the variation diagrams of all major elements versus SiO_2. This identical hyperbolic trend indicates the presence of a fractional crystallization from trachyandesites to basaltic-trachyandesites. In this diagram, while the amount of Na_2O, K_2O, and P_2O_5 increases with the increase in SiO_2 content, whereas a clear trend of decrease is observed in Fe_2O_3, CaO, MgO, Al_2O_3, TiO_2 contents with the increase in SiO_2 content.

Similarly, selected trace elements against SiO2, also display hyperbolic trend from trachyandesites to basaltic trachyandesites (Figure 6). Trace element contents are observed to increase for Ba, Rb, Nb, Zr, Th, La and Y elements together with the increase in SiO_2 content. However, a decrease is observed in Sr element.

It is also observed that the fractionation in the KV develops in the form of olivine and clinopyrosexene fractionation from basaltic-trachyandesites to trachyandesites, and petrographic data confirm this

fractionation. Traces of olivine and clinopyroxene fractionation are also evident in the Al_2O_3 versus CaO, CaO/Al_2O_3 versus MgO and Zr/Nb versus MgO diagrams (Figure 7). The fractionation in these diagrams is represented partly by olivine and partly by olivine+clinopyroxene

Table 1: Major, trace and rare earth element contents of the Karataş volcanics

Sample	K-2	K-4	K-6	K-8	K-11	K-15	K-20	K-27	K-28	K-32	K-35	K-36	K-37	K-44	K-45	K-47	K-49	K-50	K-54	K-64
SiO_2	54.68	54.55	55.14	53.57	56.09	55.09	55.45	56.61	58.45	52.56	54.20	55.45	52.79	52.68	55.42	54.36	53.92	53.07	52.09	52.26
TiO_2	0.84	0.87	0.86	0.82	0.72	0.68	0.70	0.79	0.78	0.83	0.90	0.86	0.87	0.85	0.85	0.89	0.89	0.85	0.81	0.83
Al_2O_3	19.52	19.41	18.96	18.73	19.52	19.12	19.62	18.52	18.56	18.58	19.98	19.70	18.65	18.22	19.58	20.42	19.69	19.07	18.85	18.82
Fe_2O_3	8.12	8.80	8.10	8.34	6.23	6.44	6.20	6.80	6.09	8.20	8.07	7.89	8.53	8.50	7.34	6.94	8.46	8.71	7.87	8.31
MgO	0.99	0.96	0.81	2.02	0.89	0.78	0.66	1.07	0.54	2.00	1.26	1.28	2.18	2.21	1.40	0.66	0.66	0.53	0.81	2.15
MnO	0.07	0.07	0.16	0.27	0.21	0.09	0.23	0.19	0.16	0.14	0.15	0.09	0.16	0.17	0.12	0.18	0.20	0.10	0.20	0.16
CaO	4.96	5.26	4.98	6.39	4.17	5.20	4.53	3.61	3.15	6.59	5.16	4.88	6.07	6.29	5.00	5.41	5.16	6.39	7.63	6.39
Na_2O	3.91	4.04	4.01	3.82	4.19	4.09	4.13	4.26	4.27	3.91	4.53	4.45	3.82	3.74	4.68	4.18	3.91	3.70	3.68	2.87
K_2O	3.53	3.03	2.93	2.96	4.94	4.82	4.83	5.16	5.24	3.14	2.73	2.60	3.14	3.12	2.51	3.17	3.02	3.04	3.98	3.16
P_2O_5	0.42	0.39	0.38	0.41	0.41	0.39	0.42	0.40	0.41	0.41	0.41	0.41	0.40	0.39	0.41	0.43	0.42	0.40	0.40	0.40
LOI	2.6	2.3	3.4	2.3	2.3	3.0	2.9	2.3	2.0	3.3	2.3	2.1	3.1	3.5	2.4	3.0	3.3	3.8	4.2	3.3
Total	99.64	99.68	99.73	99.63	99.67	99.70	99.67	99.71	99.65	99.66	99.69	99.71	99.71	99.67	99.71	99.64	99.63	99.66	99.52	98.65
Rb	74.4	55.7	50.5	57.6	125.8	126.5	119.6	152.7	148.0	61.2	52.1	44.5	66.4	65.7	45.2	72.5	69.0	55.0	53.9	64.4
Sr	862	784	690	802	712	777	848	661	584	730	788	759	742	736	777	830	814	808	795	789
Y	17.4	20.0	19.4	20.3	27.1	18.9	19.4	25.3	28.6	19.4	20.0	20.3	19.4	20.8	21.3	24.1	20.4	21.9	25.4	19.9
Zr	124	122	125	124	179	170	181	244	242	112	123	128	120	122	127	126	130	124	121	122
Nb	6.7	6.9	7.3	6.8	9.8	9.3	9.9	14.1	12.9	6.7	7.0	6.9	6.6	6.4	6.9	7.3	6.8	7.3	6.6	7.1
Ba	734	640	652	683	920	763	1024	687	820	679	632	600	675	653	571	749	970	671	776	693
La	24.5	23.8	25.0	22.7	40.7	29.4	31.7	36.5	36.9	22.2	25.3	24.9	23.0	22.5	26.6	26.8	24.7	26.1	25.7	23.9
Ce	50.7	47.1	51.6	46.0	67.3	56.2	59.0	66.5	66.0	44.2	51.4	49.2	44.4	47.4	50.2	48.5	48.7	46.7	48.2	47.8
Pr	6.35	5.68	5.69	5.49	8.88	6.33	6.76	7.94	7.72	5.23	5.58	5.64	5.44	5.39	5.84	6.23	5.75	5.90	5.78	5.45
Nd	24.0	22.0	24.2	22.6	38.3	25.4	27.4	30.0	31.0	21.7	23.5	23.4	21.6	22.4	23.2	25.4	22.7	24.9	22.7	21.7
Sm	5.23	4.79	4.41	5.03	7.15	4.55	5.61	5.71	5.99	4.65	4.76	4.88	4.42	4.94	5.20	5.25	5.02	4.73	4.91	4.77
Eu	1.51	1.39	1.37	1.36	1.83	1.37	1.29	1.46	1.44	1.24	1.31	1.27	1.30	1.29	1.34	1.51	1.37	1.38	1.41	1.34
Gd	4.37	4.33	4.18	4.35	6.49	4.33	4.64	5.15	5.59	4.14	4.24	4.42	4.50	4.63	4.62	5.25	4.19	4.51	4.96	4.31
Tb	0.72	0.69	0.64	0.67	0.93	0.62	0.68	0.81	0.85	0.61	0.66	0.67	0.71	0.67	0.72	0.79	0.67	0.71	0.75	0.66
Dy	3.62	3.83	3.57	3.67	4.98	3.58	3.75	4.36	4.81	3.46	3.78	3.94	3.98	3.75	4.34	4.33	3.89	3.87	4.41	3.90
Ho	0.73	0.88	0.73	0.82	1.03	0.70	0.81	0.87	1.01	0.76	0.78	0.80	0.74	0.75	0.84	0.89	0.86	0.83	0.87	0.76
Er	2.28	2.45	2.49	2.47	3.18	2.19	2.43	2.64	2.98	2.15	2.42	2.20	2.45	2.29	2.27	2.63	2.50	2.44	2.89	2.17
Tm	0.29	0.34	0.35	0.35	0.49	0.33	0.35	0.41	0.44	0.33	0.37	0.31	0.34	0.34	0.37	0.43	0.33	0.36	0.39	0.35
Yb	1.88	2.35	2.51	2.19	2.98	2.18	2.21	2.60	2.70	1.96	2.34	2.28	2.27	2.38	2.35	2.64	2.29	2.21	2.73	2.23
Lu	0.24	0.23	0.36	0.27	0.23	0.27	0.20	0.21	0.28	0.25	0.37	0.33	0.35	0.36	0.35	0.45	0.35	0.36	0.45	0.35
Th	7.5	6.7	7.0	7.2	11.9	11.3	11.2	18.4	17.1	7.0	6.4	7.3	7.0	6.7	7.6	7.1	7.5	6.9	7.3	7.3
P	1833	1702	1658	1789	1789	1702	1833	1745	1789	1789	1789	1789	1745	1702	1788	1876	1832	1745	1745	1745
K	29304	25153	24323	24572	41009	40013	40096	42835	43499	26066	22663	21584	26066	25900	20837	26315	25070	25236	24738	26232
Ti	5035	5215	5155	4915	4316	4076	4196	4735	4675	4975	5395	5155	5215	5095	5095	5335	5334	5095	4855	4975

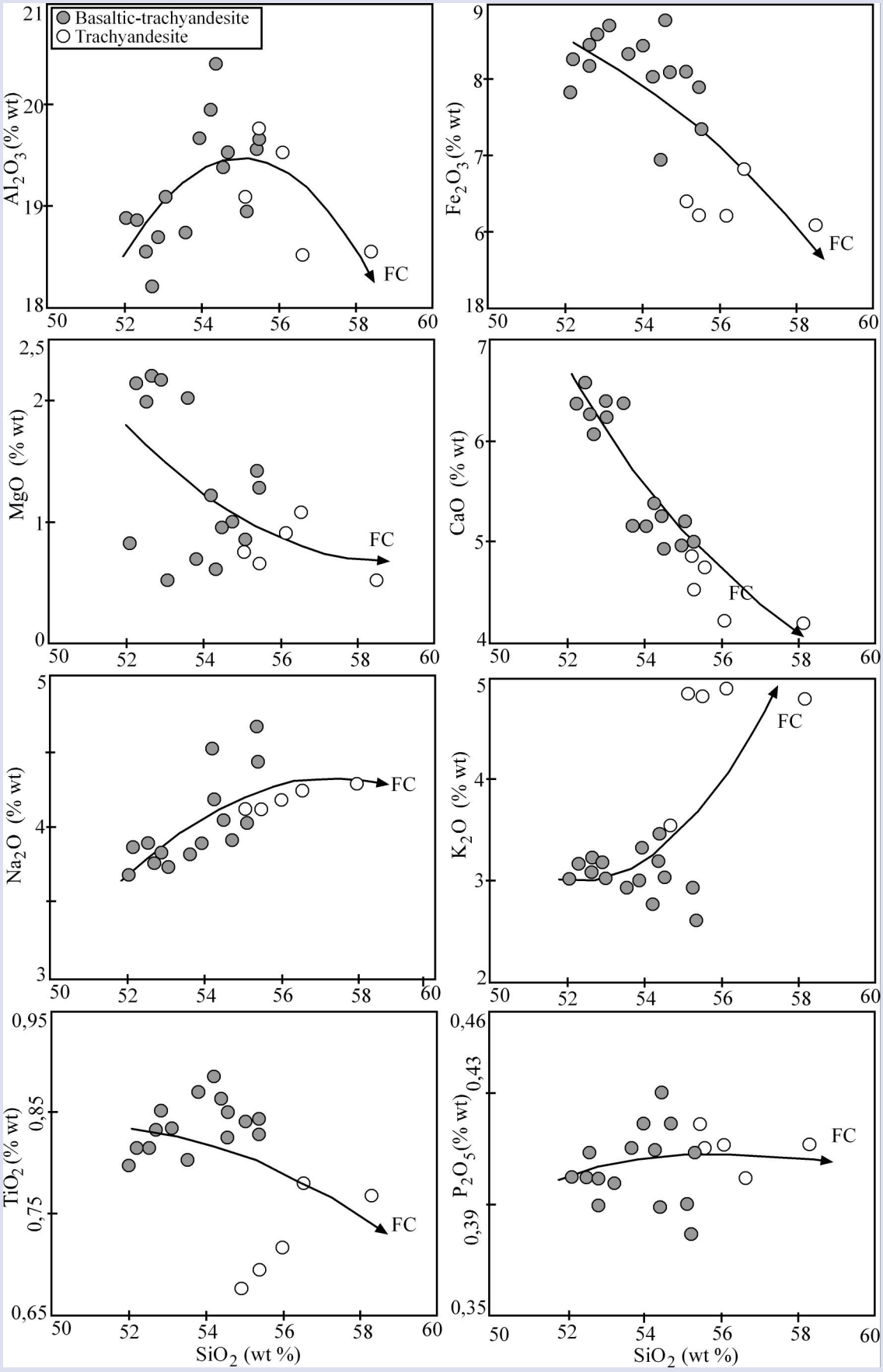

Figure 5. Variation of selected major elements versus SiO_2 for Karataş volcanics.

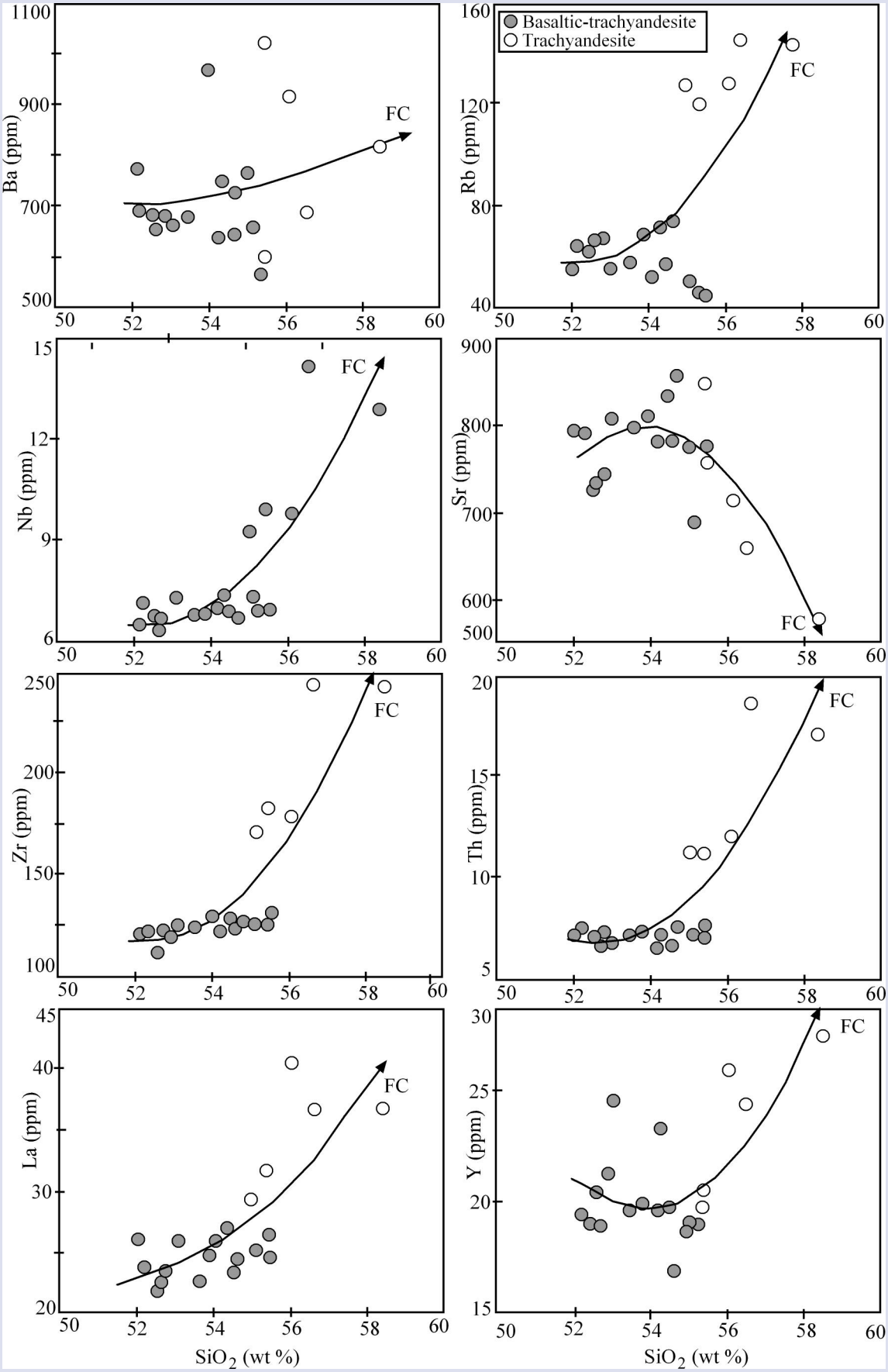

Figure 6. Variation of selected trace elements versus SiO_2 for Karataş volcanics.

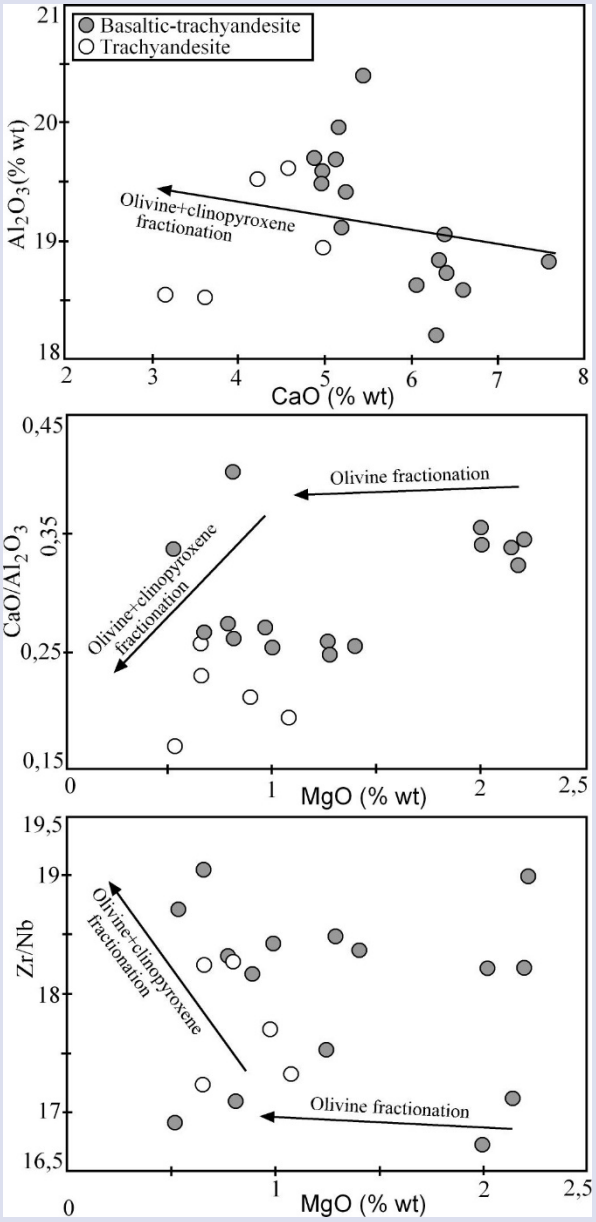

Figure 7. (a) Al2O3 versus CaO, (b) Cao/Al2O3 versus MgO, (c) Zr/Nb versus MgO for the Karataş volcanic.

Partial Melting

Table 1 shows that the MgO contents of basaltic-trachyandesite and trachyandesite forming the KV are in the range of 0.5-2.2%. Considering that the amount of partial melting increases with the increase of MgO content, it is possible to state that the amount of partial melting of basaltic trachyandesites is higher than that of trachyandesites. In addition, when we look at the Harker diagrams of trace elements relative to each other, it is clearly seen that the amount of partial melting increases from trachyandesites to basaltic-trachanadesites in the La/Lu versus La diagram (Figure 8a). Similarly, in the variation diagram Zr versus La, it is seen that the amount of partial melting in basaltic trachyandesites is higher than in trachyandesites (Figure 8b).

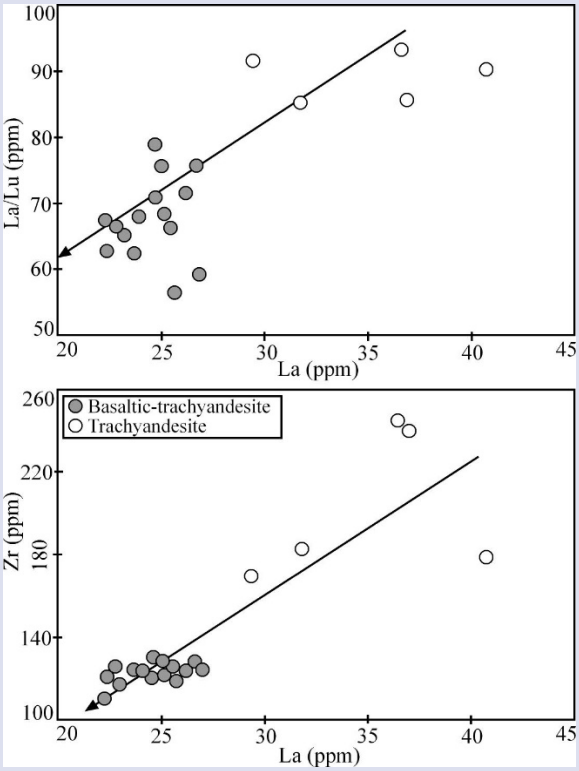

Figure 8. (a) La/Lu, Zr/La for the Karataş volcanics.

Crustal Contamination

Considering the effects of crustal contamination in the KV, crustal contamination effects are observed in both basaltic trachyandesites and trachyandesites. It is also seen that there is an increase in the effects of crustal contamination from basaltic-trachyandesites to trachyandesites (Figure 9). When the trace element profiles in the spider diagram normalized to the primary mantle and chondrite are evaluated, light rare earth elements enrichment compared to heavy rare earth elements. The enrichment of these light rare earth elements in the KV compared to the heavy rare earth elements shows that the contribution of crustal origin material is higher during the crystallization in the magma (Figure 10). While large ion lithophile (LIL) elements such as Sr, Ba, Rb in the KV show enrichment pattern, Nb and Ti show a depletion pattern (Figure 10). The enrichment pattern of the LIL elements indicates that these elements participate in the partial melting during the partial melting processes; It shows that elements with high persistence such as Nb and Ti do not participate much in partial melting processes [10] [11]. In addition, the negative Nb anomaly also shows that the crustal contamination effect is important. When geochemical environments are considered, negative Nb and Ti anomalies are also characteristic of post-collisional and subduction-related volcanics.

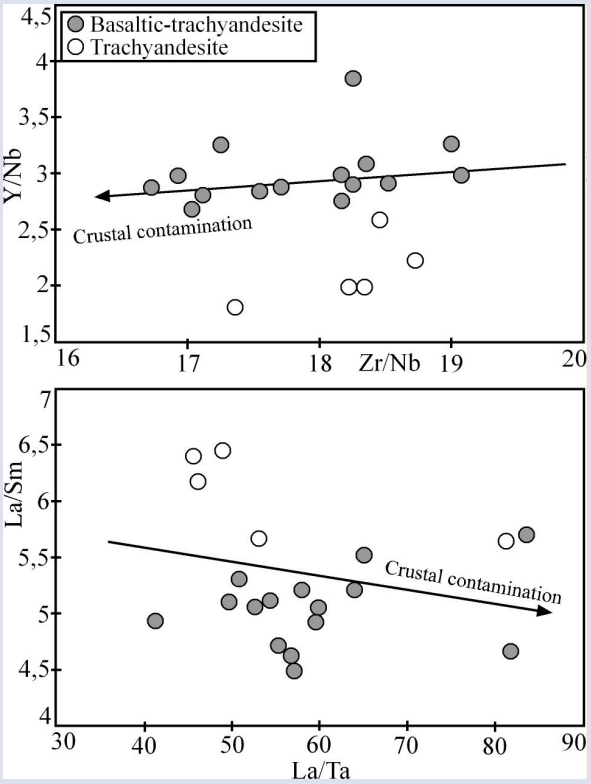

Figure 9. (a) Y/Nb versus Zr/Nb, (b) La/Sm versus La/Ta for the Karataş volcanics.

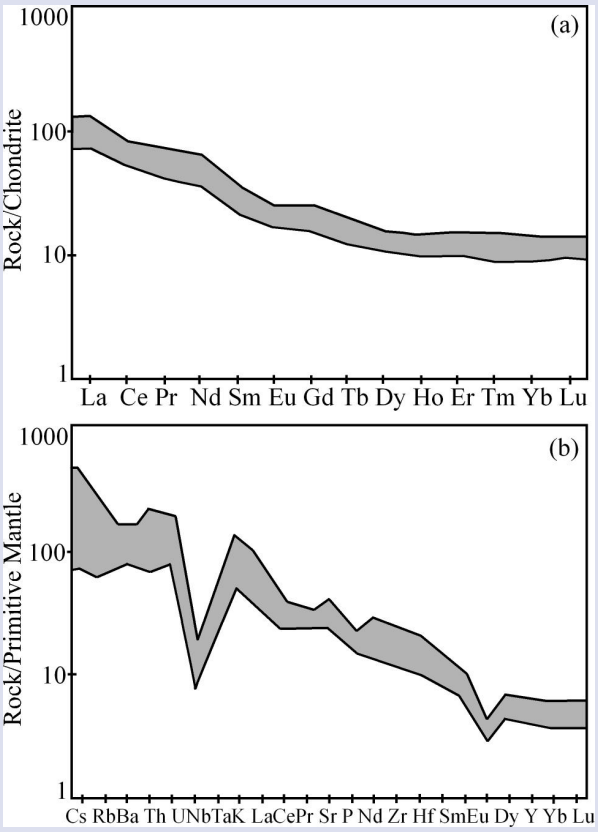

Figure 10. (a) Chondrite normalized rare earth element (REE) and (b) primitive mantle normalized multi element diagrams for the KV. Chondrite values are from [12], primitive mantle values are from [13].

Igneous rocks are formed from magma. The "primitive magma", which initially has a definite and homogeneous composition, undergoes compositional changes in the solidification process, leading to the formation of igneous rocks of different composition. These processes that cause changes in the composition of the primitive magma; It consists of processes such as fractional crystallization, partial melting, magma mixing, crustal contamination. Fractional crystallization, crustal contamination and partial melting at different rates were detected in all of the volcanic rocks observed along IAESZ.

When we look at the evolution processes of the magma forming the Eocene aged Karataş volcanism, which is formed along the İzmir-Ankara-Erzincan suture zone, consisting of basaltic-trachyandesite and trachyandesites and exhibiting alkaline character, it is seen that fractional crystallization is effective. Also, the amount of partial melting increases from basaltic trachyandesites to andesites. Crustal contamination effects are observed in both basaltic trachyandesites and trachyandesites; it is also seen that there is an increase in the effects of crustal contamination from basaltic trachyandesites to trachyandesites in KV. All these magmatic events are seen in Harker change and multi-element diagrams.

Conclusions

Middle-Upper Eocene KV, which present important outcrops in the Central-Eastern Anatolian alkaline province, are composed of basaltic-trachyandesite and trachyandesite**.** The KV, exhibiting hypocrystalline porphyritic texture, contain plagioclase minerals in the form of microliths and phenocrysts. In addition to plagioclase minerals, sanidine, augite and olivine minerals were also observed. The alkaline Karataş volcanics are geochemically display evidence of fractional crystallization (FC). Major and traces elements support the existence of a fractional crystallization from trachyandesite to basaltic-trachyandesite. It was observed that the fractionation in the Karataş volcanics is dominated by olivine and clinopyroxene. Partial melting ratio in the Karataş volcanics increased with the increase of MgO content and the partial melting ratio of basaltic-trachyandesites is higher than trachyandesites. Crustal contamination played and important role for the Karataş volcanics increasing from basaltic-trachyandesites to trachyandesites. In the Santonian-Campanian period, the oceanic crust forming the northern branch of the Neo-Tethys ocean subducted briefly beneath the Pontides (Eurasian plate). In the continuation of the subduction event, a widespread crustal thickening occurred in the region and the İzmir-Ankara-Erzincan suture zone was formed along this line [14-22]. The Middle-Upper Eocene aged Karataş volcanics are the product of an active post-collisional volcanism that occurred as a result of this collision in the region.

Conflicts of interest

There are no conflicts of interest in this work.

References

[1] Başıbüyük Z., Eosen Volkaniklerinin Hidrotermal Alterasyon Mineralojisi-Petrografisi ve Jeokimyası: Zara-İmranlı-Suşehri-Şerefiye Dörtgeninden Bir Örnek (Sivas Kuzeydoğusu, İç-Doğu Anadolu, Türkiye), Doktora Tezi, Sivas Cumhuriyet Üniversitesi, Fen Bilimleri Enstitüsü, (2006) 269.

[2] Kalkancı Ş., Suşehri Güneyinin Jeolojik ve Petrolojik Etüdü, Kösedağ Siyenitik Masifinin Jeokronolojisi (NE Sivas-Türkiye). TJK 32. Bilimsel ve Teknik Kurultayı, Bildiri Özetleri, (1974) 33-34.

[3] Yılmaz Y., Okay A., Bilgiç T., Yukarı Kelkit Çayı Yöresi ve Güneyinin Temel Jeoloji Özellikleri ve Sonuçları. MTA Rapor No*:* 7777, (1985) 124.

[4] Uysal Ş., Bedi Y., Kurt G., Kılınç F., Koyulhisar (Sivas) Dolayının Jeolojisi. MTA Rapor No: 9838, (1995) 120.

[5] Kurtman F., Sivas-Hafik-Zara ve İmranlı Bölgesinin Jeolojik ve Tektonik Yapısı, *MTA Dergisi*, 80, (1973) 1-32.

[6] MacKenzie, W.S., Guilford C., Atlas of Rock Forming Minerals in Thin Section, New York: John Wiley and Soons Inc., (1980) 192.

[7] Yardley B.W.D., MacKenzie W.S., Guilford C., Atlas of Metamorphic Rocks and Their Textures, New York: John Wiley and Soons Inc., (1990) 262.

[8] Erkan Y., Kayaç Oluşturan Önemli Minerallerin Mikroskopta İncelenmesi, 5. Baskı TMMOB Jeoloji Mühendisleri Odası, (2011) 405.

[9] Le Maitre R.W., Igneous Rocks, Cambridge: Cambridge University Press*,* (2002) 236.

[10] Pearce J.A., The Role Sub-Continental Lithosphere in Magma Genesis at Destructive Plate Margins, in Hawkesworth, C.J and Norry, M.J., eds., Continental Basalts and Mantle Xenoliths, Nantwich, U.K., Shiva, (1983) 230-249.

[11] Wilson M., Igneous Petrogenesis, London: Chapman and Hall, (1989) 466.

[12] Boynton W.V., Geochemistry of the Rare Earth Elements: Meteorite Studies. In: Henderson P. (ed), Rare Earth Element Geochemistry, Elsevier, (1984) 63114.

[13] Sun S.S., McDonough W.F., Chemical and Isotopic Systematic of Oceanic Basalts: Implications for Mantle Composition and Processes In: Sounders A.D. and Narry M.J. (Eds), Magmatism in Ocean Basins. *Geological Society of London, Special Publication* , 42 (1989) 313-345.

[14] Akın H., Geologie, Magmatismus und Lagerstattenbildung im Ostpontischen Gebirge/Türkei aus der Eicht der Pallentektonik, *Geologische Rundchau*, 68 (1979) 253-283.

[15] Şengör A.M.C., Yılmaz Y., Tethyan evolution of Turkey: A Plate Tectonic Approach, *Tectonophysics*, 75 (1981) 181-241.

[16] Harris N.B.W., Kelley S., Okay A.I., Postcollision Magmatism and Tectonics in Northwest Anatolia. *Contributions to Mineralogy and Petrology*, 117 (1994) 241-252.

[17] Yılmaz S., Boztuğ D., Space and Time Relations of Three Plutonic Phases in the Eastern Pontides, Turkey, *International Geology Review*, 38 (1996) 935-956.

[18] Okay A.I., Şahintürk Ö., Geology of the Eastern Pontides. In: Robinson, A.G. (Ed.), Regional and Petroleum Geology of the Black Sea and Surrounding Region, *AAPG Memoir*, 68 (1997) 292-311.

[19] Yılmaz Y., Tüysüz O., Yiğitbaş E., Genç S.C., Şengör A.M.C., Geology and Tectonic Evolution of the Pontides. In: Robinson, A.G. (Ed.), Regional and Petroleum Geology of the Black Sea and Surrounding Region, Am. Assoc. *Petroleum Geology Memoir*, 68 (1997) 183-226.

[20] Okay, A.I., Tansel G., Tüysüz O., Obduction, Subduction and Collision as Reflected in the Upper Cretaceous-Lower Eocene Sedimentary Record of Western Turkey, *Geological Magazine*, 138 (2001) 117-142.

[21] Şengör A.M.C., Özeren M.S., Zor E., Gene T., East Anatolian High Plateau as a Mantle-Supported, N-S Shortened Domal Structure, *Geophysics Research letters*, 30 (24) (2003) 1-12.

[22] Canbaz O., Gökçe A., Ekici T., Yılmaz H., Geochemical Characteristics of the Eocene Karataş Volcanic (Northeast Sivas, Turkey) in the İzmir-Ankara-Erzincan Suture Zone, *MTA Dergisi,* 162 (2020) 55-74.

Cumhuriyet Sci. J., 44(1) (2023) 130-142
DOI: https://doi.org/10.17776/csj.1071349

Cumhuriyet Science Journal

| csj.cumhuriyet.edu.tr | Founded: 2002 ISSN: 2587-2680 e-ISSN: 2587-246X Publisher: Sivas Cumhuriyet University

The Structure of Level-2 Semi-directed Binary Phylogenetic Networks

Nihan Özbaltan [1,a,*]

[1] *Department of Computer Engineering, Faculty of Engineering and Architecture, Bakırçay University, İzmir, Türkiye.*
**Corresponding author*

Research Article

History
Received: 10/02/2022
Accepted: 13/11/2022

ABSTRACT

Phylogenetic trees describe evolution but due to hybridization events, recombination events or lateral gene transfer, it can be represented as a phylogenetic network. In phylogenetic networks, some of the branches of tree combine and create a reticulation node. Level of a network is decided to look at how many nodes in a connected component in a network. In this research, Int this paper, the structure of directed and undirected level-2 networks and how the can be decomposed into level-2 generators is studied.

Keywords: Mathematical biology, Phylogenetics, Phylogenetic networks, Biostatistics.

[a] *nihan.ozbaltan@bakircay.edu.tr* *https://orcid.org/0000-0003-0191-312X*

Introduction

Phylogenetics is an interdisciplinary study, which is the interface of biology, mathematics, and computer science. There are different methods to construct phylogenetic trees: Maximum Parsimony (MP), Maximum Likelihood (ML), Bayesian methods, Distance-based methods and quartet-based methods. However, phylogenetic trees are not enough to explain evolution due to hybridization events, recombination events or lateral gene transfer. Phylogenetic networks are used to generalize the tree model of evolution. In a phylogenetic nework, addition branches join vertices, which are already connected by a path, defined as a reticulation. Quartet methods apply to the construction of unrooted evolutionary trees on four leaves.

In this study, phylogenetic network is a directed acyclic graph containing a single root vertex (indegree 0 and outdegree 2), leaf vertices (indegree 1 and outdegree 0) and reticulation vertex (indegree 2 and outdegree 1). A graph is biconnected, which does not contain any vertex whose removal disconnects the graph. Level of a phylogenetic network is the greatest number of reticulation vertices in a biconnected component of a graph. Phylogenetic tree is a level-0 network. My focus on this paper is level-2 network, which is illustrated in Figure 1. Each grey blob shows the biconnected component. Gambette et al. shows the structure of level-k phylogenetic networks and showed that how they can be decomposed into level-k generators [1]. Jansson and Sung constructed level-1 networks with a given set of triplets [2]. Van Iersel et al. extended Jansson's work to construct level-2 phylogenetic networks from triplets [3]

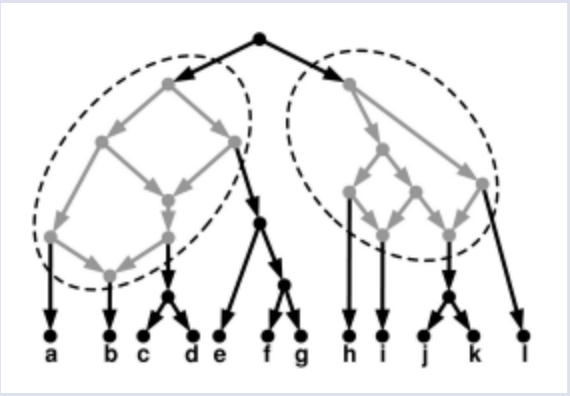

Figure 1: An example of level-2 phylogenetic network which is adapted from [8].

Unrooted and undirected network with distinguished reticulation edges is identified as a semi-directed network. This network is identifiable for Jukes-Cantor large cycle network models, which is a network with a single undirected cylce length at least four [4]. 4 leaf trees are also describes as quartets which are used in tree reconstruction [2]. When I consider the reticulation events, quartets used in network reconstruction recently; for example, SNAQ reconstruct phylogenetic from gene trees [7]. As opposed 4-leaves trees (quartets), I considered the quarnets, which are leaves networks [5]. Huebler et al. constructs level-1 phylogenetic networks from quarnets [6].

In this paper, the work of Huebler et al. by showing that, I can construct in polynomial time a semi-directed level-2 phylogenetic network is extended. An approach for

level-2 semi-directed network reconstruction is developed. This method takes the complete set of semi-directed generators displayed by a network and output the associated level-2 network. This methood is based on adding directions to an existing level-2 generator.

In the next section, definitions and notations are introduced. In section 3, a theorem to generate all level-2 generators on five leaves is proved. Finally, section 4 concludes with a discussion about the generators.

Preliminaries

Given an undirected graph G, let V (G) and E (G) be the set of vertices and edges of G, respectively. An undirected graph is biconnected if it contains no vertex whose removal disconnects the graph. A biconnected component, or blob, of an undirected graph is one of its maximal biconnected subgraphs. An unrooted binary phylogenetic network, unrooted network for short, on a set X is an undirected graph where vertices have either degree 3 (internal vertices) or degree 1 (the leaves, labeled univocally by elements in X). An unrooted network is level-k if a tree can be obtained from it by removing at most k edges per blob.

A rooted binary phylogenetic network N {rooted network for short {on a set X is a directed acyclic graph in which exactly one vertex has in-degree 0 and out-degree 2 (the root) and all other vertices have in-degree 1 and out-degree 2 (tree vertices), in-degree 2 and out-degree 1 (hybrid vertices), or in-degree 1 and out-degree 0 (the leaves, distinctly labeled by elements of X). An unrooted network N is level-k if each of its biconnected components contains at most k hybrid vertices.

Denition 1: A semi-directed binary phylogenetic networks {semi-directed networks for short on a set X, which are graphs where:

1. vertices have either degree 3 or degree 1 (the leaves, labeled univocally by elements in X);
2. vertex with degree 3 have either zero (tree vertices) or two (hybrid vertices) incoming directed edges;
3. I can direct all undirected edges to obtain a rooted binary phylogenetic networks without increasing the number of hybrid vertices, possibly having previously subdivided one of the undirected edge with a new node. An unrooted level-k generator is a biconnected unrooted level-k network, which is not level-(k-1). Rooted/semi-directed level-k generators are defined in a similar way but, for generators, unlike for general rooted/semi-directed binary networks, I allow hybrid vertices to have out-degree 0. In Fig. 3 are depicted all level-0, level-1 and level-2 generators for rooted networks, and in Fig. 24 for semi-directed networks.

For rooted/semi-directed generators, vertices of outdegree 0 and arcs are called its sides; they are empty if no subtree is hanging from them.

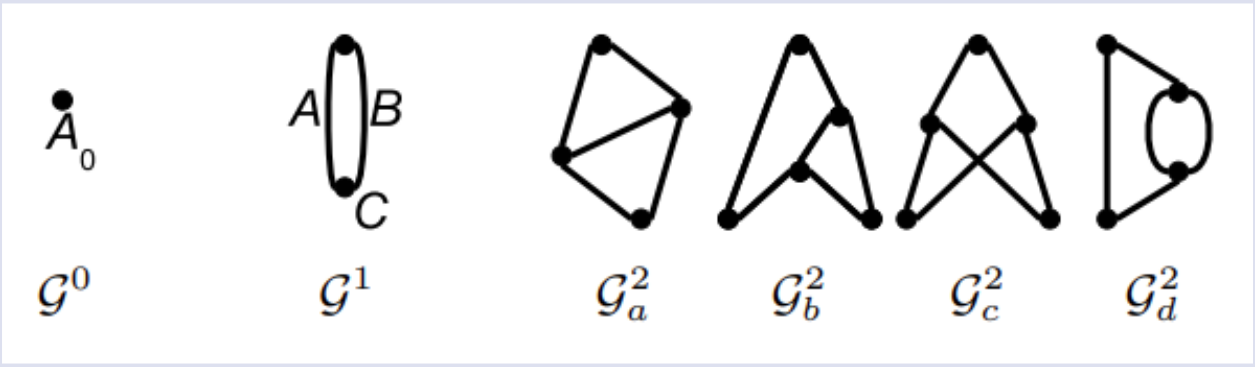

Figure 2: Level-k ≤ 2 generators for rooted networks [1]. G_0 for level-0, G_1 for level-1, and G_a^2, G_b^2, G_c^2, G_d^2 *for level* $-$ 2.

Unrooted Semi-Directed Level-2 Generators

Level-k generators to build any level-k phylogenetic networks are given in [1]. In this section, we modify these definition and theorems to generate semi-directed level-2 network from generators.

Definition 2: Let G be a level-2 generator. I can adding directed arcs to obtain semi-directed generators given in Figure 3.

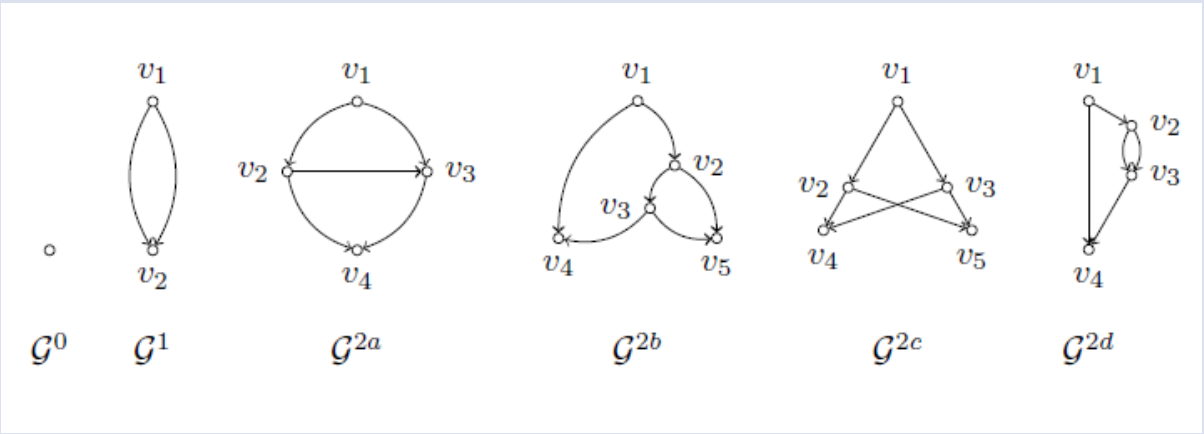

Figure 3: Level-k ≤ 2 semi-directed generators for rooted networks. G_0 for level-0, G_1 for level-1, and G_a^2, G_b^2, G_c^2, G_d^2 $for\ level-2$.

Theorem 2.1 Let G be a level-2 generator. If I adding edges to generators for rooted network to generate semi-directed networks, then the generators for level-2 semi-directed networks are isomorphic to generators for level-2 directed networks.

Proof: In semi-directed networks, it is easy to see that level-0 and level-1 generators coincide with their corresponding rooted ones. Indeed, there is a single biconnected network with no reticulation, which is the trivial network composed of only one vertex i.e., G_0 in Fig. 3. For level-1, there is only one way to have a binary biconnected graph with one hybrid vertex, which is G_1 shown in Fig. 3. In fact, if I make G_1 undirected, I can either make v_1 a hybrid vertex or v_2, obtaining $N^{11}$and N^{12}, which are both isomorphic to G_1 as seen in Figure 4.

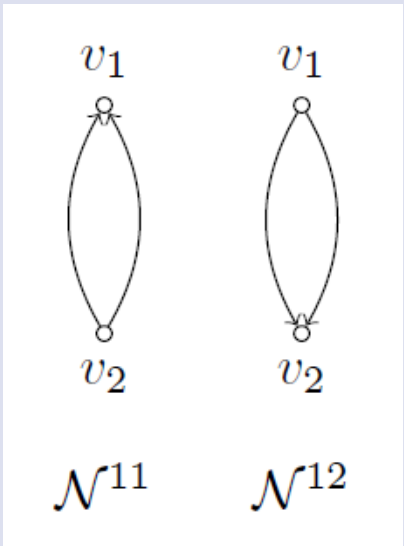

Figure 4: Level-1 semi-directed generators.

For level-2 network, there are four categories of generators, which are obtained respectively from G_a^2, G_b^2, G_c^2, G_d^2 in Fig. 3 by removing the direction of all edges and subsequently choosing a pair of nodes to be the hybrid ones.

Type G^{2a}: Since there are 4 vertices and 2 of them have to be hybrid vertices, we have 6 possible pairs of hybrid vertices: (v_1, v_2), (v_1, v_3), (v_1, v_4), (v_2, v_3), (v_2, v_4), (v_3, v_4).

Case (v_1, v_2): There is just one possible semi-directed network, which is $N^{2a,1}$ in Fig. 6.

Case (v_1, v_3): This case is equivalent to the first one since vertices v_2, and v_3 are interchangeable.

Case (v_1, v_4): There is just one possible semi-directed network, which is $N^{2a,3}$ in Fig. 6. Note that the root position is constrained here: the root needs be placed to subdivide the edge (v_2, v_3) to get a valid network.

Case (v_2, v_3): I need to choose two edges entering in v_2 and two edges entering in v_3 to be the hybrid edges. The nine possibilities are given in Fig. 5. Because of symmetries between v_1 and v_4, and between v_2 and v_3, I have to consider only networks $N^{2a,4}$.

Case (v_2, v_4): This case is equivalent to the first one since vertices v_1 and v_4 are interchangeable.

Case (v_3, v_4): This case is equivalent to the second one since vertices v_1 and v_4 are interchangeable.

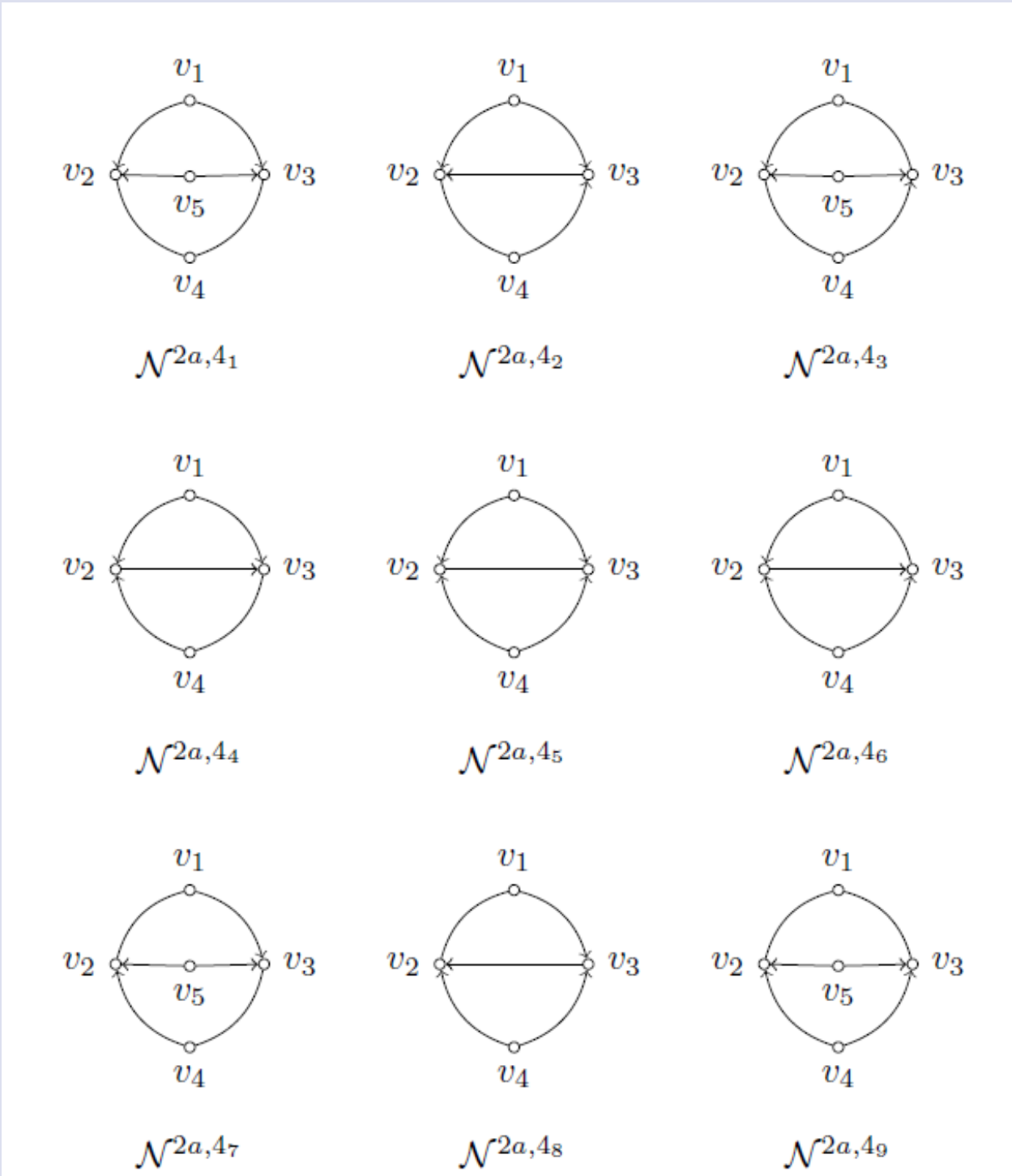

Figure 5: The 9 possible networks obtained by removing edge directions in G^{2a} and choosing v_2 and v_3 as hybrid vertices.

Therefore, I obtain 2 possible generators $N^{2a,1}$ and $N^{2a,3}$ of type (a) corresponding to G^{2a}.

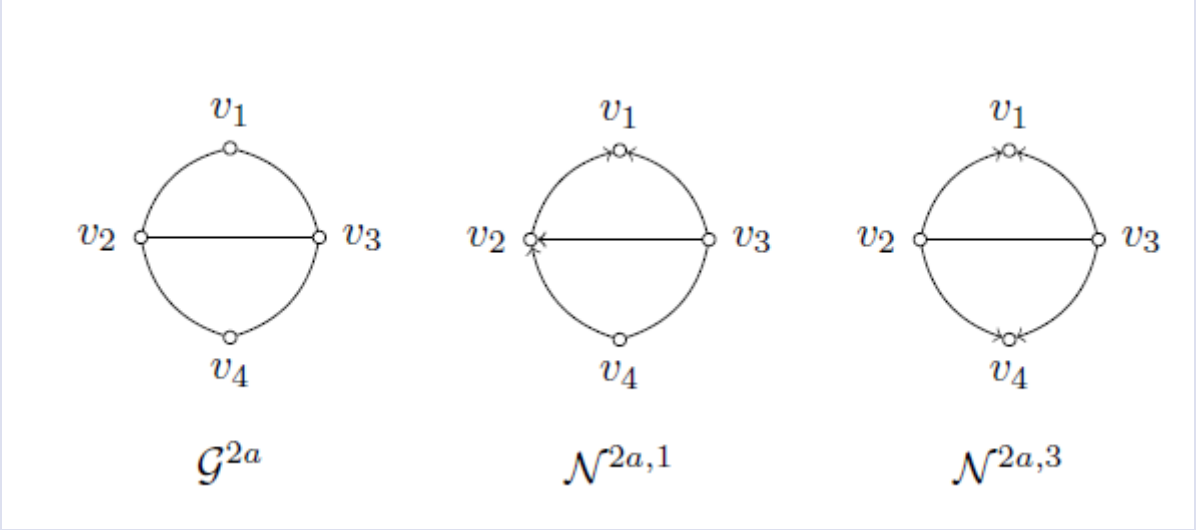

Figure 6: The directed level-2 generator G^{2a} and its corresponding semi-directed generators of type (a) $N^{2a,1}$ and $N^{2a,3}$

Type G^{2b}: Since there are 5 vertices and 2 of them have to be hybrid vertices, I have 10 possible pairs of hybrid vertices: (v_1, v_2), (v_1, v_3), (v_1, v_4), (v_1, v_5), (v_2, v_3), (v_2, v_4), (v_2, v_5), (v_3, v_4), (v_3, v_4), (v_4, v_5).

Case (v_1, v_2): There are three different cases that are shown in Fig. 7 but only $N^{2b,1_1}$is a proper Level-2 generator.

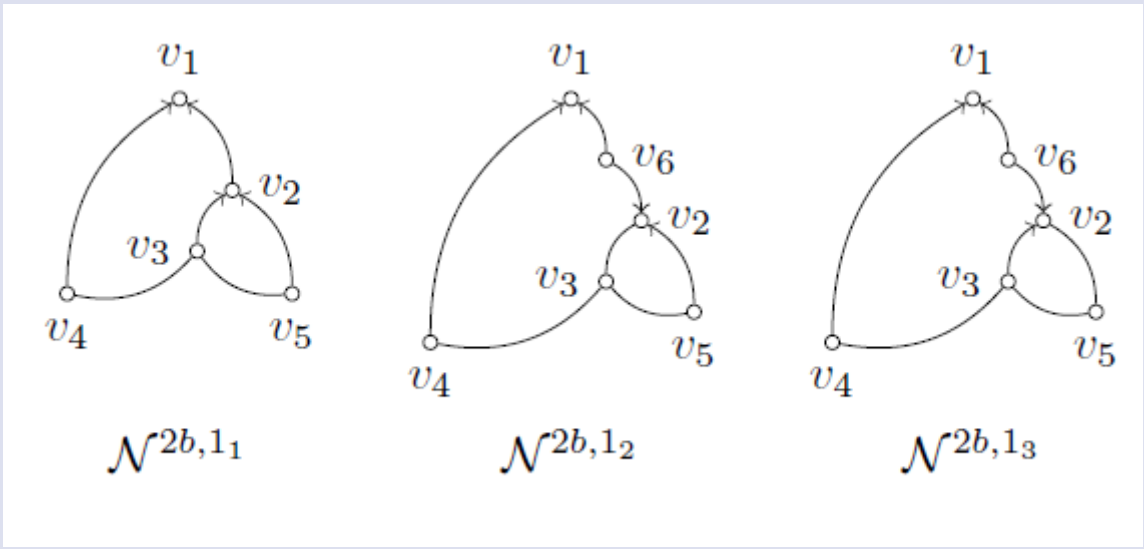

Figure 7: 3 possible $N^{2b,1}$ networks, when v_1 and v_2 are hybrid vertices.

Case (v_1, v_3): There are three different cases that are shown in Fig. 8 but only $N^{2b,1_1}$is a proper Level-2 generator.

Case (v_1, v_4): In $N^{2b,3}$, I subdivide the edge (v_1, v_4) with a vertex v_6. Assume to have the edge (v_2, v_3), then I also have (v_3, v_5) and (v_2, v_5), and I obtain a cycle (v_2, v_3, v_5). If I have the edge (v_2, v_3), I obtain the reverse cycle. Therefore, $N^{2b,3}$ cannot be a generator because there is no rooted generator that can be obtained from it.

Case (v_1, v_5): There is only one possible network $N^{2b,4}$, which is given in Fig. 14.

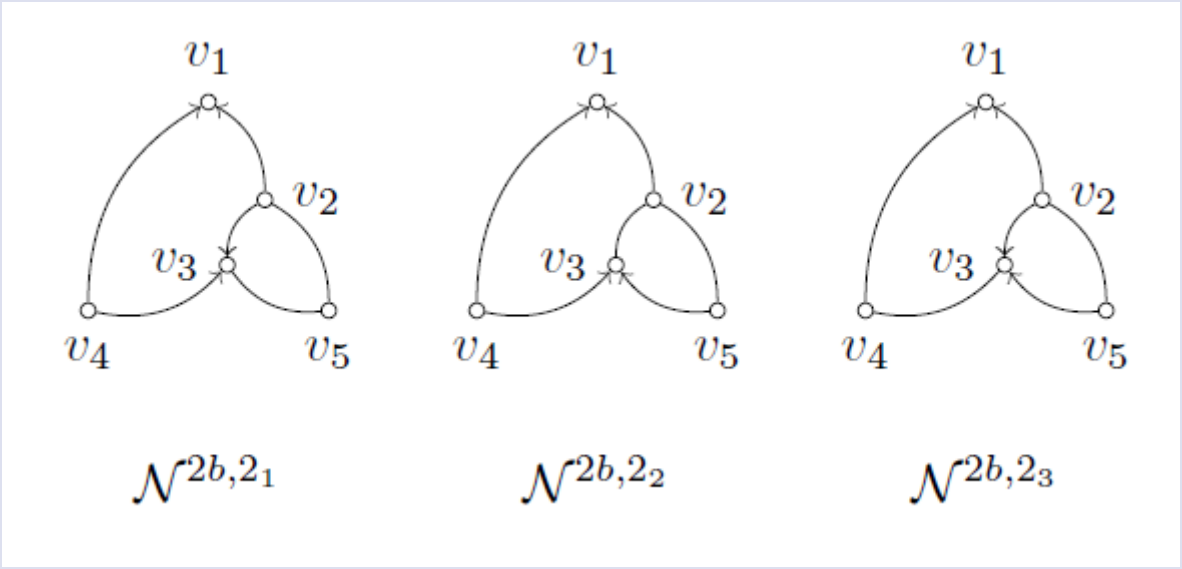

Figure 8: 3 possible $N^{2b,2}$ networks, v_1 and v_3 are hybrid vertices.

Case (v_2, v_3): there are 8 possible networks, see figure 9.

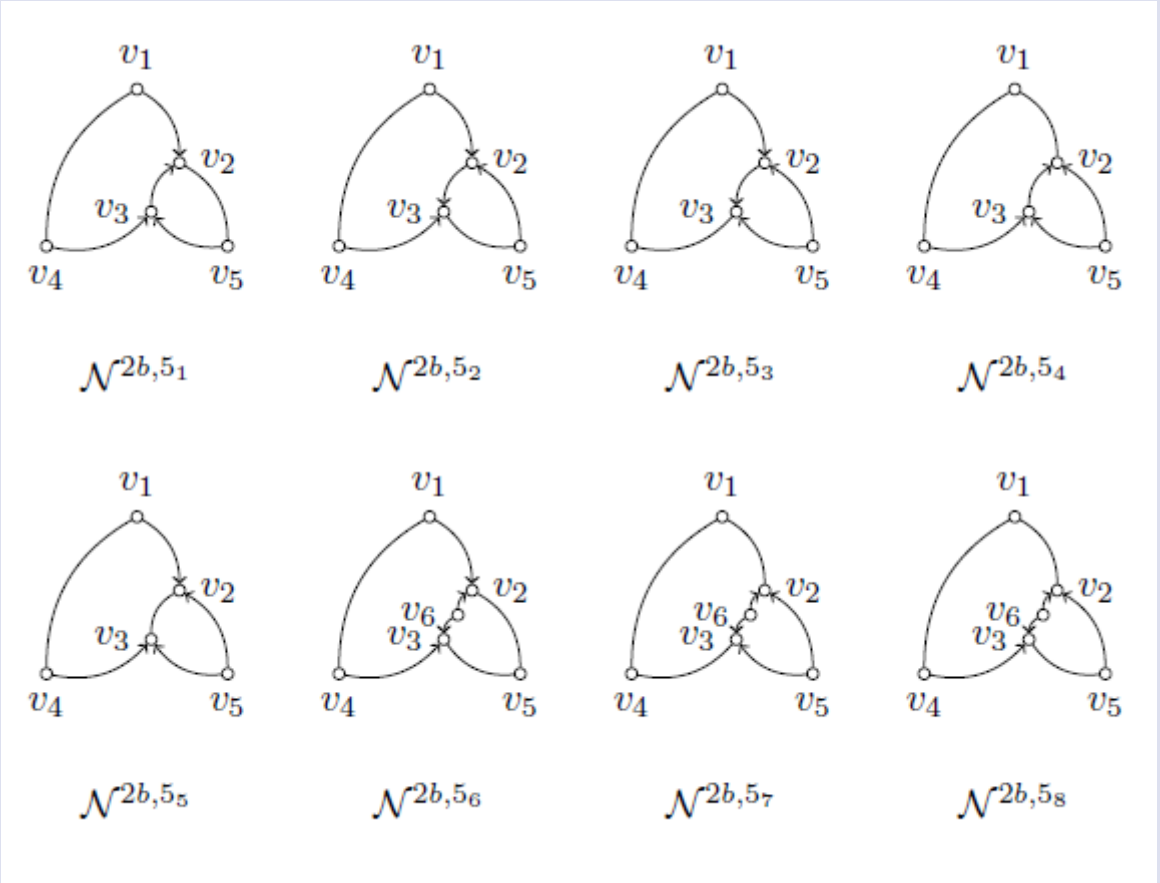

Figure 9: 8 possible $N^{2b,5}$ networks, v_2 and v_3 are hybrid vertices

Case (v_2, v_4): there are 3 possible networks, see figure 10.

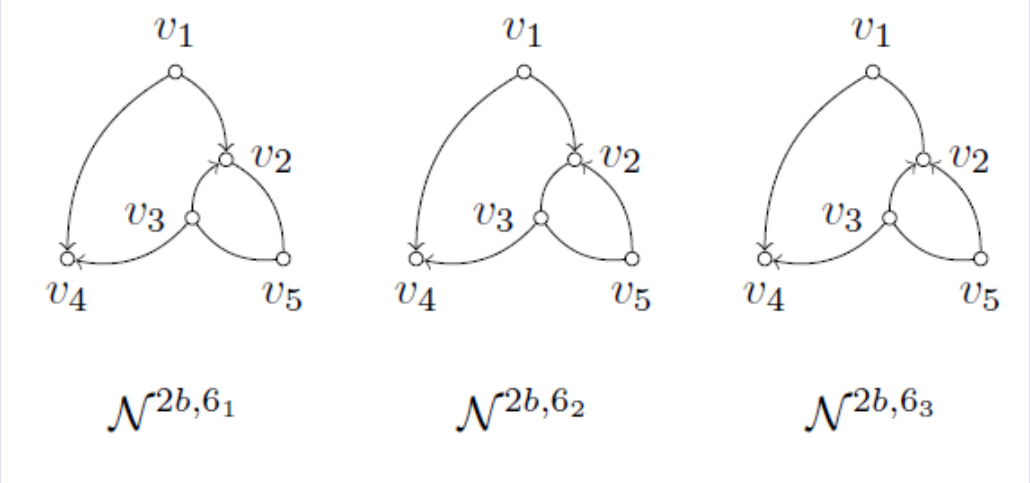

Figure 10: 3 possible $N^{2b,6}$ networks, v_2 and v_4 are hybrid vertices

Case (v_2, v_5): there are 3 possible networks, see figure 11.

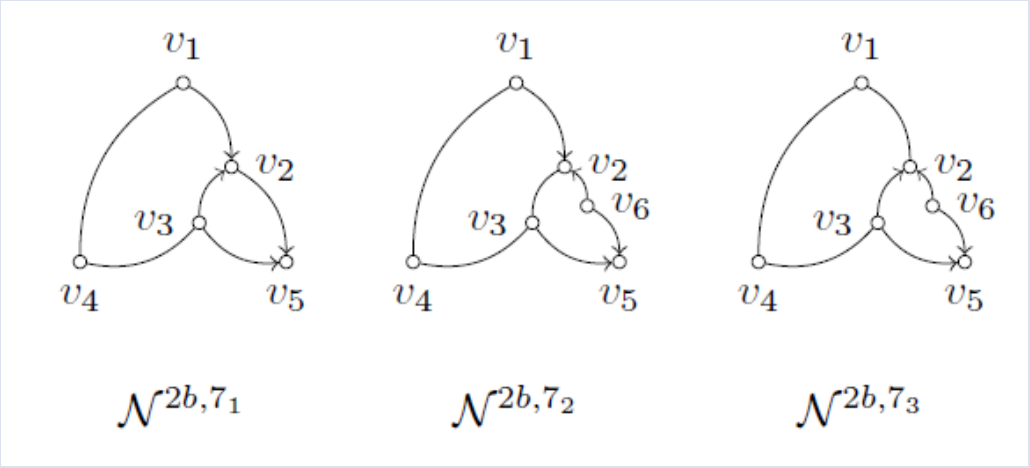

Figure 11: 3 possible $N^{2b,7}$ networks, v_2 and v_5 are hybrid vertices

Case (v_3, v_4): there are three possible networks, see figure 12.

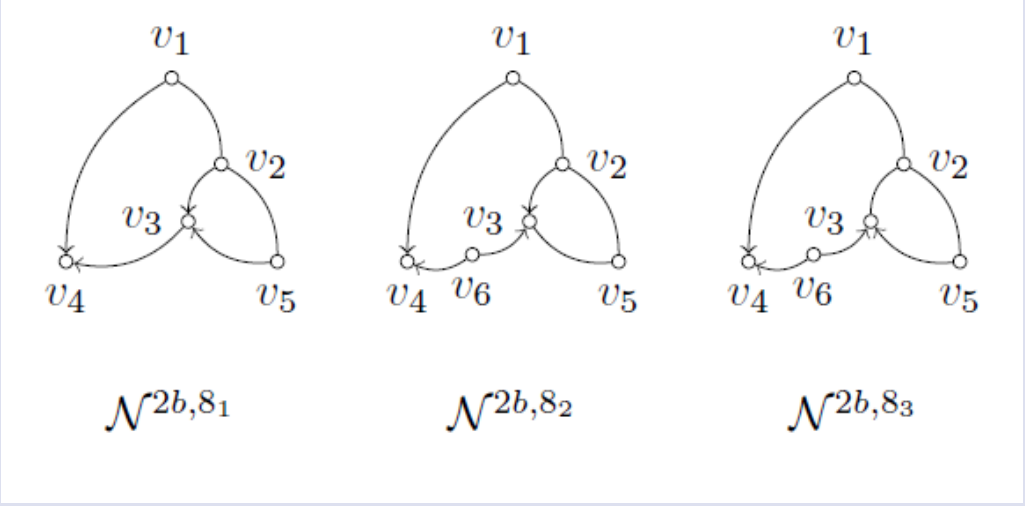

Figure 12: 3 possible $N^{2b,8}$ networks, v_3 and v_4 are hybrid vertices

Case (v_3, v_5): there are 3 possible networks, see figure 13.

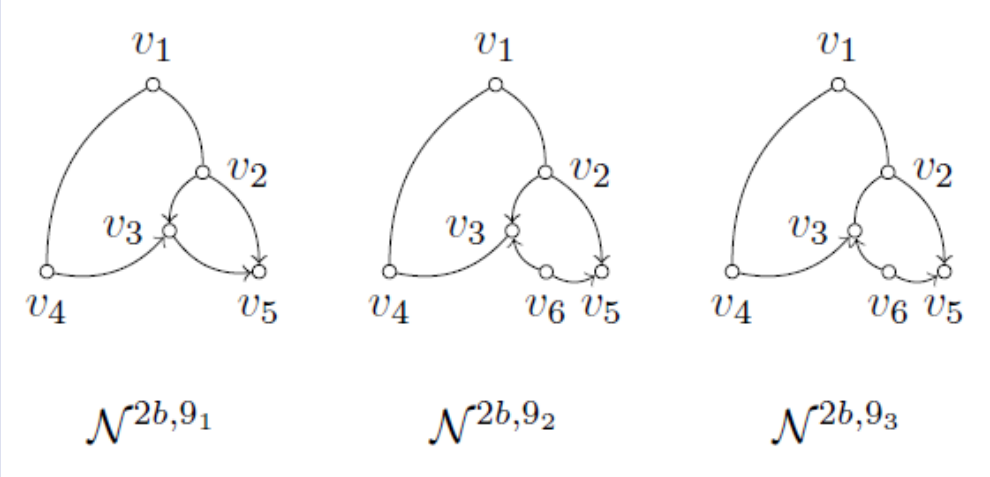

Figure 13: 3 possible $N^{2b,9}$ networks, v_3 and v_5 are hybrid vertices

Case (v_4, v_5): there is only one possible network, see figure 14.

Therefore, I obtain 4 possible generators: $N^{2b,1}$, $N^{2b,2_3}$, $N^{2b,4}$ and $N^{2b,7}$ for a semi-directed network correspondence of Level-2 type (b) generator in the directed network G^{2b} which is given in Fig. 14.

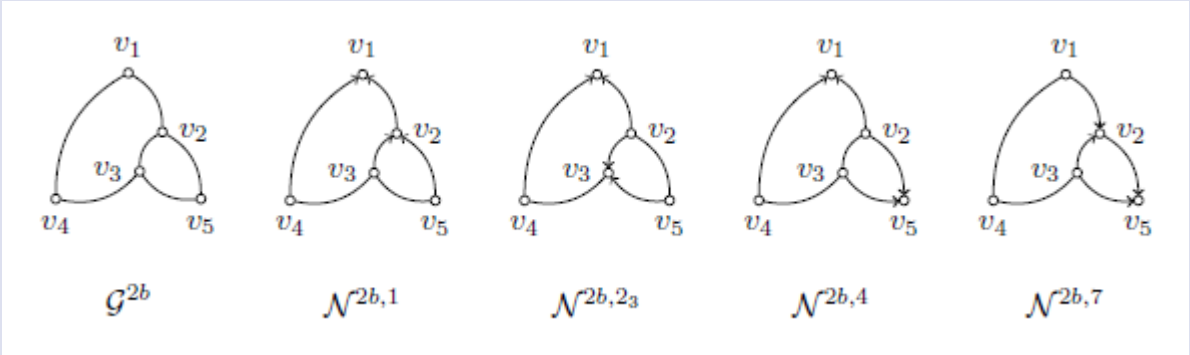

Figure 14: G^{2b} Directed Level-2 type (b) network and $N^{2b,1}$, $N^{2b,2_3}$, $N^{2b,4}$ and $N^{2b,7}$ are generators for semi-directed network Level-2 type (b) network.

For typeG^{2c}, since there are 5 vertices and 2 of them hybrid vertices, C(5, 2) = 10 possible pair of hybrid vertices: (v_1, v_2), (v_1, v_3), (v_1, v_4), (v_1, v_5), (v_2, v_3), (v_2, v_4), (v_2, v_5), (v_3, v_4), (v_3, v_4), (v_4, v_5).

Case (v_1, v_2): there are 3 possible networks, see figure 15. Network $N^{2c,1_1}$ is a possible generator.

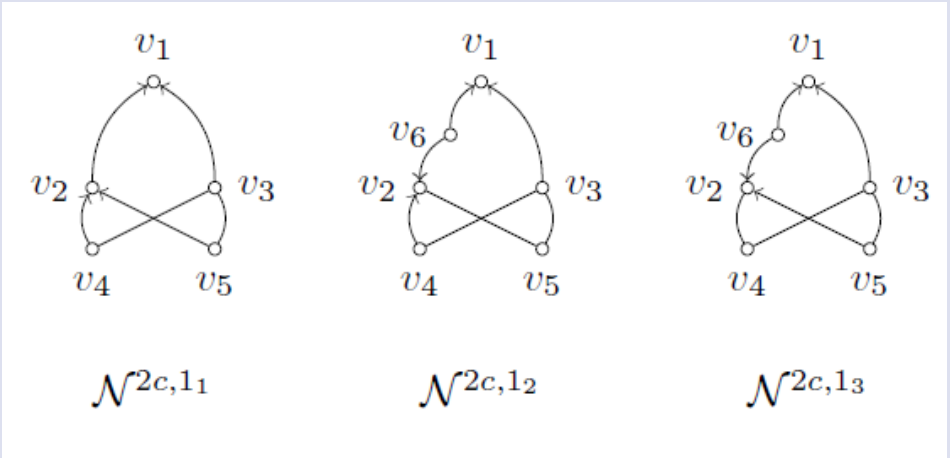

Figure 15: 3 possible $N^{2c,1}$ networks, v_1 and v_2 are hybrid vertices.

Case (v_1, v_3): there are three possible networks, see figure 15. Network $N^{2c,2}$ which are isomorphic to versions of $N^{2c,1}$.

Case (v_1, v_4): there is only one network, and it is a possible generator$N^{2c,3}$, see Fig. 19.

Case (v_1, v_5): there is only one network, and it is a possible generator $N^{2c,4}$, which is isomorphic to$N^{2c,3}$.

Case (v_2, v_3): there are 9 possible networks, see figure 16. Network $N^{2c,5_1}$ and $N^{2c,5_2}$ are possible generators.

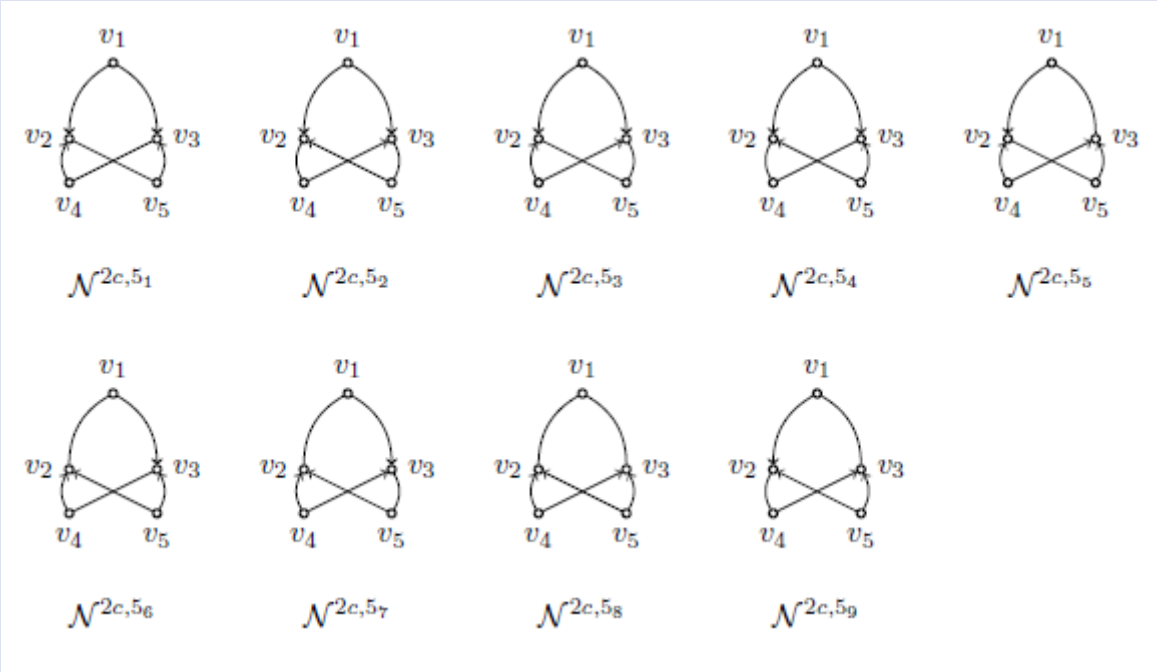

Figure 16: 3 possible $N^{2c,5}$ networks, v_2 and v_3 are hybrid vertices.

Case (v_2, v_4): There are 3 possible networks, see figure 17. Network $N^{2c,6_1}$ is a possible generator.

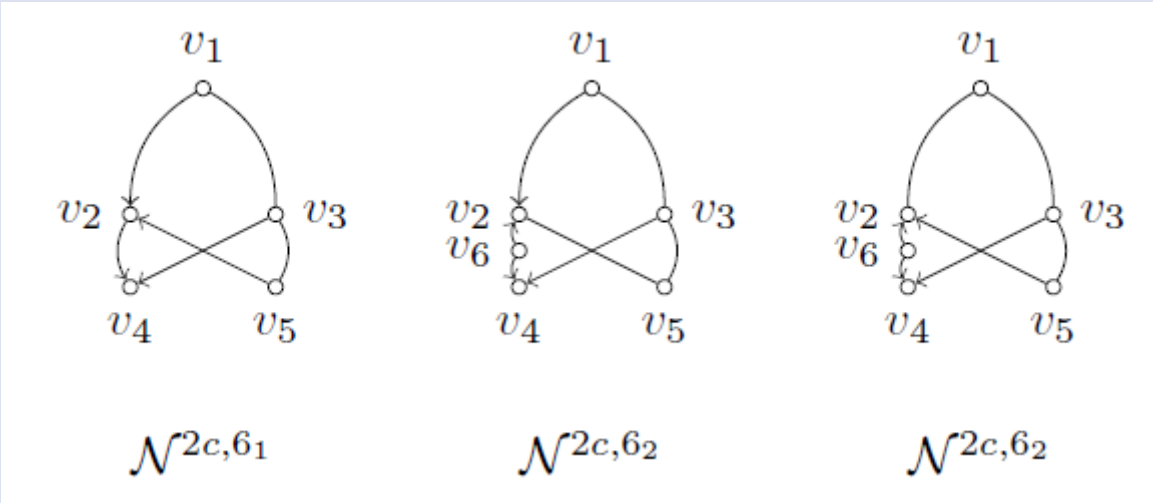

Figure 17: 3 possible $N^{2c,6}$ networks, v_2 and v_4 are hybrid vertices

Case (v_2, v_5): There are 3 possible networks, see figure 18. Network $N^{2c,7_1}$ is a possible generator.

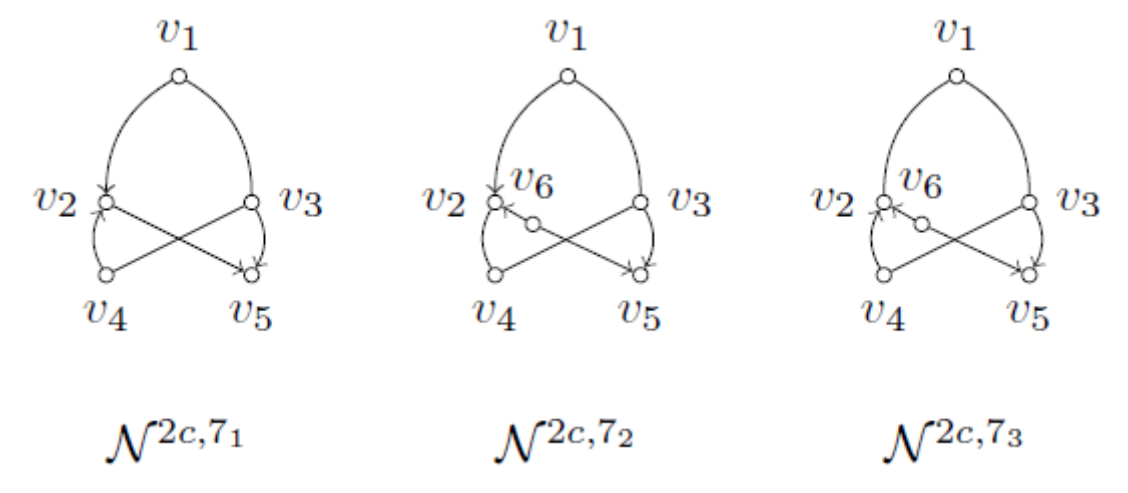

Figure 18: 3 possible $N^{2c,5}$ networks, v_2 and v_3 are hybrid vertices.

Case (v_3, v_4): I obtain 3 version of network $N^{2c,8}$ which are isomorphic to versions of $N^{2c,7}$.
Case (v_3, v_5): I obtain 3 version of network $N^{2c,9}$ which are isomorphic to versions of $N^{2c,6}$.
Case (v_4, v_5): There is only one network, and it is a possible generator $N^{2c,10}$, see Fig. 19.
Therefore, I obtain 7 possible generators $N^{2c,1_1}$, $N^{2c,3}$, $N^{2c,5_1}$, $N^{2c,5_2}$, $N^{2c,6_1}$, $N^{2c,7_1}$ and $N^{2c,10}$ for a semi-directed network correspondence of Level-2 type (c) generator in the directed network G^{2c} which is given in Fig. 19.

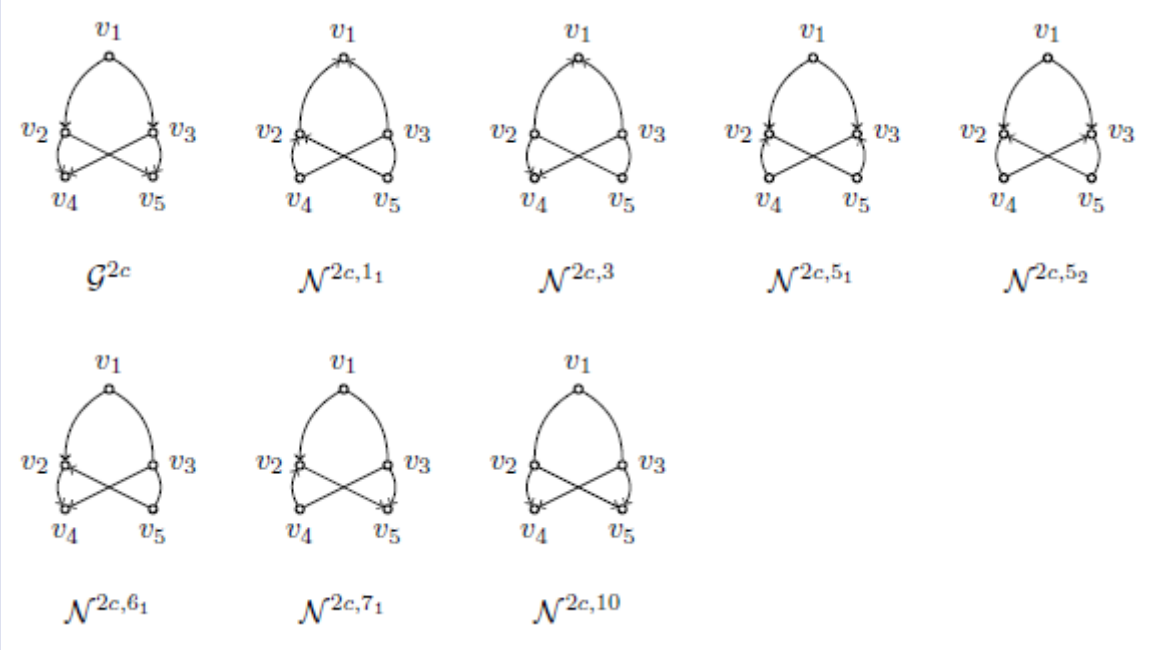

Figure 19: G^{2c} Directed Level-2 type (c) network and $N^{2c,1_1}$, $N^{2c,3}$, $N^{2c,5_1}$, $N^{2c,5_2}$, $N^{2c,6_1}$, $N^{2c,7_1}$ and $N^{2c,10}$ are generators for semi-directed network Level-2 type (c) network.

For type G^{2d}, since there are 4 vertices and 2 of them hybrid vertices, C(4, 2) = 6 possible pair of hybrid vertices: (v_1, v_2), (v_1, v_3), (v_1, v_4), (v_2, v_3), (v_2, v_4), (v_3, v_4).
Case (v_1, v_2): There are 3 possible networks, see figure 20. Network $N^{2d,1_1}$ is a possible generator.

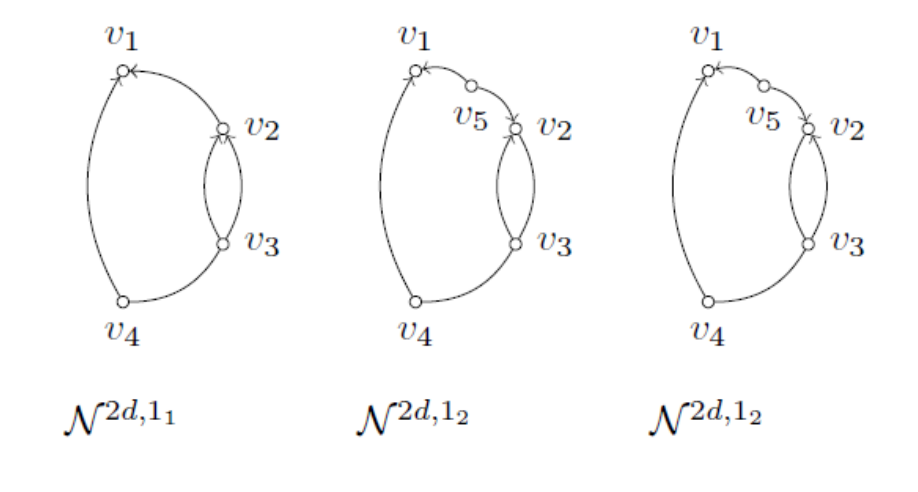

Figure 20: 3 possible $N^{2c,5}$ networks, v_2 and v_3 are hybrid vertices.

Case (v_1, v_3): There are 3 possible networks, see figure 21.

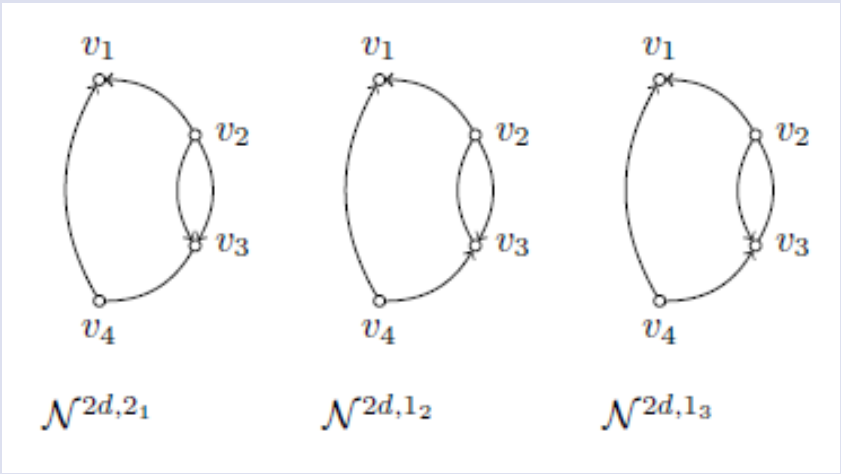

Figure 21: 3 possible $N^{2d,2}$ networks, v_1 and v_3 are hybrid vertices.

Case (v_1, v_4): There is only one network, and it is a possible generator $N^{2d,2_3}$.
Case (v_2, v_3): There are 4 possible networks, see figure 22.

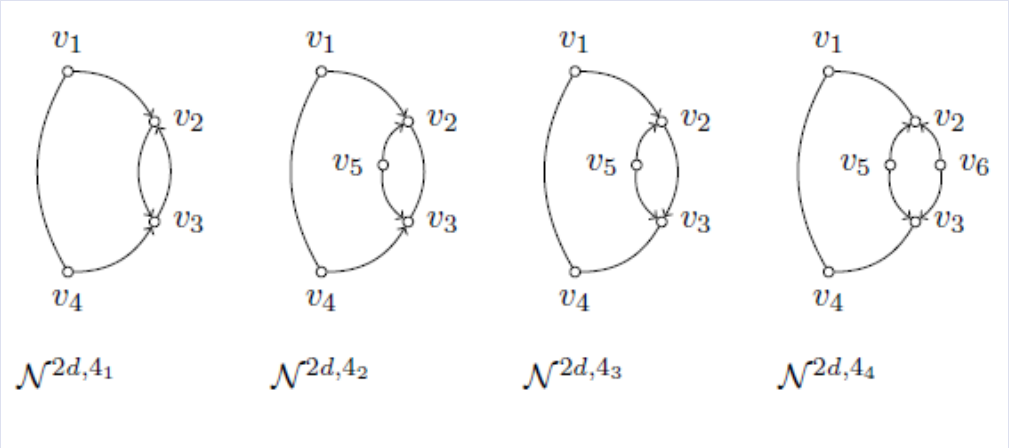

Figure 22: 4 possible $N^{2d,4}$ networks, v_2 and v_3 are hybrid vertices

Case (v_2, v_4): I obtain 3 version of network $N^{2d,5}$ which are isomorphic to versions of $N^{2d,2}$.
Case (v_3, v_4): I obtain 3 version of network $N^{2d,6}$ which are isomorphic to versions of $N^{2d,1}$.
Therefore, I obtain one possible generator $N^{2d,1_1}$ for a semi-directed network correspondence of Level-2 type (d) generator in the directed network G^{2d}, which is given in Fig. 23.

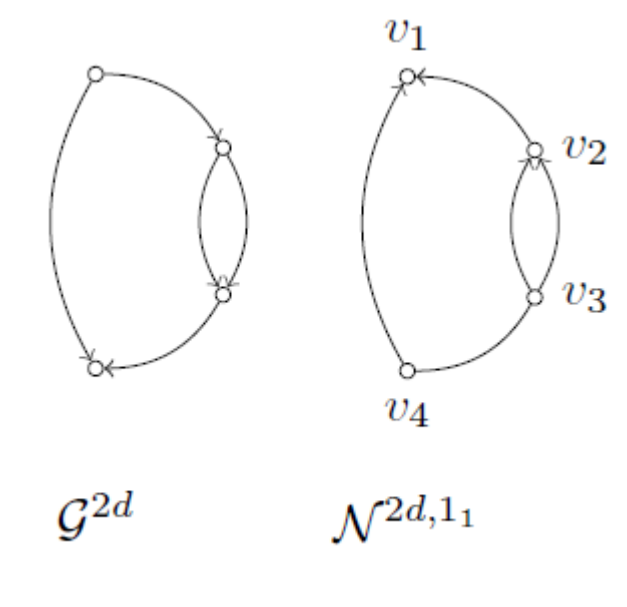

Figure 23: G^{2d} Directed Level-2 type (d) network and $N^{2d,1_1}$ are generators for semi-directed network Level-2 type (d) network.

Results and Discussion

I have shown that by considering level-k generators, I can prove that semi-directed generators isomorphic to level-k generators which is given in Figure 24. For a future work, to show that how I construct a semi-directed level-2 network when a sequence of generators is given.

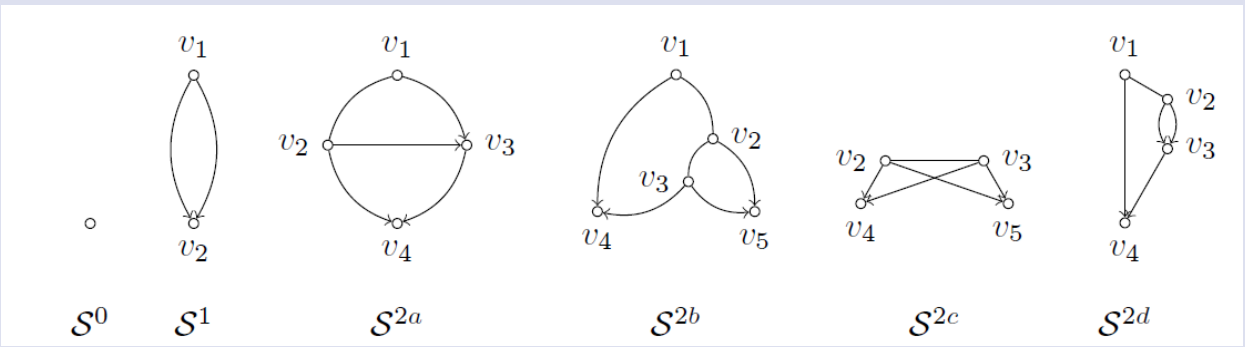

Figure 24: Level-k ≤2 generators for semi-directed networks.

Conflicts of interest

The author state that did not have conflict of interests

References

[1] Gambette P., Berry V., Paul C., The structure of level-k phylogenetic networks, *Annual Symposium on Combinatorial Pattern Matching* Springer, Berlin, Heidelberg, (2009, June). 289-300.

[2] Jansson J., Sung W. K., Inferring a level-1 phylogenetic network from a dense set of rooted triplets, *Theoretical Computer Science*, *363*(1) (2006) 60-68.

[3] Van Iersel L., Keijsper J., Kelk S., Stougie L., Hagen F., Boekhout T., Constructing level-2 phylogenetic networks from triplets, *IEEE/ACM Transactions on Computational Biology and Bioinformatics*, *6*(4) (2009) 667-681.

[4] Gross E., Long C., Distinguishing phylogenetic networks. *SIAM Journal on Applied Algebra and Geometry*, *2*(1) (2018) 72-93.

[5] Huber K. T., Moulton V., Semple C., Wu T., Quarnet inference rules for level-1 networks, *Bulletin of Mathematical Biology*, *80*(8) (2018) 2137-2153.
[6] Huebler S., Morris R., Rusinko J., Tao Y. Constructing semi-directed level-1 phylogenetic networks from quarnets, (2019) *arXiv preprint arXiv:1910.00048*.
[7] Solís-Lemus C., Ané C., Inferring phylogenetic networks with maximum pseudolikelihood under incomplete lineage sorting, *PLoS genetics*, 12(3) (2016) e1005896.

Cumhuriyet Sci. J., 44(1) (2023) 143-147
DOI: https://doi.org/10.17776/csj.1081636

Cumhuriyet Science Journal

| csj.cumhuriyet.edu.tr | Founded: 2002 ISSN: 2587-2680 e-ISSN: 2587-246X Publisher: Sivas Cumhuriyet University

The Differential Equations of Conformable Curve in IR^2

Şeyda Özel [1,a,*], **Mehmet Bektaş** [1,b]

[1] *Department of Mathematics,Faculty of Science, Fırat University, Elazığ, Türkiye.*
**Corresponding author*

Research Article

History
Received: 02/03/2022
Accepted: 19/12/2022

ABSTRACT

In this paper, we get some characterizations of conformable curve in $\mathbb{R}^2$. We investigate the conformable curve in $\mathbb{R}^2$. We define the tangent vector of the curve using the conformable derivative and the arc parameter s. Then, we get the Frenet formulas with conformable frames. Moreover, we define the location vector of conformable curve according to Frenet frame in the plane $\mathbb{R}^2$.

Finally, we obtain the differential equation characterizing location vector and curvature of conformable curve in the plane $\mathbb{R}^2$.

Keywords: Comformable curve, Location vector, Comformable frame.

[a] *s_demir2323@outlook.com* *https://orcid.org/0000-0002-1519-2418* [b] *mbektas@firat.edu.tr* *https://orcid.org/0000-0002-5797-4944*

Introduction

The fractional analysis phrase has been first appearing in a letter written by L' Hospital to Leibniz. In this letter, L' Hospital has asked Leibniz about a special structure that he used in his work for $\frac{d^n y}{dx^n}$. L' Hospital has asked how to take the derivative and what would be the result if the order of the derivative was a rational number, for instance, $n = \frac{1}{2}$ [1]. This question has created the first glint of fractional analysis. Most of the mathematical theories used in fractional analysis have been developed before the 20th century. However, to keep up with scientific developments, mathematicians have made a few changes to the structure of fractional calculus. Caputo has renewed the Riemann-Liouville fractional derivative and has introduced the Caputo derivative as a new derivative concept [2]. Many scientists, Khalil and his colleagues first came up with the definition of conformable derivative in 2014. Because of its similarity to the classical derivative definition, this derivative was the simplest of the fractional derivative definitions. Although the concepts of Riemann-Liouville and Caputo fractional derivatives are being widely used today, they are not as common as the conformable derivative because they have some deficiencies [3].The product and quotient rule, which could not be provided for the other fractional derivatives mentioned above, could be provided for this new definition of fractional derivative. In addition, a constant function has no Caputo fractional derivative among these fractional derivatives [4,5]. In a short time, many studies have been done on conformable derivatives. T. Abdejavad, J. Alzabut, F. Jarad, R.P. Agarval, A. Zbekler have studied Lyapunov type inequalities in the conformable derivative frame [6,7]. Moreover, further works have been done on the conformable derivative [8,9,10].

Finally, in this paper, the characterizations of a conformable curve in the plane $\mathbb{R}^2$ are expressed using the conformable derivative.

Geometric Preliminaries

Given a function $f:[0,\infty) \longrightarrow \mathbb{R}$. The conformable derivative of the function f of order α is defined by

$$T_\alpha f(x) = \lim_{h\to 0} \frac{f(x + hx^{1-\alpha}) - f(x)}{h} = x^{1-\alpha} f'(x) \tag{1}$$

for all $x > 0, \alpha \in (0,1)$ [11]. The function $\gamma:(0,\infty) \longrightarrow \mathbb{R}^2$ is called a conformable curve in $\mathbb{R}^2$ if γ is α −differentiable,

Let $\gamma:(0,\infty) \longrightarrow \mathbb{R}^2$ be a conformable curve. The velocity vector of γ is determined by

$$\frac{T_\alpha \gamma(t)}{t^{1-\alpha}}, \tag{2}$$

for all $t \in (0,\infty)$.

Let $\gamma:(0,\infty) \longrightarrow \mathbb{R}^2$ be a conformable curve. Then the velocity function v of γ is defined by

$$v(t) = \frac{\|T_\alpha \gamma(t)\|}{t^{1-\alpha}} \tag{3}$$

for all $t \in (0,\infty)$.

Let $\gamma:(0,\infty) \longrightarrow \mathbb{R}^2$ be a conformable curve. The arc length function s of γ is defined by

$$s = \int_t^0 \|T_\alpha \gamma(t)\| \, dt \tag{4}$$

for all $t \in (0, \infty)$, it's said that γ is a unit speed.

Now, let us define the tangent vector of the curve using the conformable derivative and the arc parameter

$$s, e_1^\alpha(s) = T_\alpha \gamma(s) = \left(T_\alpha(x(s)), T_\alpha(y(s))\right) = \left(\frac{d^\alpha x(s)}{ds^\alpha}, \frac{d^\alpha y(s)}{ds^\alpha}\right). \tag{5}$$

The norm of the tanget vector is $\|e_1^\alpha(s)\| = 1$. Furthermore,

$$e_2^\alpha(s) = \left(-T_\alpha(y(s)), T_\alpha(x(s))\right). \tag{6}$$

Here, for γ curve with the parameter s , $e_1^{(\alpha)}(s)$ and $e_2^{(\alpha)}(s)$ are the conformable unit tangent vector and unit normal vector of the curve γ, respectively, and the parameter s is the arc length. The Frenet-Serret formulas with conformable frames $e_1^\alpha(s)$, $e_2^\alpha(s)$ are given as

$$\frac{de_1^{(\alpha)}(s)}{ds} = \mathrm{K}^{(\alpha)}(s) e_2^{(\alpha)}(s) \tag{7}$$

$$\frac{de_2^{(\alpha)}(s)}{ds} = -\mathrm{K}^{(\alpha)}(s) e_1^{(\alpha)}(s), \tag{8}$$

where $K^{(\alpha)}(s)$ is curvature of the unit speed curve $\alpha = \alpha(s)$.

Location Vector of a Conformable Curve in $\mathbb{R}^2$

In this chapter, we have used the proof method and terminology of see [12].
Let us take the conformable curve $\gamma = \gamma(s)$ into consideration in the plane $\mathbb{R}^2$. In this case, we can write the location vector of $\gamma(s)$ according to Frenet frame as

$$x = x(s) = \mu_1 e_1^\alpha(s) + \mu_2 e_2^\alpha(s), \tag{9}$$

here μ_1 and μ_2 are arbitrary functions connected to s.
If we differentiate the equality (9) and use Frenet equations, we get

$$\frac{d\mu_1}{ds} - \mu_2 \mathrm{K}^{(\alpha)} = s^{\alpha-1} \tag{10}$$

and

$$\frac{d\mu_2}{ds} + \mu_1 \mathrm{K}^{\alpha} = 0. \tag{11}$$

Then, by using (10) in (11), we get

$$\frac{d}{ds}\left[\frac{1}{\mathrm{K}^\alpha}\left(\frac{d\mu_1}{ds} - s^{\alpha-1}\right)\right] + \mu_1 K(^{\alpha}) = 0. \tag{12}$$

According to μ_1, this second order differential equation is a characterization obtained from the conformable curve $\gamma = \gamma(s)$.

In equation (12), by using change of variable

$$\varphi = \frac{1}{\mathrm{K}^{(\alpha)}}, \quad \theta = \int_0^s \mathrm{K}^{(\alpha)}.ds, \tag{13}$$

we obtain

$$\frac{d\varphi}{ds}\left(\frac{d\mu_1}{ds} - s^{\alpha-1}\right) + \varphi\left(\frac{d\mu_1}{ds} - \frac{ds^{\alpha-1}}{ds}\right) + \frac{\mu_1}{\varphi} = 0. \tag{14}$$

Now, if this differential equation is tried to be solved, we obtain

$$\frac{d\varphi}{ds} = \frac{d\varphi}{d\sigma}\frac{d\theta}{ds} = \frac{d\varphi}{d\theta}\frac{1}{\varphi} \tag{15}$$

$$\frac{d\mu_1}{ds} = \frac{d\mu_1}{d\theta}\frac{d\theta}{ds} = \frac{d\mu_1}{ds}\frac{1}{\varphi} \tag{16}$$

and

$$\frac{d^2\mu_1}{ds^2} = \frac{d}{ds}\left(\frac{d\theta}{ds}\right) = \frac{d}{ds}\left(\frac{d\mu_1}{ds}\frac{1}{\varphi}\right) = \frac{d}{d\theta}\left(\frac{d\mu_1}{d\theta}\frac{1}{\varphi}\right)\frac{1}{\varphi} = \frac{1}{\varphi^2}\left[\frac{d^2\mu_1}{d\theta^2} - \frac{1}{\varphi}\frac{d\mu_1}{d\theta}\frac{d\varphi}{d\theta}\right]. \tag{17}$$

Later, by using of (15), (16), (17) in equation (14), we get

$$\frac{d^2\mu_1}{d\theta^2} + \mu_1 = \varphi^2(\alpha-1)s^{\alpha-2} + s^{\alpha-1}. \tag{18}$$

Let us try to solve the differential equation (18). This equation's solution of homogeneous is

$$y_p = c_1\cos\theta + c_2\sin\theta. \tag{18}_1$$

Due to variation of the parameters, we get this formula as following

$$y_p = v_1\cos\theta + v_2\sin\theta.$$

Here, functions v_1, v_2 are differentiable functions.

In that case, we acquire simply

$$y_p' = v_1'\cos\theta + v_2'\sin\theta - v_1.\sin\theta + v_2\cos\theta.$$

Additionally, because of

$$v_1'\cos\theta + v_2'\sin\theta = 0, \tag{19}$$

we obtain

$$y_p'' = -v_1\cos\theta - v_2\sin\theta - v_1'\sin\theta + v_2'\cos\theta,$$

and so we get

$$-v_1'\sin\theta + v_2'\cos\theta = \varphi^2(\alpha-1)s^{\alpha-2} - s^{\alpha-1}. \tag{20}$$

From the expressions (10) and (11), we acquire

$$v_1' = \sin\theta\varphi^2(\alpha-1)s^{\alpha-2} - s^{\alpha-1} \tag{21}$$

$$v_2' = \cos\theta\varphi^2(\alpha-1)s^{\alpha-2} - s^{\alpha-1}. \tag{22}$$

Afterward, if we integrate the expressions (21) and (22), respectively, we can acquire

$$v_1 = \left[\int \varphi^2\sin\theta(\alpha-1)s^{\alpha-2}d\theta - \int s^{\alpha-1}d\theta\right] \tag{23}$$

$$v_2 = \left[\int \varphi^2\cos\theta(\alpha-1)s^{\alpha-2}d\theta - \int s^{\alpha-1}d\theta\right]. \tag{24}$$

On the other side, if it is taken into account the equations $(18)_1$, (23), and (24), we can also get

$$\mu_1 = c_1\cos\theta + c_2\sin\theta + v_1e_1^{\theta} + v_2e_2^{\theta}$$

or

$$\mu_1 = c_1\cos\theta + c_2\sin\theta + \left[(\alpha-1)\int_0^s \varphi^2\sin\theta(\alpha-1)s^{\alpha-2}d\theta - \int_0^s s^{\alpha-1}d\theta\right] + + \left[(\alpha-1)\int_0^s \varphi^2\cos\theta(s^{\alpha-2}d\theta - \int_0^s s^{\alpha-1}d\theta\right].$$

On the other and, if $\frac{d\mu_1}{ds} = l(s)$ is being taken, from expression (10), we can express as follows:

$$\mu_2 = \frac{1}{\mathrm{K}^\alpha}[l(s) - s^{\alpha-1}]. \tag{25}$$

As a result, we give the following theorem:

Theorem 1: Let us assume that the curve $\gamma(s)$ is a unit speed conformable curve with α −Frenet frame in the plane $\mathbb{R}^2$. So, the location vector of the conformable curve $\gamma(s)$ is

$$\begin{aligned} x = x(s) = \Bigg\{ & c_1 \cos\theta + c_2 \sin\theta + \left[(\alpha-1)\int_0^s \varphi^2 \sin\theta s^{\alpha-2} d\theta - \int s^{\alpha-1} d\theta\right] \\ & + \left[(\alpha-1)\int_0^s \varphi^2 \cos\theta s^{\alpha-2} d\theta - \int_0^s s^{\alpha-1} d\theta\right]\Bigg\} e_1^\alpha(s) \\ & + \{\varphi[l(s) - s^{\alpha-1}]\} e_2^\alpha(s), \end{aligned} \tag{26}$$

where $\varphi = \frac{1}{\mathrm{K}^\alpha}, \theta = \int_0^s d\theta$.

Theorem 2: Let us assume that the curve $\gamma(s)$ is a unit-speed conformable curve with α −Frenet frame in the plane $\mathbb{R}^2$. Then the connection between the curvature of the α −Frenet frame conformable curve $\gamma(s)$ and the location vector can be written as follows

$$\frac{d}{ds}\left(\frac{1}{\mathrm{K}^\alpha}\left((\alpha-1)s^{\alpha-2}\frac{d\gamma}{ds} + s^{\alpha-1}\frac{d^2\gamma}{ds}\right) + \mathrm{K}^\alpha s^{\alpha-1}\frac{d\gamma}{ds} = 0\right). \tag{27}$$

Proof: Let us think $\gamma(s)$ be a unit speed conformable curve with α −Frenet frame in the plane $\mathbb{R}^2$. Then α −Frenet frame is provided by the following equations:

$$\frac{de_1^\alpha(s)}{ds^\alpha} = \mathrm{K}^\alpha e_2^\alpha(s) \tag{28}$$

and

$$\frac{de_2^\alpha(s)}{ds^\alpha} = -\mathrm{K}^\alpha e_1^\alpha(s). \tag{29}$$

By writting equation (28) in equation (29), we simply get

$$\frac{d}{ds}\left(\frac{1}{\mathrm{K}^\alpha}\frac{de_1^\alpha(s)}{ds^\alpha}\right) + \mathrm{K}^\alpha e_1^\alpha(s) = 0. \tag{30}$$

Besides, $e_1^\alpha(s) = T_\alpha\gamma(s) = s^{\alpha-1}\frac{d\gamma}{ds}$, by writting this expression in equation (30), we can obtain equations as follows:

$$\frac{d}{ds}\left(\frac{1}{\mathrm{K}^\alpha}\frac{d}{ds}\left(s^{\alpha-1}\frac{d\gamma}{ds}\right)\right) + \mathrm{K}^\alpha s^{\alpha-1}\frac{d\gamma}{ds} = 0$$

or

$$\frac{d}{ds}\left(\frac{1}{\mathrm{K}^\alpha}\left((\alpha-1)s^{\alpha-2}\frac{d\gamma}{ds} + s^{\alpha-1}\frac{d^2\gamma}{ds^2}\right) + \mathrm{K}^\alpha s^{\alpha-1}\frac{d\gamma}{ds} = 0\right).$$

As a result, the proof is being completed.

Acknowledgment

The author would like to thank the referees for their valuable comments and suggestions for the improvement of the article.

Conflicts of interest

The authors stated that there is no conflict of interest.

References

[1] Nishimoto K., An essence of Nishimoto's Fractional Calculus (Calculus in the 21st century): Integrations and Differentiations of Arbitrary Order, Descartes Press Company, Koriyama, (1991).

[2] Weilber M., Efficient Numerical Methods for Fractional Differential Equations and their Analytical Background, Ph. D. Thesis, Von der Carl-Friedrich-Gaub-Fakultur Mathematic and Informatik der Te chnis-chen University, 2005.

[3] Khalil, R., Al Harani, M., Yousef A., Sababheh M., A new definition of fractional derivative, *J. Comput and Applied Mathematics*, 264 (2014) 65-70.

[4] Baleanu, D., Vacaru, S., Constant curvature coefficients and exact solutions in fractional gravity and geometric mechanics, *Open Physics*, *9*(5) (2011) 1267-1279.

[5] Baleanu, D., Vacaru, S. I., Fractional almost Kähler–Lagrange geometry, *Nonlinear Dynamics*, *64*(4) 365-373.

[6] Abdeljawad, T., Alzabut, J., Jarad, F., A generalized Lyapunov-type inequality in the frame of conformable derivatives, *Advances in Difference Equations*, 2017(1) 1-10.

[7] Abdeljawad, T., Agarwal, R. P., Alzabut, J., Jarad, F., Özbekler, A., Lyapunov-type inequalities for mixed non-linear forced differential equations within conformable derivatives, *Journal of Inequalities and Applications*, 1 (2018) 1-17.

[8] Atangana, A., Baleanu, D., Alsaedi, A., New properties of conformable derivative, *Open Mathematics*, 13(1) (2015).

[9] Anderson, D. R., Ulness, D. J., Newly Defined Comformable Derivatives Centered Polygonal Lacunary Functions View project Dynamic Equations on Times Scales View Project Newly Defined Comformable Derivatives, Advances in Dynamical Systems and Applications, 10(2) (2015) 109-137.

[10] Aminikhah H., Sheikhani A.H.R., Rezazadeh H., Sub-equation method fort he fractional regularized long-wave equations with comformable fractional derivatives, Sci. Iran, 23 (2016) 1048-1054.

[11] Gözütok U., Çoban H., Sağıroğlu Y., Frenet frame with respect to conformable derivative, *Filomat*., *33* (6) (2019).

[12] Mağden A., Yılmaz S., Ünlütürk Y., Characterizations of special time-like curves in Lorentzian plane $\mathbb{L}^2$, *International Journal of Geometric Methods In Modern Physics.*, *14* (10) (2017).

Cumhuriyet Sci. J., 44(1) (2023) 148-159
DOI: https://doi.org/10.17776/csj.1173233

Cumhuriyet Science Journal

| csj.cumhuriyet.edu.tr | Founded: 2002 ISSN: 2587-2680 e-ISSN: 2587-246X Publisher: Sivas Cumhuriyet University

Common Fixed Point Results for Suzuki Type Contractions on Partial Metric Spaces with an Application

Kübra Özkan [1,a,*]

[1] *Department of Mathematics, Faculty of Science and Arts, Manisa Celal Bayar University, Manisa, Turkey.*
**Corresponding author*

Research Article

History
Received: 09/09/2022
Accepted: 24/01/2023

ABSTRACT

In this article, we prove a common fixed point theorem for Suzuki type contractions on complete partial metric spaces. Moreover, we state some corollaries related to Suzuki type common fixed point theorem. And we give an example where we apply our main theorem on complete partial metric spaces. Finally, to show usability of our results, we give its an application showing existence and uniqueness of a common solution for a class of functional equations in dynamic programming.

Keywords: Partial metric spaces, Fixed point theory, Completeness.

[a] *kubra.ozkan@hotmail.com* *https://orcid.org/0000-0002-8014-1713*

Introduction

In 2008, Suzuki [1] introduced a useful generalization of Banach fixed point theorem called as Suzuki fixed point theorem as follows:

Let (X,d) be a complete metric space and let T be a self-mapping on X. We consider a nonincreasing function by

$$\theta(r)=\begin{cases}1, & 0\le r\le \dfrac{\sqrt{5}-1}{2},\\ \dfrac{1-r}{r^2}, & \dfrac{\sqrt{5}-1}{2}\le r\le \dfrac{1}{\sqrt{2}},\\ \dfrac{1}{1+r}, & \dfrac{1}{\sqrt{2}}\le r<1.\end{cases}$$

Assume that there exists $r\in[0,1)$ such that

$$\theta(r)d(x,Tx)\le d(x,y)\Rightarrow d(Tx,Ty)\le rd(x,y)$$

for all $x,y\in X$. Then, there exists a unique fixed point u of T. Moreover, $\lim_{n\to\infty} T^n x=u$ for all $x\in X$. In view of this generalization, several authors generalized Suzuki's fixed point theorem, see [2-9] and the references therein. In recently, Wangwe and Kumar [10] combined Kannan and Suzuki results and introduced a new fixed point theorem in TVS valued cone metric space.

In 1994, Matthews introduced the concept of partial metric spaces [11]. They are seen as a part of the study of denotational semantics of dataflow networks and play an important role in the creation of models in the computational theory. So, many authors studied on partial metric spaces, and they gave different fixed point theorems on these type metric spaces, such as Kannan's, Caristi's, Nadler's and Suzuki's. For more details, the readers can refer to [12-19].

In this paper, we prove a common fixed point theorem for Suzuki type contractions on complete partial metric spaces. We also state some corollaries related to Suzuki type common fixed point theorem. We also give an example where we apply our main theorem on complete partial metric spaces. Finally, to show usability of our results, we give its an application showing existence and uniqueness of a common solution for a class of functional equations in dynamic programming

Preliminaries

We start by recalling a series of definitions of some fundamental notions related to partial metric spaces. In the following $\mathbb{R}^+$ stands for the set of all non-negative real numbers, i.e., $\mathbb{R}^+=[0,\infty)$.

Definition 1. Let $X\neq\varnothing$. A function $p:X\times X\to\mathbb{R}^+$ is called a partial metric, if it holds the following properties for all $x,y,z\in X$

(p1) $x=y\Leftrightarrow p(x,x)=p(x,y)=p(y,y)$,

(p2) $p(x,x)\le p(x,y)$,

(p3) $p(x,y)=p(y,x)$,

(p4) $p(x,y)\le p(x,z)+p(z,y)-p(z,z)$.

A pair (X,p) is called partial metric space. Shortly, we write PMS for the partial metric space. From (p1) and (p2), we get that if $p(x,y)=0$, then $x=y$. But the opposite may not be true. If we define partial metric as $p(x,y)=\max\{x,y\}$ for all $x,y\in\mathbb{R}^+$, then the pair $(\mathbb{R}^+,p)$ is a PMS. This is a basic for PMS [11].

p induces a T_0 topology τ_p on X having the base

$$\{B_p(a,\varepsilon): a\in X,\varepsilon>0\},$$

where $B_p(a,\varepsilon)=\{b\in X: p(a,b)<p(a,a)+\varepsilon\}$ for all $a\in X$ and $\varepsilon>0$ [9].

Definition 2. Let (X,p) be a PMS.

(1) A sequence $(x_n)_{n\in\mathbb{N}}$ in X converges to a point $x\in X$ if and only if $p(x,x)=\lim_{n\to\infty}p(x,x_n)$.

(2) A sequence $(x_n)_{n\in\mathbb{N}}$ in X is called a Cauchy sequence if there exists (and is finite)

$\lim_{n,m\to\infty}p(x_n,x_m)$.

(3) (X,p) is called complete if every Cauchy sequence $(x_n)_{n\in\mathbb{N}}$ in X converges, with respect to τ_p, to a point $x\in X$ such that $p(x,x)=\lim_{n,m\to\infty}p(x_n,x_m)$ [11].

Lemma 1. Let (X,p) be a PMS and $(x_n)_{n\in\mathbb{N}}$ be a sequence in X Suppose that $x_n\to u$ as $n\to\infty$ in a PMS (X,p) such that $p(u,u)=0$. Then $\lim_{n\to\infty}p(x_n,y)=p(u,y)$ for every $y\in X$ [20].

The function $p^s: X\times X\to[0,\infty)$ given by $p^s(x,y)=2p(x,y)-p(x,x)-p(y,y)$ is a metric on X where p is a partial metric on X [11].

Lemma 2. Let (X,p) be a PMS and $(x_n)_{n\in\mathbb{N}}$ be a sequence in X

(1) The sequence $(x_n)_{n\in\mathbb{N}}$ is a Cauchy sequence in (X,p) if and only if it is a Cauchy sequence in the metric space (X,p^s).

(2) (X,p) is complete if and only if the metric space (X,p^s) is complete. Furthermore,

$\lim_{n\to\infty}p^s(x,x_n)=0\Leftrightarrow p(x,x)=\lim_{n\to\infty}p(x,x_n)=\lim_{n\to\infty}p(x_n,x_m)$ [11].

Main Results

Theorem 1. Let (X,p) be a complete PMS, $T,S: X\to X$ be two self-maps and a nonincreasing function $\theta:[0,1)\to\left(\frac{1}{2},1\right]$ be defined by

$$\theta(r)=\begin{cases}1, & 0\le r\le\dfrac{\sqrt{5}-1}{2},\\ \dfrac{1-r}{r^2}, & \dfrac{\sqrt{5}-1}{2}\le r\le\dfrac{1}{\sqrt{2}},\\ \dfrac{1}{1+r}, & \dfrac{1}{\sqrt{2}}\le r<1.\end{cases}$$

If there exists $r\in\left[0,\frac{1}{2}\right)$ such that

$$\theta(r)\min\{p(x,Tx),p(x,Sx)\}\le p(x,y) \tag{1}$$

Implies

$$\max\left\{p(Sx,Sy),p(Tx,Ty),\frac{1}{2}\left[p(Sx,Ty)+p(Sy,Tx)\right]\right\}\le rp(x,y),$$

for all $x,y\in X$, then T and S have a unique common fixed point.

Proof. Firstly, we prove that if u is a fixed point of T (or S), then it is also fixed point of S (or T). We suppose that u is a fixed point of T, that is, $Tu=u$. We want to show that $Su=u$. Taking $x=u$ and $y=Tu$ in (1), we get

$$0 \le \theta(r)\min\left\{p(u,Tu), p(u,Su)\right\} \le p(u,Tu)$$

implies

$$p(Su,u) \le \max\left\{p(Su,STu), p(Tu,T^2u), \frac{1}{2}\left[p(Su,T^2u)+p(STu,Tu)\right]\right\}$$
$$\le rp(u,Tu).$$

Hence, we have $p(Su,u) \le rp(u,u)$. From property $(p2)$ of PMS, we get

$$p(u,u) \le p(Su,u) \le rp(u,u).$$

So, $p(u,u) = 0$. Then we get $Su = u$. Similarly, the contrary can be shown easily. Therefore, it is enough to show that T has a fixed point to complete the proof. Putting $y = Sx$ in (1), we have

$$\theta(r)\min\left\{p(x,Tx), p(x,Sx)\right\} \le p(x,Sx)$$

implies

$$\max\left\{p(Sx,S^2x), p(Tx,TSx), \frac{1}{2}\left[p(Sx,TSx)+p(S^2x,Tx)\right]\right\} \le rp(x,Sx)$$

for every $x \in X$. Hence, we get

$$\frac{1}{2}p(Sx,TSx) \le \frac{1}{2}\left[p(Sx,TSx)+p(S^2x,Tx)\right] \le rp(x,Sx). \quad (2)$$

Now, putting $y = Tx$ in (1), we have

$$\theta(r)\min\left\{p(x,Tx), p(x,Sx)\right\} \le p(x,Tx)$$

implies

$$\max\left\{p(Sx,STx), p(Tx,T^2x), \frac{1}{2}\left[p(Sx,T^2x)+p(STx,Tx)\right]\right\} \le rp(x,Tx)$$

for every $x \in X$. So, we get

$$p(Tx,T^2x) \le rp(x,Tx) \quad (3)$$

and

$$\frac{1}{2}p(Tx,STx) \le \frac{1}{2}\left[p(Sx,T^2x)+p(STx,Tx)\right] \le rp(x,Tx). \quad (4)$$

Let x_0 be an arbitrary element in X. We obtain a sequence $\{x_n\}$ such that $x_{2n+1} = Sx_{2n}$ and $x_{2n+2} = Tx_{2n+1}$ for each $n \in \mathbb{N} \cup \{0\}$. By (4), we get

$$p(x_{2n}, x_{2n+1}) = p(Tx_{2n-1}, STx_{2n-1}) \le 2rp(x_{2n-1}, Tx_{2n-1}) = 2rp(x_{2n-1}, x_{2n}).$$

And also, from (2), we get

$$p(x_{2n+1}, x_{2n+2}) = p(Sx_{2n}, TSx_{2n}) \le 2rp(x_{2n}, Sx_{2n}) = 2rp(x_{2n}, x_{2n+1}).$$

Therefore, for each $n \in \mathbb{N} \cup \{0\}$, we get

$$\begin{aligned} p(x_n, x_{n+1}) &\le 2rp(x_{n-1}, x_n) \\ &\le (2r)^2 p(x_{n-2}, x_{n-1}) \\ &\vdots \\ &\le (2r)^n p(x_0, x_1). \end{aligned} \tag{5}$$

Taking limit as $n \to \infty$ in inequality (5), we get $\lim_{n\to\infty} p(x_n, x_{n+1}) = 0$ for $r \in \left[0, \frac{1}{2}\right)$. From properties of PMS, we get

$$p(x_n, x_n) \le p(x_n, x_{n+1}) \text{ and } p(x_{n+1}, x_{n+1}) \le p(x_n, x_{n+1}).$$

Since $\lim_{n\to\infty} p(x_n, x_{n+1}) = 0$ for $r \in \left[0, \frac{1}{2}\right)$, we get

$$\lim_{n\to\infty} p(x_n, x_n) = 0 \text{ and } \lim_{n\to\infty} p(x_{n+1}, x_{n+1}) = 0. \tag{6}$$

$$\begin{aligned} p^s(x_n, x_{n+1}) &= 2p(x_n, x_{n+1}) - p(x_n, x_n) - p(x_{n+1}, x_{n+1}) \\ &\le 2p(x_n, x_{n+1}) \\ &\le 2((2r)^n p(x_0, x_1)). \end{aligned} \tag{7}$$

From (7), we have for any $k, n \in \mathbb{N}^+$

$$\begin{aligned} p^s(x_n, x_{n+k}) &\le p^s(x_n, x_{n+1}) + p^s(x_{n+1}, x_{n+2}) + \cdots + p^s(x_{n+k-1}, x_{n+k}) \\ &\le 2(2r)^n p(x_0, x_1) + 2(2r)^{n+1} p(x_0, x_1) + \cdots + 2(2r)^{n+k-1} p(x_0, x_1) \\ &= 2\left(\sum_{i=n}^{n+k-1} (2r)^i p(x_0, x_1)\right) \\ &\le 2\left(\sum_{i=n}^{\infty} (2r)^i p(x_0, x_1)\right). \end{aligned}$$

Then there exists a positive integer $n_0 \in \mathbb{N}$ such that $p^s(x_n, x_{n+k}) < \varepsilon$ for every $n \ge n_0$, all $k \in \mathbb{N}^+$ and an arbitrary $\varepsilon > 0$. We say that $\{x_n\}$ is a Cauchy sequence in the metric space (X, p^s). Since (X, p) is a complete PMS, (X, p^s) is also complete metric space. Hence, there exists $u \in X$ such that $\lim_{n\to\infty} x_n = u$ in (X, p^s). So, we get $\lim_{n\to\infty} p^s(x_n, u) = 0$ implies

$$p(u, u) = \lim_{n\to\infty} p(x_n, u) = \lim_{n,m\to\infty} p(x_n, x_m).$$

Since $\{x_n\}$ is a Cauchy sequence in the metric space (X, p^s), we get $\lim_{n,m\to\infty} p^s(x_n, x_m) = 0$. So, we have

$$\lim_{n,m\to\infty} p^s(x_n, x_m) = \lim_{n,m\to\infty} 2p(x_n, x_m) - \lim_{n,m\to\infty} p(x_m, x_m) - \lim_{n,m\to\infty} p(x_n, x_n) = 0.$$

From (6), we get

$$\lim_{n,m\to\infty} p(x_m, x_m) = \lim_{n,m\to\infty} p(x_n, x_n) = 0$$

implies $\lim_{n,m\to\infty} p(x_n, x_m) = 0$ and

$$p(u, u) = \lim_{n\to\infty} p(x_n, u) = \lim_{n,m\to\infty} p(x_n, x_m) = 0.$$

So, we get

$$\lim_{n\to\infty} p(x_{2n+1}, u) = \lim_{n\to\infty} p(x_{2n+2}, u) = 0$$

implies

$$\lim_{n\to\infty} p(Sx_{2n}, u) = \lim_{n\to\infty} p(Tx_{2n+1}, u) = 0. \tag{8}$$

We take $x, u \in X$ such that $x \neq u$. As $p(u,u) = 0$, we get, $\lim_{n\to\infty} p(x_{2n+1}, Tx_{2n+1}) = 0$

and $\lim_{n\to\infty} p(x_{2n+1}, x) \neq 0$. Then, there exists some $x_{2n_k+1} \in X$ such that

$$\theta(r)\min\{p(x_{2n_k+1}, Tx_{2n_k+1}), p(x_{2n_k+1}, Sx_{2n_k+1})\} \leq p(x_{2n_k+1}, x)$$

implies

$$\max\left\{p(Sx_{2n_k+1}, Sx), p(Tx_{2n_k+1}, Tx), \frac{1}{2}\left[p(Sx_{2n_k+1}, Tx) + p(Sx, Tx_{2n_k+1})\right]\right\} \leq rp(x_{2n_k+1}, x).$$

Hence, we get

$$p(Tx_{2n_k+1}, Tx) \leq rp(x_{2n_k+1}, x).$$

If we take the limit of both sides as $n \to \infty$, from (8), we get

$$p(u, Tx) = \lim_{n\to\infty} p(Tx_{2n_k+1}, Tx) \leq r \lim_{n\to\infty} p(x_{2n_k+1}, x) = rp(u, x).$$

Then, we have for each $x \neq u$

$$p(u, Tx) \leq rp(u, x). \tag{9}$$

To show that the equation

$$p(T^n u, u) \leq p(Tu, u) \tag{10}$$

provides for each $n \in \mathbb{N}$, we use induction. For $n = 1$, the inequality is obvious. We suppose that the inequality (10) is true for some $m \in \mathbb{N}$. So, we get

$$p(T^m u, u) \leq p(Tu, u).$$

For $n = m + 1$, if $T^m u = u$, then

$$p(T^{m+1}u, u) = p(T(T^m u), u) = p(Tu, u). \tag{11}$$

If $T^m u \neq u$, then by (9)

$$p(T^{m+1}u, u) \leq rp(T^m u, u) \leq rp(Tu, u) \leq p(Tu, u). \tag{12}$$

So, from (11) and (12), we get

$$p(T^{m+1}u, u) \leq p(Tu, u).$$

Then, inequality (10) is satisfied for all $n \in \mathbb{N}$.

Now, we will show that $Tu = u$. We assume that $Tu \neq u$. Since $0 \leq r < \frac{1}{2}$, so $\theta(r) \leq \frac{1-r}{r^2}$. Formerly, using induction, we prove that

$$p(T^n u, Tu) \leq rp(Tu, u) \tag{13}$$

for each $n \in \mathbb{N}$. For $n = 1$, it is obvious. Moreover, for $n = 2$, from (3) we get inequality (13) is satisfied. We suppose that the inequality (13) is true for some $n > 2$. So, we have

$$\begin{aligned} p(Tu, u) &\leq p(u, T^n u) + p(T^n u, Tu) - p(T^n u, T^n u) \\ &\leq p(u, T^n u) + p(T^n u, Tu) \\ &\leq p(u, T^n u) + rp(Tu, u). \end{aligned}$$

So, we get

$(1-r)p(u,Tu) \le p(u,T^n u)$.

Then, from (3), we obtain that

$$\begin{aligned}\theta(r)\min\left\{p(ST^n z,T^n u),p(T^n u,T^{n+1}u)\right\} &\le \theta(r)p(T^n u,T^{n+1}u)\\ &= \frac{1-r}{r^2}p(T^n u,T^{n+1}u)\\ &\le \frac{1-r}{r^n}p(T^n u,T^{n+1}u)\\ &\le \frac{1-r}{r^n}r^n p(u,Tu)\\ &= (1-r)p(u,Tu)\\ &\le p(u,T^n u).\end{aligned}$$

This implies

$$\begin{aligned}p(T^{n+1}u,Tu) &\le \max\left\{p(ST^n u,Su),p(T^{n+1}u,Tu),\frac{1}{2}\left[p(ST^n u,Tu)+p(Su,T^{n+1}u)\right]\right\}\\ &\le rp(u,T^n u).\end{aligned}$$

Then from (10), we get

$$p(T^{n+1}u,Tu) \le rp(T^n u,u) \le rp(Tu,u).$$

Hence, the inequality (13) is satisfied for each $n \in \mathbb{N}$.

Now, $Tu \ne u$ and (13) implies that $T^n u \ne u$. If not,

$$p(T^n u,Tu) \le rp(Tu,u) \Rightarrow p(u,Tu) \le rp(u,Tu) \le p(u,Tu)$$

for $r \in \left[0,\frac{1}{2}\right)$, which is impossible. So, from (9), we have

$$p(u,T^{n+1}u) \le rp(u,T^n u) \le r^2 p(u,T^{n-1}u) \le \cdots \le r^n p(u,Tu).$$

Taking the limit of both sides, we get

$$\lim_{n\to\infty} p(u,T^{n+1}u) = 0 = p(u,u)$$

for $r \in \left[0,\frac{1}{2}\right)$. Then, $T^n u \to u$. Since $p(T^n u,Tu) \le rp(Tu,u)$, we get

$$p(u,Tu) = \lim_{n\to\infty} p(T^n u,Tu) \le \lim_{n\to\infty} rp(Tu,u) = rp(Tu,u).$$

So, we get $p(Tu,u) = 0$, which is a contradiction. So, $Tu = u$. Hence, u is fixed point of T. Therefore, u is also a fixed point of S. As a result, u is a common fixed point of T and S.

Now, to show the uniqueness of this common fixed point, we assume that u and v are common fixed points of T and S where $u \ne v$. Taking $x = u$ and $y = v$ in inequality (1), we have

$$0 = \theta(r)\min\left\{p(u,Tu),p(u,Su)\right\} \le p(u,v)$$

implies

$$\max\left\{p(Su,Sv),p(Tu,Tv),\frac{1}{2}\left[p(Su,Tv)+p(Tu,Sv)\right]\right\}\le rp(u,v)$$

$$\Rightarrow \max\left\{p(u,v),p(u,v),\frac{1}{2}\left[2p(u,v)\right]\right\}\le rp(u,v)$$

$$\Rightarrow p(u,v)\le rp(u,v)<p(u,v).$$

So, $p(u,v)=0$ which is a contradiction. Hence, $u=v$.

In Theorem 1, if we take as $S=T$, then we get the following corollary which is Suzuki type result in partial metric spaces [15].

Corollary 1. Let (X,p) be a complete PMS, $T:X\to X$ be a self-mapping and a nonincreasing function $\theta:[0,1)\to\left(\frac{1}{2},1\right]$ be defined by

$$\theta(r)=\begin{cases}1, & 0\le r\le\dfrac{\sqrt{5}-1}{2},\\ \dfrac{1-r}{r^2}, & \dfrac{\sqrt{5}-1}{2}\le r\le\dfrac{1}{\sqrt{2}},\\ \dfrac{1}{1+r}, & \dfrac{1}{\sqrt{2}}\le r<1.\end{cases}$$

If there exists $r\in\left[0,\frac{1}{2}\right)$ such that T satisfies the condition

$$\theta(r)p(x,Tx)\le p(x,y)$$

implies

$$p(Tx,Ty)\le rp(x,y)$$

for each $x,y\in X$, then T has a unique fixed point.

Corollary 2. Let (X,p) be a complete PMS, $f,S,T:X\to X$ be three self-maps and a nonincreasing function $\theta:[0,1)\to\left(\frac{1}{2},1\right]$ be defined by

$$\theta(r)=\begin{cases}1, & 0\le r\le\dfrac{\sqrt{5}-1}{2},\\ \dfrac{1-r}{r^2}, & \dfrac{\sqrt{5}-1}{2}\le r\le\dfrac{1}{\sqrt{2}},\\ \dfrac{1}{1+r}, & \dfrac{1}{\sqrt{2}}\le r<1.\end{cases}$$

If there exists $r\in\left[0,\frac{1}{2}\right)$ such that

$$\theta(r)\min\left\{p(x,fTx),p(x,fSx)\right\}\le p(x,y)$$

implies

$$\max\left\{p(fSx, fSy), p(fTx, fTy), \frac{1}{2}\left[p(fSx, fTy) + p(fSy, fTx)\right]\right\} \leq rp(x, y), \tag{14}$$

also, if f is one to one, $fS = Sf$ and $fT = Tf$, then f, T and S have a common fixed point.

Proof. If we consider fS and fT as two maps with given contractive condition of Theorem 1, then fS and fT have a common fixed point $u \in X$. Namely, $fSu = fTu = u$. Since f is one to one, we get

$fSu = fTu = u \Rightarrow Su = Tu.$

Then, putting $x = u$ and $y = Tu$ in inequality (14)

$\theta(r)\min\left\{p(u, fTu), p(u, fSu)\right\} \leq p(u, Tu)$

implies

$$\max\left\{p(fSu, fSTu), p(fTu, fT^2u), \frac{1}{2}\left[p(fSu, fT^2u) + p(fSTu, fTu)\right]\right\} \leq rp(u, Tu)$$

$$\Rightarrow \max\left\{p(fSu, SfTu), p(fTu, TfTu), \frac{1}{2}\left[p(fSu, TfTu) + p(SfTu, fTu)\right]\right\} \leq rp(u, Tu)$$

$$\Rightarrow \max\left\{p(u, Su), p(u, Tu), \frac{1}{2}\left[p(u, Tu) + p(Su, u)\right]\right\} \leq rp(u, Tu)$$

$\Rightarrow p(u, Tu) \leq rp(u, Tu).$

Then, $p(u, Tu) = 0$. So, we get $Tu = u$ which implies $Tu = Su = u$ and also $fu = fTu = u$. So, f, T and S have a common fixed point.

Example 1. Let $X = \left\{0, \frac{1}{4}, \frac{1}{3}, 2\right\} \subset \mathbb{R}$. Define $p : X \times X \to \mathbb{R}^+$ by $p(x, y) = \max\{x, y\}$ for all $x, y \in X$. Then, it is obvious that (X, p) is a complete PMS. And define two maps T and S by

$$Tx = \begin{cases} 0 & , \quad x \neq 2 \\ \frac{1}{3} & , \quad x = 2 \end{cases}$$

and

$$Sx = \begin{cases} 0 & , \quad x \neq 2 \\ \frac{1}{4} & , \quad x = 2 \end{cases}$$

for $x \in X$. Moreover, we choose as $r = \frac{1}{6}$. So, we get $\theta(r) = 1$.

Case I If $x, y \in \left\{0, \frac{1}{4}, \frac{1}{3}\right\}$, we get

$$\theta(r)\min\left\{p(x, Tx), p(x, Sx)\right\} = \min\left\{p(x, 0), p(x, 0)\right\} = \min\left\{\max\{x,0\},\max\{x,0\}\right\}$$
$$= x \leq \max\{x, y\} = p(x, y)$$

implies

$$\max\left\{p(Sx,Sy),p(Tx,Ty),\frac{1}{2}\left[p(Sx,Ty),p(Sy,Tx)\right]\right\}=\max\left\{p(0,0),p(0,0),\frac{1}{2}[p(0,0)+p(0,0)]\right\}$$

$$=0\le\frac{1}{6}\max\{x,y\}=rp(x,y).$$

Case II If $x\in\left\{0,\frac{1}{4},\frac{1}{3}\right\}$ and $y=2$, we get

$$\theta(r)\min\left\{p(x,Tx),p(x,Sx)\right\}=\min\{p(x,0),p(x,0)\}$$

$$=\min\{\max\{x,0\},\max\{x,0\}\}$$

$$=x\le\max\{x,y\}=p(x,y)$$

implies

$$\max\left\{p(Sx,Sy),p(Tx,Ty),\frac{1}{2}\left[p(Sx,Ty),p(Sy,Tx)\right]\right\}=\max\left\{p\left(0,\frac{1}{4}\right),p\left(0,\frac{1}{3}\right),\frac{1}{2}\left[p\left(0,\frac{1}{3}\right)+p\left(\frac{1}{4},0\right)\right]\right\}$$

$$=\frac{1}{3}\le\frac{1}{6}\max\{x,2\}=rp(x,y).$$

Case III If $y\in\left\{0,\frac{1}{4},\frac{1}{3}\right\}$ and $x=2$, we get

$$\theta(r)\min\left\{p(x,Tx),p(x,Sx)\right\}=\min\left\{p\left(2,\frac{1}{3}\right),p\left(2,\frac{1}{4}\right)\right\}=2\le\max\{2,y\}=p(x,y)$$

implies

$$\max\left\{p(Sx,Sy),p(Tx,Ty),\frac{1}{2}\left[p(Sx,Ty),p(Sy,Tx)\right]\right\}=\max\left\{p\left(\frac{1}{4},0\right),p\left(\frac{1}{3},0\right),\frac{1}{2}\left[p\left(\frac{1}{4},0\right)+p\left(0,\frac{1}{3}\right)\right]\right\}$$

$$=\frac{1}{3}\le\frac{1}{6}\max\{2,y\}=rp(x,y).$$

Case IV If $x=y=2$, we get

$$\theta(r)\min\left\{p(x,Tx),p(x,Sx)\right\}=\min\left\{p\left(2,\frac{1}{3}\right),p\left(2,\frac{1}{4}\right)\right\}$$

$$=2\le\max\{x,y\}=p(x,y)$$

implies

$$\max\left\{p(Sx,Sy),p(Tx,Ty),\frac{1}{2}\left[p(Sx,Ty),p(Sy,Tx)\right]\right\}=\max\left\{p\left(\frac{1}{4},\frac{1}{4}\right),p\left(\frac{1}{3},\frac{1}{3}\right),\frac{1}{2}\left[p\left(\frac{1}{4},\frac{1}{3}\right)+p\left(\frac{1}{4},\frac{1}{3}\right)\right]\right\}$$

$$=\frac{1}{3}\le\frac{1}{6}\max\{x,y\}=rp(x,y).$$

Thus, T and S satisfy all the hypotheses of Theorem 1. So, T and S have a unique common fixed point. Moreover, it is $0\in\mathbb{R}$.

Application

Let Y and Z be Banach spaces, $S\subseteq Y$ be a state space, $D\subseteq Z$ be a decision space and $H_i : S\times D\times\mathbb{R}\to\mathbb{R}$ for $i=1,2$. The problem of dynamic programming related to the multistage process reduces to the problem of solving the following functional equation:

$$q_i(x) = \sup_{y\in D}\{H_i(x,y,q_i(x,y))\}, \quad x \in S, i = 1,2. \tag{15}$$

In this section, using Theorem 1, we show existence and uniqueness of a bounded common solution of the functional equation (15). $B(S)$ is a Banach space which consists of all bounded real functionals on S with the norm $\|h\| = \sup_{x\in S} |h(x)|$ for an arbitrary $h \in B(S)$. $(B(S), \|.\|)$ endowed with the metric d defined by

$$d(h,k) = \sup_{x\in S} |h(x) - k(x)|$$

for $h,k \in B(S)$. Then, the convergence in the space $B(S)$ corresponds to uniform convergence. So, if we take a Cauchy sequence $\{h_n\}$ in $B(S)$, the sequence $\{h_n\}$ converges uniformly to a function h^*. It is bounded. Hence, $h^* \in B(S)$. We define the partial metric such that

$$p(h,k) = d(h,k) + b \tag{16}$$

for all $h,k \in B(S)$ where $b > 0$. Then, $(B(S), p)$ is a complete PMS. Now, we define mappings $A_i : B(S) \to B(S)$ by

$$A_i h(x) = \sup_{y\in D}\{H_i(x,y,h(x,y))\} \tag{17}$$

$$A_i k(x) = \sup_{y\in D}\{H_i(x,y,k(x,y))\} \tag{18}$$

for $i = 1,2$, $h,k \in B(S)$, $x \in S$. It is clear that if the functions H_i are bounded, then A_i are well defined for $i = 1,2$.

Theorem 2. Let the functions $H_i : S \times D \times \mathbb{R} \to \mathbb{R}$ be bounded and $A_i : B(S) \to B(S)$ be defined as in (17). If there exists $r \in \left[0, \frac{1}{2}\right)$ such that

$$\theta(r)\min\{|h(t) - A_1h(t)|, |h(t) - A_2h(t)|\} \le |h(t) - k(t)| \tag{19}$$

implies

$$|H_i(x,y,h(t)) - H_j(x,y,k(t))| \le r\,|h(t) - k(t)| \tag{20}$$

for every $(x,y) \in S \times D$, $h,k \in B(S)$ and $t \in S$ and $i,j = 1,2$, then the functional equations (15) have a unique common bounded solution in $B(S)$ for $i = 1,2$.

Proof. Let ϵ be an arbitrary positive number and $h,k \in B(S)$. By (17), there exist $y_1, y_2 \in D$ such that

$$A_1h(x) < H_1(x,y_1,h(x,y_1)) + \epsilon \tag{21}$$

$$A_1k(x) < H_1(x,y_1,k(x,y_1)) + \epsilon \tag{22}$$

$$A_2h(x) < H_2(x,y_2,h(x,y_2)) + \epsilon \tag{23}$$

$$A_2k(x) < H_2(x,y_2,k(x,y_2)) + \epsilon \tag{24}$$

and

$$A_1h(x) \ge H_1(x,y_1,h(x,y_1)) \tag{25}$$

$$A_1k(x) \ge H_1(x,y_1,k(x,y_1)) \tag{26}$$

$$A_2h(x) \ge H_2(x,y_2,h(x,y_2)) \tag{27}$$

$$A_2k(x) \ge H_2(x,y_2,k(x,y_2)) \tag{28}$$

for $x \in S$. The inequality (19)

$$\theta(r)\min\{|\, h(x) - A_1h(x)\,|, |\, h(x) - A_2h(x)\,|\} \leq |\, h(x) - k(x)\,| \tag{29}$$

is satisfied for $r \in \left[0, \frac{1}{2}\right)$. Then, from (23), (24), (27) and (28), we get the functional equations

$$\begin{aligned} A_2h(x) - A_2k(x) &\leq H_2(x, y_2, h(x, y_2)) - H_2(x, y_2, k(x, y_2)) + \epsilon \\ &\leq |\, H_2(x, y_2, h(x, y_2)) - H_2(x, y_2, k(x, y_2))\,| + \epsilon \end{aligned} \tag{30}$$

and

$$\begin{aligned} A_2k(x) - A_2h(x) &\leq H_2(x, y_2, k(x, y_2)) - H_2(x, y_2, h(x, y_2)) + \epsilon \\ &\leq |\, H_2(x, y_2, k(x, y_2)) - H_2(x, y_2, h(x, y_2))\,| + \epsilon \end{aligned} \tag{31}$$

From (30) and (31), we get

$$|\, A_2h(x) - A_2k(x)\,| \leq |\, H_2(x, y_2, h(x, y_2)) - H_2(x, y_2, k(x, y_2))\,| + \epsilon$$

Using (20), we can say that

$$|\, A_2h(x) - A_2k(x)\,| \leq r\,|\, h(x) - k(x)\,| + \epsilon. \tag{32}$$

Similarly, using (20), (21), (22), (25) and (26), we get

$$|\, A_1h(x) - A_1k(x)\,| \leq r\,|\, h(x) - k(x)\,| + \epsilon. \tag{33}$$

On the other hand, from (22), (23), (26) and (27), we get

$$|\, A_2h(x) - A_1k(x)\,| \leq |\, H_2(x, y_2, h(x, y_2)) - H_1(x, y_2, k(x, y_1))\,| + \epsilon \tag{34}$$

and from (21), (24), (25) and (28), we get

$$|\, A_2k(x) - A_1h(x)\,| \leq |\, H_2(x, y_2, k(x, y_2)) - H_1(x, y_2, h(x, y_1))\,| + \epsilon \tag{35}$$

If we sum both sides of the inequalities (34) and (35) and multiply them by $\frac{1}{2}$, then we get

$$\frac{1}{2}\left[|\, A_2h(x) - A_1k(x)\,| + |\, A_2k(x) - A_1h(x)\,|\right] \leq r\,|\, h(x) - k(x)\,| + \epsilon. \tag{36}$$

Since the inequalities (32), (33) and (36) hold for any $x \in S$ and $\epsilon > 0$, we can ignore ϵ. Then, we get

$$|\, A_2h(x) - A_2k(x)\,| \leq r\,|\, h(x) - k(x)\,|, |\, A_1h(x) - A_1k(x)\,| \leq r\,|\, h(x) - k(x)\,|,$$

and

$$\frac{1}{2}\left[|\, A_2h(x) - A_1k(x)\,| + |\, A_2k(x) - A_1h(x)\,|\right] \leq r\,|\, h(x) - k(x)\,|.$$

Thus, it is true that

$$\max\left\{|A_2h(x)-A_2k(x)|+|A_1h(x)-A_1k(x)|, \frac{1}{2}[|A_2h(x)-A_1k(x)|+|A_2k(x)-A_1h(x)|]\right\} \leq r\,|\, h(x) - k(x)\,|. \tag{37}$$

Now, if we take supremum in the inequalities (29) and (37) and add $b > 0$ to them, we get from (16)

$$\theta(r)\min\{p(h(x), A_1h(x)), p(h(x), A_2h(x))\} \leq p(h(x), k(x))$$

implies

$$\max\left\{p(A_2h(x),A_2k(x)), p(A_1h(x),A_1k(x)), \frac{1}{2}[p(A_2h(x),A_1k(x))+p(A_2k(x),A_1h(x))]\right\} \leq rp(h(x), k(x))$$

for $h,k \in B(S)$, $x \in S$ and $r \in \left[0, \frac{1}{2}\right)$. So, from Theorem 1, equations (15) and (17) there exists a unique common fixed point $h^* \in B(S)$. Namely, the system of functional equations (15) has a unique common bounded solution for $i = 1,2$.

Conflicts of interest

There are no conflicts of interest in this work.

References

[1] Suzuki T., A generalized Banach contraction principle that characterizes metric completeness, *Proc. Amer. Math. Soc.*, 136 (2008) 1861-1869.

[2] Suzuki T., A new type of fixed point theorem in metric spaces, *Nonlinear Anal. Theory Methods Appl.,* 71 (2009) 5313-5317.

[3] Abbas M., Ali B., Vetro C., A Suzuki type fixed point theorem for a generalized multivalued mapping on partial hausdorff metric spaces, *Topol. Appl.,* 160 (2013) 553-563.

[4] Abbas M., Iqbal H., Petruşel A., Fixed points for multivalued Suzuki type (Theta,R)-contraction mappings with applications, *J. Funct. Spaces*, 2019 (2019) 9565804 13.

[5] Chandra N., Arya M.C., Joshi M.C., A Suzuki type common fixed point theorem, *Filomat*, 31 (2017) 2951-2956.

[6] Ciric L., Abbas M., Rajoviç M., Ali B., Suzuki type fixed point theorems for generalized multivalued mappings on a set endowed with two b-metrics, *Appl. Math. Comput*., 219 (2012) 1712-1723.

[7] Özkan K., Gürdal U., The Fixed Point Theorem and Characterization of Bipolar Metric Completeness, Konuralp J. Math., 8 (2020) 137-143.

[8] Sedghi S., Shobkolaei N., Dosenovic T., Radenovic S., Suzuki type of common fixed point theorems in fuzzy metric spaces, Math. Slovaca, 68 (2018) 451-462.

[9] Gautam P., Kumar S., Verma S., Gulati S., On some w-Interpolative contractions of Suzuki type mappings in Quasi-partial b-metric space, *J. Funct. Spaces*, 2022 (2022) Article Id. 9158199, 12 Pages.

[10] Wangwe L., Kumar S., A common fixed point theorem for generalized F-Kannan Suzuki type mapping in TVS valued cone metric space with applications, *J. Math.*, 2022 (2022) 6504663.

[11] Matthews S.G., Partial metric topology, in: Papers on General Topology and Applications, Flushing, NY, 1992, in: Ann. New York Acad. Sci., 728, New York Acad. Sci., New York, (1994) 183-197.

[12] Abbas M., Ali B., Petruşel G., Fixed points of set-valued contractions in partial metric spaces endowed with a graph, *Carpath. J. Math.*, 30 (2014) 129-137.

[13] Karapınar E., Generalizations of Caristi Kirk's theorem on partial metric spaces, *Fixed Point Theory and Appl.,* 2011 (1) (2011) Article number:4.

[14] Onsod W., Saleewong T., Kumam P., Fixed and periodic point results for generalized geraghty contractions in partial metric spaces with application, *Thai J. Math.,* 18 (3) (2020) 1247–1260.

[15] Paesano D., Vetro P., Suzuki's type characterizations of completeness for partial metric spaces and fixed points for partially ordered metric spaces, *Topol. Appl.,* 159 (3) (2012) 911–920.

[16] Paesano D., Vetro P., Fixed points and completeness on partial metric spaces, *Miskolc Math. Notes*, 16(1) (2015) 369–383.

[17] Romaguera S., A Kirk type characterization of completeness for partial metric spaces, *Fixed Point Theory and Appl.,* 2010 (1) (2009) 493–298.

[18] Romaguera S., On Nadler's fixed point theorem for partial metric spaces, *Math. Sci. Appl. E-Notes*, 1 (2013) 1–8.

[19] Shatanawi W., Samet B., Abbas M., Coupled fixed point theorems for mixed monotone mappings in ordered partial metric spaces, *Math. Comput. Model.,* 55 (3-4) (2012) 680–687.

[20] Abdeljawad T., Karapınar E., Taş K., Existence and uniqueness of a common fixed point on partial metric spaces, *Appl. Math. Lett.,* 24 (2011) 1900-1904.

Cumhuriyet Sci. J., 44(1) (2023) 160-169
DOI: https://doi.org/10.17776/csj.1120077

Cumhuriyet Science Journal

| csj.cumhuriyet.edu.tr | Founded: 2002 ISSN: 2587-2680 e-ISSN: 2587-246X Publisher: Sivas Cumhuriyet University

On Solutions Of Random Partial Differential Equations With Laplace Adomian Decomposition Method

Mehmet Merdan [1,a,*], Nihal Atasoy [1,b]

[1] *Department of Mathematical Engineering, Gümüşhane University, Gümüşhane, Turkey.*
**Corresponding author*

Research Article

History
Received: 23/05/2022
Accepted: 05/02/2023

ABSTRACT

In this study, random partial differential equations obtained by randomly choosing the coefficients or initial conditions of partial differential equations will be analyzed. With the help of Laplace Adomian Decomposition Method and Homotopy Analysis Method, approximate analytical solutions of random partial differential equations were obtained. Initial conditions and parameters are made into random variables with normal distribution and gamma distribution. Probability characteristics such as expected value, variance and confidence intervals of the obtained random partial differential equation are calculated. Obtained results will be plotted with the help of MATLAB (2013a), package program and random results will be interpreted.

Keywords: Random partial differential equation, Normal distribution, Laplace-Adomian decomposition method, Gamma distribution.

[a] *mmerdan@gumushane.edu.tr* *https://orcid.org/0000-0002-8509-3044* [b] *nihalatasoy0@gmail.com* *https://orcid.org/0000-0003-1993-5810*

Introduction

The Adomian Decomposition Method was first introduced by George Adomian in the early 1980s. Adomian is an American mathematician who developed this method for ordinary, partial, linear and nonlinear differential equations. Adomian applied this method to find approximate solutions to deterministic, stochastic, linear and nonlinear problems with boundary and initial conditions. The method is constructed by decomposing its nonlinear terms. It is defined as $Ny = \sum_{n=0}^{\infty} A_n$. Here, A_n are Adomian polynomials. Each A_n depends on the arguments $y_0, y_1, y_2, \dots, y_n$ for $n > 0$. The formulas to obtain these polynomials were developed by Adomian. Finding approximate analytical solutions of non-linear differential equations with the Adomian Decomposition Method will make the solution faster and more reliable in many areas mentioned above.

In this study, Laplace Adomian Decomposition Method (LADM) is used to calculate approximate solutions of nonlinear ordinary and partial differential equations. Laplace-Adomian Decomposition Method (LADM) is a combination of Adomian Decomposition Method and Laplace Transform Method. This method has been successfully used to solve different problems in [1-7]. Also, LADM does not require predefined dimension definition like the Runge–Kutta method. Also, LADM can be considered as an ideal method for ordinary and partial equations representing nonlinear models. Compared to other analytical methods, LADM has fewer parameters, so LADM is a useful technique that does not require discretization and linearization [8]. A comparison between LADM and ADM for analysis of FDEs is given in [9]. The Kundu-Eckhaus equation deals with quantum field theory and the analytical solution of these nonlinear PDEs is explored in [10] using LADM. The multi-step Laplace Adomian decomposition method for nonlinear FDEs is described in [11]. The analysis of the smoke model was successfully studied using LADM [12].

The motivation of this study is the previous literature on random modeling of several diseases (Merdan et al., 2017; Merdan et al., 2018; Bekiryazici and Hasimoglu et al., 2022). Gamma and Normal (Gauss) distributions will be used for the distributions of the random parameters.

The aim of this study is to analyze the solution behavior graphically by finding various probability characteristics such as expected value, variance and confidence intervals by obtaining the approximate analytical solution of random partial differential equations with the use of the Laplace-Adomian Method.

Adomian Decomposition Method Combined with Laplace Transform

Let the partial or ordinary differential equation $Fy(x,t) = g(x,t)$ be given with the initial condition $y(x,0) = f(x)$. Here F is the differential operator with linear and non-linear terms. In this case, the operator form is defined by

$$L_t y(x,t) + Ry(x,t) + Ny(x,t) = g(x,t) \quad (1)$$

$L_t = \frac{\partial}{\partial t}$, R is a linear operator with partial derivatives with respect to x, N is a nonlinear operator, and g is an inhomogeneous term independent of y.

The solution for $L_t y(x,t)$ can be expressed as

$$L_t y(x,t) = g(x,t) - Ry(x,t) - Ny(x,t) \quad (2)$$

The $\mathcal{L}$ Laplace transform is an integral transform found by Pierre-Simon Laplace. It is a powerful and practical method for solving ordinary and partial differential equations.

Definitions and Theorems

Definition 1. Given the $f(t)$ function for every $t \geq 0$; Let f be defined [13] as the Laplace transform F. Therefore,

$$F(s) = \mathcal{L}\{f(t)\} = \int_0^\infty f(t)e^{-st}dt$$

The Laplace transform of the t^n function is found as follows:

$$\mathcal{L}\{t^n\} = \frac{n!}{s^{n+1}}$$

Definition 2. Given a continuous function $f(t)$, if $F(s) = L\{f(t)\}$ then $f(t)$ is called the inverse Laplace transform of $F(s)$ and

$$f(t) = \mathcal{L}^{-1}\{F(s)\} \quad (3)$$

It is expressed by (3). The Laplace transform has derivative properties:

$$\mathcal{L}\{f^{(n)}(t)\} = s^n\mathcal{L}\{f(t)\} - \sum_{k=0}^{n-1} s^{n-1-k}f^{(k)}(0)$$

$$\mathcal{L}\{t^n f(t)\} = (-1)^n F^{(n)}(s)$$

The Laplace Adomian Decomposition Method consists of applying the Laplace transform to both sides of the equation (2).

$$\mathcal{L}\{L_t y(x,t)\} = \mathcal{L}\{g(x,t)\} - \mathcal{L}\{Ry(x,t)\} - \mathcal{L}\{Ny(x,t)\}$$

$$sy(x,s) - y(x,0) = \mathcal{L}\{g(x,t) - Ry(x,t) - Ny(x,t)\}$$

$$y(x,s) = \frac{f(x)}{s} - \frac{1}{s}\mathcal{L}\{-g(x,t) + Ry(x,t) + Ny(x,t)\}$$

Equation (2) is found and inverse Laplace transform is applied to this equation,

$$y(x,t) = f(x) - \mathcal{L}^{-1}\left[\frac{1}{s}\mathcal{L}\{-g(x,t) + Ry(x,t) + Ny(x,t)\}\right] \quad (4)$$

is obtained.
The Adomian Decomposition Method produces a series of solutions given by $y(x,t)$:

$$y(x,t) = \sum_{n=0}^{\infty} y_n(x,t) \quad (5)$$

$$Ny(x,t) = \sum_{n=0}^{\infty} A_n(y_0, y_1, \dots, y_n) \quad (6)$$

is a sequence of Adomian polynomials. A_n Adomian polynomials,

$$A_0 = f(y_0)$$

$$A_1 = y_1\frac{df(y_0)}{dy_0}$$

$$A_2 = y_2\frac{df(y_0)}{dy_0} + \frac{y_1^2}{2!}\frac{d^2f(y_0)}{dy_0^2}$$

$$A_3 = y_3\frac{df(y_0)}{dy_0} + y_1y_2\frac{d^2f(y_0)}{dy_0^2} + \frac{y_1^3}{3!}\frac{d^3f(y_0)}{dy_0^3}$$

$$A_4 = y_4 \frac{df(y_0)}{dy_0} + \left(\frac{1}{2!}y_2^2 + y_1 y_3\right)\frac{d^2 f(y_0)}{dy_0^2} + \frac{1}{2!}y_1^2 y_2 \frac{d^3 f(y_0)}{dy_0^3} + \frac{y_1^4}{4!}\frac{d^4 f(y_0)}{dy_0^4}$$

...

form can be obtained. With $\lambda \in R$ being the parameter,

$$y = \sum_{n=0}^{\infty} y_n$$

solution series of the function,

$$y = \sum_{n=0}^{\infty} \lambda^n A_n$$

and nonlinear
$f(y) = \sum_{n=0}^{\infty} \lambda^n A_n$

can be written parametrically. Adomian Polynomials can be obtained from the formula (7), provided that the $f(y)$ function at the $\lambda \in R$ point is analytical.

$$A_n = \frac{1}{n!}\left[\frac{d^n}{d\lambda^n} f\left(\sum_{i=0}^{\infty} \lambda^i y_i\right)\right]_{\lambda=0}, n \geq 0 \quad (7)$$

Using the equations (4), (5) and (6),

$$\sum_{n=0}^{\infty} y_n(x,t) = f(x) - \mathcal{L}^{-1}\left[-\frac{1}{s}\mathcal{L}\{g(x,t)\} + \frac{1}{s}\mathcal{L}\{R\sum_{n=0}^{\infty} y_n(x,t) + \sum_{n=0}^{\infty} A_n(y_0, y_1, \dots, y_n)\}\right] \quad (8)$$

is obtained. From equation (8), the following formulas are subtracted:

$$\begin{cases} y_0(x,t) = f(x) \\ y_{n+1}(x,t) = -\mathcal{L}^{-1}\left[-\frac{1}{s}\mathcal{L}\{g(x,t)\} + \frac{1}{s}\mathcal{L}\{R y_n(x,t) + A_n(y_0, y_1, \dots, y_n)\}\right], n = 0,1,2 \dots \end{cases} \quad (9)$$

Using equation (9), an approximate solution is obtained:

$$y(x,t) \approx \sum_{n=0}^{k} y_n(x,t)$$

$$\lim_{k\to\infty} \sum_{n=0}^{k} y_n(x,t) = y(x,t)$$

Application

To examine the solution behavior of random partial differential equations, an approximate solution is obtained by the Laplace-Adomian Decomposition Method. Various interpretations were made by establishing the expected value, variance and %99 confidence interval of the solution.

Example 1.

Consider the following random partial differential equation

$$y_t + y_{xx} - y^2 - y \cdot y_{xx} = 0 \quad (10)$$

subject to the initial conditions

$$y(x,0) = B\sin x \quad (11)$$

where $B \sim N(\mu, \sigma^2)$ is parameter with Normal distribution.
To solve (10)-(11) by means of Laplace-Adomian Decomposition Method, making the Laplace transform of Equation (10).

When the operations in (1)-(4) are performed, the following relation is obtained.

$$\begin{cases} y_0(x,t) = f(x) \\ y_{n+1}(x,t) = -\mathcal{L}^{-1}\left[-\frac{1}{s}\mathcal{L}\{g(x,t)\} + \frac{1}{s}\mathcal{L}\{R y_n(x,t) + A_n(y_0, y_{1,} \dots, y_n)\}\right], n = 0,1,2, \dots \end{cases} \quad (12)$$

Identifying the zeroth component $y_0(x,t)$ by $Bsinx$, the remaining components $y_n(x,t)$, $n \geq 1$, can be determined by using the recurrence relation

$$y_0(x,t) = Bsinx$$

$$A_0 = f(y_0) = {y_0}^2 = B^2 sin^2 x$$

where A_n are Adomian polynomials that represent the nonlinear term and other terms are as follows

$$A_1 = 2y_0 y_1 = 2B^2 t sin^2 x$$

$$A_2 = 2y_0 y_2 + {y_1}^2 = B^2 t^2 sin^2 x + \frac{B^2 t^2}{3} sin^2 x(3 - 2B(t-3)sinx) \quad (13)$$

…

Other polynomials can be generated similarly to enhance the accuracy of the approximation. Using equations (12) and (13) above, the following connections are found.

$$y_1(x,t) = \mathcal{L}^{-1}\left[\frac{1}{s}\mathcal{L}\{Ry_0(x,t) + A_0\}\right] = Btsinx$$

$$y_2(x,t) = \mathcal{L}^{-1}\left[\frac{1}{s}\mathcal{L}\{Ry_1(x,t) + A_1\}\right] = \frac{Bt^2}{6} sinx(3 - 2B(t-3)sinx)$$

$$y_3(x,t) = \mathcal{L}^{-1}\left[\frac{1}{s}\mathcal{L}\{Ry_2(x,t) + A_2\}\right] = -\frac{2B^4 t^5}{315} sin^4 x(5t^2 - 35t + 63) + \frac{Bt^3}{1260}\Big[210sinx + 21B^2 sin^3 x(5t^3 - 18t^2 - 10t + 40) + B\left(2cos^2 x\left(-420 + 105t - Bt^2 sinx\big(35t - 126 - 4Bsinx(5t^2 - 35t + 63)\big)\right) - 21sin^2 x(3t^2 + 10t - 80)\right)\Big]$$

…

If the $y_0(x,t),\ y_1(x,t),\ y_2(x,t),\ y_3(x,t)$ found above are written in the series, the following relation is obtained.

$$y_{LADM} = y_0(x,t) + y_1(x,t) + y_2(x,t) + y_3(x,t) + \cdots \quad (14)$$

If the values $y_0(x,t),\ y_1(x,t),\ y_2(x,t),\ y_3(x,t)$ are written and edited in (14),

$$y_{LADM} = Bsinx + Btsinx + \frac{Bt^2}{6} sinx(3 - 2B(t-3)sinx) - \frac{2B^4 t^5}{315} sin^4 x(5t^2 - 35t + 63) + \frac{Bt^3}{1260}\Big[210sinx + 21B^2 sin^3 x(5t^3 - 18t^2 - 10t + 40) + B\left(2cos^2 x\left(-420 + 105t - Bt^2 sinx\big(35t - 126 - 4Bsinx(5t^2 - 35t + 63)\big)\right) - 21sin^2 x(3t^2 + 10t - 80)\right)\Big] + \cdots \quad (15)$$

is obtained. The solution in a series form is given by y_{LADM} and using Taylor series, the exact solution

$$y(x,t) = Bsinx(1 + \frac{t}{1!} + \frac{t^2}{2!} + \frac{t^3}{3!} + \cdots) \quad (16)$$

is readily obtained.

$N[\phi(x,t;q)]$ nonlinear operator, $L[\phi(x,t;q)]$ L linear operator and $L\big(c_1(x)\big) = 0$, $c_1(x)$ integration constant; apply Homotopy Analysis Method [15-17] to equation (10) given with $y_0(x,t) = Bsinx$ initial condition.

$$N[\phi(x,t;q)] = \frac{\partial\phi(x,t;q)}{\partial t} + \frac{\partial^2\phi(x,t;q)}{\partial x^2} - \phi(x,t;q)^2 - \phi(x,t;q)\frac{\partial^2\phi(x,t;q)}{\partial x^2}$$

$$L[\phi(x,t;q)] = \frac{\partial\phi(x,t;q)}{\partial t}$$

$$L\big(c_1(x)\big) = 0,\ c_1(x)$$

Equation (18) is obtained by using equation (17).

$$L[y_m(t) - \chi_m y_{m-1}(t)] = hH(t)R_m(\vec{y}_m, t) \quad (17)$$

$$R_m[\vec{y}_{m-1}] = \frac{\partial y_{m-1}(x,t)}{\partial t} + \frac{\partial^2 y_{m-1}(x,t)}{\partial x^2} - y_{m-1}(x,t)^2 - y_{m-1}(x,t)\frac{\partial^2 y_{m-1}(x,t)}{\partial x^2} \quad (18)$$

The solution of equation (17) for $m \geq 1$ deformation of order m.

$$y_m(x,t) = \chi_m y_{m-1}(x,t) + hH(r,t)L^{-1}[R_m(\vec{y}_{m-1}(x,t))]$$

If $m \geq 1, \chi_m = 1, h = -1$ ve $H(r,t) = 1$,

$$R_1(\vec{y}_0(x,t)) = \frac{\partial y_0(x,t)}{\partial t} + \frac{\partial^2 y_0(x,t)}{\partial x^2} - y_0(x,t)^2 - y_0(x,t)\frac{\partial^2 y_0(x,t)}{\partial x^2} = -B\sin(x) \quad (19)$$

$$y_1(x,t) = \chi_1 y_0(x,t) + \hbar L^{-1}[R_1 \vec{y}_0(x,t)]$$
$$y_1(x,t) = -Bsin(x) + \hbar \int (-Bsin(x))dt$$
$$y_1(x,t) = B\sin x + Bt\sin x$$
$$y_2(x,t) = \chi_1 y_1(x,t) + \hbar L^{-1}[R_2 \vec{y}_1(x,t)]$$
$$y_2(x,t) = \frac{1}{6}\mathrm{B}\sin x(6 + 6t + 3t^2 + 2B\sin x)$$
$$y_3(x,t) = \chi_1 y_2(x,t) + \hbar L^{-1}[R_3 \vec{y}_2(x,t)]$$
$$y_3(x,t) = -\frac{1}{18}B(-3t^3\sin x - 18\sin x - 18t\sin x + B^2t^3\sin x + 3B^2t^2\sin x + 6B^2t\sin x - 9B^2t^2\sin x\, cosx^2 - 18B^2t\sin x\, cosx^2 - 3B^2t^3\sin x cosx^2 - 9t^2\sin x - 6B + 2B^3t + 6B^3tcosx^4 + 6Bcosx^2 - 8B^3tcosx^2 + 24Btcosx^2 - 12Bt)$$

Continuing in this way, the closed form solution is found as (20).

$$y(x,t) = Bsinx(1 + \tfrac{t}{1!} + \tfrac{t^2}{2!} + \tfrac{t^3}{3!} + \cdots) \tag{20}$$

Again, it has been observed that the solution obtained by Laplace-Adomian Decomposition Method is compatible with each other when compared to the Homotopy Analysis Method solution.

The parameters of the normally distributed random variable X are $B{\sim}N(\mu,\sigma^2)$. Using the moment-generating function of the normal distribution, we get

$$M_X(t) = E[e^{tX}] = e^{\frac{1}{2}\sigma^2t^2+\mu t} \tag{21}$$

from (17), the 1st and 2nd moment of the random variable $B{\sim}N(\mu,\sigma^2)$ are,

$$E[B] = \mu, \quad E[B^2] = \sigma^2 + \mu^2,$$

is calculated as. If the basic properties of the expected value for the X and Y independent random variables are used, the expected value of equations (16) and (20) is:

$$E[y(x,t)] = \left(x + tx + \tfrac{1}{2}t^2x - \tfrac{1}{6}x^3 + \cdots\right)E(B) = \left(x + tx + \tfrac{1}{2}t^2x - \tfrac{1}{6}x^3 + \cdots\right) \tag{22}$$

The expected value (22) is obtained. If $B{\sim}N(\mu = 2, \sigma^2 = 4)$ is specially selected,

$$E[y(x,t)] = 2\left(x + tx + \tfrac{1}{2}t^2x - \tfrac{1}{6}x^3 + \cdots\right)$$

is obtained. If the expected value is plotted with MATLAB (2013a) for the given parameter values, the graph in Figure 1. is obtained.

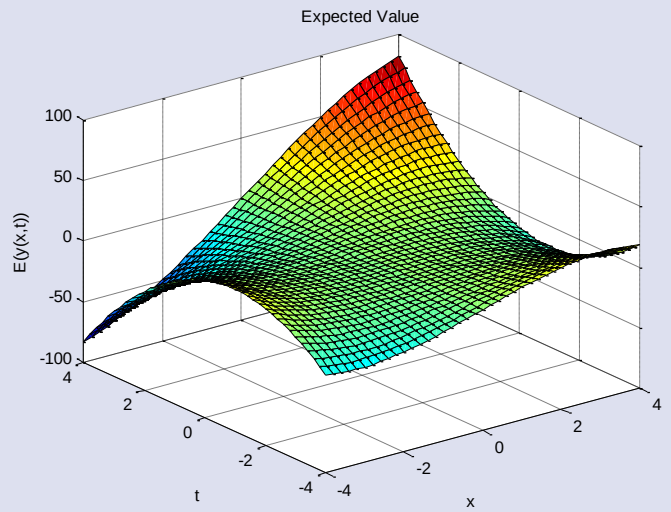

Figure 1. The solution behavior of the expected value of equations (16) and (20) for $B{\sim}N(\mu = 2, \sigma^2 = 4)$ special values..

If the basic properties of the variance are used for each random variable X, the variance of equations (16) and (20) is calculated as (24).

$$Var(B) = E(B^2) - [E(B)]^2 = \sigma^2 + \mu^2 - \mu^2 = \sigma^2 \quad (23)$$
$$Var[y(x,t)] = \left(x + tx + \frac{1}{2}t^2x - \frac{1}{6}x^3 + \cdots\right)^2 Var(B)$$

If the value in (23) is substituted,

$$Var[y(x,t)] = \left(x + tx + \frac{1}{2}t^2x - \frac{1}{6}x^3 + \cdots\right)^2 \sigma^2$$

is obtained. If $B{\sim}N(\mu = 2, \sigma^2 = 4)$ is specially selected,

$$Var[y(x,t)] = 4\left(x + tx + \frac{1}{2}t^2x - \frac{1}{6}x^3 + \cdots\right)^2$$

is obtained. Figure 2. is obtained if the variance is plotted with MATLAB (2013a) for the given parameter values.

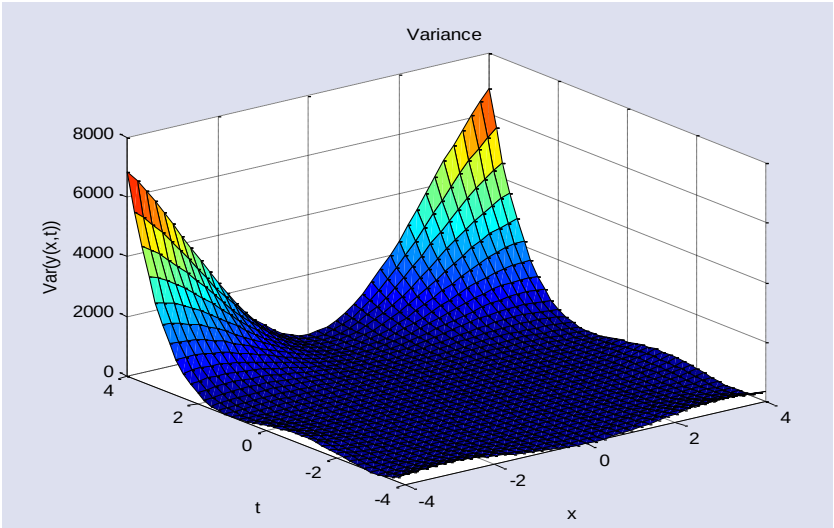

Figure 2. Solution behavior of the variance of equations (16) and (20) for $B{\sim}N(\mu = 2, \sigma^2 = 4)$ special values..

The expected value and variance values for $x = 0.5$ are given in Table 1.

Table 1. Table for the expectation value and variance with $x = 0.5$

t	$E[y(x,t)]$	$Var[y(x,t)]$
0.0	0.9583333333	0.9184027780
0.1	1.063333333	1.130677778
0.2	1.178333333	1.388469445
0.3	1.303333333	1.698677778
0.4	1.438333333	2.068802778
0.5	1.583333333	2.506944445
0.6	1.738333333	3.021802778
0.7	1.903333333	3.622677778
0.8	2.078333333	4.319469448
0.9	2.263333333	5.122677780
1.0	2.458333333	6.043402780

The standard deviation is equal to the square root of the variance.

$$std\left(y(t)\right) = \sqrt{Var\left(y(t)\right)} \tag{24}$$

Confidence intervals for expected values of random variables,

$$\left(E\left(y(t)\right) - K.std\left(y(t)\right), E\left(y(t)\right) + K.std(y(t)\right) \tag{25}$$

is equation to and this can be obtained through standard deviations. For $K = 3$, this formula gives approximately %99 confidence interval for the approximate expected value of the normally distributed random variable [14]. If the %99 confidence interval is plotted with MATLAB (2013a), the graph in Figure 3. is obtained.

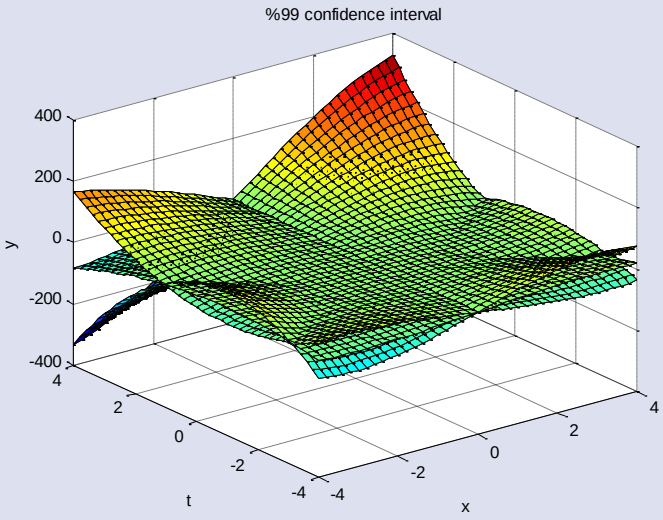

Figure 3. The solution behavior of the %99 confidence interval of equations (16) and (20) for $B{\sim}N(\mu = 2, \sigma^2 = 4)$ special values..

Example 2.

We will then consider the following random partial differential equation

$$By_t = By_{xx} + 6By - 6y^2 \tag{26}$$

random partial differential equation is subject to the following initial conditions.

$$y(x,0) = \frac{B}{(1+e^x)^2} \tag{27}$$

Where $B{\sim}Gamma\,(\omega, \lambda)$ is parameter with Gamma distribution.

To solve (26)-(27) by means of Laplace-Adomian Decomposition Method, making the Laplace transform of equation (26).

By applying the present method,

$$\begin{aligned}
y_0(x,t) &= \frac{B}{(1+e^x)^2} \\
y_1(x,t) &= \mathcal{L}^{-1}\left[-\frac{1}{s}\mathcal{L}\left\{y_{0,xx} + 6y_0 - \frac{6}{B}{y_0}^2\right\}\right] = -\frac{10Bt\left(e^{2x}+e^x\right)}{(1+e^x)^4} \\
y_2(x,t) &= \mathcal{L}^{-1}\left[-\frac{1}{s}\mathcal{L}\left\{y_{1,xx} + 6y_1 - \frac{A_1}{B}\right\}\right] = \frac{25Bt^2\left(2e^{2x}-e^x\right)}{(1+e^x)^4} \\
y_3(x,t) &= \mathcal{L}^{-1}\left[-\frac{1}{s}\mathcal{L}\left\{y_{2,xx} + 6y_2 - \frac{A_2}{B}\right\}\right] = -\frac{125Bt^3\left(4e^{3x}-7e^{2x}+e^x\right)}{3(1+e^x)^5}
\end{aligned} \tag{28}$$

$$A_0 = 6{y_0}^2 = \frac{6B^2}{(1+e^x)^4}$$

$$A_1 = 12y_0y_1 = -120\,\frac{B^2t\left(e^{2x}+e^x\right)}{(1+e^x)^6} \tag{29}$$

$$A_2 = 12y_0y_2 + 6{y_1}^2 = \frac{600B^2t^2(e^{2x}+e^x)}{(1+e^x)^8} + \frac{300B^2t^2(2e^{2x}-e^x)}{(1+e^x)^6}$$

…

equations are obtained.

If the values $y_0(x,t),\ y_1(x,t),\ y_2(x,t),\ y_3(x,t)$ are written and edited in (14),

$$y_{LADM} = \frac{B}{(1+e^x)^2} - \frac{10Bt(e^{2x}+e^x)}{(1+e^x)^4} + \frac{25Bt^2(2e^{2x}-e^x)}{(1+e^x)^4} - \frac{125Bt^3(4e^{3x}-7e^{2x}+e^x)}{3(1+e^x)^5} + \cdots \tag{30}$$

equation (30) is obtained. If the equation opens to Taylor series;

$$y(x,t) = \frac{1}{4}B - \frac{1}{4}Bx + \frac{5}{4}Bt + \frac{1}{16}Bx^2 - \frac{5}{8}Btx + \frac{25}{16}Bt^2 + \frac{1}{48}Bx^3 - \frac{5}{16}Btx^2 + \frac{25}{16}Bt^2x - \frac{125}{48}Bt^3 + \cdots \tag{31}$$

solution is obtained. If the random variable X has a gamma distribution, using the moment generating function,

$$M_X(t) = E[e^{tX}] = \left(\frac{\lambda}{\lambda - t}\right)^{\alpha}$$

from the expression, the 1st and 2nd moment of the random variable $B \sim Gamma\,(\omega, \lambda)$,

$$E[B] = \frac{\omega}{\lambda},\ E[B^2] = \frac{\omega(\omega+1)}{\lambda^2}$$

is calculated as. If the basic properties of the expected value for the X and Y independent random variables are used, the expected value of equation (31) is

$$E[y(x,t)] = \left(\frac{1}{4} - \frac{1}{4}x + \frac{5}{4}t + \frac{1}{16}x^2 - \frac{5}{8}tx + \frac{25}{16}t^2 + \frac{1}{48}x^3 - \frac{5}{16}tx^2 + \frac{25}{16}t^2x - \frac{125}{48}t^3 + \cdots\right)E(B) \tag{32}$$

is obtained. If the moment value found above is substituted in the expression (32),

$$E[y(x,t)] = \left(\frac{1}{4} - \frac{1}{4}x + \frac{5}{4}t + \frac{1}{16}x^2 - \frac{5}{8}tx + \frac{25}{16}t^2 + \frac{1}{48}x^3 - \frac{5}{16}tx^2 + \frac{25}{16}t^2x - \frac{125}{48}t^3 + \cdots\right)\frac{\omega}{\lambda} \tag{33}$$

the expected value is found as (33). If $B \sim Gamma\,(\omega = 2, \lambda = 3)$ is specially selected,

$$E[y(x,t)] = \left(\frac{1}{4} - \frac{1}{4}x + \frac{5}{4}t + \frac{1}{16}x^2 - \frac{5}{8}tx + \frac{25}{16}t^2 + \frac{1}{48}x^3 - \frac{5}{16}tx^2 + \frac{25}{16}t^2x - \frac{125}{48}t^3 + \cdots\right)\frac{2}{3}$$

is obtained. If the expected value is plotted with MATLAB (2013a) for the given parameter values, the graph in Figure 4. is obtained.

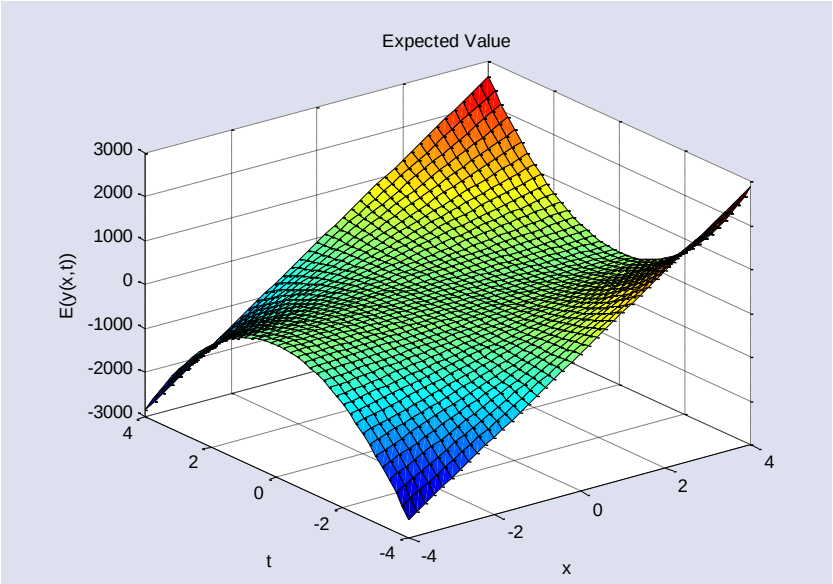

Figure 4. The solution behavior of the expected value of equation (31) for $B \sim Gamma(\omega = 2, \lambda = 3)$ special values..

$$Var(B) = \frac{\omega(\omega+1)}{\lambda^2} - \left(\frac{\omega}{\lambda}\right)^2 = \frac{\omega}{\lambda^2} \tag{34}$$

$$Var[y(x,t)] = \left(\frac{1}{4} - \frac{1}{4}x + \frac{5}{4}t + \frac{1}{16}x^2 - \frac{5}{8}tx + \frac{25}{16}t^2 + \frac{1}{48}x^3 - \frac{5}{16}tx^2 + \frac{25}{16}t^2x - \frac{125}{48}t^3 + \cdots\right)^2 Var(B) \tag{35}$$

To calculate the variance of equation (31), if (34) is substituted in (35), the variance value is calculated as follows.

$$Var[y(x,t)] = \left(\frac{1}{4} - \frac{1}{4}x + \frac{5}{4}t + \frac{1}{16}x^2 - \frac{5}{8}tx + \frac{25}{16}t^2 + \frac{1}{48}x^3 - \frac{5}{16}tx^2 + \frac{25}{16}t^2x - \frac{125}{48}t^3 + \cdots\right)^2 \frac{\omega}{\lambda^2}$$

If $B{\sim}Gamma(\omega = 2, \lambda = 3)$ is specially selected,

$$Var[y(x,t)] = \left(\frac{1}{4} - \frac{1}{4}x + \frac{5}{4}t + \frac{1}{16}x^2 - \frac{5}{8}tx + \frac{25}{16}t^2 + \frac{1}{48}x^3 - \frac{5}{16}tx^2 + \frac{25}{16}t^2x - \frac{125}{48}t^3 + \cdots\right)^2 \frac{2}{9}$$

is obtained. Figure 5. is obtained if the variance is plotted with MATLAB (2013a) for the given parameter values.

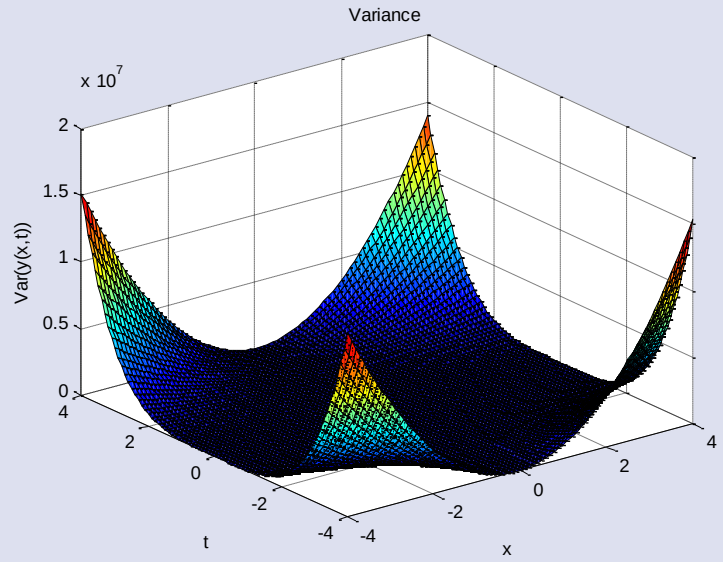

Figure 5. The solution behavior of the variance of equation (31) for $B{\sim}Gamma(\omega = 2, \lambda = 3)$ special values..

The expected value and variance values for $x = 0.5$ are given in Table 2.

Table 2. Table for the expectation value and variance with $x = 0.5$

t	$E[y(x,t)]$	$Var[y(x,t)]$
0.0	0.09548611114	0.004558798709
0.1	0.1666666667	0.01388888889
0.2	0.2586805555	0.03345781493
0.3	0.3611111111	0.06520061729
0.4	0.4635416667	0.1074354384
0.5	0.5555555556	0.1543209878
0.6	0.6267361110	0.1963990766
0.7	0.6666666669	0.2222222222
0.8	0.6649305551	0.2210663222
0.9	0.6111111110	0.1867283952
1.0	0.4947916670	0.1224093967

If (24) and (25) equations are used, for $K = 3$; If the interval $(0, 2.05)$ is taken into account, the %98 confidence interval of the expected value of the random variable showing the Gamma distribution is plotted with MATLAB (2013a), and the graph in Figure 6. is obtained.

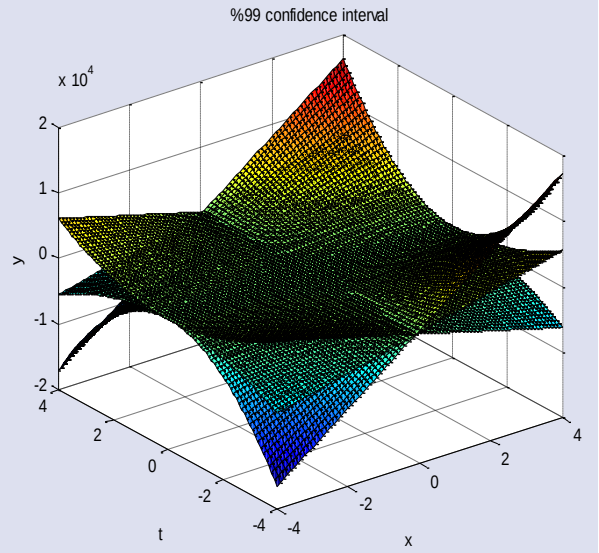

Figure 6. The solution behavior of the %99 confidence interval of equation (31) for $B{\sim}Gamma(\omega = 2, \lambda = 3)$ special values..

Conclusions

In this study, a hybrid method Laplace Addomain Decomposition Method is applied to find the solution of some important partial differential equations which are randomized with the help of Normal and Gamma distributions. We conclude that the Laplace Addomain Decomposition Method (LADM) is a powerful and efficient technique that can be used to find the approximate analytical solution of nonlinear random partial differential equations. The analytical solution of the given problem is given with the help of power series. The initial conditions or coefficients of Random PDD were selected from the Normal and Gamma distribution, and expected value, variance and confidence intervals, which are the main probability characteristics, were obtained to analyze random effects.

Acknowledgments

The authors are grateful to referees for careful reading, suggestions, and valuable comments, which have substantially improved the paper.

Conflicts of interest

There are no conflicts of interest in this work.

References

[1] Khuri S.A., A new approach to Bratu's problem, *Appl. Math. Comput*., 147 (2004) 131– 136.

[2] Kiymaz O., An algorithm for solving initial value problems using Laplace Adomian Decomposition Method, *Appl. Math. Sci.,* 3 (30) (2009) 1453–1459.

[3] Babolian E., Biazar J., Vahidi A.R., A new computational method for Laplace transforms by decomposition method, *Appl. Math. Comput.*, 150 (2004) 841–846

[4] Merdan M., Homotopy perturbation Method for solving a model for infection of CD4 +T cells, *İstanbul Ticaret Üniversitesi Fen Bilimleri Dergisi.,*12 (2007) 39–52.

[5] Yusufoglu E., Numerical solution of Duffing equation by the Laplace decomposition algorithm, *Appl. Math. Comput*., 177 (2) (2006) 572–580.

[6] Abbasbandy S., Application of He's homotopy perturbation method for Laplace transform, *Chaos Solitons Fractals*., 30 (2006) 1206–1212.

[7] Khuri S.A., A Laplace decomposition algorithm applied to a class of nonlinear differential equations, *J. Appl. Math*., 1 (4) (2001) 141–155.

[8] Jafari H, Khalique C.M., Nazari M., Application of the Laplace decomposition method for solving linear and nonlinear fractional diffusion–wave equations, *Appl. Math. Lett*., 24 (2011) 1799–1805.

[9] Mohamed M.Z., Comparison between the Laplace Decomposition Method and Adomian Decomposition in Time-Space Fractional Nonlinear Fractional Differential Equations, *Appl. Math.,* 9 (2018) 448.

[10] Gaxiola O.G., The Laplace-Adomian decomposition method applied to the Kundu–Eckhaus equation, *Int. J. Math. Its Appl.*,5 (2017) 1–12.

[11] Al-Zurigat, M., Solving nonlinear fractional differential equation using a multi-step Laplace Adomian decomposition method, *Ann. Univ. Craiova-Math. Comput. Sci. Ser.,39* (2012) 200–210.

[12] Haq F., Shah K., Rahman ur G., Shahzad M., Numerical solution of fractional order smoking model via laplace Adomian decomposition method, *Alex. Eng. J.*, 57 (2018) 1061–1069.

[13] Morales-Delgado V.F., Taneco-Hernández M.A., Gómez-Aguilar J.F., On the solutions of fractional order of evolution equations, *Eur. Phys. J. Plus*.,132 (2017) 47.

[14] Bekiryazici Z., Merdan M., Kesemen T., Modification of the random differential transformation method and its applications to compartmental models, *Communications in Statistics-Theory and Methods*., *50*(18) (2021) 4271-4292.

[15] Liao, S. J., On the proposed homotopy analysis technique for nonlinear problems and its applications. *Shanghai Jiao Tong University*, (1992).

[16] Liao S.J., An approximate solution technique which does not depend upon small parameters: a special example. *Int J Nonlinear Mech*, (1995) 30:371–80.

[17] Liao S.J., An approximate solution technique which does not depend upon small parameters (II): an application in fluid mechanics. *Int J Nonlinear Mech*, (1997) 32:815–22.

Cumhuriyet Sci. J., 44(1) (2023) 170-180
DOI: https://doi.org/10.17776/csj.1208016

Cumhuriyet Science Journal

| csj.cumhuriyet.edu.tr | Founded: 2002 ISSN: 2587-2680 e-ISSN: 2587-246X Publisher: Sivas Cumhuriyet University

α −Integral Representation of The Solution for A Conformable Fractional Diffusion Operator and Basic Properties of The Operator

Esengül Koç [1,a] , Yaşar Çakmak [1,b,*]

[1] *Department of Mathematics, Faculty of Science, Sivas Cumhuriyet University, Sivas, Türkiye.*
**Corresponding author*

Research Article

History
Received: 21/11/2022
Accepted: 06/03/2023

ABSTRACT

In this paper, we consider a diffusion operator which includes conformable fractional derivatives of order α (0<α≤1) instead of the ordinary derivatives in a traditional diffusion operator. We give an α-integral representation for the solution of this operator and obtain the conditions provided by the kernel functions in this representation. Also, by investigating the basic properties of this operator, we obtain the asymptotics of the data $\{\lambda_n, \alpha_n\}$, which are called the spectral data of the operator.

Keywords: Diffusion operator, Integral representation, Conformable fractional derivative, Spectral data.

[a] *esengul1990@hotmail.com* *https://orcid.org/0000-0002-9565-5266* [b] *ycakmak@cumhuriyet.edu.tr* *https://orcid.org/0000-0002-6820-1322*

Introduction

In 2014, the concept of conformable fractional derivative is firstly introduced by Khalil et al. (see [1]). Then, many researchers showed the basic properties of this new derivative in [2-5]. In 2017, Zhao and Luo gave a physical interpretation of this derivative (see [6]). The conformable fractional derivative has been seen in various fields such as diffusion transport, Newton mechanics and arbitrary time scale problems (see [7-9]). In [10], it has been understood that this derivative is necessary and useful for generating new types of fractional operators. Recently, important studies for various operators with conformable fractional derivatives have been published (see [11-15]).

In 1981, Gasymov and Guseinov gave an integral representation of the solution of a diffusion operator and also showed the properties which provided by kernel functions (see [16]). This integral representation for the diffusion operator is so important that many researchers have made various spectral studies by using this representation. For example, in 2007, Koyunbakan and Panakhov gave the solution of the Half inverse problem in [17], and in 2010, Yang calculated the regularized trace in [18]. In current literature, there is no such integral representation for a diffusion operator with conformable fractional derivative and this study can be considered as α generalization of the representation in [16].

α −Integral Representation of the Solution

We consider a diffusion operator with discrete boundary conditions that include conformable fractional derivatives of order α $(0 < \alpha \leq 1)$ instead of the ordinary derivatives in a traditional diffusion operator. The operator $L_\alpha = L_\alpha\big(h, H, p(x), q(x)\big)$ is called as conformable fractional diffusion operator (CFDO) and is the form

$$\ell_\alpha y := -T_x^\alpha T_x^\alpha y + [2\lambda p(x) + q(x)]y = \lambda^2 y, \ 0 < x < \pi \quad (1)$$

$$U_\alpha(y) := T_x^\alpha y(0) - hy(0) = 0 \quad (2)$$

$$V_\alpha(y) := T_x^\alpha y(\pi) + Hy(\pi) = 0 \quad (3)$$

where λ is the spectral parameter, h, $H \in \mathbb{R}$, $q(x) \in W_{2,\alpha}^1[0,\pi]$, $p(x) \in W_{2,\alpha}^2[0,\pi]$ are real valued functions, $p(x) \neq constant$ and $T_x^\alpha y$ is a conformable fractional derivative of order α of y at x, $\alpha \in (0,1]$.

In this section, we obtain an integral representation for the solution of this operator and show the conditions provided by the kernel functions in this representation.

Firstly, let's remember some important concepts of conformable fractional calculus. We note that more detailed knowledge about conformable fractional calculus can be seen in [1], [2], and [19].

Definition 2.1 Let $f: [0,\infty) \to \mathbb{R}$ be a given function. Then, the conformable fractional derivative of f of order α with respect to x is defined by

$$T_x^\alpha f(x) = \lim_{h\to 0} \frac{f(x + hx^{1-\alpha}) - f(x)}{h}, T_x^\alpha f(0) = \lim_{x\to 0^+} T_x^\alpha f(x),$$

for all $x > 0$, $\alpha \in (0,1]$. If f is differentiable that is $f'(x) = \lim_{h\to 0} \frac{f(x+h)-f(x)}{h}$, then $T_x^\alpha f(x) = x^{1-\alpha} f'(x)$.

Definition 2.2 The conformable fractional integral from 0 to x of order α is defined as follows

$$I_\alpha f(x) = \int_0^x f(t) d_\alpha t = \int_0^x t^{\alpha-1} f(t) dt, \text{for all } x > 0.$$

Definition 2.3 (α −integration by parts) Let $f, g: [a, b] \to \mathbb{R}$ be α −differentiable functions. Then,

$$\int_a^b f(x) T_x^\alpha g(x) d_\alpha x = f(x)g(x)|_a^b - \int_a^b g(x) T_x^\alpha f(x) d_\alpha x.$$

Lemma 2.4 (α −Leibniz rule) Let $f(x,t)$ be a function such that $t^{\alpha-1} f(x,t)$ and $t^{\alpha-1} f_x(x,t)$ are continuous in t and x in some regions of the (x,t)-plane, including $a(x) \le t \le b(x)$, $x_0 \le x \le x_1$. If $a(x)$ and $b(x)$ are α −differentiable functions for $x_0 \le x \le x_1$, then,

$$T_x^\alpha \left(\int_{a(x)}^{b(x)} f(x,t) d_\alpha t \right) = T_x^\alpha b(x) f\big(x, b(x)\big) b^{\alpha-1}(x) - T_x^\alpha a(x) f\big(x, a(x)\big) a^{\alpha-1}(x) + \int_{a(x)}^{b(x)} T_x^\alpha f(x,t) d_\alpha t.$$

Definition 2.5 Let $1 \le p < \infty$, $a > 0$. We called the space $L_{p,\alpha}(0,a)$ if for all functions $f: [0,a] \to \mathbb{R}$ satisfies

$$\left(\int_0^a |f(x)|^p d_\alpha x \right)^{1/p} < \infty.$$

Lemma 2.6 The space $L_{p,\alpha}(0,a)$ associated with the norm function

$$\|f\|_{p,\alpha} := \left(\int_0^a |f(x)|^p d_\alpha x \right)^{1/p}$$

is a Banach space. Moreover if $p = 2$ then $L_{2,\alpha}(0,a)$ associated with the inner product for $f, g \in L_{2,\alpha}(0,a)$

$$\langle f, g \rangle := \int_0^a f(x) \overline{g(x)} d_\alpha x$$

is a Hilbert space.

Definition 2.7 Let $1 \le p < \infty$. We called the Sobolev space $W_{p,\alpha}^1[0,a]$ if for all functions on $[0,a]$ such that $f(x)$ is absolutely continuous and $T_x^\alpha f(x) \in L_{p,\alpha}(0,a)$.

Now, let $\varphi(x,\lambda;\alpha)$ be the solution of the equation (1) satisfying the initial conditions

$$\varphi(0,\lambda;\alpha) = 1, \; T_x^\alpha \varphi(0,\lambda;\alpha) = h. \tag{4}$$

Theorem 2.8 There are the functions $A\left(x, \frac{t^\alpha}{\alpha}\right)$ and $B\left(x, \frac{t^\alpha}{\alpha}\right)$ whose second order partial derivatives are summable on $[0,\pi]$ for each $x \in [0,\pi]$ and fixed α such that the representation

$$\varphi(x,\lambda;\alpha) = \cos\left(\lambda \frac{x^\alpha}{\alpha} - \theta(x)\right) + \int_0^x A\left(x, \frac{t^\alpha}{\alpha}\right) \cos\lambda \frac{t^\alpha}{\alpha} d_\alpha t + \int_0^x B\left(x, \frac{t^\alpha}{\alpha}\right) \sin\lambda \frac{t^\alpha}{\alpha} d_\alpha t \tag{5}$$

is provided, where the functions $A\left(x, \frac{t^\alpha}{\alpha}\right)$ and $B\left(x, \frac{t^\alpha}{\alpha}\right)$ satisfy the following system of partial differential equations

$$\begin{cases} T_x^\alpha T_x^\alpha A\left(x, \frac{t^\alpha}{\alpha}\right) - q(x) A\left(x, \frac{t^\alpha}{\alpha}\right) - 2p(x) T_t^\alpha B\left(x, \frac{t^\alpha}{\alpha}\right) = T_t^\alpha T_t^\alpha A\left(x, \frac{t^\alpha}{\alpha}\right) \\ T_x^\alpha T_x^\alpha B\left(x, \frac{t^\alpha}{\alpha}\right) - q(x) B\left(x, \frac{t^\alpha}{\alpha}\right) + 2p(x) T_t^\alpha A\left(x, \frac{t^\alpha}{\alpha}\right) = T_t^\alpha T_t^\alpha B\left(x, \frac{t^\alpha}{\alpha}\right). \end{cases} \tag{6}$$

Moreover, the following relations

$$B(x,0) = 0, \; T_t^\alpha A\left(x, \frac{t^\alpha}{\alpha}\right)\Big|_{t=0} = 0, \tag{7}$$

$$\theta(x) = \int_0^x p(t) d_\alpha t, \tag{8}$$

$$A(0,0) = h, \tag{9}$$

$$A\left(x, \frac{x^\alpha}{\alpha}\right)\cos\theta(x) + B\left(x, \frac{x^\alpha}{\alpha}\right)\sin\theta(x) = h + \frac{1}{2}\int_0^x \left(q(t) + p^2(t)\right) d_\alpha t, \tag{10}$$

$$\theta(x) = p(0)\frac{x^\alpha}{\alpha} + 2\int_0^x \left(A\left(s, \frac{s^\alpha}{\alpha}\right)\sin\theta(s) - B\left(s, \frac{s^\alpha}{\alpha}\right)\cos\theta(s)\right) d_\alpha s \tag{11}$$

are satisfied. Conversely, if the second order derivatives of functions $A\left(x, \frac{t^\alpha}{\alpha}\right)$ and $B\left(x, \frac{t^\alpha}{\alpha}\right)$ are summable on $[0, \pi]$ for each $x \in [0, \pi]$, fixed α and these functions satisfy the equalities (6) and relations (7)-(11), then $\varphi(x, \lambda; \alpha)$ is a solution of equation (1) satifying the initial conditions (4).

Proof. From (5) and α −Leibniz rule, we get

$$\begin{aligned} T_x^\alpha \varphi(x,\lambda;\alpha) = \; & -\left(\lambda - T_x^\alpha \theta(x)\right)\sin\left(\lambda\frac{x^\alpha}{\alpha} - \theta(x)\right) + A\left(x, \frac{x^\alpha}{\alpha}\right)\cos\lambda\frac{x^\alpha}{\alpha} + B\left(x, \frac{x^\alpha}{\alpha}\right)\sin\lambda\frac{x^\alpha}{\alpha} \\ & + \int_0^x \left(T_x^\alpha A\left(x, \frac{t^\alpha}{\alpha}\right)\right)\cos\lambda\frac{t^\alpha}{\alpha} d_\alpha t + \int_0^x \left(T_x^\alpha B\left(x, \frac{t^\alpha}{\alpha}\right)\right)\sin\lambda\frac{t^\alpha}{\alpha} d_\alpha t \end{aligned} \tag{12}$$

and

$$\begin{aligned} T_x^\alpha T_x^\alpha \varphi(x,\lambda;\alpha) = \; & \left(T_x^\alpha T_x^\alpha \theta(x)\right)\sin\left(\lambda\frac{x^\alpha}{\alpha} - \theta(x)\right) - \left(\lambda - T_x^\alpha \theta(x)\right)^2 \cos\left(\lambda\frac{x^\alpha}{\alpha} - \theta(x)\right) \\ & + \left(T_x^\alpha A\left(x, \frac{x^\alpha}{\alpha}\right)\right)\cos\lambda\frac{x^\alpha}{\alpha} - \lambda A\left(x, \frac{x^\alpha}{\alpha}\right)\sin\lambda\frac{x^\alpha}{\alpha} \\ & + T_x^\alpha A\left(x, \frac{t^\alpha}{\alpha}\right)\Big|_{t=x}\cos\lambda\frac{x^\alpha}{\alpha} + \int_0^x \left(T_x^\alpha T_x^\alpha A\left(x, \frac{t^\alpha}{\alpha}\right)\right)\cos\lambda\frac{t^\alpha}{\alpha} d_\alpha t \\ & + \left(T_x^\alpha B\left(x, \frac{x^\alpha}{\alpha}\right)\right)\sin\lambda\frac{x^\alpha}{\alpha} + \lambda B\left(x, \frac{x^\alpha}{\alpha}\right)\cos\lambda\frac{x^\alpha}{\alpha} \\ & + T_x^\alpha B\left(x, \frac{t^\alpha}{\alpha}\right)\Big|_{t=x}\sin\lambda\frac{x^\alpha}{\alpha} + \int_0^x \left(T_x^\alpha T_x^\alpha B\left(x, \frac{t^\alpha}{\alpha}\right)\right)\sin\lambda\frac{t^\alpha}{\alpha} d_\alpha t. \end{aligned} \tag{13}$$

On the other hand, using α −integration by parts twice for the integrals at (5), we obtain

$$\begin{aligned} \varphi(x,\lambda;\alpha) = \; & \cos\left(\lambda\frac{x^\alpha}{\alpha} - \theta(x)\right) + \frac{1}{\lambda}A\left(x, \frac{x^\alpha}{\alpha}\right)\sin\lambda\frac{x^\alpha}{\alpha} - \frac{1}{\lambda}B\left(x, \frac{x^\alpha}{\alpha}\right)\cos\lambda\frac{x^\alpha}{\alpha} + \frac{1}{\lambda}B(x,0) \\ & + \frac{1}{\lambda^2}T_t^\alpha A\left(x, \frac{t^\alpha}{\alpha}\right)\Big|_{t=x}\cos\lambda\frac{x^\alpha}{\alpha} - \frac{1}{\lambda^2}T_t^\alpha A\left(x, \frac{t^\alpha}{\alpha}\right)\Big|_{t=0} \\ & - \frac{1}{\lambda^2}\int_0^x \left(T_t^\alpha T_t^\alpha A\left(x, \frac{t^\alpha}{\alpha}\right)\right)\cos\lambda\frac{t^\alpha}{\alpha} d_\alpha t + \frac{1}{\lambda^2}T_t^\alpha B\left(x, \frac{t^\alpha}{\alpha}\right)\Big|_{t=x}\sin\lambda\frac{x^\alpha}{\alpha} \\ & - \frac{1}{\lambda^2}\int_0^x \left(T_t^\alpha T_t^\alpha B\left(x, \frac{t^\alpha}{\alpha}\right)\right)\sin\lambda\frac{t^\alpha}{\alpha} d_\alpha t. \end{aligned} \tag{14}$$

From the equalities (1), (5), (13), (14) and the following equalities

$$2\lambda p(x)\int_0^x A\left(x,\frac{t^\alpha}{\alpha}\right)\cos\lambda\frac{t^\alpha}{\alpha}d_\alpha t = 2p(x)A\left(x,\frac{x^\alpha}{\alpha}\right)\sin\lambda\frac{x^\alpha}{\alpha} - \int_0^x 2p(x)\left(T_t^\alpha A\left(x,\frac{t^\alpha}{\alpha}\right)\right)\sin\lambda\frac{t^\alpha}{\alpha}d_\alpha t,$$

$$2\lambda p(x)\int_0^x B\left(x,\frac{t^\alpha}{\alpha}\right)\sin\lambda\frac{t^\alpha}{\alpha}d_\alpha t = -2p(x)B\left(x,\frac{x^\alpha}{\alpha}\right)\cos\lambda\frac{x^\alpha}{\alpha} + 2p(x)B(x,0) + \int_0^x 2p(x)\left(T_t^\alpha B\left(x,\frac{t^\alpha}{\alpha}\right)\right)\cos\lambda\frac{t^\alpha}{\alpha}d_\alpha t,$$

we get

$$\begin{aligned}
&\lambda\cos\lambda\frac{x^\alpha}{\alpha}\left(-2T_x^\alpha\theta(x)+2p(x)\right)\cos\theta(x) + \lambda\sin\lambda\frac{x^\alpha}{\alpha}\left(-2T_x^\alpha\theta(x)+2p(x)\right)\sin\theta(x)\\
&+\cos\lambda\frac{x^\alpha}{\alpha}\Big\{\left(T_x^\alpha T_x^\alpha\theta(x)\right)\sin\theta(x) + \left(T_x^\alpha\theta(x)\right)^2\cos\theta(x) - T_x^\alpha A\left(x,\frac{x^\alpha}{\alpha}\right)\\
&-T_x^\alpha A\left(x,\frac{t^\alpha}{\alpha}\right)\Big|_{t=x} + q(x)\cos\theta(x) - T_t^\alpha A\left(x,\frac{t^\alpha}{\alpha}\right)\Big|_{t=x} - 2p(x)B\left(x,\frac{x^\alpha}{\alpha}\right)\Big\}\\
&+\sin\lambda\frac{x^\alpha}{\alpha}\Big\{-\left(T_x^\alpha T_x^\alpha\theta(x)\right)\cos\theta(x) + \left(T_x^\alpha\theta(x)\right)^2\sin\theta(x) - T_x^\alpha B\left(x,\frac{x^\alpha}{\alpha}\right)\\
&-T_x^\alpha B\left(x,\frac{t^\alpha}{\alpha}\right)\Big|_{t=x} + q(x)\sin\theta(x) - T_t^\alpha B\left(x,\frac{t^\alpha}{\alpha}\right)\Big|_{t=x} + 2p(x)A\left(x,\frac{x^\alpha}{\alpha}\right)\Big\}\\
&-\lambda B(x,0) + T_t^\alpha A\left(x,\frac{t^\alpha}{\alpha}\right)\Big|_{t=0} + 2p(x)B(x,0)\\
&+\int_0^x\left[T_t^\alpha T_t^\alpha A\left(x,\frac{t^\alpha}{\alpha}\right) - T_x^\alpha T_x^\alpha A\left(x,\frac{t^\alpha}{\alpha}\right) + q(x)A\left(x,\frac{t^\alpha}{\alpha}\right) + 2p(x)T_t^\alpha B\left(x,\frac{t^\alpha}{\alpha}\right)\right]\cos\lambda\frac{t^\alpha}{\alpha}d_\alpha t\\
&+\int_0^x\left[T_t^\alpha T_t^\alpha B\left(x,\frac{t^\alpha}{\alpha}\right) - T_x^\alpha T_x^\alpha B\left(x,\frac{t^\alpha}{\alpha}\right) + q(x)B\left(x,\frac{t^\alpha}{\alpha}\right) - 2p(x)T_t^\alpha A\left(x,\frac{t^\alpha}{\alpha}\right)\right]\sin\lambda\frac{t^\alpha}{\alpha}d_\alpha t = 0.
\end{aligned}$$

Since the set of $\left\{\cos\lambda\frac{x^\alpha}{\alpha},\sin\lambda\frac{x^\alpha}{\alpha}\right\}$ is entire system for each fixed α and $p(x)\neq 0$, we immediately obtain equations (6) and (7).

From the system $\begin{cases}\left(-2T_x^\alpha\theta(x)+2p(x)\right)\cos\theta(x)=0\\ \left(-2T_x^\alpha\theta(x)+2p(x)\right)\sin\theta(x)=0\end{cases}$, the equation $T_x^\alpha\theta(x)-p(x)=0$ and hence (8) is taken.

From the equalities $T_x^\alpha\theta(x)=p(x)$, $d_\alpha A\left(x,\frac{t^\alpha}{\alpha}\right) = T_x^\alpha A\left(x,\frac{t^\alpha}{\alpha}\right)d_\alpha x + T_t^\alpha A\left(x,\frac{t^\alpha}{\alpha}\right)d_\alpha t$ and the following system

$$\begin{cases}
\left(T_x^\alpha T_x^\alpha\theta(x)\right)\sin\theta(x) + \left[\left(T_x^\alpha\theta(x)\right)^2 + q(x)\right]\cos\theta(x) - 2p(x)B\left(x,\frac{x^\alpha}{\alpha}\right)\\
-T_x^\alpha A\left(x,\frac{x^\alpha}{\alpha}\right) - T_x^\alpha A\left(x,\frac{t^\alpha}{\alpha}\right)\Big|_{t=x} - T_t^\alpha A\left(x,\frac{t^\alpha}{\alpha}\right)\Big|_{t=x} = 0\\
-\left(T_x^\alpha T_x^\alpha\theta(x)\right)\cos\theta(x) + \left[\left(T_x^\alpha\theta(x)\right)^2 + q(x)\right]\sin\theta(x) + 2p(x)A\left(x,\frac{x^\alpha}{\alpha}\right)\\
-T_x^\alpha B\left(x,\frac{x^\alpha}{\alpha}\right) - T_x^\alpha B\left(x,\frac{t^\alpha}{\alpha}\right)\Big|_{t=x} - T_t^\alpha B\left(x,\frac{t^\alpha}{\alpha}\right)\Big|_{t=x} = 0
\end{cases}$$

we get

$$\begin{cases}
T_x^\alpha A\left(x,\frac{x^\alpha}{\alpha}\right) + p(x)B\left(x,\frac{x^\alpha}{\alpha}\right) - \frac{1}{2}\left(T_x^\alpha p(x)\right)\sin\theta(x) - \frac{1}{2}\left(q(x)+p^2(x)\right)\cos\theta(x) = 0\\
T_x^\alpha B\left(x,\frac{x^\alpha}{\alpha}\right) - p(x)A\left(x,\frac{x^\alpha}{\alpha}\right) + \frac{1}{2}\left(T_x^\alpha p(x)\right)\cos\theta(x) - \frac{1}{2}\left(q(x)+p^2(x)\right)\sin\theta(x) = 0
\end{cases}.$$

In the above system, if the first equation is multiplied by $\cos\theta(x)$ and the second equation by $\sin\theta(x)$ and added side by side, we obtain

$$T_x^\alpha\left[A\left(x,\frac{x^\alpha}{\alpha}\right)\cos\theta(x) + B\left(x,\frac{x^\alpha}{\alpha}\right)\sin\theta(x)\right] = \frac{1}{2}\left(q(x)+p^2(x)\right)$$

or

$$A\left(x,\frac{x^{\alpha}}{\alpha}\right)\cos\theta(x)+B\left(x,\frac{x^{\alpha}}{\alpha}\right)\sin\theta(x)-A(0,0)=\frac{1}{2}\int_{0}^{x}\left(q(t)+p^{2}(t)\right)d_{\alpha}t.$$

Moreover, from equalities (4), (12), (7) and (8), we have that

$$T_{x}^{\alpha}\varphi(0,\lambda;\alpha)=A(0,0)=h.$$

Thus, equations (9) and (10) are obtained.

On the other hand, if the first equation is multiplied by $\sin\theta(x)$ and the second equation by $\left(-\cos\theta(x)\right)$ and added side by side, we obtain

$$T_{x}^{\alpha}\left[A\left(x,\frac{x^{\alpha}}{\alpha}\right)\sin\theta(x)-B\left(x,\frac{x^{\alpha}}{\alpha}\right)\cos\theta(x)\right]=\frac{1}{2}T_{x}^{\alpha}p(x)$$

or

$$A\left(x,\frac{x^{\alpha}}{\alpha}\right)\sin\theta(x)-B\left(x,\frac{x^{\alpha}}{\alpha}\right)\cos\theta(x)+B(0,0)=\frac{1}{2}\left(p(x)-p(0)\right).$$

From equality (7), we have that

$$B(0,0)=0.$$

Thus, equation (11) is obtained.

Basic Properties of the Operator L_{α}

In this section, we investigate some spectral properties of the operator L_{α} by supposing that the function $q(x)$ satisfies the additional condition

$$\int_{0}^{\pi}[|T_{x}^{\alpha}y(x)|^{2}+q(x)|y(x)|^{2}]d_{\alpha}x>0 \tag{15}$$

for all $y(x)\in W_{2,\alpha}^{2}[0,\pi]$ such that $y(x)\neq 0$ and

$$\left(T_{x}^{\alpha}y(0)\right)\overline{y}(0)-\left(T_{x}^{\alpha}y(\pi)\right)\overline{y}(\pi)=0. \tag{16}$$

Let the functions $\varphi:=\varphi(x,\lambda;\alpha)$ and $\psi:=\psi(x,\lambda;\alpha)$ be the solutions of the equation (1) satisfying the initial conditions (4) and

$$\psi(\pi,\lambda;\alpha)=1,T_{x}^{\alpha}\psi(\pi,\lambda;\alpha)=-H \tag{17}$$

respectively. It is clear that

$$U_{\alpha}(\varphi)=0,V_{\alpha}(\psi)=0.$$

We denote

$$\Delta_{\alpha}(\lambda)=W_{\alpha}[\psi,\varphi]=\begin{vmatrix}\psi & \varphi\\ T_{x}^{\alpha}\psi & T_{x}^{\alpha}\varphi\end{vmatrix}=\psi T_{x}^{\alpha}\varphi-\varphi T_{x}^{\alpha}\psi. \tag{18}$$

The function $\Delta_{\alpha}(\lambda)$ is called the characteristic function for the operator L_{α}, where $W_{\alpha}[\psi,\varphi]$ is the fractional Wronskian of the functions ψ and φ. Obviously, the function $\Delta_{\alpha}(\lambda)$ is entire function in λ.

Lemma 3.1 For each fixed α, $\Delta_{\alpha}(\lambda)$ does not depend on x and can be written as

$$\Delta_{\alpha}(\lambda)=V_{\alpha}(\varphi)=-U_{\alpha}(\psi). \tag{19}$$

Proof. It is clear from (18) that

$$T_x^\alpha \Delta_\alpha(\lambda) = T_x^\alpha(\psi T_x^\alpha \varphi - \varphi T_x^\alpha \psi) = \psi T_x^\alpha T_x^\alpha \varphi - \varphi T_x^\alpha T_x^\alpha \psi. \quad (20)$$

On the other hand, since the functions φ and ψ are the solutions of equation (1), the following equations are obtained

$$T_x^\alpha T_x^\alpha \varphi = (2\lambda p(x) + q(x) - \lambda^2)\varphi,$$

$$T_x^\alpha T_x^\alpha \psi = (2\lambda p(x) + q(x) - \lambda^2)\psi.$$

If these equations are substituted in (20)

$$T_x^\alpha \Delta_\alpha(\lambda) = 0$$

is obtained. Thus, the function $\Delta_\alpha(\lambda)$ is a constant with respect to x in $[0, \pi]$.

Moreover, if $x = 0$ and $x = \pi$ are substituted in equation (18) and conditions (4) and (17) are taken into account, then (19) is immediately taken.

Lemma 3.2 The zeros $\{\lambda_n\}$ of the function $\Delta_\alpha(\lambda)$ coincide with the eigenvalues of the operator L_α and for eigenfunctions $\psi_n := \psi(x, \lambda_n; \alpha)$ and $\varphi_n := \varphi(x, \lambda_n; \alpha)$ there exists a sequence $\{\beta_n\}$, such that the following relations are satisfied for each fixed α

$$\psi_n = \beta_n \varphi_n, \ \beta_n \neq 0. \quad (21)$$

Proof. Let λ_0 be an eigenvalue of the operator L_α, we show that $\Delta_\alpha(\lambda_0) = 0$. We suppose that $\Delta_\alpha(\lambda_0) \neq 0$. Then the functions $\varphi(x, \lambda_0; \alpha)$ and $\psi(x, \lambda_0; \alpha)$ are linearly independent. Thus

$$y(x, \lambda_0; \alpha) = c_1 \psi(x, \lambda_0; \alpha) + c_2 \varphi(x, \lambda_0; \alpha)$$

is a general solution of the operator L_α corresponding to $\lambda = \lambda_0$ for constants c_1 and c_2. Hence, the above equation can written for $c_1 \neq 0$ as

$$\psi(x, \lambda_0; \alpha) = \frac{1}{c_1} y(x, \lambda_0; \alpha) - \frac{c_2}{c_1} \varphi(x, \lambda_0; \alpha).$$

Thus, we get

$$\Delta_\alpha(\lambda_0) = W_\alpha[\psi(x, \lambda_0; \alpha), \varphi(x, \lambda_0; \alpha)] = \frac{1}{c_1} W_\alpha[y(x, \lambda_0; \alpha), \varphi(x, \lambda_0; \alpha)].$$

If the initial conditions (4) and especially $x = 0$ are taken into account in this equation, $\Delta_\alpha(\lambda_0) = 0$ contradiction is obtained for each fixed α.

On the other hand, let λ_0 be a zero of the function $\Delta_\alpha(\lambda)$. Then $\Delta_\alpha(\lambda_0) = 0$. So, we get $\psi(x, \lambda_0; \alpha) = \beta_0 \varphi(x, \lambda_0; \alpha)$ for $\beta_0 \neq 0$. Furthermore, the functions $\varphi(x, \lambda_0; \alpha)$ and $\psi(x, \lambda_0; \alpha)$ satisfy the initial conditions (4) and (17), respectively. So, the functions $\varphi(x, \lambda_0; \alpha)$ and $\psi(x, \lambda_0; \alpha)$ are eigenfunctions related to λ_0.

Since the eigenfunctions corresponding to each eigenvalue differ from each other by a multiplicative constant, there is a sequence $\{\beta_n\}$ such that the equality (21) is satisfied for each $n \in \mathbb{N}$ and fixed α.

Lemma 3.3 The eigenvalues of the operator L_α are real and nonzero for each fixed α.

Proof. This lemma can be proved similarly as in [20].

Denote a linear operator $L_{\alpha,0}$ with the following differential expression

$$\ell_{\alpha,0} y(x) := -T_x^\alpha T_x^\alpha y(x) + q(x) y(x)$$

and boundary conditions (2) and (3), where $y(x) \in W_{2,\alpha}^2[0, \pi]$.

Using α −integration by part and the condition (15), we get

$$\langle \ell_{\alpha,0} y, y \rangle = \int_0^\pi (\ell_{\alpha,0} y) \overline{y} \, d_\alpha x = \int_0^\pi [|T_x^\alpha y(x)|^2 + q(x)|y(x)|^2] d_\alpha x > 0.$$

Let λ_0 be an eigenvalue of the operator L_α and $y_0 = y(x,\lambda_0;\alpha)$ an eigenfunction corresponding to this eigenvalue and normalized by $\langle y_0, y_0\rangle = 1$.

It is clear that

$$-T_x^\alpha T_x^\alpha y_0 + \big(2\lambda_0 p(x) + q(x)\big)y_0 = \lambda_0^2 y_0$$

or

$$\lambda_0^2 y_0 - 2\lambda_0 p(x) y_0 - \ell_{\alpha,0} y_0 = 0. \tag{22}$$

If we take the inner product of both sides of the equation (22) by y_0, we obtain

$$\lambda_0^2 - 2\lambda_0 \langle p(x)y_0, y_0\rangle - \langle \ell_{\alpha,0} y_0, y_0\rangle = 0.$$

Hence

$$\lambda_0 = \langle p(x)y_0, y_0\rangle - \sqrt{\langle p(x)y_0, y_0\rangle^2 + \langle \ell_{\alpha,0} y_0, y_0\rangle}.$$

Since $p(x)$ is real and $\langle \ell_{\alpha,0} y, y\rangle > 0$, the proof is completed from the last relation.

Lemma 3.4 The eigenfunctions $y_n := y(x,\lambda_n;\alpha)$ and $y_k := y(x,\lambda_k;\alpha)$ corresponding to the eigenvalues λ_n and λ_k *($\lambda_n \neq \lambda_k$)* of the operator L_α are orthogonal in the sense of

$$(\lambda_n + \lambda_k)\int_0^\pi y_n y_k d_\alpha x - 2\int_0^\pi p(x) y_n y_k d_\alpha x = 0. \tag{23}$$

Proof. Take into our account that the operator $L_{\alpha,0}$ is symmetric and

$$\ell_{\alpha,0} y(x) := -T_x^\alpha T_x^\alpha y(x) + q(x)y(x) = \lambda^2 y(x) - 2\lambda p(x) y(x).$$

We have that

$$\langle \ell_{\alpha,0} y_n, y_k\rangle = \langle y_n, \ell_{\alpha,0} y_k\rangle,$$

$$\int_0^\pi (\lambda_n^2 y_n - 2\lambda_n p(x) y_n) y_k d_\alpha x = \int_0^\pi y_n (\lambda_k^2 y_k - 2\lambda_k p(x) y_k) d_\alpha x,$$

$$(\lambda_n^2 - \lambda_k^2)\int_0^\pi y_n y_k d_\alpha x - 2(\lambda_n - \lambda_k)\int_0^\pi p(x) y_n y_k d_\alpha x = 0.$$

By virtue of $\lambda_n \neq \lambda_k$ the equality (23) is obtained.

Definition 3.5 Let φ_n be the eigenfunction of the operator L_α corresponding to the eigenvalues λ_n. The numbers

$$\alpha_n = \int_0^\pi \varphi_n^2 d_\alpha x - \frac{1}{\lambda_n}\int_0^\pi p(x)\varphi_n^2 d_\alpha x \tag{24}$$

are called the normalizing numbers of the operator L_α and the data $\{\lambda_n, \alpha_n\}$ are also called the spectral data of the operator L_α.

Lemma 3.6 The equality $\dot{\Delta}_\alpha(\lambda_n) = -2\lambda_n \beta_n \alpha_n$ is valid and the eigenvalues of the operator L_α are simple, i.e., $\dot{\Delta}_\alpha(\lambda_n) \neq 0$, where $\dot{\Delta}_\alpha(\lambda) = \frac{\mathrm{d}}{\mathrm{d}\lambda}\Delta_\alpha(\lambda)$.

Proof. Since ψ and φ_n are the solutions of the equation (1), the following equalities

$$-T_x^\alpha T_x^\alpha \psi + \big(2\lambda p(x) + q(x)\big)\psi = \lambda^2 \psi,$$

$$-T_x^\alpha T_x^\alpha \varphi_n + \big(2\lambda_n p(x) + q(x)\big)\varphi_n = \lambda_n^2 \varphi_n$$

are held.

If the first equation is multiplied by φ_n, the second equation is multiplied by ψ and substracting them side by side, then the equality

$$T_x^{\alpha} W_{\alpha}[\psi, \varphi_n] = (\lambda^2 - \lambda_n^2)\varphi_n\psi - 2(\lambda - \lambda_n)p(x)\varphi_n\psi$$

is obtained. By conformable fractional integrating above equation over $[0, \pi]$ and taking into account (17) and (19), we get

$$(\lambda^2 - \lambda_n^2)\int_0^{\pi} \varphi_n\psi d_{\alpha}x - 2(\lambda - \lambda_n)\int_0^{\pi} p(x)\varphi_n\psi d_{\alpha}x = W_{\alpha}[\psi, \varphi_n]|_0^{\pi} = -\Delta_{\alpha}(\lambda).$$

Hence

$$(\lambda + \lambda_n)\int_0^{\pi} \varphi_n\psi d_{\alpha}x - 2\int_0^{\pi} p(x)\varphi_n\psi d_{\alpha}x = -\frac{\Delta_{\alpha}(\lambda)}{\lambda - \lambda_n}.$$

Passing to the limit as $\lambda \to \lambda_n$ in the last equation, it yields

$$2\lambda_n\int_0^{\pi} \varphi_n\psi_n d_{\alpha}x - 2\int_0^{\pi} p(x)\varphi_n\psi_n d_{\alpha}x = -\lim_{\lambda\to\lambda_n}\frac{\Delta_{\alpha}(\lambda)}{\lambda - \lambda_n} = -\dot{\Delta}_{\alpha}(\lambda_n).$$

From (21) and (24), we have that

$$\dot{\Delta}_{\alpha}(\lambda_n) = -2\lambda_n\beta_n\alpha_n. \tag{25}$$

It is obvious from (25) that $\dot{\Delta}(\lambda_n) \neq 0$ for $\lambda_n \neq 0$, that is, the eigenvalues are simple. Therefore, the proof is completed.

Theorem 3.7 The operator L_{α} has a countable set of eigenvalues $\{\lambda_n\}$ and the following estimate holds:

$$\lambda_n = \frac{n\alpha}{\pi^{\alpha-1}} + c_{\alpha,0} + \frac{c_{\alpha,1}}{n} + o\left(\frac{1}{n}\right), |n| \to \infty, \tag{26}$$

where

$$c_{\alpha,0} = \frac{\alpha}{\pi^{\alpha}}\int_0^{\pi} p(x)d_{\alpha}x, \quad c_{\alpha,1} = \frac{1}{\pi}\left[h + H + \frac{1}{2}\int_0^{\pi}\left(q(x) + p^2(x)\right)d_{\alpha}x\right].$$

Proof. According to (19) the relation $\Delta_{\alpha}(\lambda)$, with the help of (5) and (12), as

$$\begin{aligned}\Delta_{\alpha}(\lambda) &= -\left(\lambda - p(\pi)\right)\sin\left(\lambda\frac{\pi^{\alpha}}{\alpha} - \theta(\pi)\right) + A\left(\pi, \frac{\pi^{\alpha}}{\alpha}\right)\cos\lambda\frac{\pi^{\alpha}}{\alpha}\\ &+B\left(\pi, \frac{\pi^{\alpha}}{\alpha}\right)\sin\lambda\frac{\pi^{\alpha}}{\alpha} + H\cos\left(\lambda\frac{\pi^{\alpha}}{\alpha} - \theta(\pi)\right)\\ &+\int_0^{\pi} T_x^{\alpha}A\left(x, \frac{t^{\alpha}}{\alpha}\right)\Big|_{x=\pi}\cos\lambda\frac{t^{\alpha}}{\alpha}d_{\alpha}t + \int_0^{\pi} T_x^{\alpha}B\left(x, \frac{t^{\alpha}}{\alpha}\right)\Big|_{x=\pi}\sin\lambda\frac{t^{\alpha}}{\alpha}d_{\alpha}t\\ &+H\int_0^{\pi} A\left(\pi, \frac{t^{\alpha}}{\alpha}\right)\cos\lambda\frac{t^{\alpha}}{\alpha}d_{\alpha}t + H\int_0^{\pi} B\left(\pi, \frac{t^{\alpha}}{\alpha}\right)\sin\lambda\frac{t^{\alpha}}{\alpha}d_{\alpha}t\end{aligned} \tag{27}$$

is written.

It follows from (10) and (11)

$$\begin{cases} A\left(\pi,\frac{\pi^\alpha}{\alpha}\right)\cos\theta(\pi)+B\left(\pi,\frac{\pi^\alpha}{\alpha}\right)\sin\theta(\pi)=h+\frac{1}{2}\int_0^\pi\left(q(t)+p^2(t)\right)d_\alpha t \\ A\left(\pi,\frac{\pi^\alpha}{\alpha}\right)\sin\theta(\pi)-B\left(\pi,\frac{\pi^\alpha}{\alpha}\right)\cos\theta(\pi)=\frac{p(\pi)-p(0)}{2} \end{cases}$$

which implies that

$$\begin{cases} A\left(\pi,\frac{\pi^\alpha}{\alpha}\right)=\frac{p(\pi)-p(0)}{2}\sin\theta(\pi)+\left[h+\frac{1}{2}\int_0^\pi\left(q(t)+p^2(t)\right)d_\alpha t\right]\cos\theta(\pi) \\ B\left(\pi,\frac{\pi^\alpha}{\alpha}\right)=\frac{p(0)-p(\pi)}{2}\cos\theta(\pi)+\left[h+\frac{1}{2}\int_0^\pi\left(q(t)+p^2(t)\right)d_\alpha t\right]\sin\theta(\pi) \end{cases}$$

and hence

$$\begin{aligned} &A\left(\pi,\frac{\pi^\alpha}{\alpha}\right)\cos\lambda\frac{\pi^\alpha}{\alpha}+B\left(\pi,\frac{\pi^\alpha}{\alpha}\right)\sin\lambda\frac{\pi^\alpha}{\alpha}=\frac{p(0)-p(\pi)}{2}\sin\left(\lambda\frac{\pi^\alpha}{\alpha}-\theta(\pi)\right) \\ &+\left[h+\frac{1}{2}\int_0^\pi\left(q(t)+p^2(t)\right)d_\alpha t\right]\cos\left(\lambda\frac{\pi^\alpha}{\alpha}-\theta(\pi)\right). \end{aligned} \tag{28}$$

Take into account (28) in (27), we obtain

$$\begin{aligned} \Delta_\alpha(\lambda)=&-\left(\lambda-p(\pi)\right)\sin\left(\lambda\frac{\pi^\alpha}{\alpha}-\theta(\pi)\right)+\frac{p(0)-p(\pi)}{2}\sin\left(\lambda\frac{\pi^\alpha}{\alpha}-\theta(\pi)\right) \\ &+\left[h+H+\frac{1}{2}\int_0^\pi\left(q(t)+p^2(t)\right)d_\alpha t\right]\cos\left(\lambda\frac{\pi^\alpha}{\alpha}-\theta(\pi)\right) \\ &+\int_0^\pi T_x^\alpha A\left(x,\frac{t^\alpha}{\alpha}\right)\Big|_{x=\pi}\cos\lambda\frac{t^\alpha}{\alpha}d_\alpha t+\int_0^\pi T_x^\alpha B\left(x,\frac{t^\alpha}{\alpha}\right)\Big|_{x=\pi}\sin\lambda\frac{t^\alpha}{\alpha}d_\alpha t \\ &+H\left[\int_0^\pi A\left(\pi,\frac{t^\alpha}{\alpha}\right)\cos\lambda\frac{t^\alpha}{\alpha}d_\alpha t+\int_0^\pi B\left(\pi,\frac{t^\alpha}{\alpha}\right)\sin\lambda\frac{t^\alpha}{\alpha}d_\alpha t\right]. \end{aligned} \tag{29}$$

Thus, for $\lambda\neq p(\pi)$ the equation $\Delta_\alpha(\lambda)=0$ as

$$\begin{aligned} &\sin\left(\lambda\frac{\pi^\alpha}{\alpha}-\theta(\pi)\right)+\frac{p(\pi)-p(0)}{2}\frac{1}{\lambda-p(\pi)}\sin\left(\lambda\frac{\pi^\alpha}{\alpha}-\theta(\pi)\right) \\ &-\frac{1}{\lambda-p(\pi)}\left[h+H+\frac{1}{2}\int_0^\pi\left(q(t)+p^2(t)\right)d_\alpha t\right]\cos\left(\lambda\frac{\pi^\alpha}{\alpha}-\theta(\pi)\right)-\frac{\Delta_{\alpha,1}(\lambda)}{\lambda-p(\pi)}=0 \end{aligned}$$

is taken, where

$$\begin{aligned} \Delta_{\alpha,1}(\lambda)=&\int_0^\pi\left[T_x^\alpha A\left(x,\frac{t^\alpha}{\alpha}\right)\Big|_{x=\pi}+HA\left(\pi,\frac{t^\alpha}{\alpha}\right)\right]\cos\lambda\frac{t^\alpha}{\alpha}d_\alpha t \\ &+\int_0^\pi\left[T_x^\alpha B\left(x,\frac{t^\alpha}{\alpha}\right)\Big|_{x=\pi}+HB\left(\pi,\frac{t^\alpha}{\alpha}\right)\right]\sin\lambda\frac{t^\alpha}{\alpha}d_\alpha t=o\left(e^{|\operatorname{Im}\lambda|\frac{\pi^\alpha}{\alpha}}\right). \end{aligned}$$

Taking Taylor's expansion formula for the $\frac{1}{\lambda-p(\pi)}=\frac{1}{\lambda}+\frac{p(\pi)}{\lambda^2}+o\left(\frac{1}{\lambda^2}\right)$, $|\lambda|\to\infty$ into account, we get

$$\begin{aligned} &\sin\left(\lambda\frac{\pi^\alpha}{\alpha}-\theta(\pi)\right)+\frac{p(\pi)-p(0)}{2\lambda}\sin\left(\lambda\frac{\pi^\alpha}{\alpha}-\theta(\pi)\right)-\frac{1}{\lambda}\left[h+H+\frac{1}{2}\int_0^\pi\left(q(t)+p^2(t)\right)d_\alpha t\right]\cos\left(\lambda\frac{\pi^\alpha}{\alpha}-\theta(\pi)\right) \\ &+o\left(\frac{1}{\lambda}e^{|\operatorname{Im}\lambda|\frac{\pi^\alpha}{\alpha}}\right)=0 \end{aligned} \tag{30}$$

We take a circle $\Gamma_n = \left\{\lambda:\ |\lambda - c_{\alpha,0}| \le \frac{\alpha}{\pi^{\alpha-1}}\left(n+\frac{1}{2}\right), n = 0,1,2,\dots\right\}$ in the λ −plane and define $\Delta_\alpha(\lambda) = f(\lambda;\alpha) + g(\lambda;\alpha)$, where

$$f(\lambda;\alpha) = \sin\left(\lambda\frac{\pi^\alpha}{\alpha} - \theta(\pi)\right)$$

and

$$g(\lambda;\alpha) = \frac{p(\pi)-p(0)}{2\lambda}\sin\left(\lambda\frac{\pi^\alpha}{\alpha} - \theta(\pi)\right) - \frac{1}{\lambda}\left[h + H + \frac{1}{2}\int_0^\pi \left(q(t)+p^2(t)\right)d_\alpha t\right]\cos\left(\lambda\frac{\pi^\alpha}{\alpha} - \theta(\pi)\right) + o\left(\frac{1}{\lambda}e^{|\operatorname{Im}\lambda|\frac{\pi^\alpha}{\alpha}}\right)$$

.

For sufficiently large n and each fixed α, the number of zeros of the function $\Delta_\alpha(\lambda) = f(\lambda;\alpha) + g(\lambda;\alpha)$ in the region Γ_n is the same as the number of zeros of the function $f(\lambda;\alpha)$ from Rouche's theorem (see, e.g., [21]).

Thus, if $\sin\left(\lambda\frac{\pi^\alpha}{\alpha} - \theta(\pi)\right) = 0$, then $\lambda_n = \frac{n\alpha}{\pi^{\alpha-1}} + c_{\alpha,0}, n \in \mathbb{Z}\backslash\{0\}$ is taken, where $c_{\alpha,0} = \frac{\alpha}{\pi^\alpha}\theta(\pi) = \frac{\alpha}{\pi^\alpha}\int_0^\pi p(x)d_\alpha x$.

We conclude that $\lambda_n = \frac{n\alpha}{\pi^{\alpha-1}} + c_{\alpha,0} + \varepsilon_n,\ \varepsilon_n = o\left(\frac{1}{n}\right)$ as $|n| \to \infty$. By substituting this into (30), we obtain

$$\sin\left(n\pi + \varepsilon_n\frac{\pi^\alpha}{\alpha}\right) + \frac{p(\pi)-p(0)}{2}\frac{1}{\frac{n\alpha}{\pi^{\alpha-1}} + c_{\alpha,0} + \varepsilon_n}\sin\left(n\pi + \varepsilon_n\frac{\pi^\alpha}{\alpha}\right)$$
$$-\frac{1}{\frac{n\alpha}{\pi^{\alpha-1}} + c_{\alpha,0} + \varepsilon_n}\left[h + H + \frac{1}{2}\int_0^\pi \left(q(t)+p^2(t)\right)d_\alpha t\right]\cos\left(n\pi + \varepsilon_n\frac{\pi^\alpha}{\alpha}\right) + o\left(\frac{1}{n}\right) = 0.$$

This implies that

$$\sin\left(\varepsilon_n\frac{\pi^\alpha}{\alpha}\right) + \frac{p(\pi)-p(0)}{2}\frac{1}{\frac{n\alpha}{\pi^{\alpha-1}} + c_{\alpha,0} + \varepsilon_n}\sin\left(\varepsilon_n\frac{\pi^\alpha}{\alpha}\right) -$$
$$\frac{1}{\frac{n\alpha}{\pi^{\alpha-1}} + c_{\alpha,0} + \varepsilon_n}\left[h + H + \frac{1}{2}\int_0^\pi \left(q(t)+p^2(t)\right)d_\alpha t\right]\cos\left(\varepsilon_n\frac{\pi^\alpha}{\alpha}\right) + o\left(\frac{1}{n}\right) = 0.$$

From the following asymptotics

$$\cos\left(\varepsilon_n\frac{\pi^\alpha}{\alpha}\right) = 1 + o\left(\frac{1}{n^2}\right), \qquad \sin\left(\varepsilon_n\frac{\pi^\alpha}{\alpha}\right) = \varepsilon_n\frac{\pi^\alpha}{\alpha} + o\left(\frac{1}{n^3}\right), \qquad \frac{1}{\frac{n\alpha}{\pi^{\alpha-1}} + c_{\alpha,0} + \varepsilon_n} = \frac{\pi^{\alpha-1}}{n\alpha} + o\left(\frac{1}{n^2}\right)$$

and the above last equation, we get

$$\varepsilon_n = \frac{c_{\alpha,1}}{n} + o\left(\frac{1}{n}\right),$$

where

$$c_{\alpha,1} = \frac{1}{\pi}\left[h + H + \frac{1}{2}\int_0^\pi \left(q(t)+p^2(t)\right)d_\alpha t\right].$$

Thus, (26) is valid, i.e., the proof is completed.

Lemma 3.8 The normalizing numbers α_n of the operator L_α holds the following asymptotic formula

$$\alpha_n = \frac{\pi^\alpha}{2\alpha} + \frac{d_{\alpha,0}}{n} + o\left(\frac{1}{n}\right), \qquad |n| \to \infty, \tag{31}$$

where

$$d_{\alpha,0} = -\frac{\pi^\alpha}{2\alpha}p(0).$$

Proof. The formula (31) obtains from (24) by using the asymptotic formula (26) for λ_n.

Conflicts of interest

The authors declare that they have no conflict of interest.

Acknowledgements

This study will be included in MSc Thesis of Esengül Koç.

References

[1] Khalil R., Al Horania M., Yousefa A., et al., A New Definition of Fractional Derivative, *J. Comput. Appl. Math.*, 264 (2014) 65-70.

[2] Abdeljawad T., On Conformable Fractional Calculus, *J. Comput. Appl. Math.*, 279 (2015) 57-66.

[3] Atangana A., Baleanu D., Alsaedi A., New Properties of Conformable Derivative, *Open Math.*, 13 (2015) 889-898.

[4] Abu Hammad M., Khalil R., Abel's Formula and Wronskian for Conformable Fractional Differential Equations, *Int. J. Differ. Equ. Appl.*, 13 (3) (2014) 177-183.

[5] Birgani O.T., Chandok S., Dedovic N., Radenoviç S., A Note on Some Recent Results of the Conformable Derivative, *Adv. Theory Nonlinear Anal. Appl.*, 3 (1) (2019) 11-17.

[6] Zhao D., Luo M., General Conformable Fractional Derivative and its Physical Interpretation, *Calcolo*, 54 (2017) 903–917

[7] Zhou H.W., Yang S., Zhang S.Q., Conformable Derivative Approach to Anomalous Diffusion, *Physica A*, 491 (2018) 1001-1013.

[8] Chung W.S., Fractional Newton Mechanics with Conformable Fractional Derivative, *J. Comput. Appl. Math.*, 290 (2015) 150-158.

[9] Benkhettou N., Hassani S., Torres D.F.M., A Conformable Fractional Calculus on Arbitrary Time Scales, *J. King Saud Univ. Sci.*, 28 (2016) 93–98.

[10] Jarad F., Uğurlu E., Abdeljawad T., Baleanu D., On a New Class of Fractional Operators, *Adv. in Differ. Equ.*, 2017 (2017) Article ID 247 .

[11] Mortazaasl H., Jodayree Akbarfam A,. Trace Formula and Inverse Nodal Problem for a Conformable Fractional Sturm-Liouville Problem, *Inverse Problems in Science and Engineering*, 28 (4) (2020) 524-555.

[12] Keskin B., Inverse Problems for one Dimentional Conformable Fractional Dirac Type Integro Differential System, *Inverse Problems*, 36 (6) (2020) 065001.

[13] Adalar I., Ozkan A.S., Inverse Problems for a Conformable Fractional Sturm-Liouville Operators, *Journal of Inverse and Ill-posed Problems*, 28 (6) (2020).

[14] Çakmak Y., Inverse Nodal Problem for a Conformable Fractional Diffusion Operator, *Inverse Problems in Science and Engineering*, 29 (9) (2021) 1308-1322.

[15] Allahverdiev B.P., Tuna H., Yalçinkaya Y., Conformable Fractional Sturm-Liouville Equation, *Mathematical Methods in the Applied Sciences*, 42 (10) (2019) 3508-3526.

[16] Gasymov M.G., Gusejnov G.S., Determination of a Diffusion Operator from Spectral Data, *Akad. Nauk Azerb. SSR. Dokl.*, 37 (2) (1981) 19-23.

[17] Koyunbakan H., Panakhov E.S., Half-Inverse Problem for Diffusion Operators on the Finite Interval, *J. Math. Anal. Appl.*, 326 (2) (2007) 1024-1030.

[18] Yang C.F., New Trace Formulae for a Quadratic Pencil of the Schrodinger Operator, *Journal of Mathematical Physics*, 51 (3) (2010) 33506-33506-10.

[19] Wang Y., Zhou J., Li Y., Fractional Sobolev's Spaces on Time Scales via Conformable Fractional Calculus and Their Application to a Fractional Differential Equation on Time Scales, *Adv. Math. Phys.*, 2016 (2016) 21.

[20] Guseinov G.Sh., Inverse Spectral Problems for a Quadratic Pencil of Sturm-Liouville Operators on a Finite Interval, *Spectral Theory of Operators and Its Applications, Elm, Baku, Azerbaijan,* 7, (1986) 51–101. (In Russian)

[21] Freiling G., Yurko V.A., Inverse Sturm–Liouville Problems and Their Applications, New York: Nova Science Publishers, (2001).

Cumhuriyet Sci. J., 44(1) (2023) 181-187
DOI: https://doi.org/10.17776/csj.1209529

Cumhuriyet Science Journal

| csj.cumhuriyet.edu.tr | Founded: 2002 ISSN: 2587-2680 e-ISSN: 2587-246X Publisher: Sivas Cumhuriyet University

Spectral Decompositions of the Difference Operator Δ^m over the Sequence Space cs

Nuh Durna [1,a], Ömer Özdemir [1,b,*]

[3]*Department of Mathematics, Faculty of Science, Sivas Cumhuriyet University, Sivas, Türkiye.*
**Corresponding author*

Research Article

History
Received: 24/11/2022
Accepted: 16/03/2023

ABSTRACT

This study aims to bring together some studies on the spectra of difference operators in the literature over the cs sequence space and to provide a basis for related problems. So far, the problem has been solved up to a maximum of 2 orders on the sequence space cs. In this article, we discuss the difference operator Δ^m, represented by a (m+1) banded matrix, which generalizes the difference operators of the form Δ, Δ^2, B(r,s) and B(r,s,t) and we will give its boundedness, spectrum, fine spectrum and some spectral separations over the sequence space cs.

Keywords: Spectra, Fine spectra, Generalized difference operator, Band matrix.

[a] ndurna@cumhuriyet.edu.tr https://orcid.org/0000-0001-5469-7745 [b] sivasomer95@gmail.com https://orcid.org/0000-0003-1158-5553

Introduction

The idea of defining the sequence space with the first-order difference operator was introduced in [1] and further generalized in [2]. Then, various sequence spaces have been studied by many authors by means of difference operators of different order (see for details [3-6]. Baliarsingh et al. in [7], also combined most of the difference operators previously described and found their fine spectra in a more general way.

Spectral theory has applications in many parts of mathematics and physics, including function theory, complex analysis, differential and integral equations, control theory, and quantum physics. In the literature, there are many important studies on the calculation of spectra of difference operators and generalized difference operators over various sequence spaces. For example, the fine spectrum of the difference operator on the sequence spaces c_0, c and ℓ_p $(0 \le p < 1)$ was examined by Altay and Başar, [8-9]. The fine spectra of the operator $B(r,s)$ on c_0 and c were investigated by Altay and Başar in [10] and the fine spectra of the difference operator on the sequence spaces ℓ_p and bv_p $(1 < p < \infty)$ were calculated by Akhmedov and Başar in [11-12]. Srivastava and Kumar in [12-14] examined the fine spectra of the generalized difference operator Δ_v on sequence spaces c_0 and ℓ_1, where $a = (a_k)$ and $b = (b_k)$ are convergent sequences with certain properties, $v = (v_k)$ is a fixed or strictly decreasing sequence, and $r \in \mathbb{N}$. Recently, Akhmedov and El-Shabrawy [15], Dutta and Baliarsingh [16-17] examined the fine spectra of the generalized difference operators $\Delta_{a,b}$, Δ^2 and Δ_v^r on the sequence spaces c, c_0 and ℓ_1, respectively, where $a = (a_k)$ ve $b = (b_k)$ are convergent sequences with specific features, $v = (v_k)$ is a fixed or strictly decreasing sequence and $r \in \mathbb{N}$. In most of the studies mentioned above, the spectrum is discrete; point spectrum, continuous spectrum and residual spectrum. On the other hand, in [18] Durna and Yıldırım obtained spectral decomposition of factorable matrices on c_0 and in [19] Başar et al. studied the decomposition of the spectrum (approximate point spectrum, defect spectrum, compressed spectrum) of the generalized difference operator on some sequence spaces. In addition, in [20], Durna calculated the spectral decomposition of the Δ^{uv} generalized upper triangular double-band matrix over the sequence spaces c_0 and c. In [21] Das studied the spectrum and fine spectrum of the upper triangular matrix $U(r_1, r_2; s_1, s_2)$ on the c_0 sequence space. In [22], they studied the spectral decompositions of the generalized difference operator $B(r,s)$ on bv_0 and h sequence spaces. In [23], Tripathy and Das studied the spectrum and fine spectrum of the upper triangular matrix $U(r,0,0,s)$ on c_0 sequence space.

As mentioned above, there are many applications of spectra of bounded operators on Banach spaces. For this reason, the spectra of bounded linear operators have been studied by many people in recent years. So far, the problem on the cs sequence space has been solved up to a maximum of 2 orders. In this study, we will give the spectrum, point spectrum, continuous spectrum, residual spectrum and fine spectrum of the generalized difference operator Δ^m with $m+1$ band on the sequence space cs and calculate their spectral decomposition. Thus, the results obtained for the difference operator Δ studied in [8] and the results obtained for the generalized difference operator $B(1,-1)$ studied in [10] and [24] for $m = 1$ and the results obtained for the generalized difference operator $B(1,-2,1)$ studied in [25] for $m = 2$ will be included and generalized in this study.

Main Results

The generalized difference operator Δ^m $(m \in \mathbb{N})$ on the cs sequence space is defined by

$$\begin{aligned}(\Delta x)_k &= x_k - x_{k-1}\\ (\Delta^2 x)_k &= \Delta(\Delta x)_k = \Delta(x_k - x_{k-1})\\ &= x_k - 2x_{k-1} + x_{k-2}\\ (\Delta^3 x)_k &= x_k - 3x_{k-1} + 3x_{k-2} - x_{k-3}\\ &\vdots\\ (\Delta^m x)_k &= x_k - \binom{m}{1}x_{k-1} + \binom{m}{2}x_{k-2} + \cdots + (-1)^m x_{k-m}\\ &= \sum_{i=0}^{m}(-1)^i\binom{m}{i}x_{k-i}\\ &= x_k - mx_{k-1} + \tfrac{m(m-1)}{2!}x_{k-2} + \cdots + (-1)^m x_{k-m},\end{aligned}$$

for $k \in \mathbb{N}_0$, $\mathbb{N}_0 = \{0,1,2,\cdots\}$ and $x_k = 0$ for $k < 0$ ([7]).

It can be proven that the Δ^m operator can be represented by an (a_{nk}) matrix with $m+1$ bands. Here is

$$a_{nk} = \begin{cases}(-1)^{n-k}\binom{m}{k} & , \quad \max\{0, n-m\} \le k \le n\\ 0 & , \quad 0 \le k < \max\{0, n-m\} \text{or} k > n\end{cases}$$

for every $n, k \in \mathbb{N}_0$. Equivalently, it can be written as

$$\Delta^m = (a_{nk}) = \begin{pmatrix}1 & 0 & 0 & 0 & 0 & 0 & \cdots\\ -m & 1 & 0 & 0 & 0 & 0 & \cdots\\ \frac{m(m-1)}{2} & -m & 1 & 0 & 0 & 0 & \cdots\\ \vdots & \vdots & \vdots & \vdots & \vdots & \vdots & \cdots\\ (-1)^m & (-1)^{m-1}m & \cdots & -m & 1 & 0 & \cdots\\ 0 & (-1)^m & (-1)^{m-1}m & \cdots & -m & 1 & \cdots\\ \vdots & \vdots & \vdots & \vdots & \vdots & \vdots & \ddots\end{pmatrix}. \quad (1)$$

In this study, the fine spectrum and spectral decompositions of the Δ^m operator on the cs sequence space will be calculated, where cs is the sequence space of the form

$$cs: \left\{x = (x_n) \in w: \lim_{n\to\infty}\sum_{i=0}^{n} x_i \text{exist}\right\}.$$

If $T: cs \to cs$ is a bounded linear operator with matrix representation A, then the matrix representation of the $T^*: cs^* \to cs^* \cong bv$ adjoint operator is the transpose of matrix A (see [26]).

Spectral Decompositions of the Difference Operator Δ^m on the Sequence Space cs

In fact, the Δ^m operator is represented by a $(m+1)$-th band matrix that generalizes the difference operators of the form Δ, Δ^2, $B(r,s)$ and $B(r,s,t)$ under different conditions. First, a few basic information will be given about the linearity and boundedness of the difference operator Δ^m. Then, spectrum and fine spectrum sets such as point spectrum, continuous spectrum and residual spectrum of the Δ^m operator will be determined in the sequence space cs. Let us now give two lemmas that will be very useful in determining the subdivision of the spectrum.

Lemma 1 *Necessary and sufficient condition for the linear operator T to have a dense range is that the adjoint operator T^* is one-to-one ([27], Theorem II 3.7).*

Lemma 2 *A necessary and sufficient condition for the linear operator T to have a bounded inverse is that the adjoint operator T^* is onto ([27], Theorem II 3.7).*

Since the definitions given above are related to the spectrum of the bounded linear operator, we first need to show the boundedness of the operator Δ^m on the sequence space cs. For this, the following lemmas will be used.

Lemma 3 *Necessary and sufficient condition for the matrix $A = (a_{nk})$ to represent a $T \in B(cs)$ operator*

i) For every k, the series $\sum_n a_{nk}$ is convergent,

ii) $\sup_N \sum_k \left|\sum_{n=1}^{N}(a_{nk} - a_{n,k-1})\right| < \infty$ ([26], 8.4.6B).

Lemma 4 $\sum_{n=0}^{\infty}\sum_{k=0}^{m} b_{nk} = \sum_{k=0}^{m}\sum_{n=0}^{\infty} b_{nk}$ *is valid.*

Proof.

$$\begin{aligned}\sum_{n=0}^{\infty}\sum_{k=0}^{m} b_{nk} &= \sum_{k=0}^{m} b_{0k} + \sum_{k=0}^{m} b_{1k} + \sum_{k=0}^{m} b_{2k} + \cdots\\ &= b_{00} + b_{01} + b_{02} + \cdots + b_{0m}\\ &\quad + b_{10} + b_{11} + b_{12} + \cdots + b_{1m}\\ &\quad + b_{20} + b_{21} + b_{22} + \cdots + b_{2m} + \cdots\\ &= \sum_{n=0}^{\infty} b_{n0} + \sum_{n=0}^{\infty} b_{n1} + \cdots + \sum_{n=0}^{\infty} b_{nm}\\ &= \sum_{k=0}^{m}\sum_{n=0}^{\infty} b_{nk}.\end{aligned}$$

Theorem 1 $\Delta^m \in B(cs)$ *is valid.*

Proof. If we consider the matrix representation of the difference operator Δ^m in (1), Δ^m is a band matrix with $m+1$ bands. Therefore, it is clear that condition (i) of Lemma 3 is satisfied.

ii) We get

$$\begin{aligned}\sum_{n=1}^{N}(a_{nk} - a_{n,k-1}) &= \sum_{n=1}^{N}(-1)^{n-k}\left[\binom{m}{k} - \binom{m}{k-1}\right]\\ &= (-1)^k\left[\binom{m}{k} - \binom{m}{k-1}\right]\sum_{n=1}^{N}(-1)^n\\ &= (-1)^k\left[\binom{m}{k} - \binom{m}{k-1}\right]A\end{aligned}$$

where $A = \begin{cases}0 & , \quad N \text{ is even}\\ 1 & , \quad N \text{ is odd}\end{cases}$. Then we have

$$\begin{aligned}\sum_k\left|\sum_{n=1}^{N}(a_{nk} - a_{n,k-1})\right| &\le \sum_k\left[\binom{m}{k} + \binom{m}{k-1}\right]\\ &= \sum_{k=0}^{m}\left[\binom{m}{k} + \binom{m}{k-1}\right]\\ &\le 2^{m+1}.\end{aligned}$$

So we get $\Delta^m \in B(cs)$.

Spectrum and fine spectrum of the difference operator $\boldsymbol{\Delta^m}$ *on the* $\boldsymbol{cs}$ *sequence space*

Theorem 2 *The point spectrum of* Δ^m *on* cs *is* $\sigma_p(\Delta^m, cs) = \emptyset$.

Proof. Think of the system of linear equations $\Delta^m x = \alpha x$, with $x \neq \theta = \{0,0,0,\cdots\}$ in cs. From (1) we have

$$\begin{pmatrix} 1 & 0 & 0 & 0 & 0 & 0 & \cdots \\ -m & 1 & 0 & 0 & 0 & 0 & \cdots \\ \frac{m(m-1)}{2} & -m & 1 & 0 & 0 & 0 & \cdots \\ \cdots & \cdots & \cdots & \cdots & \cdots & \cdots & \cdots \\ (-1)^m & (-1)^{m-1}m & \cdots & -m & 1 & 0 & \cdots \\ 0 & (-1)^m & (-1)^{m-1}m & \cdots & -m & 1 & \cdots \\ \vdots & \vdots & \vdots & \vdots & \vdots & \vdots & \ddots \end{pmatrix} \begin{pmatrix} x_0 \\ x_1 \\ x_2 \\ \vdots \end{pmatrix} = \alpha \begin{pmatrix} x_0 \\ x_1 \\ x_2 \\ \vdots \end{pmatrix}$$

and so we get

$$\begin{aligned} &x_0 = \alpha x_0 \\ &-mx_0 + x_1 = \alpha x_1 \\ &\frac{m(m-1)}{2!}x_0 - mx_1 + x_2 = \alpha x_2 \\ &\tfrac{-m(m-1)(m-2)}{3!}x_0 + \tfrac{m(m-1)}{2!}x_1 - mx_2 + x_3 = \alpha x_3. \qquad (2) \\ &\qquad\qquad\qquad\qquad\qquad\qquad\qquad\qquad \vdots \end{aligned}$$

If $x_0 \neq 0$ from the first equation of the (2) system of equations, then $\alpha = 1$. So from equation 2, $-mx_0 + x_1 = x_1$ and $x_0 = 0$, which is a contradiction. Let's assume that $x_0 = 0$, then from equation 2, if $x_1 = \alpha x_1$ and $x_1 \neq 0$ then $\alpha = 1$. So from equation 3, $-mx_1 + x_2 = x_2$ and $x_1 = 0$, which is a contradiction. If we continue like this, we get $x_1 = x_2 = x_3 = \cdots = 0$. From here, there is no $x \neq 0$ with $\Delta^m x = \alpha x$. Hence $\sigma_p(\Delta^m, cs) = \emptyset$.

Corollary 1 $I_3\sigma(\Delta^m, cs) = II_3\sigma(\Delta^m, cs) = III_3\sigma(\Delta^m, cs) = \emptyset$.

Proof. Since $\sigma_p(\Delta^m, cs) = I_3\sigma(\Delta^m, cs) \cup II_3\sigma(\Delta^m, cs) \cup III_3\sigma(\Delta^m, cs)$ from [19] Table 1.2, the desired result is obtained from Theorem 2.

Theorem 3 *The point spectrum of the* $(\Delta^m)^*$ *adjoint operator on* $cs^* \cong bv$ *is the set*

$\sigma_p((\Delta^m)^*, bv) = \{\alpha \in \mathbb{C}: |1 - \alpha| \leq 2^m - 1\} \cup \{0\}$.

Proof. Let's assume that $(\Delta^m)^* x = \alpha x$ and $0 \neq x \in bv$. In this case,

$$\begin{aligned} &\binom{m}{0}x_0 - \binom{m}{1}x_1 + \binom{m}{2}x_2 - \binom{m}{3}x_3 + \cdots + (-1)^m\binom{m}{m}x_m = \alpha x_0 \\ &\binom{m}{0}x_1 - \binom{m}{1}x_2 + \binom{m}{2}x_3 + \cdots + (-1)^m\binom{m}{m-1}x_m + (-1)^m\binom{m}{m}x_{m+1} = \alpha x_1 \\ &\binom{m}{0}x_2 - \binom{m}{1}x_3 + \cdots + (-1)^m\binom{m}{m}x_{m+2} = \alpha x_2 \\ &\qquad\qquad\qquad\qquad \vdots \qquad (3) \\ &\binom{m}{0}x_k - \binom{m}{1}x_{k+1} + \binom{m}{2}x_{k+2} + \cdots + (-1)^m x_{k+m} = \alpha x_k \\ &\qquad\qquad\qquad\qquad \vdots \end{aligned}$$

system of equations is obtained from the transpose of the matrix given in (1). If we write $k = n$ and $k = n + 1$ in the equation (3) and subtract the sides,

$$\sum_{k=0}^{m}(-1)^k\binom{m}{k}(x_{k+n} - x_{k+n+1}) = \alpha(x_n - x_{n+1})$$

is obtained. Then

$$|x_n - x_{n+1}| \leq \tfrac{1}{|\alpha|}\textstyle\sum_{k=0}^{m}\binom{m}{k}|x_{k+n} - x_{k+n+1}| \qquad (4)$$

from the triangle inequality. If we write the inequality (4) for $n = 0,1,2,\cdots$ and add them side by side, we get

$$\sum_{n=0}^{\infty} |x_n - x_{n+1}| \leq \frac{1}{|\alpha|} \sum_{n=0}^{\infty} \sum_{k=0}^{m} \binom{m}{k} |x_{k+n} - x_{k+n+1}|. \tag{5}$$

If we apply Lemma 4 to the right side of the inequality (5), we get

$$\sum_{n=0}^{\infty} |x_n - x_{n+1}| \leq \frac{1}{|\alpha|} \sum_{k=0}^{\infty} \binom{m}{k} \sum_{n=0}^{m} |x_{k+n} - x_{k+n+1}|.$$

Since $\sum_{n=0}^{m} |x_{k+n} - x_{k+n+1}| \leq \sum_{n=0}^{\infty} |x_{k+n} - x_{k+n+1}| \leq \|x\|_{bv}$ and for $m < k$, $\binom{m}{k} = 0$,

$$\|x\|_{bv} \leq \frac{\|x\|_{bv}}{|\alpha|} \sum_{k=0}^{m} \binom{m}{k} = \frac{2^m}{|\alpha|} \|x\|_{bv}$$

is obtained. Thus, $|\alpha| \leq 2^m$ is found. Then $\{\alpha \in \mathbb{C}: |1-\alpha| < 2^m - 1\} \subseteq \sigma_p((\Delta^m)^*, bv)$ is obtained. Conversely, if the $|1-\alpha| < 2^m - 1$ case is considered, the $(\Delta^m)^* - \alpha I$ adjoint operator is not $1-1$, so from Lemma 1, $\Delta^m - \alpha I$ operator is not dense range in cs. So $(\Delta^m)^* - \alpha I$ is not invertible and

$$\sigma_p((\Delta^m)^*, bv) \subseteq \{\alpha \in \mathbb{C}: |1-\alpha| < 2^m - 1\}.$$

Also, in case of $m = 1$, $\alpha = 0$ for $x_0 \neq 0$ is an eigenvector corresponding to the eigenvalue $x = (x_0, 0, 0, \cdots)$. Hence $0 \in \sigma_p((\Delta^m)^*, bv)$ is obtained. If $m > 1$ anyway, 0 is contained by the set $\{\alpha \in \mathbb{C}: |1-\alpha| < 2^m - 1\}$.

Theorem 4 *The residue spectrum of the Δ^m operator on cs is the set $\sigma_r(\Delta^m, cs) = \{\alpha \in \mathbb{C}: |1-\alpha| < 2^m - 1\} \cup \{0\}$.*

Proof. Since $\sigma_r(\Delta^m, cs) = \sigma_p((\Delta^m)^*, bv) \backslash \sigma_p(\Delta^m, cs)$, the desired result is obtained from Theorem 2 and 3.

We will now calculate the spectrum of the Δ^m operator over the sequence space cs. For this we will need the $(\Delta^m - \alpha I)^{-1}$ operator. In the proof of [7, Theorem 5], under the condition $|1-\alpha| > 2^m - 1$, the operator $\Delta^m - \alpha I$ has an inverse, and its inverse is $(\Delta^m - \alpha I)^{-1} = (b_{nk})$, where

$$(b_{nk}) = \begin{pmatrix} \frac{1}{1-\alpha} & 0 & 0 & 0 & 0 & \cdots \\ \frac{m}{(1-\alpha)^2} & \frac{1}{1-\alpha} & 0 & 0 & 0 & \cdots \\ \frac{m^2}{(1-\alpha)^3} - \frac{m(m-1)}{2!(1-\alpha)^2} & \frac{m}{(1-\alpha)^2} & \frac{1}{1-\alpha} & 0 & 0 & \cdots \\ \frac{m^3}{(1-\alpha)^4} - \frac{m^2(m-1)}{(1-\alpha)^3} + \frac{m(m-1)(m-2)}{3!(1-\alpha)^2} & \frac{m^2}{(1-\alpha)^3} - \frac{m(m-1)}{2!(1-\alpha)^2} & \frac{m}{(1-\alpha)^2} & \frac{1}{1-\alpha} & 0 & \cdots \\ \vdots & \vdots & \vdots & \vdots & \vdots & \ddots \end{pmatrix}. \tag{6}$$

So we can prove the following theorem.

Theorem 5 The spectrum of Δ^m on cs is the set $\sigma(\Delta^m, cs) = \{\alpha \in \mathbb{C}: |1-\alpha| \leq 2^m - 1\}$.

Proof. Since $(\Delta^m - \alpha I)$ is a triangular matrix, its inverse exists. The matrix $(\Delta^m - \alpha I)^{-1} = (b_{nk})$ is given in (6) and

$$b_{nn} = \frac{1}{1-\alpha},$$

$$b_{n,n-1} = \frac{m}{(1-\alpha)^2},$$

$$b_{n,n-2} = \frac{m^2}{(1-\alpha)^3} - \frac{m(m-1)}{2!\,(1-\alpha)^2},$$

$$b_{n,n-3} = \frac{m^3}{(1-\alpha)^4} - \frac{m^2(m-1)}{(1-\alpha)^3} + \frac{m(m-1)(m-2)}{3!\,(1-\alpha)^2}$$

$$b_{n,n-4} = \frac{m^4}{(1-\alpha)^5} - \frac{m^3(m-1)}{(1-\alpha)^4} + \frac{m^2(m-1)(m-2)}{3!\,(1-\alpha)^3} - \frac{m^3(m-1)}{2!\,(1-\alpha)^4} + \frac{m^2(m-1)^2}{2!2!(1-\alpha)^3} + \frac{m^2(m-1)(m-2)}{3!(1-\alpha)^3} - \frac{m(m-1)(m-2)(m-3)}{4!(1-\alpha)^2}$$

$$\vdots$$

$$b_{n,n-m} = \frac{1}{1-\alpha}\left[m b_{n,n-m+1} - \frac{m(m-1)}{2} b_{n,n-m+2} + \frac{m(m-1)(m-2)}{3!} b_{n,n-m+3} + \cdots + (-1)^{m-1} b_{n,n}\right]$$

$$\vdots$$

is obtained with $n \in \mathbb{N}_0$. Let us now show that $(\Delta^m - \alpha I)^{-1} \in B(cs)$. Lemma 3 will be used for this. In the proof of [7, Theorem 5], it was shown that the $\sum_{n=0}^{\infty} |b_{nk}|$ series converges for each k. Since every absolute convergent series converges, the $\sum_n b_{nk}$ series converges and the (i) condition of Lemma 3 is obtained.
Let us now show that the condition (ii) of Lemma 3 is $\sup_N \sum_k \left|\sum_{n=1}^{N} (b_{nk} - b_{n,k-1})\right| < \infty$. Since $b_{nk} = b_{n-1,k-1}$ for all n, k,

$$\sup_N \sum_{k=1} \left|(b_{1k} - b_{1,k-1}) + (b_{2k} - b_{2,k-1}) + (b_{3k} - b_{3,k-1}) + \ldots + (b_{Nk} - b_{N,k-1})\right|$$

$$= \sup_N \sum_k |b_{N,k}| = \sup_N \sum_{k=1}^{N} |b_{N,k}|$$

$$= |b_{N1}| + |b_{N2}| + |b_{N3}| + \ldots + |b_{N,N-1}| + |b_{NN}|$$

$$= |b_{N1}| + |b_{N-1,1}| + |b_{N-2,1}| + \ldots + |b_{21}| + |b_{11}| = \sum_{n=1}^{N} |b_{nk}|$$

is obtained. If we take $S_N = \sum_{n=1}^{N} |b_{nk}|$ then the sequence (S_N) is converget for $\left|\frac{2^m - 1}{1 - \alpha}\right| < 1$ from [7, Theorem 5. So when $|1 - \alpha| > 2^m - 1$, $(\Delta^m - \alpha I)^{-1} \in B(cs)$ is valid. Hence

$$\sigma(\Delta^m, cs) \subseteq \{\alpha \in \mathbb{C}: |1 - \alpha| \leq 2^m - 1\} \tag{7}$$

is obtained. So $(\Delta^m - \alpha I)^{-1} \in B(cs)$.

Conversely, given that $\alpha \neq 1$ and $|1 - \alpha| \leq 2^m - 1$, it is clear that $\Delta^m - \alpha I$ is a triangle and therefore $(\Delta^m - \alpha I)^{-1}$ exists. As a result of Theorem 2, the image of the unit sequence $y = (1,0,0,\cdots)$ under the $(\Delta^m - \alpha I)^{-1}$ transformation, that is, the sequence $x = (\Delta^m - \alpha I)^{-1} y$ is in cs. This suggests that under the condition $|1 - \alpha| \leq 2^m - 1$ and from Theorem 3 the operator $(\Delta^m - \alpha I)^{-1}$ should not have an eigenvalue. From this it follows that $(\Delta^m)^* - \alpha I$ is not $1 - 1$. Therefore, under the condition $|1 - \alpha| \leq 2^m - 1$, the $\Delta^m - \alpha I$ operator is not dense in cs. Finally, let's prove the result for the case $\alpha = 1$. If $\alpha = 1$ then

$$\Delta^m - I = \begin{pmatrix} 0 & 0 & 0 & 0 & \cdots \\ -m & 0 & 0 & 0 & \cdots \\ \dfrac{m(m-1)}{2!} & -m & 0 & 0 & \cdots \\ -\dfrac{m(m-1)(1-2)}{3!} & \dfrac{m(m-1)}{2!} & -m & 0 & \cdots \\ \vdots & \vdots & \vdots & \vdots & \ddots \end{pmatrix}$$

is not reversible. Thus

$$\{\alpha \in \mathbb{C}: |1 - \alpha| \leq 2^m - 1\} \subseteq \sigma(\Delta^m, c) \tag{8}$$

is obtained. The proof is completed using (7) and (8).

Theorem 6 *The continuous spectrum of the operator Δ^m on cs is the set*

$$\sigma_c(\Delta^m, cs) = \{\alpha \in \mathbb{C}: |1 - \alpha| = 2^m - 1\} \backslash \{0\}.$$

Proof. The proof is obtained directly from the definition of the spectrum of the bounded linear operator and Theorems 2, 4 and 5.

Theorem 7 *If $\alpha \in (\{\alpha \in \mathbb{C}: |1 - \alpha| \leq 2^m - 1\} \cup \{0\} \backslash \{1\})$ then $\alpha \in III_2\sigma(\Delta^m, cs)$ is valid.*

Proof. Let's assume that $\alpha \in (\{\alpha \in \mathbb{C}: |1 - \alpha| \leq 2^m - 1\} \cup \{0\} \backslash \{1\})$. In this case, from Theorem 3, the operator $(\Delta^m)^* - \alpha I$ is not $1 - 1$, and hence $\alpha \in III\sigma(\Delta^m, cs)$ is obtained from Lemma 1. Moreover, it is obtained that for $\alpha \neq 1$ the operator $\Delta^m - \alpha I$ has an inverse, but for $\alpha = 0$ the operator $(\Delta^m)^* - \alpha I$ is not surjective. Thus, the operator $\Delta^m - \alpha I$ from Lemma 2 has no bounded inverse. This indicates that $\Delta^m - \alpha I$ is not continuous.

Corollary 2 $III_1\sigma(\Delta^m, cs) = \{1\}$.

Proof. From [19] Table 1.2, since $\sigma_r(\Delta^m, cs) = III_1\sigma(\Delta^m, cs) \cup III_2\sigma(\Delta^m, cs)$ and $III_1\sigma(\Delta^m, cs) \cap III_2\sigma(\Delta^m, cs) = \emptyset$, the desired result is obtained from Theorems 4 and 7.

Theorem 8 *If $\alpha \in (\{\alpha \in \mathbb{C}: |1 - \alpha| > 2^m - 1\} \backslash \{1\})$ then $\alpha \in I_1\sigma(\Delta^m, cs)$ is valid.*

Proof. Let's assume that $\alpha \in (\{\alpha \in \mathbb{C}: |1 - \alpha| > 2^m - 1\} \backslash \{1\})$. It is clear that $a \neq 1$. Therefore, the $\Delta^m - \alpha I$ operator has an inverse. This indicates that the operator $\Delta^m - \alpha I$ is surjective, so the inverse operator $(\Delta^m - \alpha I)^{-1}$ in cs has a dense range. Therefore, from Lemma 1, the $(\Delta^m - \alpha I)$ operator is dense in cs. Hence $\alpha \in I\sigma(\Delta^m, cs)$.

Moreover, since $|1-\alpha| > 2^m - 1$, the operator $\Delta^m - \alpha I$ has a bounded inverse from Theorem 5. So $\alpha \in 1\sigma(\Delta^m, cs)$. Thus, $\alpha \in I_1\sigma(\Delta^m, cs)$ is obtained for α's satisfying the $|1-\alpha| > 2^m - 1$ inequality.

Spectral decompositions of the difference operator $\boldsymbol{\Delta^m}$ on the sequence space $\boldsymbol{cs}$ that do not need to be disjoint

Theorem 9 *For the spectral decomposition of the Δ^m operator on cs, the following are vald:*
a) $\sigma_{ap}(\Delta^m, cs) = \{\alpha \in \mathbb{C}: |1-\alpha| \leq 2^m - 1\}\backslash\{1\}$,

b) $\sigma_{\delta}(\Delta^m, cs) = \{\alpha \in \mathbb{C}: |1-\alpha| \leq 2^m - 1\}$,

c) $\sigma_{co}(\Delta^m, cs) = \{\alpha \in \mathbb{C}: |1-\alpha| < 2^m - 1\} \cup \{0\}$.

Proof. a) Since $\sigma_{ap}(\Delta^m, cs) = \sigma(\Delta^m, cs)\backslash III_1\sigma(\Delta^m, cs)$ from [19] Table 1.2, the desired result is obtained from Theorem 5 and Corollary 2.

b) Since $\sigma_{\delta}(\Delta^m, cs) = \sigma(\Delta^m, cs)\backslash I_3\sigma(\Delta^m, cs)$ from [19] Table 1.2, the desired result is obtained from Theorem 5 and Corollary 1.

c) Since

$$\begin{aligned}\sigma_{co}(\Delta^m, cs) &= III_1\sigma(\Delta^m, cs) \cup III_2\sigma(\Delta^m, cs) \cup III_3\sigma(\Delta^m, cs)\\ &= \sigma_r(\Delta^m, cs) \cup III_3\sigma(\Delta^m, cs)\end{aligned}$$

from [10] Table 1.2, the desired result is obtained from Theorem 4 and Corollary 1.

Corollary 3 $\sigma_{ap}((\Delta^m)^*, bv) = \{\alpha \in \mathbb{C}: |1-\alpha| \leq 2^m - 1\}$ *and*

$\sigma_{\delta}((\Delta^m)^*, bv) = \{\alpha \in \mathbb{C}: |1-\alpha| \leq 2^m - 1\}\backslash\{1\}$ is valid.

Proof. It is obtained from [28] Proposition 1.3 and Theorem 9.

Acknowledgment

This work will be included in master's thesis of Ömer Özdemir.

Conflicts of interest

There are no conflicts of interest in this work.

References

[1] Kızmaz H., On certain sequence spaces, *Can. Math. Bull.,* 24(2) (1981) 169–176.
[2] Et M., Çolak R., On some generalized difference sequence spaces, *Soochow J. Math.,* 21(4) (1995) 377–386.
[3] Baliarsingh P., Some new difference sequence spaces of fractional order and their dual spaces, *Appl. Math. Comput.,* 219(18) (2013) 9737–9742.
[4] Bektaş C.A., Et M., Çolak R., Generalized difference sequence spaces and their dual spaces, *J. Math. Anal. Appl.*, 292 (2004) 423–432.
[5] Et M., Başarır M., On some new generalized difference sequence spaces, *Periodica Math. Hung.,* 35(3) (1997) 169–175.
[6] Malkowsky E., Mursaleen M., Suantai S., The dual spaces of sets of difference sequence sequence spaces of order m and matrix transformations, *Acta. Math. Sin. (Engl. Ser.),* 23(3) (2007) 521–532.
[7] Baliarsingh P., Mursalen M., Rakocevic V., A survey on the spectra of the difference operators over the Banach space, c. *RACSAM*, 115:57. 84(4) (2021) 1–17.
[8] Altay B., Başar F., On the fine spectrum of the difference operator on c_0 and c, *Inf. Sci.,* 168 (2004) 217–224.
[9] Altay B., Başar F., The fine spectrum and the matrix domain of the difference operator Δ on the sequence space ℓ_p, $(1 < p < \infty)$, *Commun. Math. Anal.,* 2(2) (2007) 1–11.
[10] Altay B., Başar F., On the fine spectrum of the generalized difference operator $B(r,s)$ over the sequence spaces c_0 and c, *Int. J. Math. Math. Sci.*, 18 (2005) 3005–3013.
[11] Akhmedov A.M., Başar F., The fine spectra of the difference operator Δ over the sequence space bv_p, $(1 \leq p < \infty)$, *Demonstr. Math.,* 39(3) (2006) 586–595.
[12] Akhmedov A.M., Başar F., On the fine spectra of the difference operator Δ over the sequence space ℓ_p, $(1 \leq p < \infty)$, *Acta. Math. Sin. (Engl. Ser.),* 23(10) (2007) 1757–1768.
[13] Srivastava P.D., Kumar S., On the fine spectrum of the generalized difference operator Δ_v over the sequence space c_0, *Commun. Math. Anal.,* 6(1) (2009) 8–21.
[14] Srivastava P.D., Kumar S., Fine spectrum of the generalized difference operator Δ_v on sequence space ℓ_1, *Thai. J. Math.,* 8(2) (2010) 221–233.
[15] Akhmedov A.M., El-Shabrawy S.R., On the fine spectrum of the operator $\Delta_{a,b}$ over the sequence space c, *Comput. Math. Appl.*, 61 (2011) 2994–3002.
[16] Dutta S., Baliarsingh P., On the fine spectra of the generalized rth difference operator Δ_v^r on the sequence space ℓ_1, *Appl. Math. Comput.*, 219 (2012) 1776–1784.
[17] Dutta S., Baliarsingh P., On the spectrum of $2-nd$ order generalized difference operator Δ^2 over the sequence space c_0, *Bol. Soc. Paran. Mat.,* 31(2) (2013) 235–244.
[18] Durna N., Yildirim M., Subdivision of the spectra for factorable matrices on c_0, *GUJ Sci.*, 24 (1) (2011) 45-49.
[19] Başar F., Durna N., Yildirim M., Subdivisions of the spectra for genarilized difference operator over certain sequence spaces, *Thai J. Math.*, 9(2) (2011) 285–295.

[20] Durna N., Subdivision of the spectra for the generalized upper triangular double-band matrices Δ^{uv} over the sequence spaces c_0 and c, *ADYU Sci.*, 6(1) (2016), 31-43.

[21] Das R., On the spectrum and fine spectrum of the upper triangular matrix $U(r_1, r_2; s_1, s_2)$ over the sequence space c_0, *Afr. Math.*, 28 (2017) 841-849.

[22] El-Shabrawy S.R., Abu-Janah S.H., Spectra of the generalized difference operator on the sequence spaces bv_0 and h, *Linear Multilinear Algebra*, 66(8) (2018) 1691–1708.

[23] Tripathy B.C., Das R., Fine spectrum of the upper triangular matrix $U(r, 0, 0, s)$ over the squence spaces c_0 and c, *Proyecciones J. Math.*, 37(1) (2018), 85-101.

[24] Durna N., Yildirim M., Kılıç R., Partition of the spectra for the generalized difference operator $B(r, s)$ on thesequence space cs, *Cumhuriyet Sci. J.*, 39(1) (2018) 7–15.

[25] Furkan H., Bilgiç H., Altay B., On the fine spectrum of the operator $B(r, s, t)$ over c_0 and c, *Comput. Math. Appl.,* 53(6) (2007) 989–998.

[26] Wilansky A., Summability Through Functional Analysis. North-Holland Mathematics Studies, Amsterdam (1984).

[27] Goldberg S., Unbounded Linear Operators, New York: McGraw Hill, (1966).

[28] Appell J., Pascale E.D., Vignoli A., Nonlinear Spectral Theory, New York Berlin: Walter de Gruyter, (2004).

Cumhuriyet Sci. J., 44(1) (2023) 188-196
DOI: https://doi.org/10.17776/csj.1112531

Cumhuriyet Science Journal

| csj.cumhuriyet.edu.tr | Founded: 2002 ISSN: 2587-2680 e-ISSN: 2587-246X Publisher: Sivas Cumhuriyet University

Ibuprofen and Paracetamol when They Meet: Quantum Theory of Atoms in Molecules Perspective

Cemal Parlak [1,a], Özgür Alver [2,b], Özge Bağlayan [2,c,*], Onur Demirel [3,d]

[1] *Department of Physics, Ege University, Science Faculty, İzmir, 35100, Türkiye*
[2] *Department of Physics, Eskisehir Technical University, Science Faculty, Eskisehir, 26470, Türkiye*
[3] *Faculty of Mathematics and Physics, Department of Physics, Freiburg Albert-Ludwigs University, Germany*
**Corresponding author*

Research Article

History
Received: 05/05/2022
Accepted: 16/11/2022

ABSTRACT

Ibuprofen (IBP) and paracetamol (PCM) are widely used and prescribed two drugs for particularly their effects in reducing pain and fever. For enhanced pain relief, combinations of IBP and PCM are considered another option rather than taken each drug alone. In the scope of this work, the possible structural interaction edges, some important electronic properties and the binding energy evaluations of the IBP&PCM system were examined with density functional theory (DFT) and quantum theory of atoms in molecules (QTAIM). Further, all the configurations were subjected to biological activity evaluations. It was observed that hydrogen bonding interactions are possible for the examined drug couple and configuration 4 is the most stable form whereas C1 and C6 are better inhibitors. Therefore, possible advantages and disadvantages or possible side effects must be taken into account before combining these two important drug molecules.

Keywords: Ibuprofen, Paracetamol, DFT, Hydrogen bonding, QTAIM.

[a] *cemal.parlak@ege.edu.tr* *https://orcid.org/0000-0002-6115-6098*
[b] *ozguralver@eskisehir.edu.tr* *https://orcid.org/0000-0003-0647-4242*
[c] *obaglayan@eskisehir.edu.tr* *https://orcid.org/0000-0002-0753-0325*
[d] *onurdemirel2626@gmail.com* *https://orcid.org/0000-0001-9695-9141*

Introduction

Ibuprofen and paracetamol are widely prescribed two drugs all over the world. IBP is known as a nonsteroidal anti-inflammatory drug and is extensively prescribed for the treatment of pain and inflammation [1, 2]. IBP is bound and transported in blood plasma with the help of proteins and particularly through human serum albumin [3]. Although they have different action mechanisms, PCM is also used for its analgesic, antipyretic and anti-inflammatory activities [4, 5]. In various cases such as postoperative pain, dysmenorrhoea and musculoskeletal pain the combination of IBP and PCM appeared as an effective treatment method [6-10].

At the theoretical level, DFT provides useful information about the structural properties of different types of molecular systems [11-13]. QTAIM has been widely used to analyze the real space functions and nature of interactions in various molecular systems, and to classify and understand bonding interactions in terms of a quantum mechanical parameter as electron density at the bond critical points [12-15]. Moreover, natural bond orbital (NBO) analysis provides an efficient technique for the study of hydrogen bonding interactions. It also offers a convenient basis for investigating charge transfer or conjugative interactions in molecular systems [11, 12, 16, 17].

Taking the advantages of DFT method, it is possible to find out the most possible structural energy configurations and interaction sites of the examined molecular systems. In the framework of this work, the interaction mechanisms and type of the interaction between IBP and PCM were investigated. The way they interacted and the molecular structures they build are considered important parameters for their effective treatment procedure. The blood plasma is the combination of large numbers of molecules which appears as a major limitation of this work. However, the possibility of IBP and PCM interaction should not be underestimated.

Computational Methods

IBP and PCM were first optimized by imposing no geometrical restrictions. Vibrational frequency calculations were carried out as well to see that the structures converged to a certain minimum. If any imaginary frequencies were observed at the end of vibrational frequency calculations, optimization procedures were repeated by applying small geometrical changes to the parts of the molecules where the imaginary frequencies were observed. Initial geometry configurations are very important to reach the correct optimum geometrical configurations at the end of the calculations [18]. Therefore, taking into account the previously reported works, –OH, –C=O and –NH of IBP and

PCM were selected as possible interaction sites [19, 20]. Six possible configurations were built with GaussView visualization program [21]. After building the structures, they were optimized in the way as it was mentioned above. The resultant optimized structures are given in Figures 1-6.

The binding energy calculations (E_b) between IBP and PCM were calculated as follows [22]:

$$E_b = E_{IBP\&PCM} - (E_{IBP} + E_{PCM})$$

In the given equation, $E_{IBP\&PCM}$, E_{IBP} and E_{PCM} are the optimized energies of the related structures. In the resultant E_b values, the basis sets superposition errors (BSSE) were also taken into account and calculated with the counterpoise correction method [23, 24].

The strength and the nature of possible bonding interaction sites of IBP and PCM were examined based on the QTAIM evaluations [14, 15]. In order to carry out a quantitative investigation of charge distributions and further understanding of the nature of interactions, NBO analyses were also performed [16, 17].

For the molecular optimizations of the structures from C1 to C6, the B3LYP method and 6-31G(d) basis set which yield widely acceptable results were used [25, 26]. Multiwfn program was employed for the calculations of topological parameters [14]. Finally, all the optimization and vibrational frequency calculations were carried out with Gaussian program [27]. The physicochemical properties and druglikeness of IBP...PCM were predicted by using the SwissADME website (http://swissadme.ch) [28].

Results and Discussion

In this part, all the possible conformers undertaken in this work were examined briefly taking into account the binding energies and structural properties. This is followed by the discussion of structure & biological activity relation and electronic properties.

Conformer C1

The optimized structure and the interaction sites for IBP and PCM for C1 are given in Figure 1. NBO charges of +0.242 / -0.692 for –CH / –OH and +0.507 / -0.612 for –OH / -C=O make the interaction possible for the examined conformer C1. Here NBO charges belong to the atoms given in bold letters. E_b energies were found as -7.38 and -5.09 kcal/mol, respectively. It is seen that in the water media the strength of the interaction lowered compared to gas phase calculations.

Some important topological parameters of bond critical points (BCPs) in the examined IBP&PCM system are given in Table 1. In Figure 1, the molecular topography map of the system is given. In the given map, illustrated lines show bond paths. In C1, two possible intermolecular hydrogen bondings were proposed. The first one is between hydrogen atom of the –CH in the ring of PCM and the oxygen atom of –OH in IBP. The calculated intermolecular hydrogen bonding energy (E_{HB}) energies were found as -2.05 and -7.31 kcal/mol for –CH...OH and –OH...C=O interactions, correspondingly. QTAIM calculations propose that the hydrogen bonding interactions mainly and more strongly occur at the –OH...C=O edge. It was also observed that E_{HB} energies altered in different ways that either increased or decreased or stayed constant depending on the site where the hydrogen bondings (HBs) were observed Table 2.

Table 1. Some topological parameters of BCPs for gas phase calculations.

	Type	O...BCP	BCP...H	D	ρ(r)	∇2ρ(r)	H(r)	-G/V	E_{HB}
C1	O44-H45...O33	1.210	0.686	1.896	0.0281	0.0910	-0.0003	0.987	-7.31
	C35-H40...O32	1.543	1.064	2.607	0.0068	0.0246	0.0009	1.205	-2.05
C2	C39-H43...O33	1.431	0.937	2.368	0.0120	0.0378	0.0005	1.059	-2.67
	O32-H16...O44	1.193	0.658	1.851	0.0313	0.0984	-0.0010	0.962	-8.35
C3	O44-H45...O33	1.190	0.654	1.844	0.0350	0.1075	-0.0015	0.950	-9.35
	O32-H16...O44	1.192	0.654	1.846	0.0338	0.1019	-0.0017	0.941	-9.04
C4	O32-H16...O49	1.140	0.597	1.737	0.0411	0.1289	-0.0011	0.968	-10.82
	C50-H53...O33	1.381	0.896	2.277	0.0146	0.0455	0.0003	1.028	-3.39
C5	C6-H30...C38	1.878	1.541	3.419	0.0031	0.0096	0.0019	1.462	-0.41
	C50-H51...O32	1.637	1.148	2.785	0.0056	0.0206	0.0009	1.273	-1.04
	N46-H47...O32	1.330	0.819	2.149	0.0168	0.0550	-0.0002	0.986	-4.39
	C38-H42...O32	1.691	1.211	2.902	0.0043	0.0165	0.0009	1.391	-0.72
C6	C6-H30...C38	1.806	1.308	3.114	0.0037	0.0114	0.0022	1.467	-0.47
	C50-H51...O33	1.574	1.123	2.697	0.0063	0.0230	0.0009	1.231	-1.22
	N46-H47...O33	1.275	0.763	2.038	0.0218	0.0668	-0.0004	0.978	-5.65
	C38-H42...O33	1.679	1.211	2.890	0.0046	0.0179	0.0010	1.400	-0.78

BCP: bond critical point (Å), D: bond length (Å), ρ(r): electron density (a.u.), $\nabla^2\rho(r)$: Laplacian of the electron density, H(r): electron energy density (a.u.), G(r): electron kinetic energy density, V(r): electron potential energy density (a.u.), E_{HB}: hydrogen bonding energy (kcal/mol).

Table 2. Some topological parameters of BCPs for water media calculations.

	Type	O…BCP	BCP…H	D	ρ(r)	$\nabla^2\rho(r)$	H(r)	-G/V	E_{HB}
C1	O44-H45…O33	1.619	0.647	2.266	0.0334	0.1067	-0.0007	0.975	-8.79
	C35-H40…O32	1.544	1.060	2.604	0.0071	0.0252	0.0008	1.174	-1.44
C2	C39-H43…O33	1.481	0.984	2.465	0.0010	0.0321	0.0007	1.104	-2.10
	O32-H16…O44	1.778	0.635	2.413	0.0347	0.1069	-0.0013	0.956	-9.19
C3	O44-H45…O33	1.193	0.656	1.849	0.0346	0.1058	-0.0014	0.952	-9.19
	O32-H16…O44	1.203	0.663	1.866	0.0323	0.0971	-0.0016	0.941	-8.63
C4	O32-H16…O49	1.120	0.571	1.691	0.0467	0.1430	-0.0019	0.952	-12.39
	C50-H53…O33	1.479	0.989	2.468	0.0101	0.0330	0.0006	1.087	-2.16
C5	C38-H42…C6	1.935	1.491	3.426	0.0023	0.0072	0.0014	1.400	-0.31
	C50-H51…O32	1.639	1.147	2.786	0.0054	0.0206	0.0010	1.313	-1.00
	N46-H47…O32	1.309	0.797	2.106	0.0182	0.0593	-0.0002	0.987	-4.77
	C38-H42…O32	1.653	1.166	2.819	0.0050	0.0188	0.0010	1.357	-0.88
C6	C38-H42…C6	1.935	1.491	3.426	0.0021	0.0066	0.0013	1.444	-0.28
	C50-H51…O33	1.579	1.115	2.694	0.0064	0.0236	0.0010	1.256	-1.22
	N46-H47…O33	1.248	0.733	1.981	0.0245	0.0769	-0.0006	0.971	-7.53
	C38-H42…O33	1.619	1.152	2.771	0.0055	0.0205	0.0010	1.313	-1.00

BCP: bond critical point (Å), D: bond length (Å), ρ(r): electron density (a.u.), $\nabla^2\rho(r)$: Laplacian of the electron density, H(r): electron energy density (a.u.), G(r): electron kinetic energy density, V(r): electron potential energy density (a.u.), E_{HB}: hydrogen bonding energy (kcal/mol).

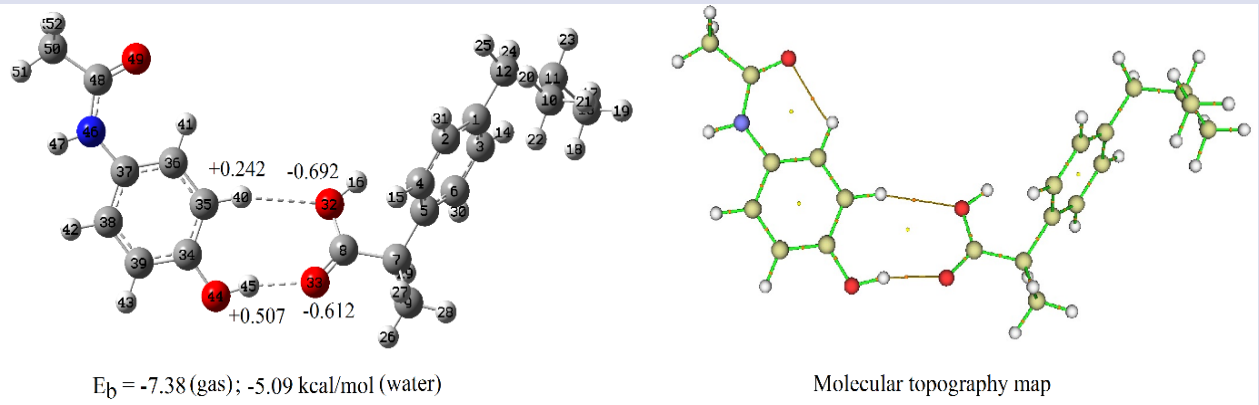

Figure 1. Optimized structure and molecular topography map of C1.

In the interpretation of topological analysis, the electron density ρ(r) and Laplacian of electron density $\nabla^2\rho(r)$ are very important parameters to understand the nature of molecular interactions. Moreover, the ratio of the kinetic electron energy density to the potential electron energy density G(r) / |V(r)| can also be used to analyze the bonding interactions. According to Rozas et. al, if $\nabla^2\rho(r)>0$ and H(r)>0 then HB can be considered as weak. Further, if $\nabla^2\rho(r)>0$ and H(r)<0 then HB interaction is supposed to be medium [29]. Therefore, for C1 conformer at the –CH…OH edge the strength of HB appears as weak, at the –OH…C=O edge it can be regarded as having medium strength. The G(r) / |V(r)| ratio with a value of slightly smaller than 1 (0.987) also refers to a medium type HB interactions for the –OH…C=O edge.

It is also possible to observe the interaction edges by following vibrational frequency shifts at the interacted edges. There are four stretching vibrations at the interaction edges. These are CH&OH of PCM and OH&C=O of IBP. They are shifted around 10, 159, 23 and 31 cm^{-1}, respectively. It is seen that the largest frequency shift appeared at –OH…C=O edge which is previously discussed as having where the medium strength HB interactions occur.

Conformer C2

The optimized structure and the interaction sites for IBP and PCM for C2 are given in Figure 2. NBO charges of C2 at the interaction edges were found as +0.273 / -0.637 for –CH / –C=O and -0.721 / +0.516 for –OH / –OH. E_b energies were calculated as -10.56 and -6.69 kcal/mol correspondingly. In Figure 2, the molecular topography map of the system can also be seen. For C2, two possible intermolecular HBs were taken into account. The first one is between the hydrogen of the –CH in the ring of PCM and the oxygen of –C=O in IBP. The second one is between –OHs of PCM and IBP. E_{HB} energies were found as -2.67 and -8.35 kcal/mol for –CH…–C=O and –OH…–OH interactions, respectively. According to QTAIM findings, HB interactions more strongly occur at the –OH…–OH edge. For –CH…–C=O interactions $\nabla^2\rho(r)$ and H(r) were found as positive. Thus, HB can be considered as weak at this edge. As for the –OH…–OH edge while $\nabla^2\rho(r)$ were found as positive, H(r) appeared as negative. Henceforth, HB interaction is supposed to be medium. The G(r) / |V(r)| ratio for the related edges also suggest that medium type HB interactions for the –OH…–OH edge (0.962) and a weak type of HB for –CH…–C=O edge (1.059).

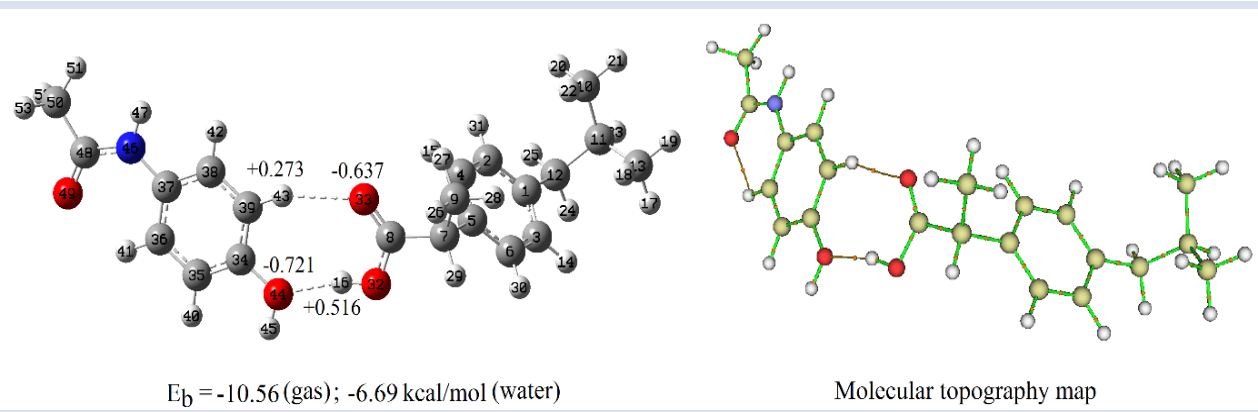

Figure 2. Optimized structure and molecular topography map of C2

In the C2 again, there are four stretching vibrations at the interaction sites. These are CH&OH of PCM and C=O&OH of IBP. They are shifted around 12, 8, 63 and 192 cm^{-1} correspondingly. The largest frequency shift was observed at –OH…–OH edge which confirms where the medium strength HB interactions occur.

Conformer C3

The optimized structure for C3 is given in Figure 3. NBO charges of C3 at the interaction sites were found as +0.512 / -0.659 for –OH / –C=O and -0.744 / +0.516 for –OH / –OH. E_b energies were calculated as -13.60 and -7.59 kcal/mol, respectively. In Figure 3, the molecular topography map of the system is given. Two possible HBs were suggested between OH of PCM and OH&C=O of IBP. E_{HB} energies were found as -9.35 and -9.04 kcal/mol for –OH…–C=O and –OH…–OH interactions respectively. QTAIM findings propose that HB interactions almost occur at the same strength for both interaction sites. Both interaction sites yielded positive $\nabla^2\rho(r)$ and negative H(r) values. Thus, HB interactions can be considered as medium strength. The G(r) / |V(r)| ratios were found slightly smaller than 1 for both edges also indicating the medium type of HB interactions.

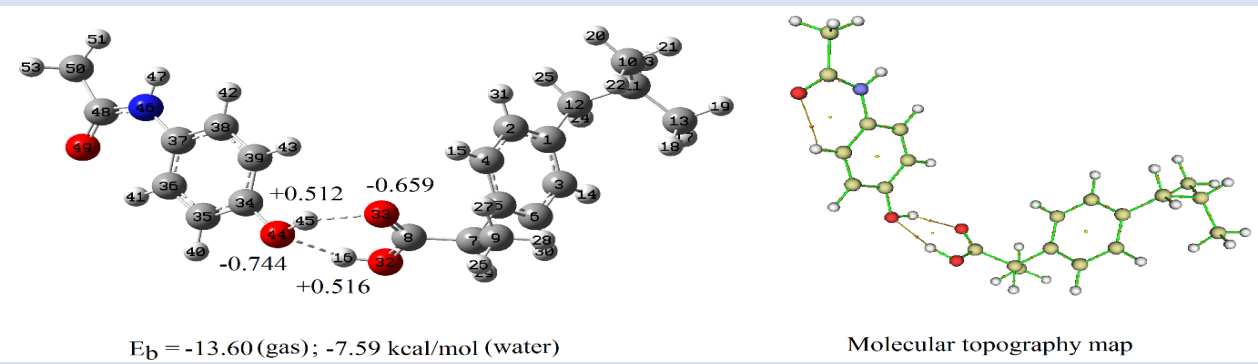

Figure 3. Optimized structure and molecular topography map of C3.

In the C3 conformer, taking the oxygen atom of PCM at the center, symmetric and antisymmetric vibrations were observed (Figure 4). The frequency shifts for OH of PCM were observed as 285 and 377 cm^{-1} for symmetric and antisymmetric vibrations correspondingly. C=O stretching vibrations of PCM was also shifted around 95 cm^{-1} upon interaction. Further, the frequency shifts for OH of IBP were calculated as 214 and 306 cm^{-1}, respectively.

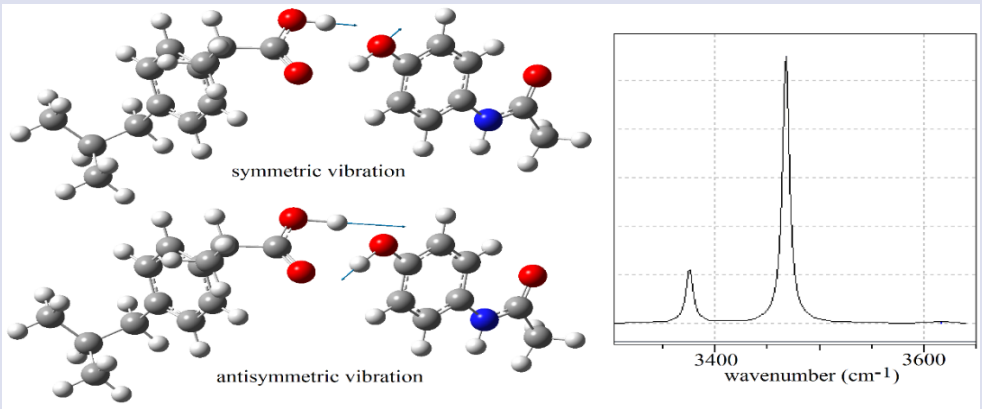

Figure 4. Symmetric and antisymmetric vibrational behavior of hydroxyl groups and their vibrational spectroscopic infrared bands.

Conformer C4

The optimized structure of C4 is given in Figure 5. NBO charges of C4 at the interaction edges were found as -0.670 / +0.517 for –C=O / –OH and +0.293 / -0.650 for –CH_3 / –C=O. The obtained E_b energies (gas/water) were found as -13.75 and -9.23 kcal/mol, respectively. In Figure 5, the molecular topography map of the system is also given. For this configuration, two possible intermolecular HBs seem possible. The first one is between the oxygen of the carbonyl group in PCM and the hydrogen of the hydroxyl group in IBP. The second possibility is between one of the hydrogens in the methyl group of PCM and the oxygen of the carbonyl group in IBP. E_{HB} energies were found as -10.82 and -3.39 kcal/mol for –C=O…-OH and –CH_3…–C=O interactions, respectively. It is clearly seen that HB interaction occurs primarily at the –C=O…–OH site where the $\nabla^2\rho(r)$ is positive and H(r) is negative addressing a medium type of interaction. At the same site the G(r) / |V(r)| ratio was found as 0.968 which confirms the previous assumption for the medium type HB connections. With both positive $\nabla^2\rho(r)$ and H(r) values and a G(r) / |V(r)| ratio larger than 1 the –CH_3…–C=O edge shows weak HB interactions. The largest vibrational shift with a value of 405 cm^{-1} in the infrared spectrum was observed with –OH of IBP which indicates that the strongest HB interactions occurs at –C=O…–OH site.

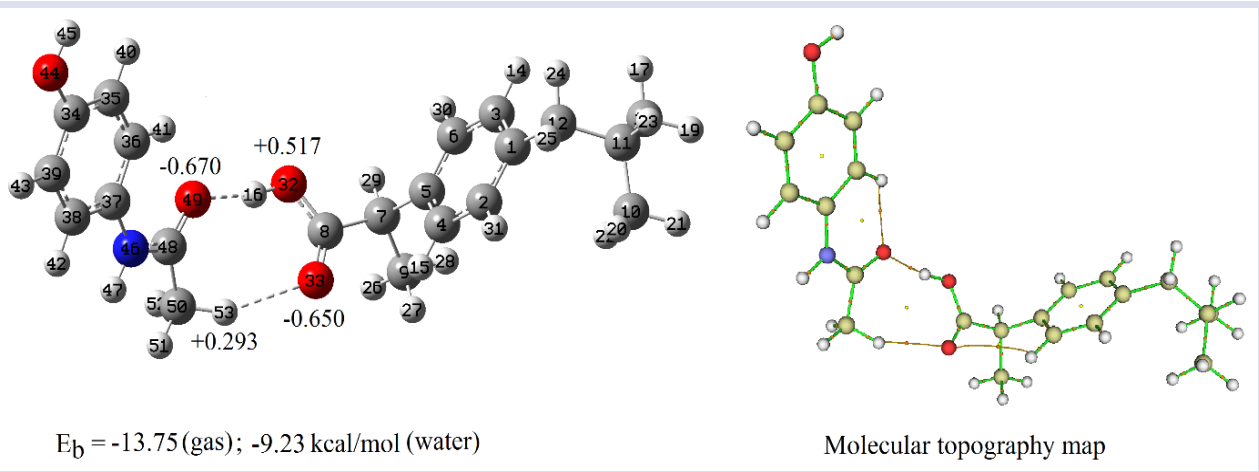

Figure 5. Optimized structure and molecular topography map of C4.

Conformer C5

The optimized structure for C5 is presented in Figure 6. NBO charges of C5 at the interaction edges were observed as -0.739 / +0.430 for –OH / –NH with E_b energies of -6.73 and -3.37 kcal/mol for gas phase and water media calculations, respectively. For C5, four intermolecular HBs were suggested by the topography map (Figure 6). However, if Table 1 is examined, it is seen that three of them is very weak in strength. The strongest HB based on the E_{HB} evaluations was identified between –NH of PCM and –OH of IBP. E_{HB} energy for this site was found as –4.39 kcal/mol with positive $\nabla^2\rho(r)$ and slightly negative H(r) (-0.0002) and with slightly smaller than 1 (0.986) G(r) / |V(r)| ratio indicating that the HB interaction is somewhere between medium and weak. The largest vibrational frequency shift in the infrared spectrum was observed with –NH of PCM with a value of 46 cm^{-1}.

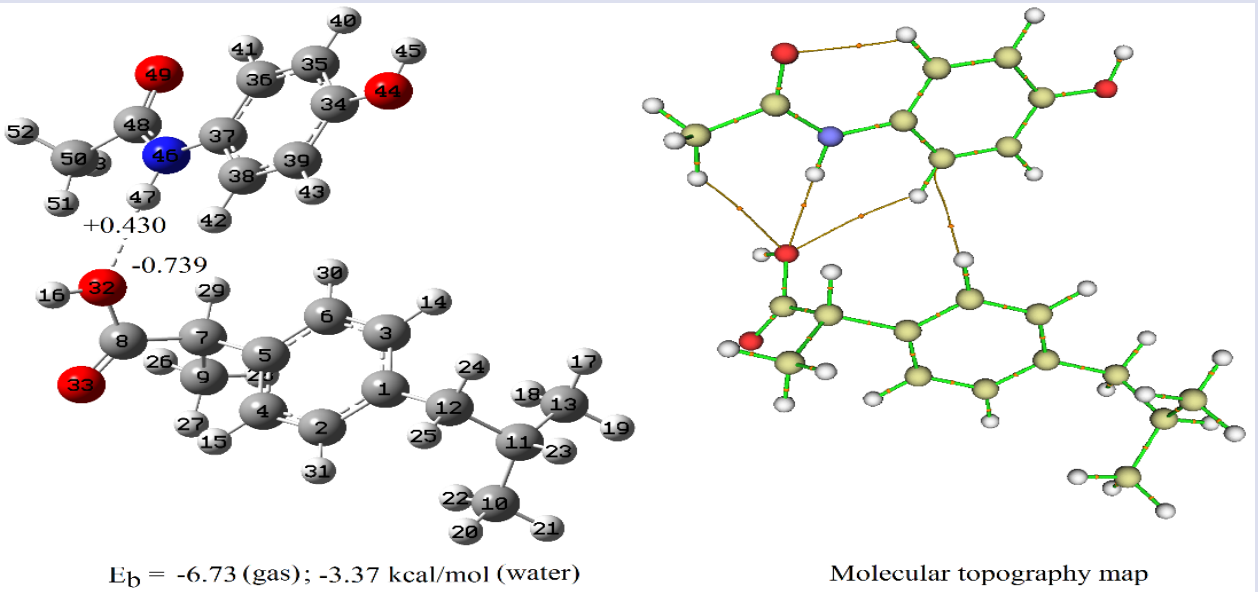

Figure 6. Optimized structure and molecular topography map of C5.

Conformer C6

NBO charges of C6 at the interaction edges were found as -0.638 / +0.438 for –C=O / –NH as can be seen in Figure 7. For gas and water media, E_b energies were found at -8.00 and -3.93 kcal/mol, respectively. C6 shows again four possible intermolecular HB interactions (Figure 7) but only HB between –C=O of IBP and –NH of PCM with E_{HB} energy of -5.65 kcal/mol seems strong (Table 1). In this interaction site $\nabla^2\rho(r)$ was found as positive and H(r) appeared as negative with a G(r) / |V(r)| ratio slightly smaller than one (0.978) indicating nearly a medium type of HB interaction. The largest vibrational frequency shift in the infrared spectrum of C6 was observed with –NH of PCM with a value of 165 cm^{-1}.

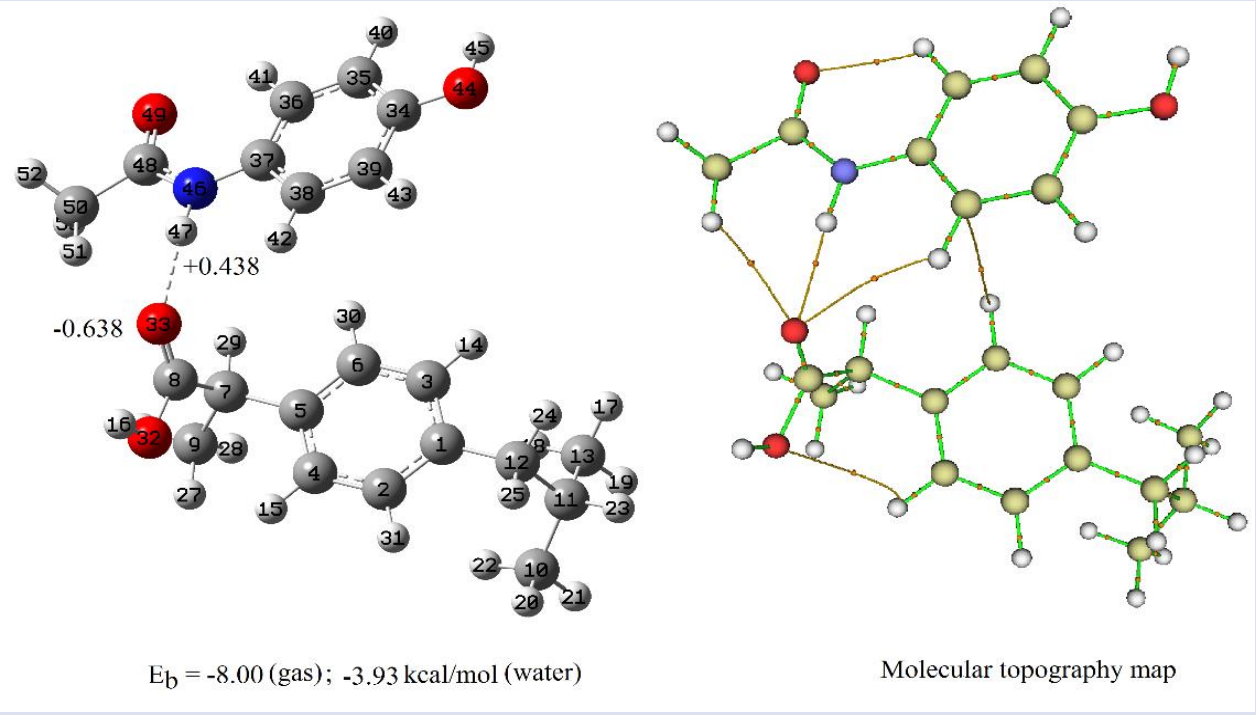

Figure 7. Optimized structure and molecular topography map of C6.

Structure–Activity Relationship

DFT was also used to search the relationships between biological activity and structure which are based on the fundamental hypothesis that biological properties are functions of the molecular structure [11, 30]. As an example, the antibacterial activity is related to the function of the lowest unoccupied molecular orbital (LUMO). Compounds which have low LUMO energy are more highly motivated to accept electrons than those with higher energy since incoming electrons are received in LUMO. LUMO energies of C1-C6 conformers were found as -0.786 (-0.484), -0.152 (-0.299), -0.434 (-0.472), -0.395 (-0.451), -0.607 (-0.481) and -0.731 (-0.570) eV correspondingly (water) while the energies of LUMO for IBP and PCM were observed as -0.563 (-0.350) and -0.074 (-0.200). C1 has the lowest LUMO energy in the gas phase whereas C6 has the lowest value in water. In addition, C1 and C6 have also lower LUMO energies in gas and water medium as compared to all the other conformers studied in this work. Thus, one can conclude the C1 or C6 conformers show higher biological activities.

Band gap (E_g) energies between the highest occupied and lowest unoccupied molecular orbitals (HOMO-LUMO) of C1-C6 conformers were found as 4.045 (4.947), 5.507 (5.458), 5.088 (5.223), 5.348 (5.303), 4.741 (5.065) and 4.446 (4.933) eV correspondingly (water) while the energies of LUMO for IBP and PCM were observed as 6.118 (6.213) and 5.403 (5.402). The values of the lowest E_g of C1-C6 conformers show same trends with the LUMO energies.

Physicochemical properties and druglikeness

The physicochemical properties give a global description of the structures of compounds. Bioavailability radar of the compounds displays a rapid evaluation of druglikeness. As seen in Table 3 and Figure 8, the bioavailability radar includes six physicochemical properties [28, 31]. In Figure 8, the pink area represents the optimal range of these properties and the red line represents the properties of the compounds. The red lines of IBP…PCM system are in the range of the pink area. Therefore, we can conclude that the interacted compounds are orally predicted bioavailable. Furthermore, druglikeness was established based on the physicochemical properties to find oral drug candidates [28]. There are five different rule-based filters which are defined as follows: (1) Lipinski's filter includes molecular weight ≤ 500, MLOGP (lipophilicity) ≤ 4.15, hydrogen bond acceptors ≤ 10, and hydrogen bond donors ≤ 5 [32]. (2) Ghose's filter includes 160 ≤ molecular weight ≤ 480, −0.4

≤ WLOGP (lipophilicity) ≤ 5.6, 40 ≤ the molar refractivity ≤ 130, and 20 ≤ number of atoms ≤ 70 [33]. (3) Veber's filter includes the number of rotatable bonds ≤ 10 and the total polar surface area ≤ 140 [34]. (4) Egan's filter includes WLOGP (Lipophilicity) ≤ 5.88 and the total polar surface area ≤ 131.6 [35]. (5) Muegge's filter includes 200 ≤ molecular weight ≤ 600, −2 ≤ XLOGP3 (lipophilicity) ≤ 5, the total polar surface area ≤ 150, the number of rings ≤ 7, the number of carbon > 4, the number of heteroatoms > 1, the number of rotatable bonds ≤15, the hydrogen bond acceptors ≤10, and the hydrogen bond donors ≤ 5 [36]. The result of drug-likeness evaluation of IBP…PCM is also shown in Figure 8 and we can conclude that IBP…PCM system fulfil all requirements of Lipinski, Ghose, Veber, Egan and Muegge rules.

Table 3. Physicochemical properties, lipophilicity and solubility of IBP…PCM.

Properties	Bioavailability	IBP…PCM
Molecular weight	Size (between 150 and 500 g/mol)	357.44
Heavy atom		26
Arom. heavy atom		12
Fraction Csp3	Saturation (not less than 0.25)	0.33
Rotatable Bond	Flexibility (not more than 9)	6
H-Bond acceptor		4
H-Bond donor		3
Molar refractivity		104.96
Polar surface area	Polarity (between 20 and 130 Å^2)	86.63
Lipophilicity		
MLOGP		3.12
WLOGP		4.23
XLOGP3	Lipophilicity (between -0.7 and +5.0)	4.24
Water Solubility	Solubility (log S not higher than 6)	
ESOL		-4.67
ALI		-5.77
SILICOS-IT		-3.44

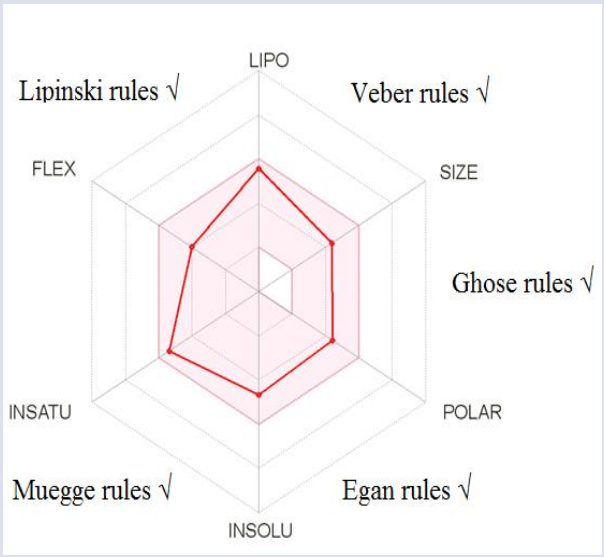

Figure 8. Bioavailability radar of IBP…PCM.

Conclusions

A detailed DFT, NBO charge and QTAIM investigations of PCM interacted IBP were carried out. The stabilities based on the binding energies of the PCM&IBP system decreased in water media calculations. C4 appeared as the most stable conformer based on the results of E_b and E_{HB} calculations in both environments. Further, all of the results obtained indicate that the strength of the interactions occurs at the physisorption level. In general, it was observed that as the interaction strength increases the larger vibrational frequency shifts were observed in the vibrational frequencies of molecular fragments at the interaction sites. The findings of this work are supposed to enlighten further biological activity studies of PCM and IBP combinations. Among the six configurations, C1 and C6 showed better biological activity. The field is further open for pharmacokinetics and clinic studies. It is also worth to note that combinations of IBP and PCM showed lower LUMO values indicating that the activity of combinations of these drugs is higher when they are used together. The drug-likeness study revealed that the interacted compounds (IBP…PCM) fulfill all requirements of Lipinski, Ghose, Veber, Egan, and Muegge rules and IBP…PCM is predicted orally bioavailable. These preliminary results provide the lead for the design of more potent and selective covid drugs.

Acknowledgment

This work was supported by Eskişehir Technical University (Project Number 20ADP133).

Conflicts of interest

There are no conflicts of interest in this work.

References

[1] Roushani M., Shahdost-Fard F., Applicability of AuNPs@N-GQDs nanocomposite in the modeling of the amplified electrochemical Ibuprofen aptasensing assay by monitoring of riboflavin, *Bioelectrochemistry*, 126 (2019) 38-47.

[2] Lazarević J.J., Uskoković–Marković S., Jelikić–Stankov M., Radonjić M., Tanasković D., Lazarević N., Popović Z.V., Intermolecular and low-frequency intramolecular Raman scattering study of racemic ibuprofen, *Spectrochim. Acta A.*, 126 (2014) 301-305.

[3] Fanali G., di Masi A., Trezza V., Marino M., Fasano M., Ascenzi P., Human serum albumin: From bench to bedside, *Mol Aspects Med.,* 33(3) (2012) 209-290.

[4] Anderson B.J., Paracetamol (acetaminophen): mechanisms of action, *Paediatr Anaesth.*, 18(10) (2008) 915-921.

[5] Langhendries J.P., Allegaert K., Van Den Anker J.N., Veyckemans F., Smets F., Possible effects of repeated exposure to ibuprofen and acetaminophen on the intestinal immune response in young infants, *Med. Hypotheses*, 87 (2016) 90-96.

[6] Derry C.J., Derry S., Moore R.A., Single dose oral ibuprofen plus paracetamol (acetaminophen) for acute postoperative pain, *Cochrane Database Syst. Rev.,* (6) CD010210 (2013).

[7] Doherty M., Hawkey C., Goulder M., Gibb I., Hill N., Aspley S., Reader S., A randomised controlled trial of ibuprofen, paracetamol or a combination tablet of ibuprofen/paracetamol in community-derived people with knee pain, *Ann. Rheum. Dis.*, 70(9) (2011) 1534-1541.

[8] Eccles R., Holbrook A., Jawad M., A double-blind, randomised, crossover study of two doses of a single-tablet combination of ibuprofen/paracetamol and placebo for primary dysmenorrhoea, *Curr. Med. Res. Opin.,* 26 (11) (2010) 2689-2699.

[9] Mehlisch D.R., Aspley S., Daniels S.E., Bandy D. P., Comparison of the analgesic efficacy of concurrent ibuprofen and paracetamol with ibuprofen or paracetamol alone in the management of moderate to severe acute postoperative dental pain in adolescents and adults: a randomized, double-blind, placebo-controlled, parallel-group, single-dose, two-center, modified factorial study, *Clin. Ther.,* 32(5) (2010) 882-895.

[10] Merry A.F., Gibbs R.D., Edwards J., Ting G.S., Frampton C., Davies E., Anderson B.J., Combined acetaminophen and ibuprofen for pain relief after oral surgery in adults: a randomized controlled trial, *Br. J. Anaesth.*, 104(1) (2010) 80-88.

[11] Kawakami J., Kakinami H., Matsushima N., Nakane A., Kitahara H., Nagaki M., Ito S., Structure-activity relationship analysis for antimicrobial activities of tryptanthrin derivatives using quantum chemical calculations, *J. Comput. Chem. Jpn.,* 12(2) (2013) 109-112.

[12] Venkataramanan N.S., Suvitha A., Kawazoe Y., Intermolecular interaction in nucleobases and dimethylsulfoxide/water molecules: A DFT, NBO, AIM and NCI analysis, *J. Mol. Graph. Model.*, 78 (2017) 48–60.

[13] Ravaei I., Haghighat M., Azami S.M., A DFT, AIM and NBO study of isoniazid drug delivery by MgO nanocage, *Appl. Surf. Sci.,* 469 (2019) 103–112.

[14] Lu T., Chen F., Multiwfn: a multifunctional wavefunction analyzer, *J. Comput. Chem.*, 33 (2012) 580–592.

[15] Bader R.F.W., Atoms in Molecules: A Quantum Theory, Clarendon, New York, 1990.

[16] Reed A.E., Weinstock R.B., Weinhold F., Natural population analysis, *J. Chem. Phys.*, 83 (1985) 735–746.

[17] Reed A.E., Curtiss L.A., Weinhold F., Intermolecular interactions from a natural bond orbital, donor-acceptor viewpoint, *Chem. Rev.*, 88 (1988) 899–926.

[18] Alver Ö., FT-IR, Raman and DFT Studies on the vibrational spectra of 2,2-bis(aminoethoxy)propane, *Bull. Chem. Soc. Ethiop.*, 30(1) (2016) 147-151.

[19] Hadad A., Azevedo D.L., Caetano E.W.S., Freire V.N., Mendonça G.L.F., Neto P.L., Albuquerque E.L., Margis R., Gottfried C., Two-level adsorption of ibuprofen on C60 fullerene for transdermal delivery: classical molecular dynamics and density functional theory computations, *J. Phys. Chem. C.*, 115(50) (2011) 24501-24511.

[20] Saikia U., Saikia N., Waters K., Pandey R., Sahariah M.B., Electronic properties of acetaminophen adsorbed on 2D clusters: A first principles density functional study, *Chemistry Select.,* 2(13) (2017) 3613-3621.

[21] Dennington R.D., Keith T.A., Millam J.M., GaussView 5.0.8, Gaussian Inc., 2008.

[22] Parlak C., Alver Ö., A density functional theory investigation on amantadine drug interaction with pristine and B, Al, Si, Ga, Ge doped C60 fullerenes, *Chem. Phys. Lett.*, 678 (2017) 85-90.

[23] Boys S.F., Bernardi F., The calculation of small molecular interactions by the differences of separate total energies. Some procedures with reduced errors, *Mol. Phys.*, 19(4) (1970) 553-566.

[24] Gutowski M., Chalasinski G., Critical evaluation of some computational approaches to the problem of basis set superposition error, *J. Chem. Phys.,* 98 (1993) 5540-5554.

[25] Beheshtian J., Peyghan A.A., Bagheri Z., Carbon nanotube functionalization with carboxylic derivatives: a DFT study, *J. Mol. Model.,* 19(1) (2013) 391–396.

[26] Peyghan A.A., Soltani A., Pahlevani A.A., Kanani Y., Khajeh S., A first-principles study of the adsorption behavior of CO on Al- and Ga-doped single-walled BN nanotubes, *Appl. Surf. Sci.*, 270 (2013) 25–32.

[27] Frisch M.J., Trucks G.W., Schlegel H.B., Gaussian 09, Revision A.1, Gaussian Inc., Wallingford, CT, 2009.

[28] Daina A., Michielin O., Zoete V., SwissADME: a free web tool to evaluate pharmacokinetics, drug-likeness and medicinal chemistry friendliness of small molecules. *Sci Rep.,* 42717(7) (2017).

[29] Rozas I., Alkorta I., Elguero J., Behavior of ylides containing N, O and C atoms as hydrogen bond acceptors, *J. Am. Chem. Soc.,* 122(45) (2000) 11154-11161.

[30] Bhattacharjee A.K., Skanchy D.J., Jennings B., Hudson T.H., Brendle J.J., Werbovetz K.A., Analysis of stereoelectronic properties, mechanism of action and pharmacophore of synthetic indolo[2,1-b]quinazoline-6,12-dione derivatives in relation to antileishmanial activity using quantum chemical, cyclic voltammetry and 3-D-QSAR Catalyst procedures, *Bioorg. Med. Chem.,* 10 (6) (2002) 1979-1989.

[31] Al Wasidi A.S., Hassan A.S., Naglah A.M., In vitro cytotoxicity and druglikeness of pyrazolines and pyridines bearing benzofuran moiety, *J. Appl. Pharm. Sci.*, 10(4) (2020) 142–148.

[32] Lipinski C.A., Lombardo F., Dominy B.W., Feeney P.J., Experimental and computational approaches to estimate solubility in drug discovery and development settings, *Adv. Drug. Deliv. Rev.,* 46(1-3) (2001) 3-26

[33] Ghose A.K., Viswanadhan V.N., Wendoloski J.J., A knowledge-based approach in designing combinatorial or medicinal chemistry libraries for drug discovery. 1. A qualitative and quantitative characterization of known drug databases, *J. Comb. Chem.,* 1(1) (1999) 55-68.

[34] Veber D.F., Johnson S.R., Cheng H.-Y., Smith B.R., Ward K.W., Kopple K.D., Molecular properties that influence the oral bioavailability of drug candidates, *J. Med. Chem.,* 45(12) (2002) 2615-2623.

[35] Egan W.J., Merz K.M., Baldwin J.J., Prediction of drug absorption using multivariate statistics, *J. Med. Chem.*, 43(21) (2000) 3867-3877.

[36] Muegge I., Heald S.L., Brittelli D., Simple selection criteria for drug-like chemical matter, *J. Med. Chem.,* 44(12) (2001) 1841-1846.

Cumhuriyet Sci. J., 44(1) (2023) 197-202
DOI: https://doi.org/10.17776/csj.1192144

Cumhuriyet Science Journal

| csj.cumhuriyet.edu.tr | Founded: 2002 ISSN: 2587-2680 e-ISSN: 2587-246X Publisher: Sivas Cumhuriyet University

Contribution of Neutralino and Chargino to Diagonal Form Factor of Majorana Neutrino in the Minimal Supersymmetric Standard Model

Coşkun Aydın [1,a,*]

[1] *Department of Physics, Faculty of Science, Karadeniz Technical University, Trabzon, Türkiye.*
**Corresponding author*

Research Article

History
Received: 20/10/2022
Accepted: 14/12/2022

ABSTRACT

In this study, we have calculated the diagonal form factor and charge radius of Majorana neutrinos in the Minimal Supersymmetry Standard Model (MSSM) using Feynman-'t Hooft gauge and dimensional regularization. From the obtained result of calculations, we have seen that the main contribution come from chargino particles in MSSM and its contribution is very small than SM contribution. It is found that $\langle r_\nu^2 \rangle = 1{,}66 \, . 10^{-32} \, cm^2$ for the charge radius of electron neutrinos which is in good agreement with results obtained from the scattering experiments.

Keywords: Standard model, Minimal supersymmetric model, Lepton, Form factors, Majorana neutrino.

[a] *coskun@ktu.edu.tr* *https://orcid.org/0000-0002-6351-0740*

Introduction

The Standard Model(SM) is a theory concerning the electromagnetic, weak and strong interactions. The SM of elementary particles is a gauge quantum field theory. The internal symmetry that defines the SM is the local $SU(3) \times SU(2) \times SU(1)$ gauge symmetry and the most general Lagrangian that describes the dynamics of the fields[1-3]. Although the SM is a beautiful model with predictive power, it includes almost 30 parameters which we are not able to know where they came from as well as some other minor problems. For example, one of them is to determine the absolute scale of the neutrino mass or the nature of the neutrino, whether it is a Dirac or a Majorana particle.We know that neutrinos are massive because neutrino oscillations have been observed in many experiments.The SM must be extended to account for the neutrino masses. Physics beyond the SM has attracted the attention of physicists for a long time. One of the most appealing theories to describe physics at the TeV scale is the minimal supersymmetric extensions of the SM (MSSM) [4-6]. Besides providing a solution to the hierarchy problem, it also provides us with a good candidate for cold dark matter(CDM),namely, the lightest neutralino which is a Majorana particle.

It is known that in quantum field theory (QFT), the interaction vertex between a single photon and a fermion can be characterized in terms of four electromagnetic (EM) form factors. In the limit of vanishing momentum transfer between the photon and fermion, the form factors encode the static EM properties of the particle [7-22].

The most general matrix element of the electromagnetic current J_μ^{EM} between neutrino mass eigentates ν_i and $\nu_j$function is given by [7,10,13]

$$< \nu_f(p_f) | J_\mu^{EM} | \nu_i(p_i) >= \overline{u_f}(p_f) \Lambda_\mu^{fi}(q) u_i(p_i) \qquad (1)$$

and

$$\Lambda_\mu^{fi}(q) = \left(\gamma_\mu - \frac{q_\mu \, q}{q^2}\right)\left[f_Q^{fi}(q^2) + f_A^{fi}(q^2)\, q^2\gamma_5) - i\sigma_{\mu\nu}q^\nu(f_M^{fi}(q^2) + i f_E^{fi}(q^2)\gamma_5)\right] \qquad (2)$$

where $q = p_i - p_j$ is the momentum transfer and f_Q is the real charge, f_A is anapole moment, f_M is magnetic moment and f_E is electric dipole moment form factor. The form factors with $f \neq i$ are called transition form factor or off-diagonal whereas those with $f = i$ are called diagonal. We note that the neutrino can not have an electric dipole moment in the CP-conserving theory.

At low neutrino energies $\Lambda_\mu^{fi}(q)$ can be expressed as follow

$$\Lambda_\mu^{fi}(q) = \left(\gamma_\mu - \frac{q_\mu \, q}{q^2}\right)\left[e_{fi} + \frac{1}{6} q^2 \left(\langle r_V^2 \rangle_{fi} + 6\gamma_5 a_{fi}\right) + \sigma_{\mu\nu}q^\nu\left(\mu_{fi} + i d_{fi}\gamma_5\right)\right] \qquad (3)$$

where $\sigma_{\mu\nu} = (\gamma_\mu\gamma_\nu - \gamma_\nu\gamma_\mu)i/2$ and $e_{fi}, \langle r_V^2 \rangle_{fi}, a_{fi}, \mu_{fi}$ and d_{fi} are respectively, the neutrino millicharge, charge radius square, anapole moment, magnetic moment and electric dipole moment.

In the nonrelativistic limit the interactions generated by the charge and anapole moment form factors that

conserve helicity, whereas the interactions generated by the magnetic and electric dipole moment form factors that flips helicity.

Let us now consider the helicity conserving (charge and anapole) parts of neutrino electromagnetic vertex function for diagonal case in Eq.(1), as

$$\Lambda_{\mu}^{Q,A}(q) = \left(\gamma_{\mu}q^2 - q_{\mu}\not{q}\right)\left[f_Q'(q^2) + f_A\ (q^2)\, q^2\gamma_5\right] \quad (4)$$

In the SM the neutrino electromagnetic form factor for small values of q^2 is given by

$$f(q^2) \cong \left(\frac{\langle r_V^2\rangle}{6} - a\right) q^2 \quad (5)$$

where $\langle \boldsymbol{r_V^2}\rangle$ is the neutrino charge radius and $\boldsymbol{a}$ is the neutrino anapole moment. For this massless case, Dirac or Majorana neutrinos are equivalent.Thus, in the SM the form factor $f(q^2)$ can be interpreted as a neutrino charge radius or as an anapole moment (or as a combination of both).

A Majorana neutrino is characterized by just one flovor diagonal electromagnetic form factor for diagonal case: the anapole moment ,that in the static limit corresponds to the axial vector charge radius $\langle \boldsymbol{r_A^2}\rangle$.

It is easy to understand the physical significance of the form factors in the nonrelativistic limit. In this limit, the interaction energy with an external electromagnetic field takes the following form

$$H_{int} = -\mu\left(\vec{\sigma}.\vec{B}\right) - d\left(\vec{\sigma}.\vec{E}\right) - a(\vec{\sigma}.\vec{j}) \quad (6)$$

where $\vec{B}$ and $\vec{E}$ are the magnetic and electric fields, $\vec{\sigma}$is the Pauli spin matrix, and $\vec{j} = \left(\vec{\nabla}\times\vec{B} - \frac{\partial}{\partial t}\vec{E}\right)$ is the electric current density at the point where the particle is situated. The form factors of the neutrinos (uncharged leptons) have been calculated in gauge field theories. The questions of whether neutrinos have masses and if so, and whether the neutrinos are Dirac or Majorana particles have been two of the most important issues in both particle physics and astrophysics. It is known that the neutrinos are massless and that it is Weyl neutrinos in the SM. There are many possible extensions of SM which reveal massive neutrino[23].

In 1980, the anapole moment of the electron was calculated by Dombey and Kennedy [18] in the SM. In 1987, H.Czyz et al. [24- 25] discussed the anapole moment of charged leptons in the context of the SM. In 2017, Whitcomb and Latimer[26] performed a scattering calculations that probes the anapole moment with a spinless charged particle. They showed that, in the non-relativistic limit, the cross sections are compatible with the quantum mechanical computation of the cross section for a spinless current scattered by an infinitesimally thin toroidal solenoid. As a result, they have obtained the effect of the charge radius or anapole moment on the scattering. Lately, it has been observed a noticeable surge of interest in the study of charge radius or anapole moment from the astrophysical as well as the particle physics point of view[27-29]. These studies also serve as basis and provide contributions to explain the dark matter [30-32].

Neutrino oscillation results imply that the flavor neutrino fields $\nu_{lL}(x)$ are the mixtures of the left-right handed components of the fields of the neutrinos, with masses defined as

$$\nu_{lL}(x) = \frac{1}{2}(1-\gamma_5)\nu_l(x) = \sum_{i=!}^{3} U_{li}\,\nu_{iL}(x)\,,\ l = e^-,\mu^-,\tau^- \quad (7)$$

where U is the unitary PMNS mixing matrix relating the neutrino mass eigenstates to the weak eigenstates and $\nu_l(x)$ is the field of neutrino (Majorana or Dirac) with mass $m_l(x)$ Flavor fields $\nu_L(x)$ enter into the SM charged current (*CC*)

$$L_I^{CC}(x) = -\frac{g}{2\sqrt{2}}\sum_{l=e,\mu,\tau}\bar{\nu}_{lL}(x)\,\gamma_{\alpha}l_L(x)W^{\alpha}(x) + h.c \quad (8)$$

and neutral current (*NC*) interactions

$$L_I^{NC}(x) = -\frac{g}{2cos\theta_W}\sum_l\left[\bar{\nu}_{lL}(x)\gamma_{\alpha}\nu_{lL} + \bar{l}\gamma_{\alpha}(g_v + g_A\gamma_5)l\right]Z^{\alpha}(x)) \quad (9)$$

is the neutrino *NC*. W^{α}(x) and Z^{α}(x) are the fields of W and Z vector bosons. g is the electroweak interaction constant and θ_w is the weak (Weinberg) angle [39]. The vector and axial-vector couplings are

$$g_V \equiv t_{3L}(l) - 2q_l sin^2\theta_W, \qquad g_A \equiv t_{3L}(l)$$

where $t_{3L}(l) = -{}^1\!/_2$ is the weak isospin charged leptons l and q_l is the charge of l in units of e, which is equal to $g\ sin\theta_W$, is the positron electric charge.

The interactions of the lepton and sneutrino with chargino (lepton-sneutino-chargino vertices), the charged lepton and the charged slepton with the neutralino (lepton-slepton-neutralino vertices) and the neutrino and slepton with chargino are correspondingly given by Lagrangian as [33-34]

$$L_I^{SUSY}(x) = \sum_l\left\{\left[\bar{l}(N^L P_L + N^R P_R)\chi^0\tilde{l} + \bar{l}(C^L P_L + C^R P_R)\chi\tilde{\nu}_l\right] + \bar{\chi}C'^L P_L\nu_l\tilde{l}\right\} + h.c \quad (10)$$

where $P_{L,R} = \frac{1}{2}(1 \mp \gamma_5)$,

$$N^L = -\frac{g}{\sqrt{2}}\sum_{AX}\left\{m_{li}M_W cos\beta N_{A3}R_{Xi}^l + 2N_{Al}tan\theta_W R_{Xi+3}^l\right\}, \quad (11)$$

$$N^R = -\frac{g}{\sqrt{2}}\sum_{AX}\left\{[-N_{A2} - N_{A1}tan\theta_W]R^l_{Xi} + \frac{m_{li}}{M_W cos\beta}N_{A3}R^l_{Xi+3}\right\}, \quad (12)$$

$$C^L = g\sum_X \frac{m_{li}}{M_W cos\beta}V_{A2}R^v_{Xi} \quad (13)$$

$$C'^L = \sum_X \left(gV_{A1}R^l_{Xi}\frac{m_{li}}{M_W cos\beta}N_{A2}R^l_{Xi+3}\right) \quad (14)$$

and $P_{L,R}$ are the project operators. N and U, V are the diagonalized matrices of neutralino and chargino mass matrix, respectively. R is the diagonalized matrix of slepton or sneutrino mass matrix. The indices A ($1...4$ for neutralinos; $1,2$ for charginos) and X ($1...6$ for sleptons; $1,2,3$ for sneutrinos) run over the dimensions of the respective matrices, whereas i as usual runs over the generations, m_l is the mass of the i^{th} charged lepton and rest of the parameters carry the standard definitions.

This paper is structured as follows: In Section 2, we present the calculations of the Majorana neutrinos' form factor in the framework of the MSSM. Finally, we present our discussion and conclusion in Section 3.

Calculation

The basic diagrams which contribute to the form factor of Majorana neutrino are shown in Fig. 1. No diagrams involving Higgs particle contribute to parity violation to this order. The simplest gauge to choose for calculating these diagrams is Feynman-'t Hooft gauge, and the calculations are performed using the dimensional regularization produce which preserves gauge in variance. This calculation is done, using above interactions Lagrangians, in framework of the minimal supersymmetric extension of the Standard Model (MSSM).There are the first three diagrams (i, ii and iii) in the SM [20,35].

We choose the Breit frame in which the neutrino has momentum initially $(p - q/2)$ and $(p + q/2)$, then we find the matrix elements for the MSSM in Fig. 1 $(i - v)$, respectively.

$$M_i = \frac{eg^2}{8}\int\frac{d^{2w}k}{(2\pi)^{2w}}\left\{\frac{\gamma^\alpha(1-\gamma_5)\left(\not{k}+\not{p}+\frac{\not{q}}{2}+m_l\right)}{\left[\left(-k+p-\frac{q}{2}\right)^2-m_l^2\right]} - \frac{\gamma^\mu\left(-\not{k}+\not{p}-\frac{\not{q}}{2}+m_l\right)\gamma^\alpha(1-\gamma_5)}{\left[\left(-k+p+\frac{q}{2}\right)^2-m_l^2\right][k^2-M_W^2]}\right\} \quad (15)$$

$$M_{ii} = \frac{eg^2}{8}\int\frac{d^{2w}k}{(2\pi)^{2w}}\left\{\frac{\gamma_\beta(1-\gamma_5)(\not{k}+m_l)\gamma_\alpha}{[k^2-m_l^2]\left[\left(-k+p-\frac{q}{2}\right)^2-M_W^2\right]} - \frac{V^{\alpha\beta\mu}\left(-k+p-\frac{q}{2},-k+p+\frac{q}{2},q\right)}{\left[\left(-k+p+\frac{q}{2}\right)^2-M_W^2\right]}\right\} \quad (16)$$

$$M_{iii} = \frac{ig}{2sin2\theta_w}\gamma^\mu(1-\gamma_5)\frac{1}{q^2-M_Z^2}\pi^{Z\gamma}_{\mu\nu}(q^2) \quad (17)$$

where $\pi^{Z\gamma}_{\mu\nu}$ is the mixing tensor for the $\gamma - Z_0$ mixing diagrams[28]. Dombey and Kennedy obtained numerically value as

$$\tilde{\pi}^{Z\gamma}_{\mu\nu}(q^2) = (3{,}83\ 10^{-3})e^2q^2g_{\mu\nu} + 0(q^4) \quad (18)$$

$$M_{iv} = e\int\frac{d^{2w}k}{(2\pi)^{2w}}\left\{\frac{\left(C'^L P_L\right)\left(-\not{k}+\not{p}-m_\chi\right)^2}{\left(k^2-m_{\tilde{l}}^2\right)\left[\left(-k+p-\frac{q}{2}\right)^2-m_\chi^2\right]}\frac{\gamma^\mu\left(-\not{k}+\not{p}+\frac{\not{q}}{2}+m_\chi\right)\left(C'^{L^\dagger}P_R\right)}{\left(-k+p+\frac{q}{2}\right)^2-m_\chi^2}\right\} \quad (19)$$

$$M_v = 2e\int\frac{d^{2w}k}{(2\pi)^{2w}}\left\{\frac{\left(C'^L P_L\right)(p-k)^\mu}{\left(k^2-m_\chi^2\right)\left[\left(-k+p-\frac{q}{2}\right)^2-m_{\tilde{l}}^2\right]}\frac{\gamma^\mu\left(\not{k}+m_\chi\right)\left(C'^{L^\dagger}P_R\right)}{\left(-k+p+\frac{q}{2}\right)^2-m_{\tilde{l}}^2}\right\} \quad (20)$$

Since the anti-particle of Majorana neutrino is equal to its particle ($\nu = \nu^c$), we didn't need to write the matrix elements of Fig.1 ($i' - \nu'$). For obtaining the total result for the Majorana neutrino, we will multiply the contribution of Fig.1 $i - \nu$) by a factor 2.

Projecting out the axial parts proportional to

$$\frac{ie}{16\pi^2}\gamma_5\gamma^\mu\frac{g^2}{M_W^2}q^2$$

and thereafter long but simple calculations, neglecting the terms of order $(m_l/M_W)^2$, we obtain the Majorana neutrino form factor expressions as follows

$$a_i^\nu = ln\left(\frac{M_W^2}{m_l^2}\right) - \frac{13}{12} \tag{21}$$

$$a_{ii}^\nu = -\frac{7}{24} \tag{22}$$

$$a_{iii}^\nu = \left(\frac{cos\theta_w}{4}\right)3{,}83\ 10^{-3} \tag{23}$$

$$a_{iv}^\nu = \left(\frac{M_W^2}{m_{\tilde{l}}^2}\right)\left[-\frac{7}{6} + 2ln\left(\frac{m_{\tilde{l}}}{m_\chi}\right)\right]\left[\frac{1}{g^2}\left(\left|C'^L\right|^2\right)\right] \tag{24}$$

$$a_v^\nu = \left(\frac{M_W^2}{m_{\tilde{\chi}}^2}\right)\left[-\frac{1}{6g^2}\left(\left|C'^L\right|^2\right)\right] \tag{25}$$

corresponding to Fig. 1((i)–(v)). Then, the total form factor of the Majorana neutrinos is

$$a_T^\nu = 2(a_i^\nu + a_{ii}^\nu + a_{iii}^\nu + a_{iv}^\nu + a_v^\nu) \tag{26}$$

Conclusion

We calculated the contribution to Majorana neutrino form factor arising from the exchange of $Z(W)$ and the leptons in the loop, as well as from the exchange of charginos (neutralino) and sleptons in the framework of the MSSM. Even though this model would be perhaps an unrealistic model, it is one of the models extending the SM. Limitations that can be obtained for this interaction from the entire body of available experimental data are investigated. We think that the most compelling constraints arise from experiments with polarized electrons. It is well known that there are many scenarios in SUYS. The leading effect inFig. 1 is approximately in the large $tan\beta$ limit.In this study we have considered only the scenario for large $tan\beta$ values and we obtained

$$a_T^\nu = ln\left(\frac{M_W^2}{m_l^2}\right) - \frac{33}{12} + \frac{m_l^2}{8}\left\{\left[-\frac{3m_{\tilde{l}}^2}{2\left(m_{\tilde{l}}^2 - m_{\tilde{\chi}^-}^2\right)} + \frac{m_l^4}{\left(m_{\tilde{l}}^2 - m_{\tilde{\chi}^-}^2\right)^3}\right] + \left[\frac{9m_{\tilde{l}}^4}{\left(m_{\tilde{l}}^2 - m_{\tilde{\chi}^-}^2\right)^3} + \frac{m_l^6}{\left(m_{\tilde{l}}^2 - m_{\tilde{\chi}^-}^2\right)^4}\right] ln\left(\frac{m_{\tilde{l}^2}}{m_{\tilde{\chi}^-}^2}\right)\right\} \tag{27}$$

It can be see that, since $m_{\tilde{l}}$ and $m_{\tilde{\nu}}$ are bigger than m_l therefore $m_l/m_{\tilde{l}}$ and $m_l/m_{\tilde{\nu}}$ become much smaller than 1. As a result, it seems unlikely possiblefrom SM that in the MSSM, even taking the limited values (see Table 1), the contribution of chargino and neutralino is extremely smaller then the contribution of SM's particle. Therefore it is unnecessary to obtain results for the different values of the parameters. This means that the terms coming from SUSY are strongly effective due to the properties of neutralino and chargino.

Here, we note that there is a long discussion on the possibility of obtaining for the neutrino charged radius which is a gauge-independent and finite quantity [36]. In the corresponding calculations, performed in the one-loop approximation including additional terms from the photon $(\gamma)$and neutral boson (Z) mixing and the box diagrams involving charge vector boson (W) and neutral vector boson (Z), the gauge invariant result for the neutrino charge radius (in fact, it is the charged radius squared) have been obtained [13,37-39] .

The numerical values of the Majorana neutrinos' charge radius for different neutrinos are obtained as

$$\langle r_\nu^2\rangle \approx \begin{cases} 1{,}66\,.\,10^{-32}\ cm^2\ \ for\ \nu_e \\ 0{,}96\,.\,10^{-32}\ cm^2\ for\ \nu_\mu \\ 0{,}30\,.\,10^{-32}\ cm^2\ for\ \nu_\tau \end{cases} \tag{28}$$

using the corresponding leptons value of m_l and mass values given in Table 1. The current contraints on the flavour neutrino charge radius $\langle r^2_{e,\mu,\tau}\rangle \leq (10^{-32} - 10^{-31})cm^2$ was obtained from the scattering experiments [38-40]. The theoretical results of $< r_\nu{}^2 >$ are smaller than the experimenal results in an magnitude of only about one order.

Table 1: The particle masses values used in the calculations [40]

Particle	**Mass** [GeV]	**Particle**	**Mass** [GeV]
e^-	$5{,}11.10^{-4}$	χ_1^0	≥ 46
μ^-	0.105	$\chi_1^\mp$	≥ 94
τ^-	1,777	$\tilde{e}$	≥ 107
Z^0	91,18	μ	≥ 94
$W^\mp$	80,39	$\tilde{\tau}$	$\geq 81{,}9$
H	125	$\tilde{\upsilon}$	≥ 41
	Some constant values		
G_F	*1,16.10-5*	$1/\alpha$	*137*
$sin^2\theta_W$	*0.229*	$tan\beta$	*20*

Without performing calculations, we can't say nothing about order of magnitude of considered contributions. A neutrino charge radius contributes to the neutrino scattering cross section on electrons and thus can be constrained by corresponding laboratory experiments.

The effect of charge radius can be included just as a shift of the vertex coupling constant

$C_V \rightarrow C_V + \left(\sqrt{2}\ \pi/\ 3G_F\ \right) < r_\nu{}^2 >$ in the weak contribution to the cross section. It has also some impact on astrophysical phenomena and cosmology. Performing at present time and planning in future very sensitive experiments on lepton magnetic, electric dipole, anapole moments and charge radius are one of main research direction in low energy experiments. For this reason presented in this work calculations have direct significance for experiment.

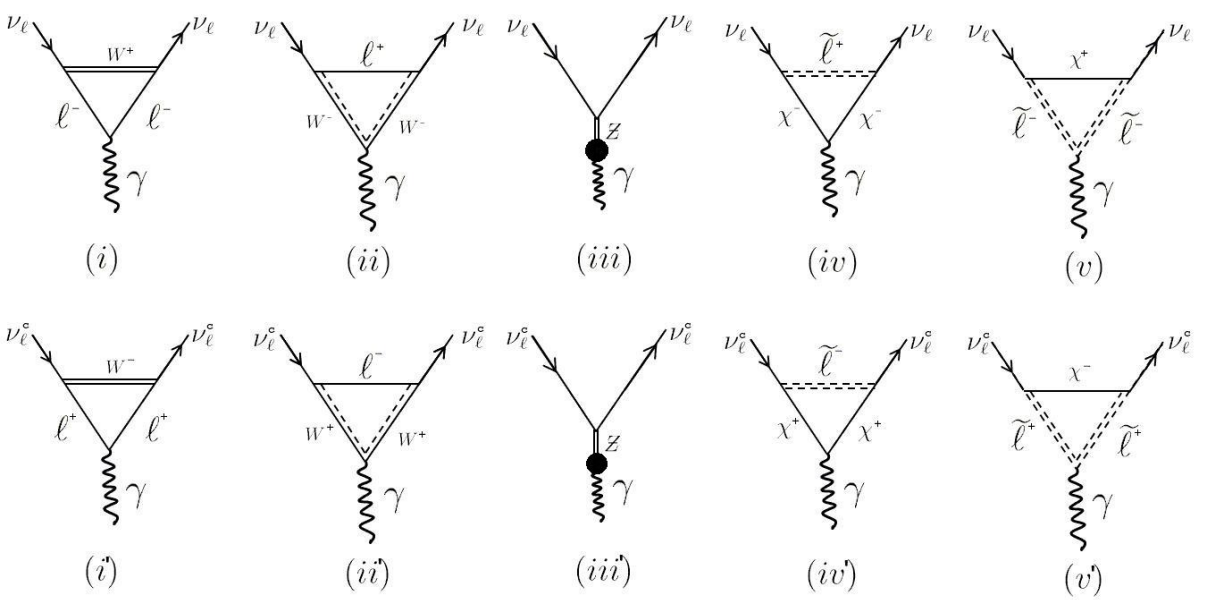

Figure 1. Basic diagram of the form factor of the Majorana neutrinos in the minimal supersymmetry standard model.

Conflicts of interest

There are no conflicts of interest in this work.

Acknowledgments

The author is greatful and would like to present his special thanks to Prof.Dr. T.M. Aliev for his careful and valuable reading of the manuscript and helpful suggestions about its revision.

References

[1] Greiner W., Müller B., Gauge Teory of Weak Interactions, 3rd ed. Berlin: Springer (2000).
[2] Langacher P., The Standard Model and Beyond. 2nd ed. New Jersey: CRC Press, (2017) 257-261.
[3] Weinberg S., The Quantum Theory of Fields, Volume 2. 1st ed. Cambridge University Press, (2005) 295-317.

[4] Mohapatra Rabindra N., Unification and Supersymmetry, 1st ed. New York: Springer, (1986) 224-243.

[5] Weinberg S., The Quantum Theory of Fields, Volume 3, Cambridge University Press (2005) 179-208

[6] Haber H. E., Kane G. L., The second for supersymmetry: Probing physics beyond the Standard model, *Phys. Pept.* 117 (1985) 75-263.

[7] Dubovik V. M., Cheshkov A. A., Multipole expansion is classical and quantum field theory and radiaton, Sov. J. Part. Nucl., 5 (1975) 318-337.

[8] Dubovik V. M.,Tosunyan L. A., Toroidal moments in the physics of electromagnetic and weak interactions, *Sov. J. Part. Nucl.,* 14 (1983) 504.

[9] Dubovik V. M., Tugushev V. V., Toroid moments in electrodynamics and solid state physics, *Phys. Rep.,* 187 (1990) 145-202.

[10] Dubovik V. M., Kuznetsov V. E.,The toroid dipole moment of the neutrina, *Int. J. Mod. Phys. A*, 13 (1998) 5257-5277.

[11] Bukina E. N., Dubovik, V. M., Kuznetsov V. E.,Transmission radiation on the neutrino toroiol dipole moment, *Phys. Lett. B,* 435 (1998) 134-138.

[12] Wood C. S. et al., Measurement of party nonconsevation anol an anapole moment in Cesium, *Science,* 275 (1997) 1759-1763.

[13] Giunti C., Studennikin A., Neutrino electromagnetic interactions: A window to new physics, *Rev. Mod. Phys.,* 87 (2015) 531-592.

[14] Kayser B., Majorana neutrinos and their electromagnetic properties, *Phys. Rev. D,* 26 (1982) 1662-1670.

[15] NievesJ. F., Electromagnetic properties of Majerana neutrinos , *Phys. Rev. D,* 26 (1998) 3152-3158.

[16] Roberts B. M. et al, Parityi-violating interactions of cosmic fields with atoms, molecules and nuclei, *Phys. Rev. D,* 90 (2014) 096005.

[17] Sakakibara S., Aachen preprint (1979) PITHA 79/17.

[18] Dombey N., Kennedy, A. D., A calculation of electron anapole moment, *Phys. Lett. B,* 91 (1980) 428-430.

[19] Paschos M. E. A., Rodriguez J.M., All electromagnetic form factors, *Eur. J. Phys.,* 26 (2005) 545-560.

[20] Abak M., Aydın C., Calculation of the Anapole moment of the neutrino, *Europhys. Lett.,* 4 (1987) 881-886.

[21] Abak M., Aydın C., Extension of SU(2)xU(1) models and the form factors of the massive Dirac Neutrinos, *Nuovo Cimento A,* 101 (1989) 597-606.

[22] Aydın C., The anapole moment of Dirac neutrinos in left-right symmetric model and in minimal supersymmetric model, *Modern Phys. Lett. A,* 16 (2001) 1823-1828.

[23] Fukugita M., Yanagida T., Physics of Neutrinos and Applications to Astrophysics, Springer-Verlag (2003).

[24] Czyz H., Kolodziej K., Zralek M.,Static properties of charged leptons and searching for a super heavy neutrino, *Physica Scripta,* 37 (1988) 205-208.

[25] Czyz H., Kolodziej K., Zralek M., Christova P., Is the anapole moment a physical observable?, *Can. J. Phys.,* 66 (1988) 132-134.

[26] Whitcomb K. M. and Latimer D. C., Scattering from a quantum anapole at low energies, *Am. J. Phys.,* 85 (2017) 932-936.

[27] Sahoo B. K., Aoki T., Das B. P., Sakemi Y., Enhanced spin dependent parity non-conservation effect is the $7s^2S_{12} \rightarrow 6d_2D_{5h}$ transition A possibility for unambigious detection of nuclear anapole moment, arXive: 1512.02055 (hep-ph).

[28] Ho C. M., Scherrer R. J., Anapole dark matter, *Phys. Lett. B,* 722 (2013) 341-346.

[29] Kopp,J., Michaels, L., Smirnov J.,Loopy constrains on leptonhilic dark matter anol internal bremsstrahlung, *JCAP04,* **(**2014) 022.

[30] Cabrel-Rosetti L. G., Mondragon M., Reyes-Perez E., Anapole moment of the lightest neutralino in the cMSSM, *Nucl. Phys. B,* 907 (2016) 1-17.

[31] Ibarra A., Yaguna, C. E., Zapata O. ,Direct detection of fermion dark matter in radiative seesaw model, *Phys. Rev. D,* 93 (2016) 035012

[32] Rosiek J., Complete et of Feynman rule for the minimal supersymmetric extenion of the standard model, *Phys. Rev. D,* 41 (1995) 3464-3501.

[33] Moroi T., Muon anomalous magnetic dipole moment in the minimal supersymmetric standard model, *Phys. Rev. D* 53 (1996) 65656575; Erratum: *Phys. Rev. D,* 56 (1997) 4424.

[34] Sun K. S., Chen, J. B. Yang, X. Y. and Cui, S. K., LFV decays of Z boson in Minimal R-symmetric Supersymmetric Standard Model, *Chin. Phys. C,* 43 (2019) 043101.

[35] Aydın C., Anapole Moment of Leptons in the Minimal Supersymmetric Standard Model, arXiv:1910.09545v3 (hep-ph).

[36] Musolf M. J., Holstein B. R.,Observability of the anapole moment and charge radius , *Phys. Rev. D,* 43 (1991) 2956-2970.

[37] Cadeddu M., Dordei F., Giunti C., Li Y.F., Picciau E., Yang Y.Y., Physics results from the first COHERENT observation of coherent elastic neutrino-nucleus scattering in argon and their combination with cesium-iodide data, *Phys. Rev. D,* 102 (2020) 015030.

[38] Khan A.N., Constraints on general light mediators from PandaX-II electron recoil data, *Phys. Lett. B,* 819 (2021) 136415.

[39] Guinti C., Gruszko J., Jones B., Kaufman L., Parno D., Pocar A., Report of Topical Group on Neutrino Properties for Snowmass 2021, arXiv :2209.03340(hep-ph).

[40] Workman R.L. et al., Review of Particle Physics (Particle Data Group), *Prog.Theor. Exp. Phys.*, 2022, 083C01 (2022).

Cumhuriyet Sci. J., 44(1) (2023) 203-208
DOI: https://doi.org/10.17776/csj.1187724

Cumhuriyet Science Journal

| csj.cumhuriyet.edu.tr | Founded: 2002 ISSN: 2587-2680 e-ISSN: 2587-246X Publisher: Sivas Cumhuriyet University

Analyzing of the Evolution and the Scaling Properties of a Sinusoidal Mound

Ahmet Türker Tüzemen [1,a,*]

[1]*Department of Mathematics and Science Education, Faculty of Education, Sivas Cumhuriyet University, Sivas, Türkiye.*
**Corresponding author*

Research Article

History
Received: 12/10/2022
Accepted: 15/12/2022

ABSTRACT

The evolution of an initial surface (below its roughening temperature) bounded by a sinusoidal function and consisting of concentric circular steps in two dimensions has been investigated in the Diffusion Limited (DL) regime. Assuming that there were entropic interactions between steps and the local mass transfer took place due to the surface diffusion, the solution of the diffusion equation has been obtained by using polar coordinates in two dimensions. The results obtained in this investigation with analyzing the surface height's evolution as a function of time are as follows: The surface's height approximately decreases as τ^{α} $(\alpha \approx 0.35)$ and α is independent of the amplitude and the wavelength of the initial surface. The variations in the heights of the surfaces which have different amplitudes (A_{01}, A_{02}) and wavelengths (λ_1, λ_2) scale as $(A_{01}/A_{02})(\lambda_1/\lambda_2)^3$.

Keywords: Mass transfer, Surface structure, Surface processes, Diffusion limited regime.

[a] *atuzemen@cumhuriyet.edu.tr* *https://orcid.org/0000-0002-6120-6008*

Introduction

Knowing the morphological structures of semiconductor crystal surfaces and how they reach their equilibrium surface structures are issues that need to be emphasized in terms of designing and fabricating new semiconductor devices. The dynamics in the surface's evolution to equilibrium structure provide us detailed information about the surface's structure and the driving forces that enable the surface to reach its equilibrium structure. Monatomic steps which have terraces between them are observed on the surfaces under their roughening temperature. The events in the growth and reaching the equilibrium shape of a crystal take place through monatomic steps and the existence of steps on the surface affects significantly the morphological evolution of the surface. The evolution of surface morphology occurs due to the tendency to decrease the free energy of the surface.

There are lots of theoretical and experimental works done from past to present about decaying of crystalline surfaces. Rettori and Villain [1] have studied on a crystal surface below its roughening temperature and examined the decaying of a profile produced artificially. Uwaha [2] investigated the relaxation of crystal shapes caused by step movement. The flattening of a corrugated crystal surface which has monoatomic steps where mass transport occurs by surface diffusion has been studied by Ozdemir and Zangwill [3]. In their study where they explained the morphological changes of the gratings with annealing, Umbach et al. [4] have studied on atomic step arrays on Si(001) using scanning tunneling microscope. Israeli and Kandel [5] have examined a cone surface's equilibration which has a regular shape for Diffusion Limited (DL) and Attachment-Detachment Limited (ADL) regimes. Ichimiya et al. [6] have studied the silicon mounds' decay experimentally in the DL regime and determined that the mound's height decreases as a function of time as $t^{1/4}$ or $t^{2/5}$. In another study the decay characteristics of three-dimensional (3D) islands have been examined theoretically by Li et al. [7]. Kodambaka et al [8, 9] presented the coarsening/decay kinetics of 2D TiN adatom islands in their experimental works. Kellogg and Bartelt [10] have investigated the island decay on Rh(001) surface using low-energy electron microscopy. Esen et al. [11] put forth a study about the equilibration of a conic shaped surface using the Kinetic Monte Carlo method. In Diffusion Limited (DL) regime, the different shaped surfaces owned circular monoatomic steps have been examined by Tüzemen et al. [12]. They have assumed that there were only repulsive interactions between the steps. They found that the scaling characteristics of the surfaces' height variations. In addition, they determined that the surfaces' heights characteristically decreased with τ^{α} $(\alpha \approx 0.36$ for the sinusoidal surface they dealt with) in time. Moreover, Tüzemen et al. [13] have investigated the morphology of a conic shaped initial surface in two dimensions in DL regime. They have included the repulsive interaction as well as the attractive interaction between steps in their calculations. The surface's height evolution and morphology have been studied in the presence of only repulsive interactions and both attractive and repulsive interactions between steps.

In this work, the evolution of an initial surface (below its roughening temperature) which consists of concentric circular steps in two dimensions and whose edge structure coincide with a sinusoidal function has been investigated. In our investigation, we examined the changes in interested surfaces' heights as a function of time during the surface's evolution for only Diffusion Limited (DL) regime. It was supposed that the local mass transfer takes place because of the surface diffusion while the initial surface's evolution happens. In addition, it was considered that there are entropic interactions between steps on the surface. With these admissions, the diffusion equation

has been solved in two dimensions by using polar coordinates and an equation of motion for each circular step's radius was obtained. Later the solution of these coupled equations was achieved numerically. The organization of the work is as follows: the definitions and the problem's theoretical solution are given in section 2, in section 3 obtained numerical results and their discussions are presented and in the section 4 conclusions are given.

Theory

In this study, an initial surface which consisting of concentric circular steps owned monoatomic height is examined. There are finite number of steps on the surface. The flat terraces separate these steps, as shown in Figure 1. The borders of i^{th} terrace are i and $i+1$ from above and below respectively. The surface's evolution occurs by the steps' motion by attachment (detachment) of particles to (from) step edges. In the case of no flux to the surface, the diffusion equation for i^{th} terrace atom concentration can be given as follows,

$$D_s \nabla^2 C_i(\vec{r}) = \frac{\partial C_i(\vec{r})}{\partial t} \quad (1)$$

Here D_s represents the surface diffusion constant. There isn't any desorption from the surface. The steady state diffusion equation is written as [5]

$$\frac{\partial^2 C_i(\vec{r})}{\partial r^2} + \frac{1}{r}\frac{C_i(\vec{r})}{\partial r} = 0 \quad (2)$$

The solution of Eqn. (2) is $C_i(\vec{r}) = A_i \ln r + B_i$. The arbitrary constants A_i and B_i are calculated by using suitable boundary conditions which are defined at the step edges and given as below,

$$D_s \frac{\partial C_i}{\partial r}\Big|_{r_i} = k\left[C_i|_{r_i} - C_i^{eq}\right] \quad (3)$$
$$-D_s \frac{\partial C_i}{\partial r}\Big|_{r_{i+1}} = k\left[C_i|_{r_{i+1}} - C_{i+1}^{eq}\right]$$

while k shows the attachment/detachment coefficient (it is assumed that attachment/detachment coefficients belonging to the up and down steps have the same value) and C_i^{eq} expresses the value of atoms' equilibrium concentration on the adjacent terrace to the i^{th} step.

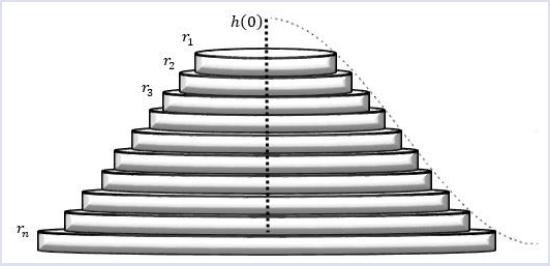

Figure 1. The initial surface consists of monoatomic circular steps with radii $r_1, r_2, r_3, \ldots\ldots r_n$ of separated by terraces and $h(0)$ shows the extrapolated initial surface height. The shape of the sinusoidal function in which the edge structure is coincident is also given with dashed lines.

The expressions of the arbitrary constant A_i and the step's velocity can be given as follows by using boundary conditions in Eqn. (3) and conservation of mass at the step edge respectively,

$$A_i = \frac{c_i^{eq} - C_{i+1}^{eq}}{ln\frac{r_i}{r_{i+1}} - \frac{D_S}{k}\left(\frac{1}{r_i} + \frac{1}{r_{i+1}}\right)} \quad (4)$$

$$\frac{dr_i}{dt} = \Omega D_s \left(\frac{\partial C_i}{\partial r} - \frac{\partial C_{i-1}}{\partial r}\right)\Big|_{r_i} = \Omega D_s \frac{A_i - A_{i-1}}{r_i} \quad (5)$$

Ω is the area on the surface occupied by an atom. According to the Gibbs-Thompson relation C_i^{eq} is explained as

$$C_i^{eq} = \bar{C}^{eq} exp\left(\frac{\mu_i}{T}\right) \approx \bar{C}^{eq}\left(1 + \frac{\mu_i}{T}\right) \quad (6)$$

Boltzman's constant is used as 1 in the calculation because of the used units. The step chemical potential (μ_i) which is dependent on entropic [14] and elastic [15,16] interactions between the nearest neighbor steps with the island curvature can be approximately given as under the assumption that the distances between steps are smaller than the radii [5,17,18].

$$\mu_i = \frac{\Omega\Gamma}{r_i} + \Omega G\left(\frac{2r_{i+1}}{(r_{i+1}+r_i)}\frac{1}{(r_{i+1}-r_i)^3} - \frac{2r_{i-1}}{(r_i+r_{i-1})}\frac{1}{(r_i-r_{i-1})^3}\right) \quad (7)$$

Here, while G shows the strength of the interaction between steps and Γ expresses the step line tension. The dimensionless expressions (ρ_i and τ) of the radii and time can be written as follows by using Ref. [5],

$$\rho_i = \frac{T}{\Omega\Gamma} r_i \quad (8)$$

$$\tau = D_s \bar{C}^{eq} \Omega \left(\frac{T}{\Omega\Gamma}\right)^2 \left(1 + \frac{D_S T}{k\Omega\Gamma}\right)^{-1} t \quad (9)$$

By using these expressions with the Eqns. (3)-(5), the equations of the steps' motion can be obtained as below.

$$\dot{\rho}_\iota = \frac{d\rho_i}{d\tau} = \frac{a_i - a_{i-1}}{\rho_i} \quad (10)$$

The arbitrary constant a_i is given by

$$a_i = \frac{\varepsilon_i - \varepsilon_{i+1}}{(1-q)ln\frac{\rho_i}{\rho_{i+1}} - q\left(\frac{1}{\rho_i}+\frac{1}{\rho_{i+1}}\right)} \quad (11)$$

and ε_i is written as

$$\varepsilon_i = \frac{1}{\rho_i} + g\left(\frac{2\rho_{i+1}}{(\rho_{i+1}+\rho_i)}\frac{1}{(\rho_{i+1}-\rho_i)^3} - \frac{2\rho_{i-1}}{(\rho_i+\rho_{i-1})}\frac{1}{(\rho_i-\rho_{i-1})^3}\right) \quad (12)$$

where g measures G relative to Γ and equals to $(T^2G/\Omega^2\,\Gamma^3)$. If the constant a_i is analyzed, it can be easily seen that it depends on q and g. The parameter q determines the surface evolution regime. In the case of $q = 0$, the evolution of the surface comes true in the Diffusion Limited (DL) regime. On the other hand, the surface evolves in the Attachment/Detachment Limited (ADL) regime for $q = 1$.

Results and Discussion

In this work, We consider an initial surface which consists of monoatomic circular steps of separated by flat terraces and whose edge structure coincide with a sinusoidal function in the form of $A_0 \sin(2\pi x/\lambda)$ and investigate its approach to equilibrium in time. A_0 and λ are the amplitude and the wavelength of the sinusoidal surface respectively. The side view of this surface is shown in Figure 2. During the investigation, we have studied the evolutions of the initial surfaces only in the Diffusion Limited regime ($q = 0$ in Eqn. (11)). The cases in which the initial surfaces' evolutions take place in the Attachment/Detachment Limited regime ($q = 1$) have not been examined.

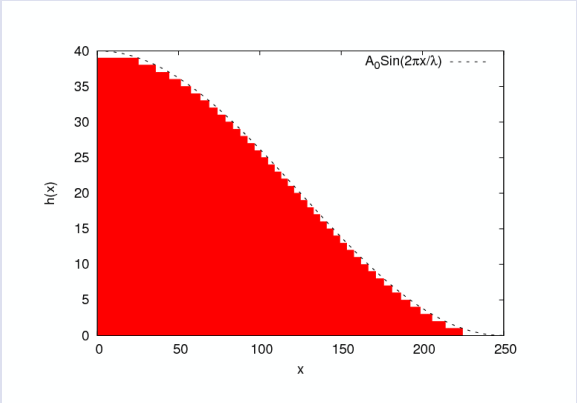

Figure 2. An example of investigated surface which has a sine structure. The units of all used lengths are a lattice constant a_0.

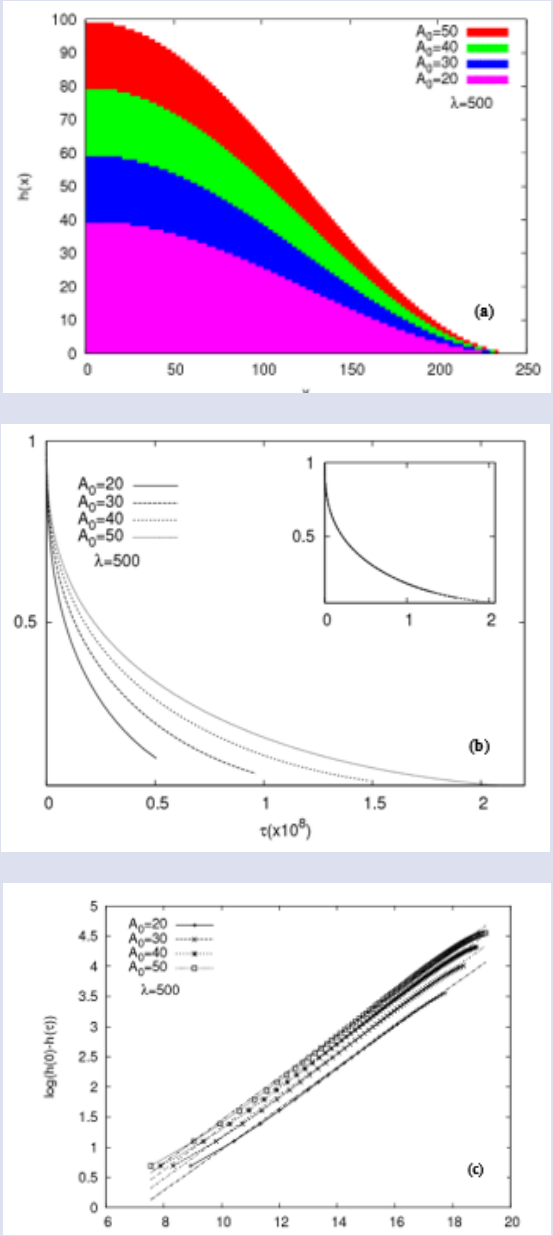

Figure 3. (a) The initial surfaces which have the same wavelength $(\lambda = 500)$ and different amplitudes $(A_0 = 20, 30, 40, 50)$ (b) The variations in the surface's scaled heights as a function of time for the initial surfaces defined in (a). The inset gives the scaling relation in the surface's height with respect to scaled time. All curves are scaled with respect to the curve with $A_0 = 50$. Scaling parameter is given by $\beta' = (A_{01}/A_{02})$. The scaling factors are given as follows $(5/2)$ $(5/3)$, $(5/4)$ and 1 for the amplitudes of the initial surfaces $A_0 = 20, 30, 40$ and 50 respectively, (c) The $log\big(h(0) - h(\tau)\big) - log(\tau)$ plots of the initial surfaces given in (a). The slope values (α) of all curves are equal and nearly 0.35.

Firstly, we considered the initial surfaces that have the same wavelength $(\lambda = 500)$ and different amplitudes (as 20, 30, 40 and 50). The number of steps on these initial surfaces

were $40, 60, 80$ and 100 (shown in Figure 3a). The variations of these surfaces' heights as a function of time have been examined for $g = 10^{-6}$ (in Eqn. 12) firstly. When the evolution of studied surface starts, the radius of the top most step starts to reduce and it disappears from the surface after a while. The surface height also decreases with the disappearance of the topmost step. This phenomenon also applies to other steps. During these events, the particles continuously transfer from the disappeared step to other steps and they grow them. This process continues to take place until last few steps remain. The normalized height variation of the surface happens as given in Figure 3b in this case.

It can be easily seen that all surface heights decrease depending on time. The initial surface, which has the greater wavelength (more steps), needs more time to complete its evolution. The scaling here is related to the surfaces' normalized heights evolution in time forms with the amplitudes' ratios (the number of steps' ratios) of the initial surface.

$$h_{A_{01}}(\tau) = h_{A_{02}}(\beta\tau') \tag{13}$$

Here β equals the ratio A_{01}/A_{02}. The inset in Figure 3b shows the scaling behavior for two initial surfaces which have the same wavelength and different amplitudes. Other finding from this investigation is that the surface's height decreases as follows [19, 6]

$$h(0) - h(\tau) = k\tau^{\alpha} \tag{14}$$

$h(0)$ expresses the initial height of the surface and k is a constant. The $log\big(h(0) - h(\tau)\big) - log(\tau)$ plots of the initial surfaces given in Figure 3a are shown in Figure 3c. The slopes of all curves are obtained as approximately (independent of wavelength) $\alpha \approx 0.35$. The advantage of determining the form of the surface height decreases is that it gives us about the events (driving forces that cause events) took place during evolution. The driving forces which affect the evolution of the interested initial surfaces are the entropic interaction between the steps and the line tension due to the step curvature. The same results have been obtained for $g = 10^{-5}, 10^{-4}$ and 10^{-3} values under the same initial surface conditions.

In the second part, we examined the initial surfaces that have the same amplitude (number of steps) $(A_0 = 40)$ and the different wave lengths $(\lambda = 300, 400, 500, 600)$ (Figure 4a). The value of g was again taken as 10^{-6} firstly, when the heights' variations of the surfaces are investigated. Figure 4b shows the variations of the heights of the surfaces as a function of time. The surface which has the biggest wavelength completes its evolution in the longest time. The scaling of the curves belonging to the height variations is shown in the inset of Figure 4b. In this situation, the scaling happens with the cube of the ratio of the initial surfaces' wavelengths.

$$h_{\lambda_1}(\tau) = h_{\lambda_2}(\beta'\tau') \tag{15}$$

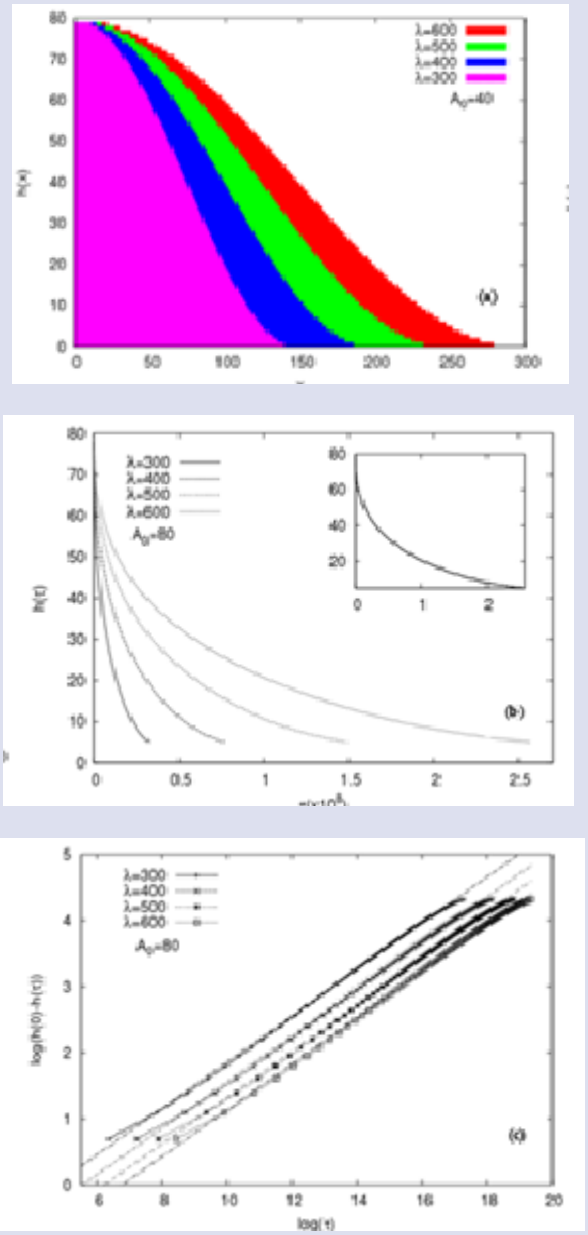

Figure 4. (a) The initial surfaces which have the same amplitude $(A_0 = 40)$ and different wavelengths $(\lambda = 300, 400, 500, 600)$ (b) The changes in the surface's scaled heights as a function of time for the initial surfaces defined in (a). The scaling relation between the surfaces' heights is given inset. All curves are scaled with respect to the curve with $\lambda = 600$. Scaling parameter is given by $\beta' = (\lambda_1/\lambda_2)^3$. The scaling factors are given as follows $(6/3)^3$, $(6/4)^3$, $(6/5)^3$ and 1 for the wavelengths of the initial surfaces $\lambda = 300, 400, 500$ and 600 respectively (c) The $log\big(h(0) - h(\tau)\big) - log(\tau)$ plots belonging the initial surfaces indicated in (a). The slope values (α) of all curves are approximately 0.35..

β' is equal to $(\lambda_1/\lambda_2)^3$. Figure 4c shows the $log\big(h(0)-h(\tau)\big)-log(\tau)$ curves for the cases examined in Figure 3b. The slope of all curves is $\alpha \approx 0.35$. In this part of the investigation, we acquired the same scaling behaviors and the α values for $g = 10^{-5}, 10^{-4}$ and 10^{-3} values under the same initial surface conditions. In our old study [12], we have examined a sinusoidal initial surface similar to the one studied here. Because of this, the scaling characteristics obtained in equations (13) and (15) are the same with found out ones in Ref. [12] as expected. While the slope of the $log\big(h(0)-h(\tau)\big)-log(\tau)$ curves belonging to the studied sinusoidal surfaces was found as $\alpha \approx 0.36$ in Ref. [12], it was found as $\alpha \approx 0.35$ for the sinusoidal surfaces studied here. The α values are close to each other due to the surface similarity.

In the last part of the study, we analyzed the initial surfaces which have different amplitudes and different wavelengths. While the amplitudes of the chosen initial surfaces are $20, 30, 40$ and 50, the wavelengths of these surfaces are $300, 400, 500$ and 600 respectively (shown in Figure 5a). Similarly, first of all we examined that how these surfaces' scaled heights vary as a function of time for $g = 10^{-6}$. The curves drawn for this investigation are given in Figure 5b. As a result, it has been found that the evolutions of the surfaces' normalized heights scales according to the following expression,

$$h_{A_{01},\lambda_1}(\tau) = h_{A_{02},\lambda_2}(\eta\tau') \qquad (16)$$

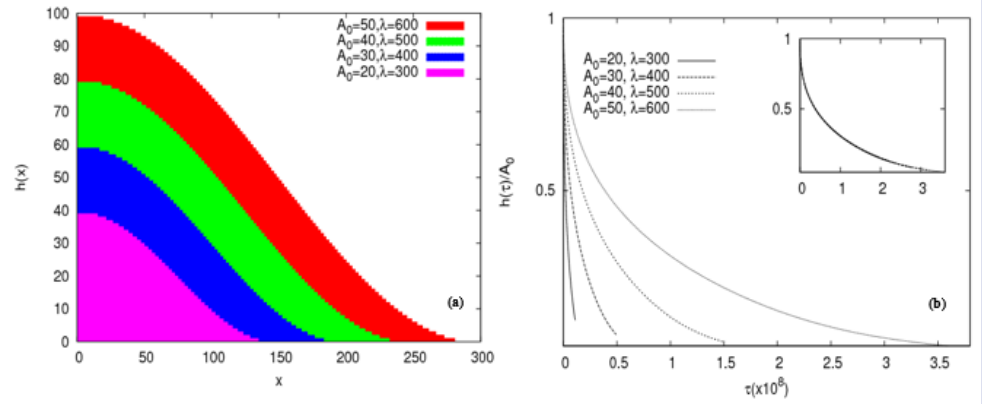

Figure 5. (a) The initial surfaces which have the different amplitudes $(A_0 = 20, 30, 40, 50)$ and wavelengths $(\lambda = 300, 400, 500, 600)$ (b) The changes in the surface's scaled heights as a function of time for the initial surfaces. The scaling behaviors of the surfaces' heights is given inset. All curves are scaled with respect to the curve with $A_0 = 50$ and $\lambda = 600$. Scaling parameter is given by $\eta = (A_{01}/A_{02})(\lambda_1/\lambda_2)^3$. The scaling factors are given as follows $(5/2)(6/3)^3$, $(5/3)(6/4)^3$, $(5/4)(6/5)^3$ and 1 for the amplitudes of the initial surfaces $A_0 = 20, 30, 40$ and 50 respectively.

Here, η is given by $\beta.\beta'$. So $\eta = \left(\frac{A_{01}}{A_{02}}\right)\left(\frac{\lambda_1}{\lambda_2}\right)^3$. The scaled curves are given in inset of Figure 5b. In addition, we plotted the $log\big(h(0)-h(\tau)\big)-log(\tau)$ plots of initial surfaces which are given in Figure 5a and determined that all obtained curves' slopes were $\alpha \approx 0.35$. Again, in the last part of the study, we determined that the scaling property and α value has not been changed in the cases of taking the values of g as $10^{-5}, 10^{-4}$ and 10^{-3}.

Although it is not shown here, the different initial surfaces (surfaces in the form of $z(x) = h(0) - ax^{\gamma}$ for the values of $\gamma = 1/3, 1/2, 1, 2, 3$) which have been discussed in our study [12] have been examined under the last investigation's conditions. When these initial surfaces had different numbers of steps (N) and the different intersection points (x_0) with the x axis (similar to the initial surfaces investigated in Figure 5), it has been determined that the scaling property of the changes of these surfaces' scaled heights as a function of time was similar to the expression given in eqn. (16). It can be written as follows,

$$h_{N_1,x_{01}}(\tau) = h_{N_2,x_{02}}(\eta'\tau') \qquad (17)$$

The value of η' has been found as $\left(\frac{N_1}{N_2}\right)\left(\frac{x_{01}}{x_{02}}\right)^3$ independent of the g value.

Conclusions

We examined the evolution of a sinusoidal initial surface (below its roughening temperature) in Diffusion Limited regime. The examined surface consists of concentric monoatomic circular steps in two dimensions separated by terraces. The diffusion equation has been solved in two dimensions by using polar coordinates and an equation of motion for each circular step's radius was obtained by assuming the line tension of steps and the entropic repulsion between neighboring steps. In this investigation, we obtained the results by analyzing the surface height's evolution as a function of time are as follows: The surface's height approximately decreases as τ^{α} $(\alpha \approx 0.35)$ and α is independent of the amplitude and the wavelength of the initial surface. The variations in the heights of the surfaces which have different amplitudes (A_{01}, A_{02}) and wavelengths (λ_1, λ_2) scale as $\left(\frac{A_{01}}{A_{02}}\right)\left(\frac{\lambda_1}{\lambda_2}\right)^3$. Moreover, we determined that obtained results were independent of the "g" value.

Acknowledgment

This research did not receive any specific grant from funding agencies in the public, commercial, or not-for-profit sectors.

Conflicts of interest

There are no conflicts of interest in this work.

References

[1] Rettori A., Villain J., Flattening of Grooves on a Crystal Surface: A Method of Investigation of Surface Roughness, *J. Phys. France,* 49 (1988) 257–267.

[2] Uwaha M., Relaxation of Crystal Shapes Caused by Step Motion, *J. Phys. Soc. Jpn.,* 57 (1988) 1681–1686.

[3] Ozdemir M., Zangwill A., Morphological Equilibration of a Corrugated Crystalline Surface, *Phys. Rev. B,* 42 (1990) 5013.

[4] Umbach C.C., Keeffe M.E., Blakely J.M., Scanning Tunneling Microscopy of One Dimensional Periodic Corrugated Silicon Surfaces, *J. Vac. Sci. Technol. A,* 9 (1991) 1014.

[5] Israeli N., Kandel D., Profile of a Decaying Crystalline Cone, *Phys. Rev. B,* 60 (1999) 5946.

[6] Ichimiya A., Hayashi K., Williams E.D., Einstein T.L., Uwaha M., Watanabe K., Decay of Silicon Mounds: Scaling Laws and Description with Continuum Step Parameters, *Appl. Surf. Sci.,* 175–176 (2001) 33–35.

[7] Li M., Wendelken J.F., Liu B., Wang E.G., Zhang Z., Decay Characteristics of Surface Mounds with Contrasting Interlayer Mass Transport Channels, *Phys. Rev. Lett.,* 86 (2001) 2345.

[8] Kodambaka S., Petrova V., Vailionis A., Petrov I., Greene J.E., In Situ High-Temperature Scanning Tunneling Microscopy Studies of Two-Dimensional TiN Island Coarsening Kinetics on TiN (001), *Surf. Sci.,* 526 (2003) 85–96.

[9] Kodambaka S., Israeli N., Bareno J., Swiech W., Ohmori K., Petrov I., Greene J.E., Low Energy Electron Microscopy Studies of Interlayer Mass Transport Kinetics on TiN (111), *Surf. Sci.,* 560 (2004) 53–62.

[10] Kellogg G.L., Bartelt N.C., Surface-Diffusion-Limited Island Decay on Rh(001), *Surf. Sci.,* 577 (2005) 151-157.

[11] Esen M., Tüzemen A.T., Ozdemir M., Equilibration of a Cone: KMC Simulation Results, *Eur. Phys. J. B,* 85 (2012) 117.

[12] Tüzemen A.T., Esen M., Ozdemir M., Scaling Properties of Equilibrating Semiconductor Mounds of Various Initial Shapes, *J. Cryst. Growth*, 470 (2017) 94–98.

[13] Tüzemen A.T., Esen M., Ozdemir M., The Investigation of the Morphology of a Decaying Conic Mound in the Presence of Repulsive and Attractive Step Interactions, *J. Cryst. Growth*, 501 (2018) 1–6.

[14] Gruber E.E., Mullins W.W., On the Theory of Anisotropy of Crystalline Surface Tension, *J. Phys. Chem. Solids.*, 28 (1967) 875-887.

[15] Andreev A.F., Kosevich A.Y., Capillary Phenomena in the Theory of Elasticity, *Sov. Phys. JETP*, 54 (1981) 761.

[16] Marchenko V.I., Parshin A.Ya., Elastic Properties of Crystal Surfaces, *Zh. Eksp. Teor. Fiz.,* 79 (1980) 257-260.

[17] Tanaka S., Bartelt N.C., Umbach C.C., Tromp R.M., Blakely J.M., Step Permeability and the Relaxation of Biperiodic Gratings on Si(001), *Phys. Rev. Lett.,* 78 (1997) 3342.

[18] Jeong H.C., Williams E.D., Steps on Surfaces: Experiment and Theory, *Surf. Sci. Rep*. 34 (1999) 171–294.

[19] Israeli N., Kandel D., Profile Scaling in Decay of Nanostructures, *Phys. Rev. B*, 80 (1998) 3300.

Cumhuriyet Sci. J., 44(1) (2023) 209-217
DOI: https://doi.org/10.17776/csj.1184107

Cumhuriyet Science Journal

| csj.cumhuriyet.edu.tr | Founded: 2002 ISSN: 2587-2680 e-ISSN: 2587-246X Publisher: Sivas Cumhuriyet University

Reclaim of Wrecked Bi-Te Based Materials In Peltier Modules In Thermopower Properties By Mechanical Milling

Mehmet Çetin [1,a], Gizem Durak Yüzüak [2,b], Ercüment Yüzüak [1,c,*]

[1] *Department of Energy Systems, Faculty of Engineering and Architecture, Recep Tayyip Erdogan University, Rize, Türkiye.*
[2] *Rare Earth Elements Application and Research Center, Munzur University, Tunceli, Türkiye.*
**Corresponding author*

Research Article

History
Received: 04/10/2022
Accepted: 26/02/2023

ABSTRACT

We thoroughly evaluated the effects of various treatments on the structural and electrical properties of the two as-cast materials, "Sb-doping Bi-Te (p-type)" and "Se-doping Bi-Te (n-type)" which are frequently present in abandoned Peltier modules. To investigate the thermoelectric properties of Bi_2Te_3-based materials, waste alloys characterized by electrical conductivity using the hot-end method. Alloys were purified by performing arc melting on a water-cooled copper crucible in a vacuum of at least 10^{-3} mbar, with five times melting sessions to assure homogeneity. A single and long milling period of 144 hours is applied. After the compressing operation, the resulting discs with nanostructures were annealed for an hour at 600 K under vacuum conditions. The discs' structural properties were characterized using X-ray diffraction (XRD) and their surfaces and stoichiometries were determined using scanning electron microscopy with an energy dispersive feature. The Seebeck coefficient of the nanoparticle formed n-type Bi-Te based sample is -35.3 $\mu V.K^{-1}$ and p-type Bi-Te based sample is 100 $\mu V.K^{-1}$ (15% of mean error margin). It was found that a notable improvement was attained in comparison to the initial state with the addition of nanoparticles.

Keywords: Peltier modules, BiTe-based, Thermoelectric.

[a] *mehmet_cetin21@erdogan.edu.tr* *https://orcid.org/0000-0001-6422-4634* [b] *gizemdurakyuzuak@munzur.edu.tr* *https://orcid.org/0000-0002-2358-8789*
[c] *ercument.yuzuak@erdogan.edu.tr* *https://orcid.org/0000-0002-2521-9362*

Introduction

Thermoelectric energy conversion (TEC) has been demonstrated as an alternate method to capture the waste heat, which is frequently situated in our environment, and convert it into electrical energy in a very cost-effective manner. TEC-based generators and derivatives have the possibility of providing an alternate option to encounter the world's energy needs and to act as a source for numerous novel ideas, such as self-generating gadgets and wearable energy technology [1, 2]. The efficiency of the material used for energy conversion is one of the most significant issues that arise in thermoelectric applications. More effective materials can be generated thanks to advancements in thermoelectric material production processes, and innovative-technologies can boost the electrical outputs and efficiencies of currently used materials. The characteristics in yield can be used to categorize energy systems lead out of thermoelectric materials, and these production parameters are influenced by the material properties used. The figure of merit (ZT), a term used to describe the performance of materials, also be used to describe these materials;

$$ZT = \frac{S^2 \sigma T}{\kappa} \quad (1)$$

where, S ($\mu V.K^{-1}$) is Seebeck coefficient, σ ($S.m^{-1}$) is electrical conductivity, T is temperature (K) and κ ($W.K^{-1}.m^{-1}$) is thermal conductivity [1]. Materials having a high Seebeck coefficient, high electrical conductivity, and low thermal conductivity are required for a good ZT output, per the equation, which we can define as the coefficient of performance.

Investigators set their sights on increasing the value of ZT from its default value of one of Eq. 1, considered a threshold. All investigations that have succeeded in increasing the performance coefficient above this amount have employed nano-structured material engineering [3]. Many novel techniques, such alloying nano systems [4], nano wires [5], and thin-film layered structures [6], have been introduced to increase material yield, and there have been extensive investigations into the progress of the thermoelectric effect and, by extension, thermoelectric materials. When Li et al. [7] exhibited a picture of the combined electrical structure and phonon mismatch in a single Sn-Se crystal system, they provided novel insight into how to attain low thermal conductivity. Equation 1 reveals that decreasing heat conductivity is an excellent strategy. However, other strategies have been developed to boost thermoelectric efficiency, including expanding the Seebeck coefficient by electronic band topologies and band changes [8] and decreasing thermal conductivity via nano-induced-configuration as thin films and/or ball-milled [9-18].

Seebeck coefficient, which allows for improvement of both the performance coefficient and the electrical output, is a highly essential parameter in the creation of improved thermoelectric materials since it yields better

results with the usage of nano-sized systems. There are a variety of approaches that have been used to create materials with improved output performances. Progress was accomplished in present work by raising the Seebeck coefficient and employing a mechanical grinding mechanism to decrease large-scale thermoelectric materials to nano dimensions, resulting in an unusual shape. Mechanical grinding is employed, and the method chosen is one that can be used and maintained at minimal expense. Having been removed from an inoperable Peltier module, the thermoelectric materials that undergo grinding are considered trash. Thus, impressive outcomes have been achieved, with the potential for a Seebeck coefficient rise of up to a factor of 2. It has been demonstrated, however, that discarded thermoelectric materials may be re-evaluated and put to a good use through a variety of methods.

Degradation or damage to the thermoelectric material is a typical cause of thermoelectric module failure [19]. Temperature extremes, corrosion, and mechanical wear and tear are only some of the potential causes. In order to get non-functional thermoelectric materials back into service, it is usually required to pinpoint the root of the problem and fix it. If the thermoelectric material failed due to corrosion or oxidation, for instance, it can be salvageable by scraping off the corroded or oxidized outer layers and applying a protective coating or through an annealing procedure. It may be essential to modify the module to reduce stress on the material, or to repair or replace the damaged components, if the breakdown was brought on by thermal stress or mechanical damage. When trying to enhance the effectiveness of a thermoelectric material, it's not enough to just deal with the material-specific issues that can affect performance; the module design also needs to be optimized. By optimizing the temperature gradient across the module, heat transport can be enhanced, and parasitic losses can be minimized.

The performance and dependability of thermoelectric materials and modules have been the subject of several investigations. New materials and production methods have been the focus of recent research for thermoelectric device improvement [20, 21]. Others have studied what causes thermoelectric modules to degrade and fail, and they have provided solutions to these problems [22-24]. In conclusion, research into re-activating inactive thermoelectric materials in Peltier modules is an important topic with the potential to increase the durability and efficiency of thermoelectric devices in a variety of settings.

The purpose of bringing inoperable thermoelectric materials back into use in Peltier modules is to get them working again so they can be put to use in thermoelectric applications. Peltier modules use thermoelectric materials to create power from a temperature difference between their heated and cooled sides. However, the effectiveness of the module can diminish or be rendered useless if the thermoelectric materials deteriorate or are destroyed over time. Restoring the functioning of non-functional thermoelectric materials requires determining what caused the material's failure or degradation, then adopting solutions to fix the problems. Methods for this include cleaning the surface of the material to get rid of any impurities or corrosion, fixing or replacing any broken parts, and adjusting the module's design for better heat transfer and less stress. The purpose of putting the Peltier module back into service is not just to restore its original functionality, but to enhance its performance as well. The module's performance and its capacity to convert thermal energy into electrical energy can be enhanced by addressing the reasons that have contributed to material degradation or failure. The overall objective of re-operating inoperable thermoelectric materials in Peltier modules is to increase the lifespan of these modules and improve their performance, which can have significant implications for a variety of applications in fields like energy harvesting, cooling, and temperature sensing. This research serves as a set of answers to the question posed in the above. Separating the Peltier modules' n and p type materials allowed scientists to use the nanoparticle production process to the wasteful materials in an effort to reclaim some re-usable product.

Experimental

The electrical conductivity type was used to sort out the waste Peltier module and eliminate the Bi-Te alloys at first. The hot-end technique is used to determine if a semiconductor material is n- or p-type. A source-meter was used to assess the sort of conductivity present in the materials by measuring the voltage produced by the semiconductor when different temperatures were applied to each end.

Thermoelectric characteristics may be characterized and explored once waste Bi_2Te_3-based materials have been sorted according to conductivity classes. The arc melting technique was used to remove impurities like carbon (C) and oxygen (O) and to give a homogeneous appearance. As part of the arc melting procedure, the components were initially put in a copper crucible cooled with water before being subjected to a vacuum of up to 10^{-3} mbar and heated to melting point. This process, performed in an Edmund Bühler arc furnace, was carried out five times to provide sufficient uniformity and purity.

Initially, bulk samples were obtained; thereafter, a mechanical grinding technique was developed to conceive uniform nanostructures from Bi_2Te_3-based material. A ball mill system was constructed using steel balls, a grinding chamber, and a rotating mechanism, and grinding was performed using the planetary grinding principle with a ball-to-material ratio of 10:1 and rotation values of 150 rpm. By rotating the chamber on its own axis, centrifugal force is generated, causing the materials and balls within to move around the chamber. Due to the constant movement and wall contact of the balls, the materials in the chamber are constantly being broken down into ever-smaller increments. We used present method throughout the course of 144 hours. The nanoparticles obtained from

the grinding process were annealed for 1 hour in a vacuum environment at 600 K using a Pfeiffer brand Hi-Cube vacuum station in order to avoid oxidation, decrease stress, and homogenize them. The powder was then compressed to the required particle size and pore type in an alloy pressing process. After milling the samples into a powder, they were cold pressed for an hour at 10 MPa. The procedure used to process the samples is depicted in Figure 1. Connections were built between n- and p-type materials, electrically in series and thermally in parallel, to characterize the materials' electrical properties and build a thermoelectric module.

.

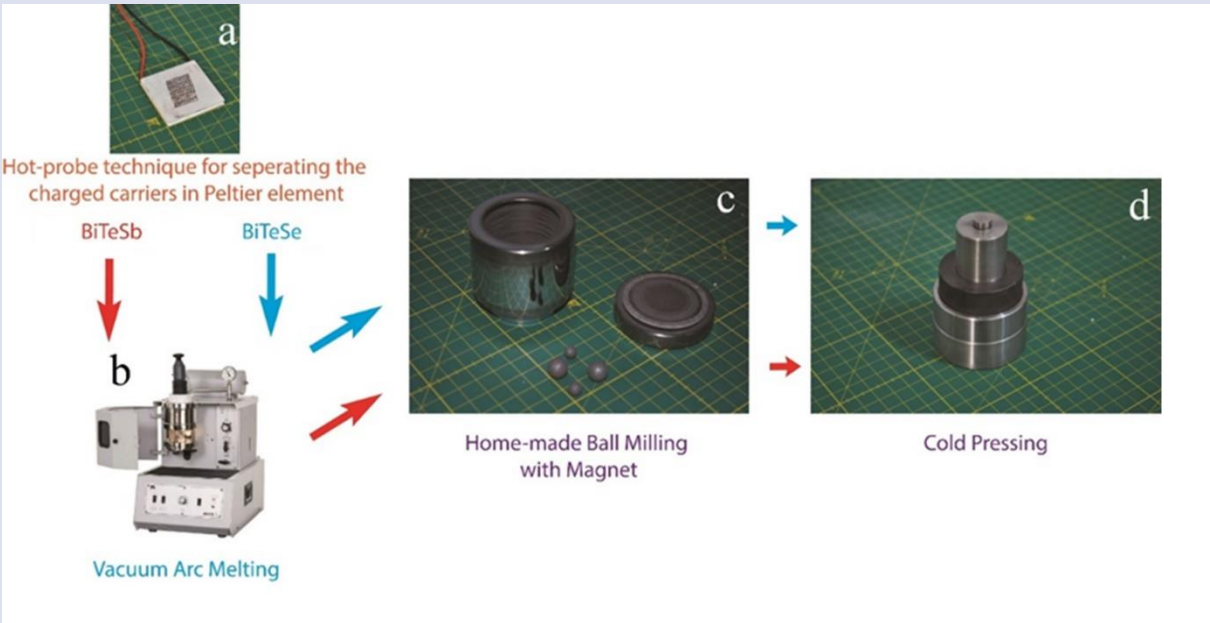

Figure 1. Processing of waste thermoelectric materials **a)** Separating n- and p-type semiconductors from the Peltier module, **b)** Preparing the samples by arc melting method, **c)** Performing the grinding process with the designed mechanical grinding system, **d)** Bringing the samples into the desired form by applying press.

Thermoelectric measurements were done after the silver paste connection was made by heating one side of the material while cooling the other. Figure 2a displays the results of the efficient and cost-effective hot-end approach used to characterize BiSbTe and BiSeTe nanoparticles (NPs). Via this method, copper wires are attached to the voltage meter's positive and negative terminals to reduce the meter's temperature rise. A distance of 1 cm must be maintained between the hot spot end of the copper wire pair and the cold end of the wire throughout the duration of the measurement to guarantee a fair comparison. A rapid increase in temperature at the probe's tip rather than the more gradual rise in temperature that would occur over a longer distance might lead to inaccurate voltage measurements. This has prompted investigations into the precise relationship between the reported voltage, the measured temperature, and the measured particle size. Instruments like the Keithley 2461 time-dependent source-meter, the Lakeshore 335 with a Si diode for temperature readings, and the Keithley 2220 electronic programmable power supply all contribute to the so-called "hot-end approach" (Figure 2b). With the use of a Keithley 2461, the difference in electrical potential between the module's two terminals was determined. A thermal imaging camera and Si-diode were used to take temperature readings from the sample's contact sites at various current levels. The error margin for the reported voltage per temperature values was 15% on average. This figure is rather close to what has been found in another research [1]. The structural and morphological features of the manufactured materials were analyzed by X-ray diffraction (XRD), scanning electron microscopy (SEM), and energy dispersive x-ray (EDX) techniques.

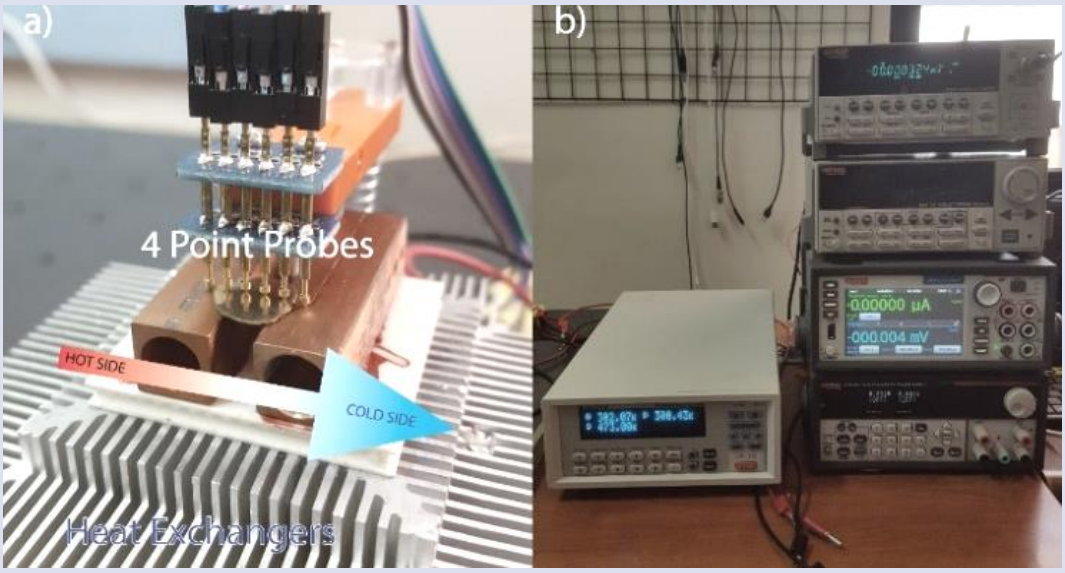

Figure 2. **a)** The hot-end measurement system designed for the characterization of the produced nanoparticles, **b)** The used devices in the study (Keithley 2461, Lakeshore 335, Keithley 2230).

Results and Discussions

X-ray diffraction analysis was used to learn more about the nanostructured discs of BiSbTe and BiSeTe that were synthesized. The as-cast and NPs' of BiSbTe and BiSeTe of XRD patterns are shown in Figures 3a and 3b, respectively. In the range of 2θ=20-110°, BiTe was identified by its diffraction peaks at 17°, 28°, 38°, 41°, 43°, 50°, 56°, and 70°. Diffraction peaks of milled alloys show the absence of several peaks ((0 0 6), (0 0 15), and (0 0 21)) that were previously present in the un-milled Sb-doping Bi-Te and Se-doping Bi-Te samples. Deformation caused by milling at room temperature is confirmed by the removal or decrease in peak intensities of reflections from basal planes. Both 2θ=26.5° and 29.5° were investigated in detail to highlight the distinctions between BiSbTe and BiSeTe in Figure 3b. It was predicted that there would be a difference of around 0.5° between the Bragg locations of the n-type and p-type materials that were produced. This scenario agrees with findings from earlier research [15, 16, 17]. Based on using the well-known Debye-Scherrer equation (D=(kλ/β.cosθ)) depicted in Figure 3b, we may infer the crystallite size and the lattice strain generated by the milling operation. Results showed that both crystal-sizes decreased without substantially altering the unit cell. Furthermore, the XRD analysis reveals that the full-with-half-maximum values of the patterns rise with essentially no change in the unit cell characteristics for both the "Sb doped" and the "Se doped" samples after the long-term low alloying technique has been applied. As a result of minimizing flaws and applying low energy to the materials over a prolonged period of time, nanoparticles have been formed. Based on the XRD data, it appears that the ball milling has a systematic effect on the crystal orientation, as seen in Figure 3b.

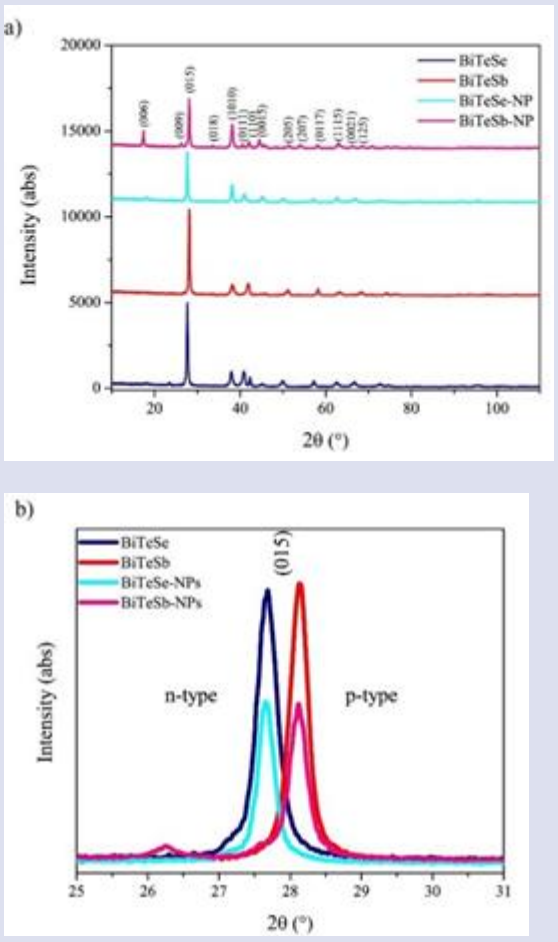

Figure 3. a) XRD patterns of as-cast and NPs' of n- and p-type BiTe alloys, and b) $(015)_{hkl}$ Bragg position of n-type and p-type materials, nanoparticles are named NPs'.

SEM was used for energy dispersive X-ray (EDX) examination to learn about the elemental composition and presence of contaminants. Figures 4a and 4b display SEM images that reveal surface information. The samples show a uniform surface roughness. The results of the EDX study may be seen in Figures 4c and 4d. It was predicted that one sample would have a high Sb content and the other a high Se content, and both predictions turned out to be true. We were able to extrapolate some information about the materials' n-type and p-type behaviors from this finding. Figures 4e and 4f also provide elemental mapping analyses, which reveal the realization of elemental distributions like Bi, Sb, Se, and Te inside the material. In order to prevent confusion, we ignore elements that make up less than 1% of the atom. The intended meaning was preserved while providing a clear interpretation.

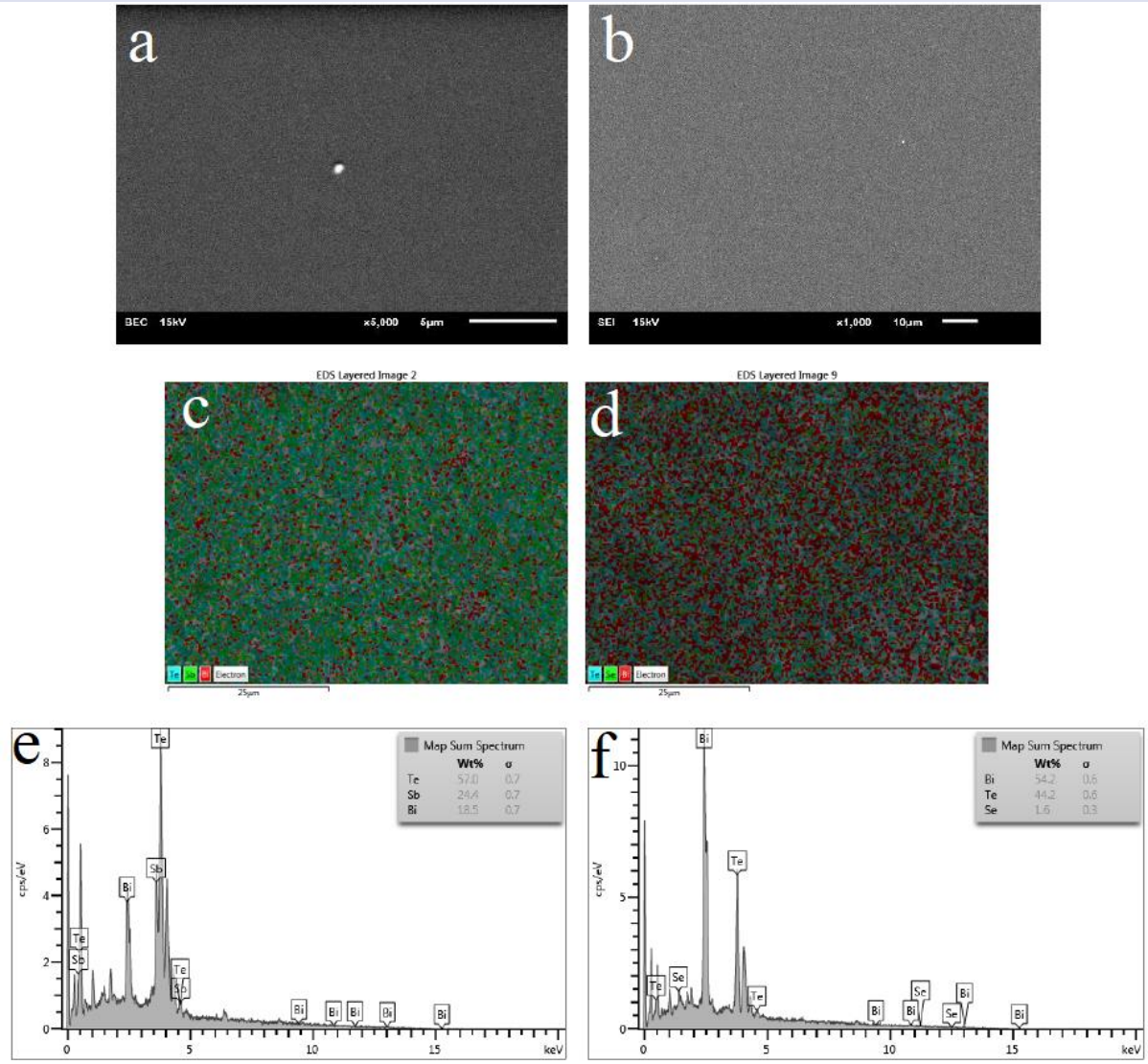

Figure 4. Structural and morphological analysis of materials, a) BiSbTe SEM image, b) BiSeTe SEM image, c) BiSbTe elemental mapping analysis, d) BiSeTe elemental mapping analysis, e) BiSbTe elemental spectrum, f) BiSeTe elemental spectrum.

Electrical measurements were taken of the materials, and the surface temperatures were measured using a thermal camera so that the Seebeck coefficients could be calculated (Figures 5a and 5b). Individual temperature calibrations and measurements were done for n and p type materials before the connections were established. Following that, it was mixed with silver paste and subjected to the aforementioned procedures again and again while still in module form. During the measurement, we subjected the heater capsule on the hot side of the manufactured module to varying currents while keeping a close eye on the temperature variations in the module's legs using a thermal imaging camera. Silver paste was used to link the legs of p-type BiSbTe and n-type BiSeTe alloys to copper wires, and the resulting resistance changes were measured.

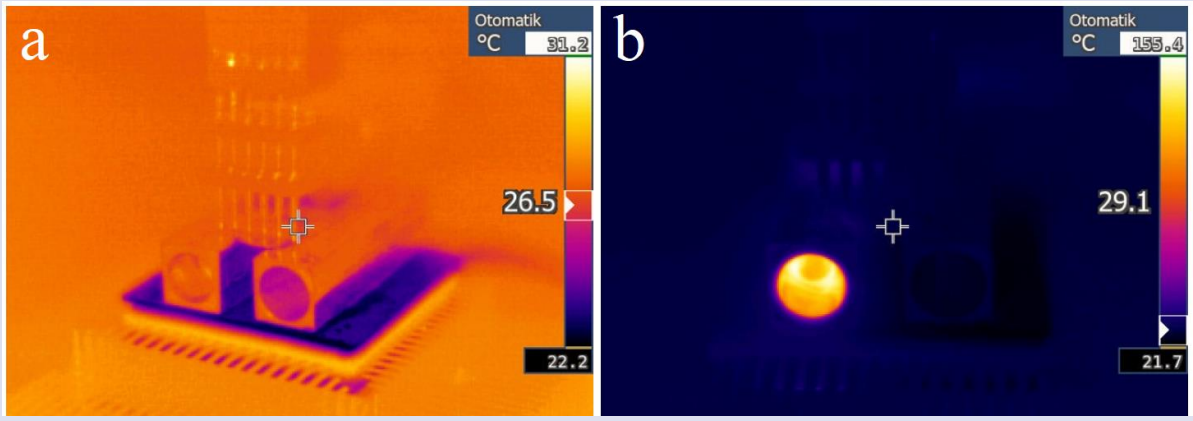

Figure 5. Thermal camera images taken from the samples, a) the temperature measured when 0 A current is applied, and b) the temperature values measured under the current of 1.4 A.

As a result, we placed in the hot tip to varying currents, ranging from minimum (0 A, as seen in Figure 5a to maximum (1.4 A), and recorded the resulting temperatures at various intervals. The maximum recorded temperature was 428 K (155°C). However, when this highest value that can be obtained brings with it some problems for the measurement system that is not in a vacuum atmosphere, in this study, the software has been developed for a programmable power supply up to a maximum current value of 0.5 A, so that the temperature difference of 22.5 K will be achieved. The thermal camera photos were taken in real time, therefore the values discovered are accurate representations of what was happening within the resistor capsule.

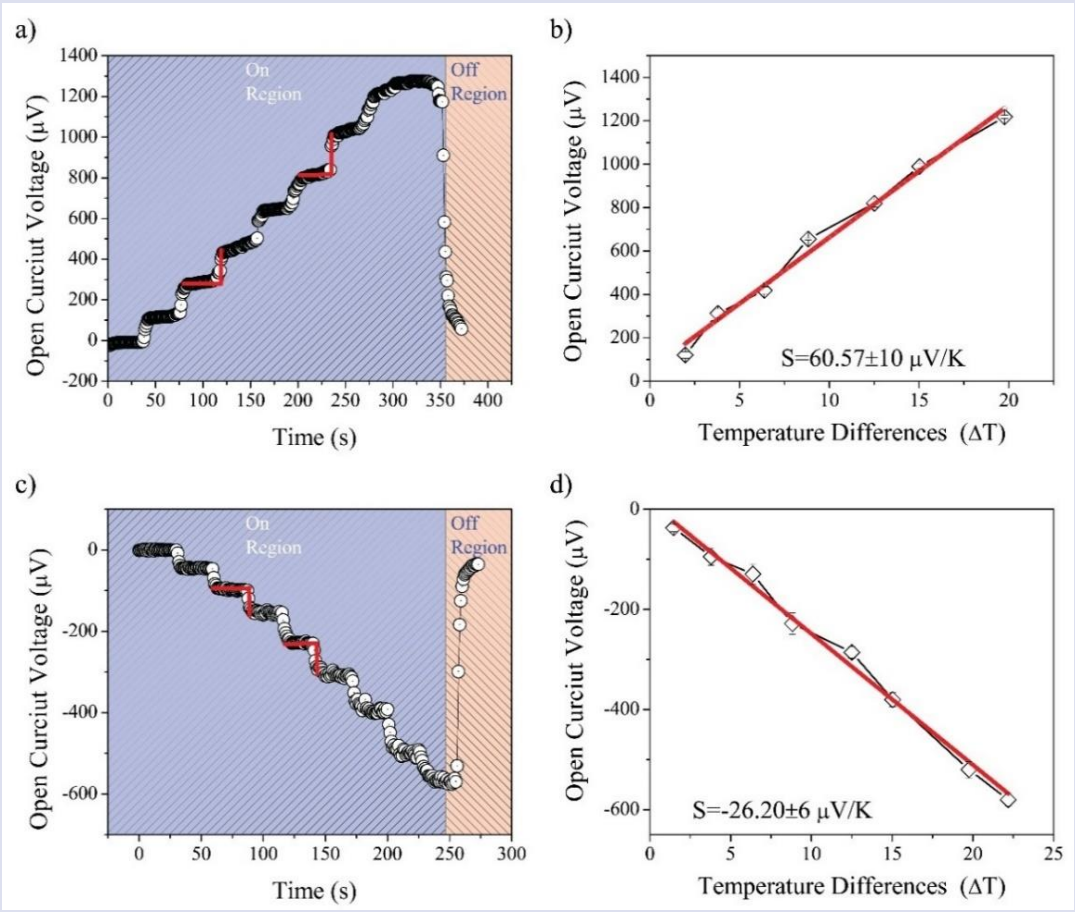

Figure 6. As-cast formed **a)** and **b)** p-type (Sb-doping), **c)** and **d)** n-type (Se-doping) materials time dependent voltage values and calculated Seebeck coefficient, respectively.

Figures 6 and 7 reveal the time- and temperature gradient-dependent electrical open circuit voltage curves of n-type and p-type materials, respectively, acquired prior to NPs' synthesis. It's easy to tell the difference between the n-type and p-type BiTe curves because of the different symmetry of the two materials. Figures 6a and 6b show the results of the Seebeck coefficient calculation using the temperature differential determined from the contact locations on the sample surface using a thermal camera. Figures 7a and 7b display the electrical values recorded following the fabrication and annealing of nanoparticles. Table 1 lists the calculated Seebeck coefficients based on these values.

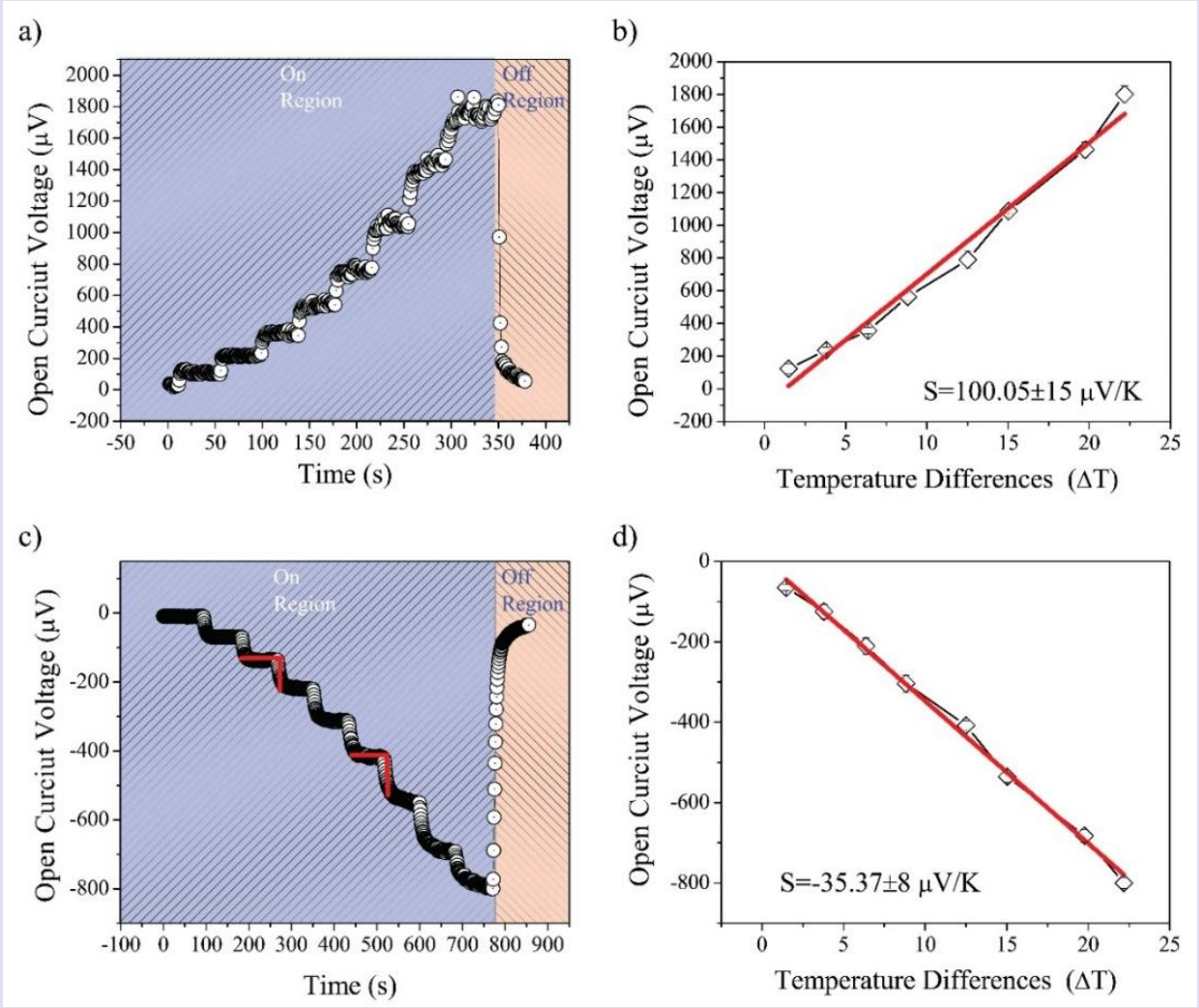

Figure 7. NPs' formed **a)** and **b)** p-type (Sb-doping), **c)** and **d)** n-type (Se-doping) materials' time dependent voltage values and calculated Seebeck coefficient, respectively.

Contrarily, there has been a lot of study done on thermoelectric materials based on thin films and milled alloys that make better use of nanostructures. Studies of thin films and milled alloys have also been substantial, and the possibility of incorporating such structures with textile goods by exploiting their adaptability has been considered [10, 11]. Table 1 provides information on the electrical outputs of a few thermoelectric materials. As can be seen in table 1, various significant advances have been made in order to increase the ZT of thin-formed and milled alloys for thermoelectric materials. The power factor improvement or the thermal conductivity reduction from microstructure engineering is the root causes of the ZT improvement.

Table 1. Electrical outputs from a selection of published nanoparticles' research

Material System	Seebeck Coefficient, S (μV/K)	Electrical Conductivity, σ (S/cm)	Electrical Resistivity, ρ ($10^{-3}\Omega.cm$)	Thermopower (S2σ) (10^{-4} W/m.K^2)
n-Bi-Te *[11]*	-118.6	674	1,48	9,5
n-Bi-Te *[12]*	-242	360	2,77	21
n-Bi-Te *[13]*	-163	1025	0,97	27,3
n-Bi-Te *[14]*	-175	1204.3	0,83	35,2
p-Sb-Te *[14]*	155	1612.9	0,62	35,9
p-Bi-Te *[15]*	170	450	2,22	13
p-Bi-Te *[25]*	32.6	188.1	5.31	2
n-Bi-Te *[26]*	-105	1265.8	0.79	13.9
n-Bi-Te *[27]*	-172	69.9	14.3	2.07
Present Study Commercial n-Bi-Te	-26.2	1200	0.83	0.8
Present Study Commercial p-Bi-Te	60.5	900	1.11	3.2
Present Study NP n-Bi-Te	-35.3	1100	0.9	1.3
Present Study NP p-Bi-Te	100	750	1.31	7.5

Conclusions

In the present report, nanostructured Bi-Te-based alloys in defunct Peltier modules were made using conventional arc melting and a ball-milling method, and their structural, electrical, and thermal characteristics were investigated and employed to show off high-efficiency TEG modules for a heat-recovery scheme. Present advancements in this field have focused on simplifying, cheapening, and scaling up the manufacture of nanostructured materials, all in service to the creation of more effective thermoelectric devices. The following are some of the goals of this research along these lines:

Two distinct types of n-type (Se-doping) and p-type (Sb-doping) in BiTe systems were identified based on the nano-structuring used.

In order to better understand the thermoelectric effects, the argument suggests that additional study into energy harvesting from discarded gadgets is required. When the system is being subjected to temperature-induced changes, it is necessary to gain temperature dependency of thermal conductivity and Seebeck curves. If these actions are taken, it will be possible to gather valuable data that will advance the field.

Because low-speed rates inhibit the recovery and recrystallization process and encourage fracture, nanostructures with high density interfaces and defects (dislocation) can be obtained in a short amount of time by milling at low-speed rates in the nanoparticle manufacturing process (low speed - long time grinding).

The research provides more evidence that nano-structured materials can boost thermopower. As a last research recommendation, it is crucial to understand the significance of the ZT value by determining the thermal conductivity coefficient of such substances.

Acknowledgments

This work was supported by the Scientific and Technological Research Council of Turkey-TÜBİTAK, 2209-A Research Project Support Program for Undergraduate Students and it was performed at the Functional Materials Research Laboratory in Recep Tayyip Erdogan University. The authors would like to thank Sedanur Baltacı and Gaye Dülger for their helpful contributions.

Conflicts of interest

The authors declare that they have no conflict of interest.

References

[1] Shi X.-L., Zou J., and Chen Z.-G., Advanced Thermoelectric Design: From Materials and Structures to Devices, *Chemical Reviews,* 120 (2020) 7399-7515.

[2] Finn P.A., Asker C., Wan K., Bilotti E., Fenwick O., Nielsen C.B., Thermoelectric Materials: Current Status and Future Challenges, *Frontiers in Electronic Materials,* 1 (2021) 677845.

[3] Rojas J.P., Singh D., Inayat S.B., Sevilla G.A.T., Fahad H.M., Hussain M.M., Micro and nano-engineering enabled new generation of thermoelectric generator devices and applications, *ECS Journal of Solid-State Science and Technology,* 6 (3) (2017) N3036.

[4] Pan Y., Li J.F., Thermoelectric performance enhancement in n-type $Bi_2(TeSe)_3$ alloys owing to nanoscale inhomogeneity combined with a spark plasma-textured microstructure, *NPG Asia Materials,* 8 (6) (2016) e275-e275.

[5] Boukai A.I., Bunimovich Y., Tahir-Kheli J., Yu J.-K., Goddard III W.A., Heath J.R., Silicon nanowires as efficient thermoelectric materials, *Nature,* 451 (7175) (2008) 168-171.

[6] Yüzüak G.D., Çiçek M.M., Elerman Y., Yüzüak E., Enhancing the power factor of p-type BiSbTe films via deposited with/without Cr seed layer, *Journal of Alloys and Compounds*, 886 (2021) 161263.

[7] Li C.W., Hong J., May A.F., Bansal D., Chi S., Hong T., Ehlers G., Delaire O., Orbitally driven giant phonon anharmonicity in SnSe, *Nature Physics,* 11 (12) (2015) 1063-1069.

[8] Pei Y., Wang H., Snyder G.J., Band engineering of thermoelectric materials, *Advanced Materials,* 24 (46) (2012) 6125-6135.

[9] Zhao L.D., Wu H.J., Hao S.Q., Wu C.I., Zhou X.Y., Biswas K., He J.Q., Hogan T.P., Uher C., Wolverton C., Dravid V.P., Kanatzidis M.G., All-scale hierarchical thermoelectrics: MgTe in PbTe facilitates valence band convergence and suppresses bipolar thermal transport for high performance, *Energy & Environmental* Science, 6 (11) (2013) 3346-3355.

[10] Goncalves L.M., Couto C., Alpuim P., Rolo A.G., Völklein F., Correia J.H., Optimization of thermoelectric properties on Bi_2Te_3 thin films deposited by thermal co-evaporation, *Thin Solid Films,* 518 (10) (2010) 2816-2821.

[11] Nuthongkum P., Sakdanuphab R., Horprathum M., Sakulkalavek A., [Bi]:[Te] Control, Structural and Thermoelectric Properties of Flexible Bi_xTe_y Thin Films Prepared by RF Magnetron Sputtering at Different Sputtering Pressures, *Journal of Electronic Materials,* 46 (11), (2017), 6444-6450.

[12] Wang X., He H., Wang N., Miao L., Effects of annealing temperature on thermoelectric properties of Bi_2Te_3 films prepared by co-sputtering, *Applied Surface Science,* 276 (2013) 539-542.

[13] Kurokawa T., Mori R., Norimasa O., Chiba T., Eguchi R., Takashiri M., Influences of substrate types and heat treatment conditions on structural and thermoelectric properties of nanocrystalline Bi_2Te_3 thin films formed by DC magnetron sputtering, *Vacuum,* 179 (2020) 109535.

[14] Lee C.W., Kim G.H., Choi J.W., An K.-S., Kim J.-S., Kim H., Lee Y.K., Improvement of thermoelectric properties of Bi_2Te_3 and Sb_2Te_3 films grown on graphene substrate, *Physica Status Solidi (RRL)–Rapid Research Letters,* 11 (6) (2017) 1700029.

[15] Budnik A.V., Rogacheva E.I., Pinegin V.I., Sipatov A.Y., Fedorov A.G., Effect of initial bulk material composition on thermoelectric properties of Bi_2Te_3 thin films, *Journal of Electronic Materials*, 42 (7) (2013) 1324-1329.

[16] Ahiska R., Mamur H., Uliş M., Termoelektrik modülün jeneratör olarak modellenmesi ve deneysel çalışması, *Gazi Üniversitesi Mühendislik Mimarlık Fakültesi Dergisi,* 26 (4) (2011) 889-896.

[17] Hayati M., Bhuiyan M.R.A., Korkmaz F., Nil M., A review on bismuth telluride (Bi_2Te_3) nanostructure for thermoelectric applications, *Renewable and Sustainable Energy Reviews,* 82 (2018) 4159-4169.

[18] Yüzüak G.D., Özkan S., Yüzüak E., Unraveling energy consumption by using low-cost and reevaluated thermoelectric Thin Films, *Turkish Journal of Physics,* 44 (5) (2020) 442-449.

[19] Rocha Liborio Tenorio H.C., Vieira D.A., De Souza C.P., Measurement of parameters and degradation of thermoelectric modules, *IEEE Instrumentation & Measurement Magazine*, 20(2) (2017) 13-19.

[20] Zebarjadi M., Esfarjani K., Dresselhaus M.S., Ren Z.F., Chen G., Perspectives on thermoelectrics: from fundamentals to device applications, *Energy & Environmental Science*, 5 (1) (2012) 5147-5162.

[21] He J., Tritt T.M., Advances in thermoelectric materials research: Looking back and moving forward, *Science*, 357 (6358) (2017) 1-9.

[22] Shilpa M.K., Raheman M.A., Aabid A., Baig M., Veeresha R.K., Kudva N., A Systematic Review of Thermoelectric Peltier Devices: Applications and Limitations, *FDMP-Fluid Dynamics & Materials Processing,* 19 (1) (2023) 187–206.

[23] Barako M.T., Park W., Marconnet A.M., Asheghi M., Goodson K.E., Thermal Cycling, Mechanical Degradation, and the Effective Figure of Merit of a Thermoelectric Module, *Journal of Electronic Materials,* 42 (3) (2013) 372–381.

[24] Karri N.K., Mo C., Geometry optimization for structural reliability and performance of a thermoelectric generator, *SN Applied Sciences,* 1 (9) (2019) 1097.

[25] Anandan P., Omprakash M., Azhagurajan M., Arivanandhan M., Rajan Babu D., Koyama T., Hayakawa Y., Tailoring bismuth telluride nanostructures using a scalable sintering process and their thermoelectric properties, *Cryst.Eng.Comm.*, 16 (34) (2014) 7956-7962.

[26] Kim C., Kim D.H., Han Y.S., Chung J.S., Park S.H., Him H., Fabrication of bismuth telluride nanoparticles using a chemical synthetic process and their thermoelectric evaluations, *Powder technology*, 214 (3) (2011) 463-468.

[27] Zou P., Xu G., Wang S., Thermoelectric Properties of Nanocrystalline $Bi_2(Te_{1-x}Se_x)_3$ Prepared by High-Pressure Sintering, *Journal of Electronic Materials*, 44 (6) (2015) 1592-1598.

Cumhuriyet Sci. J., 44(1) (2023) 218-223
DOI: https://doi.org/10.17776/csj.1193669

Cumhuriyet Science Journal

| csj.cumhuriyet.edu.tr | Founded: 2002 ISSN: 2587-2680 e-ISSN: 2587-246X Publisher: Sivas Cumhuriyet University

Description of 2_3^+, 0_3^+ Intruder States in ^{130}Xe Nucleus by Mixing of Transitional Hamiltonian and O(6) Casimir Operator

Zahra Jahangiri Tazekand [1,a,*], Hadi Sabri [1,b]

[1] *Department of Physics, University of Tabriz, 51664-16471,Tabriz, Iran.*
**Corresponding author*

Research Article

History
Received: 24/10/2022
Accepted: 13/03/2023

ABSTRACT

In this paper, we tried to describe the 2_3^+, 0_3^+ intruder stats in ^{130}Xe nucleus in a configuration mixing framework. To this aim, we have used a transitional Hamiltonian based in the affine SU(1,1) lie algebra in the framework of interacting boson model. Also, we perturbed this Hamiltonian in the version 2 with adding a new term, the O(6) Casimir operator, due to the nature of these intruder states. The results confirm the accuracy of this mixing configuration in the description of all considered energy levels and especially, the intruder states. Also, these results suggest same approach with adding other Casimir operators of different symmetry chains to extend the ability of this transitional Hamiltonian.

Keywords: Affine algebra, Casimir operator, Intruder state, Transitional Hamiltonian.

[a] z.jahangiri@tabrizu.ac.ir https://orcid.org/0000-0002-5089-0836 [b] h-sabri@tabrizu.ac.ir https://orcid.org/0000-0002-5919-3295

Introduction

The existence of states belong to excited enrgy bands between the levels of ground band of energy refered to the mixing of symmetries. As have been shown in various spectroscopic selective experiments, *e.g.* transfer reactions in particular, very near to closed shells (the In and Sb nuclei at Z=50 but also in other mass regions, *e.g.* the Tl and Bi nuclei at Z=82) some low-lying extra states, so-called intruder states have been observed with a conspicuous energy dependence on the number of free valence neutrons, hinting for 2*p*-2*h* excitations as their origin [1-9]. If these excitations are proton excitations combined with the neutron degree of freedom appearing on both sides of the Z=50 closed shell, such as condition which are available for ^{130}Xe isotope, it is a natural step to suggest that low-lying extra 0^+ excitations will also show up in the even-even nuclei in between. Because the^{130} Xe isotope with a large number of valence neutrons are situated near to the -stability line, they could be studied and must describe by such formalism which perturbed by some excitation [1-2]. The interacting boson model (IBM) Hamiltonian is regards as the most successful formalism in description of such concepts. IBM was written from the beginning in second quantization form in terms of the generators of the U(6) unitary lie algebra. The model assumes that low-lying collective excitations of the nucleus can be described in terms of the number *N* bosons. The bosons correspond to pairs of nucleons in valance shell, coupled to angular momentum j=0 and j=2 which correspond respectively to s and d boson and N is constant for a given nucleus and equal to half its number of valance nucleons [3-15]. The phenomenological IBM in terms of U(5), SU(3) and O(6) dynamical symmetries has been employed in describing the collective properties of several medium and heavy mass nuclei. These dynamical symmetries correspond to harmonic vibrator, axial rotor and $\gamma-$unstable rotor as the geometrical analogues, respectively. These symmetries are fairly successful in the investigation of low-lying nuclear states of nuclei located in three dynamical limits of IBM. On the other hand, the analytic description of structure at the critical point of phase transition is considered as issue, recently great analyses has been performed to describe them. Iachello in Refs [16-22] have established a new set of dynamical symmetries, i.e. *E*(5) and *X*(5), for nuclei which are located at the critical point of transitional regions. The *E*(5) symmetry describes a second order phase transition which corresponds to the transitional states in the region from *U*(5) to *O*(6) symmetries in the IBM [22-24].

Different studies on the^{130} *Xe* nucleus report the excitation of as intruder states. The low-lying 2_3^+ and 0_3^+ levels arises either from the intruder 2p-2h or from the normal 0p-0h configuration ,low-lying of these isotope are formed from the mixing of two intrinsic states of different deformations These levels are classified as two phonon states where must describe by 2p-2h excitation [26-37] A method to describe the intruder excitations in the IBM framework proposed to associate the different shell-model spaces of 0P-0h, 2p-2h,etc excitations. In this approach, two or four protons in the *z*=50-82 major shell can be excited to next major shell. These excitations make the corresponding boson spaces including *N,N+2,*... bosons which $N= N_\pi + N_\nu$,The Hamiltonians of formalisms

in description of such levels have the $\hat{H} = \hat{H}_{reg} + \hat{H}_{2p-2h}$ form where mixes the regular (0*p*-0*h*) and (2p-2h) configurations. The correlation between valence protons and neutrons is enhanced [8-22] due to this cross-shell excitation of protons resulting in the lowering of excited 2_3^+ and 0_3^+ states and therefore, classified them as intruder states.

In this paper we used i) the *U*(5)-*SO*(6) transitional Hamiltonian which is defined in the affine *SU*(1,1) algebra and ii) Due to the nature of the considered intruder levels, we added the *O*(6) Casimir operator as the perturbation to the both regular Hamiltonians. The efficiency of these both approaches are analyzed with comparison of their predictions for different energy levels and the experimental counterparts.

Theoretical Framework

The nature of $0_3^+, 2_3^+$ in ^{130}Xe is reported in Ref [9] which correspond with *SO* (6) symmetry of IBM. In the first part of this study we used a transitional Hamiltonian which describe both *U*(5) and *O*(6) limits as regular part to cover the spherical properties of the considered nucleus. The analytic description of nuclear structure at the critical point of phase transitions has attracted extensive interest in the recent decades. One has to employ some complicated numerical methods to diagonalize the transitional Hamiltonian in these situations but Pan et al. [23-24] have proposed a new solution based on algebraic technique and explores the properties of nuclei classified in the U(5)↔SO(6) transitional region of IBM. Hamiltonian with two control parameters was used in which the results for the control parameter of transitional Hamiltonian offer a combination of spherical and deformed shapes in different isotopic Also, this Hamiltonian extended by adding a corresponding *O*(6) operator to increase the effect of *O*(6) symmetry and increase the accuracy of this formalism in description of intruder levels as:

$$\hat{H}_{extended} = \hat{H}_{SU(1,1)} + \eta \hat{C}_{2(SO(6))}, \quad (1)$$

η is a constant which extract in comparison with experimental data. By employing the generators of SU(1,1) algebra, a Hamiltonian construct which is suitable for the investigation of such nuclei which located between U(5) and SO(6) limits The SU(1,1) algebra has been described in Refs[23-24]. Here, we briefly outline the basic ansatz and summarize the results. The lie algebra corresponds to the SU(1,1)lie algebra is generated by $S^\nu, \nu = 0$ and $\pm$, which satisfies the following commutation relations:

$$[S^0, S^\pm] = \pm S^\pm \ , \quad [S^+, S^-] = -2S^0 \quad (2)$$

The Casimir operator of *SU*(1,1) group can be written as:

$$\hat{C}_2 = S^0(S^0 - 1) - S^+S^- \equiv \hat{C}_{2(SO(6))} \quad (3)$$

We would use this operator to describe some intruder states which have *SO*(6) nature which detailed are present in the following. Representations of *SU*(1,1) are determined by a single number κ, thus the representation of Hilbert space is spanned by orthonormal basis $|\kappa\mu\rangle$ where κ can be any positive number and $\mu = \kappa, \kappa+1, \ldots$. Therefore,

$$\hat{C}_2(SU(1,1))|\kappa\mu\rangle = \kappa(\kappa-1)|\kappa\mu\rangle \ , \ S^0|\kappa\mu\rangle = \mu|\kappa\mu\rangle \quad (4)$$

In IBM, the generators of s and $d-$bosons pairing algebra is created by:

$$S^+(d) = \frac{1}{2}(d^\dagger . d^\dagger) \ , \ S^-(d) = \frac{1}{2}(\tilde{d} . \tilde{d}) \ , \ S^0(d) = \frac{1}{4}\sum_\nu (d_\nu^\dagger d_\nu + d_\nu d_\nu^\dagger) \quad (5)$$

$$S^+(s) = \frac{1}{2}s^{\dagger 2} \quad , \quad S^-(s) = \frac{1}{2}s^2 \quad , \quad S^0(s) = \frac{1}{4}(s^\dagger s + ss^\dagger) \quad (6)$$

On the other hand, the infinite dimensional *SU*(1,1) algebra is generated by using of [23-24]:

$$S_n^\pm = \sum_t c_{s;t}^{2n+1} S^\pm(s;t) + c_{d;t}^{2n+1} S^\pm(d;t) \quad , \quad S_n^0 = \sum_t c_{s;t}^{2n} S^0(s;t) + c_{d;t}^{2n} S^0(d;t) \quad (7)$$

And the sum is over proton, π, and neutron, ν, indices Where c_S and c_d are real parameters and *n* can be $0, \pm1, \pm2, \ldots$. These generators satisfy the commutation relations,

$$[S_m^0, S_n^\pm] = \pm S_{m+n}^\pm \ , \quad [S_m^+, S_n^-] = -2S_{m+n+1}^0 \quad (8)$$

Then, $\{S_m^{\mu}, \mu=0,+,-;\pm1,\pm2,...\}$ generates an affine lie algebra *SU*(1,1) without central extension. By employing the generators of *SU*(1,1) algebra, the following Hamiltonian is constructed for the transitional region between $U(5)\leftrightarrow SO(6)$ limits [23-24]:

$$\hat{H} = g\ S_0^+ S_0^- + \varepsilon\ S_1^0 + \gamma_1\ \hat{C}_2(SO_\pi(5)) + \gamma_2\ \hat{C}_2(SO_\nu(5)) + \delta_1\ \hat{C}_2(SO_\pi(3)) + \delta_2\ \hat{C}_2(SO_\nu(3)) + \delta\ \hat{C}_2(SO(3)) \quad (9)$$

g, ε, γ and δ are real parameters and $\hat{C}_2(SO(3))$ and $\hat{C}_2(SO(5))$ denote the Casimir operators of these groups. It can be seen that Hamiltonian (9) would be equivalent with $SO(6)$ Hamiltonian if $c_s = c_d$ and with $U(5)$ Hamiltonian when $c_s = 0$ & $c_d \neq 0$. Therefore, the $c_s \neq c_d \neq 0$ requirement just corresponds to the $U(5)\leftrightarrow SO(6)$ transitional region. To control this transitional Hamiltonian via single parameter and also due to the *O*(5) sub algebras which joint symmetry for both *U*(5) and *O*(6) dynamical limits, we take c_d (=1) constant value and c_s vary between 0 and c_d.

Eigenstates of Hamiltonian(9) can obtain with using the Fourier-Laurent expansion of eigenstates and *SU*(1,1) generators in terms of unknown $c-$number parameters x_i with $i = 1,2,...,k$. It means, one can consider the eigenstates as [23-24]:

$$\left|k;\beta;\nu_s^\pi,\nu_s^\nu,\nu^\pi,\nu^\nu;n_\Delta^\pi L_\pi, n_\Delta^\nu L_\nu; LM\right\rangle = \sum_{n_i \in Z} a_{n_1} a_{n_2} ... a_{n_k} x_1^{n_1} x_2^{n_2} ... x_k^{n_k} S_{n_1}^+ S_{n_2}^+ ... S_{n_k}^+ \left|lw\right\rangle \quad (10)$$

Due to the analytical behavior of wave functions, it suffices to consider x_i near zero. With using the commutation relations between the generators of SU(1,1) algebra, i.e. Eq(10), wave functions can be considered as:

$$\left|k;\beta;\nu_s^\pi,\nu_s^\nu,\nu^\pi,\nu^\nu;n_\Delta^\pi L_\pi, n_\Delta^\nu L_\nu; LM\right\rangle = N S_{x_1}^+ S_{x_2}^+ ... S_{x_k}^+ \left|lw\right\rangle \quad (11)$$

N is the normalization factor and

$$S_{x_i}^+ = \sum_t \frac{c_{s;t}}{1 - c_{s;t}^2 x_i} S^+(s;t) + \frac{c_{d;t}}{1 - c_{d;t}^2 x_i} S^+(d;t) \quad (12)$$

The c-numbers x_i are determined through the following set of equations as:

$$\frac{\epsilon}{x_i} = \sum_t g\left(\frac{c_{s;t}{}^2(\nu_s^t + \frac{1}{2})}{1 - c_{s;t}{}^2 x_i} + \frac{c_{d;t}^2(\nu^t + \frac{5}{2})}{1 - c_{d;t}^2 x_i}\right) - \sum_{i \neq j} \frac{2}{x_i - x_j} \quad \text{for i=1,2,...,k} \quad (13)$$

Eigenvalues of Hamiltonian (9), i.e. $E^{(k)}$, can be expressed as

$$E^{(k)} = \sum_{i=1}^k \frac{\varepsilon}{x_i} + \gamma_1 \nu^\pi(\nu^\pi + 3) + \gamma_2 \nu^\nu(\nu^\nu + 3) + \delta_1 L_\pi(L_\pi + 1) + \delta_2 L_\nu(L_\nu + 1) + \delta L(L+1) + \varepsilon \Lambda_1^0$$
$$\Lambda_1^0 = \sum_t \frac{1}{2}\left[c_{s;t}^2(\nu_s^t + \frac{1}{2}) + c_{d;t}^2(\nu^t + \frac{5}{2})\right] \quad (14)$$

Similarly, the eigenvalues of Hamiltonian (1), i.e. $E_{extended}(k)$, can be expressed as:

$$\hat{C}_2[SO(6)] = h^{(k)}, \qquad h^{(k)} = \sum_{i=1}^{k} \frac{\varepsilon}{x_i} \quad (15)$$

$$E_{extended}(k) = E(k) + \sum_{i=1}^{k} \frac{\varepsilon}{x_i}, \quad E^{(k)} = \sum_{i=1}^k \frac{\varepsilon}{x_i} + \gamma_1 \nu^\pi(\nu^\pi + 3) + \gamma_2 \nu^\nu(\nu^\nu + 3) + \delta_1 L_\pi(L_\pi + 1) + \delta_2 L_\nu(L_\nu + 1) + \delta L(L+1) + \varepsilon \Lambda_1^0 \quad (16)$$

The quantum number *k*, is related to total boson number *N*, by

$$2k = N_\pi + N_\nu - \nu_s^\pi - \nu_s^\nu - \nu^\pi - \nu^\nu$$

To obtain the numerical results for E(k), we have followed the prescriptions have introduced in Refs.[38-39], namely a set of non-linear Bethe-Ansatz equations (BAE) with $k-$ unknowns for $k-$ pair excitations must be solved. To this aim we have changed the variables as:

$$\grave{o} = \frac{\varepsilon}{g}(g = 1\ \ keV) \quad , \quad c = \frac{c_s}{c_d} \leq 1 \quad , \quad y_i = c_d^2 x_i \tag{17}$$

so, the new form of Eq.(13) would be

$$\frac{\epsilon}{y_i} = \sum_t \left(\frac{c_t{}^2(\nu_s^t + \frac{1}{2})}{1 - c_t{}^2 y_i} + \frac{(\nu^t + \frac{5}{2})}{1 - y_i}\right) - \sum_{i \neq j} \frac{2}{y_i - y_j} \qquad \text{for i=1,2,...,k} \tag{18}$$

We have solved Eq.(18) with definite values of c and ε for $i = 1$ to determine the roots of Beth-Ansatz equations (BAE) with specified values of ν_s and ν, similar to procedure which have done in Refs [38-39]. Then, we have used "Find root" in the Maple17 to get all $y_j^{'}$s. We carry out this procedure with different values of c and ε to provide energy spectra (after inserting γ and δ) with minimum variation as compared to the experimental counterparts:

$$\sigma = \left(\frac{1}{N_{tot}^{\ 2}} \sum_{i=1} \left| E_{\exp}(i) - E_{cal}(i) \right|^2\right)^{1/2}$$

Which N_{tot} is the number of energy levels where are included in extraction processes. We have extracted the best set of Hamiltonian's parameters, i.e. γ and δ, via the available experimental data [25-29] for excitation energies of selected states, $0_1^+, 2_1^+, 4_1^+, 0_2^+, 2_2^+, 4_2^+$ and *etc*, e.g. 12 levels up to 2_4^+, or two neutron separation energies for nuclei which are considered in this study. In summary, we have extracted γ and δ externally from empirical evidences and other quantities of Hamiltonian, e.g. c and ε would determine through the minimization of σ.

Results

In this paper We try to increase the accuracy of heoretical prediction in the determination of energy levels in ^{130}Xe nucleus with using an extension of transitional Hamiltonian. As have explained in the previous parts, due to the nature of considered intruder levels, 2*p*-2*h* excitation, we added a *O*(6) Casimir to improve our methods. we calculated all the roots of Eq (18) and then extracted the constants of energy formula with least square method, then, we determined the energy of different states with Eq (14), namely without the mixing term. Also we carried out these calculations with using different values of c_s, δ, $\gamma$and ε to get the best corresponding between theoretical predictions and experimental counterparts. These results are presented in Table 1 and the best arrangement which yield by C_s*=0.7 and* σ =137 Also, for excited energy levels and especially, intruder levels, we need to add new terms to optimize our theoretical predictions. The new results which yield with using Eq (16) are presented in Table 2. Also, the best corresponding between theoretical predictions and experimental counterparts yield via C_s*=0.8 and* σ =183, are presented in Table 2.

Table 1. The parameters of IBM-2 Hamiltonian for ^{130} Xe isotope which are extracted by least square method from experimental data were taken from [25-29] σ is regarded as the quality for extraction processes (N=5 the Boson number)

Cs	γ_1	γ_2	δ_1	δ_2	Δ	ε	σ
0.2	76.41	43.75	80.33	-105.49	11.74	500	228
0.3	80.35	42.77	85.42	-110.08	11.09	500	302
0.4	88.26	42.32	94.64	-118.57	10.99	500	270
0.5	91.76	41.98	110.21	-133.77	9.89	500	230
0.6	101.43	40.64	150.55	-140.58	7.83	500	244
0.7	120.65	39.85	170.76	-146.04	3.16	500	137
0.8	118.87	44.45	180.90	-190.41	2.75	500	267
0.9	112.98	45.32	210.48	-220.88	1.74	500	280

Table 2. The parameters of extended IBM-2 Hamiltonian for ^{130} Xe isotope which are extracted by least square method from experimental data were taken from [25-29]. σ is regarded as the quality for extraction processes.(N=5 the Boson number)

Cs	γ_1	γ_2	δ_1	δ_2	Δ	ε	σ
0.2	101.32	80.65	110.95	-90.76	13.99	500	230
0.3	110.67	77.09	130.09	-95.54	11.74	500	210
0.4	118.21	71.39	145.88	-100.89	9.09	500	225
0.5	124.12	68.44	160.37	-110.55	7.78	500	218
0.6	133.45	60.56	177.05	-116.04	6.45	500	190
0.7	155.38	57.34	198.29	-126.47	5.63	500	198
0.8	160.44	44.45	188.94	-130.66	3.88	500	183
0.9	140.77	49.32	200.44	-149.68	2.95	500	205

Obviously, this extended formalism improve theoretical predictions and confirm our idea to add this term in description of intruder levels of ^{130}Xe nucleus. A detailed report on the results of these two formalisms about each levels are showed in Table 3 and Figure 1.

Table 3. Theoretical predictions of both normal and extended Hamiltonian for ^{130}Xe nucleus. All energies are in *keV*.

level	$E_{experimental}$	$E_{SU(1,1)}$	$E_{extended\ SU(1,1)}$
0_1^+	0	0	0
2_1^+	536	499	510
4_1^+	1204	1290	1180
6_1^+	1944	2015	1902
2_2^+	1122	1200	1100
3_1^+	1632	1550	1675
4_2^+	1808	1700	1878
0_2^+	1793	1500	1750
2_3^+	2150	2430	2220
0_3^+	2017	2221	2430

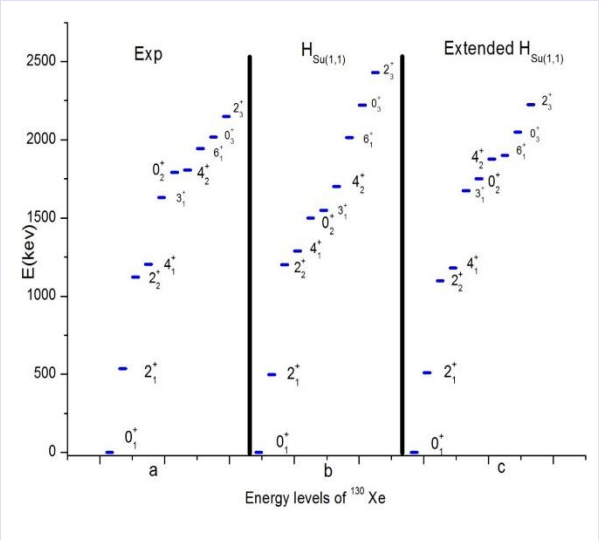

Figure 1. The basal latencies of rats before and after operation (paired student t-test, *p<0.05)

Figure1.energy spectra of ^{130}Xe nucleus, a) experimental spectra together b) theoretical predictions based on *SU*(1,1) transitional Hamiltonian and c) extended Hamiltonian.

Conclusions and Summary

These results show the advantages of the considered transitional Hamiltonian in the description of only the states of ground band. This confirm the spherical nature of this nucleus and therefore, explain the reason of using such transitional Hamiltonian for this nucleus. On the other hand, we got the biggest differences between theoretical predictions and experimental data in 2_3^+ and 0_3^+ states which as reported have *O*(6) nature. To optimize our theoretical predictions, we need to add new term as explained in Eq.(1) and due to the properties of these intruder states, the $\hat{C}_{2(SO(6))}$, e.g. Eq.(3), is our selection. By using same method which have used to get roots and predictions of the transitional Hamiltonian In transitional Hamiltonian, we changed the control parameter of this model which describe symmetries mixing, together the excitation term to describe the energy spectra with high accuracy. The results of normal and perturbed Hamiltonians show the advantages of perturbed one for all of the considered states and especially 2_3^+ and 0_3^+ intruder states. Also, the changes in the control parameters of this transitional Hamiltonian verify the superposition of two *U*(5) and *O*(6) nature of this nucleus. The better agreement which yield by the extended Hamiltonian suggest the partial symmetry-like structure in this nucleus which is type-II and only, these intruder states belong to this additional symmetry.

Acknowledgment

This work is supported by the Research Council of the University of Tabriz.

Conflict of interests

Conflict-of-interest statement the authors have no conflicts of interest to declare. The authors have seen and agree with the contents of the manuscript and there is no

financial interest to report. We certify that the submission is original work and is not under review at any other publication.

References

[1] Heyde K., Jolie J., Phase transitions versus shape coexistence, *Physical Review. C*., 69(2004) 054304-36.

[2] Heyde K., Wood J., Shape coexistence in atomic nuclei, *Reviews of Modern Physics*., 83 (2011)1467-1655.

[3] Garcia-Ramos J.,Heyde K., Nuclear shape coexistence: A study of the even-even Hg isotopes using the interacting boson model with configuration mixing, *Physical Review. C*, 89 (2014) 014306-48.

[4] Nomura K., Otsuka T., Shape coexistence in the microscopically guided interacting boson model, *Journal of Physics. G*.,43 (2016) 024008- 2.

[5] Fossion F.,Shape Coexistence in the Lead Isotopes Using Algebraic Models, *Acta Physica Polonica*. B., 36 (2005) 1351-1360.

[6] Fossion R., Heyde K., Intruder bands and configuration mixing in lead isotopes, *Physical Review.C*., 67 (2003) 024306.

[7] Van Isacker P., Particle-hole excitations in the interacting boson model (IV). The U(5)-SU(3) coupling, *Nuclear Physics. A.* ,651(1999) 31-55

[8] Garcia-Ramose J.E.,Heyde K., Disentangling the nuclear shape coexistence in even-even Hg isotopes using the interacting boson model, *EPJ Web of Conferences*., 93 (2015) 01004.

[9] Chuu D.S., Hsieh S.T., Structure of even-even Dy nuclei in the interacting boson model with two-quasiparticle states, *Physical Review.C.,*38 (1988) 960-968.

[10] McCutchan E.A., A piece in the Pt intruder state puzzle, *Physics of Atomic Nuclei*., 70 (2007) 1587-1591.

[11] Garcia-Ramos J.E., Hellemans V., Heyde K., Platinum nuclei: Concealed configuration mixing and shape coexistence, *Physical Review.C.*, 84 (2011) 12-45.

[12] Garcia-Ramos J.E.,Heyde K., Comparing the Interacting Boson Model with configuration mixing and the extended consistent-Q formalism, *Nuclear Physics.A.,* 825 (2009) 39-79.

[13] Delion D.S., Florescu A., Microscopic Description of Alpha Decay to Intruder 0+2 States in Pb, Po, Hg, and Pt Isotopes, *Physical Review Letters*., 74(1995) 15-20.

[14] Jolie J., Heyde K., Consistent description of intruder states, *Physical Review.C*., 42 (1990) 1-6.

[15] Soramel F.,Farenea E., Study of very neutron deficient nuclei ^{178}Pt and ^{181}Au, *The European Physical. J. A*., 4 (1999) 17-19.

[16] Oros A.M., Shape coexistence in the light Po isotopes, *Nuclear Physics. A*., 645 (1999) 107-142.

[17] Heyde K., Van Isaker P., A shell-model interpretation of intruder states and the onset of deformation in even-even nuclei, *Physics Letters. B*., 155 (1985) 303-308.

[18] Bijnens N.,Intruder states and the onset of deformation in the neutron-deficient even-even polonium isotopes, *Physical Review Letters*., 75 (1995) 18-25.

[19] Garcia-Ramos J.E., Heyde K., A study of the even-even Hg isotopes using the interacting boson model with configuration mixing, *Physical Review.C*., 89 (2014) 172-200.

[20] Heyde K., A shell-model description of 0+ intruder states in even-even nuclei, *Nuclear Physics. A*., 466 (1987) 189-226.

[21] Xu Y., Krane K.S., Gummin M.A., Shape coexistence and electric monopole transitions in 184Pt, *Physical Review Letters* ., 68 (1992) 3853-3856.

[22] Pan F., Dongkang L., Exactly solvable configuration mixing scheme in the vibrational limit of the interacting boson model, *Physical Review. C*, 97 (2018) 1-10.

[23] Pan F., Draayer J.P., New algebraic solutions for SO (6)↔ U (5) transitional nuclei in the interacting boson model, *Nuclear Physics .A*., 636 (1998) 156-168.

[24] Pan F., Draayer J.P., Algebraic solutions of an sl-boson system in the U(2l + 1) ⟷ O(2l + 2) transitional region , *Journal of Physics A: Mathematical and General*., 35 (2002) 7173-7185.

[25] National Nuclear Data Center,(Brookhaven National laboratory), chart of nuclides, (http://www.nndc.bnl.gov/chart/reColor.jsp?newColor=dm)

[26] Sergeenkov V., Nuclear Data sheets for A=130, *Nuclear Data Sheets*., 58 (1989) 765-870.

[27] Jalili A., Pan F., Nuclear structure and band mixing in 194Pt, *Physical Review. C*.,103 (2021) 1-8.

[28] Jalili A.,Sabri H., Properties of giant dipole resonances within an extended pairing model with a focus on spectral statistics , *Physical Review. C* .,104 (2021) 024332-2.

[29] Heyde K., Intruder analog states: New classification of particle-hole excitations near closed shells, *Physical Review. C*., 46 (1992) 541-560.

[30] Sabri H., Jahangiri Z., Investigation of shape coexistence in $^{118–128}$Te isotopes, *Nuclear Physics. A*., 946 (2016) 11-28.

[31] Sabri H., A theoretical study of energy spectra and two-neutron separation energies of $^{106–122}$Cd isotopes in the transitional region of IBM, *The European Physical Journal Plus*., 129 (2014) 138-149.

[32] Fathi H., Investigation of shape phase transition in the U(5) ↔ SO(6) transitional region by catastrophe theory and critical exponents of some quantities, *International Journal of Modern Physics .E*., 23 (2014) 1-15.

[33] Subber A.,Hamilton W.D.,An application of the dynamic deformation model to the tellurium isotopes, *Journal of Physics G: Nuclear Physics.*,13 (1987) 161-173.

[34] Walker P.M., E0 transitions in the light tellurium isotopes: evidence for intruder states, *Journal of Physics G: Nuclear Physics,* 13(1987) 95-103.

[35] Iachello F.,Arima A., The Interacting Boson Model, Cambridge University Press, Cambridge., (1987) 19-98.

[36] Casten R.F.,Zamfir N.V., Evidence for a Possible E(5) Symmetry in 134Ba , *Physical Review Letters*., 85 (2000) 3584-6.

[37] Paul E.S., Shape coexistence in 132Ba, *Physical Review. C*., 40 (1989) 1255-1264.

[38] Arima A., Iachello F., Interacting Boson Model of Collective States I The Vibrational Limit, *Annals of Physics*.,281 (2000) 2-64.

[39] Casten R.F., Warner D.D., The interacting boson approximation, *Reviews of Modern Physics*., 60 (1988) 389-465.

[40] Dieperink A. E. L., Scholten O., Iachello F., Classical Limit of the Interacting-Boson Model, *Physical Review Letters*, 44 (1980) 1747-1750.

Cumhuriyet Sci. J., 44(1) (2023) 224-228
DOI: https://doi.org/10.17776/csj.1171453

Cumhuriyet Science Journal

| csj.cumhuriyet.edu.tr | Founded: 2002 ISSN: 2587-2680 e-ISSN: 2587-246X Publisher: Sivas Cumhuriyet University

Parameters Estimation for the Unit log-log Distribution

Mustafa Çağatay Korkmaz [1,a], Kadir Karakaya [2,b,*], Yunus Akdoğan [2,c], Yener Ünal [3,d]

[1] *Department of Measurement and Evaluation, Faculty of Education, Artvin Çoruh University, Artvin, Türkiye*
[2] *Department of Statistics, Faculty of Science, Selçuk University, Konya, Türkiye*
[3] *Department of Statistics and Computer Science, Faculty of Science, Sivas Cumhuriyet University, Sivas, Türkiye*
**Corresponding author*

Research Article

History
Received: 06/09/2022
Accepted: 11/01/2023

ABSTRACT

In this paper, point estimation problem of two unknown parameters of the unit log-log distribution is examined. For point estimation, six methods of estimate such as maximum likelihood, maximum product spacing, Anderson-Darling, least squares, weighted least squares, and Cramer-von Mises are examined in detail. Extensive simulation experiments are conducted to compare the effectiveness of these estimators based on bias and mean squared errors. According to the simulation results, it is seen that all estimators performed well in terms of two criteria and take close values in case of large sample. Moreover, practical data applications are performed for all estimators. Results of the Kolmogorov-Smirnov statistics are reported for all estimators in practical applications.

Keywords: Unit log-log distribution, Estimation, Monte Carlo simuation, Kolmogrov-Smirnov statistic.

[a] *mcagatay@artvin.edu.tr* *https://orcid.org/0000-0003-3302-0705*
[b] *kkarakaya@selcuk.edu.tr* *https://orcid.org/0000-0002-0781-3587*
[c] *yakdogan@selcuk.edu.tr* *https://orcid.org/0000-0003-3520-7493*
[d] *uyener@cumhuriyet.edu.tr* *https://orcid.org/0000-0002-4796-8276*

Introduction

In recent years, the need to model proportional data has been increasing. Beta and Kumaraswamy [1] distributions are the best-known distributions for modeling these data. However, in recent years, many new distributions have been proposed as alternatives to these distributions. Some of these can be presented as [2-4]. One of the unit distributions proposed in recent years is the unit log-log (ULL) distribution introduced by Korkmaz and Korkmaz [5]. The ULL distribution was obtained by converting the log-log distribution [6] to the range of (0,1). The probability density function (pdf), cumulative distribution function of the ULL distribution are given, respectively, by

$$f(x,\alpha,\beta)=\frac{\alpha\log\beta\left(-\log x\right)^{\alpha-1}\beta^{\left(-\log x\right)^{\alpha}}}{x}e^{1-\beta^{\left(-\log x\right)^{\alpha}}},\ x\in(0,1) \quad (1)$$

and

$$F(x,\alpha,\beta)=e^{1-\beta^{\left(-\log x\right)^{\alpha}}},x\in(0,1), \quad (2)$$

where $\alpha>0$ and $\beta>1$ are the distribution parameters. The following is the quantile function of the ULL model, which we also use to generate numbers for the simulation study:

$$x_u(\alpha,\beta)=\exp\left[-\left(\frac{\log(1-\log u)}{\log\beta}\right)^{1/\alpha}\right], \quad (3)$$

where $u\in(0,1)$. The pdf plots for some choices of α and β is presented in Figure 1. The ULL distribution has U-shaped, N-shaped, decreasing unimodal shapes and increasing, as shown in Figure 1.

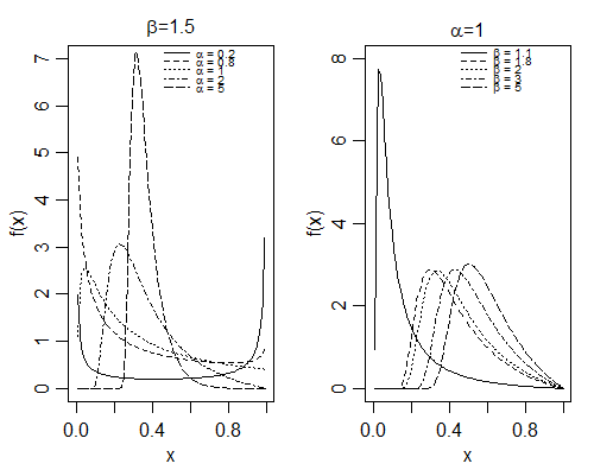

Figure 1. The pdf plots for ULL model

Some mathematical properties of the ULL model, including moments, stochastic ordering, order statistics, etc., were studied in detail by Korkmaz and Korkmaz [5]. Korkmaz and Korkmaz [5] proposed a new quantile regression model based on the ULL distribution as an alternative to beta regression [7], Kumaraswamy regression [8], and unit-Weibull regression [9]. Both

parameters of ULL distribution and regression parameters were estimated by the maximum likelihood methodology in [5]. Korkmaz and Korkmaz [5] conducted comprehensive simulation experiments for the estimate of both the model parameters"" and the regression parameters under various scenarios. Korkmaz and Korkmaz [5] used only the maximum likelihood technique to estimate unknown parameters of the ULL model. The aim of the current research is to evaluate some estimators for the parameters of the ULL distribution in detail. The rest of the paper is organized as follows: Section 2 presents six estimators. In Section 3, a simulation experiment is conducted to assess the performance of these estimators based on bias and mean squared errord (MSE). Two real data applications are examined in Section 4. The study is completed with the concluding remarks in Section 5.

Estimation of Parameters Using Different Methods

In this section, six estimators are examined for the estimation of two parameters of the ULL model. These estimators are: maximum likelihood (MLE), least squares (LSE), maximum product spacing (MPS), weighted least squares (WLSE), Anderson-Darling (AD), and Cramer-von Mises (CVM). These estimators are often preferred for estimating unknown parameter of distributions. Some studies using this estimator can be given as [10-13].

Maximum Likelihood Estimation

In this subsection, we derive estimations of the parameters α and β via method of the MLE. Let $X_1, X_2, \ldots, X_n$ be a random sample from the ULL distribution with observed values $x_1, x_2, \ldots, x_n$, and $\boldsymbol{\Xi} = (\alpha, \beta)^T$ be the vector of the model parameters. Then, the log-likelihood function is given by

$$\ell(\boldsymbol{\Xi}) = n\log\alpha + n\log(\log\beta) + (\alpha-1)\sum_{i=1}^{n}\mathrm{l}'' + \log\beta\sum_{i=1}^{n}(-\log x_i)^{\alpha} + n - \sum_{i=1}^{n}\beta^{(-\log x_i)^{\alpha}}. \quad (4)$$

The MLE of α and β, say $\hat{\alpha}$ and $\hat{\beta}$, are derived by

$$\frac{\partial}{\partial\alpha}\ell(\boldsymbol{\Xi}) = \frac{n}{\alpha} + \sum_{i=1}^{n}\log(-\log x_i) + \log\beta\sum_{i=1}^{n}(-\log x_i)^{\alpha}\log(-\log x_i)\left[1-\beta^{(-\log x_i)^{\alpha}}\right] = 0 \quad (5)$$

and $$\frac{\partial}{\partial\beta}\ell(\boldsymbol{\Xi}) = \frac{n}{\beta\log\beta} + \frac{1}{\beta}\sum_{i=1}^{n}(-\log x_i)^{\alpha} - \sum_{i=1}^{n}(-\log x_i)^{\alpha}\beta^{(-\log x_i)^{\alpha}-1} = 0. \quad (6)$$

The $\hat{\alpha}$ and $\hat{\beta}$ are not obtained analytically from above equations. A software can be used in this regard, like R, Matlab, or Mathematica to obtain estimations via numerical methods.

Maximum Product Spacing Estimation

MPS technique was presented by [14]. Let be the $X_{(1)}, X_{(2)}, \ldots, X_{(n)}$ ordered statistics from ULL distribution with sample size *n* and $x_{(1)}, x_{(2)}, \ldots, x_{(n)}$ be the ordered observed values from the ULL distribution. Geometric mean (GM) of the differences is given as

$$GM = \sqrt[n+1]{\prod_{i=1}^{n+1}\left[F(x_{(i)},\alpha,\beta) - F(x_{(i-1)},\alpha,\beta)\right]}, \quad (7)$$

where $F(x_{(n+1)},\alpha,\beta) = 1$ and $F(x_{(0)},\alpha,\beta) = 0$. MPSE, $\hat{\alpha}_{MPS}$ and $\hat{\beta}_{MPS}$, of the α and β parameters are acquired by maximizing GM. If we take the logarithm of the above expression, we get the following:

$$MPS(\boldsymbol{\Xi}) = \frac{1}{n+1}\sum_{i=1}^{n+1}\log\left[e^{1-\beta^{(-\log x_{(i)})^{\alpha}}} - e^{1-\beta^{(-\log x_{(i-1)})^{\alpha}}}\right]. \quad (8)$$

Least Squares Estimation

The LSE $\hat{\alpha}_{LSE}$ and $\hat{\beta}_{LSE}$, of α and β, respectively, are achieved by minimizing the following

$$LSE(\boldsymbol{\Xi}) = \sum_{i=1}^{n}\left(e^{1-\beta^{(-\log x_{(i)})^{\alpha}}} - \frac{i}{n+1}\right)^2. \quad (9)$$

Weighted Least Squares Estimation

The WLSE, $\hat{\alpha}_{WLSE}$ and $\hat{\beta}_{WLSE}$, of the α and β parameters are achieved by minimizing the following

$$WLSE(\Xi)=\sum_{i=1}^{n}\frac{(n+2)(n+1)^2}{i(n-i+1)}\left(e^{1-\beta^{\left(-\log x_{(i)}\right)^{\alpha}}}-\frac{i}{n+1}\right)^2. \tag{10}$$

Anderson-Darling Estimation

The AD, $\hat{\alpha}_{AD}$, $\hat{\beta}_{AD}$, of the α, β parameters are obtained by minimizing

$$AD(\Xi)=-n-\sum_{i=1}^{n}\frac{2i-1}{n}\left[\log\left\{e^{1-\beta^{\left(-\log x_{(i)}\right)^{\alpha}}}\right\}+\log\left\{1-e^{1-\beta^{\left(-\log x_{(i)}\right)^{\alpha}}}\right\}\right]. \tag{11}$$

Cramer-von Mises Estimation

The CVM, $\hat{\alpha}_{CVM}$ and $\hat{\beta}_{CVM}$, of the α and β parameters are acquired by minimizing

$$CVM(\Xi)=\frac{1}{12n}+\sum_{i=1}^{n}\left[e^{1-\beta^{\left(-\log x_{(i)}\right)^{\alpha}}}-\frac{2i-1}{2n}\right]^2. \tag{12}$$

Because Equations (4), (8)-(12) involve non-linear functions, explicit forms of all estimators cannot be obtained directly. As a result, numerical tecniques like quasi-Newton and Newton-Raphson algorithms must be used to solve them.

Simulation Study

In this section, the success of the estimators for ULL model parameters are examined different sample size *n*. It is genetared $N=1000$ samples of size $n=20,25,\ldots,1000$ from the ULL model based on the true parameter values $\alpha=5$ and $\beta=5$. The constrOptim coomand in the R is used to acquire all estimations. In addition, for comparisons between the methods, we calculate the bias and MSE of the estimators. The bias and MSE are computed as for $h=\alpha$ or β

$$Bias_h(n)=\frac{1}{N}\sum_{i=1}^{N}\left(h_i-\hat{h}_i\right), \tag{13}$$

and

$$MSE_h(n)=\frac{1}{N}\sum_{i=1}^{N}\left(h_i-\hat{h}_i\right)^2, \tag{14}$$

respectively.

Figures 2-7 illustrate the outcomes of this simulation experiment. Figures 2-7 indicate that six estimators are consistent, as MSE, bias decrease and the empirical means are goes true parameters values with increasing *n*. In addition, six estimators are asymptotic unbiased. Quantity of biases and MSEs in the MLE methodology are initially higher than other methods, but they become very close as the sample size increases. Although the bias criteria suggests that LSE is the best estimator, as *n* increases, the bias of all estimators approach one another and finally reach zero. According to MSE criterion, MPS method is better than other methods. As a result, it can be concluded that any estimator can be chosen for the ULL model in case of large sample. For other parameter settings, same results can be achieved.

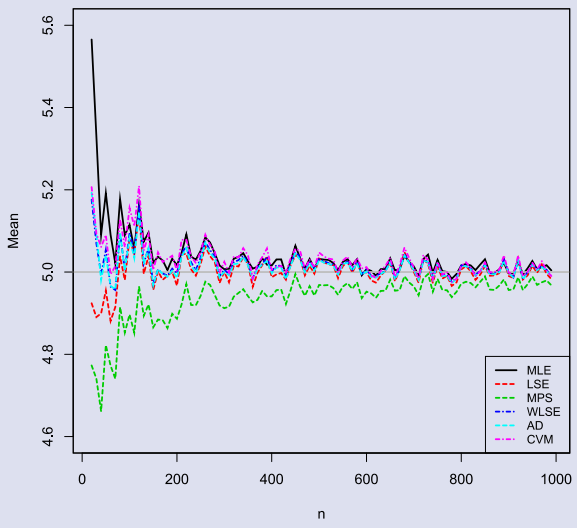

Figure 2. The empirical means of parameter for all estimators

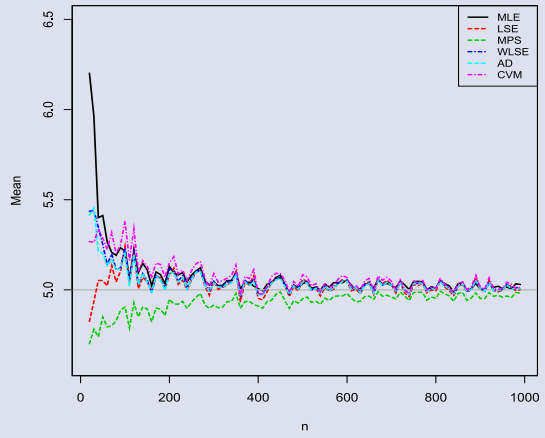

Figure 3. The empirical means of parameter for all estimators

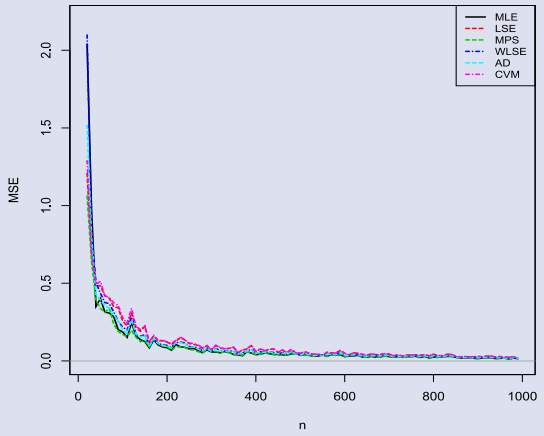

Figure 6. The MSEs of parameter α for all estimators

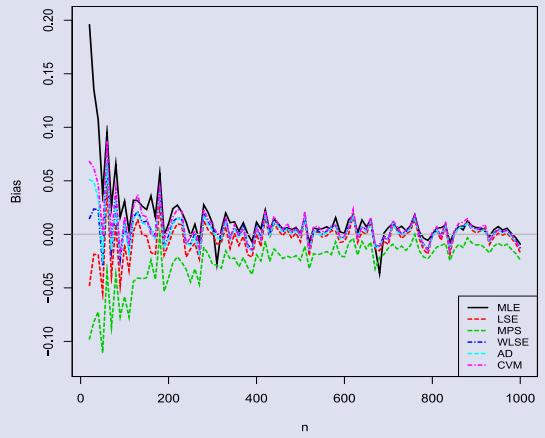

Figure 4. The biases of parameter α for all estimators

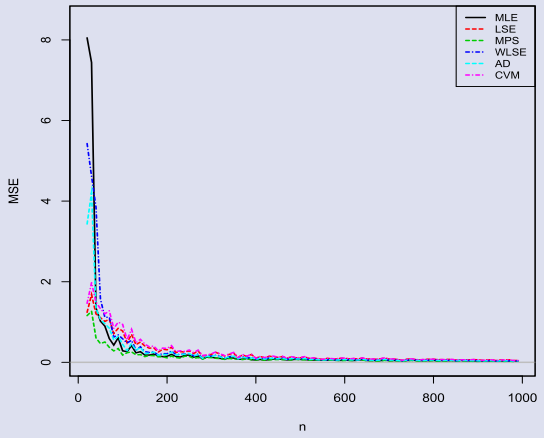

Figure 7. The MSEs of parameter β for all estimators

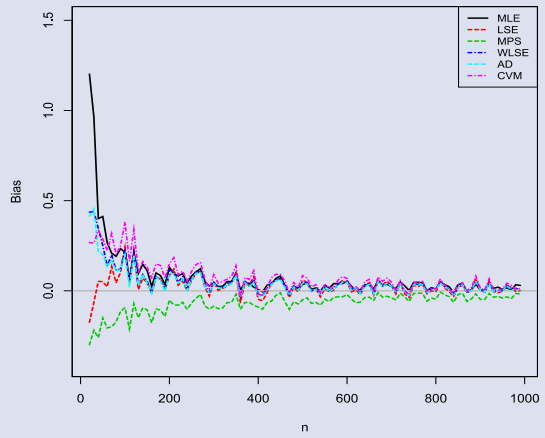

Figure 5. The biases of parameter β for all estimators

Applications Based on Real Data

In this section, two real data applications for ULL distribution are examined. The ULL distribution is modelled to two practical datasets by estimating the two unknown parameters using the all estimators discussed in Section 2. The MLE, LSE, QE, WLSE, AD, and CVM the parameters α and β of ULL distribution are obtained by BFGS algorithm. The results and Kolmogorov-Smirnov statistics (KS) and related p values for all estimators are reported in Table 1.

The first data is originates from [15] and indicates the Susquehanna River flood levels in Harrisburg, Pennsylvania. The data are 0.654, 0.613, 0.315, 0.449, 0.297, 0.402, 0.379, 0.423, 0.379, 0.3235, 0.269, 0.740, 0.418, 0.412, 0.494, 0.416, 0.338, 0.392, 0.484 and 0.265. For the first data, some descriptive statistics are as follows: there are 20 observations, the mean is 0.4231,

the standard deviation is 0.1252, the median is 0.4070, the skewness is 1.1560, and the kurtosis is 1.1530.

The second data set taken from [16] and represents the strengths of 1.5 cm glass fibers, which were first measured by researchers at the UK National Physical Laboratory. The data are 0.17, 0.13, 0.16, 0.14, 0.20, 0.15, 0.13, 0.11, 0.15, 0.12, 0.12, 0.15, 0.12, 0.16, 0.21, 0.20, 0.23, 0.16, 0.12, 0.10, 0.32, 0.33, 0.33, 0.36, 0.38, 0.20 and 0.26. For the second data, some descriptive statistics are as follows: there are 27 observations, the mean is 0.1930, the standard deviation is 0.0831, the median is 0.1600, the skewness is 1.0710, and the kurtosis is -0.056.

Table 1: Results of the parameter estimations and KS for two data sets for all estimators

		Parameter		KS	
Data	**Estimators**	α	β	**Statistics**	**p-values**
Flood levels	MLE	2.9192	1.9334	0.1366	0.8493
	LSE	2.7806	1.9296	0.1360	0.8529
	MPS	2.5363	1.9388	0.1354	0.8099
	WLSE	2.6582	1.9170	0.1390	0.8339
	AD	2.8151	1.9312	0.1359	0.8535
	CVM	3.0179	1.9503	0.1317	0.8783
Glass fiber	MLE	4.3774	1.0422	0.1120	0.8868
	LSE	3.7747	1.0602	0.1063	0.9200
	MPS	3.9008	1.0574	0.1107	0.8589
	WLSE	3.8547	1.0583	0.1046	0.9291
	AD	3.9660	1.0544	0.1050	0.9271
	CVM	3.9888	1.0525	0.0990	0.9538

Concluding Remarks

The ULL distribution introduced by [5] is studied in this work with relation to six point estimation methods. For one parameter setting as $\alpha = 5$ and $\beta = 5$ and different sample sizes, simulations are performed. When the sample size is increased, the MSEs and biases are observed to decrease and approach zero. In addition, the estimations and KS outcomes for all estimators are examined for two real datasets. The simulation results show that all estimators perform well on the bias and MSE criteria and close each other in a large sample.

Conflicts of interest

The authors state that did not have a conflict of interests

References

[1] Kumaraswamy, P., A generalized probability density function for double-bounded random processes , *J. Hydrol.*, 46 (1980), 79-88.

[2] Gómez-Déniz, E., Sordo, M.A., Calderín-Ojeda, E., The log–lindley distribution as an alternative to the beta regression model with applications in insurance, *Insurance Math. Econ.*, 54 (2014), 49-57.

[3] Mazucheli, J., Menezes, A.F.B., Chakraborty, S., On the one parameter unit-Lindley distribution and its associated regression model for proportion data, *J. Appl. Stat*., 46 (2019), 700-714.

[4] Korkmaz, M.Ç., Chesneau, C. On the unit burr-xii distribution with the quantile regression modeling and applications, *Comput. Appl. Math*., 40 (2021), 1-26.

[5] Korkmaz, M.Ç., Korkmaz, Z.S., The unit log–log distribution: a new unit distribution with alternative quantile regression modeling and educational measurements applications, *Journal of Applied Statistics*, (2021) 1-20.

[6] Pham, H., A vtub-shaped hazard rate function with applications to system safety, *Int. J. Reliab. Appl.*, 3 (2002), 1–16.

[7] Ferrari, S., Cribari-Neto, F., Beta regression for modelling rates and proportions, *Journal of Applied Statistics*, 31(7) (2004) 799–815.

[8] Mitnik, P.A., Baek, S., The Kumaraswamy distribution: Median-dispersion re-parameterizations for regression modeling and simulation-based estimation, *Stat. Pap*., 54 (2013) 177–192.

[9] Mazucheli, J., Menezes, A., Fernandes, L., de Oliveira, R., Ghitany, M., The unit-Weibull distribution as an alternative to the Kumaraswamy distribution for the modeling of quantiles conditional on covariates, *Journal of Applied Statistics*, 47 (2020) 954–974.

[10] Kınacı, İ., Kuş, C., Karakaya, K., Akdoğan, Y., APT-Pareto Distribution and its Properties. *Cumhuriyet Science Journal,* (2019) 40 (2) 378-387.

[11] Karakaya, K., Tanış, C., Different methods of estimation for the one parameter Akash distribution, *Cumhuriyet Science Journal*, (2020) 41 (4) 944-950 .

[12] Tanış, C., Saraçoğlu, B., Kuş, C., Pekgör, A., Transmuted complementary exponential power distribution: properties and applications. *Cumhuriyet Science Journal*, (2020) 41 (2) 419-432.

[13] Hamedani, G.G., Korkmaz, M.Ç., Butt, N.S., Yousof, H.M., The Type I Quasi Lambert Family, *Pakistan Journal of Statistics and Operation Research*, 17(3) (2021) 545-558.

[14] Cheng, R.C.H., Amin, N.A.K., Maximum product of spacings estimation with application to the lognormal distribution, Math Report, (1979) 791.

[15] Dumonceaux, R., Antle, C.E., Discrimination between the log-normal and the Weibull distributions, *Technometrics*, 15(4) (1973) 923-926.

[16] Elgarhy, M., Exponentiated generalized Kumaraswamy distribution with applications, *Annals of Data Science*, 5(2) (2018) 273-292.

Cumhuriyet Sci. J., 44(1) (2023) 229-235
DOI: https://doi.org/10.17776/csj.1122736

Cumhuriyet Science Journal

| csj.cumhuriyet.edu.tr | Founded: 2002 ISSN: 2587-2680 e-ISSN: 2587-246X Publisher: Sivas Cumhuriyet University

Evaluating the Goodness of Fit of Generalized Nakagami Distribution

Deniz Özonur [1,a,*]

[1] *Department of Statistics, Faculty of Science, Gazi University, Teknikokullar, Ankara, Türkiye.*
**Corresponding author*

Research Article

History
Received: 28/05/2022
Accepted: 27/02/2023

ABSTRACT

The Generalized Nakagami distribution is a popular distribution in wireless communication. This distribution includes the Nakagami distribution as a special case. Likelihood ratio, score, and two C(α) tests are developed to evaluate the fit of Nakagami distribution against Generalized Nakagami distribution. A Monte Carlo simulation study is performed in order to investigate the performance of these tests with regard to Type I errors and powers of tests. Finally, two data sets are analyzed using the proposed goodness of fit tests.

Keywords: C(α) test, Generalized Nakagami Distribution, Likelihood ratio test, Power of test, Score test.

[a] *denizozonur@gazi.edu.tr* *https://orcid.org/0000-0002-7622-1008*

Introduction

Modeling of wireless channels is crucial in many applied sciences such as engineering, medicine, and hydrology. In wireless communications, signals usually do not reach the receiver directly during transmission, and degradation of signal quality known as fading occurs. In the literature, various models such as Rayleigh, Rician, Nakagami, and K-models are used to model the fading in wireless channels. Since the modeling of the statistical properties of the fading channels is flexible, differences arise among these models. These models also differ in terms of parameter numbers. Among these models, the Nakagami model can model fading of signals reasonably well. The Generalized Nakagami distribution (GND) is produced by adding a new parameter that takes into account the tails of the density function of the Nakagami distribution [1]. The probability density function (pdf) of the GND is given as follows:

$$f(y;s,m,\Omega)=\frac{2sm^m}{\Gamma(m)\Omega^m}y^{2ms-1}e^{-\left(\frac{m}{\Omega}\right)y^{2s}},\ y>0, \qquad (1)$$

where $m\geq 0.5$ and $s>0$ are shape parameters and $\Omega>0$ is scale parameter. Note that the GND is related to the generalized gamma distribution introduced by Stacy [2]. It can be noted that the Generalized Nakagami random variable is generated by taking the square root of the generalized gamma random variable.

The probability densities of GND are plotted for various parameter combinations in Figure 1.

The GND converts to some special distributions such as when $s=1$, the GND becomes the ND; when $m=s=1$ the GND reduces to the Rayleigh distribution and when $m=1, s=1/2$ the GND reverts to exponential distribution.

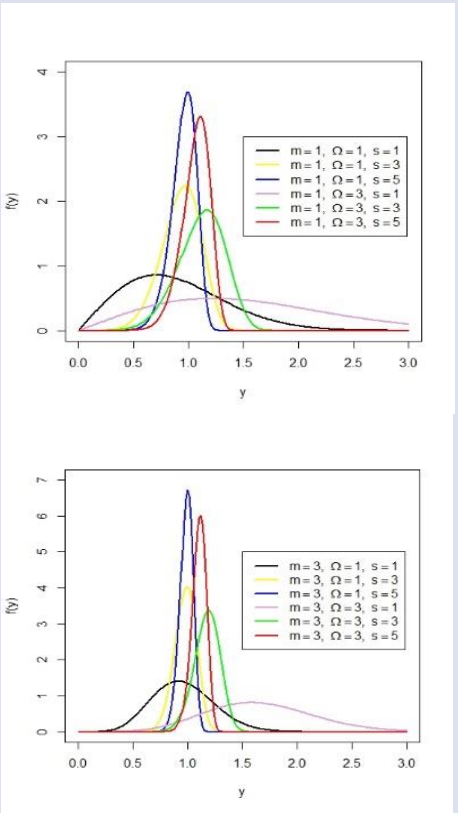

Figure 1. Generalized Nakagami densities for various parameter combinations.

It is essential to identify an appropriate distribution to be fitted for a given data. Increasing of number of parameters can cause some complications such as estimations of parameters depend on each other. In real applications, distributions with fewer parameters may be sufficient to describe data or provide better fit than distribution which have more parameters or complete opposite of this situation may occur. For example, Shankar [1] has reported that the GND is likely to match ultrasound data much better than the ND. Hence, in this study the ND is considered as a special case of the GND, and some goodness of fit tests are constructed to decide which distribution will have better fitting.

The ND was proposed by Nakagami to model fading of radio signals [3]. Although many statistical distributions describe the fading of signals such as Weibull, Rician, Rayleigh, and lognormal distributions, the ND matches some empirical data better than the other distributions [4].

Applications of the ND have been carried out in many scientific fields such as modelling of high-frequency seismogram envelopes, communications engineering, medical imaging studies etc. The usefulness of ND for dealing with high frequency seismogram envelopes has been demonstrated [5]. Sarkar et al. [6, 7] have examined performance of the ND to derivation of unit hydrographs in hydrology. Datta et al. [8] have modelled ultrasound kidney images with the ND. Alavi et al. [9] have analyzed performance of the ND for wind speed data. Since the ND has memoryless property, Ahmad et al. [10] have used the distribution to model hazard rate in reliability studies. Ramos et al. [11,12] have proposed new estimator for the ND and presented Bayesian inference considering objective priors for the ND parameters. Kumar et al. [13] have used the ND as a lifetime model. Ozonur et al. [14] have adapted some tests to evaluate Rayleigh distribution against the ND. Ozonur and Paul [15] have developed tests of fit of the generalized gamma distribution.

Goodness of fit tests are statistical tools evaluating adequacy of a distribution. Although goodness of fit of the ND is examined in the literature, asymptotically optimal goodness of fit tests such as the Neyman's $C(\alpha)$, Rao's score and likelihood ratio tests are firstly developed in this study to check whether the GND is statistically superior to the ND for a given data set. In order to decide whether a random sample has been taken from the ND or GND, null and alternative hypotheses can be constructed as below:

$$H_0 : s = 1 \\ H_1 : s \neq 1. \qquad (2)$$

The Neyman's $C(\alpha)$, Rao's score and likelihood ratio tests are asymptotically optimal, and they provide tests with good properties in large samples [16]. Although there are various studies including these goodness of fit tests [17,18], these tests have not been taken into consideration for the GND. Goodness of fit problem of the distribution is considered in the study due to pervasive usage in many scientific areas. In this context, the main focus of this study is to test goodness of fit of the ND against the GND.

The rest of the article is designed as follows. Firstly, the goodness of fit tests such as the likelihood ratio, score, and two $C(\alpha)$ tests are proposed to test the null hypothesis against the alternative hypothesis. Secondly, simulation study is performed to evaluate the performance of the tests with regard to Type I errors and powers of tests. In the subsequent section, two real data sets are analyzed and finally, some conclusions are provided.

Materials and Methods

Goodness of Fit Tests

$Y_1,\ldots,Y_n$ is a random sample from the GND with pdf given in Equation (1) with the parameter vector $\gamma = (s,\beta^T)^T$ where $\beta = (m,\Omega)^T$. The aim of this study is to test the $H_0 : s = 1$ against the $H_1 : s \neq 1$ treating the $\beta = (m,\Omega)^T$ as nuisance parameter.

Likelihood ratio test

The log-likelihood function of the GND is given by

$$l(\gamma;Y) = n\left[\log(2s) + m\log(m) - \log\Gamma(m) - m\log(\Omega)\right] + (2ms-1)\sum_{i=1}^{n}\log(y_i) - \frac{m}{\Omega}\sum_{i=1}^{n}y_i^{2s}. \qquad (3)$$

The maximum likelihood estimate (MLE) of γ under the full model, say $\tilde{\gamma} = (\tilde{s},\tilde{m},\tilde{\Omega})^T$, is a simultaneous solution of the following equations:

$$\frac{n}{s} + 2m\sum_{i=1}^{n}\log(y_i) - \frac{m}{\Omega}\sum_{i=1}^{n}2y_i^{2s}\log(y_i) = 0$$

$$n\left[\log(m) + 1 - \Psi(m) - \log(\Omega)\right] + 2s\sum_{i=1}^{n}\log(y_i) - \frac{1}{\Omega}\sum_{i=1}^{n}y_i^{2s} = 0$$

$$\frac{-nm}{\Omega} + \frac{m}{\Omega^2}\sum_{i=1}^{n}y_i^{2s} = 0$$

where $\Psi(m)$ is digamma function, i.e., $\Psi(m)=\dfrac{\partial \log\Gamma(m)}{\partial m}$. Similarly, the MLE of γ under the reduced model, say $\hat{\gamma}=\left(1,\hat{m},\hat{\Omega}\right)^{\mathrm{T}}$, can be obtained by solving the following equations :

$$n\log(m)+n-n\Psi(m)-n\log\Omega+2\sum_{i=1}^{n}\log y_i-\frac{1}{\Omega}\sum_{i=1}^{n}y_i^2=0$$

$$\frac{-nm}{\Omega}+\frac{m}{\Omega^2}\sum_{i=1}^{n}y_i^2=0.$$

Since the MLE equations of the full and reduced models have no direct solutions, iterative methods must be used to solve the equations. The MLEs of γ under the full and reduced models are derived using the mle2 function in R 3.4.1.

The likelihood ratio test statistic (LR) is given as follows:

$$LR=2\left(l(\tilde{\gamma};Y)-l(\hat{\gamma};Y)\right),$$

where $\tilde{\gamma}=\left(\tilde{s},\tilde{m},\tilde{\Omega}\right)^{\mathrm{T}}$ and $\hat{\gamma}=\left(1,\hat{m},\hat{\Omega}\right)^{\mathrm{T}}$ are the MLEs of γ under the full model and reduced model, respectively. Then the statistic LR asymptotically follows χ_1^2 under the null hypothesis.

C(α) and score tests

Rao proposed the score test as an alternative to the likelihood ratio test and Neyman introduced the $C(\alpha)$ test as a generalization of the Rao's score test [19, 20]. The $C(\alpha)$ and score test statistics are based on score functions. The score functions are the partial derivatives of the log-likelihood function with respect to the parameter of interest and nuisance parameter evaluated under the null hypothesis.

Consider testing $H_0: s=1$ against $H_1: s\neq 1$ where the parameter vector $\gamma=(s,\beta^T)^T$ is partitioned into the parameter of interest s and nuisance parameter $\beta=(m,\Omega)^T$. Similarly, score vector and information matrix can be partitioned as $U=\begin{bmatrix}U_s\\U_\beta\end{bmatrix}$ and $I=\begin{bmatrix}I_{ss} & I_{s\beta}\\ I_{\beta s} & I_{\beta\beta}\end{bmatrix}$, respectively. Under the null hypothesis, we obtained elements of the U and I as follows:

$$U_s=\left.\frac{\partial l(\gamma;Y)}{\partial s}\right|_{s=1}=n+2m\sum_i\log y_i-\frac{2m}{\Omega}\sum_i y_i^2\log y_i,$$

$$U_\beta=\frac{\partial l(\gamma;Y)}{\partial\beta}=\left(\frac{\partial l(\gamma;Y)}{\partial m},\frac{\partial l(\gamma;Y)}{\partial\Omega}\right)^T\Bigg|_{s=1}$$

$$=\left(n\left(\log m+1-\Psi(m)-\log\Omega\right)+2\sum_i\log y_i-\frac{1}{\Omega}\sum_i y_i^2,\quad \frac{-nm}{\Omega}+\frac{m}{\Omega^2}\sum_i y_i^2\right)^T,$$

$$I_{ss}=-E\left[\left.\frac{\partial^2 l(\gamma;X)}{\partial s\partial s}\right|_{s=1}\right]=n+\frac{n}{\Gamma(m)}\left[\Gamma(m+1)\log^2\left(\frac{\Omega}{m}\right)+2\Gamma'(m+1)\log\left(\frac{\Omega}{m}\right)+\Gamma''(m+1)\right]$$

$$I_{s\beta}=-E\left[\left.\frac{\partial^2 l(\gamma;X)}{\partial s\partial\beta^T}\right|_{s=1}\right]=\left[\frac{n}{m},-\frac{nm}{\Omega}\left(\log\left(\frac{\Omega}{m}\right)+\Psi(m+1)\right)\right]^T,$$

$$I_{\beta\beta}=-E\left[\left.\frac{\partial^2 l(\gamma;X)}{\partial\beta\partial\beta^T}\right|_{s=1}\right]=\begin{bmatrix}-\dfrac{n}{m}+n\Psi'(m) & 0\\ 0 & \dfrac{nm}{\Omega^2}\end{bmatrix},$$

where trigamma function $\Psi'(m)$ is derivative of the digamma function $\Psi(m)$.

Define adjusted score as $R=U_s-BU_\beta$, where B is the matrix of partial regression coefficients. Bartlett [21] showed that $B=I_{s\beta}I_{\beta\beta}^{-1}$ and variance covariance matrix of R is $I_{ss.\beta}=I_{ss}-I_{s\beta}I_{\beta\beta}^{-1}I_{\beta s}$. The Neyman's $C(\alpha)$ statistic is given by

$$C=\frac{R^2}{I_{ss.\beta}}.$$

The main advantage of the $C(\alpha)$ test is that it only requires the estimates under the null hypothesis. Hence, estimate of the nuisance parameter $\beta=(m,\Omega)^T$ is only required and if the nuisance parameter is replaced by $\sqrt{n}$ -consistent estimate, then the $C(\alpha)$ statistic is asymptotically distributed as χ_1^2 under the null hypothesis. In addition, if the nuisance parameter

$\beta=\left(m,\Omega\right)^T$ is replaced by its MLE $\hat{\beta}=\left(\hat{m},\hat{\Omega}\right)^T$, then the $C(\alpha)$ statistic becomes the Rao's score test statistic (S) which is given as follows:

$$S=\frac{U_s^2}{I_{ss.\beta}}.$$

Under the null hypothesis, the MLE $\hat{\beta}=\left(\hat{m},\hat{\Omega}\right)^T$ can be obtained as mentioned in the reduced model of the likelihood ratio test. In order to calculate the $C(\alpha)$ statistic, two different moment based estimates of the nuisance parameter, say $\breve{\beta}_1=\left(\breve{m}_{AK},\breve{\Omega}\right)^T$ and $\breve{\beta}_2=\left(\breve{m}_{CB},\breve{\Omega}\right)^T$, are used. Under the null hypothesis k. moment of the data is $\mu_k=E\left[Y^k\right]=\frac{\Gamma\left(m+k/2\right)}{\Gamma\left(m\right)}\left(\frac{\Omega}{m}\right)^{k/2}$.

The moment estimate of Ω is obtained as $\breve{\Omega}=\mu_2$. Since the moment estimate of m cannot be obtained from first moment equation, Abdi and Kaveh [22] have suggested a moment-based estimator for the m fading parameter as $\breve{m}_{AK}=\frac{\mu_2^2}{\mu_4-\mu_2^2}$. In addition, Cheng and Beaulieu [23] have reported the estimator of m as $\breve{m}_{CB}=\frac{\mu_1\mu_2}{2\left(\mu_3-\mu_1\mu_2\right)}$. In this study, we have used both estimators of m and we have denoted the $C(\alpha)$ statistics by C_{CB} and C_{AK} using the estimators of m as $\breve{m}_{CB}$ and $\breve{m}_{AK}$, respectively.

Asymptotically, it has been shown in the literature that the likelihood ratio test is equivalent to the $C(\alpha)$ or score test and the test statistics C_{CB}, C_{AK} and S are asymptotically follow χ_1^2 under the null hypothesis [24, 25].

Simulation Study

Monte Carlo simulation study is performed to demonstrate quality of the proposed tests LR, C_{CB}, C_{AK} and S in terms of Type I errors and powers of tests by using statistical software R 3.4.1. In the simulation study, critical values of the goodness of fit tests are obtained by simulating 10000 samples of size n from the GND with $s=1$. Using the critical values, the Type I errors are calculated by generating 5000 random samples from the GND with $s=1$ for various combinations of levels $(\alpha=0.10,0.05,0.01)$, sample sizes $(n=20,30,50)$ and parameters $(m=0.75,1)$. The Type I errors and powers of the tests are not affected as the value of Ω changes. So, all simulation results are obtained based on $\Omega=1$. The Type I errors of the tests are summarized in Table 1. In addition, we have obtained the powers of the tests under the GND using various combinations of sample sizes n and parameters $(m=0.75,1;\ s=1,3,5,7,9,11,13,15)$. The power study is performed with 5000 iterations and nominal level of 0.05. The powers of the tests are presented in Table 2.

Table 1. Type I errors of the tests for different m parameters, nominal levels and sample sizes.

Sample Sizes	Level	m	C_{CB}	C_{AK}	S	LR
20	0.10	0.75	0.0970	0.0970	0.0978	0.0954
		1	0.1026	0.1026	0.1070	0.1082
	0.05	0.75	0.0476	0.0450	0.0504	0.0482
		1	0.0524	0.0510	0.0590	0.0546
	0.01	0.75	0.0102	0.0106	0.0100	0.0122
		1	0.0124	0.0122	0.0118	0.0112
30	0.10	0.75	0.1008	0.1026	0.1050	0.1068
		1	0.1038	0.1042	0.0964	0.0960
	0.05	0.75	0.0494	0.0518	0.0518	0.0518
		1	0.0516	0.0530	0.0478	0.0520
	0.01	0.75	0.0082	0.0082	0.0092	0.0104
		1	0.0116	0.0128	0.0060	0.0098
50	0.10	0.75	0.0984	0.0966	0.0928	0.0948
		1	0.0920	0.0936	0.0912	0.0980
	0.05	0.75	0.0462	0.0454	0.0514	0.0484
		1	0.0426	0.0430	0.0442	0.0472
	0.01	0.75	0.0102	0.0110	0.0108	0.0098
		1	0.0056	0.0054	0.0092	0.0052

As shown in Table 1, Type I errors of all the four tests close to nominal levels irrespective of values of parameters and sample sizes. As shown in Table 2, as the sample size increases powers of all the tests increase. Also, powers of the tests increase as the s moves away from the null. It can be stated that when s is smaller than 7, the LR is the most powerful test and S provides slightly lower power than the LR. However, the score test S shows better performance among the four tests when $s>7$ in terms of powers of tests. For all sample sizes and parameter combinations, the C_{AK} is the least powerful test among all these tests. The C_{CB} has better performance than the C_{AK} between the Neyman $C(\alpha)$ tests using moment estimators. The score test S shows generally better performance than the C_{CB} and C_{AK} tests in terms of powers of tests. It is pointed out that for all sample sizes, as m parameter increases, powers of LR, C_{CB} and C_{AK} tests decrease. However, as m parameter increases, the power of S test decreases when $s<7$, and increases when $s>7$.

Table 2. Powers of the tests for nominal level 0.05, $m=0.75,1$ and $n=20,30,50$.

n	m	Statistics	s							
			1	3	5	7	9	11	13	15
20	0.75	C_{CB}	0.0580	0.1540	0.1974	0.2114	0.2070	0.2226	0.2356	0.2256
		C_{AK}	0.0562	0.1198	0.1274	0.1298	0.1172	0.1182	0.1224	0.1110
		S	0.0548	0.1712	0.2606	0.3238	0.3998	0.5688	0.7200	0.8230
		LR	0.0544	0.2086	0.3064	0.3568	0.3808	0.4106	0.4216	0.4206
	1	C_{CB}	0.0580	0.1446	0.1674	0.1790	0.1818	0.1668	0.1830	0.1806
		C_{AK}	0.0560	0.1082	0.1126	0.1114	0.1026	0.0892	0.0904	0.0852
		S	0.0504	0.1472	0.2118	0.3096	0.4884	0.6952	0.8102	0.8450
		LR	0.0542	0.1798	0.2544	0.3186	0.3296	0.3268	0.3520	0.3646
30	0.75	C_{CB}	0.0544	0.2572	0.3156	0.3478	0.3660	0.3924	0.3874	0.3908
		C_{AK}	0.0540	0.2106	0.2340	0.2444	0.2486	0.2512	0.2458	0.2468
		S	0.0572	0.2630	0.3674	0.4436	0.5438	0.6954	0.8442	0.9002
		LR	0.0546	0.2794	0.3960	0.4586	0.5018	0.5214	0.5318	0.5508
	1	C_{CB}	0.0460	0.2188	0.2960	0.3114	0.3256	0.3368	0.3276	0.3444
		C_{AK}	0.0480	0.1774	0.2110	0.2182	0.2234	0.2208	0.2060	0.2188
		S	0.0480	0.2100	0.3244	0.3974	0.6130	0.8144	0.8912	0.9372
		LR	0.0468	0.2250	0.3466	0.3770	0.4128	0.4324	0.4358	0.4556
60	0.75	C_{CB}	0.0496	0.4334	0.5624	0.6050	0.6364	0.6462	0.6662	0.6666
		C_{AK}	0.0484	0.3728	0.4676	0.5002	0.5050	0.4986	0.5294	0.5276
		S	0.0488	0.4110	0.5840	0.6508	0.7188	0.8412	0.9506	0.9604
		LR	0.0488	0.4360	0.6136	0.6762	0.7106	0.7352	0.7554	0.7698
	1	C_{CB}	0.0536	0.4106	0.5114	0.5454	0.5874	0.6102	0.6070	0.6204
		C_{AK}	0.0532	0.3582	0.4294	0.4512	0.4804	0.4940	0.4960	0.4924
		S	0.0514	0.3674	0.5096	0.5808	0.7774	0.9332	0.9606	0.9898
		LR	0.0504	0.3670	0.5218	0.5836	0.6310	0.6542	0.6596	0.6780

Real Data Examples

Notice that all the tests discussed above asymptotically follow chi-square distribution. However, the asymptotic distribution may be poor for small or moderate sample sizes; hence, p-values based on the asymptotic distribution may not always be reliable. Therefore, we obtain parametric bootstrap p-values for the following real data examples. The parametric bootstrap procedure is performed as follows.

Calculate the test statistic value T_0 from original data. Then generate a bootstrap sample according to the null hypothesis using the MLE and compute the test statistic T_0 with this bootstrap sample and call it T_0^*. Replicate this sampling a large number of times, say B times. Thus, the T_0^* values are $T_{01}^*, T_{02}^*, \ldots, T_{0B}^*$. The bootstrap p-value of T_0 is calculated as $p^* = \left\{ \#\left(T_{0i}^* > T_0\right) \right\} / B \quad (i = 1,2,\ldots,B)$. Reject the null hypothesis if the bootstrap p-value is smaller than nominal level of test. In the real data examples, we have considered the nominal level $\alpha = 0.05$ and the replication number $B = 100000$.

Example 1

In the first example, we have considered daily wind speed data analyzed by [26]. This data is presented in Table 3.

Table 3. Daily wind speed data

5.5	4.0	5.3	5.7	4.1	6.7	5.4	3.9	2.8	3.7	2.9	4.7	3.8	3.4	2.5
3.3	3.5	2.6	4.1	3.3	6.9	2.7	2.0	2.5	2.8	2.0	3.2	2.6	3.8	4.0

The MLEs of the parameters for the data are obtained as $\hat{m} = 2.516$ and $\hat{\Omega} = 15.973$ under the null hypothesis and $\tilde{s} = 0.134$, $\tilde{m} = 131.981$, $\tilde{\Omega} = 1.416$ under the alternative hypothesis. We calculate values of the tests statistics $LR = 2.436$ and $S = 2.072$ with parametric bootstrap p-values 0.040 and 0.116, respectively. Although the ND sufficiently fits the wind speed data according to the p-value of the S statistic, the GND provides a better fit than the ND according to p-the value of the LR statistic.

Example 2

As the second example, we have analyzed a real data of remission times (in months) of patients with bladder cancer [27]. The data is presented in Table 4.

Table 4. Remission times

0.08	2.09	3.48	4.87	6.94	8.66	13.11	23.63	0.20	2.23	3.52	4.98
6.97	9.02	13.29	0.40	2.26	3.57	5.06	7.09	9.22	13.80	25.74	0.50
2.46	3.64	5.09	7.26	9.47	14.24	25.82	0.51	2.54	3.70	5.17	7.28
9.74	14.76	6.31	0.81	2.62	3.82	5.32	7.32	10.06	14.77	32.15	2.64
3.88	5.32	7.39	10.34	14.83	34.26	0.90	2.69	4.18	5.34	7.59	10.66
15.96	36.66	1.05	2.69	4.23	5.41	7.62	10.75	16.62	43.01	1.19	2.75
4.26	5.41	7.63	17.12	46.12	1.26	2.83	4.33	5.49	7.66	11.25	17.14
79.05	1.35	2.87	5.62	7.87	11.64	17.36	1.40	3.02	4.34	5.71	7.93
11.79	18.10	1.46	4.40	5.85	8.26	11.98	19.13	1.76	3.25	4.50	6.25
8.37	12.02	2.02	3.31	4.51	6.54	8.53	12.03	20.28	2.02	3.36	6.76
12.07	21.73	2.07	3.36	6.93	8.65	12.63	22.69				

The MLEs of the parameters for the data are obtained as $\hat{m}=0.503$ and $\hat{\Omega}=193.327$ under the null hypothesis and $\tilde{s}=0.257$, $\tilde{m}=3.875$, $\tilde{\Omega}=2.804$ under the alternative hypothesis. We obtain values of the tests statistics $LR=42.485$ and $S=509.530$ with the bootstrap p-values 0.000 and 0.000, respectively. So, our conclusion is that the GND sufficiently fits the remission times data.

Conclusion

The Generalized Nakagami distribution is popular distribution in engineering, survival analysis, medical studies, and hydrology. The distribution contains the Nakagami distribution as a special case. When the reduced model may be adequate for the considered data, the Generalized Nakagami distribution may be a redundant and complex distribution.

Since it is important to decide whether reduced distribution is sufficient to describe data, four goodness of fit tests, namely, the $C(\alpha)$ tests C_{CB} and C_{AK}; score test S and likelihood ratio test LR are developed to test goodness of fit of the Nakagami distribution against the Generalized Nakagami distribution. These tests are then compared by a Monte Carlo simulation study for various sample size and parameter scenarios. Simulation study suggests that the LR and S tests provide better performance than the C_{CB} and C_{AK} tests. Although, the LR is the most powerful test and the S provides slightly lower power than the LR for small values of m and s, the score test S is the most powerful test for large values of m and s. So, our recommendation is to use the LR and S tests for small m and s values and the S test for large m and s values.

Conflicts of interest

There are no conflicts of interest in this work.

References

[1] Shankar P.M., Ultrasonic tissue characterization using a generalized Nakagami model, *IEEE Trans. Ultrason. Ferroelectr. Freq. Control*, 48 (6) (2001) 1716-1720.

[2] Stacy E.W., A generalization of the gamma distribution, *Ann. Math. Stat.*, 33 (3) (1962) 1187-1192.

[3] Nakagami M., The m-distribution: a general formulation of intensity distribution of rapid fading, Statistical Method in Radio Wave Propagation, W.C. Hoffman (ed.), Pergamon, (1960) 3–36.

[4] Ibnkahla M., Signal Processing for Mobile Communications, CRC Press, Washington, (2004).

[5] Nakahara H., Carcolé E., Maximum-likelihood method for estimating coda Q and the Nakagami-m parameter, *Bulletin of the Seismological Society of America*, 100 (6) (2010) 3174-3182.

[6] Sarkar S., Goel N.K., Mathur B.S., Adequacy of Nakagami-m distribution function to derive GIUH, *J. Hydrol. Eng.*, 14 (10) (2009) 1070-1079.

[7] Sarkar S., Goel N.K., Mathur B.S., Performance investigation of Nakagami-m distribution to derive flood hydrograph by genetic algorithm optimization approach, *J. Hydrol. Eng.,* 15 (8) (2010) 658-666.

[8] Datta P., Gupta A., Agrawal R., Statistical modeling of B-Mode clinical kidney images, Medical Imaging, m-Health and Emerging Communication Systems (MedCom), Greater Noida, (2014) 222-229.

[9] Alavi O., Mohammadi K., Mostafaeipour A., Evaluating the suitability of wind speed probability distribution models: A case of study of east and southeast parts of Iran, *Energy Convers. Manage.*, 119 (2016) 101-108.

[10] Ahmad K., Ahmad S.P., Ahmed A., Classical and Bayesian approach in estimation of scale parameter of Nakagami distribution, *J. Probab. Stat.*, (2016) 2016.

[11] Ramos P.L., Louzada F., Ramos E., An Efficient, Closed-Form MAP Estimator for Nakagami-m Fading Parameter, *IEEE Commun. Lett.,* 20 (11) (2016) 2328-2331.

[12] Ramos P.L., Louzada, F., Ramos, E., Posterior Properties of the Nakagami-m Distribution Using Noninformative Priors and Applications in Reliability, *IEEE Trans. Reliab.*, 67 (1) (2017) 105-117.

[13] Kumar K., Garg, R., Krishna, H., Nakagami distribution as a reliability model under progressive censoring, *Int. J. Syst. Assur. Eng. Manag.*, 8 (1) (2017) 109-122.

[14] Ozonur D., Akdur, H.T.K., Bayrak, H., Optimal Asymptotic T ests for Nakagami Distribution, *SDU J. Nat. Appl. Sci.*, 22 (2 018) 487-492.

[15] Ozonur D., Paul, S., Goodness of fit tests of the two-parameter gamma distribution against the three-parameter generalized gamma distribution, *Commun. Stat.-Simul. Comput.*, 51 (3) (2022) 687-697.

[16] Rayner, J.C., Thas, O., Best, D.J., Smooth tests of goodness of fit: using R. John Wiley & Sons, Singapore, (2009).

[17] Bera A.K., Bilias Y., Rao's score, Neyman's C (α) and Silvey's LM tests: an essay on historical developments and some new results, *J. Stat. Plann. Inference*, 97 (1) (2001) 9-44.

[18] Balakrishnan N., Kannan N., Nagaraja H.N., Advances in ranking and selection, multiple comparisons, and reliability: methodology and applications, Birkhauser, Boston, (2005).
[19] Rao C.R., Large sample tests of statistical hypotheses concerning several parameters with application to problems of estimation, *Proceedings of Cambridge Philosophical Society,* 44 (1948) 50-57.
[20] Neyman J., Optimal asymptotic tests of composite statistical hypotheses, Probability and statistics, Wiley, New York (1959).
[21] Bartlett M.S., Approximate confidence intervals, *Biometrika*, 40 (1/2) (1953) 12-19.
[22] Abdi A., Kaveh M., Performance comparison of three different estimators for the Nakagami m parameter using Monte Carlo simulation, *IEEE Commun. Lett.*, 4 (4) (2000) 119-121.
[23] Cheng J., Beaulieu N.C., Generalized moment estimators for the Nakagami fading parameter, *IEEE Commun. Lett.*, 6 (4) (2002) 144-146.
[24] Moran P.A., On asymptotically optimal tests of composite hypotheses, *Biometrika,* 57 (1) (1970) 47-55.
[25] Cox D.R., Hinkley D.V., Theoretical Statistics, Chapman & Hall, London, (1974).
[26] Tilbi D., Seddik-Ameur N., Chi-squared goodness-of-fit tests for the generalized Rayleigh distribution, *J. Stat. Theory Pract.,* 11 (4) (2017) 594-603.
[27] Lee E.T., Wang J., Statistical methods for survival data analysis, Vol. 476, John Wiley & Sons, (2003).

AUTHOR GUIDELINES

Thank you for choosing to submit your paper to Cumhuriyet Science Journal. The following instructions will ensure we have everything required so your paper can move through pre-evaluating, peer review, production and publication smoothly. Please take the time to read and follow them as closely as possible, as doing so will ensure your paper matches the journal's requirements.

Submission

Cumhuriyet Science Journal is an international, peer-reviewed, free of charge journal covering the full scope of both natural and engineering sciences. Manuscripts should be submitted by one of the authors of the manuscript as online submission after registration to the Cumhuriyet Sciences Journal. Microsoft Word (.doc, .docx, .rtf), files can be submitted. There is no page limit. If there is a problem while uploading the files of manuscript, please try to reduce their file size, especially manuscripts including embedded figures. Submissions by anyone other than one of the authors will not be accepted. The submitting author takes responsibility for the paper during submission and peer review. If for some technical reason submission through the online submission systme is not possible, the author can contact csj@cumhuriyet.edu.tr for support.

Submission or processing charges

Cumhuriyet Science Journal does not charge any article submission, processing charges, and printing charge from the authors.

Terms of Submission

Papers must be submitted on the understanding that they have not been published elsewhere (except in the form of an abstract or as part of a published lecture, review, or thesis) and are not currently under consideration by another journal. The submitting author is responsible for ensuring that the article's publication has been approved by all the other coauthors. It is also the authors' responsibility to ensure that the articles emanating from a particular institution are submitted with the approval of the necessary institution. Only an acknowledgment from the editorial office officially establishes the date of receipt. Further correspondence and proofs will be sent to the author(s) before publication unless otherwise indicated. It is a condition of submission of a paper that the corresponding author permit editing of the paper for readability. All enquiries concerning the publication of accepted papers should be addressed to csj@cumhuriyet.edu.tr. Please note that Cumhuriyet Science Journal uses iThenticate software to screen papers for unoriginal material. By submitting your paper to Cumhuriyet Science Journal are agreeing to any necessary originality checks your paper may have to undergo during the peer review and production processes. Upon receiving a new manuscript, the Editorial office conducts initial pre-refereeing checks to ensure the article is legible, complete, correctly formatted, original, within the scope of the journal in question, in the style of a scientific article and written in clear English. Any article that has problems with any of the journal criteria may be rejected at this stage.

Peer Review

This journal operates a single blind review process. All contributions will be initially assessed by the editor for suitability for the journal. Papers deemed suitable are then typically sent to a minimum of two independent expert reviewer to assess the scientific quality of the paper. The author is required to upload the revised article to the system within 15 days by making the corrections suggested by the referee. The article will be rejected if there are no fixes in it. The Editor is responsible for the final decision regarding acceptance or rejection of articles. The Editor's decision is final

Title and Authorship Information

The following information should be included

Paper title

Full author names

Full institutional mailing addresses

Corresponding address

Email address

Abstract

The manuscript should contain an abstract. The researchers who are native speakers of Turkish have to add Turkish title and abstract as well. The abstract should be self-contained and citation-free and should be 250-300 words.

Keywords

Keywords of the scientific articles should be selected from the web address of www.bilimadresleri.com

Introduction

This section should be succinct, with no subheadings.

Materials and Methods

This part should contain sufficient detail so that all procedures can be repeated. It can be divided into subsections if required.

Conflicts of interest

Sample sentence if there is no conflict of interest: The authors stated that did not have conflict of interests.

Acknowledgements

Sample sentences for acknowledgements: The work was supported by grants from CUBAP (T-11111). We would like to acknowledge Prof. Mehmet Sözer, MD, for his precious technical and editorial assistance. We would like to thank

References

References to cited literature should be identified by number in the text in square brackets and grouped at the end of the paper in numerical order of appearance. Each reference must be cited in the text. Always give inclusive page numbers for references to journal articles and a page range or chapter number for books. References should be styled and punctuated according to the following examples

[1] Karaca E., Ulusoy S., Morgül Ü., Ulusoy H.I., Development of Analytical Method for Sensitive Determination of Streptozotocin based on Solid Phase Extraction, Cumhuriyet Sci. J., 41 (4) (2020) 826-831. (sample reference for journals)

[2] Keskin B., Ozkan A.S., Inverse Spectral Problems for Dirac Operator with Eigenvalue Dependent Boundary and Jump Conditions, Acta Math. Hungar., 130 (2011) 150-159(sample reference for journals)

[3] Mazur M.T., Kurman R.J., Dysfunctional Uterine Bleeding. In: Mazur M.T., Kurman R.J., (Eds). Diagnosis of endometrial biopsies and curettings, A practical approach. 2nd ed. Berlin: Springer, (2005) 100-120. (sample reference for book chapters)

[4] Mazur M.T., Kurman R.J.,Diagnosis of endometrial biopsies and curettings, A practical approach. 2nd ed. Berlin, (2005) 100-120. (sample reference for book)

[5] National Cancer Institute, Surveillance Epidemiology and End Results. Cancer of the Corpus and Uterus, NOS. Available at: http://seer.cancer.gov/statfacts/html/corp.html?statfacts_page=corp. Retrieved March 2, 2008. (sample reference for websites)

[6] Surname N., Title of thesis, PD or master thesis, Name of university, name of institue, year. (sample reference for thesis)

[7] Surname N., Title of fulltext conference paper, name of conference, city, year, pages. (sample reference for Abstratcs in conferences are not accepted as a valid reference except full text)

Preparation of Figures

Each figure can be integrated in the paper body or separately uploaded and should be cited in a consecutive order. Figure widths can be 4-6 inch as 300 dpi. The labels of the figures should be clear and informative. The name and the subtitles of the figures must be 9-point font.

Preparation of Tables

Tables should be cited consecutively in the text. Every table must have a descriptive title and if numerical measurements are given, the units should be included in the column heading. Tables should be simple with simple borders and text written as left text. The name and the subtitle of the tables must be 9-point font

Proofs

Corrected proofs must be returned to the publisher within 2 weeks of receipt. The publisher will do everything possible to ensure prompt publication. It will therefore be appreciated if the manuscripts and figures conform from the outset to the style of the journal.

Copyright

Ethical Guidelines

New methods and ethically relevant aspects must be described in detail, bearing in mind the following:

Human Experiments. All work must be conducted in accordance with the Declaration of Helsinki (1964). Papers describing experimental work on human subjects who carry a risk of harm must include:

A statement that the experiment was conducted with the understanding and the consent of the human subject.

A statement that the responsible Ethical Committee has approved the experiments.

Animal Experiments. Papers describing experiments on living animals should provide:

A full description of any anaesthetic and surgical procedure used.

Evidence that all possible steps were taken to avoid animal suffering at each stage of the experiment. Papers describing experiments on isolated tissues must indicate precisely how the donor tissues were obtained.

Submission Preparation Checklist

As part of the submission process, authors are required to check off their submission's compliance with all of the following items, and submissions may be rejected that do not adhere to these guidelines.

The submission has not been previously published, nor is it before another journal for consideration (or an explanation has been provided in Comments to the Editor).

The submission file is in Microsoft Word document file (Times New Roman) format.

Where available, URLs for the references have been provided.

The text is single-spaced; uses a 11-point font; employs italics, rather than underlining (except with URL addresses); and all illustrations, figures, and tables are placed within the text at the appropriate points, rather than at the end.

The text adheres to the stylistic and bibliographic requirements outlined in the Author Guidelines, which is found in About the Journal.

If submitting to a peer-reviewed section of the journal, the instructions in Ensuring a Double-Blind Review have been followed.